NUMERICAL STUDY OF HYDROFOILS FOR WATER TURBINES

A Thesis

by

RICHARDS CHIZHUTHANICKEL SUNNY

Submitted to the Office of Graduate and Professional Studies of
Texas A&M University
in partial fulfillment of the requirement for the degree of

MASTER OF SCIENCE

Chair of Committee,	Hamn-Ching Chen
Committee Members,	Richard Mercier
	Zhizhang Xie
Head of Department,	Sharath Girimaji

August 2016

Major Subject: Ocean Engineering

ABSTRACT

The major objective of this research was to suggest a water turbine design with higher power efficiency by conducting a parametric study of hydrofoil shapes, modified hydrofoil shapes with circular void, tip speed ratio, pitch angle and solidity. The other objectives of this research included answering the question of whether the efficiency of a chosen Gorlov turbine design can be increased by including circular void in the hydrofoil sections and studying the variation in lift and drag forces on hydrofoil sections with different circular voids in a steady state. The design was intended for a specific case of Gulf Stream ocean currents. Research was carried out using a series of 75 computational fluid dynamic (CFD) 2D simulations which consists of 67 rotating turbine simulations (RTS) and 8 steady state simulations (SSS) using the commercial CFD software, STAR-CCM+. Through this research, the power efficiency of the base case turbine was improved from 31.5%. to 49.92% according to the simulation results. Results of this research showed that it is possible to increase the power efficiency of the turbine using the modified hydrofoils with voids.

To my Lord Jesus, To mother Mary, To my parents , To my brother , To my grandmother,

To all my friends and To all my teachers.

ACKNOWLEDGMENTS

I would like to express my deepest appreciation to my committee chair, Dr. H C Chen and to my committee members, Dr. Richard Mercier, Dr. Zhizhang Xie for their guidance and support through the course of this research. I would also like to thank Dr. Dean Baskin for serving as a committee member for my thesis defense. I thank my dear parents, my brother and my friends for their love, prayers and support. I specially thank Mrs. Maya Varyani and IIT Madras Alumni Association for the Dr. K S Varyani Memorial Award which funded my entire Master's program. I thank Texas A&M University for the opportunity to be part of this great campus. I thank my friends Alwin, Jobin, Johnson, Manu and Naveen for their support during difficult times. Also I extend my gratitude to the supercomputer center, Texas A&M University and above all, I thank God for all his blessings and love which made all of this possible.

NOMENCLATURE

NOAA	National Oceanic and Atmospheric Administration
GoMRI	Gulf of Mexico Research Initiative
GW	Gigawatt
MW	Megawatt
HYCOM	Hybrid Coordinate Ocean Model
MCT	Marine Current Turbines
TGL	Tidal Generation Limited
P_a	Available Power
ρ	Density
P_p	Produced Power
A	Area
V	Flow Velocity
T	Torque
ω	Rotational Velocity
η	Efficiency
σ	Solidity
ϕ	Helical Angle
C	Chord Length

n	Number of Blades
h	Height
d	Diameter
Re	Reynolds' Number
TSR	Tip Speed Ratio
λ	Tip Speed Ratio
β	Pitch Angle
H	Hydrofoil Shape
$NACA$	National Advisory Committee for Aeronautics
P	Pressure
R	Radius of Turbine
μ	Viscosity of Water
U	Free Stream Velocity
C_p	Power Coefficient
L	Lift Force
D	Drag Force
F_n	Froude Number
CFD	Computational Fluid Dynamics
CAD	Computer Aided Design
$R.O.$	Regional Oceanography

TABLE OF CONTENTS

LIST OF FIGURES

LIST OF TABLES

1 INTRODUCTION

The major objective of this research was to suggest a water turbine design with higher power efficiency, by modifying the turbine blade hydrofoil cross sections, for extracting renewable energy from Gulf Stream ocean currents. The other main objective includes answering the question whether an inclusion of a void in the hydrofoil can increase its efficiency.

1.1 Background

When we look into the future it is not possible, not to stop at the possibility of energy crisis. Renewable energy resources are one of the solutions to solve the energy crisis [5]. Researches says that in the past 30 years, energy usage has been increased by 200% [6]. Some scientific predictions say fossil fuels would be exhausted in a century [7]. In this scenario, from ocean perspective, renewable energy consists of energy from waves, tides and ocean currents. For this research water turbine for extracting ocean current energy is given the focus.

Ocean currents are formed from effects of temperature, wind, salinity, bathymetry, and the rotation of the earth. Ocean currents are the continuous flow of water in ocean in specific directions and it may differ very much depending on the causes mentioned. Driving forces for ocean currents include importantly Sun which causes winds and temperature differences. Ocean currents have steady speed which are good for deploying

energy extraction devices. Gulf stream currents are rich in kinetic energy as the flow velocity can reach up to 2.5m/s and density of water is 1000 kg/m^3. Major fast ocean currents are surface currents and they are driven mainly by shear stress due to wind and generates anti clockwise loops in southern hemisphere and in northern hemisphere, clockwise loops Fig. 1.1.

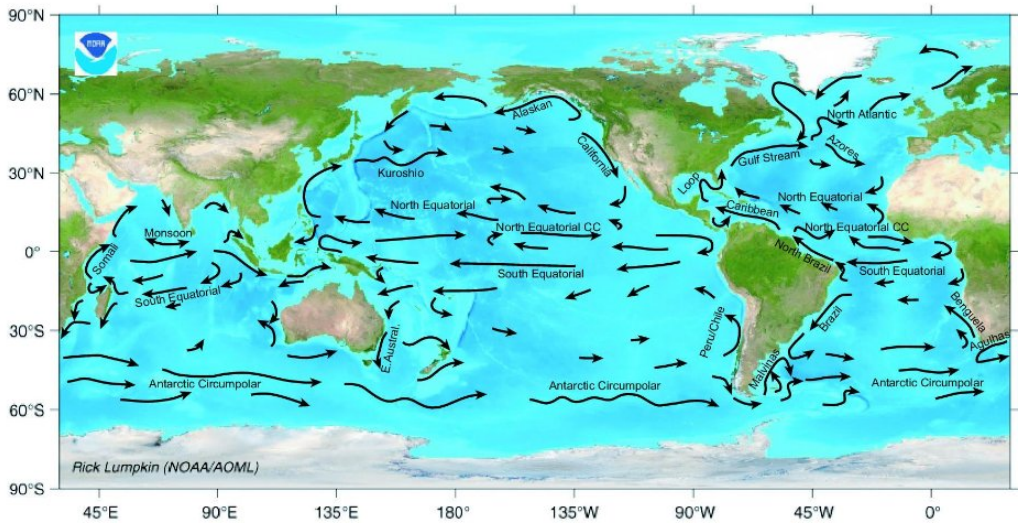

Figure 1.1: Major Ocean Surface Currents (Source NOAA)

Gulf Stream currents is a classic case of currents made by wind in northern hemisphere. Due to Coriolis Effect, these currents gets stronger near the western boundary of Atlantic region [8]. It is an ocean current which have been studied the most. Gulf Stream has a width of 90 *km* and depth of 1000 *m* on an average. The average speed of current as fast as 2m/s near the surface [9] to [10] and slowly decrease by depth. Gulf Stream velocity profile in depth could be seen from Fig. 1.2 and Fig. 1.3.

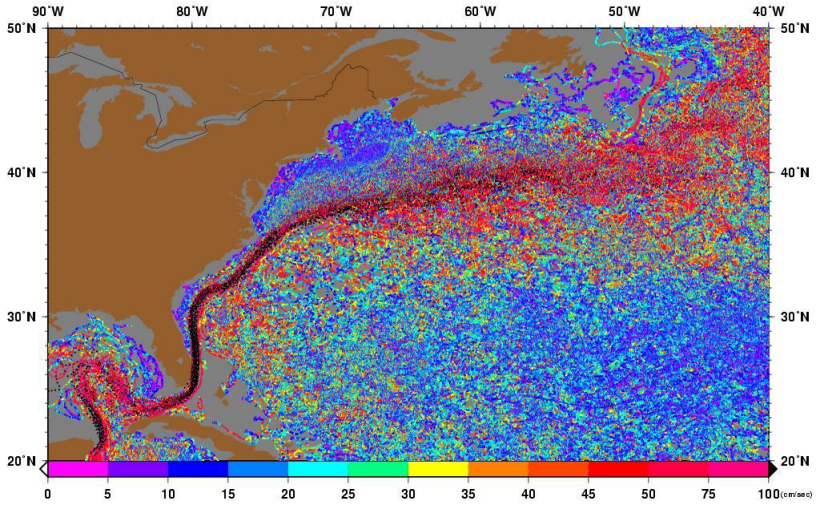

Figure 1.2: Gulf Stream Velocity Profile (Source: GoMRI)

Numerous estimations of power potential from ocean current energy in Gulf Stream have been carried out in past. An estimation of power that could be extracted is given by Lissaman and Radkey in their research paper "Coriolis Program: A Review of the status of the ocean turbine energy system" in 1970s which estimates about 83 MW energy from one turbine and around 10 GW from 120 such turbines [11]. According to US Department of the Interior, 0.1% of total energy available from Gulf Stream is sufficient for 35% of electrical needs in Florida [12]. A different assessment by Von Arx, Stewart, and Apel [13] shows about 1 GW power from Gulf Stream currents. This is achieved through water turbines in arrays. A recent research by Duerr and Dhanak [14] asses about 20-25GW from ocean currents in Florida. This research used Hybrid Coordinate Ocean Model(HYCOM) data for analysis. But with the help of implied ocean circulation model and considering collective effect from power extraction, the limit of power from Florida current portion was predicted around 5 GW by Yang et al. [15] for an average current condition.

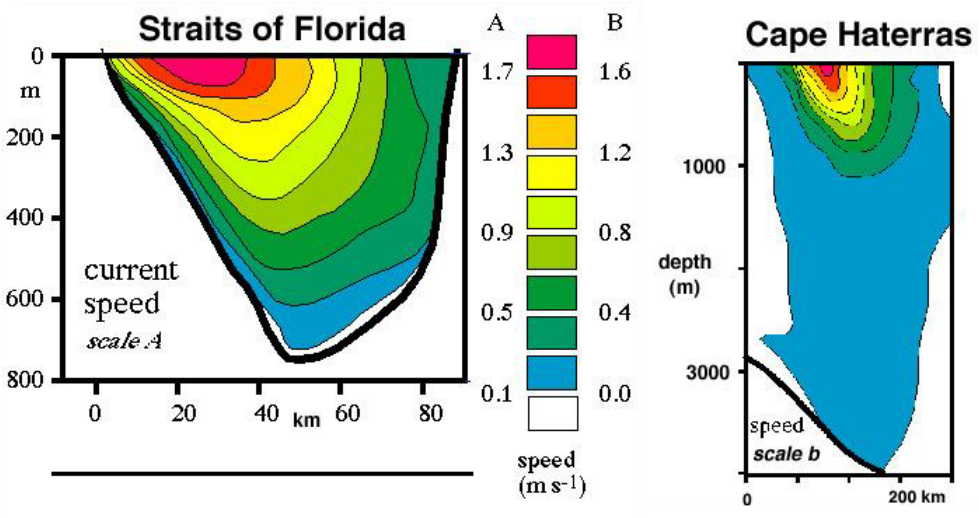

Figure 1.3: Gulf Stream Depth Velocity (Source: R.O. an Introduction)

1.2 Water Turbines

A water turbine is a rotating machine which can extract hydro energy, which is the sum of potential and kinetic energy of water, into mechanical work. Hydro energy available per unit area is higher than the wind energy due to thousand times higher density of water than that of air. It was in the 19th century that these turbines were proven and they were used to produce power for industrial purposes. Even though the high head hydraulic turbines have been used efficiently and widely since then, it is not the case with low head flows such as ocean currents and river currents. Since many decades' scientists have been working unsuccessfully on manipulating higher pressure head turbines to work efficiently in lower pressure head applications [16].For ultra-low head or free stream hydroelectric stations, water turbines in high pressure heads are expensive [16]. Among the low head water turbines, lift- based turbines have the better efficiency compared to drag-based turbines

[17]. Depending on the flow direction, there are two classes of turbo machines, axial and radial. When fluid flows in the direction of shaft, as in the case of propellers it is called axial and when fluid is coming perpendicular to shaft or rotating axis, it is called radial turbo machines. The turbines which can use both the radial and axial flow of fluid are called cross flow turbines. Studies shows that there are more than sixty kinds of hydro turbine designs are in development [18]. Majority of those use the lift based forces. All the lift based turbines are mainly recognized by the type of blade cross section which is used. Depending on this cross section shape these turbines can work at various flow speed. Compared to the drag based turbine, lift based turbine is more efficient in case of low head or free flow. Only a very less number of free flow commercial power plants exists. The famous one is the dual axial turbines by Siemens [19], [20] which are called MCT or Marine Current Turbines. Recently a famous one, the 1.2MW SeaGen with double rotors was constructed in Strangford, Northern Ireland for tidal energy. Other notable ones areHammerfest and TGL (Tidal Generation Limited). The former is by Andritz which is in Eday Island and latter one is situated in Orkney. The largest free flow power plant till now is the Uldolmok Tidal Power Plant [21], [22], [23]. Vertical helical blade turbines are used to generate 2.4 GWh electricity annually. Mean flow speed at the location is about 2.4m/s. Considering the success of this power plant with vertical axis helical turbine (Gorlov Turbine), the same is used for this research. Also Alexander Gorlov, the inventor of this turbine has suggested the possibility and feasibility of large-scale floating power farm using the Gorlov turbines [16] in Gulf Stream. The major reasons for choosing vertical turbines are also due to its

low construction cost, possibility of designing smaller since torque required to start is low, and non-necessity of altering yaw angle according to the varying flow direction. Also considering the environmental effects such as safety of fishes, vertical axis turbine is claimed to be better [24]. The major issue with vertical axis turbine when it was first designed by Darrieus in 1931 was its possibility of mechanical fatigue due to the periodically varying force and torque with rotating azimuthal angle. Two major turbine design modification for overcoming this was suggested by Kobold [25] and Gorlov [26], [27], [28]. While Kobold designed passive varying blades for reducing the change of angle of attack, Gorlov used helical blades.

1.3 Gorlov and Darrieus Helical Turbine

Gorlov turbine Fig. 1.4 was designed in 1990s by Alexander Gorlov in order to improve the Darrieus turbine Fig. 1.5. These two have unidirectional rotation in every flow direction. Both of these designs uses lift based force for hydro energy extraction. Due to this mechanism, these turbines can achieve a rotational velocity which is greater than the free stream velocity itself.

The available power(P_a) of a flowing fluid across an area of A is given by

$$P_a = \frac{1}{2}\rho A V^3$$

where ρ is the density of fluid and V is the velocity. The energy produced by the turbine

Figure 1.4: Gorlov Turbine

P_p is given by

$$P_p = T\omega$$

where T is the moment or torque produced by the fluid while turbine is rotating at a speed of ω. The efficiency (η) is given by

$$\eta = \frac{1}{2}\frac{T\omega}{\rho A V^3}$$

ratio of produced power by available power. The research on hydrodynamics of Gorolv and Darrieus turbine is very less. But there are dependable experimental results. One of them is the work done by Shiono, Suzuki and Kiho [1], comparing Gorlov and Darrieus turbine. Their studies show that when we try to eliminate the periodic effect by making the blades of turbine helical, the efficiency of the turbine reduces. Thus Darrieus turbine efficiency is the limiting case of Gorlov turbine efficiency for the same parameters. But from a practical scenario, the reduction of efficiency up to certain limit is admissible if we can produce a steady moment as Gorlov do. And when inventor claims an efficiency of 35% [16] for varying current speed it sounds good. In order to do the comparative study,

Figure 1.5: Darrieus Turbine

they [29] have considered two non-dimensional parameters mainly. solidity (σ) and helical angle (ϕ), where σ is ratio of length occupied by foil section to the perimeter of circle in rotating plane.

$$\sigma = \frac{nC}{\pi d}$$

where n is the number of blades, d is the diameter and C is the chord length. ϕ is defined as the helical angle which could be found out by

$$\sigma = \frac{nC}{\pi d}$$

$$\phi = \tan^{-1} \frac{nh}{\pi d}$$

where h is the height. So one of the area of interest is the solving the issue of reduction in efficiency as ϕ gets smaller. The Fig. 1.6 shows the efficiency of particular Gorlov turbine with chord of foils $C = 0.125m$, $n = 3$, $\sigma = 0.4$ inlet velocity $V = 1.2m/s$. Reynolds

number of $Re = 0.1510^6$. The results show a maximum efficiency of Darrieus turbine is about 34% ($\phi = 90°$) and that of Gorlov turbine with $\phi = 60°$) is around 22% both occurring at a TSR $\lambda = 1.3 - 1.4$. According to the results as the ϕ value increases efficiency also increases for Gorlov turbine. So the optimum ϕ of Gorlov turbine will be defined by the maximum height possible without effecting the rigidity of the blade which is a function of blade material properties and foil cross section. An efficiency of 39% was reported by a research carried out by Verdant Power LLC and GCK Technology Inc. in 2005 for $\phi = 67°$ but the chord length and velocity were different. According to Gorlov [16] efficiency is 35% for the design with three blades, 0.6096m diameter and 0.8636m height ($\phi = 53.6°$) for a flow velocity of $1.524 m/s$. The other resource to study for the Uldolmok channel, "Evaluation of Helical Turbine Efficiency for Tidal Current Power Plant Based on In-Situ Experiment [29].

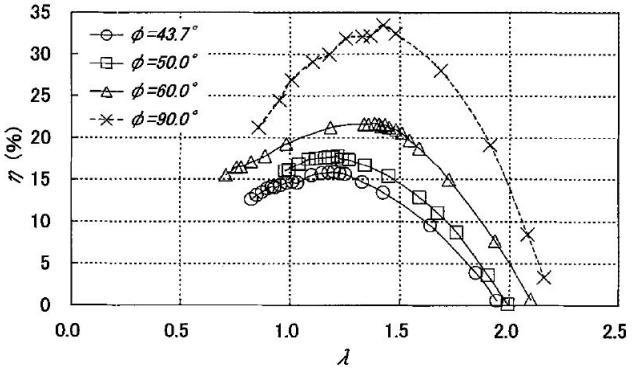

Figure 1.6: Gorlov Turbine Efficiency [1]

Gorlov turbine of diameter 2.2 m and height 2.5 m was rotated for different TSR

and current velocity and its torques was measured. The research paper states that the efficiency of 35% is feasible even though the maximum efficiency by their results shows 30%. Coming to the starting performance, Gorlov turbine stands much ahead of Darrieus turbine. At every rotation angle with respective to inlet, Gorlov turbine produces the same torque. But in case of Darrieus turbine, if it is positioned at the least torque position, it is difficult to start. This is a very important factor considering a large scale power plant with many small turbines in gulf stream. So ability to start by itself at low water velocities has given much importance in considering Gorlov turbine for the project. The change from periodic change of moment to a steady moment is a significant quality of Gorlov turbine over Darrieus turbine which have periodic fluctuation with a time interval of $\frac{T}{n}$, where T is the time for one rotation and n is the number of blades. This is possible due to the continuous helical blade structure, each blade covering $\frac{2\pi}{n}$. This effect reduces significantly the fatigue stress, vibration and power reduction due to the variation. These are very important factors in practical scenario since it can severely effect the cost efficiency of system over many years. The tip speed ratio λ of Gorlov turbine ranges for maximum efficiency is found to be between 0.9 to 2.5 [1]. This result is used to estimate the maximum efficient rotational velocity ω of the turbine in this project. A Gorlov turbine design and operation could be defined geometrically using five parameters, such as diameter (D), height (h), number of blades (n), chord length (C), hydrofoil cross section shape (H), flow velocity (v), tip speed ratio (TSR) and pitch angle (β). The non-dimensional parameters helical angle (ϕ) and solidity (σ) can be found out using above parameters. For this project the

focus is given on studying the variation in power efficiency with parameters, hydrofoil cross section shape (H), tip speed ratio (TSR), pitch angle (β) solidity (σ). The velocity is made constant ($v = 2m/s$). The base design parameters value was chosen as same as that of the initial design suggested for gulf stream by Gorlov [16] which are hydrofoil shape $H = NACA0020$, diameter $D = 0.6096m(24')$, height $h = 0.8696m(34'')$ and chord length $C = 0.1178m(7'')$ and tip speed ratio $TSR = 0.958$

1.4 Hydrofoil Cross Sections

Darrieus and Gorlov turbine are lift based turbines and the hydrofoil shape and is one of the main determining factor for efficiency. A study of 14 different hydrofoil cross section shapes and 14 cases of modification with void in shape of circle on one hydrofoil section (NACA0020) has been carried out for this research in order to find the best hydrofoil section with best modification for increasing the efficiency. All the fourteen cases of hydrofoil sections were taken from NACA 4 digit airfoils. National Advisory Committee for Aeronautics(NACA) was founded to make better flight wings and study their dynamics. NACA presented report no.460 in 1933 titled "The Characteristics of 78 Related Airfoil Sections from Tests in the Variable-Density Wind Tunnel". It includes data of 78 airfoil shapes NACA tested in their wind tunnels. This report is the basis for four digit NACA foils. The four digits in series define the shape of the foil. The first digit 'm' says the percentage value of maximum camber compared to chord length. Second digit gives the position on the chord of the maximum camber in tenths of the chord and

is represented with the letter 'p'. The final two digits 't' denotes the maximum thickness of the airfoil in percentage of the chord length. This could be seen from Fig. 1.7. NACA four digit airfoils could be generated using just these four digits and few mathematical equations. Due to this reason they are very easy to create. For this research since the chord length is constant 0.1778m all foils are scaled by a factor of 0.1778. Fourteen different NACA foils have been used for this research. NACA design has inspiration from Clark Y and Göttingen 398 airfoils which were the best designs in 1930's.

Last Name	First Name	Lab 7 assignme
Meserole	Tyler	--
Boykin	Tyler	--
Swinnea	James	0.00
Rhodes	Rowdee	0.00
Whitfield	Conner	0.00

Figure 1.7: NACA 4 Digit Airfoil

1.4.1 NACA Hydrofoils With Voids

During the course of theoretical approach to utilize the vortex induced forces, this was a thought to introduce a possibility of vortex in a hydrofoil, which can create an extra Kutta lift. During literature survey on this idea, it was found that in airfoils this technique has already been used. Lift enhancement possibility by introducing vortices has been shown by Vernon [30] and Chernyshenko [31]. On further research understood that idea of trapped vortices has mentioned as early as 1960s by Ringleb [32] and by Adkins [33] after that. The very recent studies done in regards of project VortexCell2050 was also

proving this technique. But Iollo and Zannetti [34] showed that a trapped vortex can have a limited stability region. Even though this is successful in air it is a matter of question about its behavior in water due to the high viscosity and density of water. So as part of choosing the best hydrofoil design for the Gorlov turbine, the idea was to carry out few non rotating simulations with voids of different size and position and try the best void among them into the best hydrofoil from rotating simulations. The basic hydrofoil which was used is NACA0020. As a part of this 14 different cases of hydrofoils with voids were tested at eight different angle of attacks. And their variations were studied. This is a new attempt to use foils with cavity for a water turbine. The hydrofoil shape (H) with modifications of voids is denoted by (HM) in this thesis. An example for HM could be seen in Fig. 1.8.

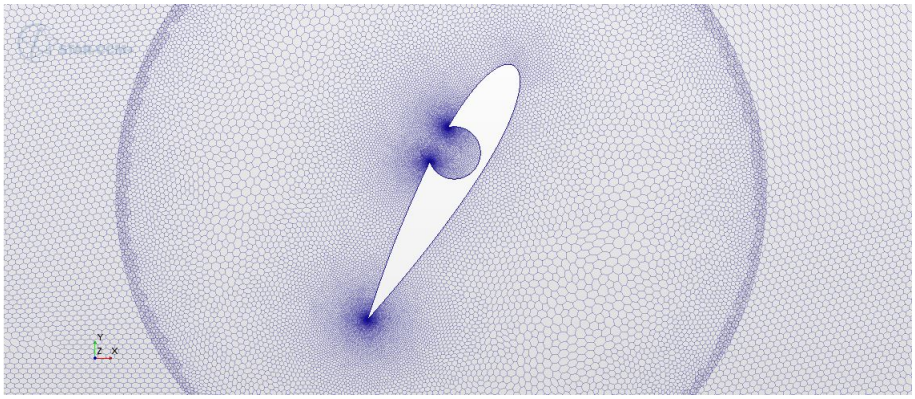

Figure 1.8: Modified NACA Airfoil Section With Circular Void

1.5 Hydrodynamics

Well defined theoretical analysis methods for behavior of water turbine like wind turbines has not been developed. The major available techniques are aerodynamics of wind turbine and hydrodynamics of marine propellers [35]. The basic equations applicable for a turbine with any fluid is the Bernoulli's equation for incompressible flow which basically shows the energy balance Eqn. 1.1 at any point in a stream line. In the equation v is the flow velocity at a point on a stream line, z is the height of the point, g is the acceleration due to gravity, with the positive z-direction pointing upward, p is the pressure, and ρ represents the density of the fluid.

$$\frac{v^2}{2} + gz + \frac{P}{\rho} = constant \tag{1.1}$$

The maximum possible efficiency of a horizontal axis turbine estimated by Betz law is called Betz limit which statess that, independent of the design of a wind turbine in open flow, no turbine can capture more than 16/27 (59.3%) of the kinetic energy in wind. The factor is called as Betz coefficient. Commercial wind turbines usually achieve around 75% to 80% of this limit. This limit is derived by applying the law of mass conservation and Bernoulli equation assuming fluid to be incompressible. But this limit is not applicable to vertical axis turbines. Turbines are normally designed for a constant speed of rotation and it could be varied by the turbine controller. The non-dimensional parameter which represent the rotational speed is called tip speed ratio (TSR) or λ which is the ratio of maximum radius R times rotational speed ω to current velocity V.

$$\lambda = \frac{R\omega}{V}$$

The non-dimensional number which represent the viscous nature is the Reynolds' number Re.

$$Re = \frac{\rho V L}{\mu}$$

where ρ is density of water V is the current velocity, L is the characteristic length and μ is the viscosity of water This number defines whether the flow is laminar, transient or turbulent. This is very important since the physics model for solving the Navier Stokes equation is depending mostly on Reynolds number. The power produced (P_p) of turbine could be found out by the equation Eqn. 1.2

$$P_p = \frac{1}{2} A V (V^2 - U^2) \tag{1.2}$$

where U is the velocity upstream and V is the velocity downstream of turbine and A is the sweep area. Power coefficient C_p shows the performance of the turbine. It is the ratio of produced power to the available power (P_a) which is given by Eqn. 1.3

$$P_a = \frac{1}{2} \rho A U^3 \tag{1.3}$$

where ρ is density of fluid U is the current velocity and A is the sweep area of turbine. From hydrodynamics point of view, the case of vertical axis turbine is more complex than that of horizontal axis turbine mainly because they have axis of rotation perpendicular to the water flow. The high angle of attack during the rotation and the non-uniform flow with vortices on one side of rotating blades makes problem difficult. The forces on the hydrofoils section during rotation can be seen from Fig. 1.9. The parameters which the hydrodynamics of a hydrofoil depends are the relative velocity V_r, angle of attack α,

rotational angle θ, axial force F, Lift force L, Drag Force D, tangential force and the tangential velocity. The Fig. 1.10 shows the schematic representation of this quantities. According to Consul [36], the performance of Gorlov and Darrieus turbine is depended on six non dimensional groups which are Reynolds number (Re), tip speed ratio (λ), Froude number (Fn), blockage ratio, solidity (σ) and the number of blades (n). As the tip speed ratio increases the maximum angle of attack reduces which is favorable, as the tip speed ratio increases which is directly proportional to the rotational speed, the effect of free flow velocity in relative speed reduces and angle of attack approaches the pitch angle. The negative maximum angle of attack is smaller than that of positive maximum in magnitude due to the flow velocity. When angle of attack of hydrofoil rises above certain value, the fluid flow will separate and creates wake region. With the increase in angle of attack this separation point moves from trailing edge to the leading edge. This state is called deep stalling. In this phenomenon is not favorable since during this state the lift to drag ratio is relatively small. The radius of the nose of hydrofoil and the Reynolds number determines at which angle deep stalling occurs. Another important phenomenon is called the dynamic stalling when the angle of incidence changes fast. Due to this, a hysteresis happens in lift and drag, between the increasing and decreasing angle of incidence. A disturbance similar to vortices is shed and move over the low pressure region due to this phenomenon. This phenomenon is important in case of Gorlov and Darrieus turbine since they are susceptible to it mainly at low rotational rate. The non-uniform inflow with wakes to the blades in downstream is the result of dynamic stall. The first relevant visualization research on

this topic has been carried out by Brochier et al. [37] on a Darrieus wind turbine with NACA0018 foil at a Reynolds number of 10,000 and tip speed ratio varying from one to eight. LDV and hydrogen bubbles were used for visualization. According to him leading edge first vortex is formed and it combines with the second vortex which is formed at the trailing edge forming doublet of two counter rotating vortices which travels down to meet the blade in downstream. This observation is confirmed by the research done by Fujisawa and Shibuya [4] Fig. 1.11

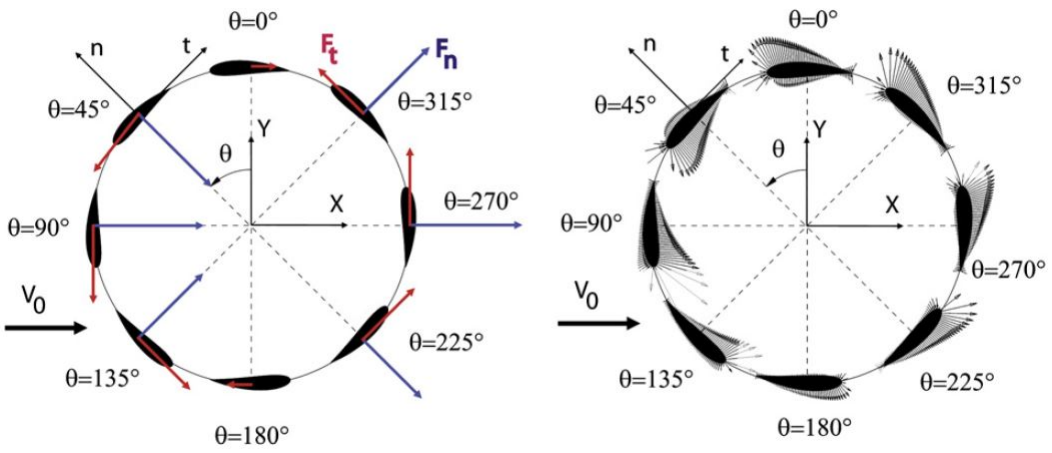

Figure 1.9: Forces on Darrieus Turbine [2]

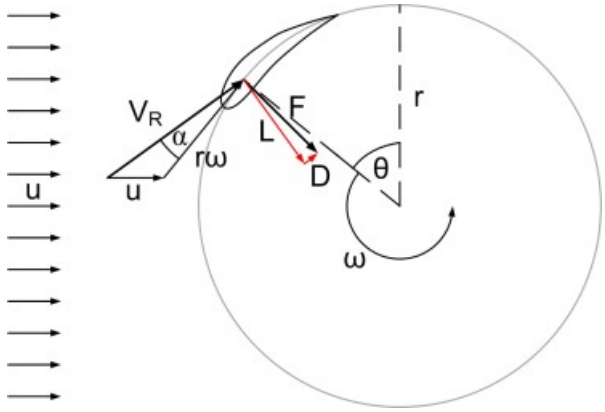

Figure 1.10: Basic Flow Mechanics of Darrieus Turbine [3]

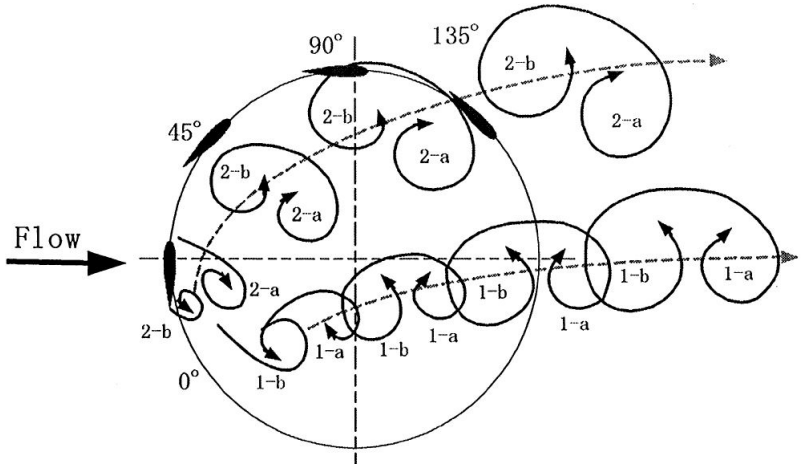

Figure 1.11: Dynamic Stall of Darrieus Turbine [4]

1.6 Computational Fluid Dynamics

Computational fluid dynamics (CFD) belongs to the family of fluid mechanics which use numerical analysis and algorithms to solve and analyze issues which is related to fluid flows. Computers do the calculations for simulating the interaction of liquids and gases whose boundary conditions define the surfaces. Unsteady, compressible, viscous, turbulent and separated can be solved using this. Most of the CFD solvers available uses solving methods such as finite elements, finite volumes, finite differences and spectral elements.

The famous finite element method (FEM) codes include commercial COMSOL Multi-physics and the freely available FEniCS. Other famous commercial codes such as ANSYS CFX, ANSYS Fluent and StarCCM+ and freely available code OpenFoam uses finite volume method (FVM). Experiments required for this thesis is done using the commercial CFD software STAR-CCM+. This software provides a broad engineering physics simulation tools. It is an entire engineering process for solving problems involving flow (of fluids or solids), heat transfer, and stress. It provides a suite of integrated components that combine to produce a package that can address a variety of modeling needs. The components of this software includes 3D-CAD modeler, CAD embedding, surface preparation tools, automatic meshing, physics modeling, turbulence modeling, post-processing and CAE Integration. This software is based on object-oriented programming technology. The methods used for the simulations in STAR-CCM+ are explained in detail in coming chapters.

2 OBJECTIVE

The major objective of this research was to suggest a water turbine design with higher power efficiency by conducting a parametric study of hydrofoil shapes, hydrofoil shape modifications with circular void, tip speed ratio, pitch angle and solidity. The other main objectives of this research included answering the question whether the efficiency of the chosen turbine can be increased by including circular void in the hydrofoil sections, and studying the variation in lift and drag of a hydrofoil section with different circular voids in a steady state. The design has been intended to specific case of Gulf Stream ocean currents with flow velocity of 2m/s. The base water turbine design which was selected for this research was a Gorlov turbine and the base geometry was selected according to the research paper by its inventor himself Alexander Gorlov [16]. Hydrofoil section which was selected was symmetric hydrofoil NACA0020 with a chord length of $C = 0.1778m$, with three blades $n = 3$, diameter of $D = 0.6096m$, solidity of $\sigma = 0.2785$, tip speed ratio of $\lambda = 0.958$, pitch angle of $\beta = 0°$ and height of $h = 0.8696m$. The claimed efficiency of this specific vertical axis Gorlov turbine design is 35% [16]. So the objective was to suggest a modification in design as well as operating condition in order to increase the efficiency. Since the quantitative accuracy of the two dimensional numerical simulation results for predicting real three dimensional performances will be less, performance is predicted based on comparison with the two dimensional simulation performance of the base case.

3 METHODOLOGY

The tool used for this research was computational fluid dynamics numerical simulations. The software that was used for this research was STAR CCM+ which is a commercial CFD software. All the numerical simulations were two dimensional simulations considering the Blade Element Theory (BET). The required output of the simulations of the turbine was the moment, lift and drag over each of the three hydrofoil sections in time, from which power produced and efficiency could be evaluated. The parametric study was conducted by changing only one parameter at a time while other parameters remaining same as that of the base design. The base design was a Gorlov turbine with hydrofoil cross section $H = NACA0020$, chord length $C = 0.1778m$, number of blades $n = 3$, diameter $D = 0.6096m$, solidity $\sigma = 0.2785$ (Eqn. 3.1), tip speed ratio $\lambda = 0.958$ (Eqn. 3.2), pitch angle of $\beta = 0°$, height $h = 0.8636m$ and helical angle $\phi = 53.5°$ (Eqn. 3.3), flow velocity $V = 2m/s$. The effect of helical angle ϕ cannot be captured by these simulations since these are two dimensional simulations. So the forces, moment and power determined by these simulations using BET actually predicts that of an ideal case Gorlov turbine which have a helical angle $\phi = 90°$. In order this to be possible Gorlov turbine should be infinitely long or high, or else it could be though as Darrieus turbine which have $\phi = 90°$ for blades, but no helical structure. As the efficiency of the Gorlov turbine reduces when ϕ become smaller [1], the determined power would be the upper limit for variation in ϕ.

$$\sigma = \frac{nC}{\pi D} \tag{3.1}$$

$$\lambda = \frac{D\omega}{2V} \tag{3.2}$$

$$\phi = \tan^{-1}(\frac{nh}{\pi D}) \tag{3.3}$$

The representation of these parameters could be seen from the snapshot of one of the simulation that was carried out Fig.3.1. The parametric study was conducted in a specific manner in order to achieve the desired result. The first parameter which studied was Hydrofoil cross section shape (H). For selecting the best H, fourteen different hydrofoil section shapes were chosen with all other parameters remaining same as that of the base case. For the cases of asymmetric hydrofoils, two simulations were carried out for each H, one being camber pointing radially outwards and other being camber pointing radially inwards.In the section 3.1 it is explained how two dimensional results are used to determine the three dimensional. In the following sections geometry, meshing and setting up simulations in star ccm+ are explained.

3.1 Blade Element Theory (BET)

Blade element theory (BET) is a mathematical method made by William Froude, David Taylor and Stefan Drzewiecki to understand the behavior of propellers. In BET, blade of the propeller is broken into small pieces and forces on all pieces is found out. These forces are integrated along blade length and over one complete rotation of rotor and thus obtain the forces and moment produced by the entire propeller or rotor. This

theory is used for this research in order to determine the three dimensional results from two dimensional results. For helical angle $\phi = 90°$, every cross section of the turbine blade is same in the vicinity neglecting the pressure difference due to the water head corresponding to the height in case of vertically placed Gorlov turbine and corresponding to the diameter in case of horizontally placed ones. The two dimensional simulation results of forces and moment from STAR-CCM+ were estimated for a unit depth of one meter. So utilizing BET theory when the forces and moment results got from the software is multiplied by the height of turbine which is 0.8636m gives the three dimensional results for the turbine with $\phi = 90°$. Since this is case of Darrieus turbine an assumption is made in order to compare the results for a Gorlov turbine. The assumption is that the ratio of efficiency of two Darrieus turbines A_D and B_D will be directly proportional to that of two corresponding Gorlov turbines A_G and B_G for a given helical angle ϕ. This relation could be defined as Eqn. 3.4 where f is the function of ϕ alone. We know that $f(90°) = 1$ and $f(\phi) > 0$. So with this assumption, for $\phi = 53.5°$ we can say that order of efficiency determined using the two dimensional simulations will be same as that of corresponding three dimensional Gorlov turbines. So it could be stated as " If $\eta(A_{DS}) > \eta(B_{DS})$ the $\eta(A_G) > \eta(B_G)$ " where 'DS' Darrieus turbine from simulation and 'G' represent three dimensional Gorlov turbine. Comparisons are done on this basis in this research.

$$\frac{\eta(A_D)}{\eta(B_D)} = f(\phi)\frac{\eta(A_G)}{\eta(B_G)} \tag{3.4}$$

3.2 Geometry

The geometry required for all numerical simulations were created using AutoCAD computer aided designing (CAD) software. For the two dimensional rotating turbine simulations the initial geometry created in AutoCAD had the outer dimension a box of 14 m in length, 8 m in height and 0.1 m in depth.

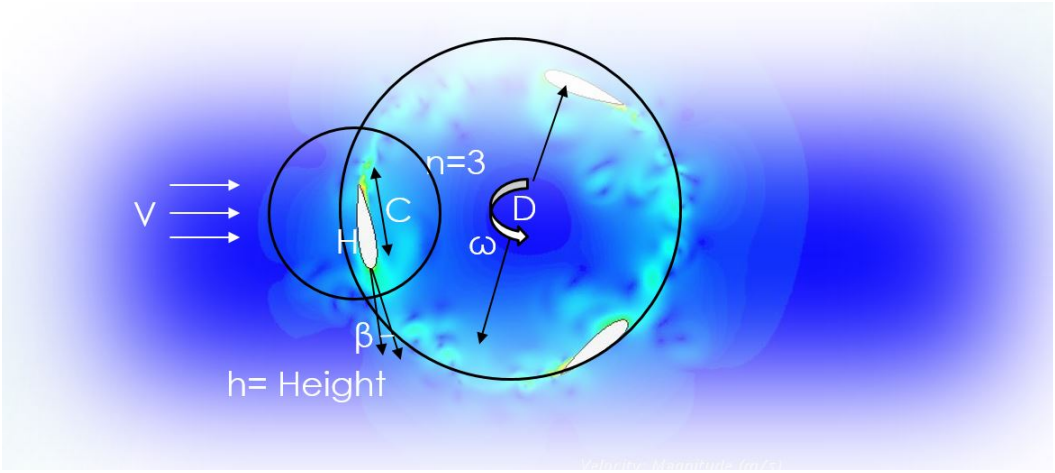

Figure 3.1: Parameters of Gorlov Turbine

The center of the turbine was located 4 m from the velocity inlet. The origin of the global coordinate system is the center of the turbine on the upper plane of the box, which is 4 m along X axis from inlet and 4 m along Y axis from the side boundary. The vertical position of the turbine The outlet was 10 m away from center. The base diameter of the turbine was 0. 6096m.This could be seen from the Fig. 3.2

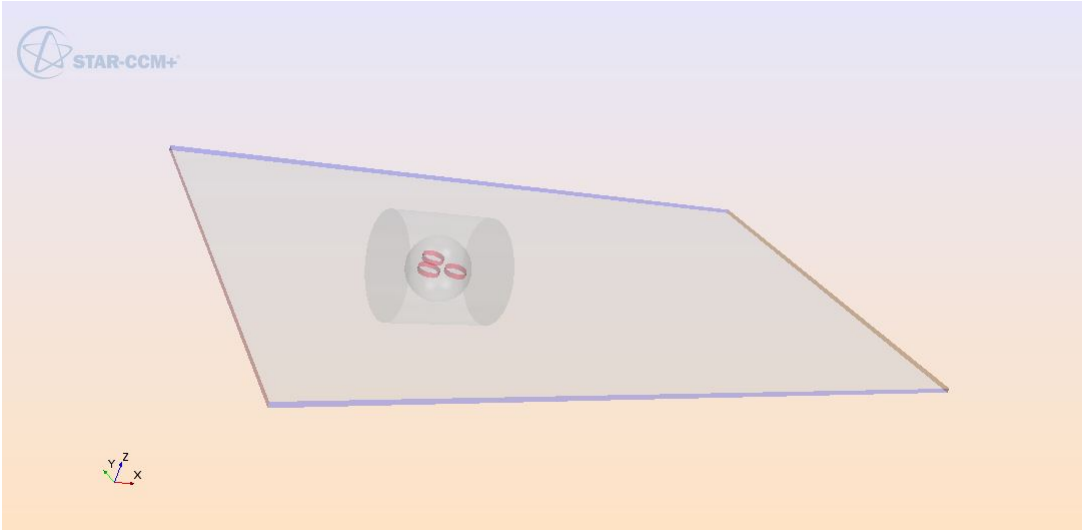

Figure 3.2: 3D Geometry of Simulating Region

3.2.1 Geometry for Overset and Fine Meshing

In order to use the Overset meshing technique in STAR CCM+, which makes it easier to rotate and translate some parts of the geometry without recreating the entire geometry again. The base diameter of turbine was 0.6096 m. Overset region for three of the hydrofoils were three cylinders each of diameter of 0.4 m centered at the midpoint of the chord of hydrofoil and with same depth as that of the box, 0.1 m. While doing the automatic two dimensional meshing, in order to do fine meshing near the hydrofoil region, a sphere and a cylinder is created. Sphere is centered at the origin of the global coordinate (GC) with a diameter of 1.0 m. The cylinder is centered at the origin in GC with a length of 2m along X axis and have a diameter of 2 m. Geometry for the fine meshing simulation could be understood from the Fig. 3.3. The cylinder, sphere and the hydrofoils are visible in this figure.

The red cylindrical surfaces that could be seen are the surfaces of three overset cylinder regions. Three local Cartesian Coordinate (LC) systems have been also constructed at the center of the three hydrofoils which would rotate along with the overset mesh. The X, Y and Z axis in the local coordinate system points in the same direction as that of global coordinate system. Once the 3D CAD model was generated in AutoCAD software, then it is exported in STAR-CCM+ as an IGES file.

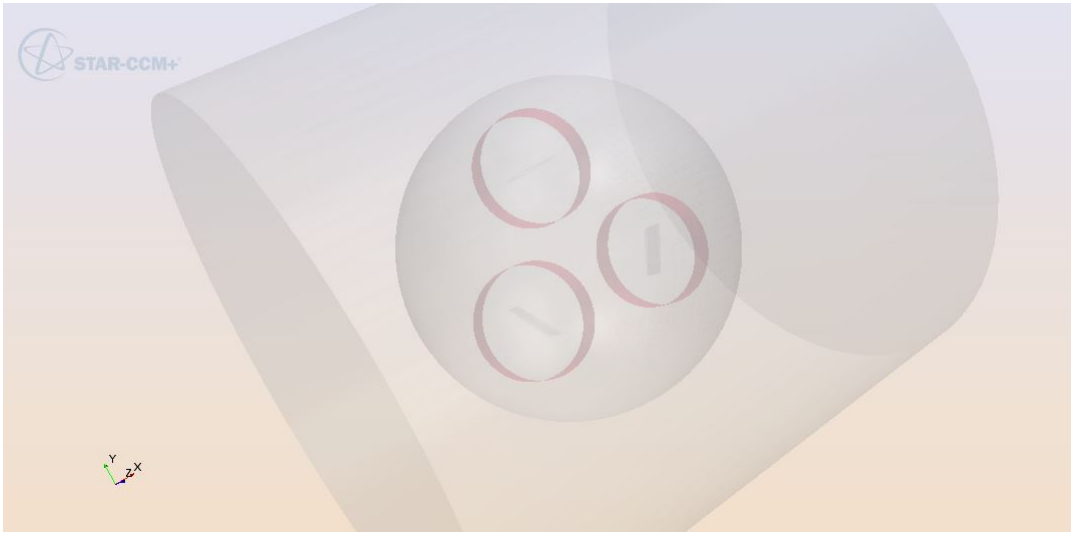

Figure 3.3: Geometry for Fine Meshing

3.2.2 Geometry of Hydrofoils (H)

All the hydrofoil sections that are used for this research are NACA airfoil shapes. The chord length of all the hydrofoils are same $C = 0.1778m$. For the simulations for comparison, chord length $C = 0.125$. The coordinates of the NACA foils were taken from public domain. hydrofoil geometry was created using 200 points distributed with cosine spacing. The coordinates were then scaled to the chord length and then imported as points

in to AutoCAD. The twelve different NACA foils other than NACA0020 which is the base case that are used for this research are given in the Table 3.1.

Table 3.1: NACA Foils for Simulations

H1	NACA0006	H7	NACA2408
H2	NACA0009	H8	NACA2411
H3	NACA0012	H9	NACA2414
H4	NACA0018	H10	NACA2424
H5	NACA0024	H11	NACA4421
H6	NACA1410	H12	NACA6409

In total six symmetric and seven asymmetric hydrofoils were used for this research. Each of the hydrofoil shapes (H) is named in order to understand from the name of simulation which hydrofoil shape is used. The base hydrofoil shape NACA0020 is named as 'H00'. The names are given as it is in the table. These NACA foils were selected considering the data base information available on their lift coefficient (C_L), drag coefficient (C_D) for a range of Reynolds' number (Re) and angle of attack (α). The NACA foil geometry used for this research could be regenerated using the equations provided by NACA. Foils used were 4 digit NACA foils. The first digit 'm' says the percentage value of maximum camber compared to chord length. Second digit gives the position on the chord of the maximum camber in tenths of the chord and is represented with the letter 'p'. The final two

digits 't' denotes the maximum thickness of the airfoil in percentage of the chord length. Considering origin at the nose of the airfoil with left hand Cartesian coordinate system, the coordinates of the upper and lower surfaces of NACA foil could be found out using the following equations Eqn. 3.5 to Eqn. 3.8 where subscript u denotes the upper surface and l denotes the lower surface. Note that 'c' represent chord length in the equations in this section.

$$x_u = x - y_t \sin(\theta) \tag{3.5}$$

$$y_u = y_c + y_t \cos(\theta) \tag{3.6}$$

$$x_l = x + y_t \sin(\theta) \tag{3.7}$$

$$y_l = y_c - y_t \cos(\theta) \tag{3.8}$$

The x in the equations represent the position along the chord, y_t is the corresponding distribution of thickness and θ is the angle between previous and the current points. The thickness distribution y_t is defined by the equation Eqn. 3.9.

$$\begin{aligned} \pm y_t = 5tc \Bigg[& 0.2969\sqrt{\frac{x}{c}} \pm (-0.1260)\left(\frac{x}{c}\right) \\ & \pm (-0.3516)\left(\frac{x}{c}\right)^2 \pm 0.2843\left(\frac{x}{c}\right)^3 \pm (-0.1015)\left(\frac{x}{c}\right)^4 \Bigg] \end{aligned} \tag{3.9}$$

t is the maximum thickness as a fraction of the chord. The leading edge radius is defined

by the equation Eqn. 3.10

$$r_t = 1.1019t^2 \tag{3.10}$$

The equation of (y_c) for the cambered NACA 4 digit airfoils is given by the equations Eqn. 3.11 and Eqn. 3.12.

$$y_c = m\frac{x}{p^2}\left(2p - \frac{x}{c}\right) \qquad 0 \leq x \leq pc \tag{3.11}$$

$$y_c = m\frac{c-x}{(1-p)^2}\left(1 + \frac{x}{c} - 2p\right) \qquad pc \leq x \leq c \tag{3.12}$$

Angle between earlier point and current point θ is found out using equation Eqn. 3.13

$$\theta = \tan^{-1}\frac{dy_c}{dx} \tag{3.13}$$

$\frac{dy_c}{dx}$ could be found out using the equations Eqn. 3.14 and Eqn. 3.15

$$\frac{dy_c}{dx} = \frac{2m}{p^2}\left(p - \frac{x}{c}\right) \qquad 0 \leq x \leq pc \tag{3.14}$$

$$\frac{dy_c}{dx} = \frac{2m}{(1-p)^2}\left(p - \frac{x}{c}\right) \qquad pc \leq x \leq c \tag{3.15}$$

The geometry of thirteen cases of hydrofoils that were used of research could be seen from figures Fig. 3.4 and Fig. 3.5c These figures are taken from the two dimensional meshes. It could be seen as the last two digits of foil name increases the hydrofoil becomes thicker and when the first digit increases camber increases. The foils shapes H01 to H05 are symmetric and H06 to H12 are asymmetric. H00 is the base hydrofoil NACA0020. The tail of all the hydrofoils are modified with fillet tool in AutoCAD with a fillet radius of $R_f = 0.001m$. This was done in order to prevent the sharp angle at the tail which would cause difficulty in meshing as well as during simulation.

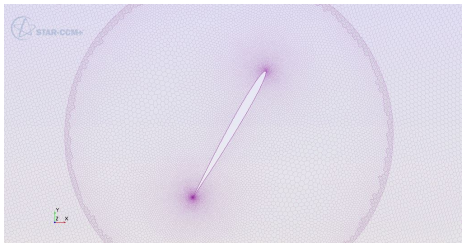

(a) NACA0006 (H1)

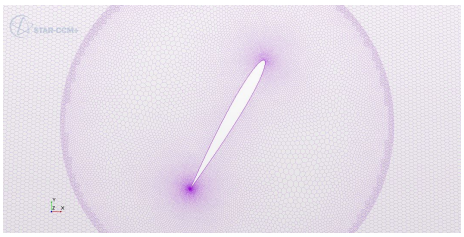

(b) NACA0009 (H2)

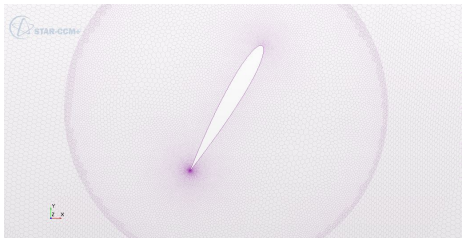

(c) NACA0012 (H3)

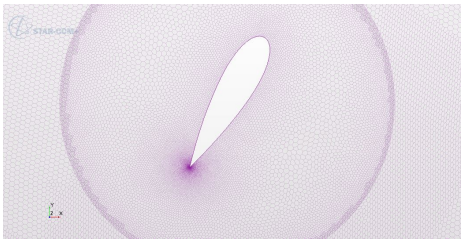

(d) NACA0018 (H4)

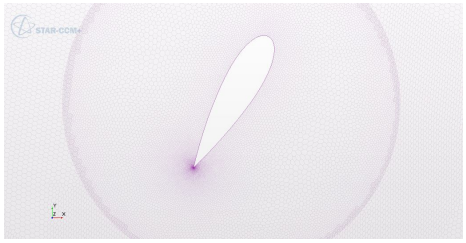

(e) NACA0024 (H5)

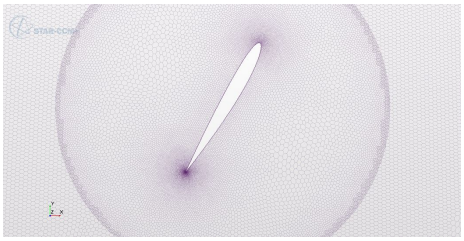

(f) NACA1410 (H6)

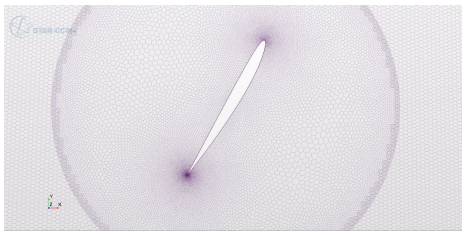

(g) NACA2408 (H7)

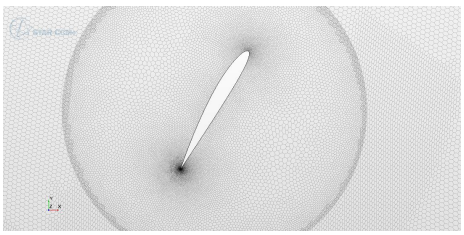

(h) NACA0006 (H8)

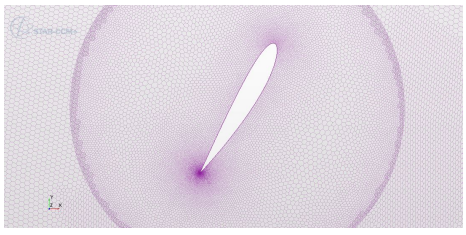

(i) NACA2411 (H9)

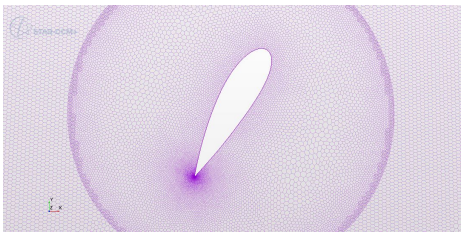

(j) NACA2414 (H10)

Figure 3.4: NACA Hydrofoils H1 to H10

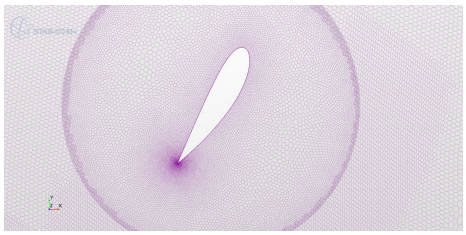

(a) NACA2424 (H11)

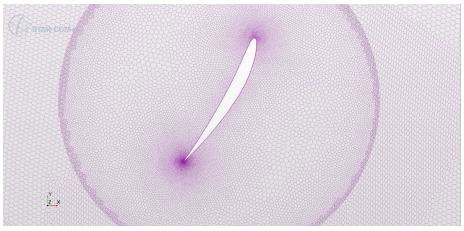

(b) NACA4421 (H12)

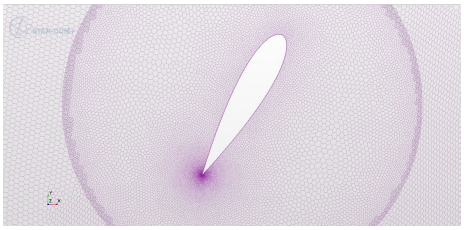

(c) NACA0020 (H0)

Figure 3.5: NACA Hydrofoils H11, H12 and H0

3.2.3 Modified Hydrofoils (HM)

For this research thirteen different cases of circular voids were made on the base hydrofoil NACA0020. The best void from the steady state simulations considering the lift and drag forces were tried for the rotating simulation case. Voids were made circular for the easiness of defining the void as well as the easiness in replicating for further research. It was a secondary objective of this research to study the variation of lift and drag of a hydrofoil in a steady state for different positions and sizes of void. For this purpose, a base modification in the hydrofoil with circular void was defined which was named as 'HM00'. The variations in the void was done for three parameters, radius of the void R_v, X coordinate of the center of the void X_v and the Y coordinate of the center of the void Y_v. R_V was represented as the percentage value of maximum thickness t, Y_V was represented as the percentage of Y coordinate of maximum thickness and the X coordinate at which

the maximum thickness occurs b. The coordinate system and the parameters could be seen form the Fig. 3.6.

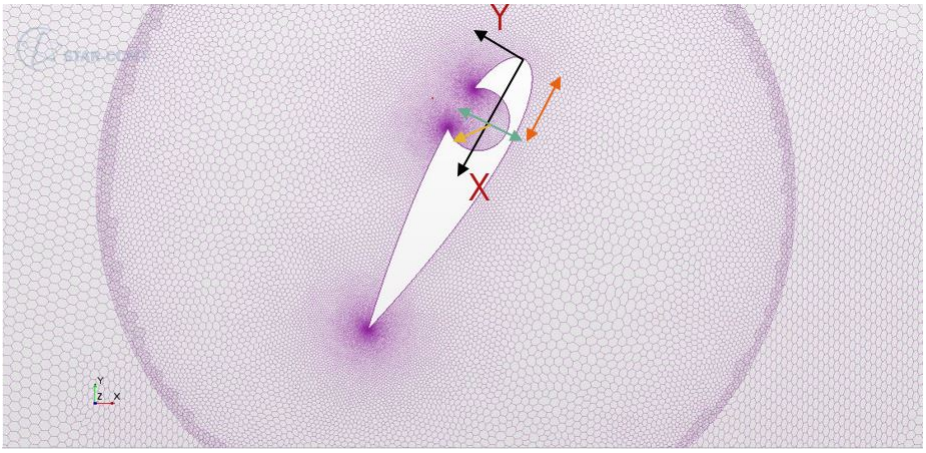

Figure 3.6: Geometry for Fine Meshing for HM

Radius R_v and Y coordinate Y_v were defined in percentage of t while X_v is defined in percentage of b. For the base modified case HM00, $R_v = 50$, $Y_v = 30$ and $X_v = 100$. The joining edges where circular void meets the airfoil, are modified with a fillet radius of 0.001m like the tail of hydrofoils. The cases were chosen such that five data points for each of the parameters were available in order to study the variation. Now during the rotating hydrofoils, they have large value of positive and negative angle of attack α. So the modified hydrofoil which may be more efficient than another in a steady state for a certain pitch angle need not be more efficient for the rotating case. Due to the constraint in number of simulations that could be carried out, the method adopted was like the following. In one simulation steady state performance of thirteen different cases which include four specific cases each for studying the parametric variation with R_v, Y_v and X_v and one base case for

a specific pitch angle β. Eight simulations were carried out of eight different values of β. The modified hydrofoil which performed best in overall eight simulations in terms of lift force was considered for the rotating case. It cannot be said from the cases which were studied in this research, which is the best modified hydrofoil for the turbine case, since the performance in steady state may not be directly correlated to the performance in the rotating case. But since the objective was just to answer whether these type of modifications can improve the efficiency of a turbine or not, the idea was to stop when a modified case which would have higher efficiency is found out. The scope of finding the best modified hydrofoil shape was considered only for the future not, in this research. But the data from this research for steady state for different pitch angles was intended to help to find a correlation between performance in steady state and rotating state in future research. The thirteen different cases of HM can be classified in to three as mentioned below and their geometry definition and the naming could be understood from the tables Table 3.2, Table 3.3 and 3.4.

NACA0020 is used for all the modified hydrofoils (HM) and base case of HM, HM00 is $R_v = 50$, $Y_v = 30$ and $X_v = 100$. The range of radius of the void R_v and Y_v was chosen such that for the largest R_v and the smallest Y_v, at least twenty percent of maximum thickness is remaining in order to provide the structural strength. The interval between the values was chosen such that two values each to the left and right of the base case could be achieved in number line.

Table 3.2: Modified Hydrofoils (HM) With Varying R_v

Modified Hydrofoil (HM)	Radius of circular void R_v
HM01	45
HM02	47.5
HM00	50
HM03	52.5
HM04	55

In order to verify two modifications in Gorlov turbine, which was suggested by inventor [16]' one first being using a skewed hydrofoil which have the radius of curvature for chord R_c same as that of the radius of turbine (Fig. 3.7).

Table 3.3: Modified Hydrofoils (HM) With Varying Y_v

Modified Hydrofoil (HM)	Y coordinate of center of circular void Y_v
HM05	20
HM06	25
HM00	30
HM07	35
HM08	40

Table 3.4: Modified Hydrofoils (HM) With Varying X_v

Modified Hydrofoil (HM)	X coordinate of center of circular void X_v
HM09	80
HM10	90
HM00	100
HM11	110
HM12	120

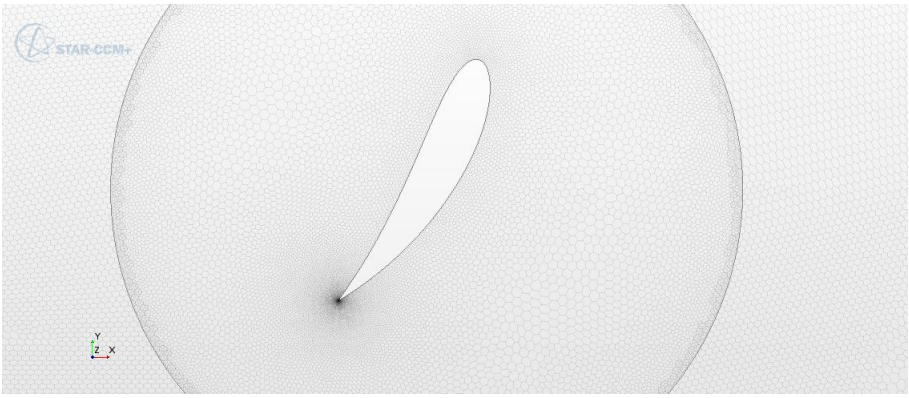

Figure 3.7: Skewed NACA0020 Hydrofoil (H13)

The second one being turbine with two layer of hydrofoils with 60° phase difference (Fig. 3.8). Two layer hydrofoils are named as 'HH'. For skewed case NACA0020 was used. For the two layer case H00, H04 and H04 HM12 were used. The geometry of one of the double layer mesh crated could be seen from the Fig. 3.8.

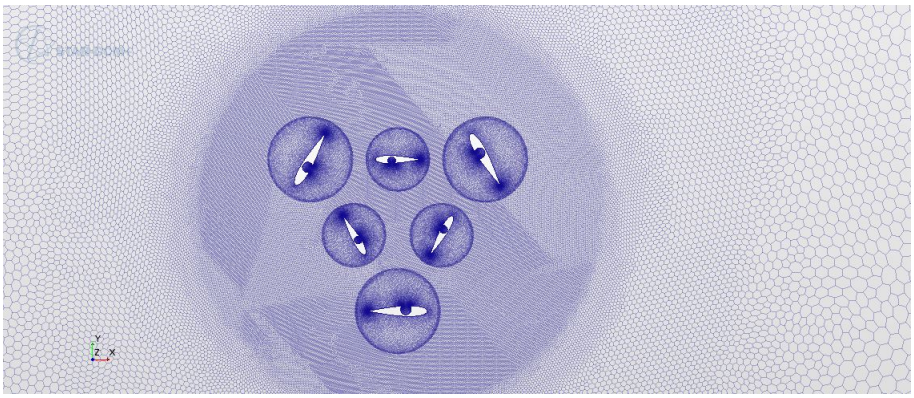

Figure 3.8: Double Layer Hydrofoil Mesh (HH4HM12)

For creating the skewed hydrofoil shape named as H13, chord length was made equal to the arc length which is connected by the equation $L_A = R\theta$ where L_A is the arc length of skewed hydrofoil and θ is the angle made by the hydrofoil to the center of the turbine. The angle between two consecutive points for skewed case was determined using the equation $\frac{dx}{C} = \frac{d\theta}{\theta}$. The Y coordinates of the hydrofoils were taken radially inwards and outwards. For the two-layer hydrofoil turbine, the inner layer was scaled by 75% of the outer layer and its radius was half the radius.

3.3 Simulations

Sixty-two different rotating turbine simulations (RTS) were and eight different steady state simulations (SSS) were used for this research. Details of simulations are given in next chapter. Sixty-two RTS were carried out in order to do the parametric study on H, σ, λ and independent cases of skewed hydrofoil and double layer turbine. Eight SSS were carried out in order to do the parametric study on HM with R_v, X_v and Y_v for eight different pitch angles (β). In order to compare with an experimental result, five RTS simulations were

carried out with five different tip speed ratio (λ).

3.3.1 Naming of Simulations

The naming of the simulations is given and explained in this section. The tables Table 3.5 to Table 3.7 show how hydrofoil shape (H) and modified hydrofoil shape (HM) are defined. The other parameters include tip speed ratio λ, pitch angle β, solidity (σ) and number of layers (N). There are two kind of simulations, RTS and SSS. Simulations are named as follows. Name starts with 'S' followed by first digit '1' or '2', where '1' represents RTS and '2' represents SSS. For the RTS cases with first digit '1', the second digit could be again '1' or '2' which represents number of layers N. The third and the fourth digit represents the hydrofoil shape H, the fifth digit could be '0', '1' or '2' representing to which direction camber of asymmetric hydrofoil and void of a symmetric is pointed. For symmetric it is 0. If it is away from center of turbine, it is '1' and if it is towards the center it is '2'. The sixth and the seventh digit represents the modified hydrofoil shape (HM) from 00 to 13. The eighth and the ninth digit represent tip speed ratio λ (L) according to the Table 3.5 from 01 to 12. The tenth digit represents β (B) according to the Table 3.6 from 1 to 8 and the eleventh digit represent σ (S) according to the Table 3.7 from 1 to 6. For SSS second and third digit followed by '2' represents H and fourth digit represents β according to the Table 3.6.

For the simulations for comparison, C is added after S, 'SC'. For steady state simulations S is added after S, making 'SS'. All the 70 simulations are named also in serial order which are given in Table 3.8 to Table 3.14 along with the corresponding simulation name.

SIM stands for the serial number of simulation, CA stands for the cases RTS or SSS, CM stands for camber and in case of HM void, N stands for number of layers, H stands for hydrofoil shape, HM stands for modified hydrofoil shape. For cases with no modification 'XX' is given.

Table 3.5: Tip Speed Ratio (λ) for Simulations

Representation (L)	Tip Speed Ratio λ
L01	0.88
L02	0.96
L03	1.00
L04	1.05
L05	1.20
L06	1.25
L07	1.36
L08	1.45
L09	1.51
L10	1.68
L11	1.75
L12	2.00

Table 3.6: Pitch Angle (β) for Simulations

Representation (B)	Pitch Angle (β)
B1	$-8°$
B2	$-4°$
B3	$-2°$
B4	$0°$
B5	$1°$
B6	$2°$
B7	$4°$
B8	$8°$

Table 3.7: Solidity (σ) for Simulations

Representation (S)	Solidity (σ)
S1	0.1
S2	0.15
S3	0.2
S4	0.2875
S5	0.4
S6	0.5

Table 3.8: Naming for Simulations SIM01 to SIM10

SIM	Name	CA	N	H	CM	HM	λ	β	σ
SIM01	S11010XX0244	RTS	1	H01	0	HMXX	L02	B4	S4
SIM02	S11020XX0244	RTS	1	H02	0	HMXX	L02	B4	S4
SIM03	S11030XX0244	RTS	1	H03	0	HMXX	L02	B4	S4
SIM04	S11040XX0244	RTS	1	H04	0	HMXX	L02	B4	S4
SIM05	S11050XX0244	RTS	1	H05	0	HMXX	L02	B4	S4
SIM06	S11061XX0244	RTS	1	H06	1	HMXX	L02	B4	S4
SIM07	S11071XX0244	RTS	1	H07	1	HMXX	L02	B4	S4
SIM08	S11081XX0244	RTS	1	H08	1	HMXX	L02	B4	S4
SIM09	S11091XX0244	RTS	1	H09	1	HMXX	L02	B4	S4
SIM10	S11101XX0244	RTS	1	H10	1	HMXX	L02	B4	S4

3.4 Setup of Rotating Turbine Simulation

Numerical simulations were carried out in Star CCM+. In this section the various setups that were used for the rotating turbine simulation in Star CCM+ is explained.

3.4.1 Geometry Import

The 3D geometry was created in AutoCAD was imported to Star CCM+ as an IGES file. The file was imported as a surface mesh. The import mode was to create a new part. The mark feature edges in IGES import option was selected as sharp CAD edges with sharp edge angle of 30° with a sewing tolerance of 0.001. Create part contacts from coincident

entities option was selected with a coincidence tolerance of $1.0x10^{-5}m$. Medium tessellation density was chosen which have curve chord tolerance of 0.03%, curve chord angle of 8°, surface plane tolerance of 0.03% and surface plane angle of 8°.

Table 3.9: Naming for Simulations SIM11 to SIM20

SIM	Name	CA	N	H	CM	HM	λ	β	σ
SIM11	S11110XX0244	RTS	1	H11	0	HMXX	L02	B4	S4
SIM12	S11120XX0244	RTS	1	H12	0	HMXX	L02	B4	S4
SIM13	S11000XX0244	RTS	1	H00	0	HMXX	L02	B4	S4
SIM14	S11001090244	RTS	1	H00	1	HM09	L02	B4	S4
SIM15	S11062XX0244	RTS	1	H06	2	HMXX	L02	B4	S4
SIM16	S11072XX0244	RTS	1	H07	2	HMXX	L02	B4	S4
SIM17	S11082XX0244	RTS	1	H08	2	HMXX	L02	B4	S4
SIM18	S11092XX0244	RTS	1	H09	2	HMXX	L02	B4	S4
SIM19	S11102XX0244	RTS	1	H10	2	HMXX	L02	B4	S4
SIM20	S11112XX0244	RTS	1	H11	2	HMXX	L02	B4	S4

3.4.2 Creating Surfaces

When geometry is imported, four bodies are created, one being the fluid domain and other three being the hydrofoils. When bodies are created, only one surface is created for one body. So it needed to be split and named. Surfaces are divided using split by patch

option and surfaces are named. For the fluid domain body there are six surfaces; flow inlet surface, flow outlet surface, two side surfaces and top and bottom surfaces. This could be seen from Fig. 3.9

Table 3.10: Naming for Simulations SIM21 to SIM30

SIM	Name	CA	N	H	CM	HM	λ	β	σ
SIM21	S11122XX0244	RTS	1	H11	2	HMXX	L02	B4	S4
SIM22	S11002090244	RTS	1	H00	2	HM09	L02	B4	S4
SIM23	S11000XX0234	RTS	1	H00	0	HMXX	L02	B3	S4
SIM24	S11000XX0224	RTS	1	H00	0	HMXX	L02	B2	S4
SIM25	S11000XX0264	RTS	1	H00	0	HMXX	L02	B6	S4
SIM26	S11000XX0274	RTS	1	H00	0	HMXX	L02	B7	S4
SIM27	S11040XX0264	RTS	1	H04	0	HMXX	L02	B6	S4
SIM28	S11002090264	RTS	1	H00	2	HM09	L02	B6	S4
SIM29	S11001130244	RTS	1	H00	1	HM13	L02	B4	S4
SIM30	S11001130244	RTS	1	H00	1	HM13	L02	B4	S4

The hydrofoil body surface is split in to four surfaces, which are cylindrical surface, hydrofoil surface, cylinder top surface and cylinder bottom surface. This could be seen from Fig. 3.10. This method is continued for all the three hydrofoils. Only fluid region is created in Star CCM+ which means the hydrofoil is identified by its outer surface. Thus the surface creation and naming of surfaces is completed.

Table 3.11: Naming for Simulations SIM31 to SIM40

SIM	Name	CA	N	H	CM	HM	λ	β	σ
SIM31	S11042090244	RTS	1	H04	2	HM09	L02	B4	S4
SIM32	S11042090264	RTS	1	H04	2	HM09	L02	B6	S4
SIM33	S11042120244	RTS	1	H04	2	HM12	L02	B4	S4
SIM34	S11042120264	RTS	1	H04	2	HM12	L02	B6	S4
SIM35	S11040XX0164	RTS	1	H04	0	HMXX	L01	B6	S4
SIM36	S11000XX0164	RTS	1	H00	0	HMXX	L01	B6	S4
SIM37	S11040XX0464	RTS	1	H04	0	HMXX	L04	B6	S4
SIM38	S11000XX0464	RTS	1	H00	0	HMXX	L04	B6	S4
SIM39	S11040XX0564	RTS	1	H04	0	HMXX	L05	B6	S4
SIM40	S11042120564	RTS	1	H04	2	HM12	L05	B6	S4

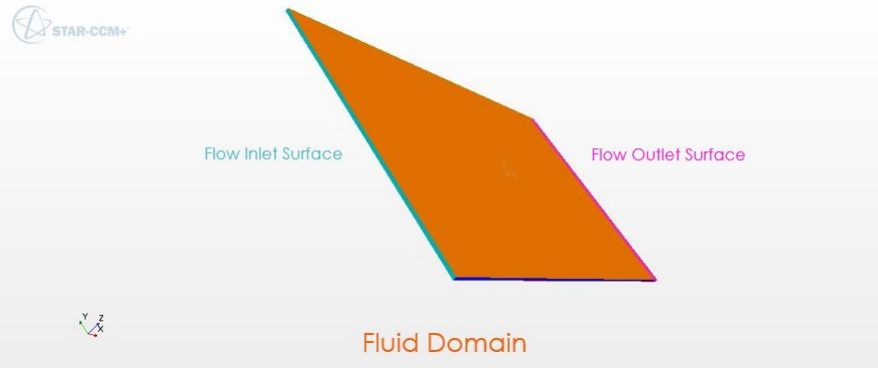

Figure 3.9: Fluid Domain

Table 3.12: Naming for Simulations SIM41 to SIM50

SIM	Name	CA	N	H	CM	HM	λ	β	σ
SIM41	S11040XX0764	RTS	1	H04	0	HMXX	L07	B6	S4
SIM42	S11042120764	RTS	1	H04	2	HM12	L07	B6	S4
SIM43	S11040XX0964	RTS	1	H04	0	HMXX	L09	B6	S4
SIM44	S11042120964	RTS	1	H04	2	HM12	L09	B6	S4
SIM45	S11040XX1064	RTS	1	H04	0	HMXX	L10	B6	S4
SIM46	S110420121064	RTS	1	H04	2	HM12	L10	B6	S4
SIM47	S1104212AU44	RTS	1	H04	2	HM12	LAU	B4	S4
SIM48	S11040XXAU64	RTS	1	H04	0	HMXX	LAU	B6	S4
SIM49	S11000XXAU64	RTS	1	H00	0	HMXX	LAU	B6	S4
SIM50	S12040XX0744	RTS	2	H04	0	HMXX	L07	B4	S4

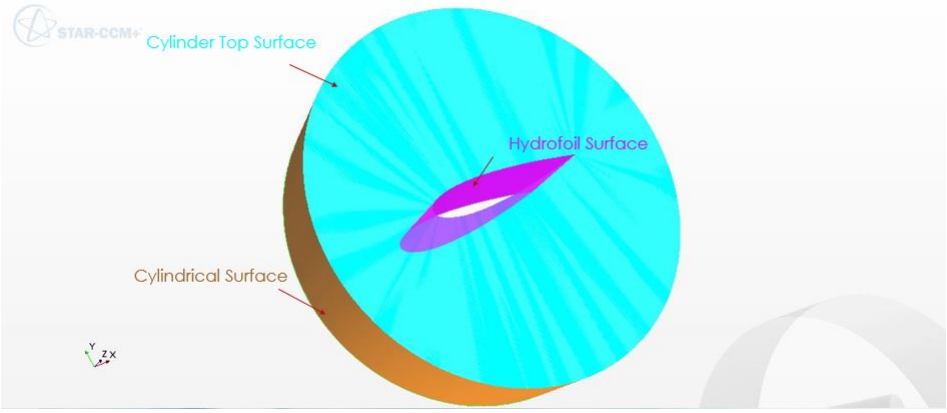

Figure 3.10: Hydrofoil Inside Cylinder

Table 3.13: Naming for Simulations SIM51 to SIM60

SIM	Name	CA	N	H	CM	HM	λ	β	σ
SIM51	S12042120744	RTS	2	H04	2	HM12	L07	B4	S4
SIM52	S12040XX0764	RTS	2	H04	0	HMXX	L07	B6	S4
SIM53	S11040XX0761	RTS	1	H04	0	HMXX	L07	B6	S1
SIM54	S11040XX0762	RTS	1	H04	0	HMXX	L07	B6	S2
SIM55	S11040XX0763	RTS	1	H04	0	HMXX	L07	B6	S3
SIM56	S11040XX0765	RTS	1	H04	0	HMXX	L07	B6	S5
SIM57	S11040XX0766	RTS	1	H04	0	HMXX	L07	B6	S6
SIM58	SC11040XX0845	RTS	1	H04	0	HMXX	L08	B4	S5
SIM59	SC11040XX0345	RTS	1	H04	0	HMXX	L03	B4	S5
SIM60	SC11040XX0645	RTS	1	H04	0	HMXX	L06	B4	S5

3.4.3 Creating Regions

Meshing and physics can only be assigned to regions and not to parts. So before meshing and assigning physics models, parts of all bodies need to be assigned to regions. This is done by choosing assign parts to region option, in which further it had chosen as create a region for each part and create a boundary for each part surface. Create interface from contact option is not selected since the cylinder hydrofoil region is an overset region.

Table 3.14: Naming for Simulations SIM61 to SIM70

SIM	Name	CA	N	H	CM	HM	λ	β	σ
SIM61	SC11040XX1145	RTS	1	H04	0	HMXX	L11	B4	S5
SIM62	SC11040XX1245	RTS	1	H04	0	HMXX	L12	B4	S5
SIM63	SS2008	SSS	-	H00	-	-	-	B8	-
SIM64	SS2007	SSS	-	H00	-	-	-	B7	-
SIM65	SS2006	SSS	-	H00	-	-	-	B6	-
SIM66	SS2005	SSS	-	H00	-	-	-	B5	-
SIM67	SS2004	SSS	-	H00	-	-	-	B4	-
SIM68	SS2003	SSS	-	H00	-	-	-	B3	-
SIM69	SS2002	SSS	-	H00	-	-	-	B2	-
SIM70	SS2001	SSS	-	H00	-	-	-	B1	-

3.4.4 Meshing

All the simulations that were done for this research was two dimensional simulations. Even though Star CCM+ is designed mainly for the three dimensional simulations, it also has the option for doing the two dimensional simulations. The two dimensional simulation was used in order to reduce the computing time as there are many simulations has to be carried out. In order to carry out 2D simulation, the regions which need to be considered for it should be executed with an operation called badge for 2D meshing. So all the regions that were created is selected for 2D badge and when executed all the surfaces which are

coinciding Z=0 plane are ready for 2D meshing. After this a new operation of automated 2D mesh is created. For this operation the fluid domain region in selected first. The meshing type selected was polygonal meshing. Curvature refinement and proximity refinement were selected which is optional. In the expert polygonal mesher properties options where selected to retain geometric features and to create aligned meshes. Minimum face quality was chosen as 0.05. The base size was given as 0.1m as the same order that of chord length. Project to CAD option is selected. The target surface size was chosen as same as that of base size, 0.1m. The minimum surface size was given as 5% of the base size, 0.005m. The surface curvature was selected as 36 points per circle. Surface growth rate was given as 1.05. After this in order to do the fine meshing in the regions near to the hydrofoils, custom control in automated 2D mesh is used. A cylinder of diameter 2m, length of 2m and a sphere of 1m radius is created for this. Both are centered at the center of turbine blades as it can be seen in the Fig. 3.3. In custom control for both cylinder and sphere 2D surface mesher control was selected. For the cylinder custom size was selected as 20% of the base size, 0.02m. For the sphere custom size selected was 5%, 0.005m. These specific values were given after many trials and the mesh verification was carried out before choosing this values. Details of mesh verification is proved in later section. The 2D that were created with these values can be seen from the Fig. 3.11

It could be seen from Fig. 3.11 that near the center of turbine in shape of a rectangle there is fine mesh which corresponds to the cylinder and there is finer mesh inside a circle which corresponds to the region inside sphere. Closer look at the mesh near the center

could be seen from the Fig. 3.12

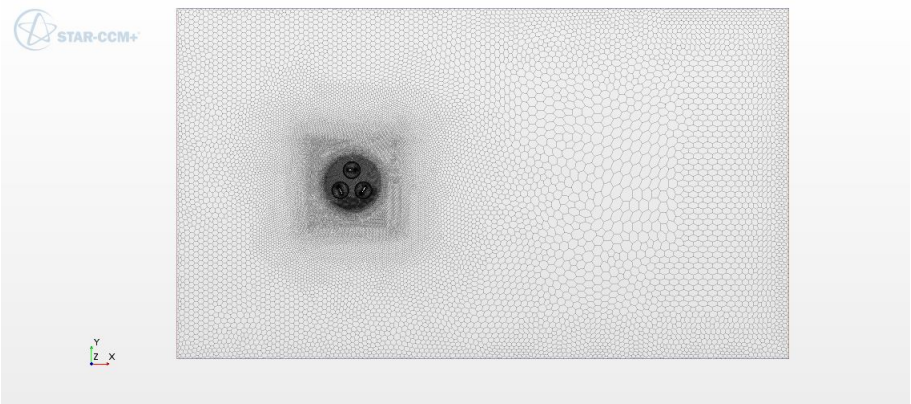

Figure 3.11: 2D Mesh for Rotating Turbine

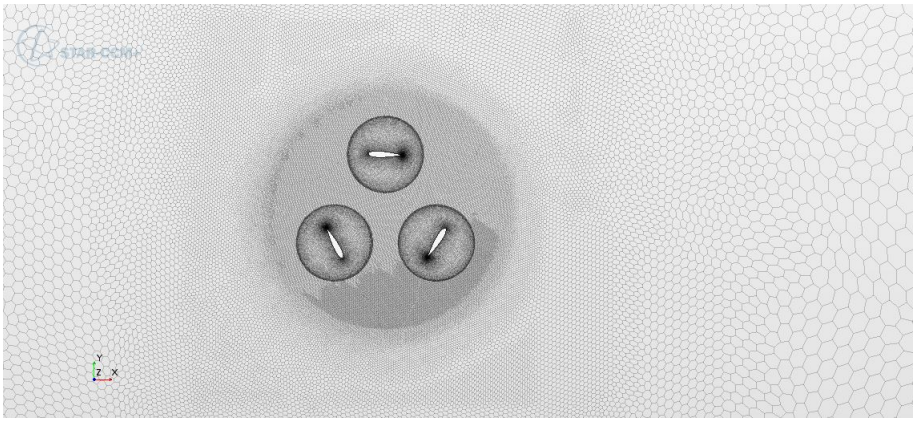

Figure 3.12: 2D Fine Mesh With Custom Control

After the meshing of fluid domain, the next part is the meshing of three cylindrical hydrofoil regions. The meshing type selected was polygonal meshing and prism layer meshing. For polygonal meshing, curvature refinement and proximity refinement were selected which is optional. In the expert polygonal mesher properties options where selected to retain geometric features and to create aligned meshes. Minimum face quality

was chosen as 0.05. The base size was given as 0.002m. Target surface size was selected as same as that of base size, 0.002m. Minimum surface size was selected as 1% of the base size $2x10^{-5}m$. Basic surface curvature was selected as 36 points per circle. Surface growth rate was selected as 1.05. The meshing around the hydrofoil can be seen in the Fig. 3.13.

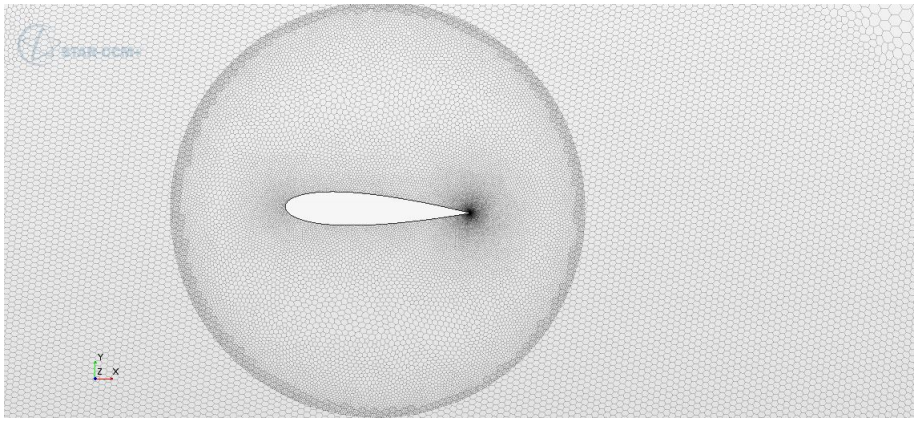

Figure 3.13: Mesh Around Hydrofoil

For the prism layer meshing, stretching function was given as geometric progression. Distribution mode was chosen as stretch factor. Gap fill was given as 25%. Minimum thickness was given as 10%. Layer reduction was given as 50%. In expert prism layer mesher properties, boundary march angle was given as 50°. Concave angle limit was given as 0° and convex angle limit was given as 360°. Number of prism layer was chosen as 5. Prism layer stretching factor was given as 1.5. Total thickness of prism layer was given as 1% of base size, $2x10^{-5}m$. The prism layer meshing could be seen from the Fig. 3.14

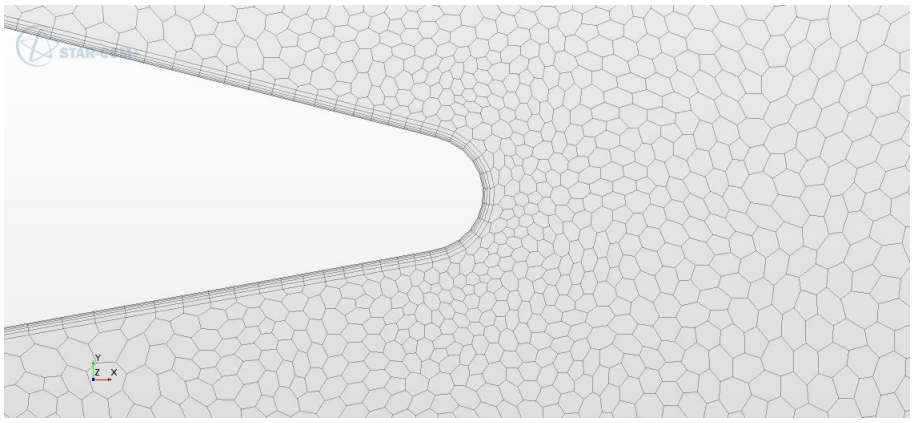

Figure 3.14: Prism Layer Meshing

3.4.5 Overset Meshing

Overset meshes are used to discretize a computational domain with several different meshes that overlap each other in an arbitrary manner. They are used mostly in problems dealing with multiple or moving bodies, as well as optimization studies. This meshes are also called as 'Chimera' meshes or overlapping meshes. For the rotating turbine simulation this meshing techniques is used since there are multiple moving bodies. Also in order to do the parametric study with change in pitch angle this was useful since only the overset regions of three hydrofoils need to be with respective to their local coordinate system, rather than creating entirely new simulation for all the different pitch angles. The overset meshing during the simulation for a velocity field could be seen from the Fig. 3.15

There are three overset mesh region which consists of three cylindrical hydrofoil regions. when overset meshes are used, overset mesh interfaces are created. Physics conditions are linearly interpolated at the interface. The overlapping of meshes at the interface could be seen from the Fig. 3.16.

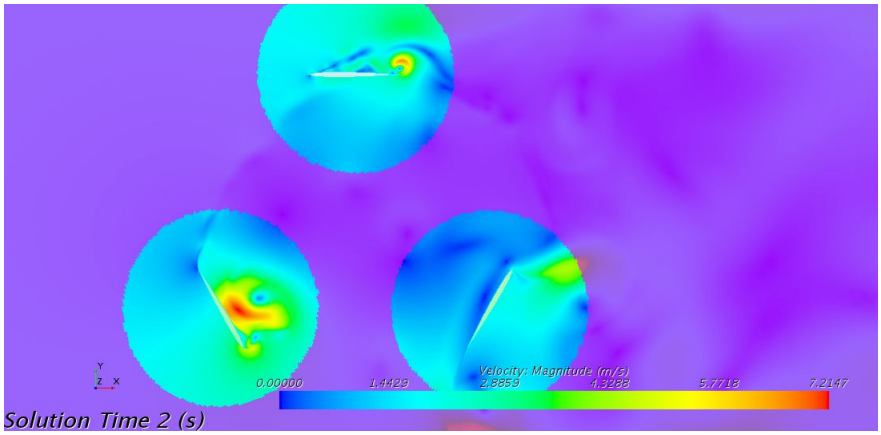

Figure 3.15: Overset Meshing

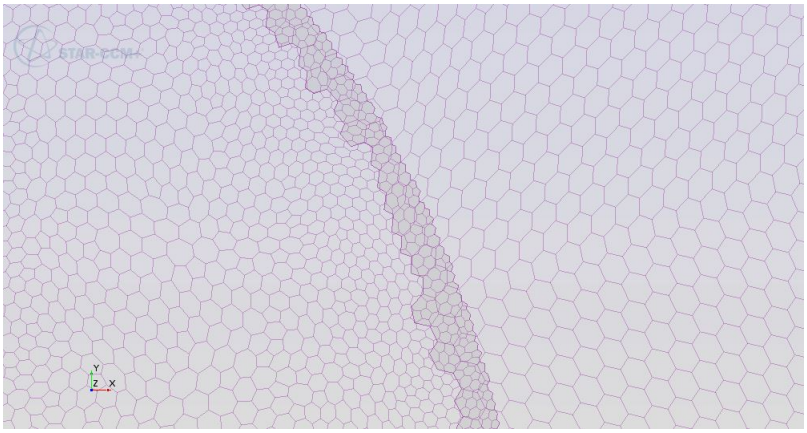

Figure 3.16: Overset Mesh Overlap

3.4.6 Physics Continua

After creating mesh, the next step is to define the physics for all the regions. For the case considered there is only one kind of physics is required for the entire domain. The fluid is selected as water with constant density of $997.56 kg/m^3$ with a dynamic viscosity of $8.89x10^{-4} Pa\,s$. The implicit unsteady model is chosen for rotating case. The flow is solved by solving Reynolds Averaged Navier - Stokes (RANS) model equations. RANS equations

are equations of motion which are averaged in time for fluid flow. The method used for this is called Reynolds decomposition, in which quantity in a time instant is split into its time-averaged and fluctuating quantities. These equations are used mainly for modelling turbulent flows. By knowing the properties of the turbulent flow, RANS equations can give approximate time-averaged solutions for the Navier – Stokes equations. These equations for a stationary, incompressible Newtonian fluid, is given in equation Eqn. 3.16

$$\rho \bar{u}_j \frac{\partial \bar{u}_i}{\partial x_j} = \rho \bar{f}_i + \frac{\partial}{\partial x_j}\left[-\bar{p}\delta_{ij} + \mu\left(\frac{\partial \bar{u}_i}{\partial x_j} + \frac{\partial \bar{u}_j}{\partial x_i}\right) - \rho\overline{u_i' u_j'}\right]. \tag{3.16}$$

Equation Eqn. 3.16 shows the change in fluid element average momentum causing from the convection by the mean flow and unsteadiness in the mean flow. The isotropic stress from pressure field, average body force, the viscous stresses, and apparent stress $\left(-\rho\overline{u_i' u_j'}\right)$ due to the fluctuating velocity field, which is normally called as Reynolds stress balances this difference. Many different turbulent model creations were led by the attempt to make additional modelling to close this nonlinear Reynolds stress. The turbulence model selected for the simulations was $K-\omega$ turbulence model. $K-\omega$ is a two-equation turbulence model, which is used as a closure for RANS equations. This turbulence model tries to predict the turbulence by two partial differential equations, each for two variables, k and ω, with the first variable being the turbulence kinetic energy (k) and the second (ω) is the specific rate of dissipation of the turbulence kinetic energy k into internal thermal energy. The eddy viscosity v_T, as needed in the RANS equations, is given by: $v_T = k/\omega$, and the evolution of k and ω is modeled as given in equations Eqn. 3.17 and Eqn. 3.18

$$\frac{\partial(\rho k)}{\partial t}+\frac{\partial(\rho u_j k)}{\partial x_j}=P-\beta^*\rho\omega k+\frac{\partial}{\partial x_j}\left[\left(\mu+\sigma_k\frac{\rho k}{\omega}\right)\frac{\partial k}{\partial x_j}\right],\qquad P=\tau_{ij}\frac{\partial u_i}{\partial x_j}, \quad (3.17)$$

$$\frac{\partial(\rho\omega)}{\partial t}+\frac{\partial(\rho u_j\omega)}{\partial x_j}=\frac{\gamma\omega}{k}P-\beta\rho\omega^2+\frac{\partial}{\partial x_j}\left[\left(\mu+\sigma_\omega\frac{\rho k}{\omega}\right)\frac{\partial\omega}{\partial x_j}\right]+\frac{\rho\sigma_d}{\omega}\frac{\partial k}{\partial x_j}\frac{\partial\omega}{\partial x_j} \quad (3.18)$$

Segregated solver algorithm was selected for the simulation. In segregated solver approach, the governing equations are solved in sequential order segregated from one another. Since the governing equations are coupled and nonlinear, numerous iterations of the solution loop need to be carried out before solution is converged. Convection for this solving algorithm was selected as second order. Minimum absolute pressure was selected as 1000 Pa. Flow boundary diffusion and secondary gradients options were selected. Curvature correction option was not selected for $k-\omega$ model. Durbin scale limiter was selected as the realizability option. Minimum Tke and minimum Sdr value was selected as $1x10^{-10}$. These are the minimum values that the transported variable k and ω is permitted to have respectively. An appropriate value is a small number that is greater than the floating point minimum of the computer. Secondary gradients are selected on. Kappa value was given as $\kappa = 0.41$, $\beta^\star$ was given a value of 0.09. Other constant values that were given are $\beta_1 = 0.075$, $\sigma_{k1} = 0.85$, $\sigma_{w1} = 0.5$, $\beta_2 = 0.0828$, $\sigma_{k2} = 1.0$, $\sigma_{w2} = 0.856$, $a_1 = 0.31$, $\zeta^\star = 1.5$, realizability coefficient = 0.6. Hybrid Gauss-LSQ gradient method and Venkatakrishnan limiter method was used for gradient properties. Custom accuracy level was selected as two. Flat cells curvature criterion, cell skewness criterion and Chevron cell criterion was selected. Least squares tensor minimum Eigen values ratio was given as 0.1. Normalized flat cells curvature factor was given as 1.0. Maximum safe skewness angle was given as

75°. Minimum unsafe skewness angle was given as 88°. Acceptable field variation factor was given as 0.05. For the reference value minimum allowable wall distance was given as $1.0x10^{-6}m$. Reference pressure was given as atmospheric pressure, $101325Pa$. Initial pressure was same as reference pressure. Initial turbulence intensity value was given as 0.01. Turbulence condition was selected as intensity + viscosity ratio. Turbulence velocity scale was selected as 2m/s. Turbulent viscosity ratio was given as 10.0.

3.4.7 Physics in Regions

For the fluid domain region, velocity inlet is selected for inlet surface with velocity vector $2\hat{i}+0\hat{j}+0\hat{k}$ m/s. Velocity for the simulations for comparison is $1.2\hat{i}+0\hat{j}+0\hat{k}$ m/s. For the outlet surface, pressure outlet option was selected with back flow pressure as environmental pressure. The two surfaces with normal in Y and -Y direction were selected as symmetric planes. Now for the cylinder with hydrofoils, overset meshing was activated. Reference frame for three hydrofoils is region reference frame which is rotating with respective to lab frame with same rotational speed of the turbine. Shear stress specification for the hydrofoil surface was given No-Slip condition. Wall surface specification was given as smooth. For blended wall function log law offset E was given a value of 9.0 and Von Karman constant κ was given as 0.42. The cylindrical surface of hydrofoil was selected as overset boundary.

3.4.8 Solvers

Implicit- unsteady solvers were used for this simulation with a time step of 0.001s. The verification of the time step is given in later section. The temporal discretization was

selected as second order. For the overset solver for load balancing, acceptor weight was given as 1.0. The re-balance limit was given as 0.8 and re-balance period was given as 10 iterations. Domain partitioning method was selected per continuum. For the wall distance properties minimum tree size threshold value was given as $5x10^5$. For the segregated flow solver properties bad cell minimum scaling pressure correction value was given as 0.8. Acceptable volume cell change was given as 0.001. For velocity corrections, maximum unlimited velocity was given as 20m/s. Acceptable velocity increase rate is 0.15. Under-relaxation factor for velocity was given 0.8 and for pressure 0.2. For algebraic multigrid method (AMG) linear solver for velocity maximum number of cycles were given as 30, convergence tolerance was given as 0.1. Flexible type cycle was selected. Maximum direct solver equations were 32. Relaxation scheme was Gauss - Siedel. For the flexible cycle restriction tolerance was given as 0.9, prolongation tolerance value was 0.5. For the pressure AMG solver fixed type cycle was selected with maximum number of levels as 50 and post-sweeps as 2 and with no pre-sweeps. Under relaxation factor for $k-\omega$ turbulence was given as 0.8. AMG linear solver properties for this was same as that of the velocity solver. $k-\omega$ turbulent viscosity was given an under relaxation factor of 1.0 with a maximum ration of 10^5.

3.4.9 Rotational Motion

A rotating reference frame was created with the same rotational speed of the turbine with respective to the laboratory frame. The rotational motion was assigned to three overset cylinders with hydrofoil surface. The rotational speed for the base case was

60rpm. Three kind of rotational method was used for this research. First one with constant rpm, second with linearly varying rpm and one with automatically changing rpm after calculating the rotational acceleration. The last case resembles the real case turbine kept in ocean current. For the second case the rotational velocities at certain times are given in a table format. Star CCM+ would read it and linearly interpolate the rotational velocity in between and gives as input. The base case rpm was determined by using this method when turbine was allowed to start with 50 rpm and to increase up to 100 rpm in 5 seconds. The peak moment was around 60 rpm and thus it was selected. For the third kind idea was to create a new field function needed to be created which intake the moment each time, then calculate rotational acceleration and update the velocity. It was not working since it created loop since rotational velocity is not saved in two time levels. So a java macro was created to resolve the issue. This was done with the help of open resource from CFD forum website by author abdul099.The java macro script is given below.

```
packagemacro;
importstar.base.report.Report;
importstar.common.ImplicitUnsteadySolver;
importstar.common.PhysicalTimeStoppingCriterion;
importstar.common.Simulation;
importstar.common.StarMacro;
importstar.motion.MotionManager;
importstar.motion.RotatingMotion;
```

```
publicclassChangeOmegaextendsStarMacro{
publicvoidexecute(){
Simulationsim = getActiveSimulation();
RotatingMotionrotation = (RotatingMotion)
sim.get(MotionManager.class).getObject("Rotation");
ReporttorqueReport = sim.getReportManager().getReport("Totalmf123");
PhysicalTimeStoppingCriterionmaxTimeStoppingCriterion =
(PhysicalTimeStoppingCriterion)
sim.getSolverStoppingCriterionManager().
getSolverStoppingCriterion("MaximumPhysicalTime");
doublerotationRate = 0;
doubletimeStep = ((ImplicitUnsteadySolver)
sim.getSolverManager().
getSolver(ImplicitUnsteadySolver.class)).getTimeStep().getValue();
do{
if(sim.getSolution().getPhysicalTime() > 0){
doublecurrentTorque = torqueReport.getReportMonitorValue();
rotationRate = rotationRate + currentTorque * 1.5335 * timeStep;
rotation.getRotationRate().setValue(rotationRate);
}
sim.getSimulationIterator().step(1);
```

$\}while(!maxTimeStoppingCriterion.getIsSatisfied());$

$\}\}$

The rotational acceleration α_R is given by the relation M/I where M is the moment and I is the moment of inertia. Rotational velocity V_R is updated by adding $\alpha_R dt$ to the current V_R. The I value of $1.5335 kgm^2$ was found out using the equation $I = 3 \times 1 \times A_H \times \rho_w \times R^2$, where A_H is the area of the hydrofoil, depth is one meter, ρ_w is the density of wood and R is the radius of the turbine.

3.4.10 Stopping Criteria and Reports

The maximum inner iteration for the simulation was given as 20. This was selected after verification which is discussed in later section. Simulations were run for a physical time of two seconds considering the rotation per minute (rpm). Time history of drag force, lift force and moment on each of the hydrofoils and all combined was reported for all simulations.

3.5 Setup of Steady State Simulations

The setup for the steady state simulations are explained in this section. The setups which are identical with the rotational turbine case are not explained again.

3.5.1 Geometry and Import

The geometry of steady state simulation (SSS) consists of 15 bodies. Fourteen of them are the cylinders with hydrofoils each kept apart with a distance of 0.6m. This consists of 13 hydrofoil modified shapes (HM) from H00 HM00 to H00 HM12 of NACA0020

(H00) and H00 without modification. The definition of those modified shapes are given in the section 3.2.3. The fluid domain has the dimension of $9.6m \times 3.0m \times 0.5m$. The 3D geometry was created in AutoCAD was imported to Star CCM+ as an IGES file. The file was imported as a surface mesh. The geometry of the fluid domain can be seen from the Fig. 3.17

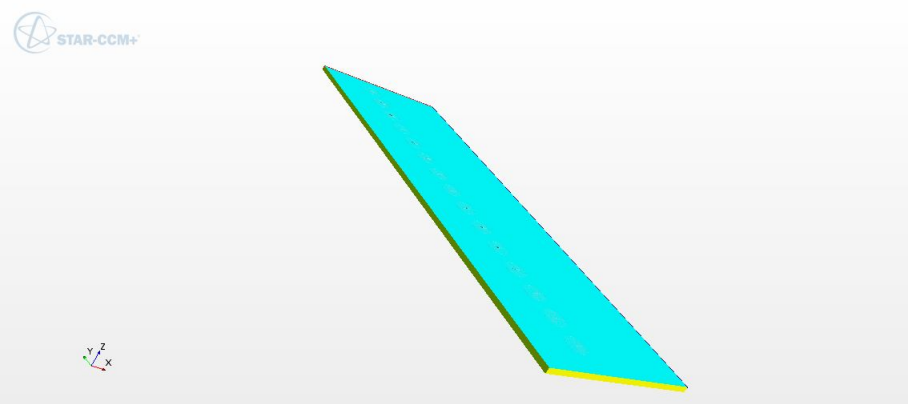

Figure 3.17: Geometry of SSS

The geometry of one of the overset cylinder with hydrofoil could be seen from the Fig. 3.18. The import mode was to create a new part. The mark feature edges in IGES import option was selected as sharp CAD edges with sharp edge angle of 30° with a sewing tolerance of 0.001. Create part contacts from coincident entities option was selected with a coincidence tolerance of $1.0x10^{-5}m$. Medium tessellation density was chosen which have curve chord tolerance of 0.03%, curve chord angle of 8°, surface plane tolerance of 0.03% and surface plane angle of 8°.

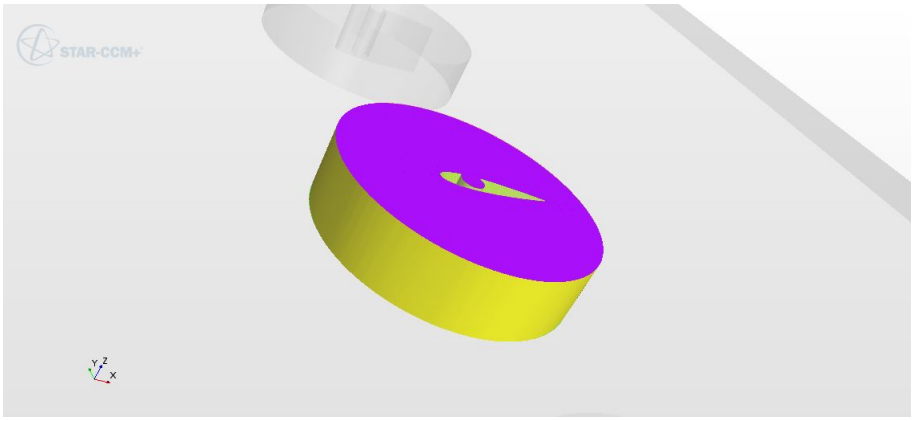

Figure 3.18: Overset Cylinder Hydrofoil Geometry

3.5.2 Creating Surfaces and Regions

Surfaces and regions for SSS are created in the same fashion as that of rotating turbine simulation (RTS) case. This is explained in section 3.3.2 and 3.3.3. There are 15 regions for this case instead of four for the RTS.

3.5.3 Meshing

The meshing type selected for SSS was polygonal meshing. Curvature refinement and proximity refinement were selected which is optional. In the expert polygonal mesher properties options were selected to retain geometric features and to create aligned meshes. Minimum face quality was chosen as 0.05. The base size was given as 0.01m as the same order that of chord length. Project to CAD option is selected. The target surface size was chosen as same as that of base size, 0.01m. The minimum surface size was given as 1% of the base size, 1×10^4. The surface curvature was selected as 36 points per circle. Surface growth rate was given as 1.1. After this in order to do the fine meshing in the regions near to the hydrofoils, custom control in automated 2D mesh was used. For each hydrofoil, a

cylinder of diameter 0.2m, length of 0.7m along X axis was used. In order to do the fine meshing in the region of void, another small cylinder of radius 0.03m and length of 0.05m along the y axis was used for all the fourteen hydrofoils. The mesh of SSS could be seen in the Fig. 3.19

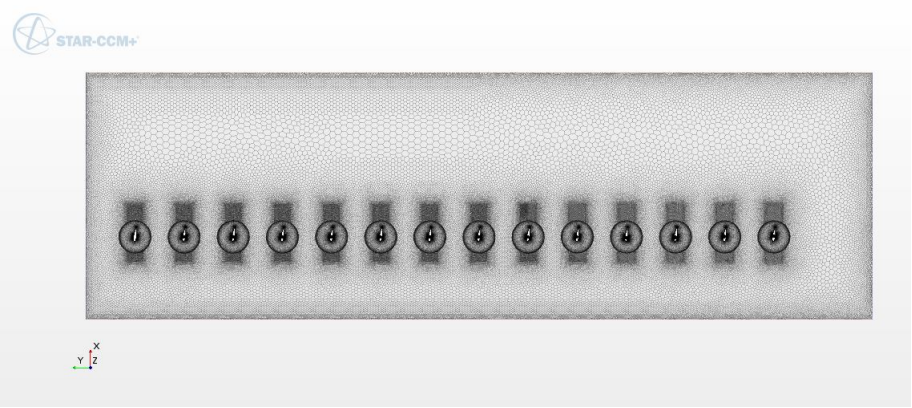

Figure 3.19: Mesh for Steady State Simulation

The fine meshing cylinder around hydrofoils could be seen in the Fig. 3.20. In custom control for both cylinders 2D surface mesher control was selected. For the larger cylinder custom size was selected as 40% of the base size, 0.004m. For the cylinder around cavity custom size selected was 20%, 0.0004m. It could be seen from Fig. 3.20 that along the x axis direction of hydrofoil fine mesh in shape of a rectangle which corresponds to the bigger cylinder and there was finer mesh at the void corresponds to the region inside smaller cylinder. Closer look at the mesh near the center could be seen from the Fig. 3.21

After the meshing of fluid domain, the next part was the meshing of fourteen cylindrical hydrofoil regions. The meshing type selected was polygonal meshing and prism

layer meshing. For polygonal meshing, curvature refinement and proximity refinement were selected which is optional. In the expert polygonal mesher properties options were selected to retain geometric features and to create aligned meshes. Minimum face quality was chosen as 0.05. The base size was given as 0.002m. Target surface size was selected as same as that of base size, 0.002m. Minimum surface size was selected as 1% of the base size $2x10^{-5}m$. Basic surface curvature was selected as 36 points per circle. Surface growth rate was selected as 1.1. For the prism layer meshing, stretching function was given as geometric progression. Distribution mode was chosen as stretch factor. Gap fill was given as 25%. Minimum thickness was given as 10%. Layer reduction was given as 50%. In expert prism layer mesher properties, boundary march angle was given as 50°. Concave angle limit was given as 0° and convex angle limit was given as 360°. Number of prism layer was chosen as 5. Prism layer stretching factor was given as 1.5. Total thickness of prism layer was given as 25% of base size, $5x10^{-4}m$. The prism layer meshing could be seen from the Fig. 3.22

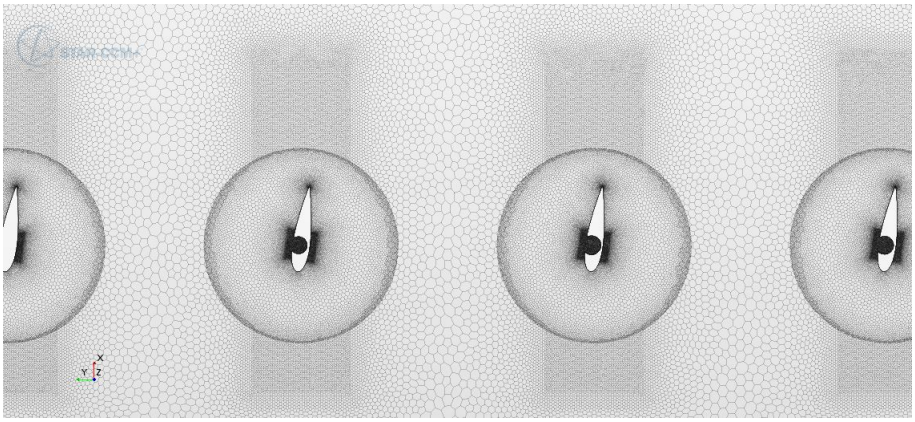

Figure 3.20: Fine and Overset Meshing for SSS

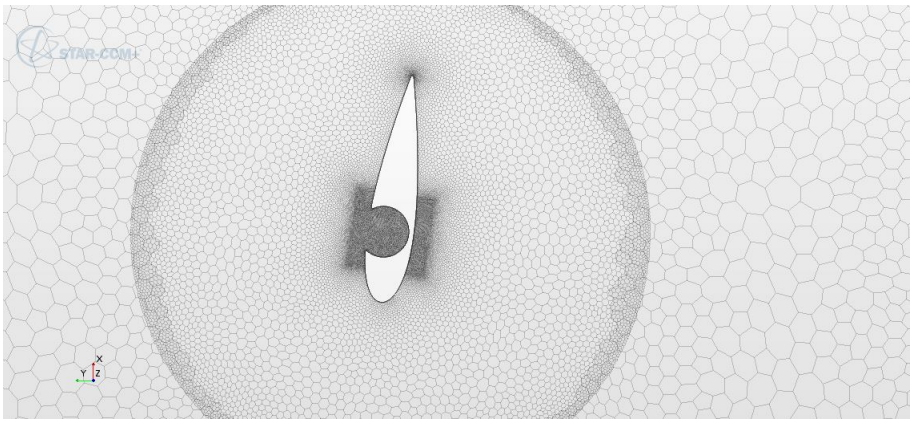

Figure 3.21: 2D Fine Mesh Near Hydrofoil

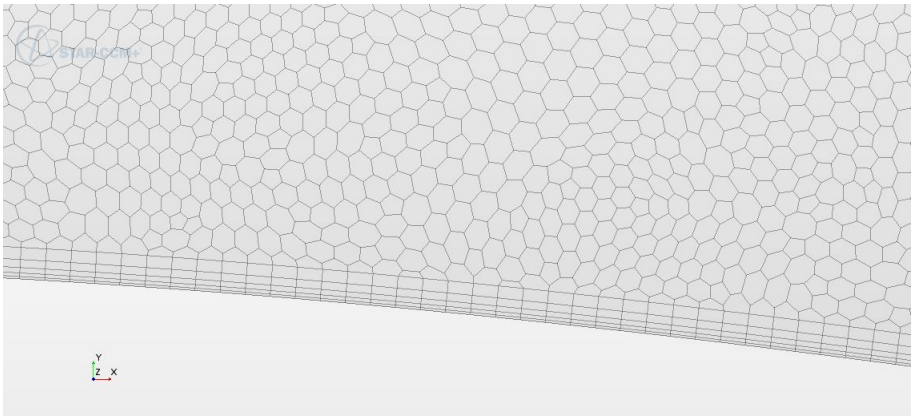

Figure 3.22: Prism Layer Meshing for SSS

3.5.4 Overset Meshing

Overset meshes that were used for Steady State Simulations are same as that of the rotating turbine simulation except that instead of three overset regions, there were fourteen overset regions. The details of overset meshing for RTS is given in section 3.3.5.

3.5.5 Physics for SSS

For the case considered there is only one kind of physics is required for the entire domain. The fluid is selected as water with constant density of $997.56 kg/m^3$ with a dy-

namic viscosity of $8.89x10^{-4} Pa\ s$. The implicit unsteady model was selected. The flow was solved by solving Reynolds Averaged Navier - Stokes (RANS) model equations. The turbulence model selected for the simulations was $K-\omega$ turbulence model. Segregated solver algorithm was selected for the simulation. Convection for this solving algorithm was selected as second order. Minimum absolute pressure was selected as 1000 Pa. Flow boundary diffusion and secondary gradients options were selected. Curvature correction option was not selected for $k-\omega$ model. Durbin scale limiter was selected as the realizability option. Minimum Tke and minimum Sdr value was selected as $1x10^{-10}$. Secondary gradients are selected on. Kappa value was given as $\kappa = 0.41$, $\beta^{\star}$ was given a value of 0.09. Other constant values that were given are $\beta_1 = 0.075$, $\sigma_{k1} = 0.85$, $\sigma_{w1} = 0.5$, $\beta_2 = 0.0828$, $\sigma_{k2} = 1.0$, $\sigma_{w2} = 0.856$, $a_1 = 0.31$, $\zeta^{\star} = 1.5$, realizability coefficient = 0.6. Hybrid Gauss-LSQ gradient method and Venkatakrishnan limiter method was used for gradient properties. Custom accuracy level was selected as two. Flat cells curvature criterion, cell skewness criterion and Chevron cell criterion was selected. Least squares tensor minimum Eigen values ratio was given as 0.1. Normalized flat cells curvature factor was given as 1.0. Maximum safe skewness angle was given as 75°. Minimum unsafe skewness angle was given as 88°. Acceptable field variation factor was given as 0.05. For the reference value minimum allowable wall distance was given as $1.0x10^{-6}m$. Reference pressure was given as atmospheric pressure, $101325Pa$. Initial pressure was same as reference pressure. Initial turbulence intensity value was given as 0.01. Turbulence condition was selected as intensity + viscosity ratio. Turbulence velocity scale was selected as 4m/s. Turbulent

viscosity ratio was given as 10.0. For the fluid domain region, velocity inlet is selected for inlet surface with velocity vector $4\hat{i}+0\hat{j}+0\hat{k}$. For the outlet surface, pressure outlet option was selected with back flow pressure as environmental pressure. The two surfaces with normal in Y and -Y direction were selected as symmetric planes. Now for the cylinder with hydrofoils, overset meshing is activated. Shear stress specification for the hydrofoil surface was given no-slip condition. Wall surface specification was given as smooth. For blended wall function log law offset E was given a value of 9.0 and Von Karman constant κ was given as 0.42. The cylindrical surface of hydrofoil was selected as overset boundary.

3.5.6 Solvers

Implicit-unsteady solvers were used for this simulation with a time step of 0.001s. The verification of the time step is given in appendix. The temporal discretization was selected as second order. For the overset solver for load balancing, acceptor weight was given as 1.0. The re-balance limit was given as 0.8 and re-balance period was given as 10 iterations. Domain partitioning method was selected per continuum. For the wall distance properties minimum tree size threshold value was given as $5x10^5$. For the segregated flow, solver properties bad cell minimum scaling pressure correction value was given as 0.8. Acceptable volume cell change was given as 0.001. For velocity corrections, maximum unlimited velocity is given as 20m/s. Acceptable velocity increase rate is 0.15. Under-relaxation factor for velocity was given 0.8 and for pressure 0.2. For algebraic multigrid method (AMG) linear solver for velocity maximum number of cycles were given as 30, convergence tolerance was given as 0.1. Flexible type cycle was selected. Maximum

direct solver equations were 32. Relaxation scheme was Gauss - Siedel. For the flexible cycle restriction tolerance was given as 0.9, prolongation tolerance value was 0.5. For the pressure AMG solver fixed type cycle is selected with maximum number of levels as 50 and post-Sweeps as 2 and with no pre-Sweeps. Under relaxation factor for $k-\omega$ turbulence was given as 0.8. AMG linear solver properties for this was same as that of the velocity solver. $k-\omega$ turbulent viscosity was given an under relaxation factor of 1.0 with a maximum ration of 10^5.

3.5.7 Stopping Criteria and Reports

The maximum inner iteration for the simulation was given as 20. This was selected after verification which is discussed in later section. Simulations were run for a physical time of one second. Time history of drag force and lift force on each of the fourteen hydrofoils was reported for all eight simulations.

3.6 Running the Simulation

All the simulations were run using parallel computing. More than 7000 computing hours were used for this research. Ada super computer cluster provided by Texas A&M University was used for this. Number of cores were selected after running simulation for 10-time step with different number of core. The version of software used for this research is Star CCM+ 10.06.010. This results are given in verification section. An example batch job script for the simulation looks as follows.

#BSUB -J starccm

```
#BSUB -o starccm.
#BSUB -L /bin/bash
#BSUB -W 3:00
#BSUB -M 1000
#BSUB -R 'rusage[mem=1000]'
#BSUB -n 10
#BSUB -R 'span[ptile=20]'
module load STAR-CCM+
starccm + -rsh blaunch -np 20 -batch ChangeOmega.java -
collab ND4_Auto2nd.sim -machinefile $LSB_DJOB_HOSTFILE
```

4 CFD SIMULATIONS

This chapter show the outputs of the 70 numerical simulations that were carried out for this research. the parameter input for all simulations SIM01 to SIM70 are given in tables from Table 3.8 to Table 3.14 in section 3.3.1. The 70 simulations could be divided in to five sections. The first section consists of Rotating Turbine simulations(RTS). These simulations were performed to find the best hydrofoil shape (H) among all the tested ones for the maximum power efficiency. The second section of simulations consists of simulations for finding the best modified hydrofoil shape (HM). The third section of simulations consists of finding the best pitch angle (β). The fourth section consists of finding the best tip speed ratio (λ), the fifth section consists of finding the best solidity value (σ). Other sections which consists of simulation of double layer foils and comparison of experimental result in the same scale is given in appendix. In this chapter all the simulation outputs are not included since there are many. The outputs of all the simulations are provided in the appendix. Only relevant simulation results are presented here.

4.1 Section I Simulations

The section I consists of simulations which were carried out in order to find the best hydrofoil cross section shape (H). All the hydrofoils used for these simulations are NACA foils. For the asymmetric foils there are two cases, one with camber pointing towards center and camber pointing outwards. There are 20 simulations in this section, SIM01 to SIM21

except SIM14 which is a modified case. The only variation from the base case for these simulations are the hydrofoil shape H. These are without modifications, i.e HMXX. The input parameters could be understood from the simulation name explained in the naming section in methodology chapter. The definitions of the hydrofoil shapes (H) are given in Table 3.1. Hydrofoil shape used for all the simulations in this section is given in Table 4.1 and Table 4.2. CM in tables stands for camber. 0 for CM stands for symmetric hydrofoil, 1 represents camber pointing outwards and 2 represents camber pointing inwards. Hydrofoils in all rotating turbine simulations are named as A, B and C where A corresponds the hydrofoil making 0° with Y axis at time t = 0s in anti-clockwise direction, the hydrofoil making 120° is named as B and hydrofoil C makes an angle of 240° with Y axis. For the plot of moment with θ angle corresponds to the rotation angle of turbine starting with 0° at t = 0 s.

4.1.1 Base Case Simulation SIM13

The base case parameters are flow velocity V=2m/s, hydrofoil shape H= NACA0020, Chord length C = 0.1778m, diameter D = 0.6096m, solidity σ = 0.2785 (S4), tip speed ratio λ = 0.958 (L02), Number of layers N=1, number of blades n=3 and pitch angle $\beta = 0°$ (B4). The final velocity profile of this simulation is given in the Fig. 4.1 and the final pressure profile of final the simulation is given in the Fig. 4.2 The final time is 2 seconds. The time history of the moment on each of the hydrofoils and total moment is given in the Fig. 4.3

From analyzing the Fig. 4.3 in MATLAB, it could be seen that the first maximum moment peak of hydrofoil A happens as t = 0.178s with a value of 279.9Nm and at an

angle of 64.08°. The next maximum moment peak is for hydrofoil C. The maximum moment peak of hydrofoil C happens as t = 0.551s with a value of 252.8Nm and at an angle of 198.36°. The position of C is 78.36°.

Table 4.1: Simulations SIM01 to SIM10 Properties

SIM	Name	H	CM
SIM01	S11010XX0244	H01	0
SIM02	S11020XX0244	H02	0
SIM03	S11030XX0244	H03	0
SIM04	S11040XX0244	H04	0
SIM05	S11050XX0244	H05	0
SIM06	S11061XX0244	H06	1
SIM07	S11071XX0244	H07	1
SIM08	S11081XX0244	H08	1
SIM09	S11091XX0244	H09	1
SIM10	S11101XX0244	H10	1

The first maximum moment peak of hydrofoil B happens as t = 0.891s with a value of 240.6Nm and at an angle of 320.76°. The position of B at this point is 80.76°. The second maximum moment peak of the hydrofoil A occurs at time t = 1.225s with a value of 232.7 Nm and at a rotation angle of 441°. The position of the hydrofoil A at this time is 81°. The second maximum moment peak of hydrofoil C happens as t = 1.561s with a

value of 242.3Nm and at an angle of 561.96°. The position of hydrofoil C at this point is 81.96°. The second maximum moment peak of hydrofoil B happens as t = 1.892s with a value of 230.0Nm and at an angle of 681.12°. The position of hydrofoil C at this point is 81.12°.

Table 4.2: Simulations SIM11 to SIM20 Properties

SIM	Name	H	CM
SIM11	S11110XX0244	H11	0
SIM12	S11120XX0244	H12	0
SIM13	S11000XX0244	H00	0
SIM15	S11062XX0244	H06	2
SIM16	S11072XX0244	H07	2
SIM17	S11082XX0244	H08	2
SIM18	S11092XX0244	H09	2
SIM19	S11102XX0244	H10	2
SIM20	S11112XX0244	H11	2
SIM21	S11122XX0244	H11	2

Analyzing the position of hydrofoils with peak moment it is found that maximum moment occurs at every time between 78° to 82° for all the hydrofoils A, B and C except for the first peak for hydrofoil A which occurs at 64°. But looking at the plot it could be understood that for at least the initial 100° of rotation angle it is not stabilized. So

we neglect the moment time history till the first 120°. Results from other simulations also shows instability for initial 100° of rotation angle. So while calculating the average moment for all simulations, first 120° is not considered. The velocity profile at second peak of hydrofoil A is shown in the Fig. 4.4. A close look at hydrofoil position at 81 could be seen in the Fig. 4.5. The pressure profile at the maximum moment point seen in the Fig. 4.6. The pressure profile around the hydrofoil at maximum moment position could be seen in the Fig. 4.7

The time history of lift and drag force on the hydrofoils in global coordinate system could be seen from the figures Fig. 4.9 and Fig. 4.8 respectively. GC stands for global coordinate and LC stands for local coordinate, where M is the moment produced by considered hydrofoil at the center of turbine, $D_{(LC)}$ is drag force in local coordinate (LC) is the lift force in local coordinate and DP is lever-arm for lift force. For t = 1.225 s, for hydrofoil A M=232.7Nm, $D_{(LC)} = -612N$, $L_{LC} = -2000N$, substituting we get DP (1.225) = 0.02308m.

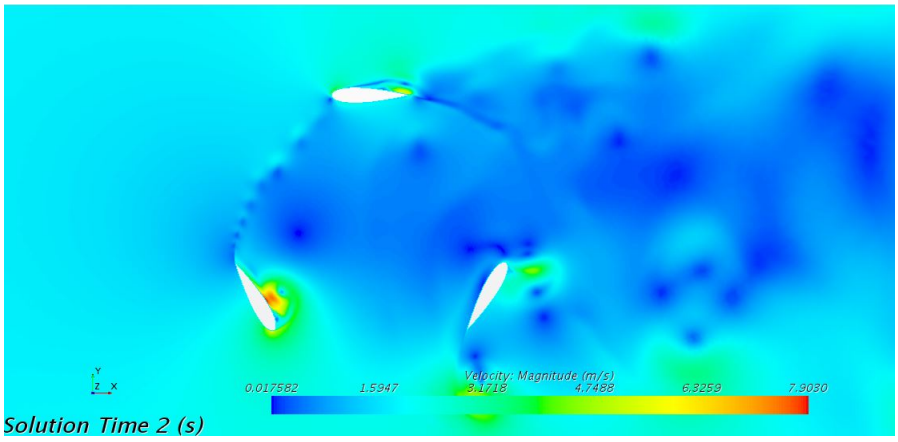

Figure 4.1: Base Case SIM13 Velocity Profile at 2 Seconds

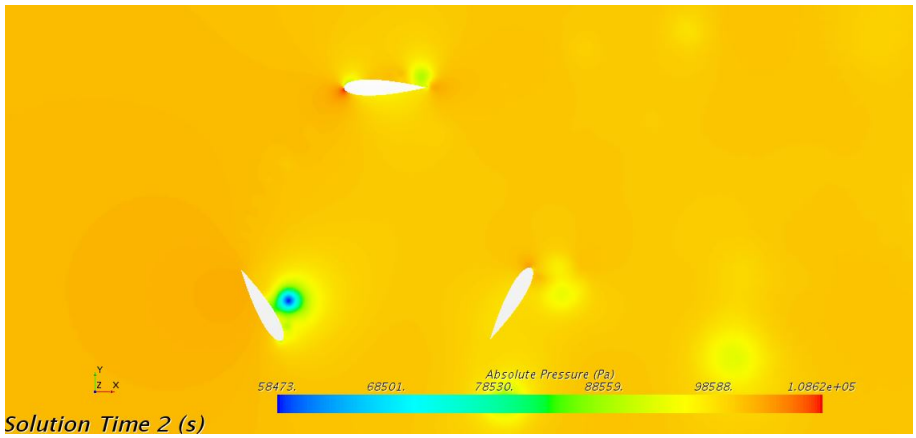

Figure 4.2: Base Case SIM13 Pressure Profile at 2 Seconds

The angle of attack α at hydrofoil position of θ is given by the equation Eqn. 4.10 and the relative velocity to a hydrofoil along X axis tail pointing toward positive X axis is $(R\omega + V\cos(\theta))\hat{i} - V\sin(\theta)\hat{j}$. The variation of angle of attack α with hydrofoil position θ is given in the Fig. 4.12. The variation of magnitude of relative velocity with hydrofoil position is given in the Fig. 4.13. So using these the angle of attack and relative velocity magnitude for maximum moment hydrofoil position is $-41.56°$ and $2.978 m/s$.

The angle of attack and pitch angle of hydrofoils varies throughout the rotation. So in order to understand the physics better the lift force in local coordinate (LC) is derived from GC using the equations Eqn. 4.1, Eqn. 4.2 and Eqn. 4.3.

$$L_{A(LC)}(t) = L_{A(GC)}(t)\cos(\theta) - D_{A(GC)}(t)\sin(\theta) \tag{4.1}$$

$$L_{B(LC)}(t) = L_{B(GC)}(t)\cos(\frac{2\pi}{3} + \theta) - D_{B(GC)}(t)\sin(\frac{2\pi}{3} + \theta) \tag{4.2}$$

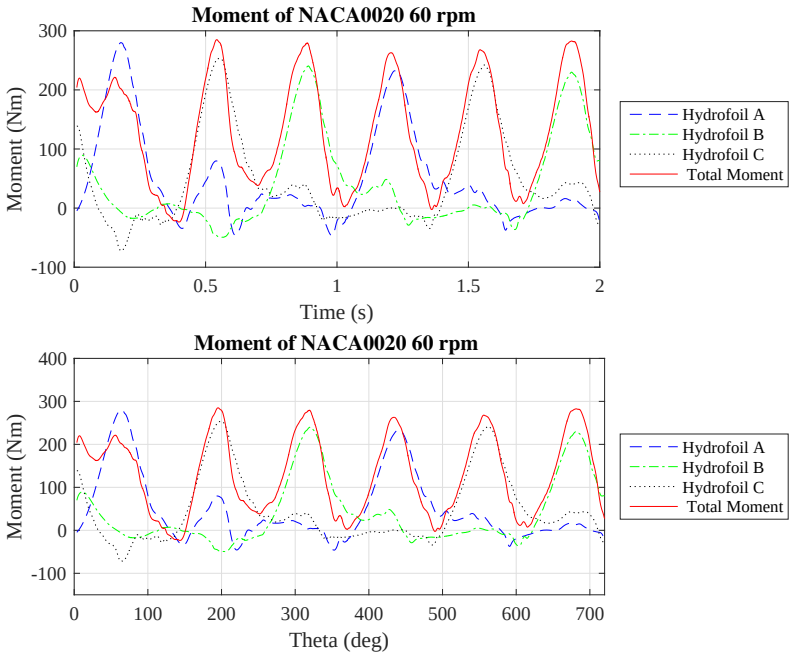

Figure 4.3: Base Case SIM13 Moment Plot

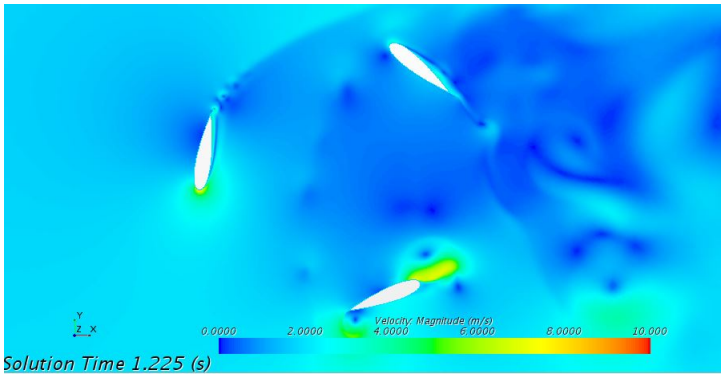

Figure 4.4: Maximum Moment Velocity Profile t = 1.225 s SIM13

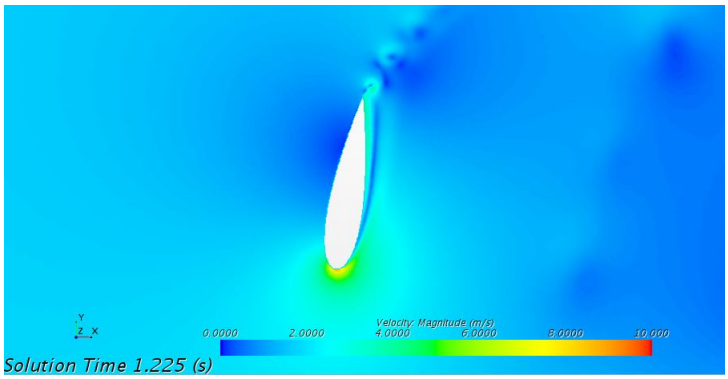

Figure 4.5: Velocity Profile Around Hydrofoil at Maximum Moment

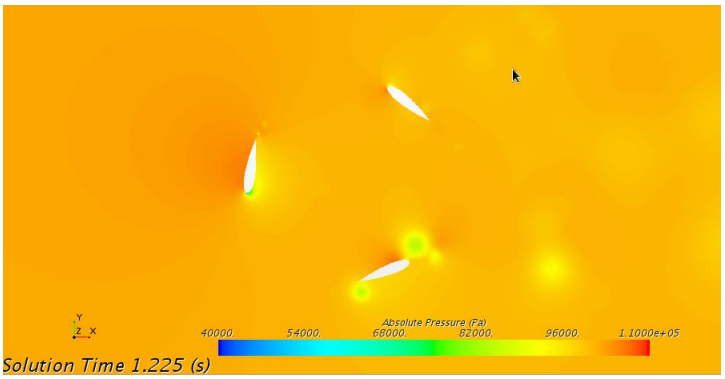

Figure 4.6: Pressure Profile of Turbine at Maximum Moment Position

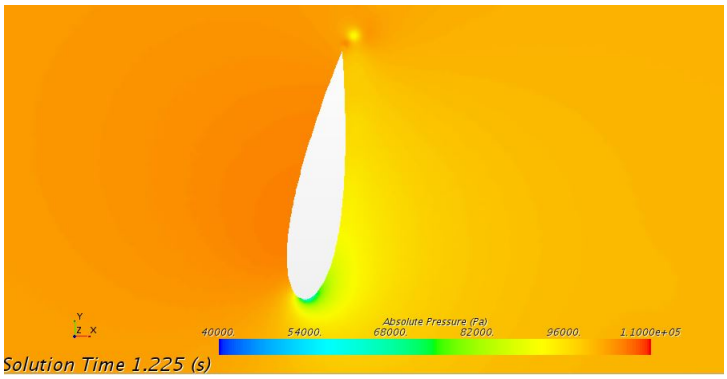

Figure 4.7: Pressure Profile of Turbine at t = 1.225 s

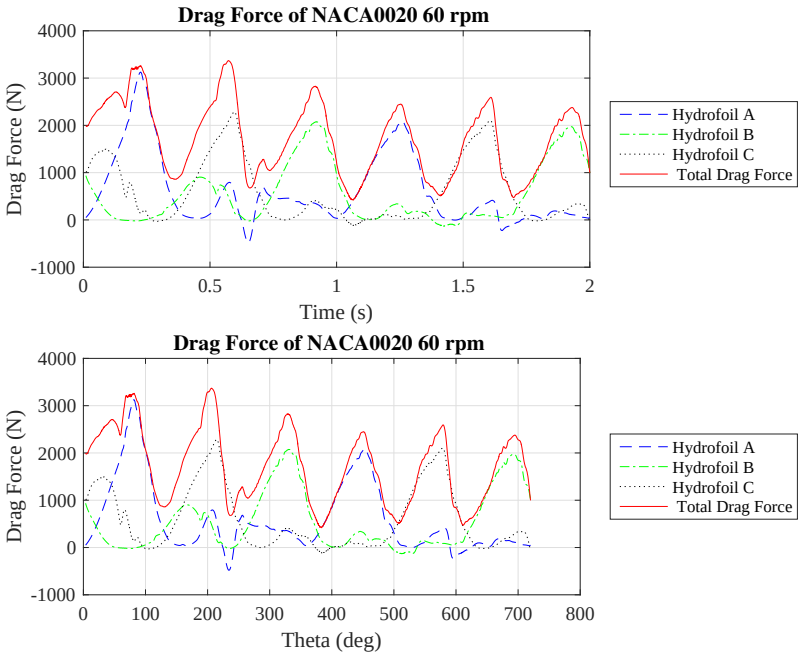

Figure 4.8: Drag Force of SIM 13 in GC

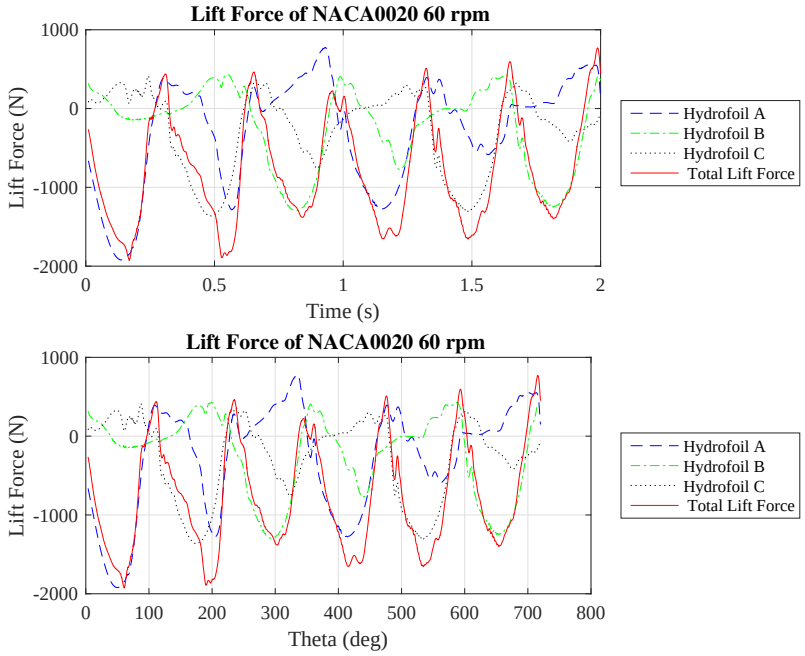

Figure 4.9: Lift Force of SIM13 in GC

$$L_{C(LC)}(t) = L_{C(GC)}(t)\cos(\frac{4\pi}{3}+\theta) - D_{C(GC)}(t)\sin(\frac{4\pi}{3}+\theta) \tag{4.3}$$

Similarly, the drag force in LC for each hydrofoil could be found out using the equations Eqn. 4.4, Eqn. 4.5 and Eqn. 4.6.

$$D_{A(LC)}(t) = L_{A(GC)}(t)\sin(\theta) + D_{A(GC)}(t)\cos(\theta) \tag{4.4}$$

$$D_{B(LC)}(t) = L_{B(GC)}(t)\sin(\frac{2\pi}{3}+\theta) + D_{B(GC)}(t)\cos(\frac{2\pi}{3}+\theta) \tag{4.5}$$

$$D_{C(LC)}(t) = L_{C(GC)}(t)\sin(\frac{4\pi}{3}+\theta) + D_{C(GC)}(t)\cos(\frac{4\pi}{3}+\theta) \tag{4.6}$$

Using these equations, lift and drag force in local coordinate system are plotted in the Fig. 4.10

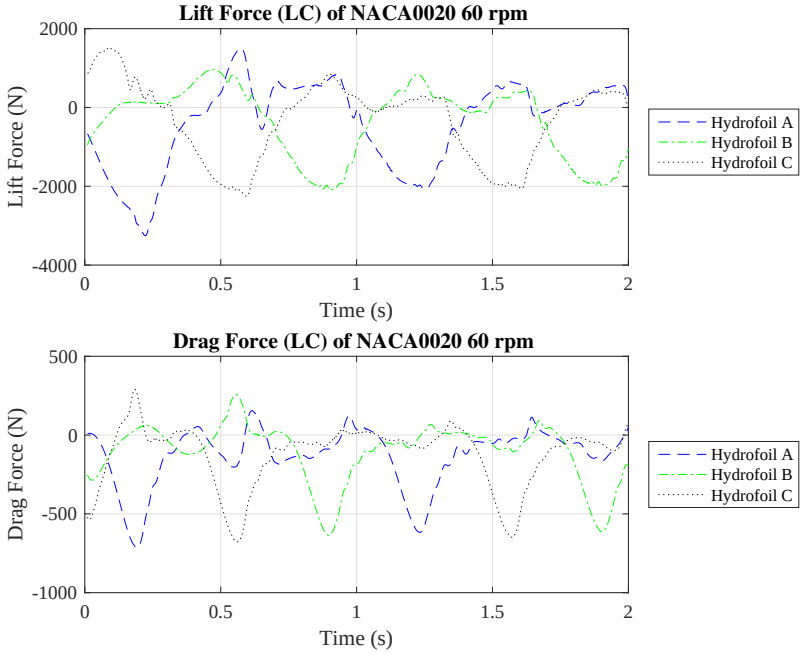

Figure 4.10: Lift and Drag Force of SIM13 in LC

Using the local coordinate lift and drag force and knowing the moment, the per-

pendicular distance from center of pressure (DP) to the center of the LC system could be found out approximately using the equation. It is derived based on the Fig. 4.11. This is an approximation. The exact center of pressure has also been found it. For this for required time step, the required hydrofoil is split into 100 bins in X and Y (GC) direction when forces on each bin in Y and X (GC) is extracted. Then their moments are calculated with respective to center of turbine and center of pressure is determined. The equation Eqn. 4.8 and Eqn. 4.9 shows this where CP_X is the X coordinate (GC) of the center of pressure.

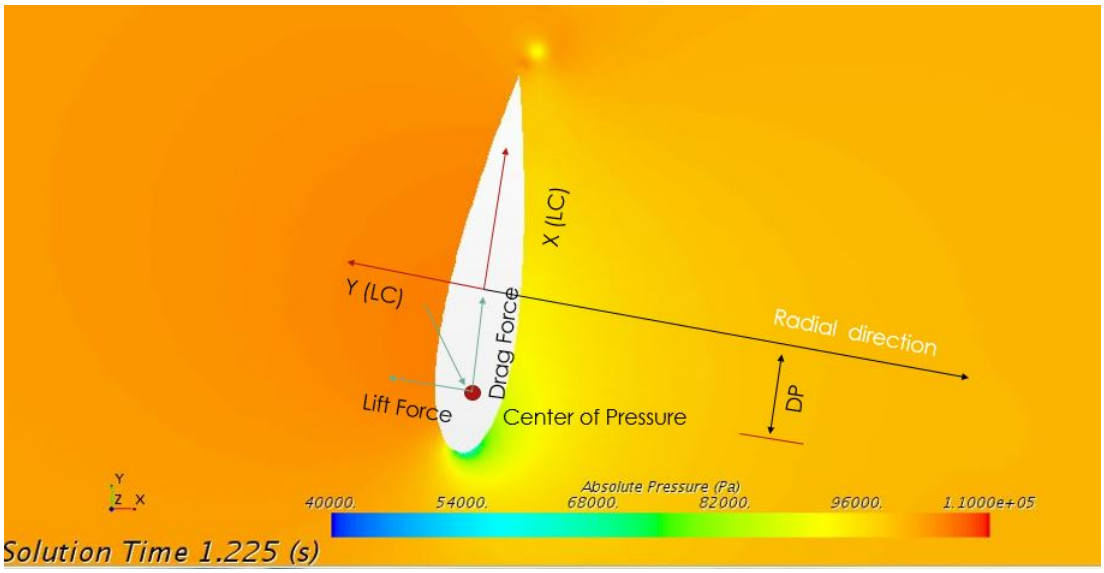

Figure 4.11: Estimation of DP

$$DP(t) = -\frac{M + \left(D_{(LC)}R\right)}{L_{LC}} \tag{4.7}$$

$$CP_X = \frac{\Sigma(-Y \times F_X)}{\Sigma F_X} \tag{4.8}$$

$$CP_Y = \frac{\Sigma(X \times F_Y)}{\Sigma F_Y} \tag{4.9}$$

$$\alpha = \tan^{-1} \frac{-V \sin(\theta)}{R\omega + V \cos(\theta)} \tag{4.10}$$

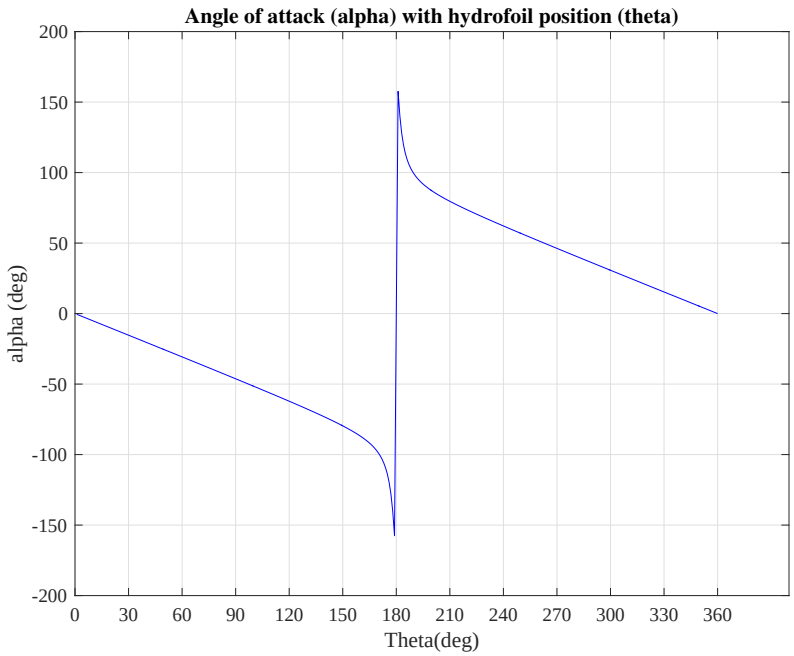

Figure 4.12: Angle of Attack and Hydrofoil Position

4.1.2 Average Moment of Section I Simulations

The average total moment of section I simulations is given in the Table 4.3. Focus is given only for those hydrofoils with the best and worst average moment with and without camber. For the calculation of average moment average is taken from trough of the first peak total moment to the trough of fifth peak. First peak is not considered due to the initial instability and the last peak is not considered since it is not complete. AM stands for average moment in the table and Hyd. stands for hydrofoil. The unit is Nm for all values

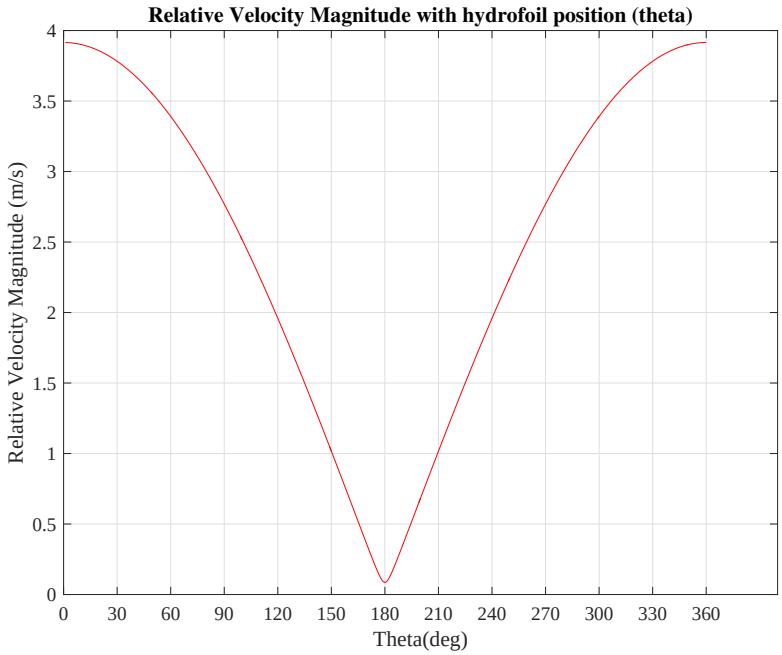

Figure 4.13: Angle of Attack and Velocity Magnitude

According to the results of the section I simulations, the simulation with maximum total average moment is SIM04 corresponding to hydrofoil H04 which is NACA0018 with a moment of 135.72Nm. The simulation with the least total average moment comes to be SIM01 corresponding to hydrofoil H01 which is NACA0006 with a moment of 43.84Nm. The range of total average moment of symmetric foil is 43.84 Nm to 135.72 while the range of asymmetric hydrofoils is from 51.56Nm for SIM12 to 129.58 for SIM19 corresponding to NACA6409 and NACA2424. Among cases with camber pointing outwards the range is from 51.56Nm to 121.75Nm corresponding to NACA6409 and NACA2424. Among the cases with camber pointing inwards the range is from 68.7Nm to 129.58 corresponding to NACA2408 and NACA2424. The considerable difference in the mean moment values of

hydrofoil A, B and C is due to the reason that individually they are not averaged in same phases. Each of them have completed one rotation but not two. So cannot be compared. This is the reason it could be seen that all cases average moments are in specific order as C>A>B. From this analysis two cases of simulations are chosen in order to compare with the base case, SIM04 and SIM01 the Simulations with best and least performance.

4.1.3 Most Efficient Turbine of Section I SIM04

The hydrofoil shape for SIM04 was H= NACA0018. Other input parameters are flow velocity V=2m/s, Chord length C = 0.1778m, diameter D = 0.6096m, solidity σ = 0.2785 (S4), tip speed ratio λ = 0.958 (L02), Number of layers N=1, number of blades n=3 and pitch angle $\beta = 0°$ (B4). The final velocity profile of this simulation is given in the Fig. 4.15 and the final pressure profile of final the simulation is given in the Fig. 4.14 The final time is 2 seconds. The time history of the moment on each of the hydrofoils and total moment is given in the Fig. 4.16.

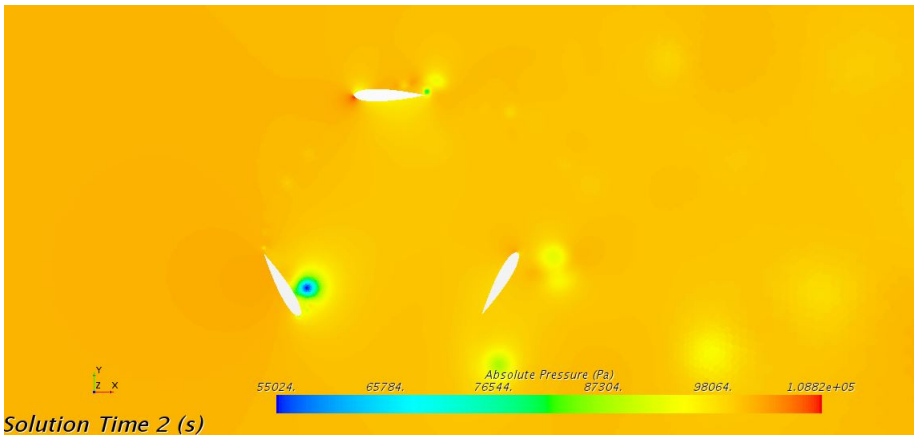

Figure 4.14: SIM04 Pressure Profile at 2 Seconds

Table 4.3: Average Total Moments of Section I SIM01 - SIM10

SIM	Total AM	Hyd. A AM	Hyd. B AM	Hyd. C AM
SIM01	43.84	11.44	8.06	24.33
SIM02	70.20	18.65	14.97	36.58
SIM03	98.60	28.90	21.00	48.68
SIM04	135.72	38.00	30.13	67.59
SIM05	135.70	41.32	29.81	64.57
SIM06	81.90	20.42	20.90	40.58
SIM07	55.01	16.19	8.53	30.28
SIM08	87.22	24.54	21.68	40.99
SIM09	112.99	34.31	25.93	52.74
SIM10	121.75	33.61	28.24	59.90

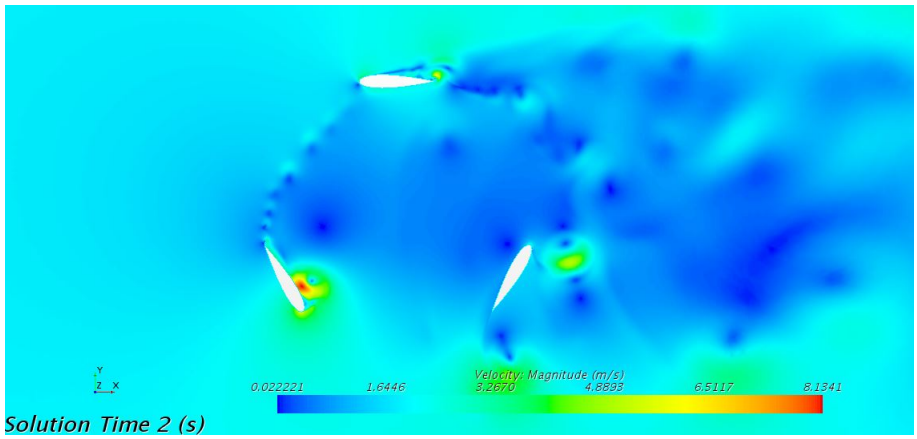

Figure 4.15: SIM04 Velocity Profile at 2 Seconds

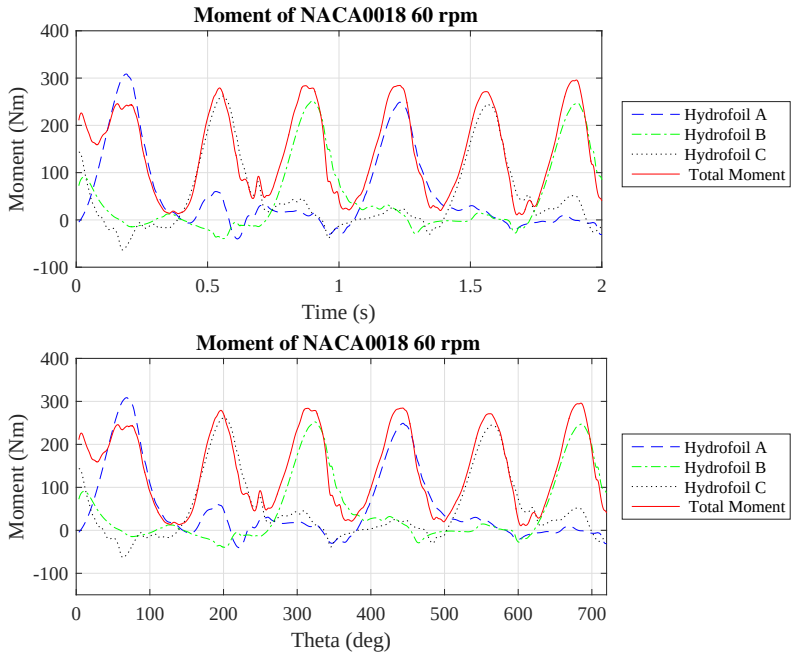

Figure 4.16: SIM04 Moment Plot

In order to compare with the base case, the second maximum moment peak of hydrofoil A is chosen. The second maximum moment (MM) peak of the hydrofoil A occurs at time t = 1.232s with a value of 249 Nm and at a rotation angle of 443.52°. The position of the hydrofoil A at this time is 83.52°. But the nearest stored data points for velocity profile are at t = 1.22s and t = 1.24s. So t = 1.22 s is selected for analysis where moment is 245Nm and position is 79.2°. The velocity profile at second peak of hydrofoil A is shown in the Fig. 4.17. A close look at hydrofoil position at 79.2° could be seen in the Fig. 4.18. The pressure profile at the maximum moment point seen in the Fig. 4.19. The pressure profile around the hydrofoil at maximum moment position could be seen in the Fig. 4.20

Table 4.4: Average Total Moments of Section I SIM11 -SIM21

SIM	Total AM	Hyd. A AM	Hyd. B AM	Hyd. C AM
SIM11	110.26	32.97	25.51	51.78
SIM12	51.56	21.90	15.14	14.52
SIM13	122.47	34.83	25.07	62.57
SIM15	84.62	20.60	18.33	45.68
SIM16	68.70	16.76	11.91	40.03
SIM17	98.50	27.32	19.68	51.50
SIM18	121.51	33.59	26.43	61.49
SIM19	129.58	35.43	25.78	68.37
SIM20	122.69	32.90	22.69	67.10
SIM21	101.95	25.69	19.32	56.94

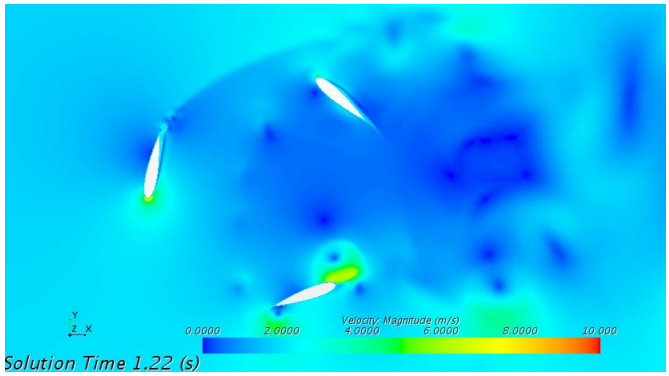

Figure 4.17: Velocity Profile at t = 1.22 s SIM04

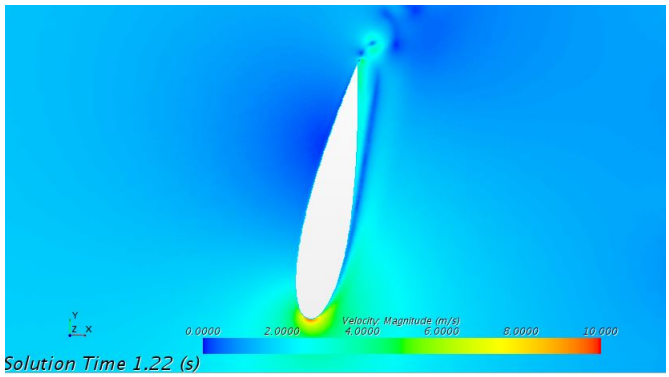

Figure 4.18: Velocity Profile Around Hydrofoil at Maximum Moment SIM04

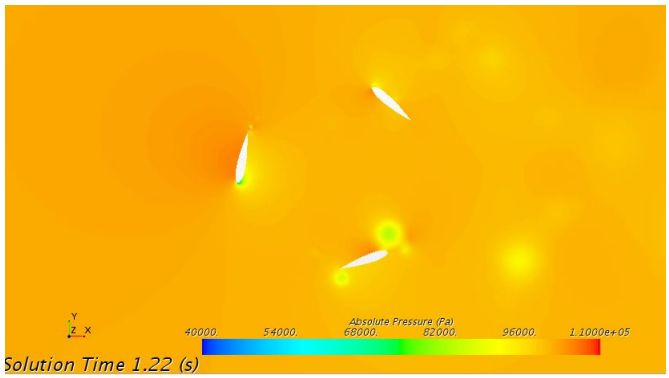

Figure 4.19: Pressure Profile of Turbine at t = 1.22 s SIM04

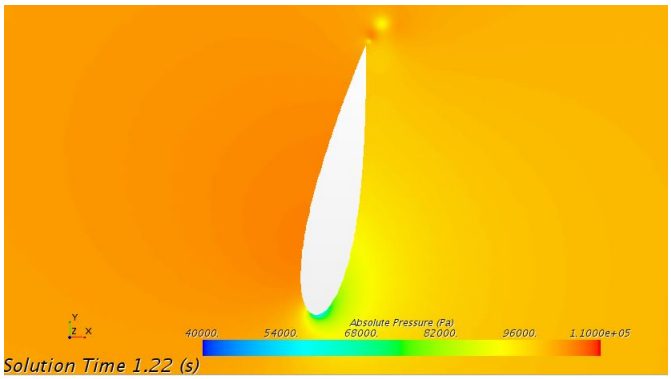

Figure 4.20: Pressure Profile Around Hydrofoil at Peak Moment

The time history of lift and drag force on the hydrofoils in global coordinate system could be seen from the figures Fig. 4.22 and Fig. 4.21 respectively. GC stands for global

coordinate and LC stands for local coordinate.

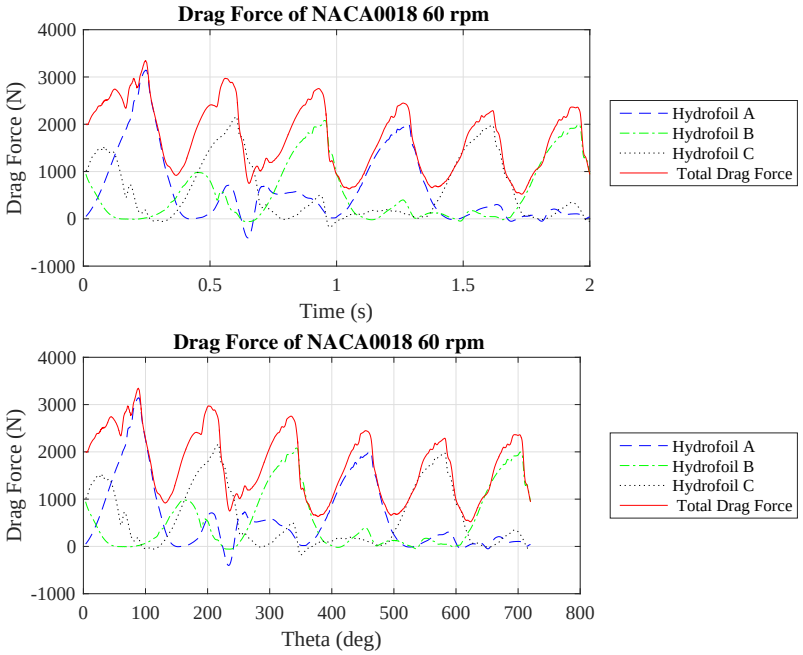

Figure 4.21: Drag Force of SIM04 in GC

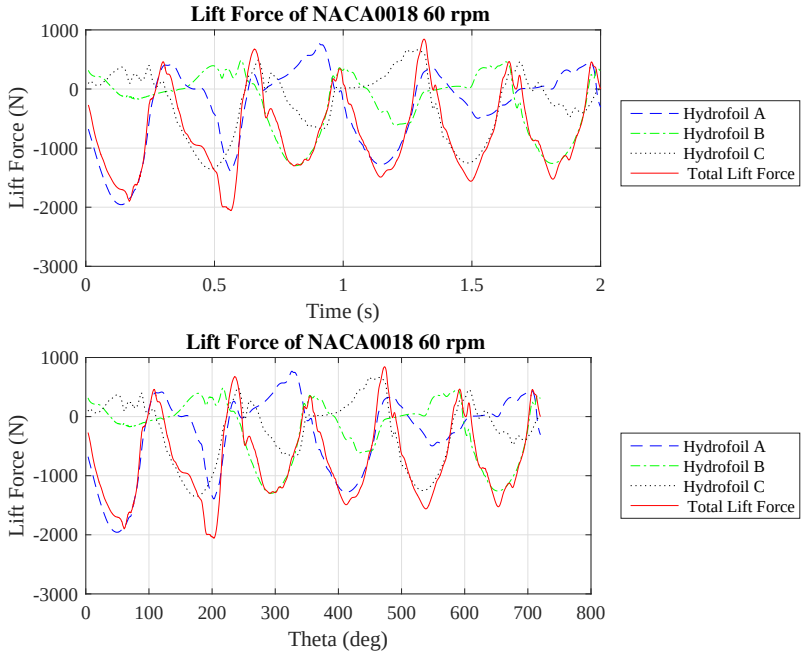

Figure 4.22: Lift Force of SIM04 in GC

The lift and drag force of SIM04 in local coordinate (LC) are plotted in the Fig. 4.23

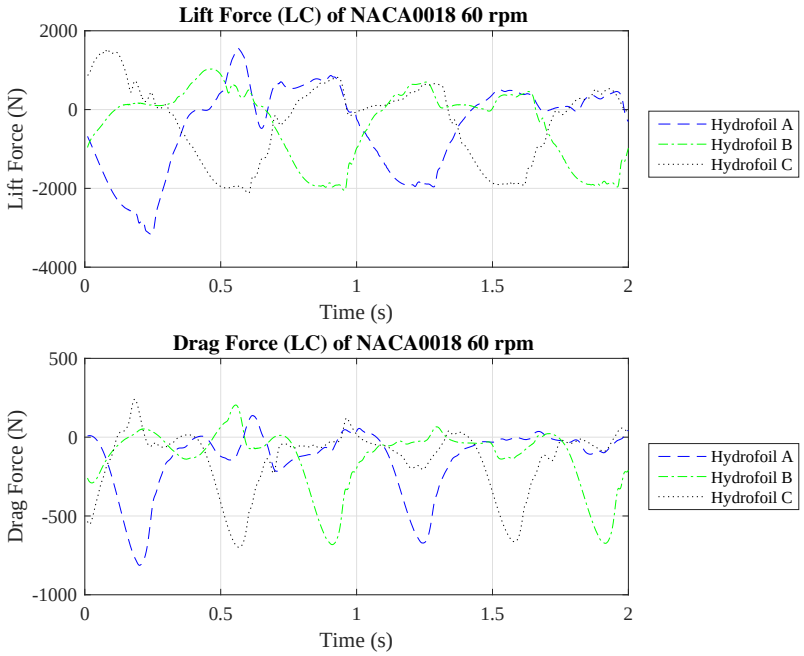

Figure 4.23: Lift and Drag Force of SIM04 in LC

For SIM04 the lift force in LC for hydrofoil A at t = 1.232s is $L_{LC} = -1842N$ and drag force is $D_{(LC)} = -657N$, substituting in Eqn. 4.11 we get DP (1.232) = 0.0265m. From these values it can be seen that the negative lift force of SIM04(1842N) is smaller than that SIM13(2000N).So it is not due to the increase in the lift that NACA0018 have better performance. The negative drag force of SIM04 (657N) is higher than that of SIM13(612N). The distance to center of pressure is larger for SIM04 (0.0265m) than SIM13 (0.02308m). So the lever arm for lift force is higher. The increase in moment from lift force for SIM04 is $2000 \times 0.02308 - 1842 \times 0.0265 = 2.65Nm$. Now the increase in moment from drag force for SIM04 $657 \times R - 612 \times R = 45 * 0.3048 = 13.716Nm$. So it can be said that the major reason for better performance of SIM04 with NACA0018 is due to the higher

negative drag force around hydrofoil near the hydrofoil position of $\theta = 75°$ to 85°.

4.1.4 Least Efficient Turbine Among Section I SIM01

The hydrofoil shape for SIM01 was H= NACA0006. Other input parameters are flow velocity V=2m/s, Chord length C = 0.1778m, diameter D = 0.6096m, solidity σ = 0.2785 (S4), tip speed ratio λ = 0.958 (L02), Number of layers N=1, number of blades n=3 and pitch angle $\beta = 0°$ (B4). The final velocity profile of this simulation is given in the Fig. 4.24 and the final pressure profile of final the simulation is given in the Fig. 4.25 The final time is 2 seconds.

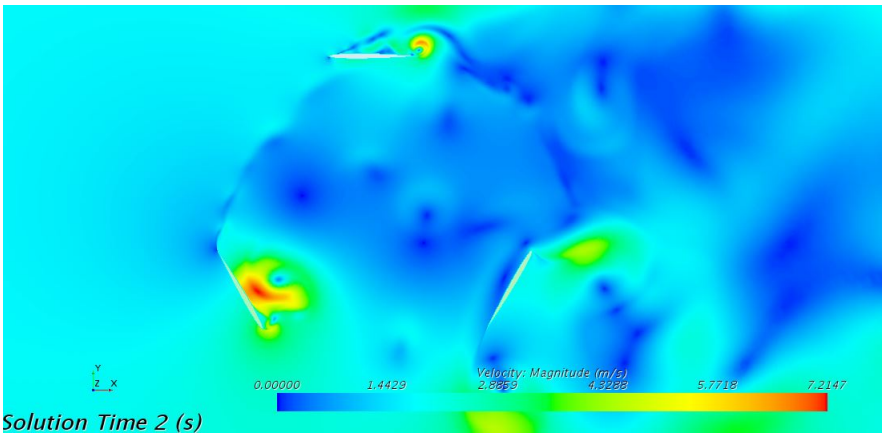

Figure 4.24: SIM01 Velocity Profile at 2 Seconds

The time history of the moment on each of the hydrofoils and total moment is given in the Fig. 4.26. In order to compare with the base case, the second maximum moment peak of hydrofoil A is chosen. The second maximum moment (MM) peak of the hydrofoil A occurs at time t = 1.167s with a value of 112.8 Nm and at a rotation angle of 420.12°. The position of the hydrofoil A at this time is 60.12°. But the nearest stored data points

for velocity profile are at t = 1.16s and t = 1.18s. So t = 1.16 s is selected for velocity and pressure profile.

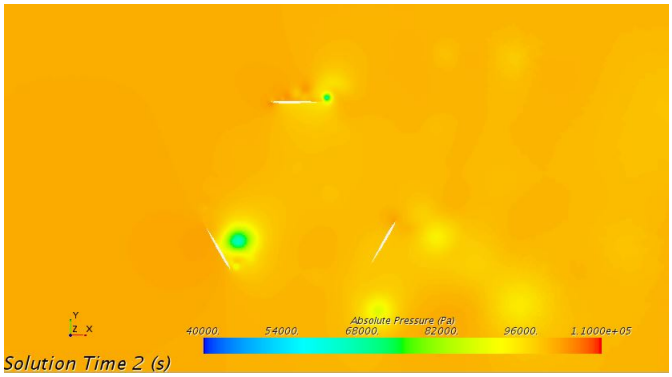

Figure 4.25: SIM01 Pressure Profile at 2 Seconds

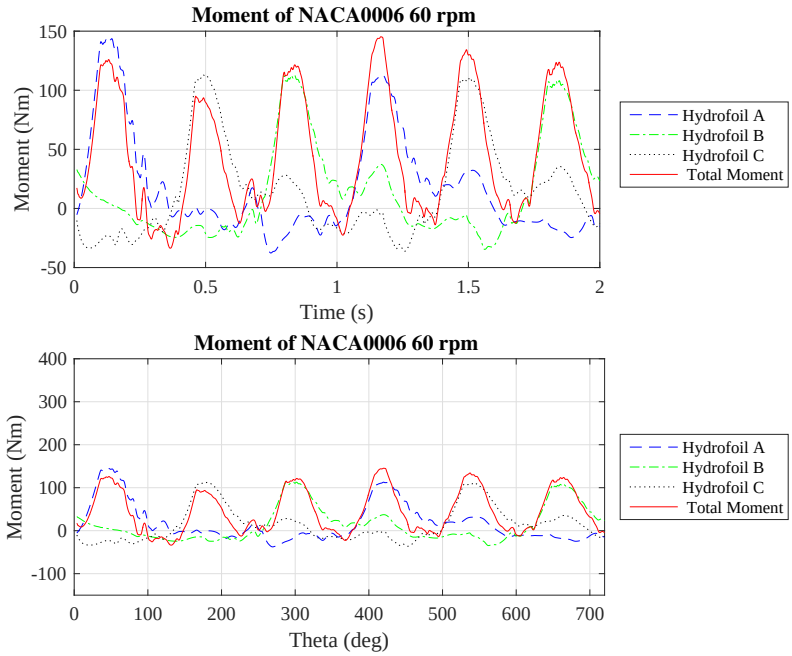

Figure 4.26: SIM01 Moment Plot

The velocity profile at second peak of hydrofoil A is shown in the Fig. 4.27. A close look at hydrofoil position at 60.2° could be seen in the Fig. 4.28. The pressure profile at the

maximum moment point seen in the Fig. 4.29. The pressure profile around the hydrofoil at maximum moment position could be seen in the Fig. 4.30

The time history of lift and drag force on the hydrofoils in global coordinate system could be seen from the figures Fig. 4.32 and Fig. 4.31 respectively. GC stands for global coordinate and LC stands for local coordinate.

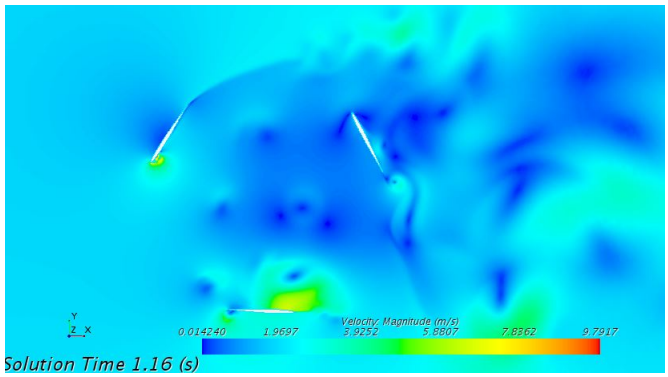

Figure 4.27: Velocity Profile at t = 1.16 Seconds SIM01

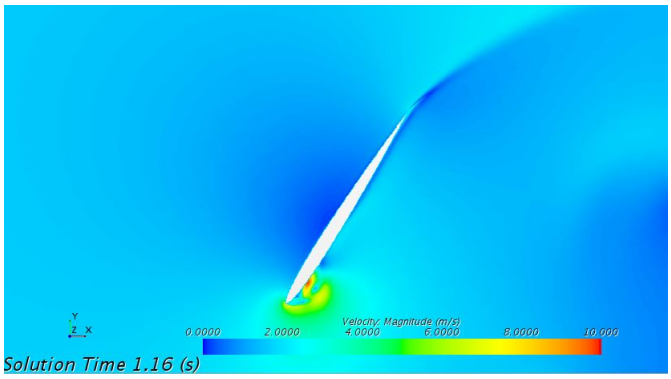

Figure 4.28: Velocity Profile Around Hydrofoil at Maximum Moment SIM01

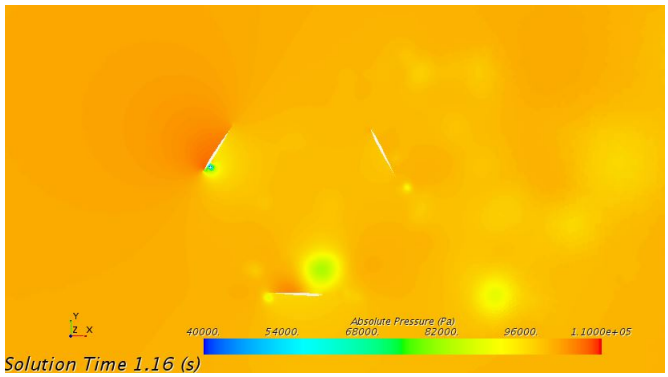

Figure 4.29: Pressure Profile of Turbine at t = 1.16 Seconds SIM01

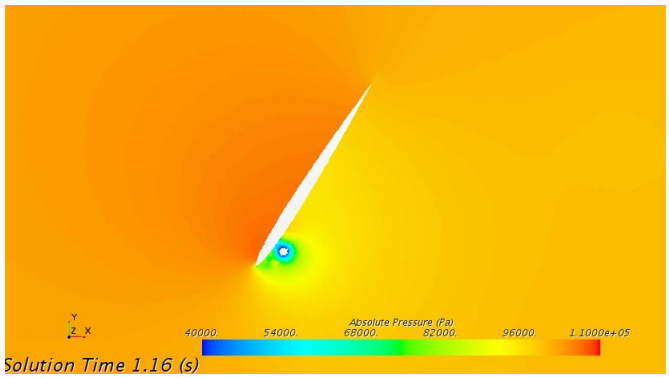

Figure 4.30: Pressure Profile Around Hydrofoil at Peak Moment SIM01

The lift and drag force of SIM04 in local coordinate (LC) are plotted in the Fig. 4.33. For SIM04 the lift force in LC for hydrofoil A at t = 1.167s is $L_{LC} = -2270N$ and drag force is $D_{(LC)} = -128N$, moment = 112.8Nm substituting in Eqn. 4.11 we get DP (1.167) = 0.0325m. From these values it can be seen that the negative lift force of SIM01(2270N) is higher than that SIM13(2000N). The negative drag force of SIM01 (128N) is higher than that of SIM13(612N). The distance to center of pressure is larger for SIM01 (0.0325m) than SIM13 (0.02308m). So the lever arm for lift force is higher.

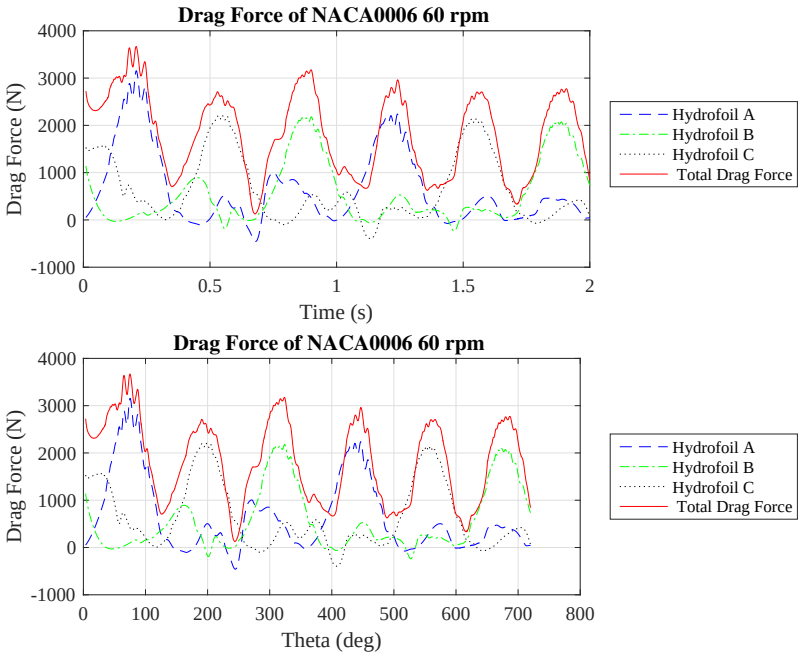

Figure 4.31: Drag Force of SIM01 in GC

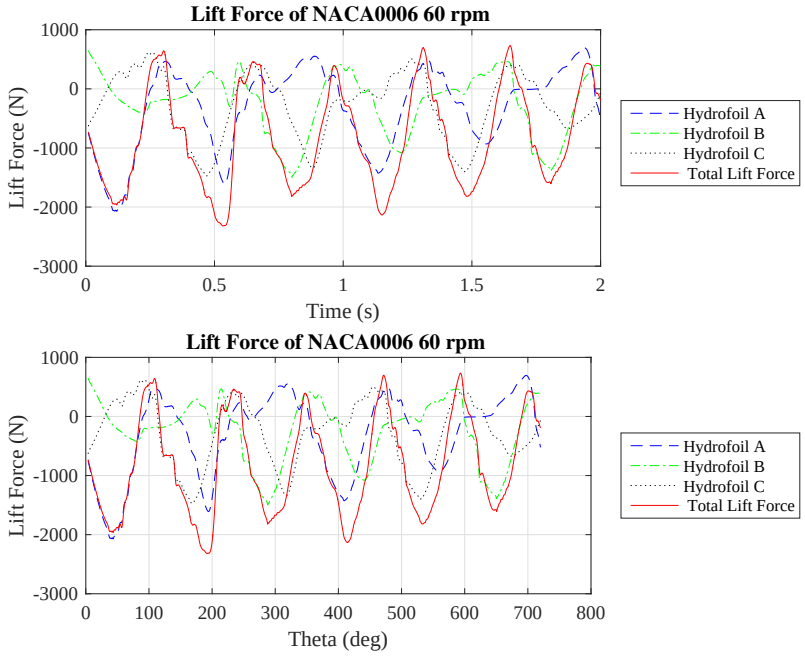

Figure 4.32: Lift Force of SIM01 in GC

The increase in moment from lift force for SIM01 is 24.97Nm. Now the decrease in

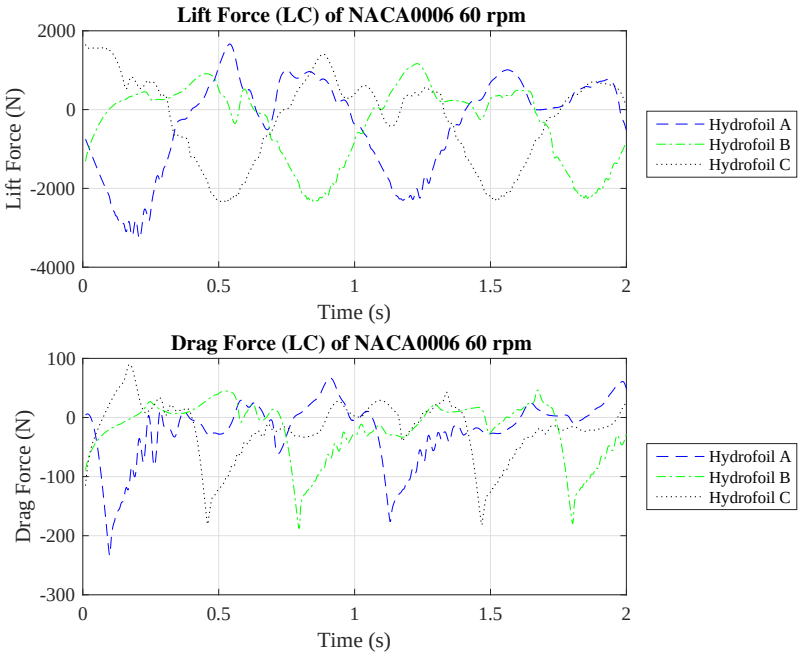

Figure 4.33: Lift and Drag Force of SIM01 in LC

moment from drag force for SIM01 147.52Nm. So it can be said that the major reason for poor performance of SIM01 with NACA0006 is due to the very low negative drag force around hydrofoil near the hydrofoil position.

4.2 Section II Simulations

The objective of section II simulations is to select a modification to hydrofoil (HM). This section simulation results of consists of 8 steady state simulations (SSS) and few () rotating turbine simulations (RTS). From the SSS, for 8 pitch angles each with thirteen modifications, two hydrofoil modifications are chosen and then they have used in RTS and compared with same case without modification.

4.2.1 Steady State Simulations

The geometry of steady state simulation (SSS) consists of 15 bodies. Fourteen of them are the cylinders with hydrofoils each kept apart with a distance of 0.6m. This consists of 13 hydrofoil modified shapes (HM) from H00 HM00 to H00 HM12 of NACA0020 (H00) and H00 without modification. The definition of those modified shapes are given in the section 3.2.3. The flow velocity is 4m/s and the input parameters used are explained in section 3.5.5. The variation is the steady flow pattern and pressure field for different cases and different pitch angles are not identifiable to eye and hence only the velocity and pressure profiles for only two cases for two pitch angles are shown in this the section. The other results are provided in appendix. The variation of pitch angles for the SSS are given in the Table 4.5.

Table 4.5: Steady State Simulation Input Pitch Angle (β)

Simulation Number	Representation (B)	Pitch Angle (β)
SIM63	B8	8°
SIM64	B7	4°
SIM65	B6	2°
SIM66	B5	1°
SIM67	B4	0°
SIM68	B3	−2°
SIM69	B2	−4°
SIM70	B1	−8°

Velocity Profiles

The velocity profile of only two cases are provided here. The two cases are SIM63 with $\beta = 8°$ and SIM70 with $\beta = -8°$. The velocity profile of SIM63 can be seen in the figures Fig. 4.34 and Fig. 4.35. The Fig. 4.34 shows velocity profile of the cases HMXX, HM00, HM04, HM03, HM02, HM01 and HM05 respectively from left to right. The Fig. 4.35 shows the velocity profile of the cases HM06, HM07, HM08, HM09, HM10, HM11 and HM12 respectively from left to right. A closer look at velocity profile around hydrofoil with circular void HM12 and without void HMXX could be seen in the Fig. 4.36b. Comparing the figures HMXX and HM12 it could be seen that for HM12 the velocity above the nose region along y axis is slightly less than that of HMXX. inside the void velocity at the center of vortex is near 0 and the velocity near the void surface is around 3m/s.

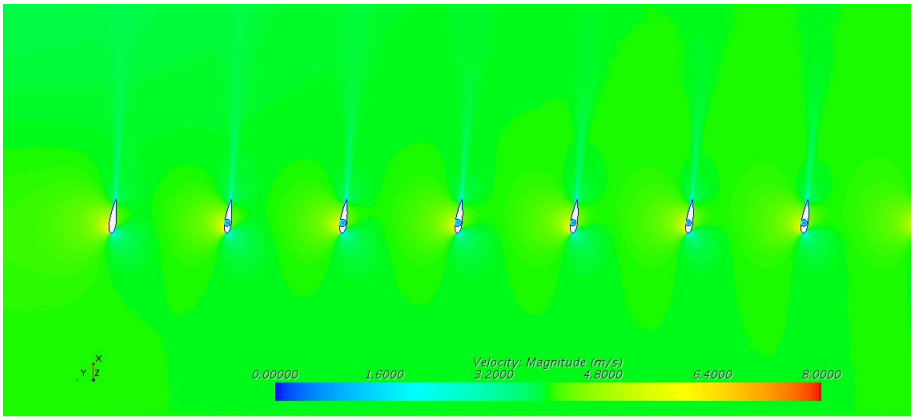

Figure 4.34: SIM63 Velocity Profile $\beta = 8°$ a

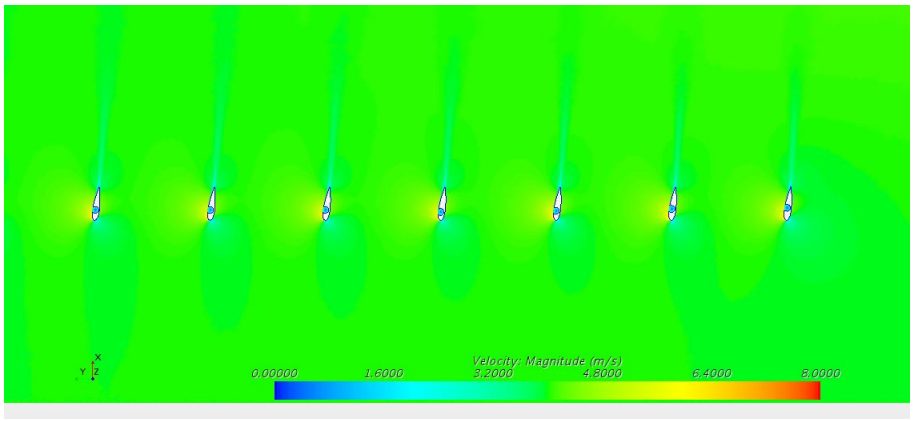

Figure 4.35: SIM63 Velocity Profile $\beta = 8°$ b

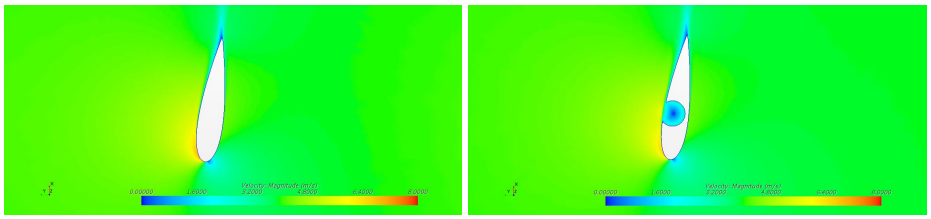

(a) SIM63 Velocity HMXX $\beta = 8°$ (b) SIM63 Velocity HM12 $\beta = 8°$

Figure 4.36: Velocity Profile of HMXX and HM12 of SIM63

The velocity profile of SIM70 can be seen in the figures Fig. 4.37 and Fig. 4.38. The Fig. 4.37 shows velocity profile of the cases HMXX, HM00, HM04, HM03, HM02, HM01 and HM05 respectively from left to right. The Fig. 4.38 shows the velocity profile of the cases HM06, HM07, HM08, HM09, HM10, HM11 and HM12 respectively from left to right. A closer look at velocity profile around hydrofoil with circular void HM12 and without void HMXX could be seen in the Fig. 4.39b. Comparing the figures HMXX and HM12 it could be seen that for HM12 the velocity near the nose is not effected by the void. Inside the void, velocity at the center of vortex is near 0 and the velocity near the void surface is around 3m/s which is almost same as that of the SIM63 case.

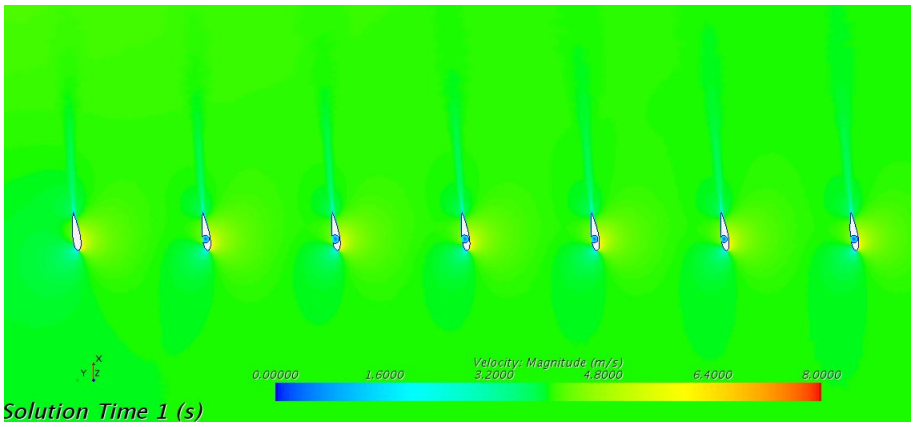

Figure 4.37: SIM70 Velocity Profile $\beta = -8°$ a

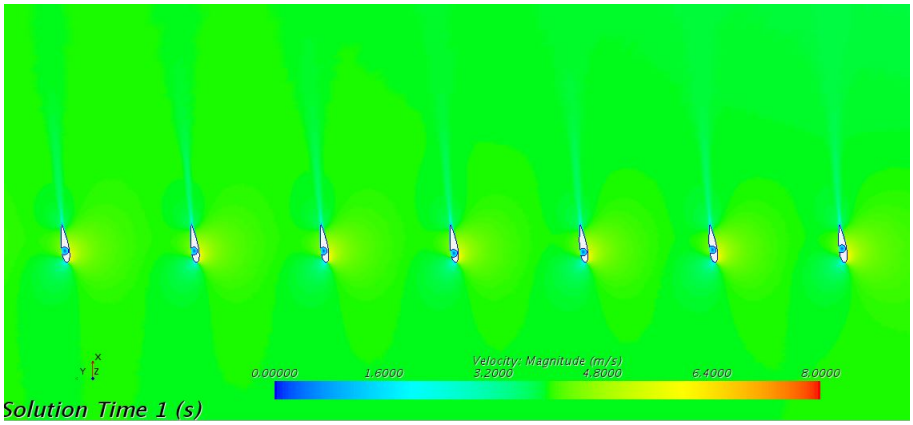

Figure 4.38: SIM70 Velocity Profile $\beta = -8°$ b

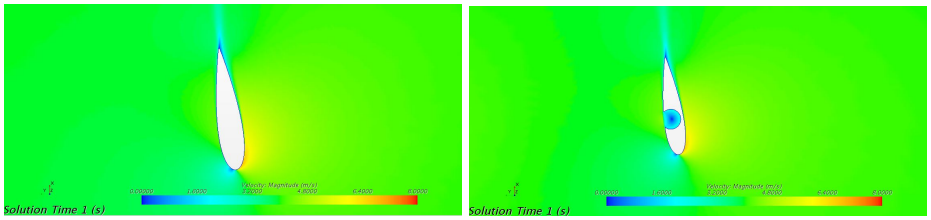

(a) SIM70 Velocity HMXX $\beta = -8°$ (b) SIM70 Velocity HM12 $\beta = -8°$

Figure 4.39: Velocity Comparison of HMXX and HM12

Pressure Profiles

The pressure profiles of only two cases are provided here. The two cases are SIM63 with $\beta = 8°$ and SIM70 with $\beta = -8°$. The pressure profile of SIM63 can be seen in the figures Fig. 4.40 and Fig. 4.41. The Fig. 4.40 shows pressure profile of the cases HMXX, HM00, HM04, HM03, HM02, HM01 and HM05 respectively from left to right. The Fig. 4.41 shows the velocity profile of the cases HM06, HM07, HM08, HM09, HM10, HM11 and HM12 respectively from left to right. A closer look at pressure profile around hydrofoil with circular void HM12 and without void HMXX could be seen in the Fig. 4.36b.

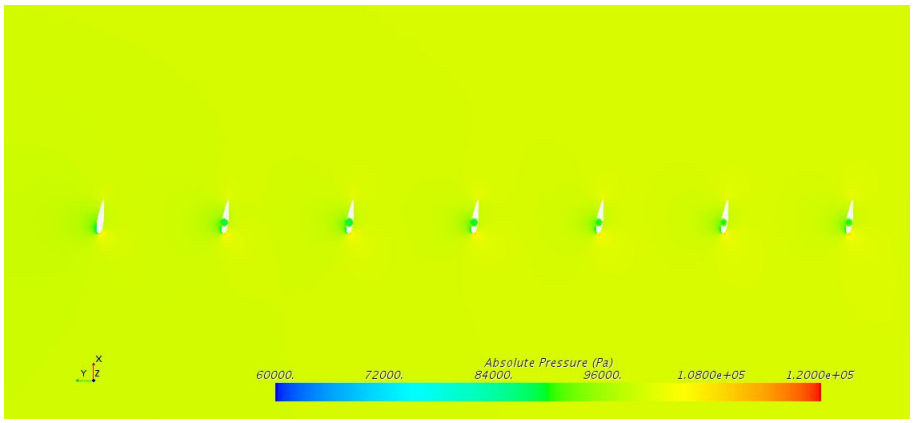

Figure 4.40: SIM63 Pressure Profile $\beta = 8°$ a

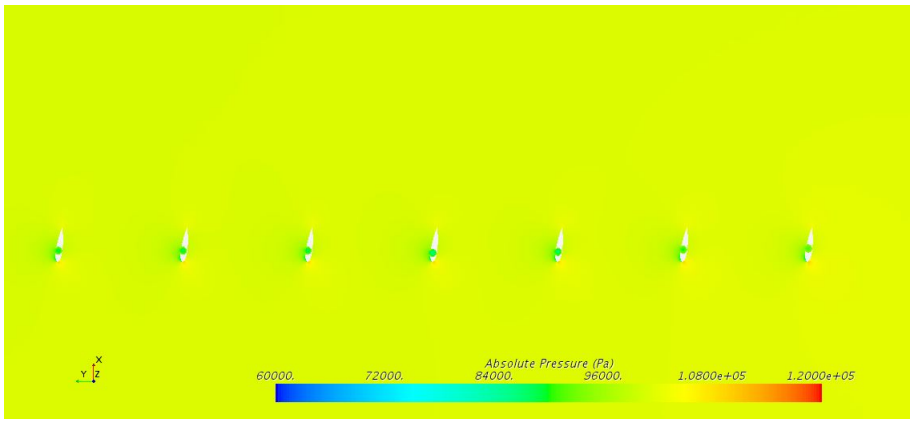

Figure 4.41: SIM63 Pressure Profile $\beta = 8°$ b

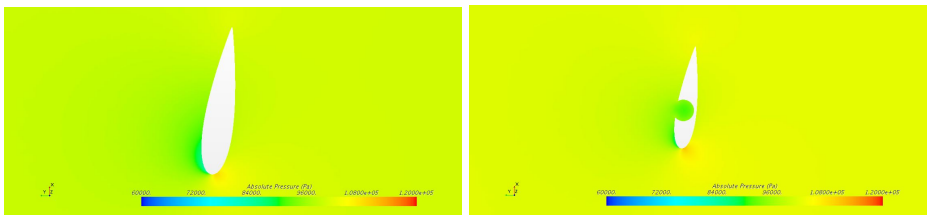

(a) SIM63 Pressure HMXX $\beta = 8°$ (b) SIM63 Pressure HM12 $\beta = 8°$

Figure 4.42: Pressure Comparison of HMXX and HM12 of SIM63

The pressure profile of SIM70 can be seen in the figures Fig. 4.43 and Fig. 4.44. The Fig. 4.43 shows velocity profile of the cases HMXX, HM00, HM04, HM03, HM02, HM01 and HM05 respectively from left to right. The Fig. 4.44 shows the velocity profile of the cases HM06, HM07, HM08, HM09, HM10, HM11 and HM12 respectively from left to right. A closer look at velocity profile around hydrofoil with circular void HM12 and without void HMXX could be seen in the Fig . 4.45b.

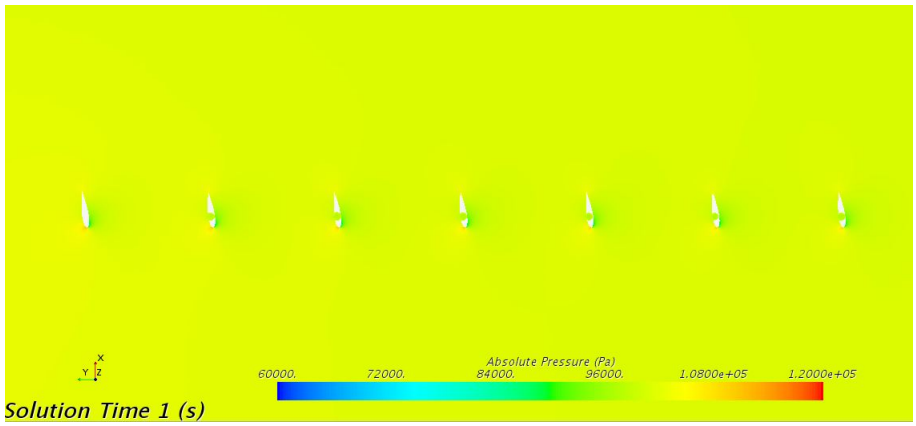

Figure 4.43: SIM70 Pressure Profile $\beta = -8°$ a

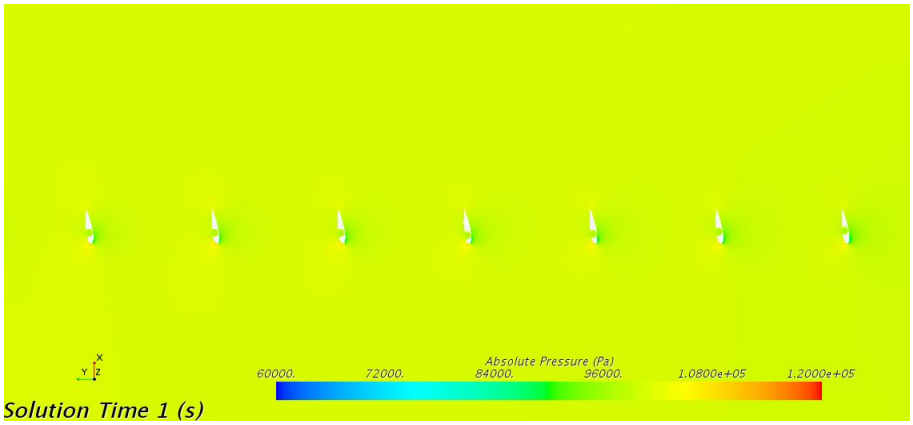

Figure 4.44: SIM70 Pressure Profile $\beta = -8°$ b

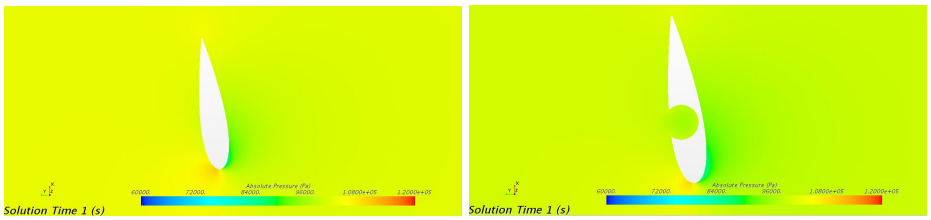

(a) SIM70 Pressure HMXX $\beta = -8°$ (b) SIM70 Pressure HM12 $\beta = -8°$

Figure 4.45: Pressure Comparison of HMXX and HM12 of SIM70

Lift and Drag Results of Steady State Simulations

The lift force and drag force result on each of all 13 modified hydrofoils at 8 pitch angles are discussed in this section. This section is divided in to three more parts, first one being the variation of lift and drag with pitch angle in time, the second one being the variation of lift and drag with radius of the void R_V, third section discuss the variation with Y coordinate of center of void Y_V and final section discuss the variation with X coordinate of center of void X_V. The HMs are named in this section as cases. The cases include HMXX (NACA0020) and they are in the same order as that in the SSS from left to right. The name of cases is given as per the Table 4.6 Radius R_v and Y coordinate Y_v are defined in percentage of t while X_v is defined in percentage of b. For the base modified case HM00, $R_v = 50$, $Y_v = 30$ and $X_v = 100$. Case CA01 is the NACA0020 hydrofoil without void HMXX, CA02 is the base modified case HM00, cases CA03 to CA06 have variation only in R_V with CA02. Cases CA07 to CA10 have variation only in Y_V with CA02. Cases CA11 to CA14 have variation only in X_V with CA02.

Table 4.6: Average Total Moments of Section II SIM11 -SIM21

Cases	Hydrofoil Modification HM	R_V	Y_V	X_V
CA01	HMXX	-	-	-
CA02	HM00	50	30	100
CA03	HM04	55	30	100
CA04	HM03	52.5	30	100
CA05	HM02	47.5	30	100
CA06	HM01	45	30	100
CA07	HM05	50	20	100
CA08	HM06	50	25	100
CA09	HM07	50	35	100
CA10	HM08	50	40	100
CA11	HM09	50	30	80
CA12	HM10	50	30	90
CA13	HM11	50	30	110
CA14	HM12	50	30	120

4.2.2 Variation of Lift and Drag With Pitch

In this section the variation of lift and drag force in time with pitch is discussed. This is the result that are combined from all Steady State Simulations, SIM63 to SIM70.

Case CA01

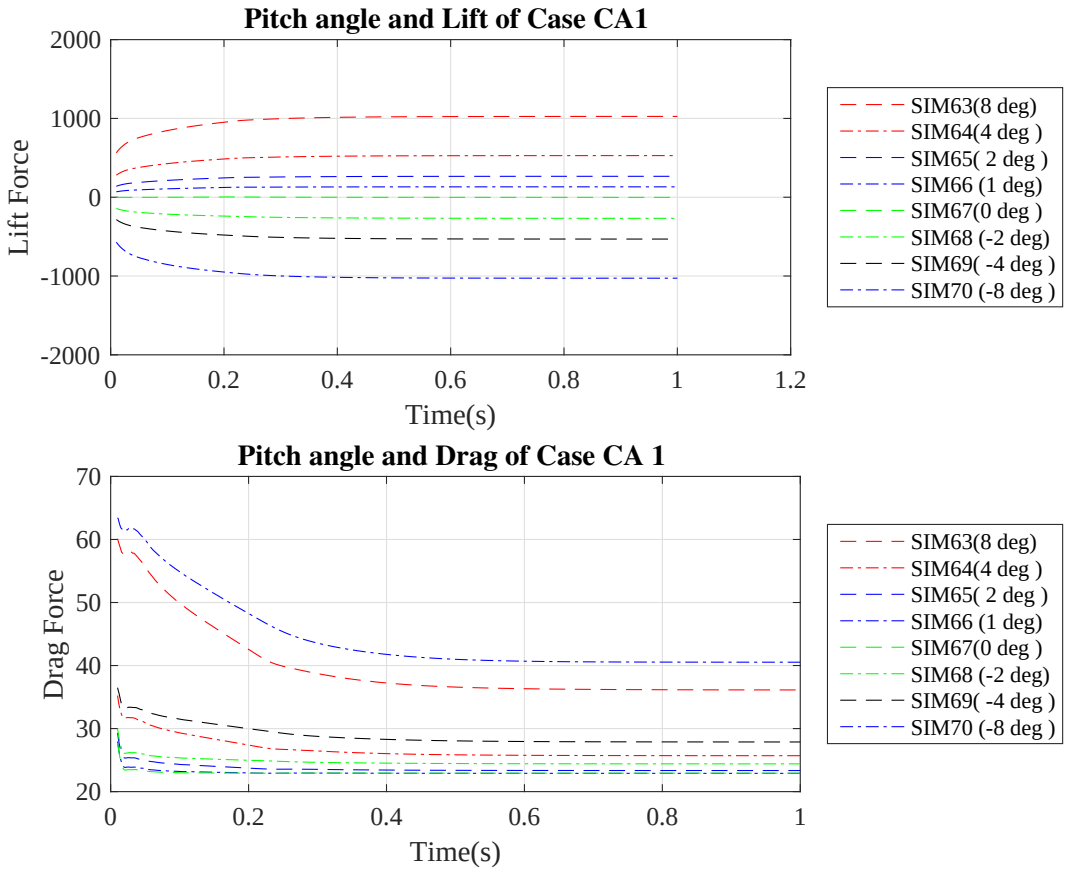

Figure 4.46: Lift and Drag of CA01

For CA01 the minimum lift force is -1028N for pitch angle $\beta = -8°$ and maximum lift force is 1026N for pitch angle $\beta = 8°$. Steady state has been reached around 0.6s. The minimum drag force is around 22N for $\beta = 0°$ and maximum is around 40N for pitch angle

$\beta = 8°and -8°$.

Case CA02

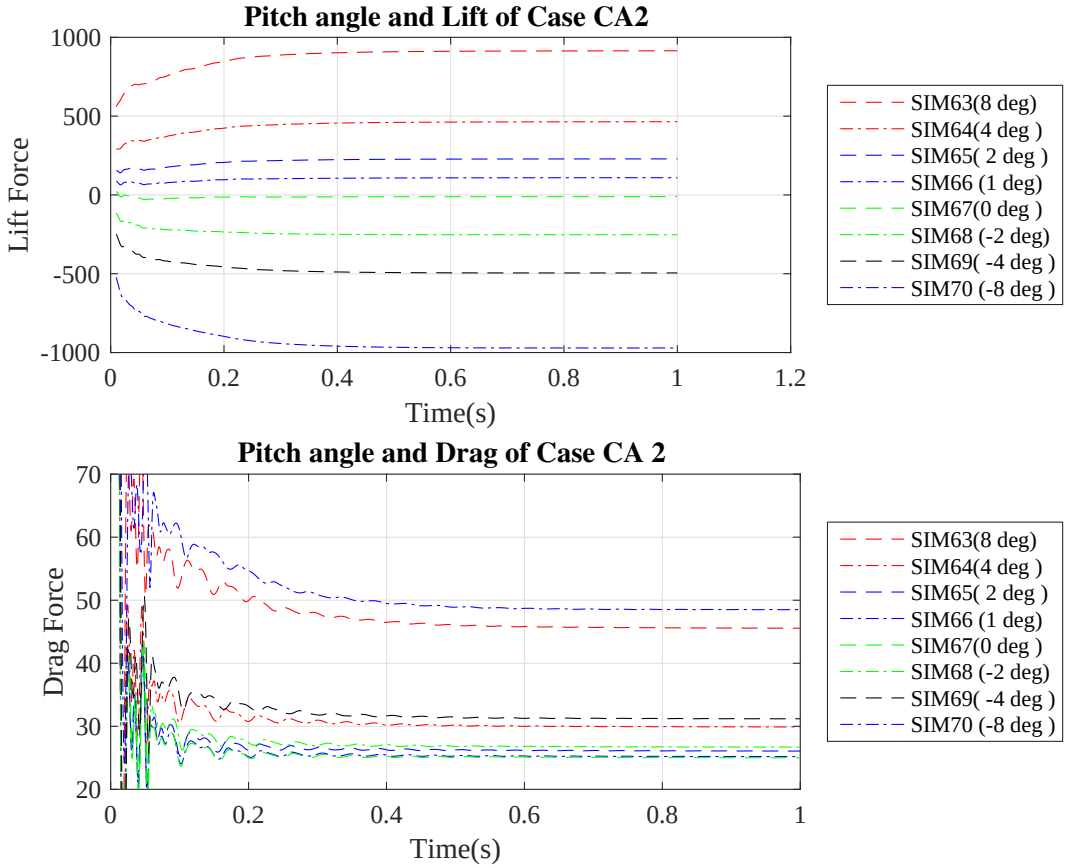

Figure 4.47: Lift and Drag of CA02

For CA02 the minimum lift force is -971N for pitch angle $\beta = -8°$ and maximum lift force is 914N for pitch angle $\beta = 8°$. The minimum drag force is around 25N for $\beta = 0°$ and maximum is around 48N for pitch angle $\beta = -8°$.

Case CA03

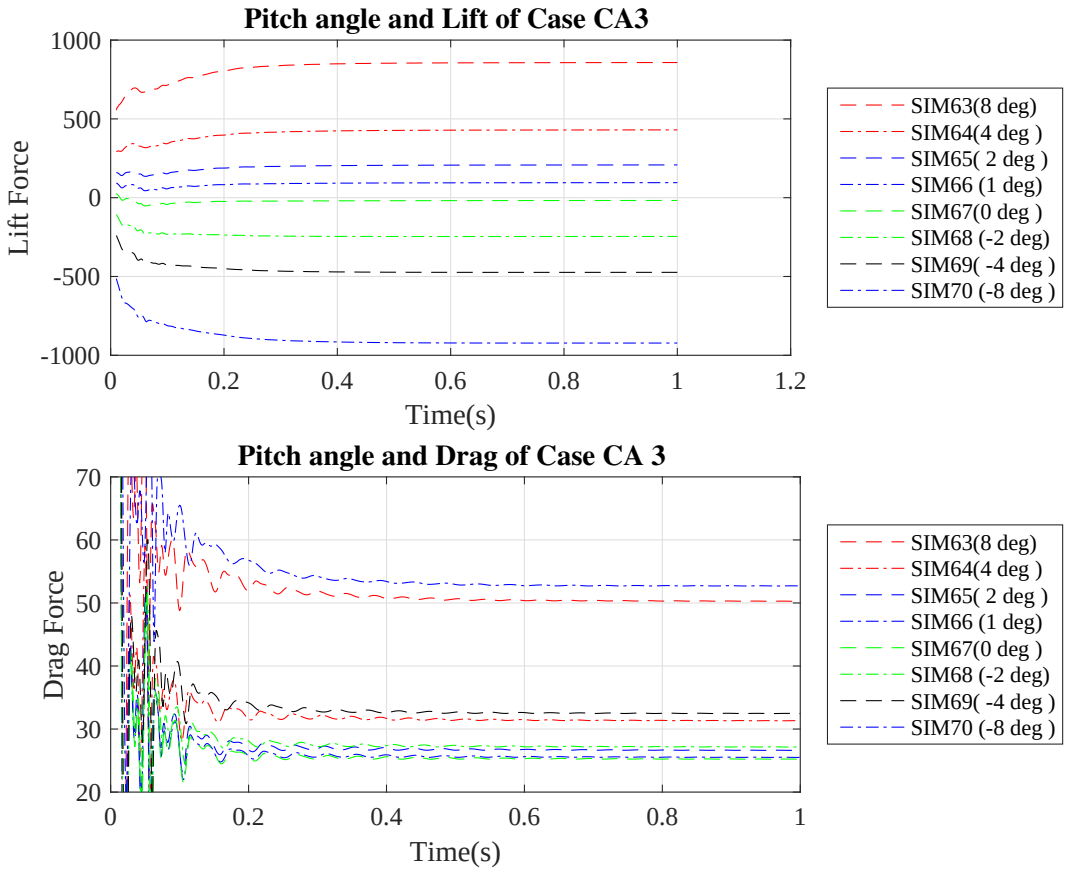

Figure 4.48: Lift and Drag of CA03

For CA03 the minimum lift force is -922N for pitch angle $\beta = -8°$ and maximum lift force is 857N for pitch angle $\beta = 8°$. The minimum drag force is around 25N for $\beta = 0°$ and maximum is around 52N for pitch angle $\beta = -8°$.

Case CA04

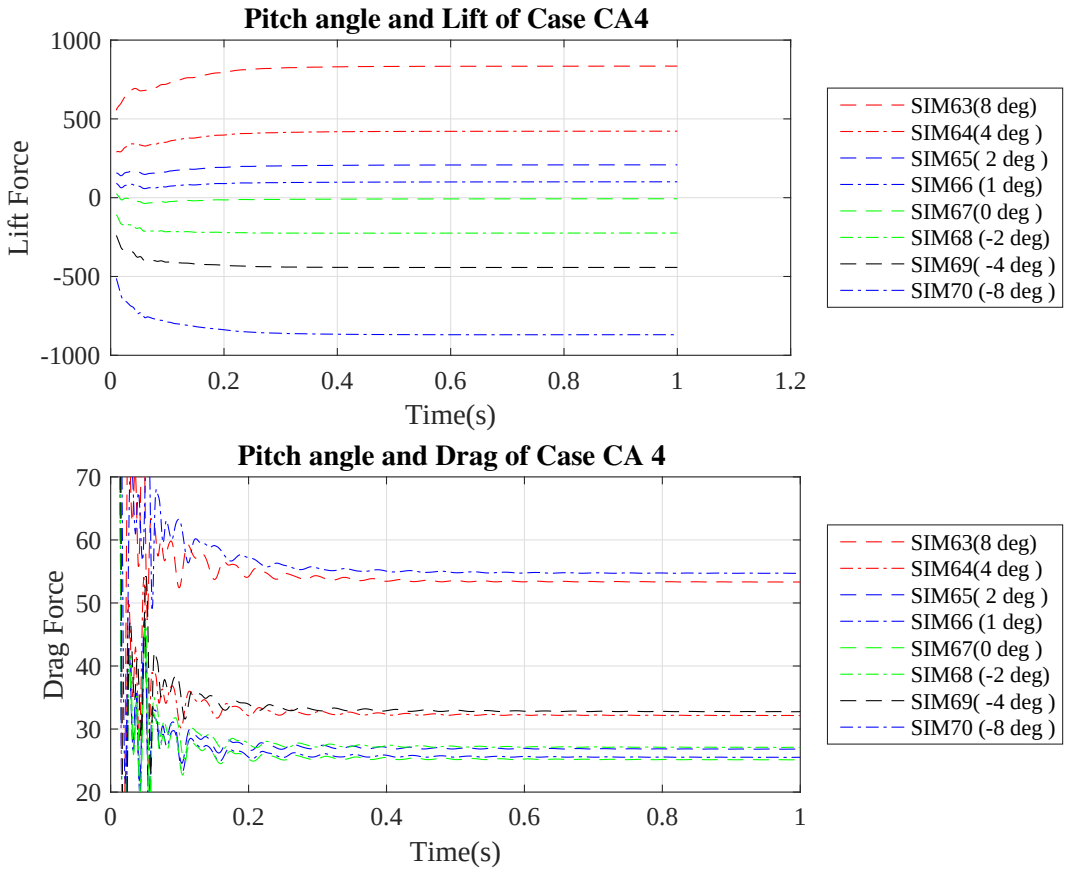

Figure 4.49: Lift and Drag of CA04

For CA04 the minimum lift force is -869N for pitch angle $\beta = -8°$ and maximum lift force is 834N for pitch angle $\beta = 8°$. The minimum drag force is around 25N for $\beta = 0°$ and maximum is around 55N for pitch angle $\beta = -8°$.

Case CA05

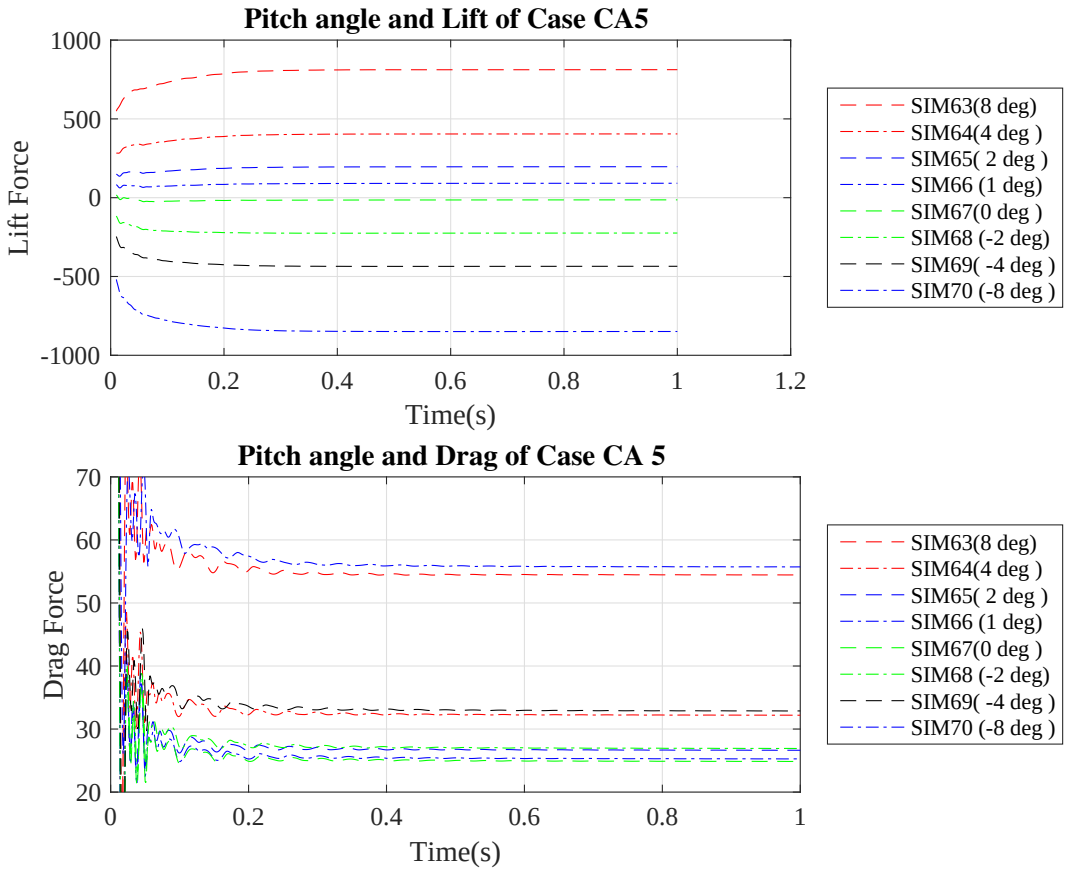

Figure 4.50: Lift and Drag of CA05

For CA05 the minimum lift force is -849N for pitch angle $\beta = -8°$ and maximum lift force is 812N for pitch angle $\beta = 8°$. The minimum drag force is around 25N for $\beta = 0°$ and maximum is around 56N for pitch angle $\beta = -8°$.

Case CA06

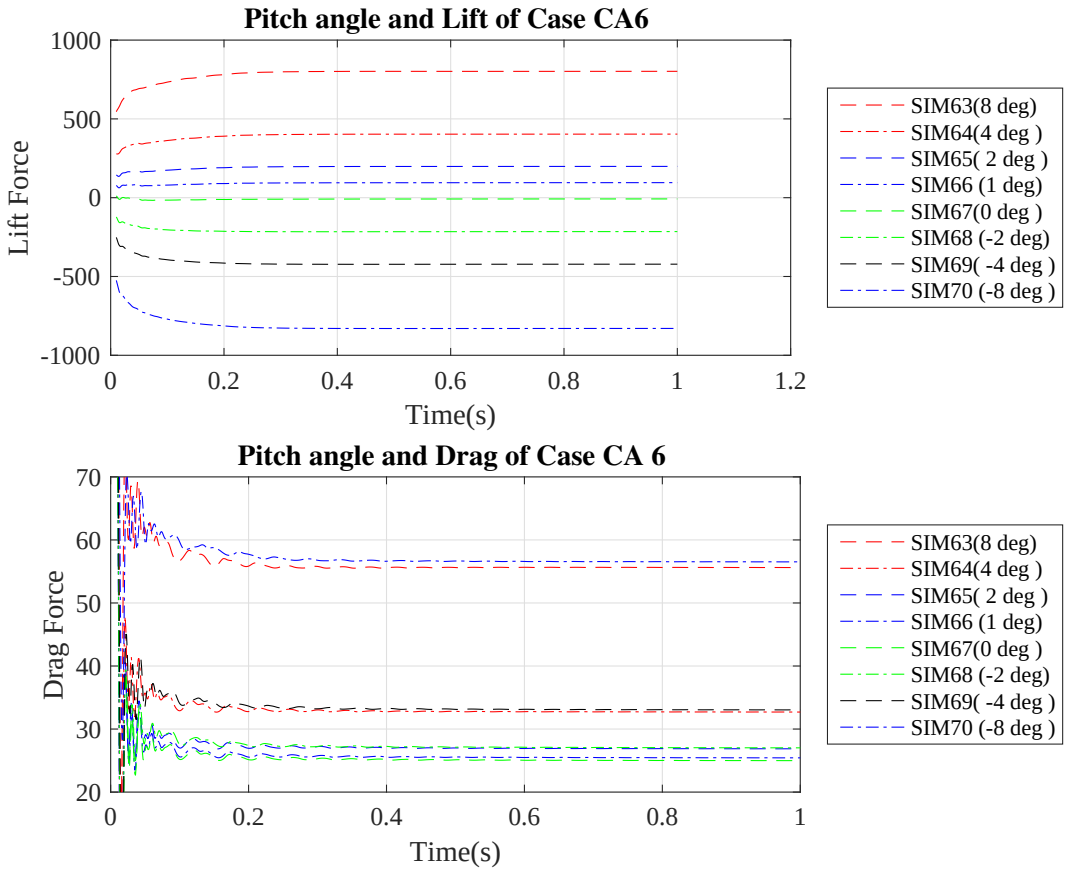

Figure 4.51: Lift and Drag of CA06

For CA06 the minimum lift force is -849N for pitch angle $\beta = -8°$ and maximum lift force is 812N for pitch angle $\beta = 8°$. The minimum drag force is around 25N for $\beta = 0°$ and maximum is around 56N for pitch angle $\beta = -8°$.

Case CA07

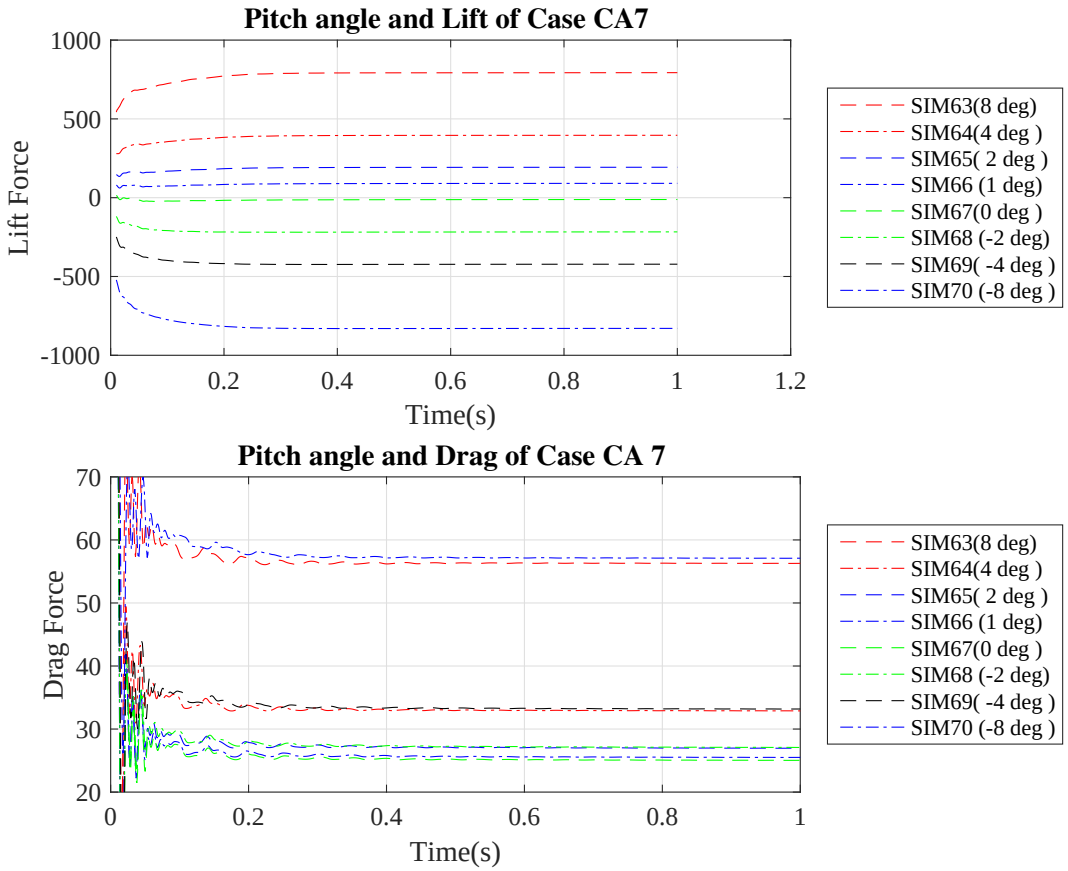

Figure 4.52: Lift and Drag of CA07

For CA07 the minimum lift force is -829N for pitch angle $\beta = -8°$ and maximum lift force is 793N for pitch angle $\beta = 8°$. The minimum drag force is around 25N for $\beta = 0°$ and maximum is around 57N for pitch angle $\beta = -8°$.

Case CA08

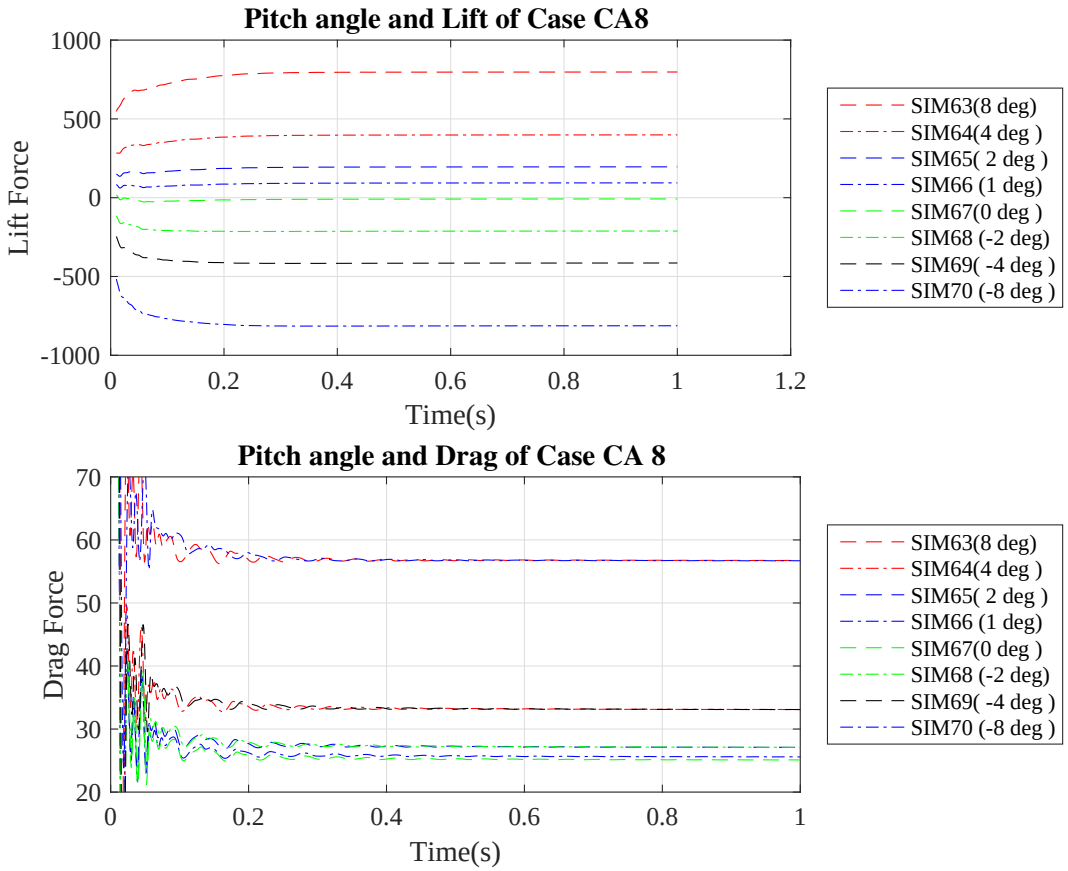

Figure 4.53: Lift and Drag of CA08

For CA08 the minimum lift force is -829N for pitch angle $\beta = -8°$ and maximum lift force is 793N for pitch angle $\beta = 8°$. The minimum drag force is around 25N for $\beta = 0°$ and maximum is around 57N for pitch angle $\beta = -8°$.

Case CA09

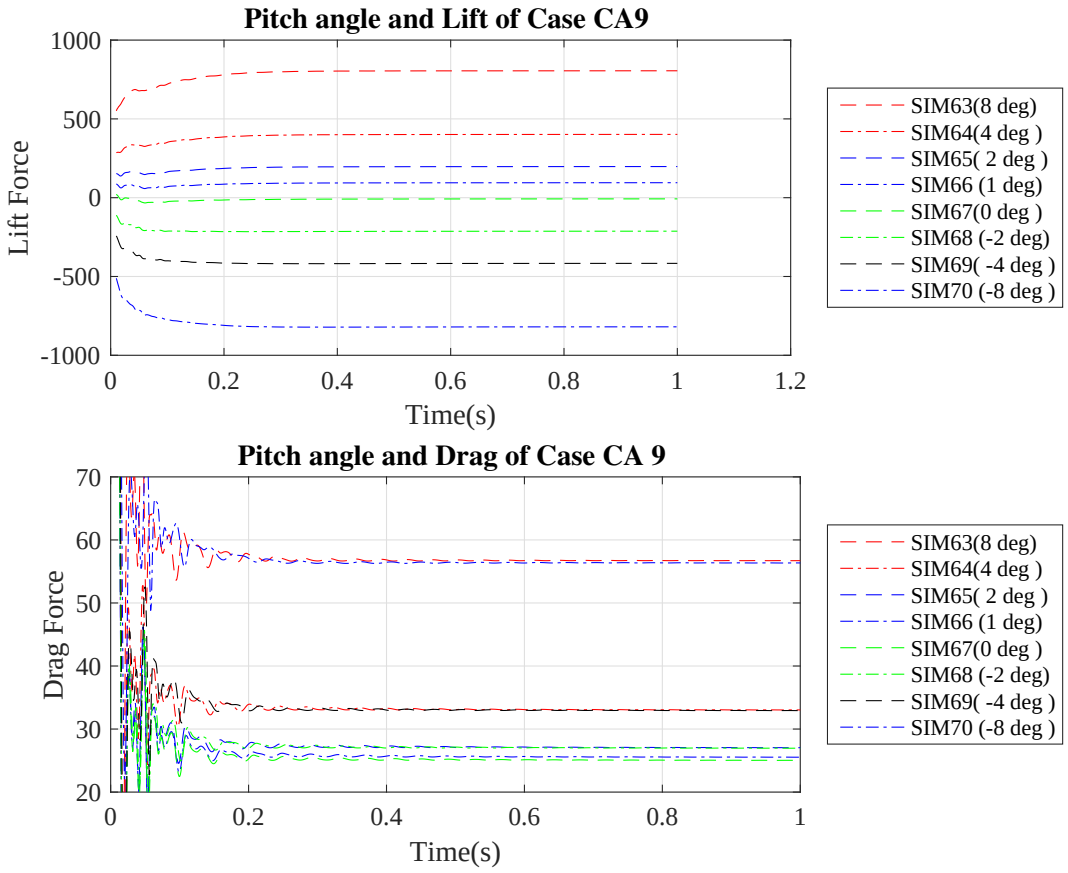

Figure 4.54: Lift and Drag of CA09

For CA09 the minimum lift force is -819N for pitch angle $\beta = -8°$ and maximum lift force is 805N for pitch angle $\beta = 8°$. The minimum drag force is around 25N for $\beta = 0°$ and maximum is around 57N for pitch angle $\beta = -8°$.

Case CA10

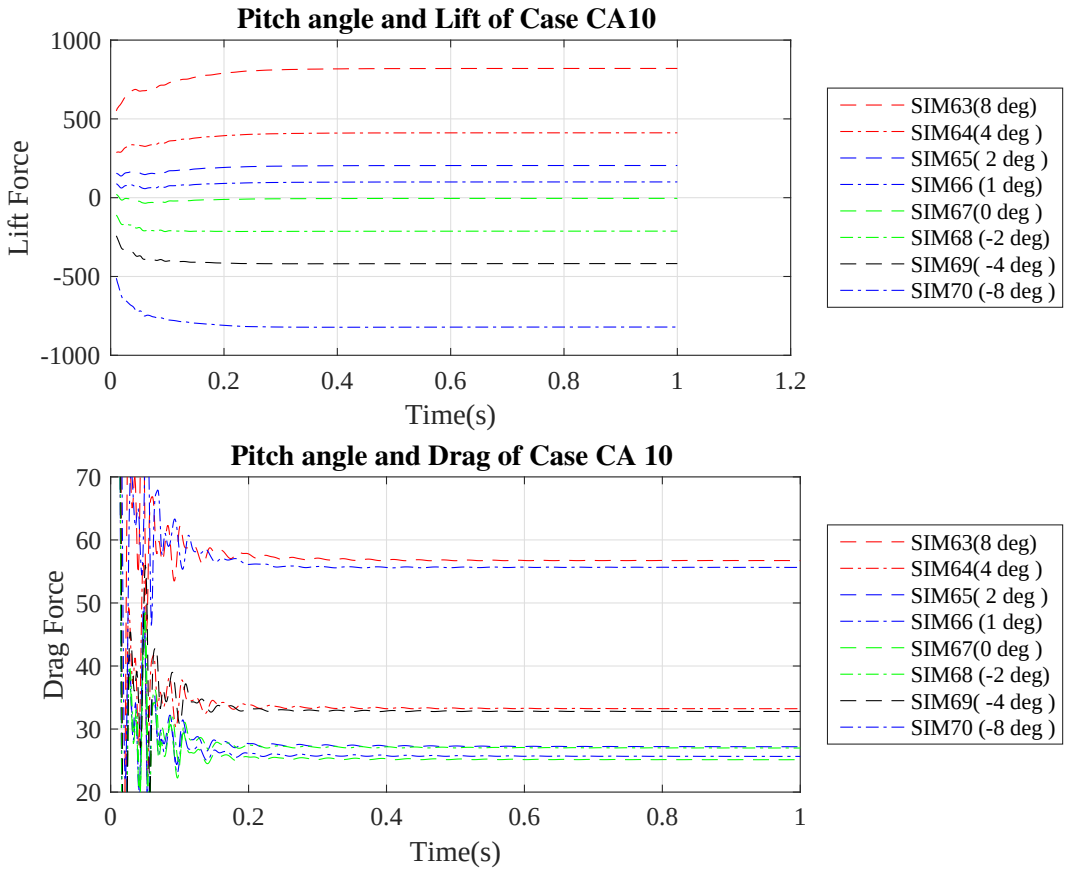

Figure 4.55: Lift and Drag of CA10

For CA10 the minimum lift force is -820N for pitch angle $\beta = -8°$ and maximum lift force is 820N for pitch angle $\beta = 8°$. The minimum drag force is around 25N for $\beta = 0°$ and maximum is around 57N for pitch angle $\beta = -8°$.

Case CA11

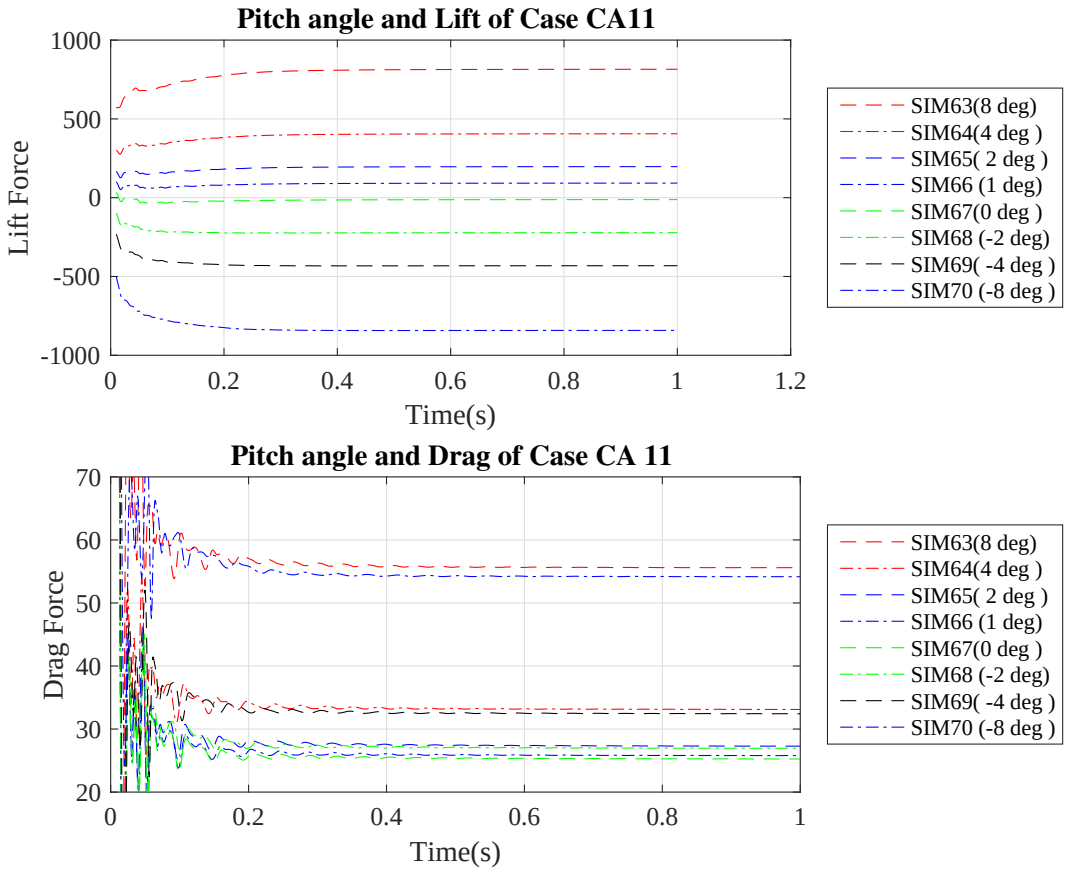

Figure 4.56: Lift and Drag of CA11

For CA11 the minimum lift force is -842N for pitch angle $\beta = -8°$ and maximum lift force is 814N for pitch angle $\beta = 8°$. The minimum drag force is around 25N for $\beta = 0°$ and maximum is around 56N for pitch angle $\beta = -8°$.

Case CA12

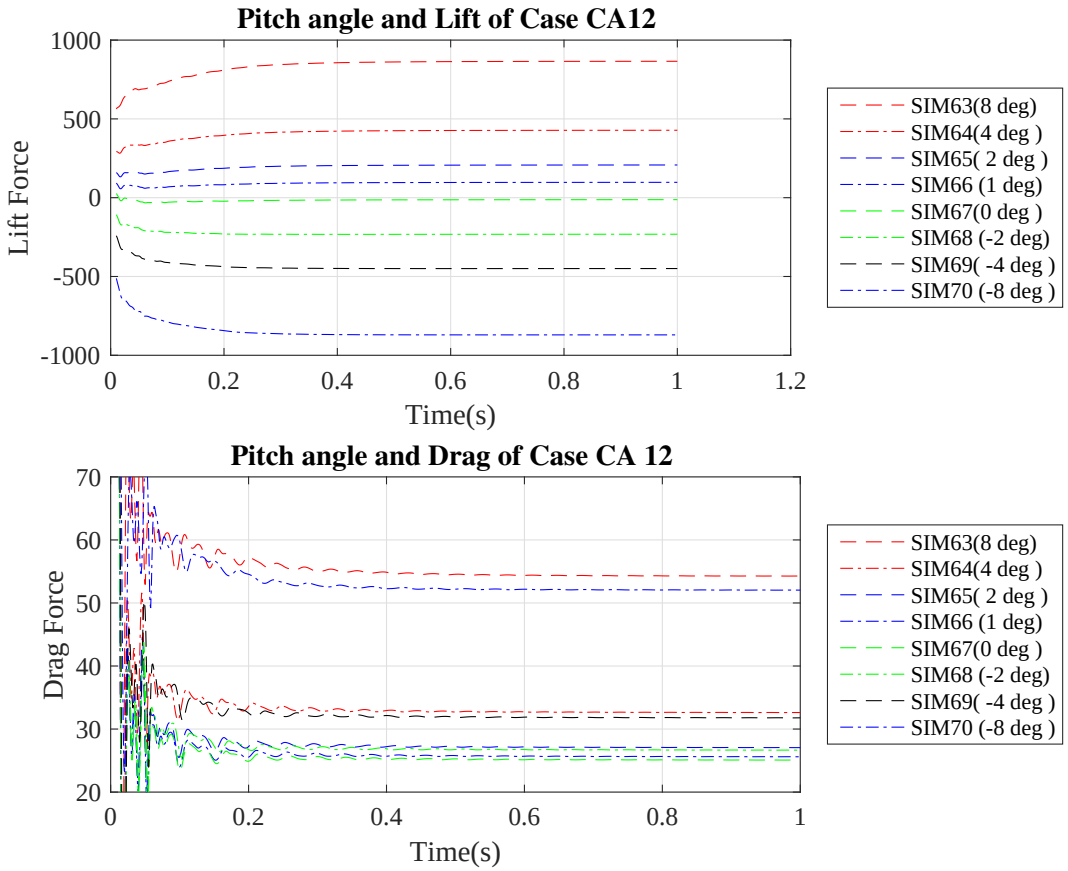

Figure 4.57: Lift and Drag of CA12

For CA12 the minimum lift force is -870N for pitch angle $\beta = -8°$ and maximum lift force is 865N for pitch angle $\beta = 8°$. The minimum drag force is around 25N for $\beta = 0°$ and maximum is around 54N for pitch angle $\beta = -8°$. Case CA13

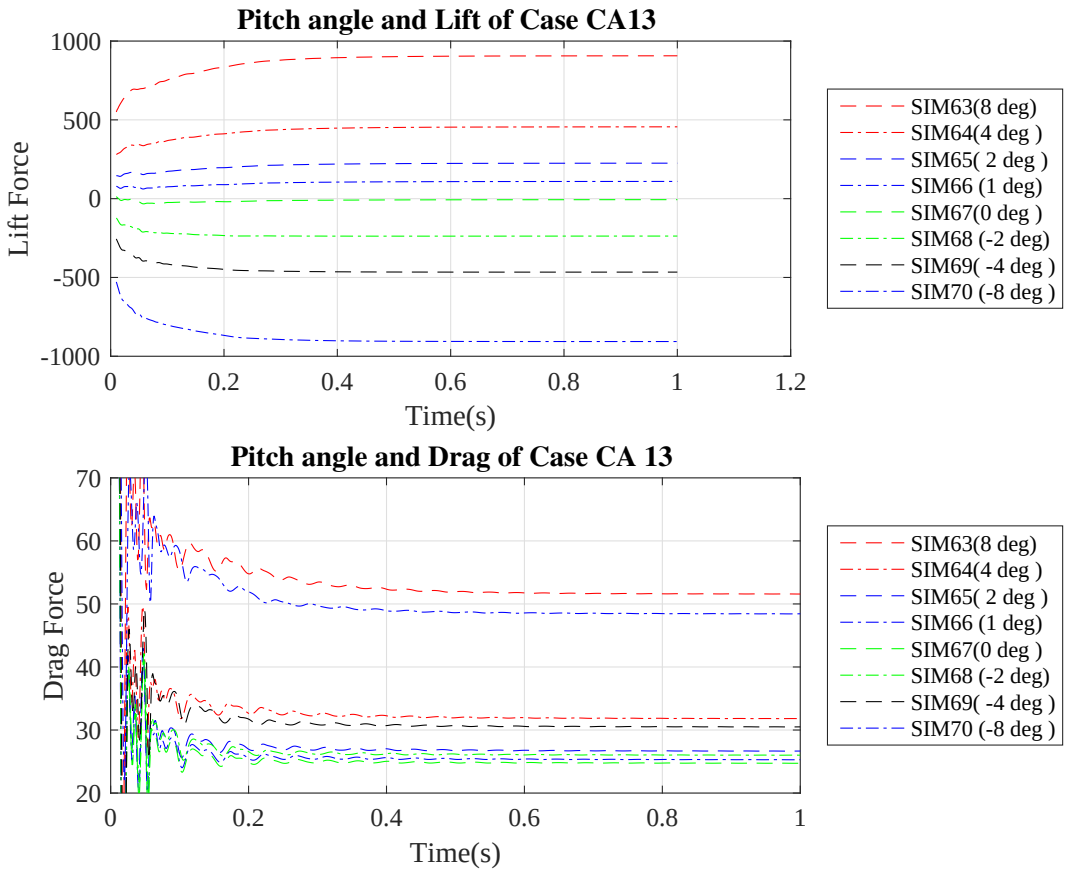

Figure 4.58: Lift and Drag of CA13

Case CA13

For CA13 the minimum lift force is -906N for pitch angle $\beta = -8°$ and maximum lift force is 906N for pitch angle $\beta = 8°$. The minimum drag force is around 25N for $\beta = 0°$ and maximum is around 51N for pitch angle $\beta = -8°$.

Case CA14

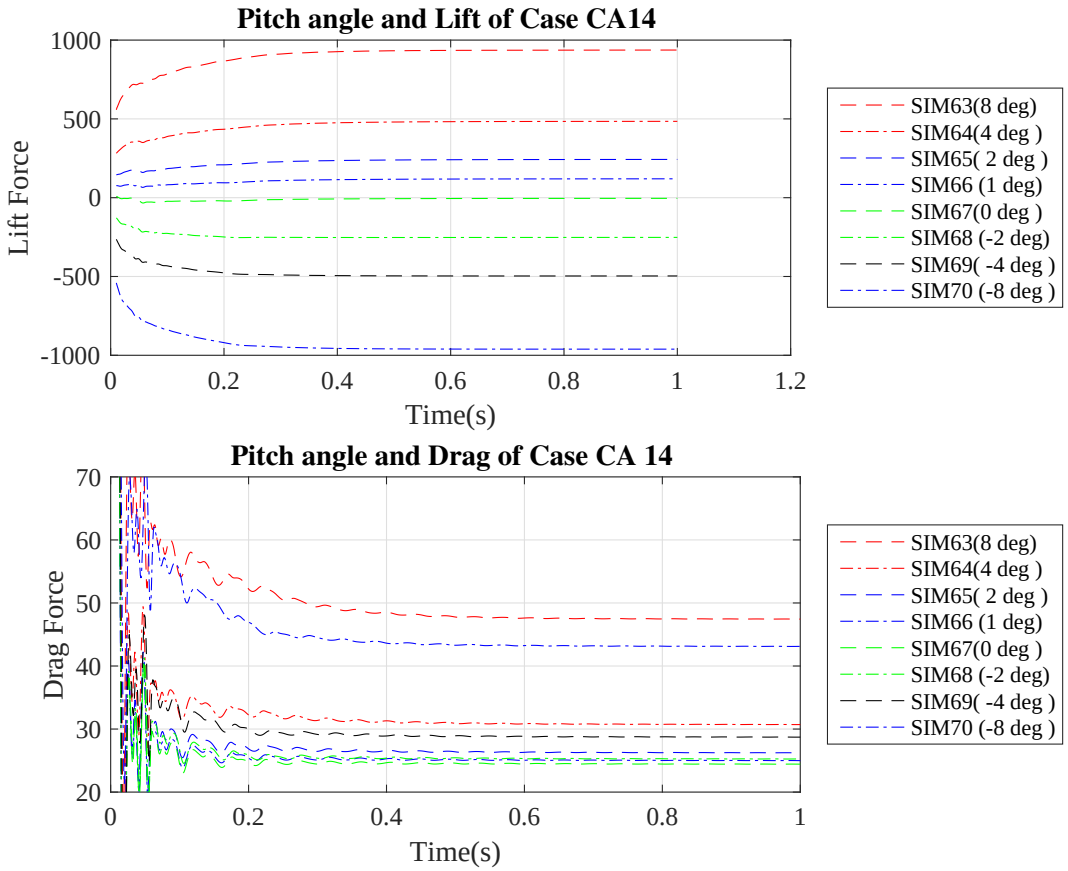

Figure 4.59: Lift and Drag of CA14

For CA14 the minimum lift force is -961N for pitch angle $\beta = -8°$ and maximum lift force is 936N for pitch angle $\beta = 8°$. The minimum drag force is around 24N for $\beta = 0°$ and maximum is around 47N for pitch angle $\beta = -8°$.

The maximum lift force among the modified hydrofoil is for the case CA14. During the initial 0.1s case CA11 have the highest lift. These two cases where selected for the rotating turbine simulations with modified hydrofoils.

4.2.3 Variation of Lift and Drag With Void Radius

In this section the variation of lift and drag force in time with circular void radius R_V is discussed. This is the result that are combined from cases CA02 to CA06. There are 8 results corresponding to the 8 pitch angles.

SIM63 Lift and Drag Variation With R_V

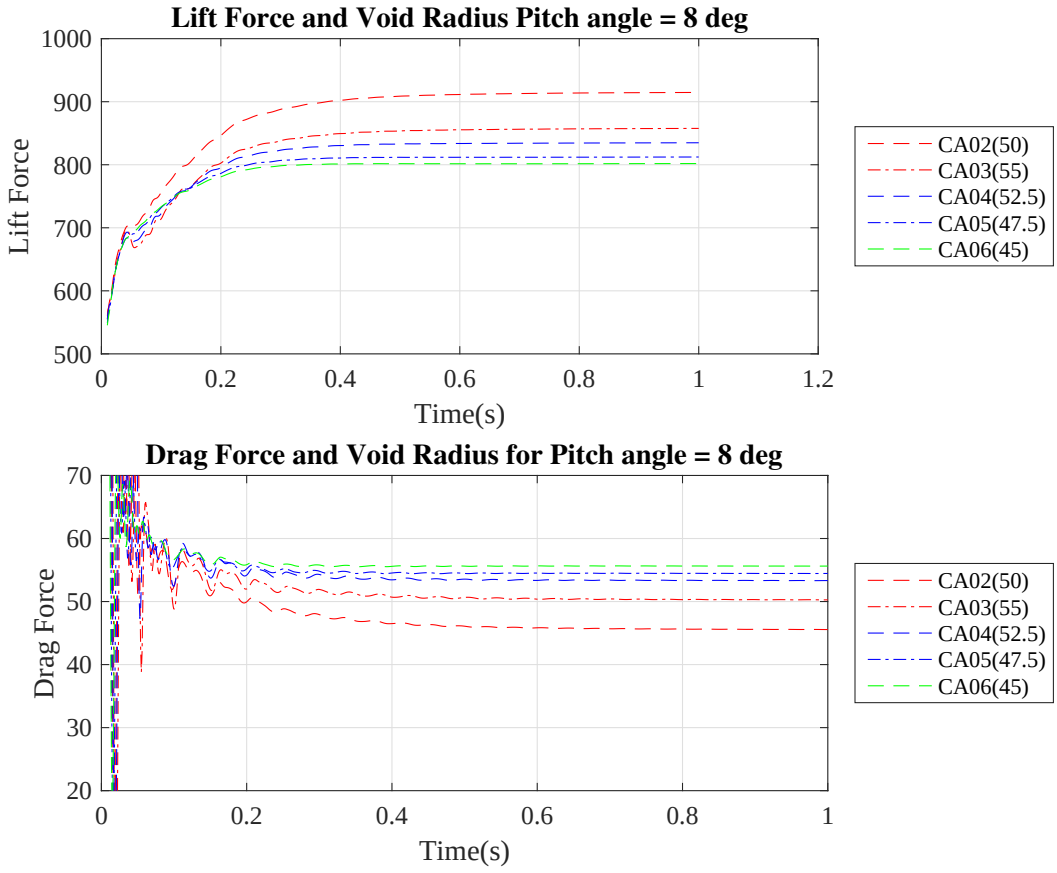

Figure 4.60: Lift and Drag With Void Radius SIM63 (8°)

For simulation SIM63 minimum steady state lift force is for case CA06 of 801N and maximum steady state lift force is for case CA02 of 915N. The minimum steady state drag

force is for case CA02 of 45N and maximum steady state drag force is for case CA06 of 56N.

SIM64 Lift and Drag Variation With R_V

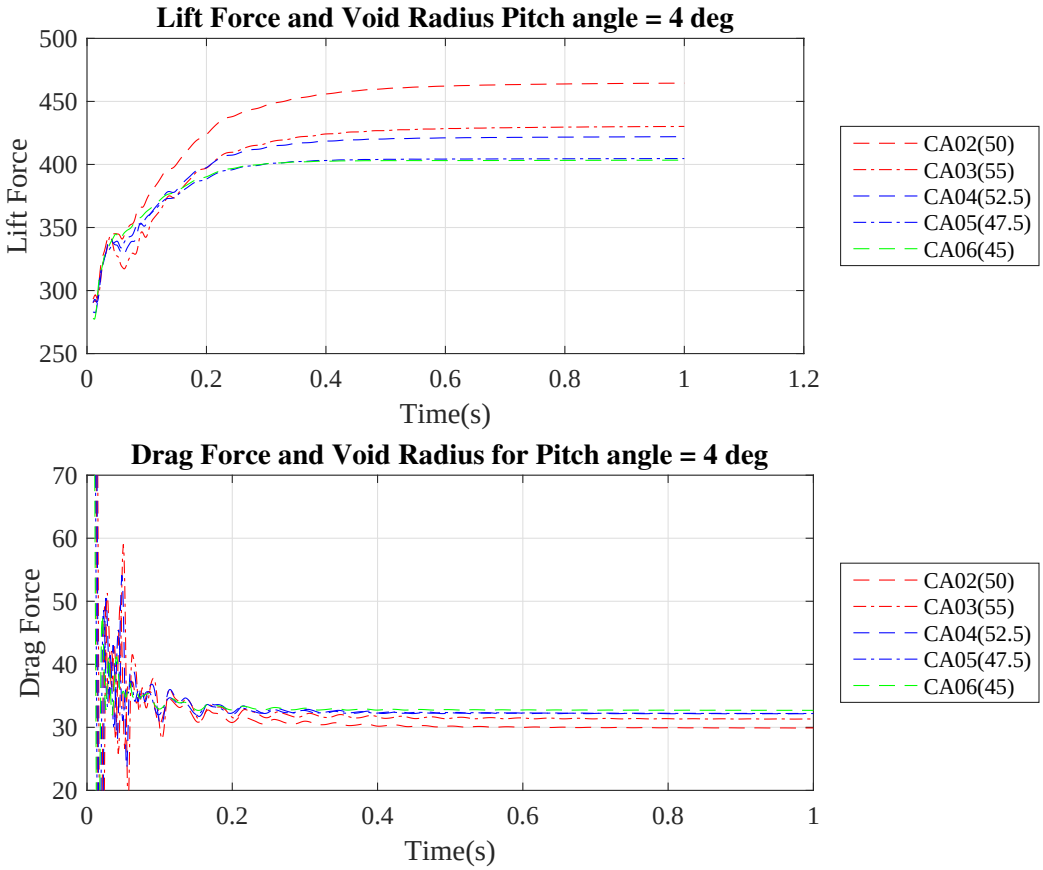

Figure 4.61: Lift and Drag With Void Radius SIM64 (4°)

For simulation SIM64 minimum steady state lift force is for case CA06 of 403N and maximum steady state lift force is for case CA02 of 464N. The minimum steady state drag force is for case CA02 of 29N and maximum steady state drag force is for case CA06 of 33N.

SIM65 Lift and Drag Variation With R_V

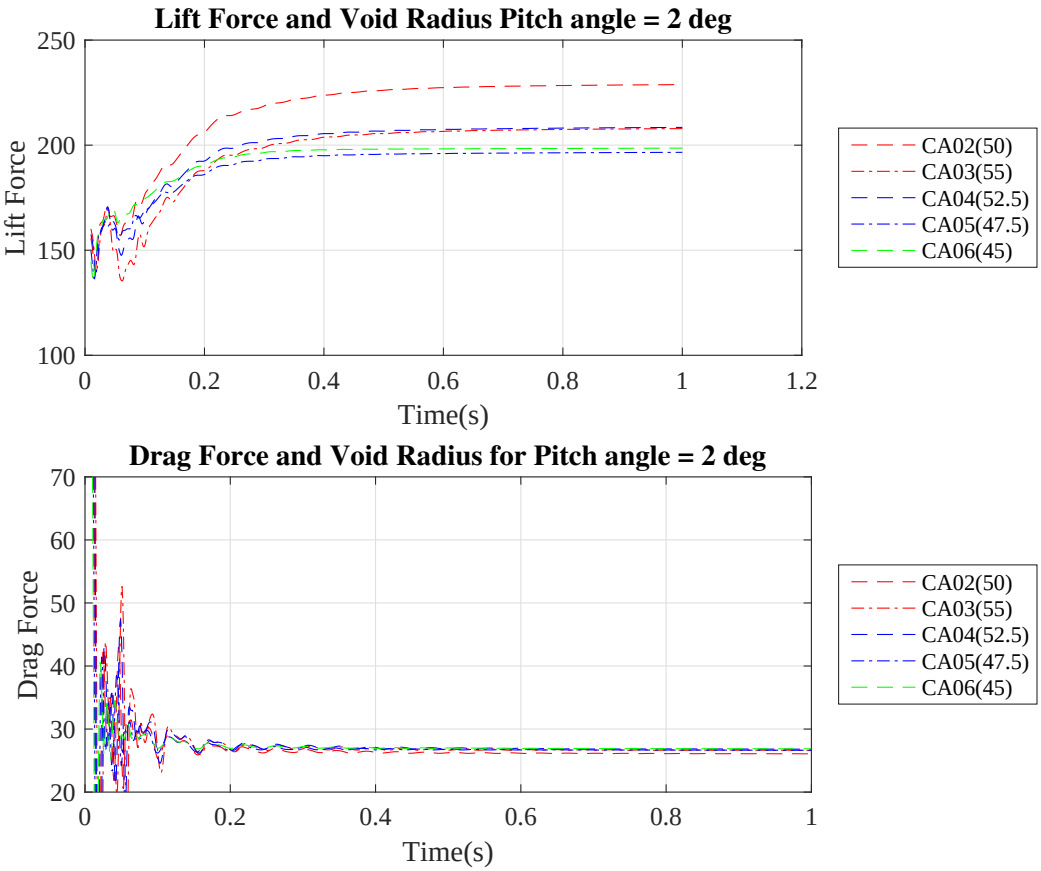

Figure 4.62: Lift and Drag With Void Radius SIM65 (2°)

For simulation SIM65 minimum steady state lift force is for case CA05 of 197N and maximum steady state lift force is for case CA02 of 228N. The minimum steady state drag force is for case CA02 of 26N and maximum steady state drag force is for case CA06 of 26.8N.

SIM66 Lift and Drag Variation With R_V

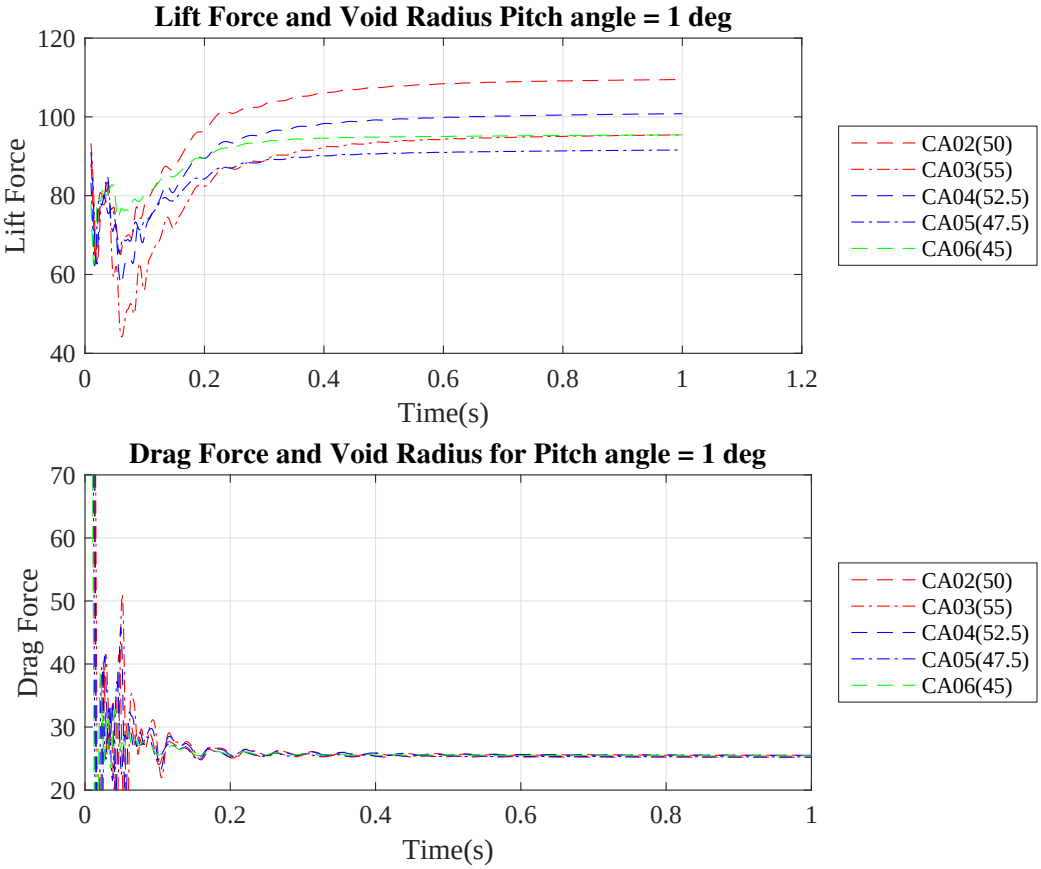

Figure 4.63: Lift and Drag With Void Radius SIM66 (1°)

For simulation SIM66 minimum steady state lift force is for case CA05 of 91.6N and maximum steady state lift force is for case CA02 of 109.5N. The minimum steady state drag force is for case CA02 of 25.18N and maximum steady state drag force is for case CA04 of 25.52N.

SIM67 Lift and Drag Variation With R_V

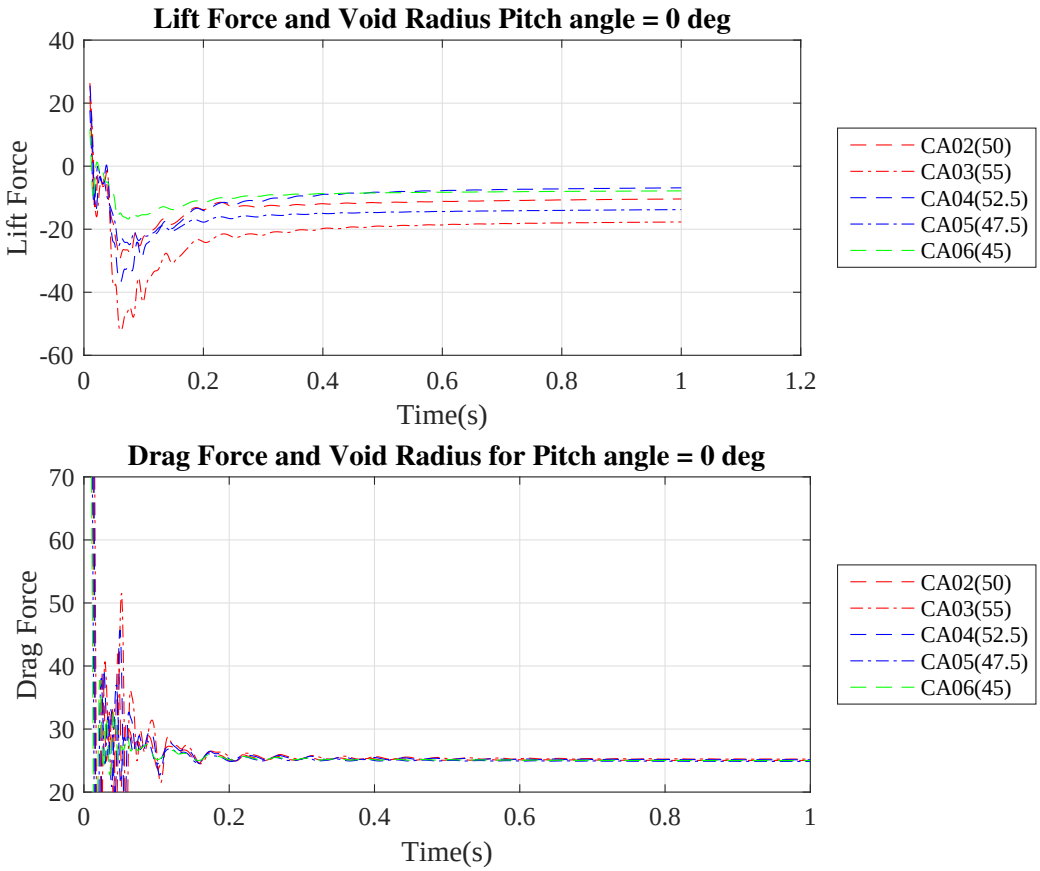

Figure 4.64: Lift and Drag With Void Radius SIM67 (0°)

For simulation SIM67 minimum steady state lift force is for case CA03 of -17.7N and maximum steady state lift force is for case CA04 of -6.8N. The steady state drag force for all cases are almost same of 25.00N.

SIM68 Lift and Drag Variation With R_V

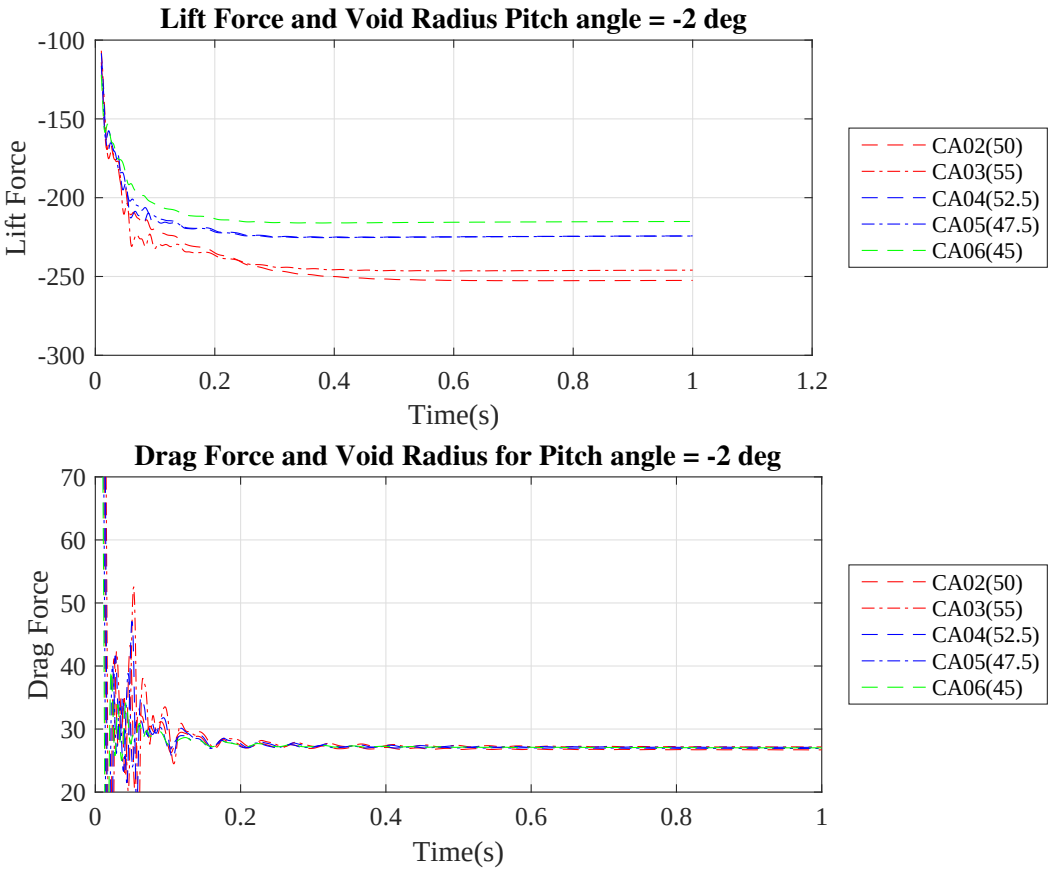

Figure 4.65: Lift and Drag With Void Radius SIM68 (-2°)

For simulation SIM68 minimum steady state lift force is for case CA02 of -252N and maximum steady state lift force is for case CA06 of -215N. The minimum steady state drag force is for case CA02 of 26.70N and maximum steady state drag force is for case CA03 of 27.16N.

SIM69 Lift and Drag Variation With R_V

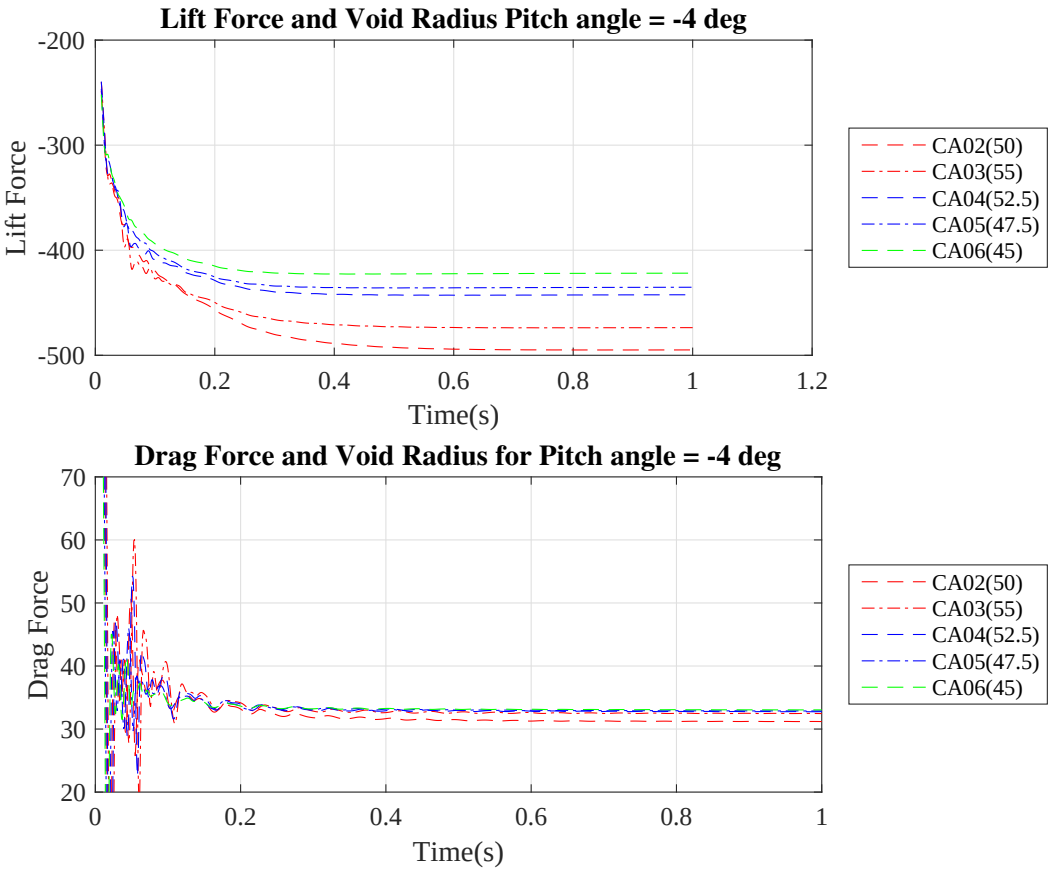

Figure 4.66: Lift and Drag With Void Radius SIM69 (-4°)

For simulation SIM69 minimum steady state lift force is for case CA02 of -494.9N and maximum steady state lift force is for case CA06 of -421.8N. The minimum steady state drag force is for case CA02 of 31.18N and maximum steady state drag force is for case CA06 of 33.04N.

SIM70 Lift and Drag Variation With R_V

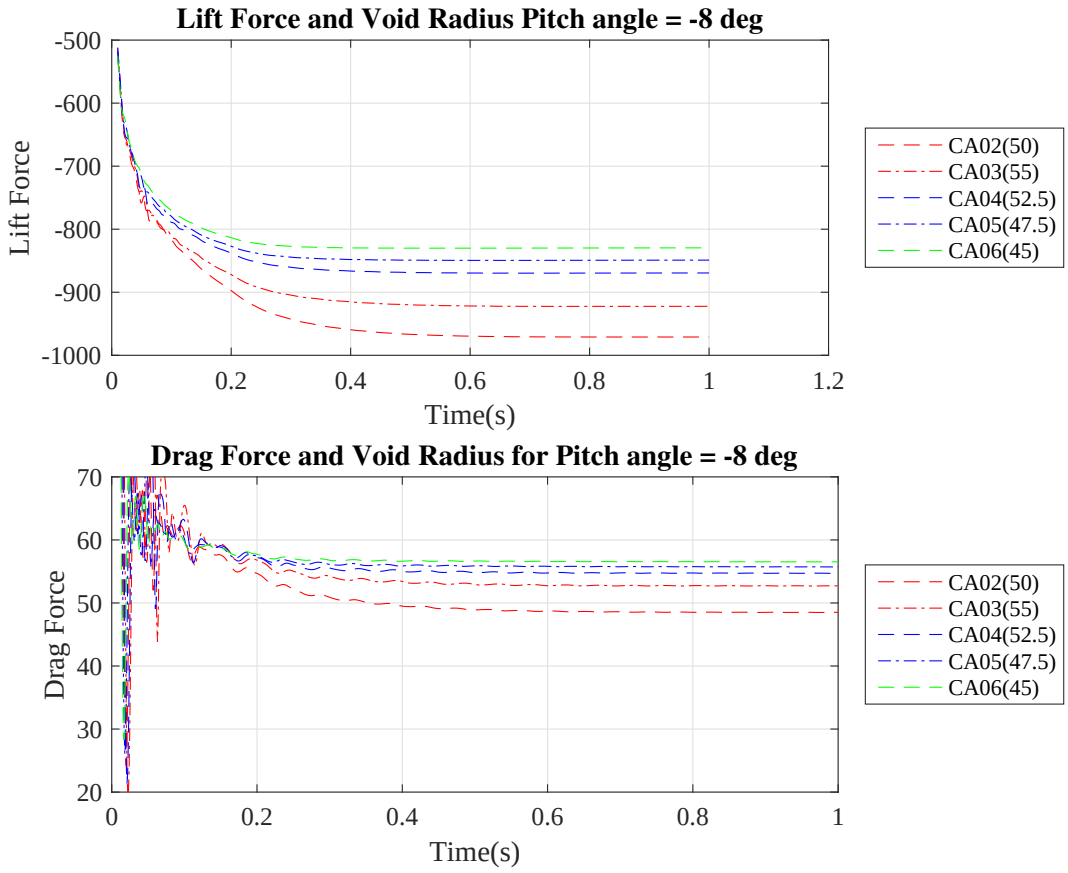

Figure 4.67: Lift and Drag With Void Radius SIM70 (-8°)

For simulation SIM70 minimum steady state lift force is for case CA02 of -970.98N and maximum steady state lift force is for case CA06 of -829.55N. The minimum steady state drag force is for case CA02 of 48.51N and maximum steady state drag force is for case CA06 of 56.52N.

From these results the case CA02 have the maximum lift for all positive pitch angles and it have the negative maximum lift for negative drag in pitch angles which is favorable. Also it shows least in most cases. case CA06 seems to be the least efficient. Case CA02

is the base case and hence the best R_V is selected that of CA02 which is 50.

4.2.4 Variation of Lift and Drag With Y Coordinate of the Void

In this section the variation of lift and drag force in time with Y coordinate of circular void Y_V is discussed. This is the result that are combined from cases CA02 and CA07 to CA10. There are 8 results corresponding to the 8 pitch angles.

SIM63 Lift and Drag Variation With Y_V

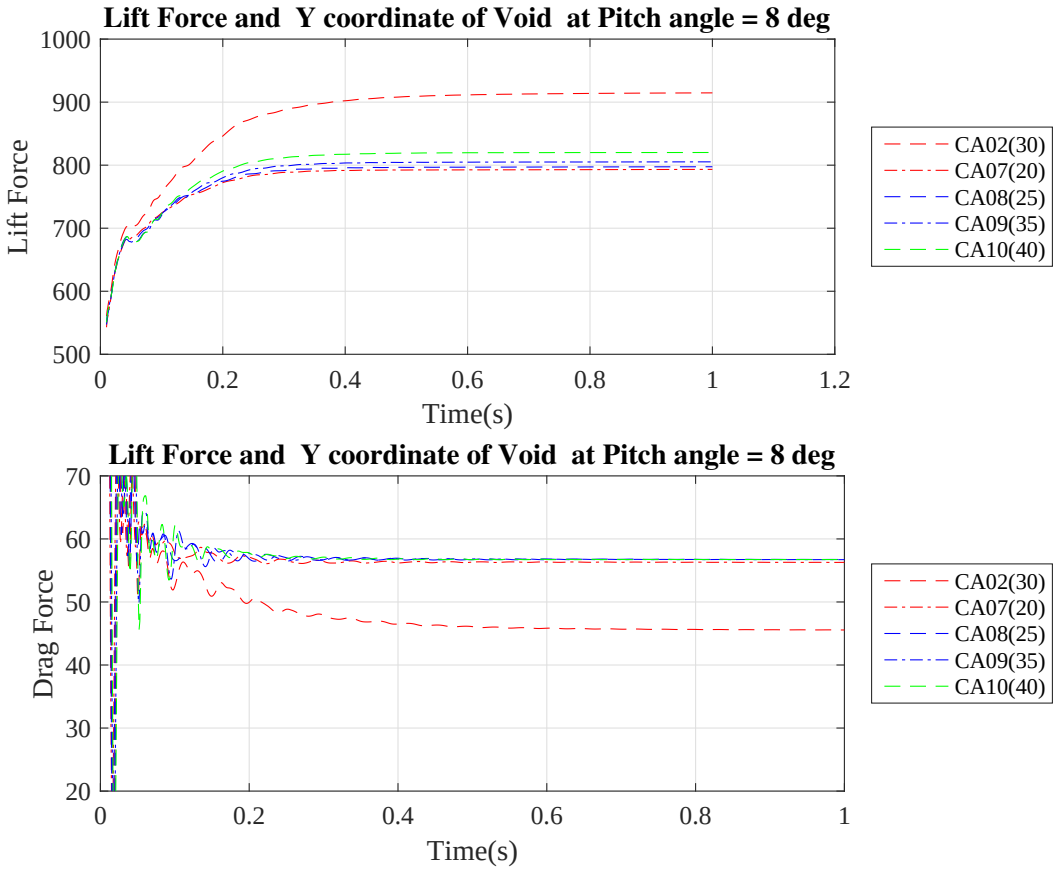

Figure 4.68: Lift and Drag With Y Coordinate of Void SIM63 (8 °)

For simulation SIM63 minimum steady state lift force is for case CA07 of 793.32N and maximum steady state lift force is for case CA02 of 914.68N. The minimum steady

state drag force is for case CA02 of 45.55N and maximum steady state drag force is for case CA08 of 56.73N.

SIM64 Lift and Drag Variation With Y_V

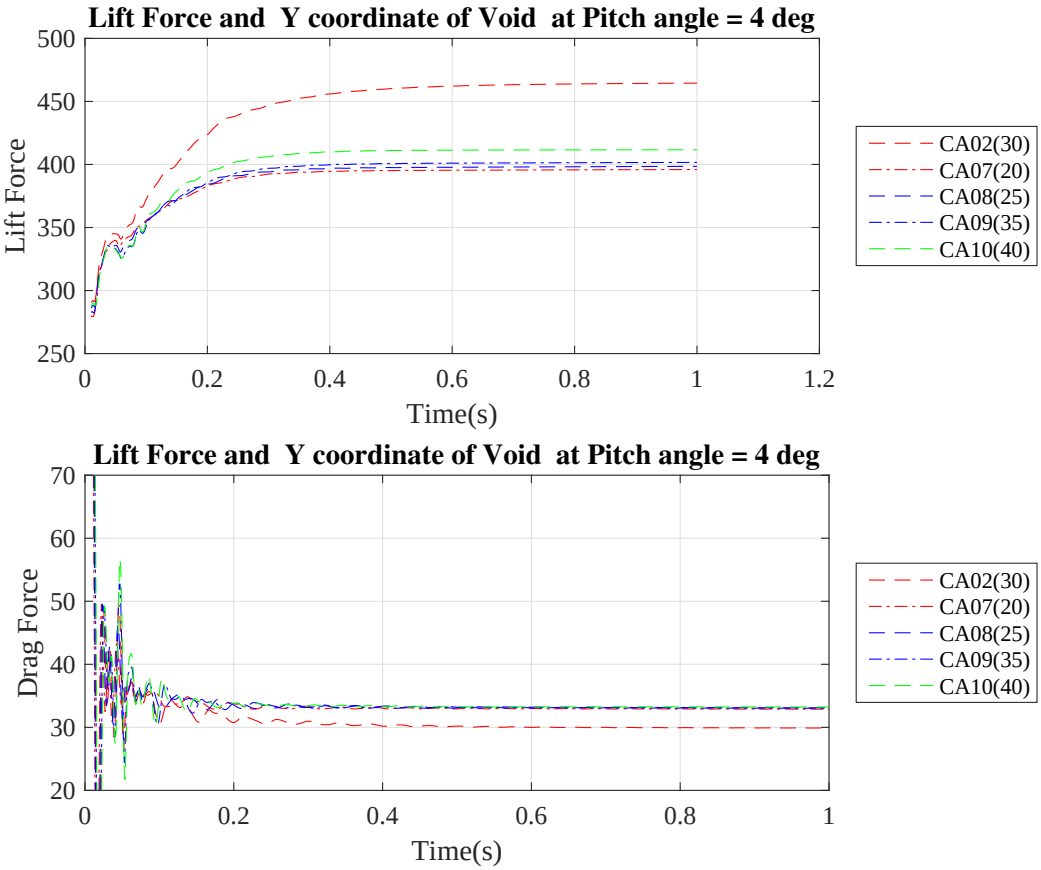

Figure 4.69: Lift and Drag With Y Coordinate of Void SIM64 (4 °)

For simulation SIM64 minimum steady state lift force is for case CA07 of 395.98N and maximum steady state lift force is for case CA02 of 464.51N. The minimum steady state drag force is for case CA02 of 29.9N and maximum steady state drag force is for case CA10 of 33.2N.

SIM65 Lift and Drag Variation With Y_V

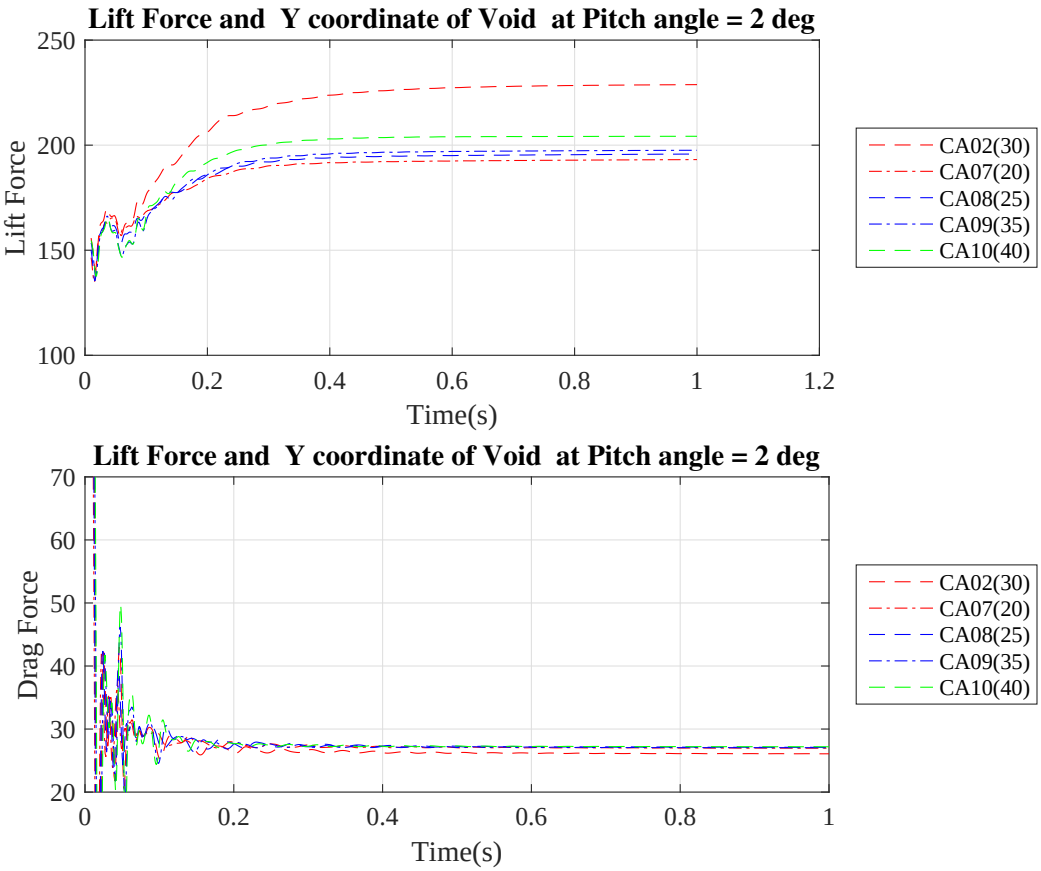

Figure 4.70: Lift and Drag With Y Coordinate of Void SIM65 (2 °)

For simulation SIM65 minimum steady state lift force is for case CA07 of 193.13N and maximum steady state lift force is for case CA02 of 228.80N. The minimum steady state drag force is for case CA02 of 26.071N and maximum steady state drag force is for case CA10 of 27.192N.

SIM66 Lift and Drag Variation With Y_V

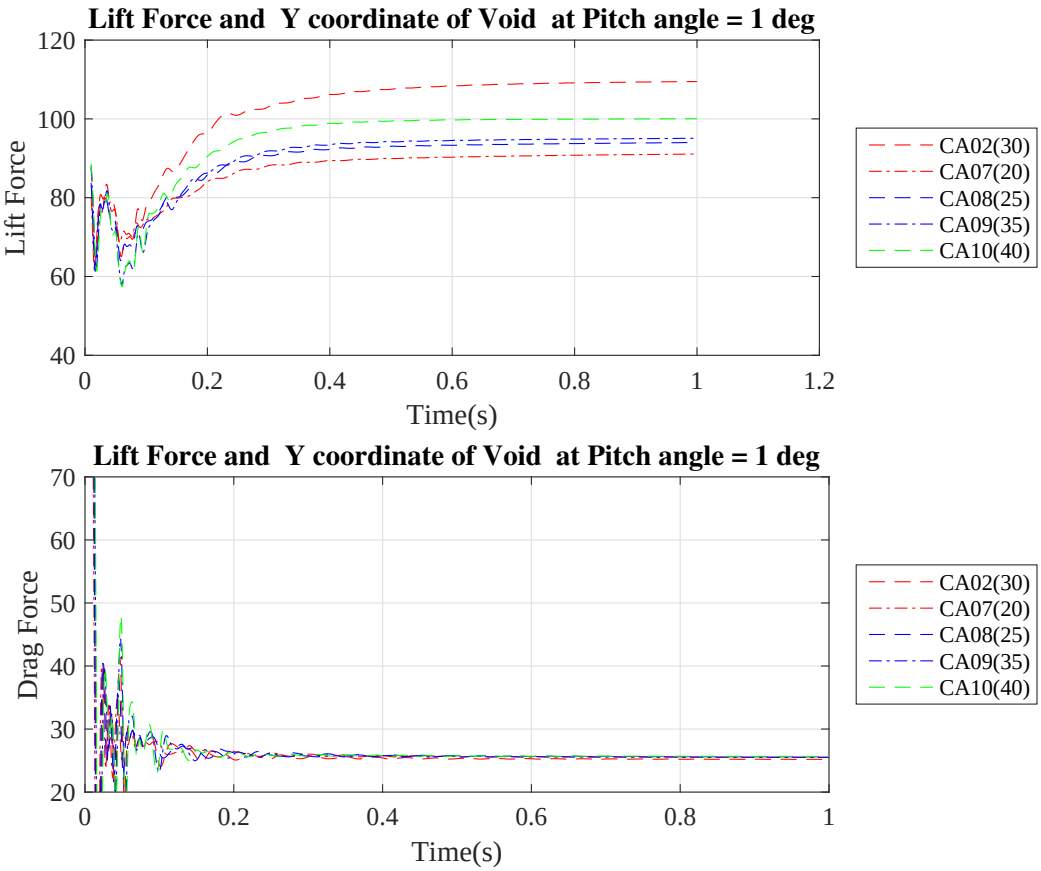

Figure 4.71: Lift and Drag With Y Coordinate of Void SIM66(1 °)

For simulation SIM67 minimum steady state lift force is for case CA07 of 91.08N and maximum steady state lift force is for case CA02 of 109.47N. The minimum steady state drag force is for case CA02 of 25.18N and maximum steady state drag force is for case CA10 of 25.66N.

SIM67 Lift and Drag Variation With Y_V

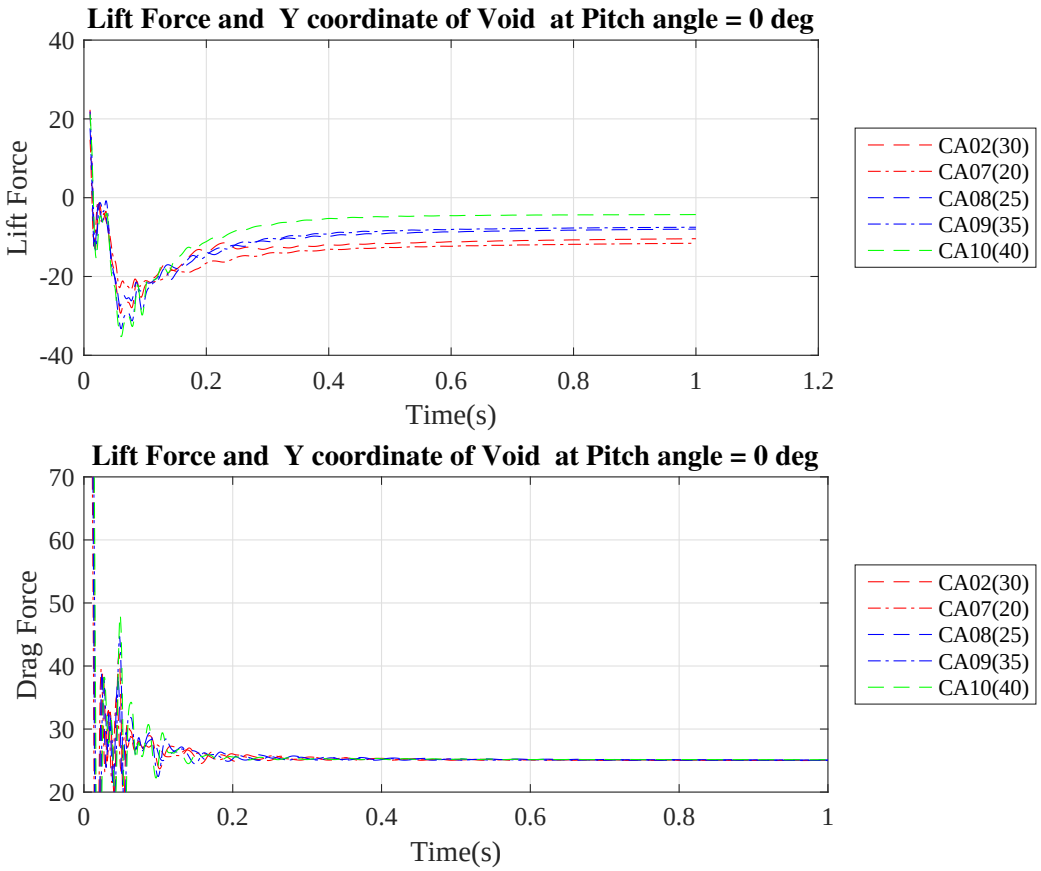

Figure 4.72: Lift and Drag With Y Coordinate of Void SIM67 (0 °)

For simulation SIM67 minimum steady state lift force is for case CA02 of -11.56N and maximum steady state lift force is for case CA10 of -4.28N. The minimum steady state drag force is for all cases is around 25N.

SIM68 Lift and Drag Variation With Y_V

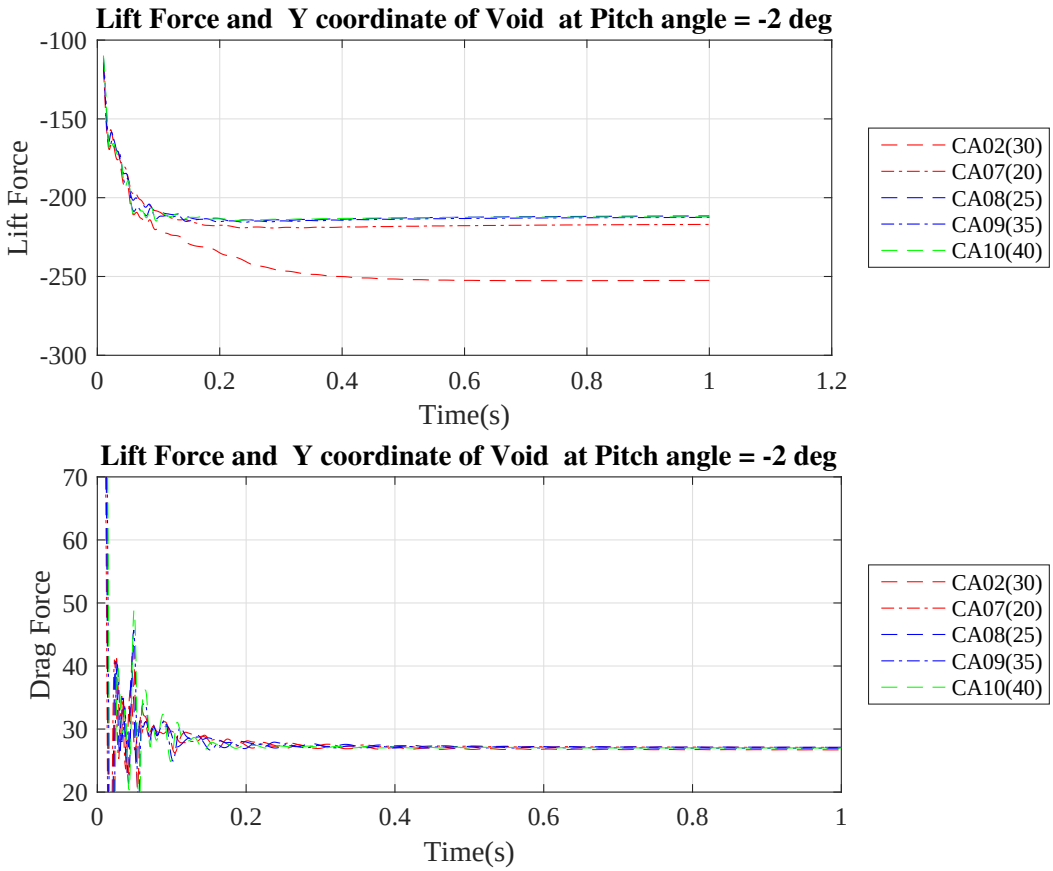

Figure 4.73: Lift and Drag With Y Coordinate of Void SIM68 (-2 °)

For simulation SIM68 minimum steady state lift force is for case CA02 of -252.49N and maximum steady state lift force is for case CA08 of -211.59N. The minimum steady state drag force is for case CA02 of 26.70N and maximum steady state drag force is for case CA08 of 27.10N.

SIM69 Lift and Drag Variation With Y_V

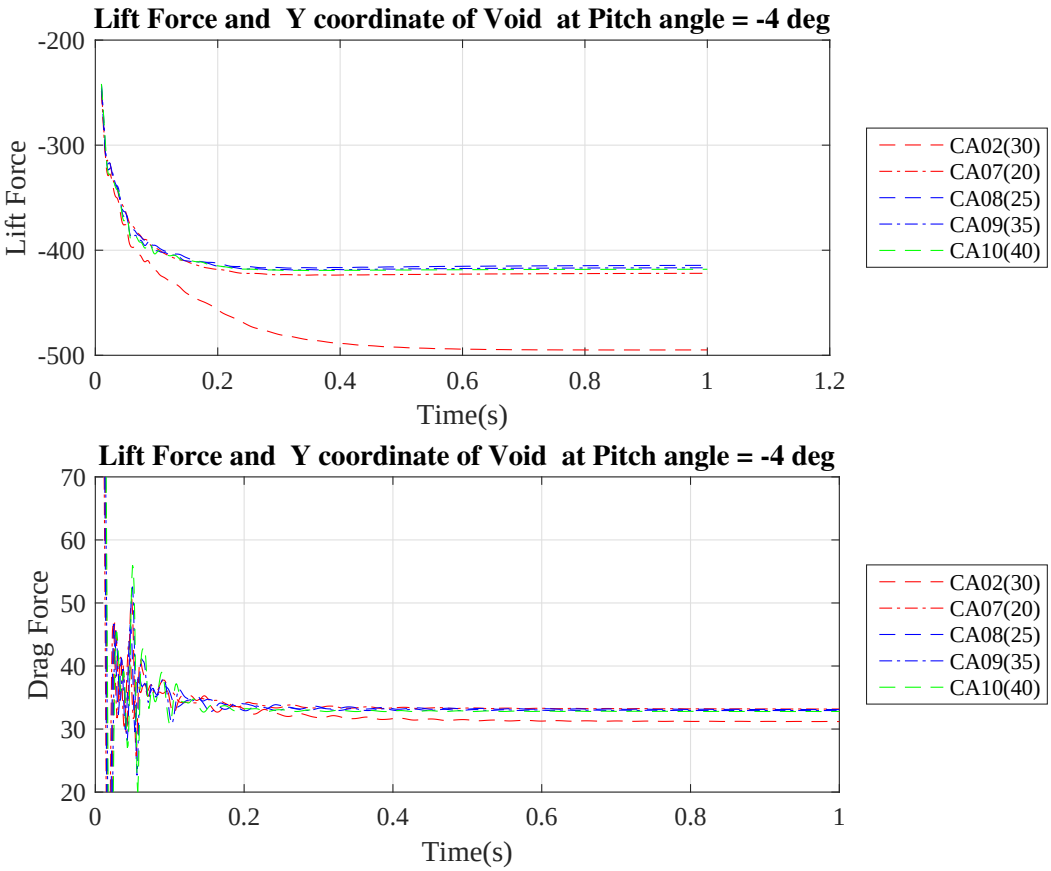

Figure 4.74: Lift and Drag With Y Coordinate of Void SIM69 (-4 °)

For simulation SIM69 minimum steady state lift force is for case CA02 of -494.89N and maximum steady state lift force is for case CA08 of -414.40N. The minimum steady state drag force is for case CA02 of 31.18N and maximum steady state drag force is for case CA07 of 33.18N.

SIM70 Lift and Drag Variation With Y_V

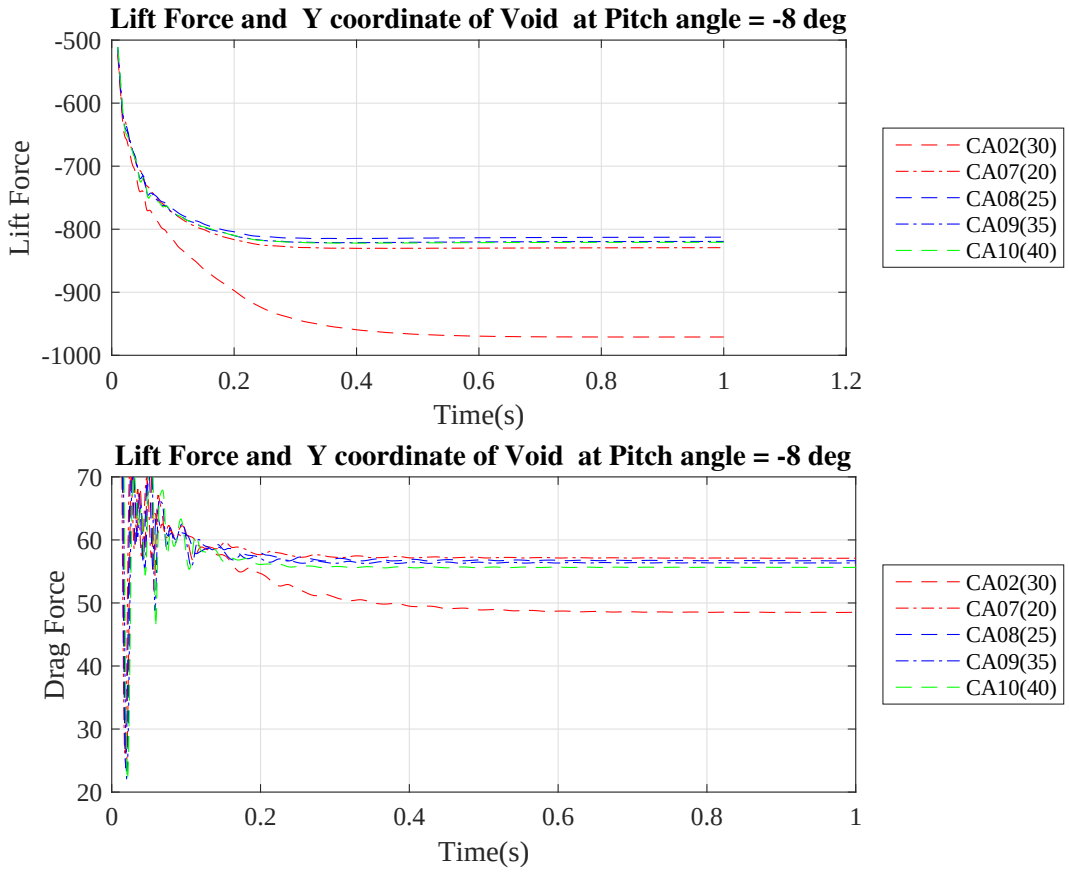

Figure 4.75: Lift and Drag With Y Coordinate of Void SIM70 (-8 °)

For simulation SIM70 minimum steady state lift force is for case CA02 of -970.98N and maximum steady state lift force is for case CA08 of -829.28N. The minimum steady state drag force is for case CA02 of 48.51N and maximum steady state drag force is for case CA07 of 57.01N.

From these results the case CA02 have the maximum lift for all positive pitch angles and it have the negative maximum lift for negative drag in pitch angles which is favorable. Also it shows least drag in most cases. case CA08 seems to be the least efficient. Case

CA02 is the base case and hence the best Y_V is selected that of CA02 which is 30.

4.2.5 Variation of Lift and Drag With X Coordinate of the Void

In this section the variation of lift and drag force in time with X coordinate of circular void X_V is discussed. This is the result that are combined from cases CA02 and CA11 to CA14. There are 8 results corresponding to the 8 pitch angles.

SIM63 Lift and Drag Variation With X_V

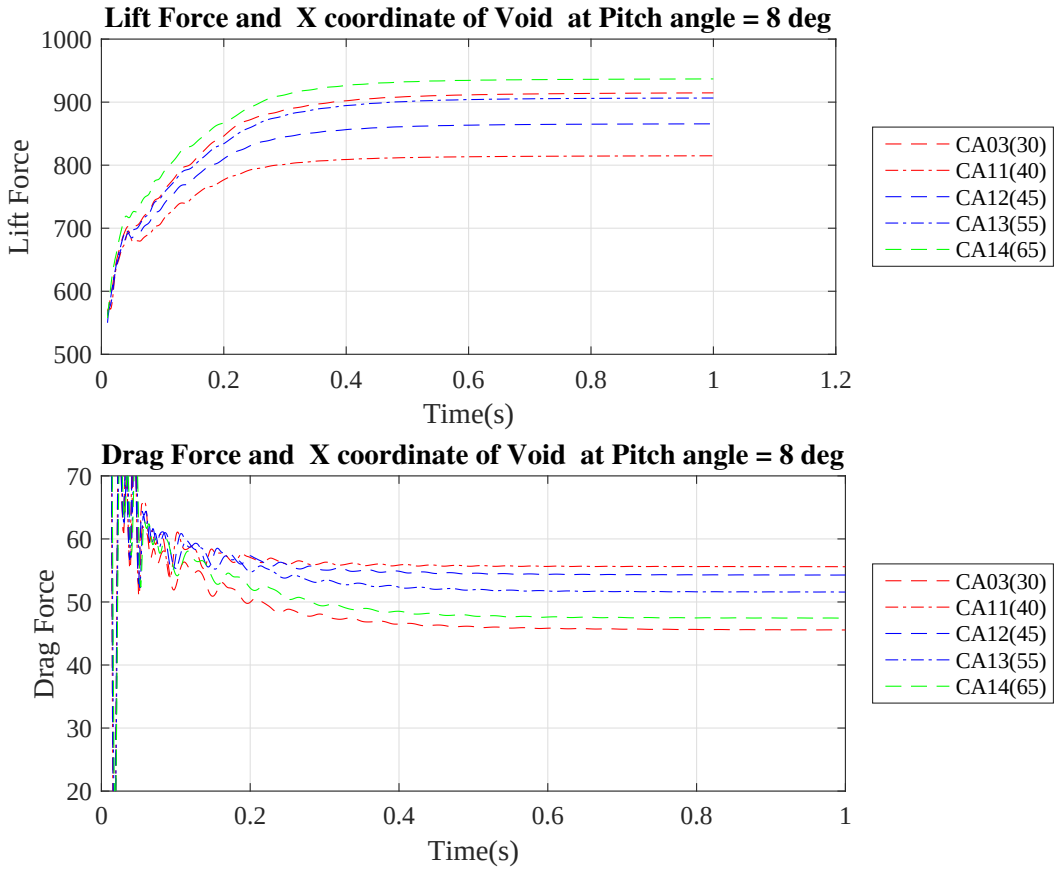

Figure 4.76: Lift and Drag With X Coordinate of Void SIM63 (8 °)

For simulation SIM63 minimum steady state lift force is for case CA11 of 814.88N and maximum steady state lift force is for case CA14 of 936.81N. The minimum steady

state drag force is for case CA02 of 45.55N and maximum steady state drag force is for case CA11 of 55.59N.

SIM64 Lift and Drag Variation With X_V

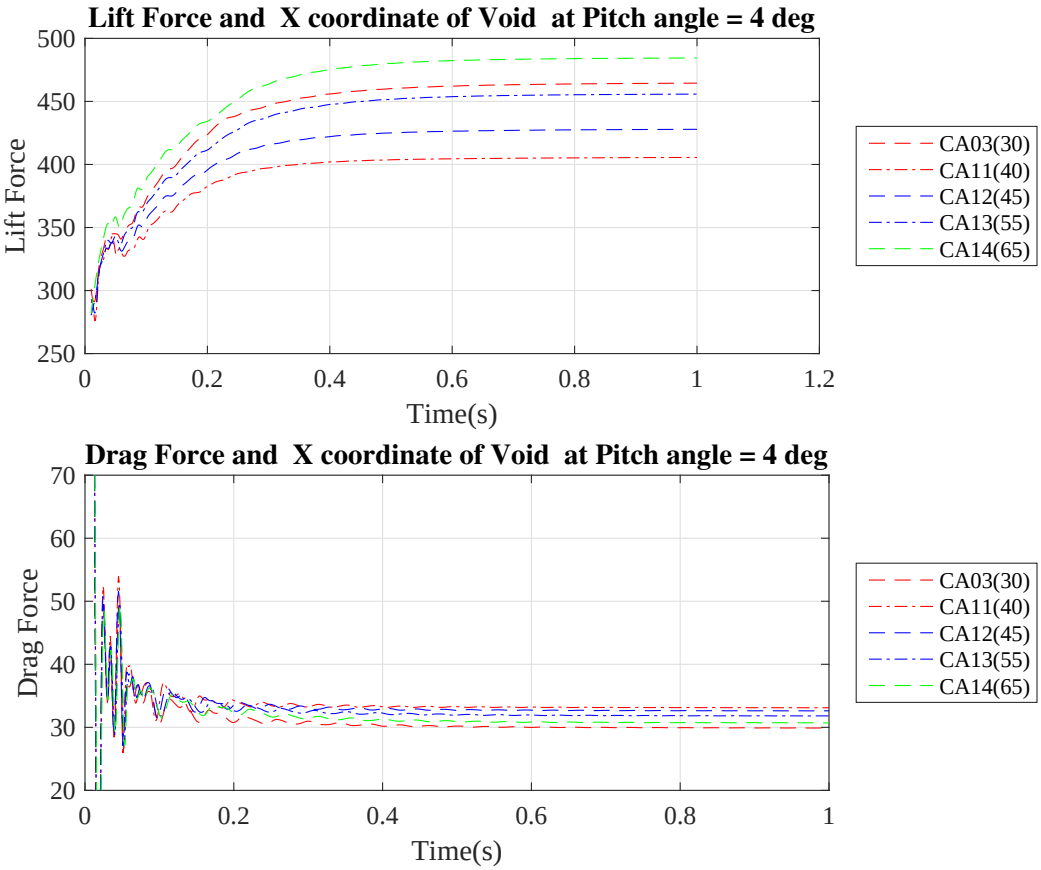

Figure 4.77: Lift and Drag With X Coordinate of Void SIM64 (4 °)

For simulation SIM64 minimum steady state lift force is for case CA11 of 405.57N and maximum steady state lift force is for case CA14 of 484.45N. The minimum steady state drag force is for case CA02 of 29.90N and maximum steady state drag force is for case CA11 of 33.30N.

SIM65 Lift and Drag Variation With X_V

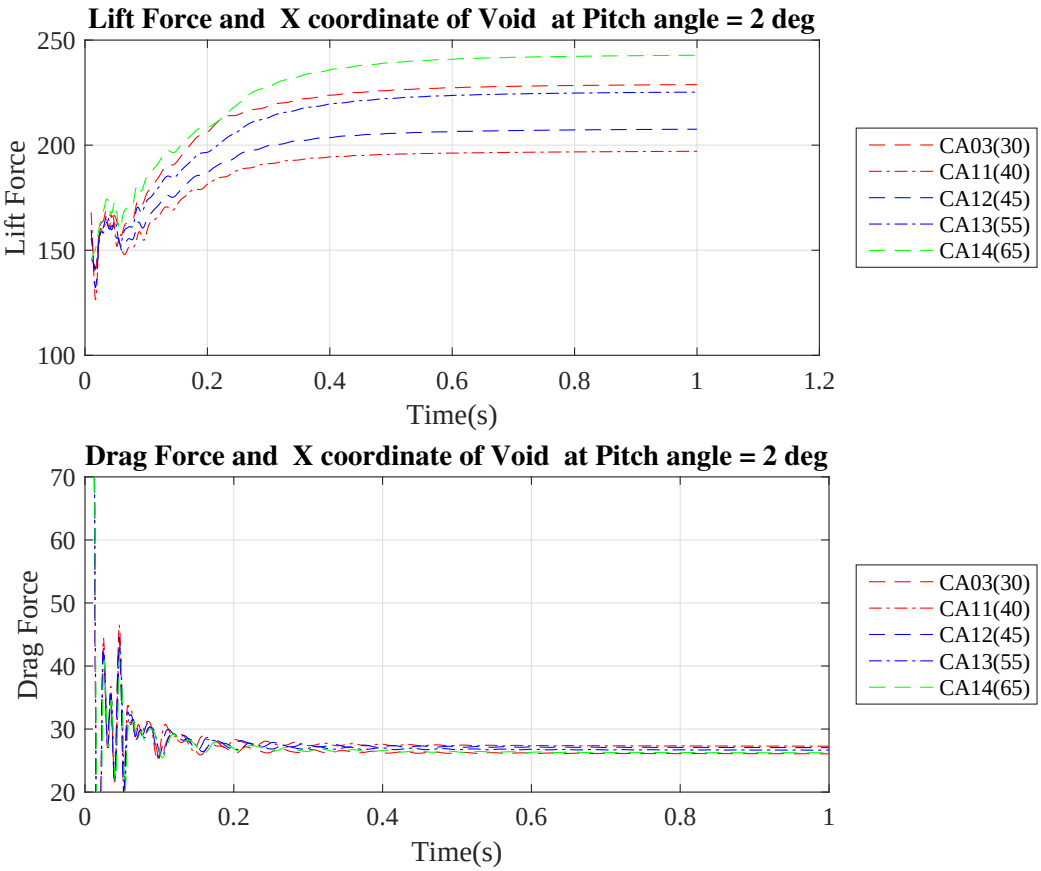

Figure 4.78: Lift and Drag With X Coordinate of Void SIM65 (2 °)

For simulation SIM65 minimum steady state lift force is for case CA11 of 197.07N and maximum steady state lift force is for case CA14 of 242.77N. The minimum steady state drag force is for case CA02 of 26.07N and maximum steady state drag force is for case CA11 of 27.29N.

SIM66 Lift and Drag Variation With X_V

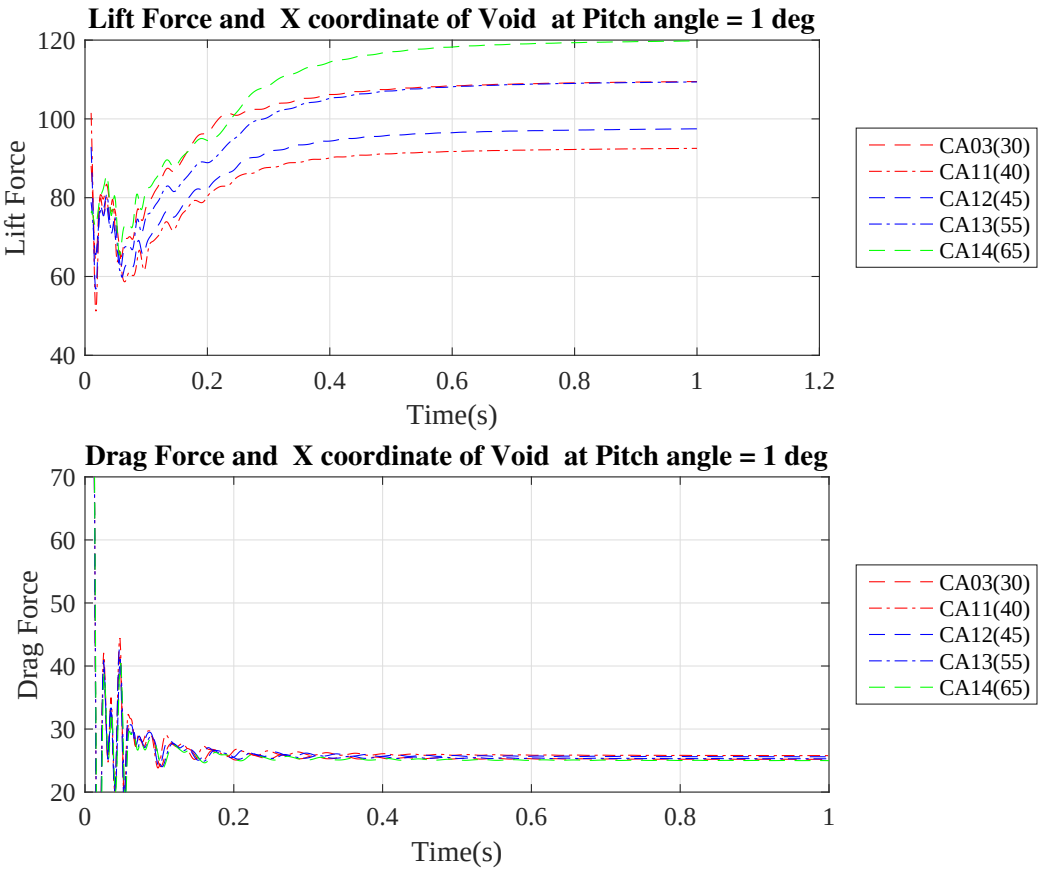

Figure 4.79: Lift and Drag With X Coordinate of Void SIM66(1 °)

For simulation SIM66 minimum steady state lift force is for case CA11 of 92.51N and maximum steady state lift force is for case CA14 of 119.78N. The minimum steady state drag force is for case CA14 of 24.99N and maximum steady state drag force is for case CA11 of 25.78N.

SIM67 Lift and Drag Variation With X_V

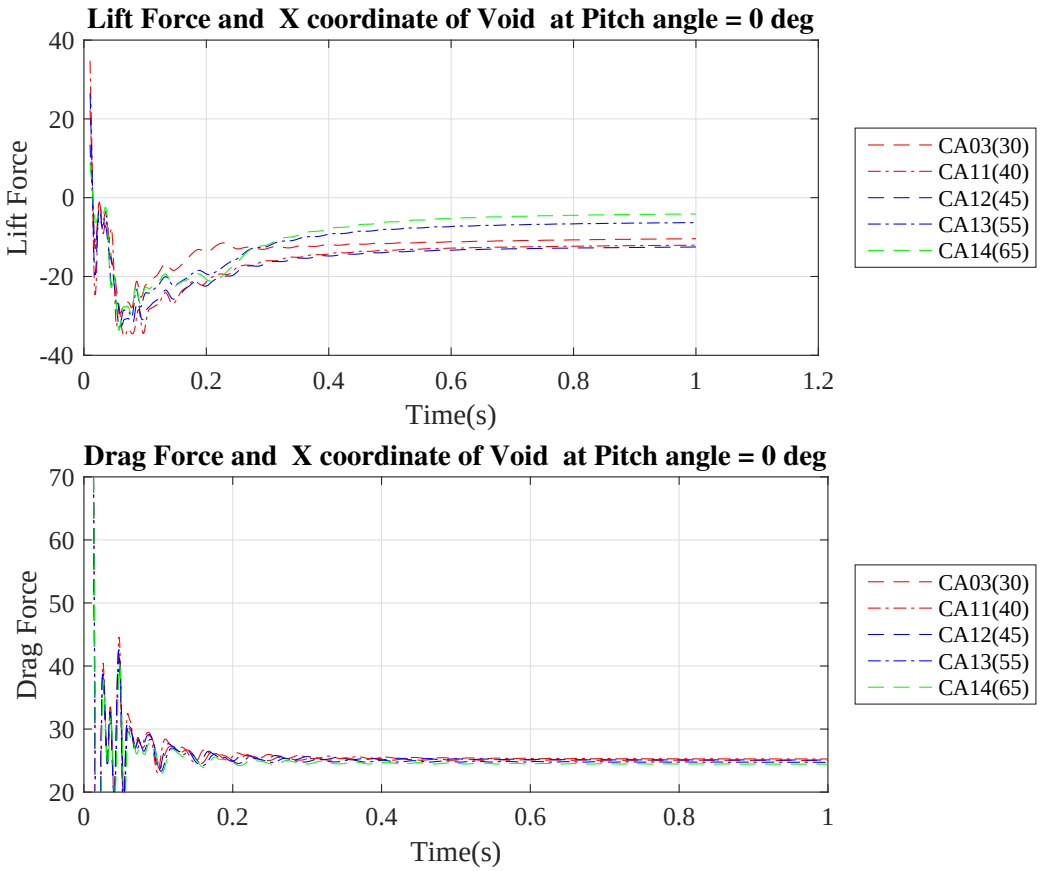

Figure 4.80: Lift and Drag With X Coordinate of Void SIM67 (0 °)

For simulation SIM67 minimum steady state lift force is for case CA02 of -12.05N and maximum steady state lift force is for case CA14 of -4.12N. The minimum steady state drag force is for case CA14 of 24.43N and maximum steady state drag force is for case CA11 of 25.25N.

SIM68 Lift and Drag Variation With X_V

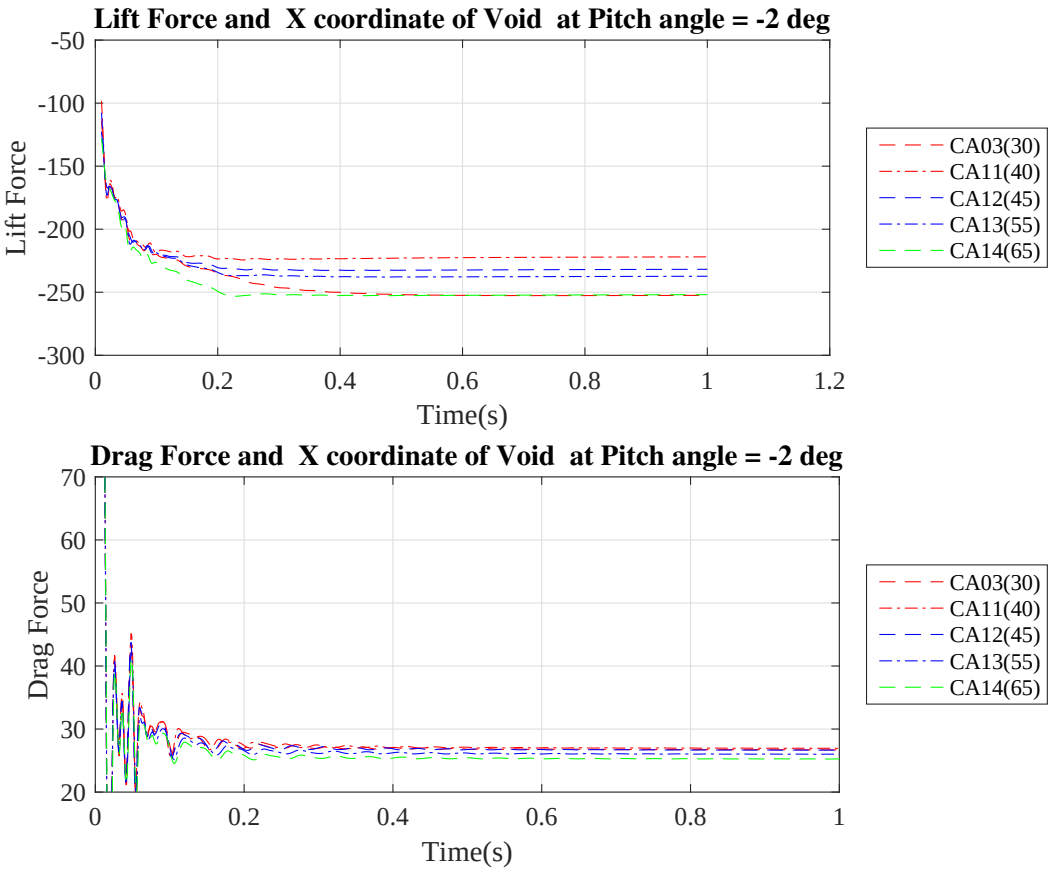

Figure 4.81: Lift and Drag With X Coordinate of Void SIM68 (-2 °)

For simulation SIM68 minimum steady state lift force is for case CA02 of -252.49N and maximum steady state lift force is for case CA11 of -221.94N. The minimum steady state drag force is for case CA13 of 26.001N and maximum steady state drag force is for case CA11 of 26.91N.

SIM69 Lift and Drag Variation With X_V

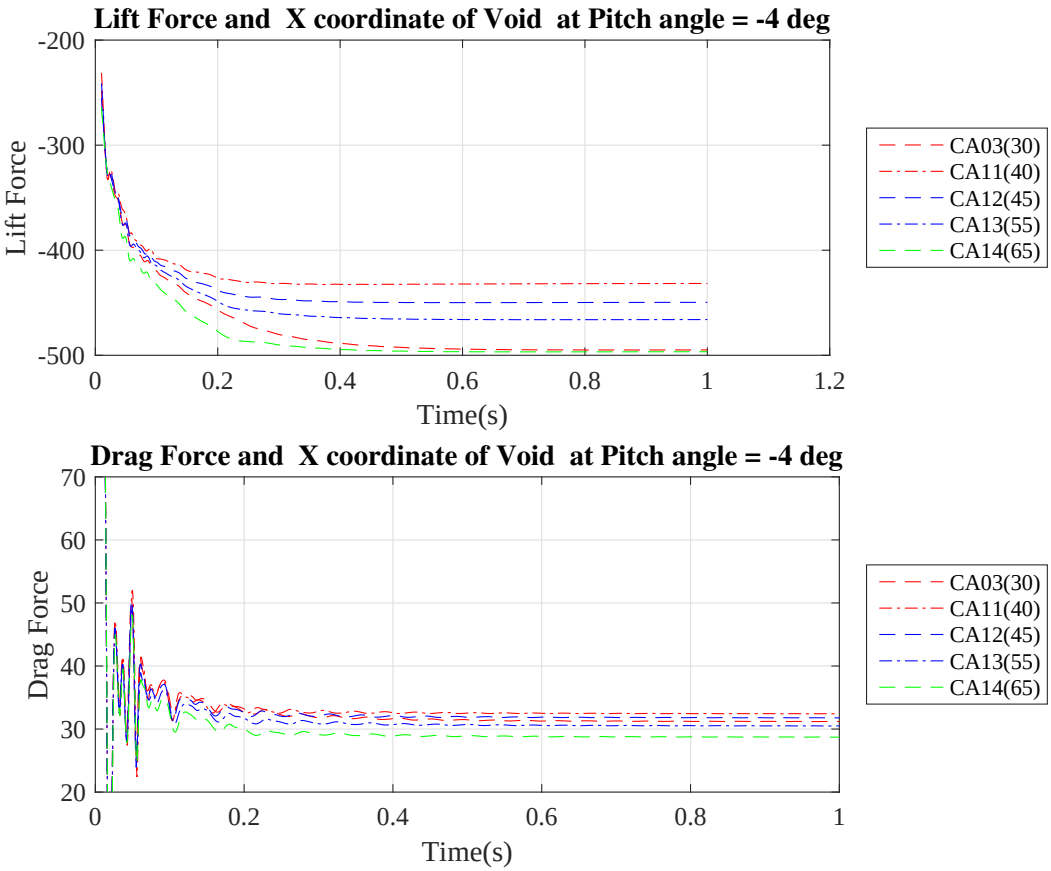

Figure 4.82: Lift and Drag With X Coordinate of Void SIM69 (-4 °)

For simulation SIM69 minimum steady state lift force is for case CA02 of -496.59N and maximum steady state lift force is for case CA06 of -431.62N. The minimum steady state drag force is for case CA14of 28.72N and maximum steady state drag force is for case CA11 of 32.41N.

SIM70 Lift and Drag Variation With X_V

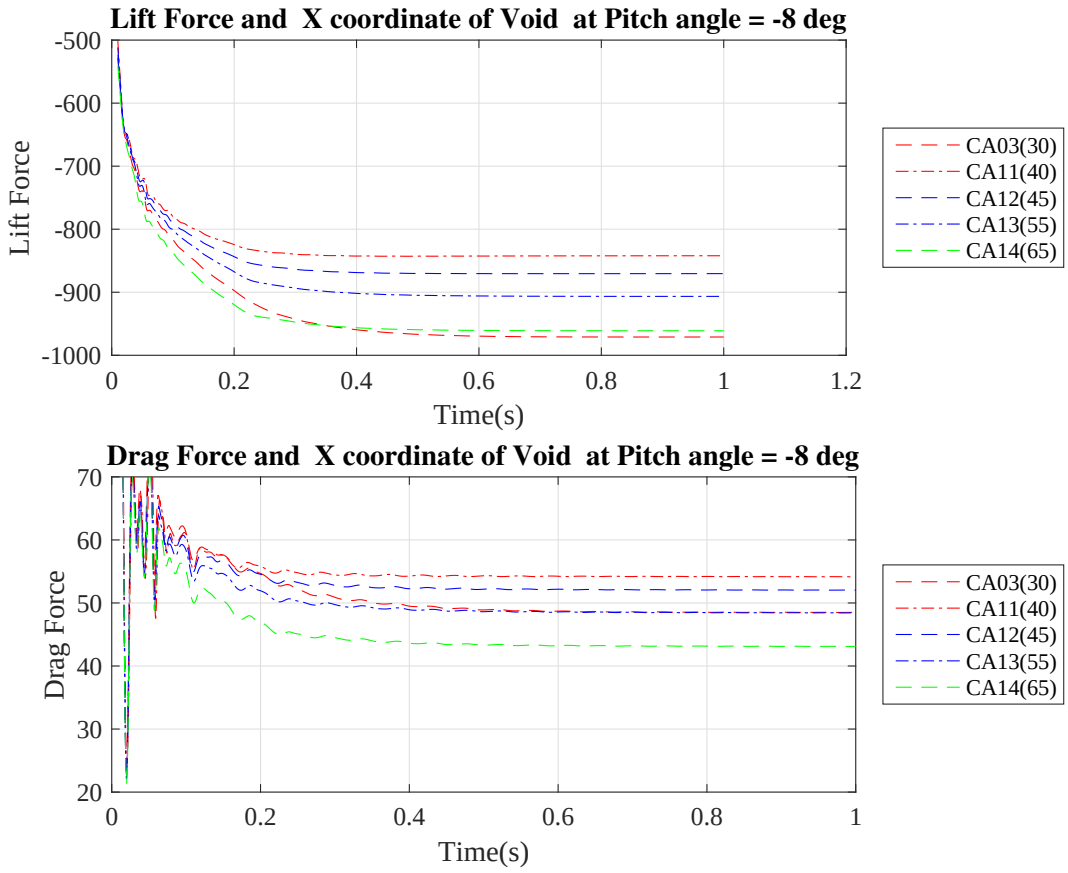

Figure 4.83: Lift and Drag With X Coordinate of Void SIM70 (-8 °)

For simulation SIM70 minimum steady state lift force is for case CA02 of -970.98N and maximum steady state lift force is for case CA11 of -842.55N. The minimum steady state drag force is for case CA14 of 43.11N and maximum steady state drag force is for case CA11 of 54.16N.

From these results the case CA14 have the maximum lift for most of the positive pitch angles and maximum negative drag for negative pitch angles. Case CA11 have least lift magnitude in most cases. For few negative pitch angles CA02 performed better. Con-

sidering the drag CA14 and CA02 equally good. Case CA11 is the least efficient. Selected X_V is that of case CA14 which is 120.

Selected Modification for Hydrofoil

From the results selected R_V=50, Y_V=30 and X_V=120which coincides with case CA14. SO the selected modification for the rotating turbine simulations is HM12 corresponding to the void size and position.

4.2.6 Rotating Turbine Simulations (RTS) With Modified Hydrofoil

The two modifications that are used for RTS are HM12 and HM09. The details of the RTS with modified cases are given in the Table 4.7. SIM stands for the serial number of simulation, CA stands for the cases RTS or SSS, CM stands for camber and in case of HM, void, N stands for number of layers, H stands for hydrofoil shape, HM stands for modified hydrofoil shape. The modification is applied for two hydrofoil shapes H, H00 which is the base case and H04 which was selected from the Section I simulations. The RTS with modified hydrofoils are compared with simulations with all other parameters same but without modification or HMXX.

The average moment and efficiency of RTS with modified hydrofoils is compared with RTS with same other input parameter except no modification in hydrofoil shape H, HMXX. This results are shown in the Table 4.8 where AM is the average moment, η is the power efficiency in percentage. XX stands for the simulations with same other input parameter except no modification in hydrofoil shape H, HMXX. The power efficiency η in percentage is found out using the equation Eqn. 4.11. where AM is average moment, ρ

is the density of the water, A is the sweep area of turbine which is diameter $\times$ depth and V is the flow velocity.

$$\eta = \frac{AM \times \omega}{\frac{1}{2} \times \rho \times A \times V^2} \tag{4.11}$$

Table 4.7: Simulations With Modified Hydrofoils

SIM	Name	CA	N	H	CM	HM	λ	β	σ
SIM14	S11001090244	RTS	1	H00	1	HM09	L02	B4	S4
SIM22	S11002090244	RTS	1	H00	2	HM09	L02	B4	S4
SIM29	S11001130244	RTS	1	H00	1	HM13	L02	B4	S4
SIM31	S11042090244	RTS	1	H04	2	HM09	L02	B4	S4
SIM33	S11042120244	RTS	1	H04	2	HM12	L02	B4	S4
SIM40	S11042120564	RTS	1	H04	2	HM12	L05	B6	S4
SIM42	S11042120764	RTS	1	H04	2	HM12	L07	B6	S4
SIM44	S11042120964	RTS	1	H04	2	HM12	L09	B6	S4
SIM46	S110420121064	RTS	1	H04	2	HM12	L10	B6	S4

Table 4.8: Comparison of Average Moment and Power Efficiency With HM

SIM	HM	CM	AM (Nm)	η %	SIM XX	AM XX (Nm)	η XX %
SIM14	HM09	1	110.53	28.48	SIM13	122.47	31.56
SIM22	HM09	2	128.723	33.16	SIM13	122.47	31.56
SIM29	HM13	1	107.73	27.76	SIM04	135.72	34.97
SIM31	HM09	2	124.53	32.09	SIM04	135.72	34.97
SIM33	HM12	2	136.52	35.18	SIM04	135.72	34.97
SIM40	HM12	2	138.03	44.46	SIM39	138.64	44.66
SIM42	HM12	2	136.74	49.92	SIM41	132.76	48.46
SIM44	HM12	2	118.89	48.21	SIM43	119.95	48.94
SIM46	HM12	2	106.81	48.16	SIM45	108.59	48.97

From the comparison it could be seen that in for three simulations, modified hydrofoil showed better efficiency than that of hydrofoil with no modifications. Also among all simulations, maximum efficiency is shown by SIM42 which have the modified hydrofoil HM. In this section the detailed comparison is done only for this case.

SIM42 With Modified Hydrofoil HM12

The hydrofoil shape for SIM42 was H= NACA0018. Other input parameters are flow velocity V=2m/s, Chord length C = 0.1778m, diameter D = 0.6096m, solidity σ = 0.2785 (S4), tip speed ratio λ = 1.36 (L07), Number of layers N=1, number of blades n=3 and pitch angle $\beta = 0°$ (B4). The final velocity profile of this simulation is given in the Fig. 4.84 and the final pressure profile of final the simulation is given in the Fig. 4.85 The final time is 2 seconds. For SIM42 the lift force in LC for hydrofoil A at t = 0.891s is $L_{LC} = -2211N$ and drag force is $D_{(LC)} = -619.5N$. Moment is 251.4Nm substituting in Eqn. 4.11 we get DP (0.891) = 0.0283m.

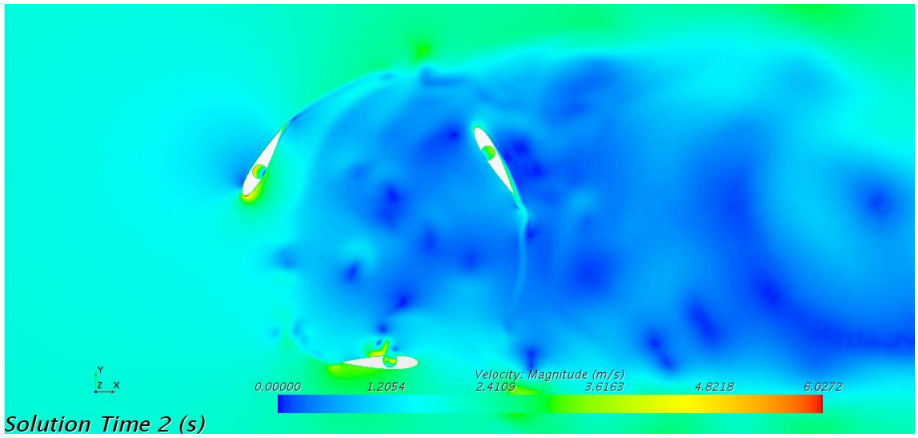

Figure 4.84: SIM42 Velocity Profile at 2 s

The time history of the moment on each of the hydrofoils and total moment is given in the Fig. 4.86

In order to compare with the base case, the second maximum moment peak of hydrofoil A is chosen. The second maximum moment (MM) peak of the hydrofoil A occurs at time t = 0.891s with a value of 251.4 Nm and at a rotation angle of 454.41°. The position

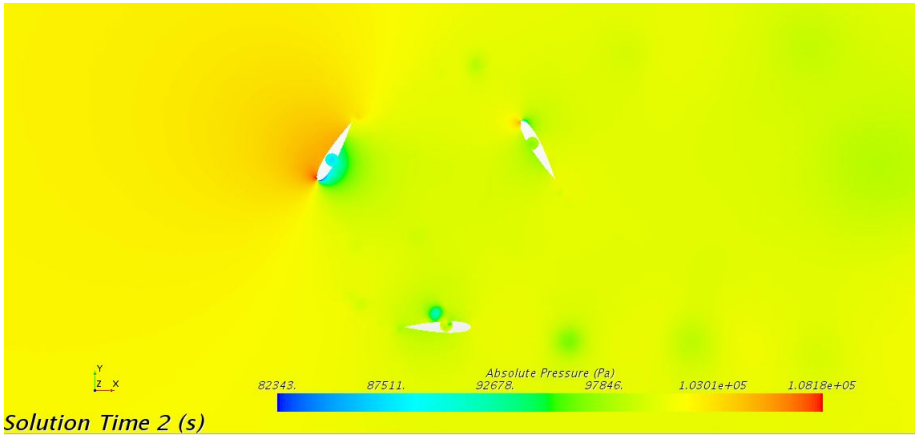

Figure 4.85: SIM42 Pressure Profile at 2 s

of the hydrofoil A at this time is 94.41°. But the nearest stored data points for velocity profile are at t = 0.88s and t = 0.90s. So t = 0.88 s is selected for velocity and pressure profiles. The velocity profile at second peak of hydrofoil A is shown in the Fig. 4.87. A close look at hydrofoil position at 94° could be seen in the Fig. 4.88. The pressure profile at the maximum moment point seen in the Fig. 4.89. The pressure profile around the hydrofoil at maximum moment position could be seen in the Fig. 4.90

The time history of lift and drag force on the hydrofoils in global coordinate system could be seen from the figures Fig. 4.92 and Fig. 4.91 respectively. GC stands for global coordinate and LC stands for local coordinate.

The lift and drag force of SIM42 in local coordinate (LC) are plotted in the Fig. 4.93

SIM41 Hydrofoil Without Modification HMXX

The hydrofoil shape for SIM41 was H= NACA0018. Other input parameters are flow velocity V=2m/s, Chord length C = 0.1778m, diameter D = 0.6096m, solidity σ =

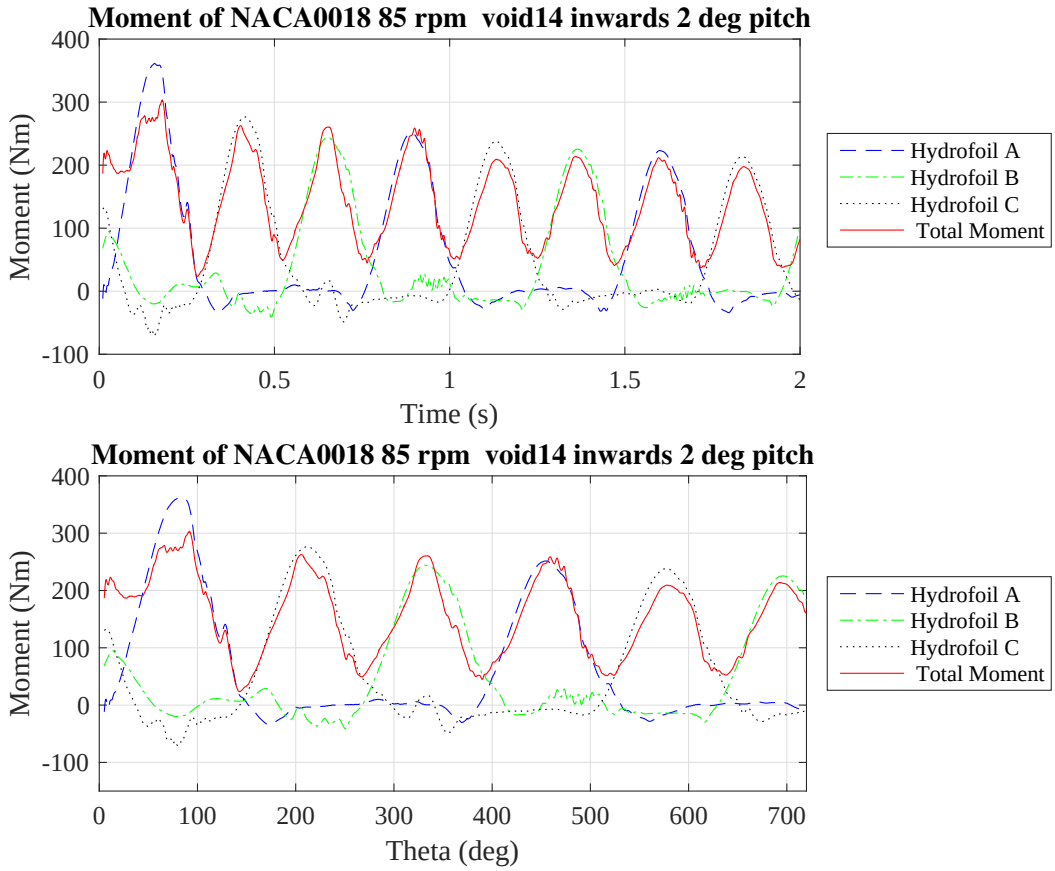

Figure 4.86: SIM42 Moment Plot

0.2785 (S4), tip speed ratio λ = 1.36 (L07), Number of layers N=1, number of blades n=3 and pitch angle $\beta = 0°$ (B4). The final velocity profile of this simulation is given in the Fig. 4.94 and the final pressure profile of final the simulation is given in the Fig. 4.95 The final time is 2 seconds.

The time history of the moment on each of the hydrofoils and total moment is given in the Fig. 4.96

In order to compare with the base case, the second maximum moment peak of hydrofoil A is chosen. The second maximum moment (MM) peak of the hydrofoil A occurs at

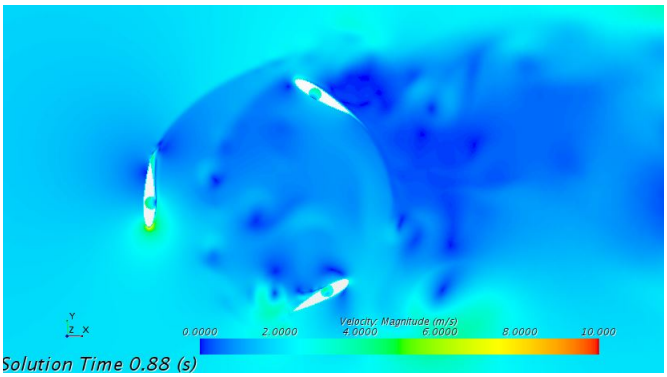

Figure 4.87: Velocity Profile at t = 0.88 s SIM42

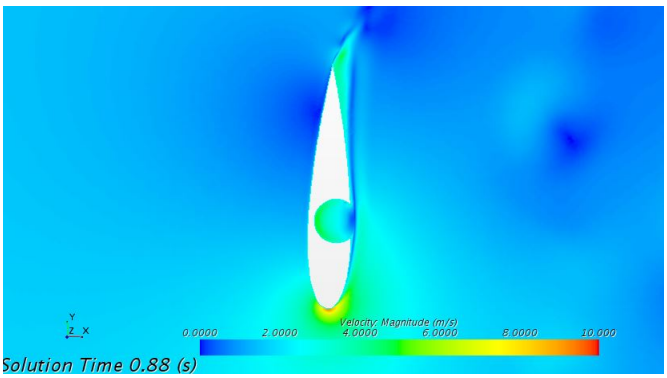

Figure 4.88: Velocity Profile Around Hydrofoil at Maximum Moment SIM42

time t = 0.893s with a value of 260.4 Nm and at a rotation angle of 455.43°. The position of the hydrofoil A at this time is 95.41°. But the nearest stored data points for velocity profile are at t = 0.88s and t = 0.90s. So t = 0.88 s is selected for velocity and pressure profiles. The velocity profile at second peak of hydrofoil A is shown in the Fig. 4.97. A close look at hydrofoil position at 94° could be seen in the Fig. 4.98. The pressure profile at the maximum moment point seen in the Fig. 4.99. The pressure profile around the hydrofoil at maximum moment position could be seen in the Fig. 4.100

The time history of lift and drag force on the hydrofoils in global coordinate system could be seen from the figures Fig. 4.102 and Fig. 4.101 respectively. GC stands for global

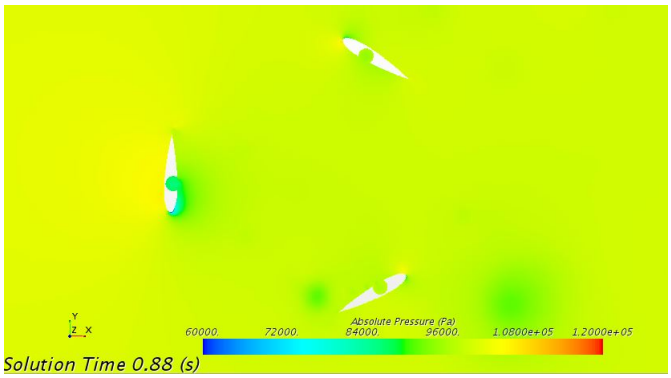

Figure 4.89: Pressure Profile of Turbine at t = 0.88 s SIM42

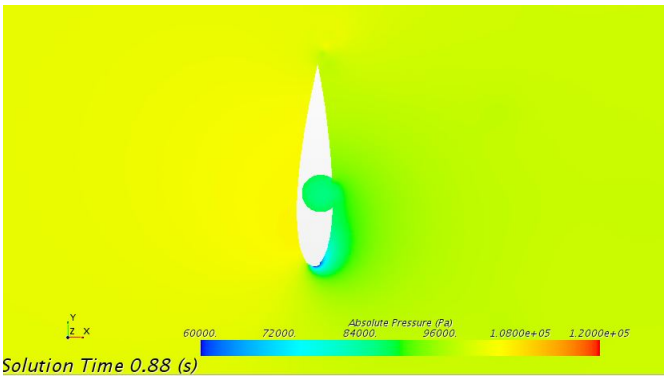

Figure 4.90: Pressure Profile Around Hydrofoil at Peak Moment

coordinate and LC stands for local coordinate.

The lift and drag force of SIM42 in local coordinate (LC) are plotted in the Fig. 4.103

For SIM41 the lift force in LC for hydrofoil A at t = 0.891s is $L_{LC} = -2104N$ and drag force is $D_{(LC)} = -642.9N$. Moment is 260.8Nm substituting in Eqn. 4.11 we get DP (0.891) = 0.0308m.

From these values it is seen that the peak moment of SIM41 which has HMXX is greater than that of SIM42 HM12 even though the average is lesser than SIM42. It can be seen that the negative lift force of SIM41(2104N) is smaller than that SIM42(2211N). The negative drag force of SIM42 (641N) is higher than that of SIM42(619.5N). The distance

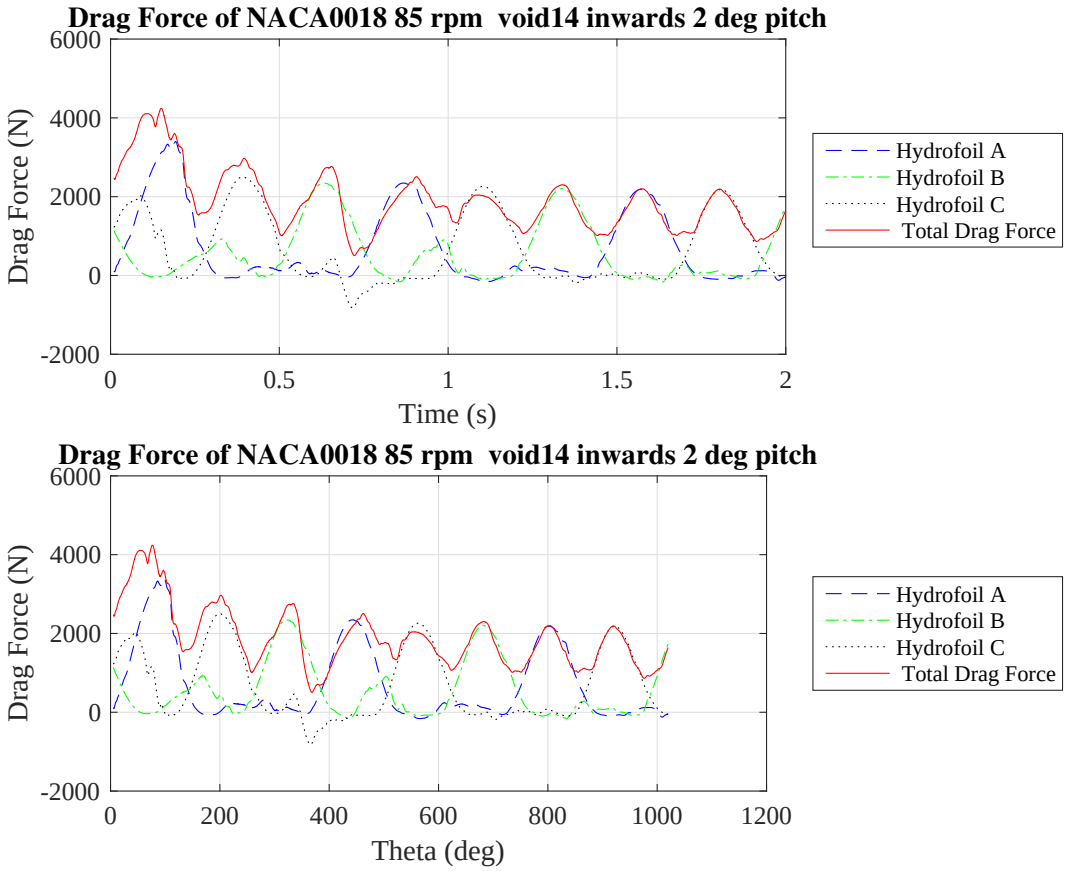

Figure 4.91: Drag Force of SIM42 in GC

to center of pressure is larger for SIM41 (0.0308m) than SIM42 (0.02830m). So the lever arm for lift force is higher.

The increase in moment from lift force for SIM41 is 2.27Nm. Now the increase in moment from drag force for SIM41 = 7.13Nm. So it can be said that the major reason for peak moment of SIM41 with NACA0018 is due to the higher negative drag force around hydrofoil. But the reason for higher average of SIM42 to be investigated. For that the moment plot of hydrofoil A, B and C are compared for both cases in Fig. 4.104, Fig 4.105 and Fig. 4.106. It could be seen from the figures that both overlap almost but on the

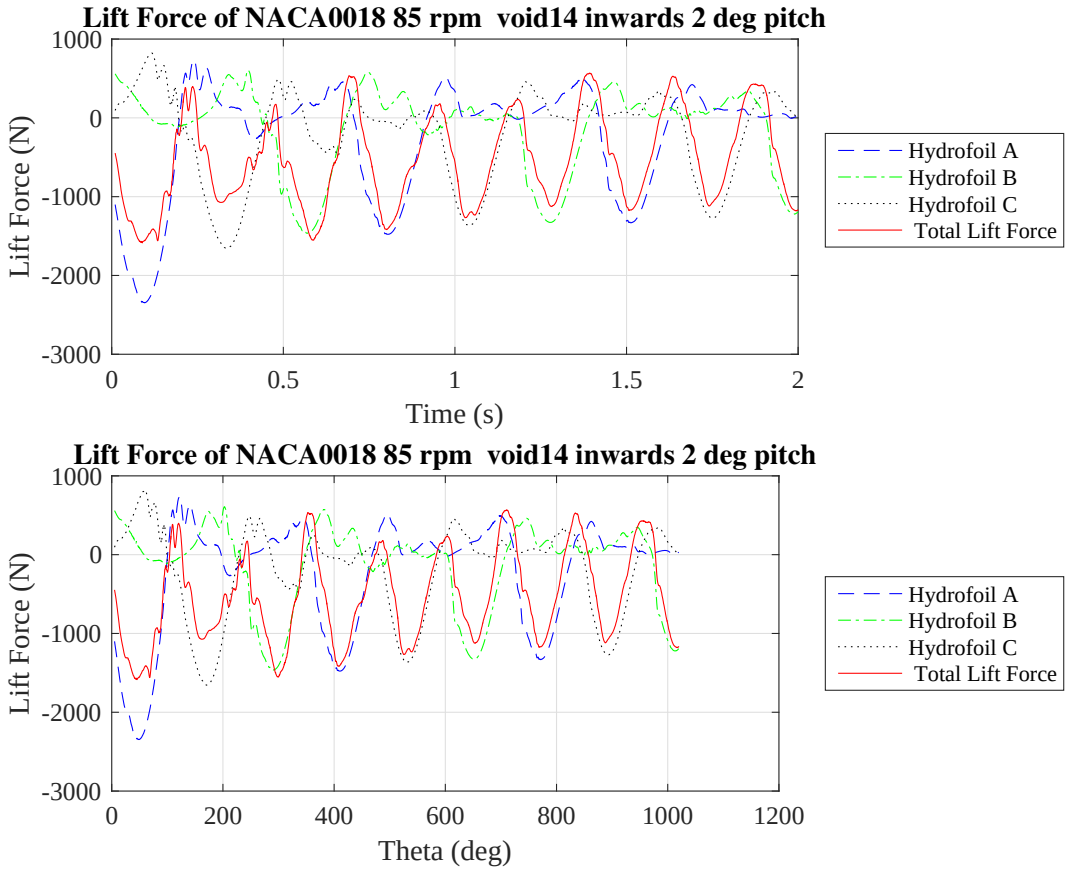

Figure 4.92: Lift Force of SIM42 in GC

right side of the peak SIM42 is slightly wider especially in the region where trough starts. Since this pattern is seen in all three hydrofoils it can be considered as a non-temporary pattern. For hydrofoil C it starts at t = 1.22s to 1.35s, θ=142° to 208.5°. For hydrofoil A it starts at t = 0.99s to 1.11s, θ=145° to 206°. For hydrofoil B it starts at t = 0.76s to 0.88s, θ=147° to 208°. So to investigate the pressure profiles in this region t = 1.28s is selected for hydrofoil C for SIM41 and SIM42. This can be seen from figures Fig. 4.107 and Fig. 4.108. The moment of hydrofoil C for SIM41 at t = 1.28s is -16.21Nm, lift is -387.9N and drag is 51.43N. So dp = -0.0014 for SIM41. Moment due to drag is -15.67Nm and that

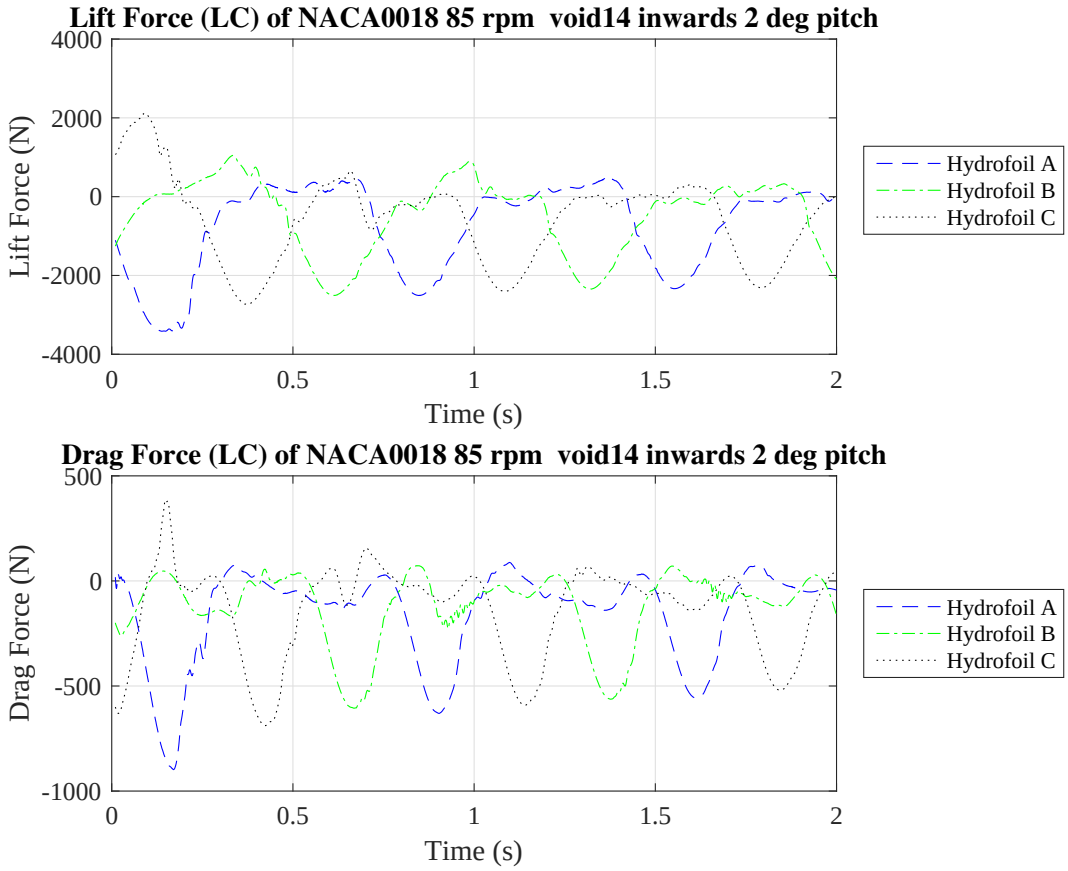

Figure 4.93: Lift and Drag Force of SIM42 in LC

due to lift is -0.54Nm for SIM41.Now the moment of hydrofoil C for SIM42 at t = 1.28s is -3.80Nm, lift is -31.34N and drag is 33.14N. So dp = 0.2011 for SIM42. Moment due to drag is -10.10Nm and that due to lift is 6.3Nm for SIM42. From the velocity figures it can be seen that a vortex with high velocity is passing through the inner side of the hydrofoil. Due to the presence of void for SIM42 vortex partially breaks and positive moment is created due to lift instead of negative moment in case of SIM41 in this region.

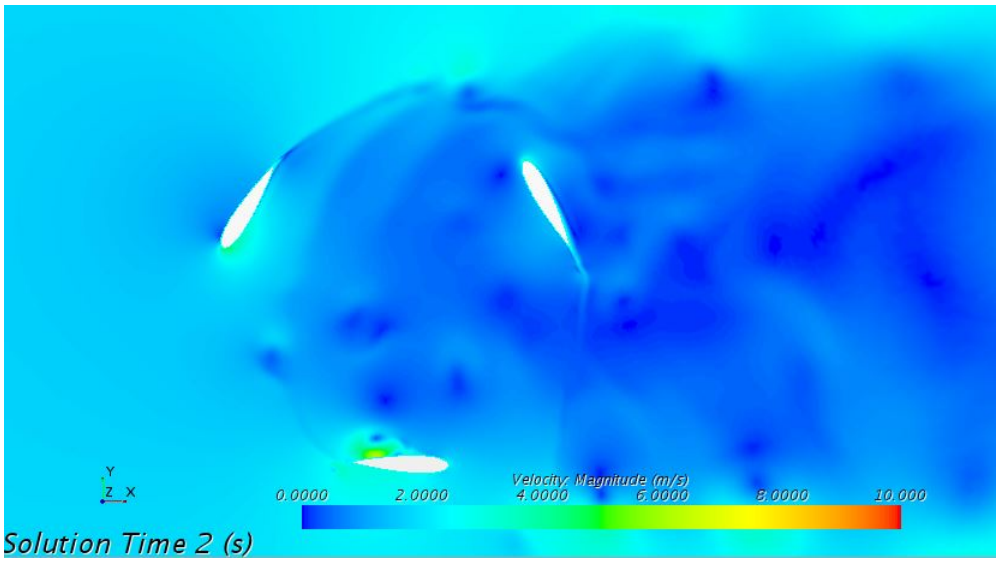

Figure 4.94: SIM41 Velocity Profile at 2 s

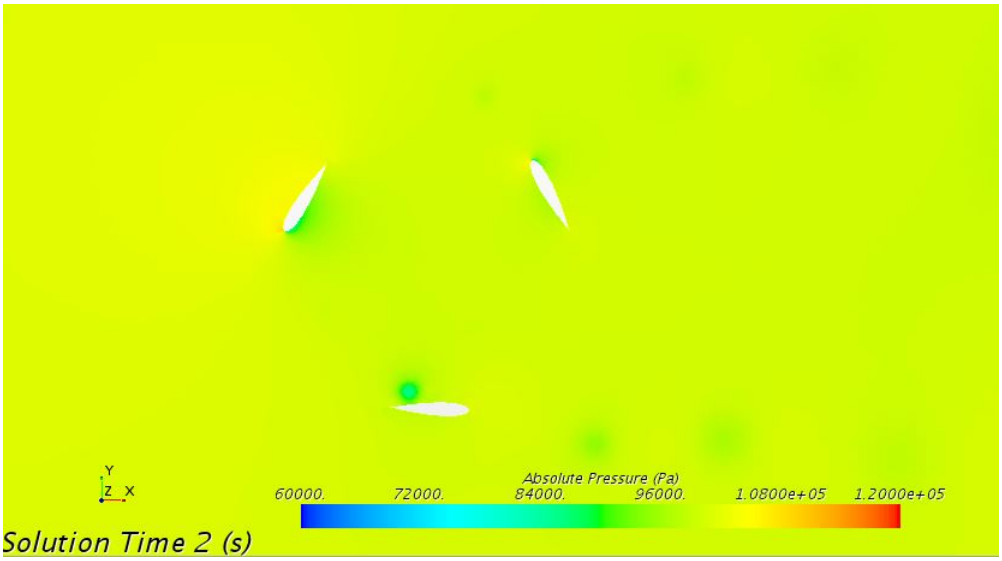

Figure 4.95: SIM41 Pressure Profile at 2 s

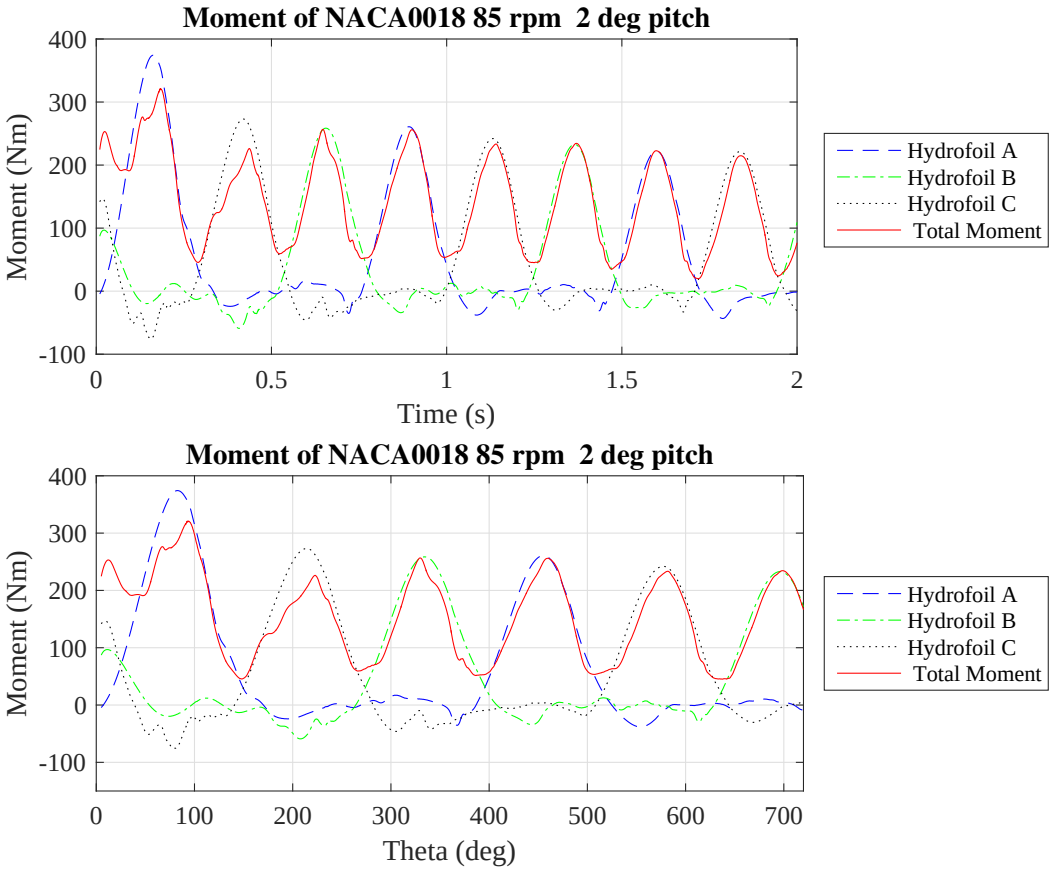

Figure 4.96: SIM41 Moment Plot

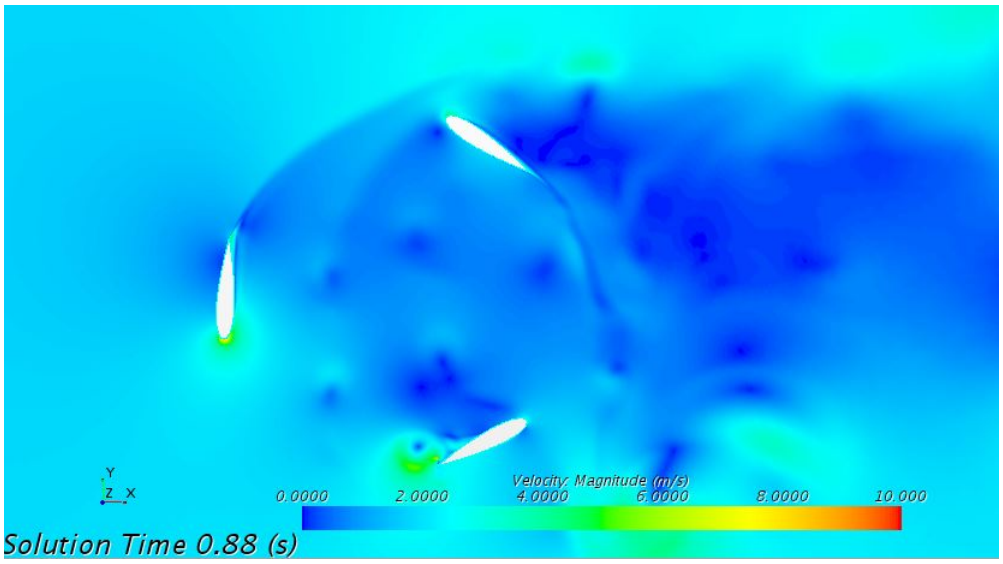

Figure 4.97: Velocity Profile at t = 0.88 s SIM42

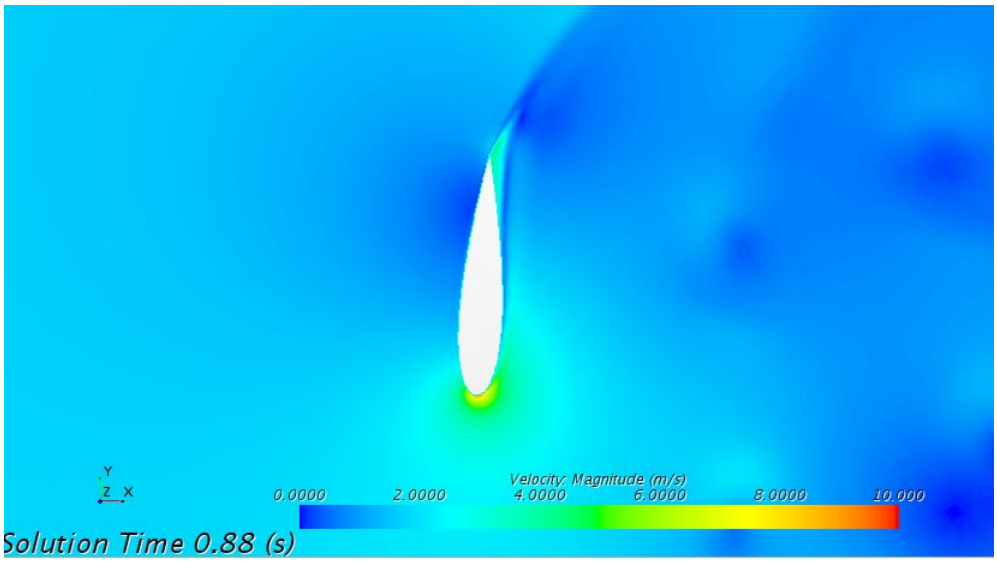

Figure 4.98: Velocity Profile Around Hydrofoil at Maximum Moment SIM41

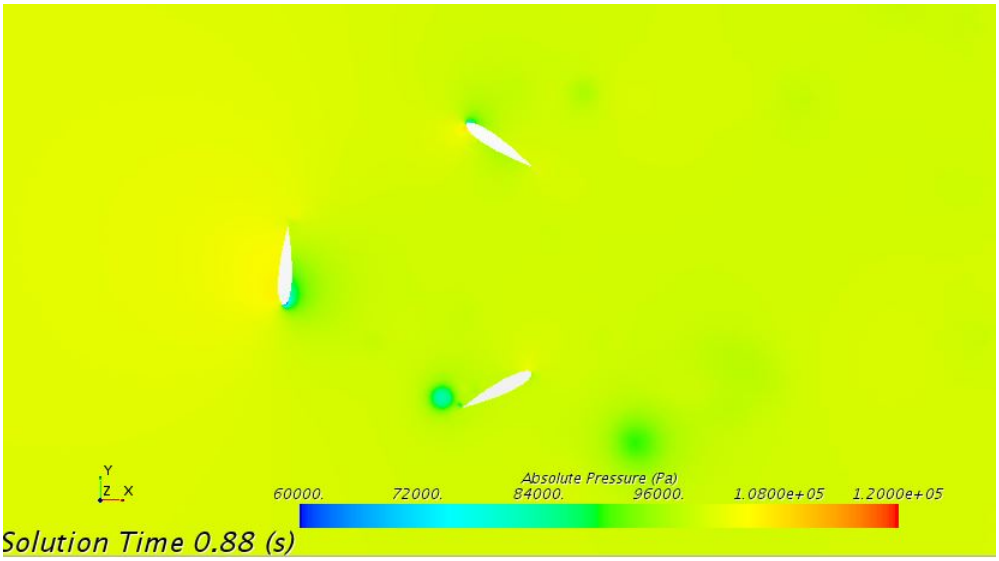

Figure 4.99: Pressure Profile of Turbine at t = 0.88 s SIM42

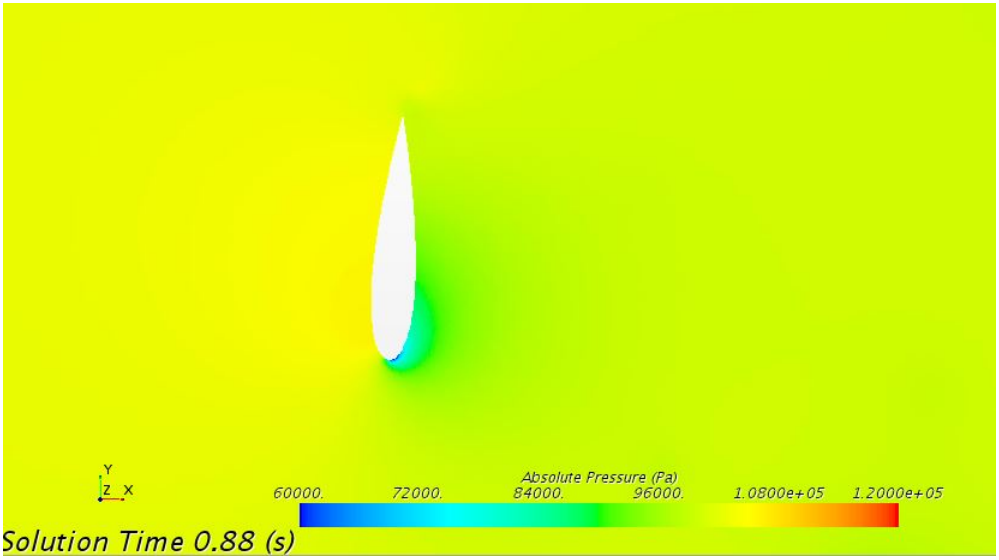

Figure 4.100: Pressure Profile Around Hydrofoil at Peak Moment

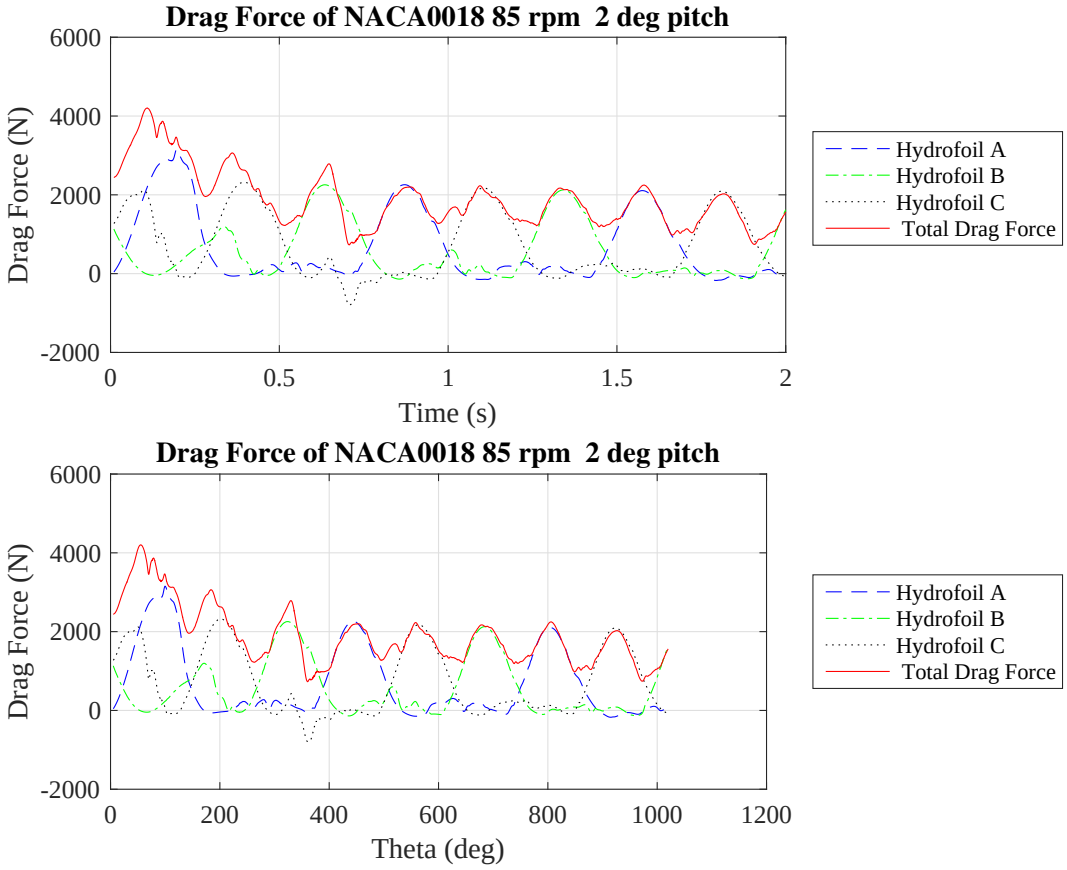

Figure 4.101: Drag Force of SIM41 in GC

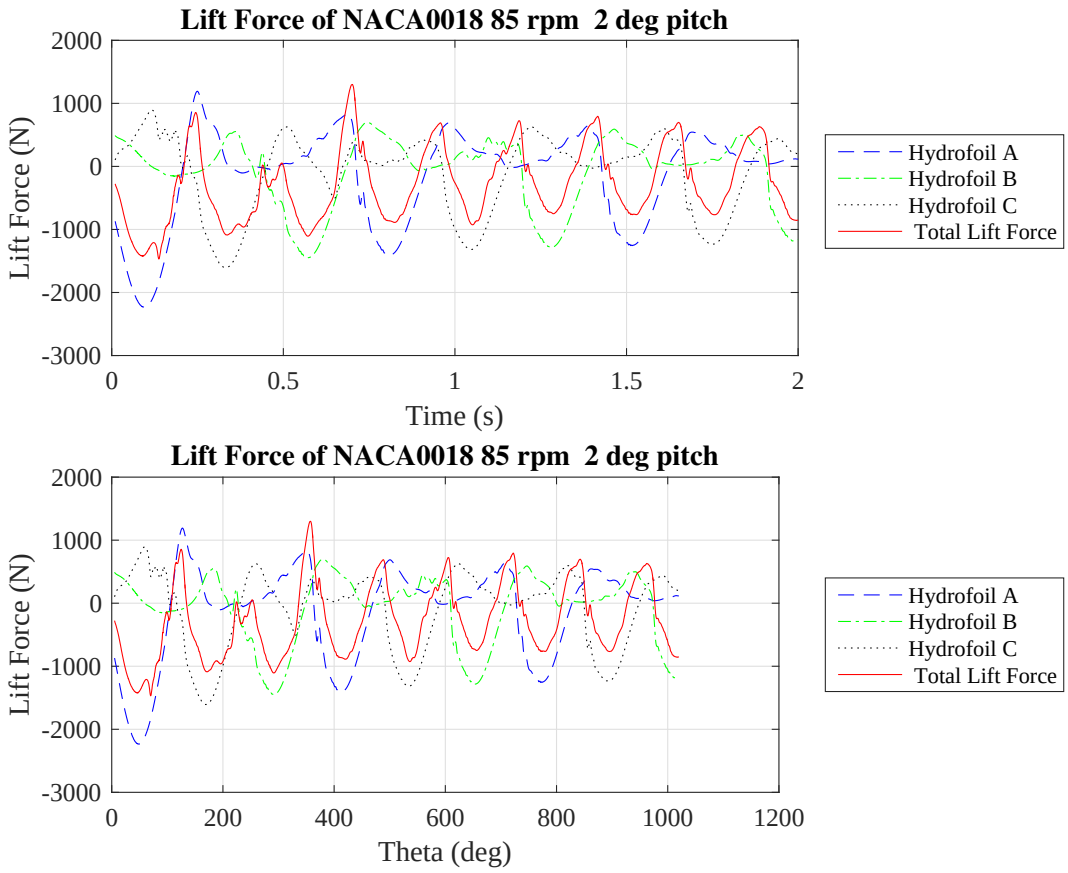

Figure 4.102: Lift Force of SIM41 in GC

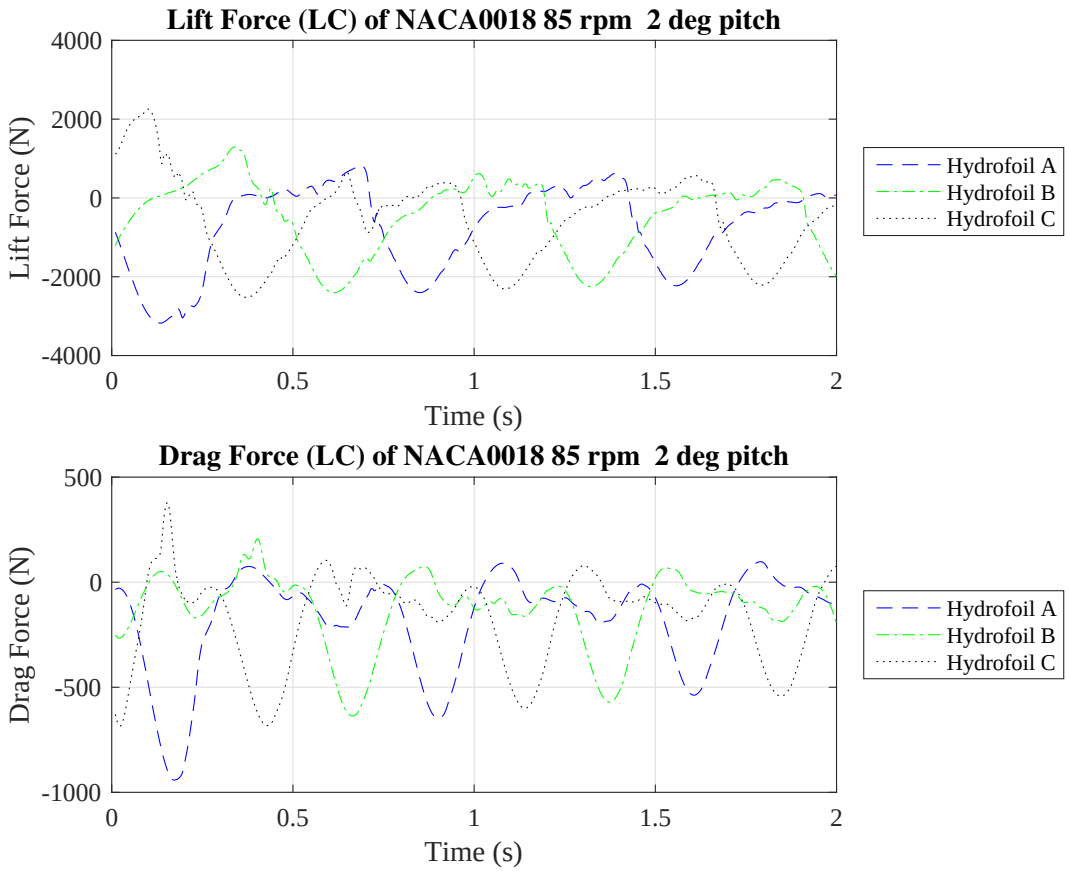

Figure 4.103: Lift and Drag Force of SIM41 in LC

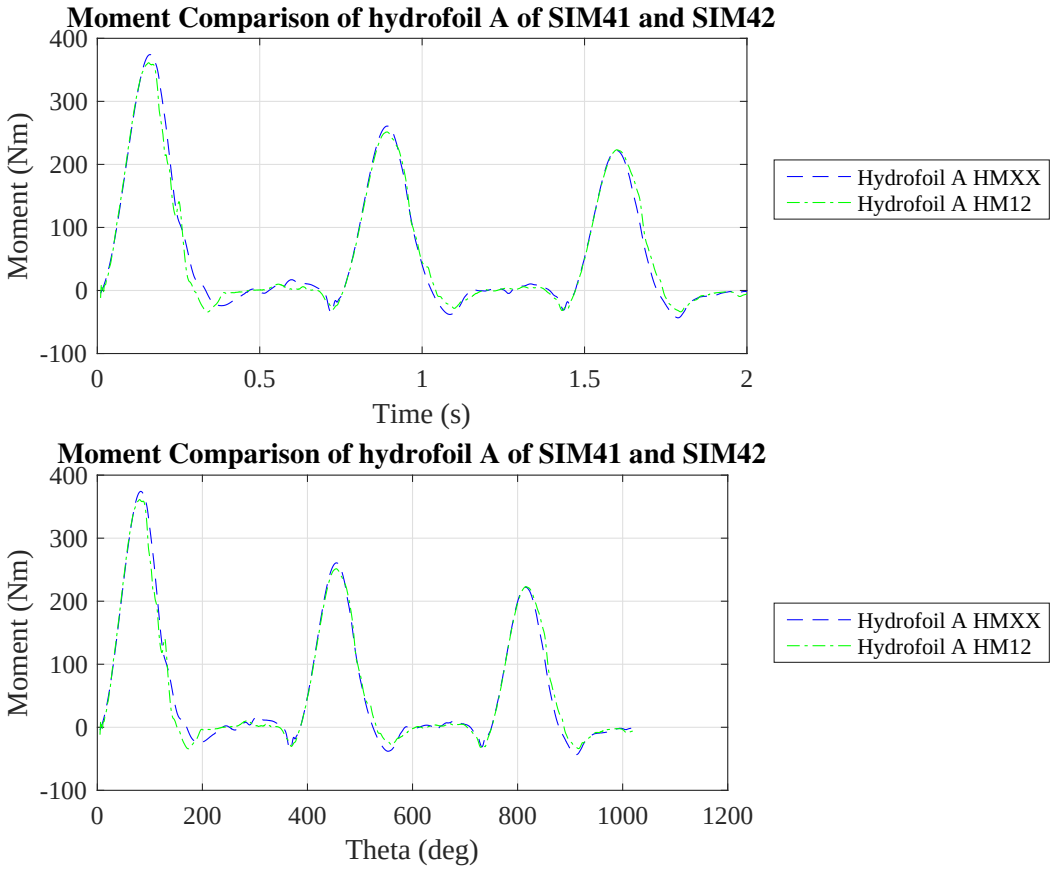

Figure 4.104: Moment Comparison of Hydrofoil A of SIM41 and SIM42

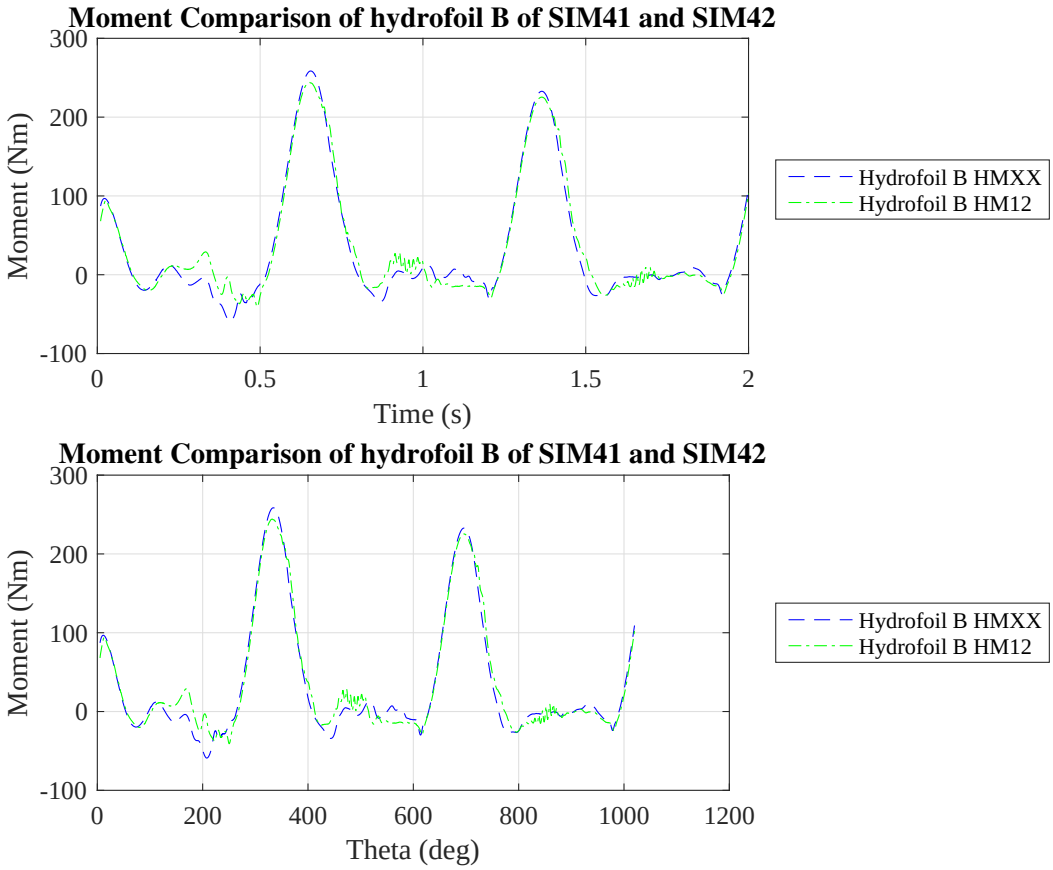

Figure 4.105: Moment Comparison of Hydrofoil B of SIM41 and SIM42

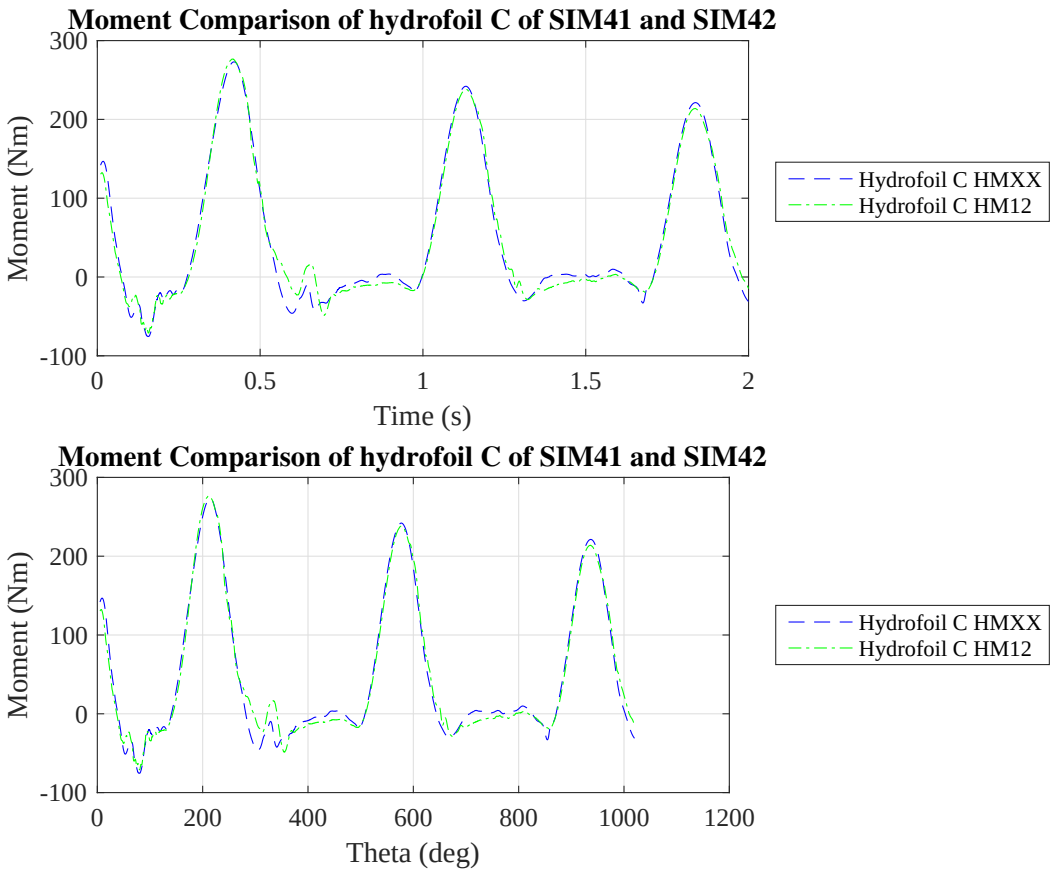

Figure 4.106: Moment Comparison of Hydrofoil C of SIM41 and SIM42

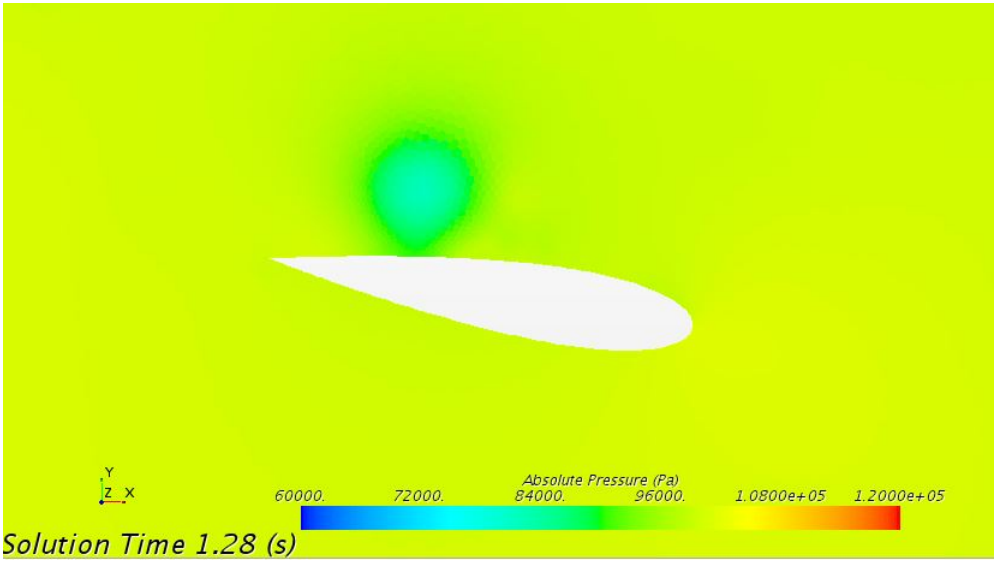

Figure 4.107: Pressure Comparison of Hydrofoil B of SIM41 and SIM42

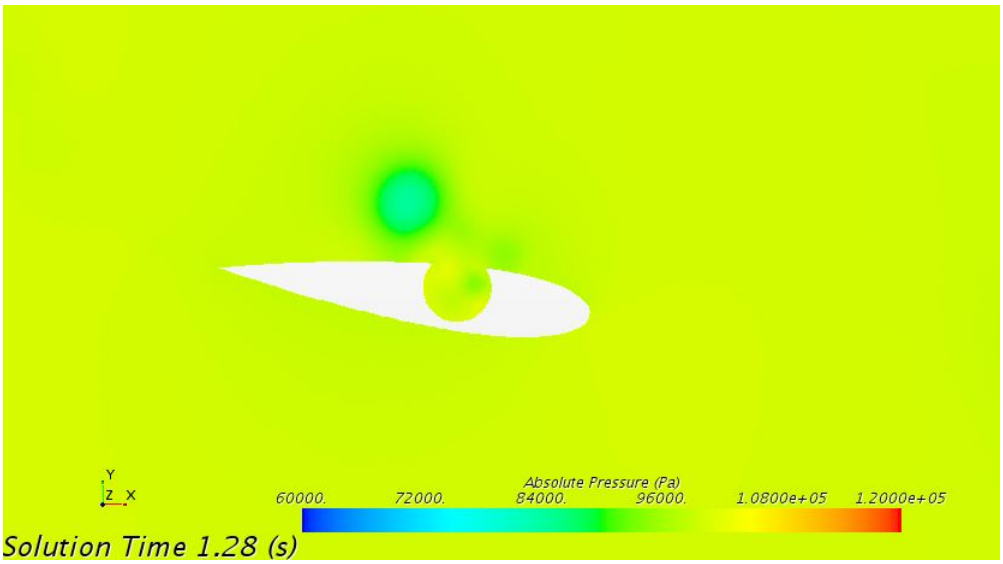

Figure 4.108: Pressure Comparison of Hydrofoil C of SIM41 and SIM42

4.3 Section III Simulations

Simulations in this section are rotating turbine simulations (RTS) with 5 different pitch angles $\beta = -4°, -2°, 0°, 2°$ and $4°$. The simulations considered for this section are given in the Table 4.9 The average moment and efficiency of RTS with non-zero pitch angle is compared with RTS with zero pitch angle. This results are shown in the Table 4.10 where AM is the average moment, η is the power efficiency in percentage.

Table 4.9: Section III Simulation Parameters

SIM	Name	CA	N	H	CM	HM	λ	β	σ
SIM23	S11000XX0234	RTS	1	H00	0	HMXX	L02	B3	S4
SIM24	S11000XX0224	RTS	1	H00	0	HMXX	L02	B2	S4
SIM25	S11000XX0264	RTS	1	H00	0	HMXX	L02	B6	S4
SIM26	S11000XX0274	RTS	1	H00	0	HMXX	L02	B7	S4
SIM27	S11040XX0264	RTS	1	H04	0	HMXX	L02	B6	S4
SIM32	S11042090264	RTS	1	H04	2	HM09	L02	B6	S4
SIM34	S11042120264	RTS	1	H04	2	HM12	L02	B6	S4

Table 4.10: Section III Simulation Results

SIM	β	AM	η %	SIM $\beta = 0°$	AM	η
SIM23	$-2°$	114.05	29.39	SIM13	122.47	31.55
SIM24	$-4°$	105.77	27.25	SIM13	122.47	31.55
SIM25	2°	125.18	32.25	SIM13	122.47	31.55
SIM26	4°	124.63	32.11	SIM13	122.47	31.55
SIM27	2°	137.29	35.37	SIM04	135.72	34.97
SIM32	2°	127.35	32.81	SIM31	124.53	32.09
SIM34	2°	136.44	35.15	SIM33	136.52	35.17

From the comparison, it could be seen that when pitch angle is negative, efficiency reduces also when pitch angle increases from 2° to 4°, efficiency reduces. But at a pitch angle of 2° efficiency is higher except for SIM34 which have modified hydrofoil with void. The velocity, pressure profiles, moment, lift and drag results for these simulations are given in the appendix.

4.4 Section IV Simulations

This Section consists of 7 rotating turbine simulations with varying tip speed ratio. The hydrofoil shape for SIM41 was H= NACA0018. Other input parameters are flow velocity V=2m/s, Chord length C = 0.1778m, diameter D = 0.6096m, solidity σ = 0.2785 (S4), Number of layers N=1, number of blades n=3 and pitch angle $\beta = 0°$ (B4). The tip speed ratio considered for these simulations are L01, L02, L04, L05, L07, L09 and L10 The

simulations considered for this section are given in the Table 4.11 The average moment and efficiency of RTS with non-zero pitch angle is compared with RTS with zero pitch angle. This results are shown in the Table 4.12 where AM is the average moment, η is the power efficiency in percentage.

From this table it can be seen that the efficiency reaches the peak at tip speed ratio $\lambda = 1.36$. After that till $\lambda = 1.68$ it is around the same value. The final velocity profile for the RTS with least and maximum λ is given in the figures Fig. 4.109 and Fig. 4.110.

Table 4.11: Section IV Simulation Parameters

SIM	Name	CA	N	H	CM	HM	λ	β	σ
SIM35	S11040XX0164	RTS	1	H04	0	HMXX	L01	B6	S4
SIM36	S11000XX0164	RTS	1	H00	0	HMXX	L01	B6	S4
SIM37	S11040XX0464	RTS	1	H04	0	HMXX	L04	B6	S4
SIM38	S11000XX0464	RTS	1	H00	0	HMXX	L04	B6	S4
SIM39	S11040XX0564	RTS	1	H04	0	HMXX	L05	B6	S4
SIM40	S11042120564	RTS	1	H04	2	HM12	L05	B6	S4
SIM41	S11040XX0764	RTS	1	H04	0	HMXX	L07	B6	S4
SIM42	S11042120764	RTS	1	H04	2	HM12	L07	B6	S4
SIM43	S11040XX0964	RTS	1	H04	0	HMXX	L09	B6	S4
SIM44	S11042120964	RTS	1	H04	2	HM12	L09	B6	S4
SIM45	S11040XX1064	RTS	1	H04	0	HMXX	L10	B6	S4
SIM46	S110420121064	RTS	1	H04	2	HM12	L10	B6	S4

Table 4.12: Section IV Simulation Results

SIM	λ	AM	η %	SIM $\lambda = 0°$	AM	η
SIM35	0.88	121.95	28.80	SIM27	137.29	35.37
SIM36	0.88	112.98	26.68	SIM25	125.18	32.25
SIM37	1.05	146.62	40.93	SIM27	137.29	35.37
SIM38	1.05	134.16	37.45	SIM25	125.18	32.25
SIM39	1.20	138.64	44.65	SIM27	137.29	35.37
SIM40	1.20	138.03	44.46	SIM34	136.44	35.15
SIM41	1.36	132.76	48.46	SIM27	137.29	35.37
SIM42	1.36	136.74	49.91	SIM34	136.44	35.15
SIM43	1.51	119.95	48.93	SIM27	137.29	35.37
SIM44	1.51	118.18	48.21	SIM34	136.44	35.15
SIM45	1.68	108.59	48.97	SIM27	137.29	35.37
SIM46	1.68	106.81	48.16	SIM34	136.44	35.15

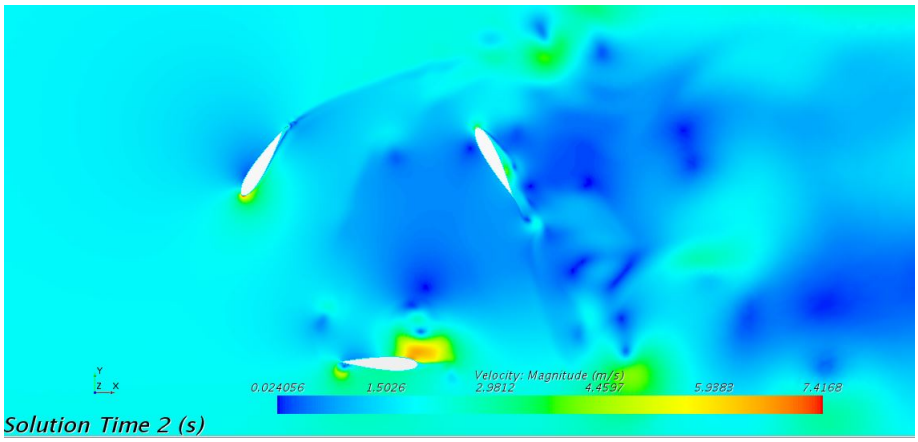

Figure 4.109: Velocity Profile $\lambda = 0.88$

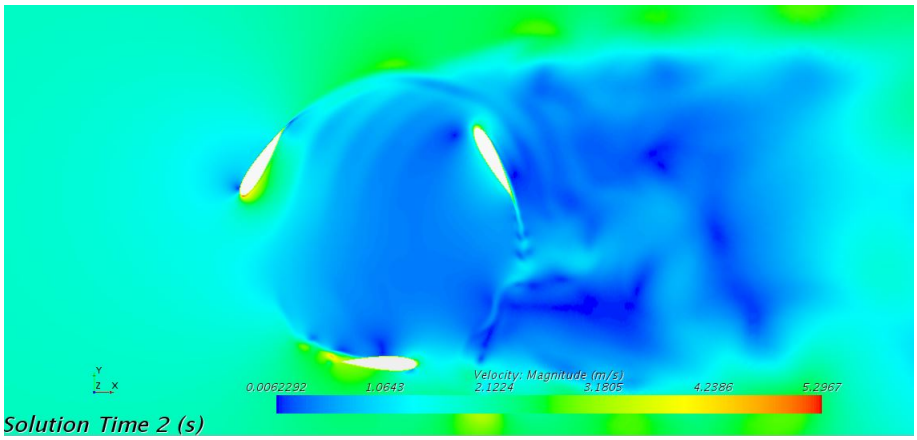

Figure 4.110: Velocity Profile $\lambda = 1.68$

4.5 Section V Simulations

This Section consists of 5 rotating turbine simulations with varying solidity. The hydrofoil shape for SIM41 was H= NACA0018. Other input parameters are flow velocity V=2m/s, Chord length C = 0.1778m, tip speed ratio λ= 0.96, Number of layers N=1, number of blades n=3 and pitch angle $\beta = 0°$ (B4). The solidity values considered for these simulations are S1 to S6 The simulations considered for this section are given in

the Table 4.13 The average moment and efficiency of RTS with non-zero pitch angle is compared with RTS with zero pitch angle. This results are shown in the Table 4.14 where AM is the average moment, η is the power efficiency in percentage. Highest efficiency is for the solidity 0.2785 which is the base case.

Table 4.13: Section V Simulations Parameters

SIM	Name	CA	N	H	CM	HM	λ	β	σ
SIM53	S11040XX0761	RTS	1	H04	0	HMXX	L07	B6	S1
SIM54	S11040XX0762	RTS	1	H04	0	HMXX	L07	B6	S2
SIM55	S11040XX0763	RTS	1	H04	0	HMXX	L07	B6	S3
SIM56	S11040XX0765	RTS	1	H04	0	HMXX	L07	B6	S5
SIM57	S11040XX0766	RTS	1	H04	0	HMXX	L07	B6	S6

Table 4.14: Section V Simulation Results

SIM	σ	AM	η %	SIM $\sigma = 0.2875°$	AM	η
SIM53	0.1	830.38	39.07	SIM41	132.76	48.46
SIM54	0.15	230.62	24.41	SIM41	132.76	48.46
SIM55	0.2	214.04	40.281	SIM41	132.76	48.46
SIM56	0.4	58.67	44.18	SIM41	132.76	48.46
SIM57	0.5 30.33	35.68	SIM41	132.76	48.46	

5 RESULTS

The final results and analysis of 70 CFD simulations which consists of 62 rotating turbine simulation (RTS) and 8 Steady State Simulations (SSS) is given in this chapter over all simulations are divided in to five sections, in order to find out the best modification to the base geometry and operating condition of selected Gorlov turbine. Section I simulations consists of 20 rotating turbine simulations which includes 13 different NACA foils, 6 symmetric and 7 asymmetric hydrofoils. All of the hydrofoils in section I does not have any modification (HMXX). These simulations are carried out for finding the best hydrofoil shape H. For asymmetric hydrofoil shapes there are two cases, one with camber pointing towards center and other being camber pointing outwards. All other input parameters except H is same for this section simulations. Hydrofoil shape H04 was selected as the best H. The objective of section II simulations is to select a modification to hydrofoil (HM). This section simulation results of consists of 8 steady state simulations (SSS) and 9 rotating turbine simulations (RTS). From the SSS, for 8 pitch angles each with thirteen modifications, two hydrofoil modifications HM are chosen which are HM09 and HM12 then they have used in RTS and compared with same case without modification. Two hydrofoil shapes which were considered for this modification are the base case H00 and the best case of section I simulations H04. Also the case of skewed hydrofoil modification HM13 has been carried out. Hydrofoil modification of HM12 was selected as the best HM. Simulations in section III are rotating turbine simulations (RTS) with 5 different pitch angles $\beta = -4°, -2°, 0°, 2°$

and 4°. The average moment and efficiency of RTS with non-zero pitch angle is compared with RTS with zero pitch angle. Pitch angle of 2° was selected as best for hydrofoils without modification and pitch angle of 0° was selected for those with modification. Section IV simulations consists of 7 rotating turbine simulations with varying tip speed ratio. The tip speed ratio considered for these simulations are L01, L02, L04, L05, L07, L09 and L10. The average moment and efficiency of RTS with tip speed ratio of L02 is compared with RTS with other tip speed ratios. The best tip speed ratio was found out to be L07. The final section V consists of 5 rotating turbine simulations with varying solidity. The hydrofoil shape for section V was H04 and tip speed ratio is L07. The solidity values considered for these simulations are S1 to S6. The best solidity value was found out to be S4. The base case parameters for RTS were H00, flow velocity V=2m/s, chord length C = 0.1778m, diameter D = 0.6096m, solidity σ = 0.2785 (S4), Number of layers N=1, number of blades n=3, tip speed ratio $\lambda = 0.96$ (L02) and pitch angle $\beta = 0°$ (B4).

5.1 Section I Simulations

Section I consists of 20 rotating turbine simulations which includes 13 different NACA foils, 6 symmetric and 7 asymmetric hydrofoils. For the asymmetric foils there are two cases, one with camber pointing towards center and camber pointing outwards. There are 20 simulations in this section, SIM01 to SIM21 except SIM14 which is a modified case. The only variation from the base case for these simulations are the hydrofoil shape H. These are without modifications, i.e. HMXX. The results of section I simulation could

be understood from three figures which shows their average moment, average power produced and average power efficiency. Numbers in X axis corresponds to the simulation number like 15 means SIM15. SIM14 is not part of this section. Fig. 5.1 shows the average moment, Fig. 5.2 shows the average power produced and Fig. 5.3 shows the predicted average power efficiency.

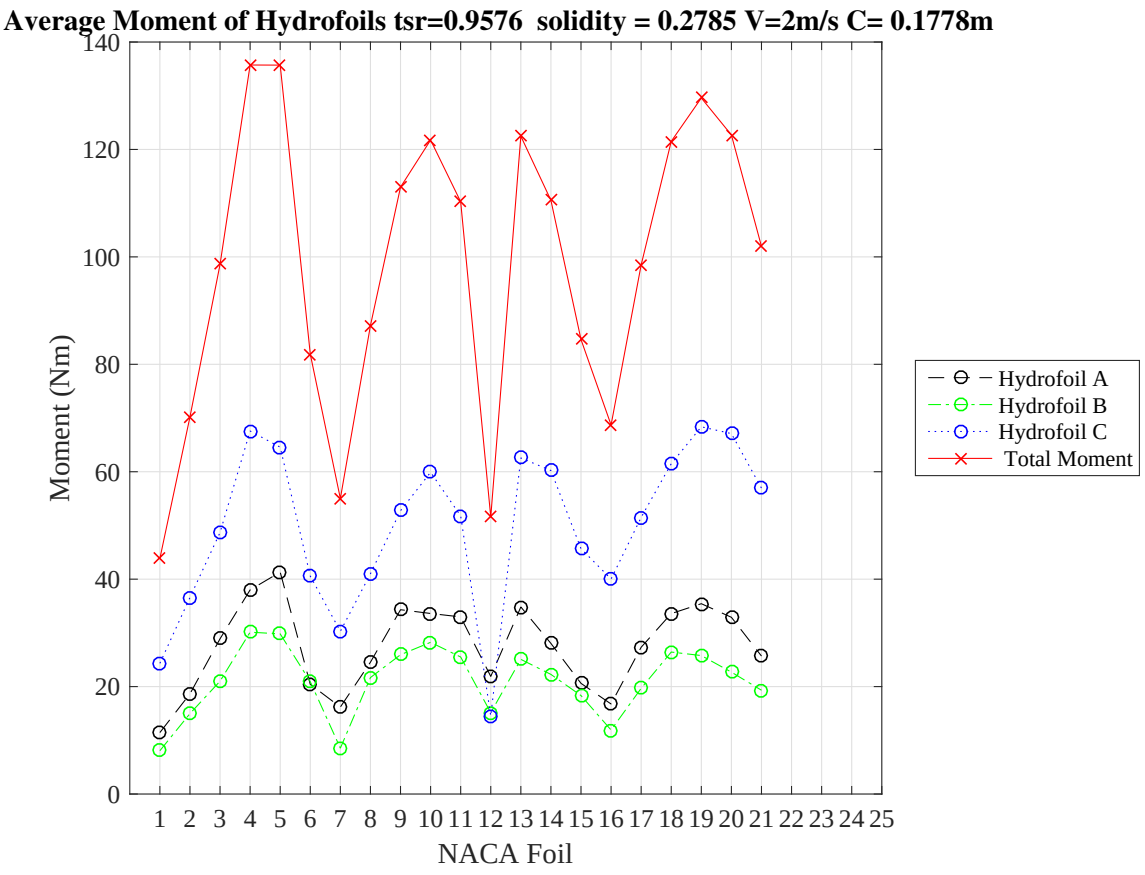

Figure 5.1: Average Moment of Section I Simulations

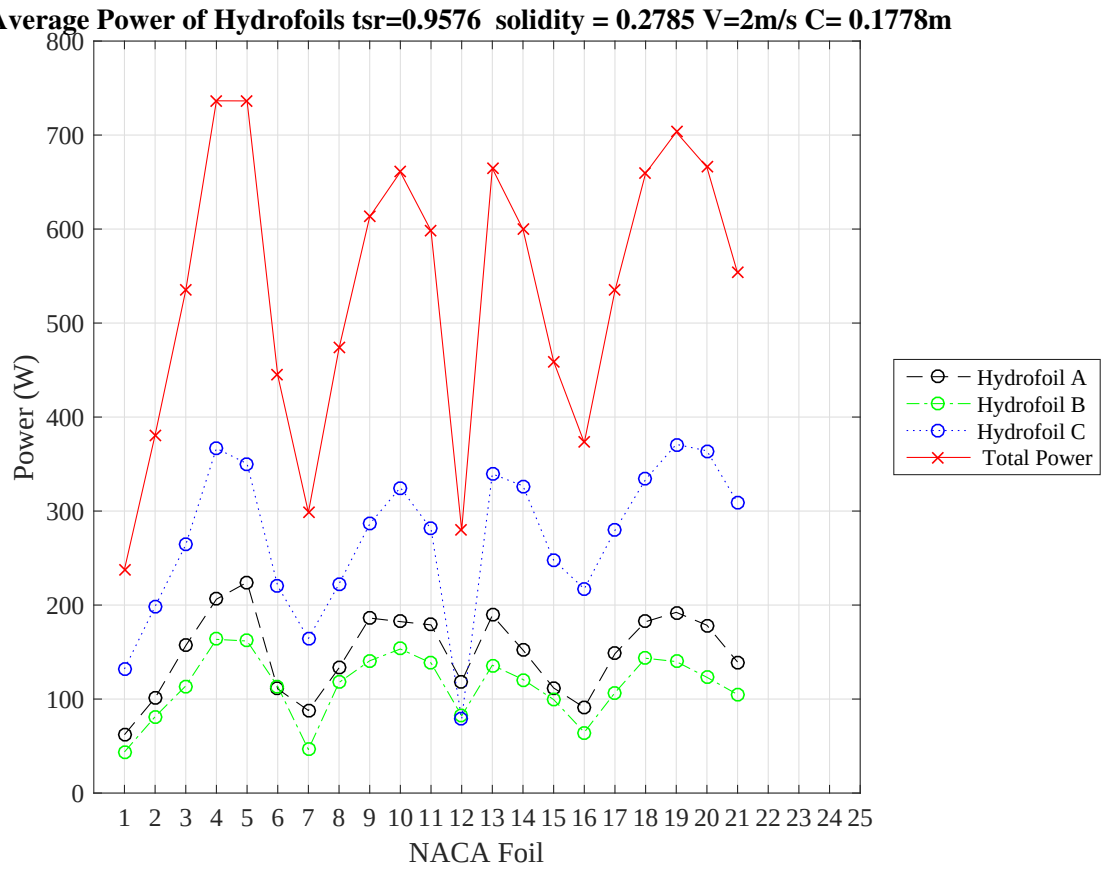

Figure 5.2: Average Power of Section I Simulations

From the Fig. 5.1, it can be seen that the average moment is for simulation SIM04 with 135.72Nm. SIM05 also have about the same moment of 135.69Nm. After that there is dip and next comes SIM19 with 129.58Nm. The least average moment is for the simulation SIM01 with 43.83Nm. The hydrofoil shape for the best performing simulation SIM04 is H04 which is NACA0018. The second best case simulation SIM05 uses H05 which have NACA0024. NACA0018 and NACA0024 are symmetric hydrofoils with maximum thickness of first being 18% and that of the second being 24% of the chord length. The base case simulation is SIM13 with hydrofoil shape H00 which uses NACA0020. The average

moment produced by the base case is 122.47N. From the Fig. 5.2 when analyzing it can be seen that the average power produced have the same pattern as that of the moment. It is expected as the rotational speed is constant. The maximum average power produced is for simulation SIM04 with 736.44W. The simulation SIM01 with NACA0006 have the least power with 237.88W. The base case turbine produces power of 664.56N. Average Power efficiency also have the same pattern as that of average power as they are directly proportional. The maximum average power efficiency shown by SIM04 which uses NACA0018 comes to about 34.97%. For the base case the efficiency is around 31.56%. The least efficiency is SIM01 with 11.29%.

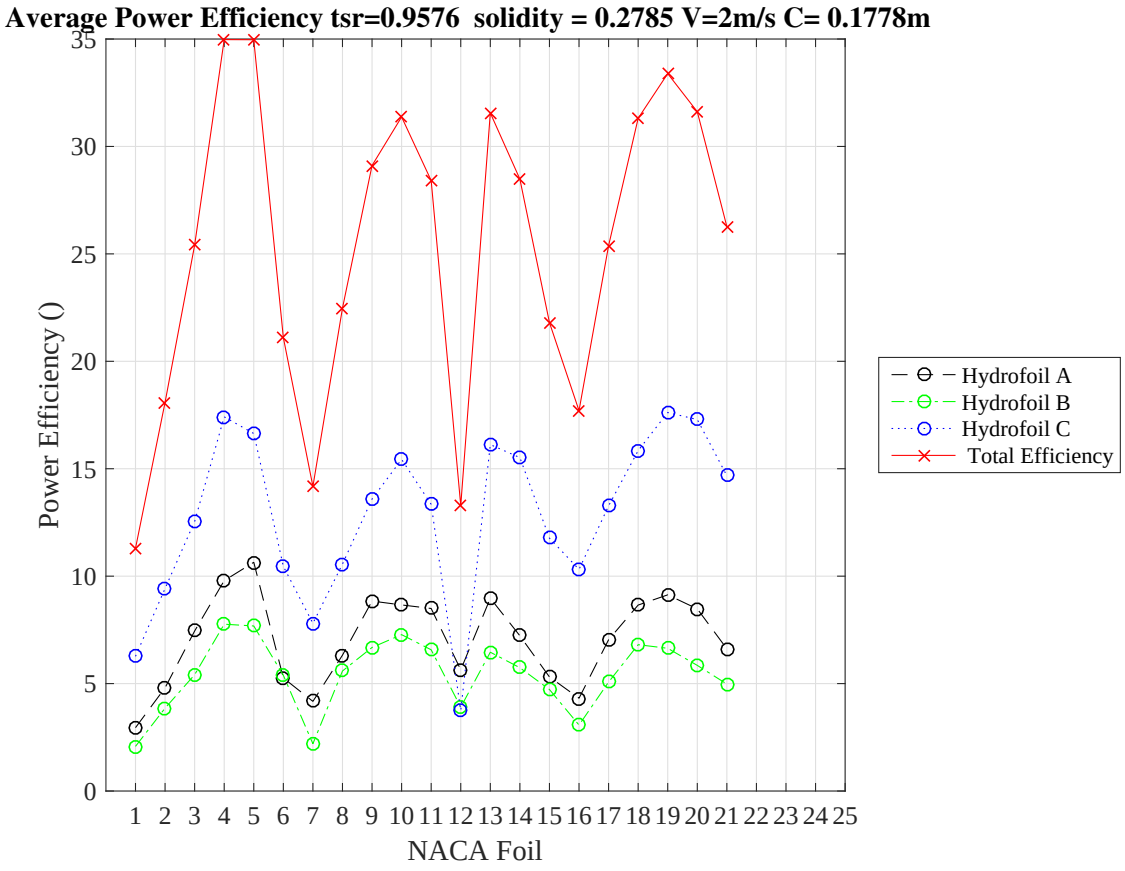

Figure 5.3: Average Power Efficiency of Section I Simulations

5.2 Section II Simulations

The objective of section II simulations is to select a modification to hydrofoil (HM). This section simulation results of consists of 8 steady state simulations (SSS) and 9 rotating turbine simulations (RTS). From the SSS, for 8 pitch angles each with thirteen modifications, two hydrofoil modifications are chosen and then they have used in RTS and compared with same case without modification. The results of steady state simulations could be understood from the Fig. 5.4 to Fig. 5.11. The variation of lift force and drag force with pitch is shown in Fig. 5.4 and Fig. 5.5. The variation of lift force and drag force with R_V is shown in Fig. 5.6 and Fig. 5.7. The details of input parameters can be understood from Table 4.7 and Table 4.8. The variation of lift force and drag force with Y_V is shown in Fig. 5.8 and Fig. 5.9. The variation of lift force and drag force with X_V is shown in Fig. 5.10 and Fig. 5.11.

The variation of lift force with pitch angle is almost linear for all the cases of hydrofoil. Case CA01 shows the highest lift of 1025.5N for pitch angle $\beta = 8°$. Case CA01 is the base case hydrofoil shape H00 without modification HMXX. The highest negative lift is also for the same case CA01 which is expected as it is a symmetric foil with value of -1027N for $\beta = 8°$. The slope of the of linear variation is $128N/°$. The base modified case CA02 with HM00 shows lift of 914.8N for pitch angle $\beta = 8°$. The highest negative lift for this case -970.98N. The slope for positive pitch angles is $115.63N/°$. The slope for negative pitch angles is $120.6N/°$. For the selected case for RTS, CA14 with HM12 shows lift of 936.8N for pitch angle $\beta = 8°$ which is the highest value among

modified cases. The highest negative lift for this case -961.02N. The slope for positive pitch angles is $117.5N/°$. The slope for negative pitch angles is $119.5N/°$. For the least efficient case, CA07 with HM05 shows lift of 793.3N for pitch angle $\beta = 8°$. The highest negative lift for this case -829.3N. The slope for positive pitch angles is $99.16N/°$. The slope for negative pitch angles is $103.6N/°$.

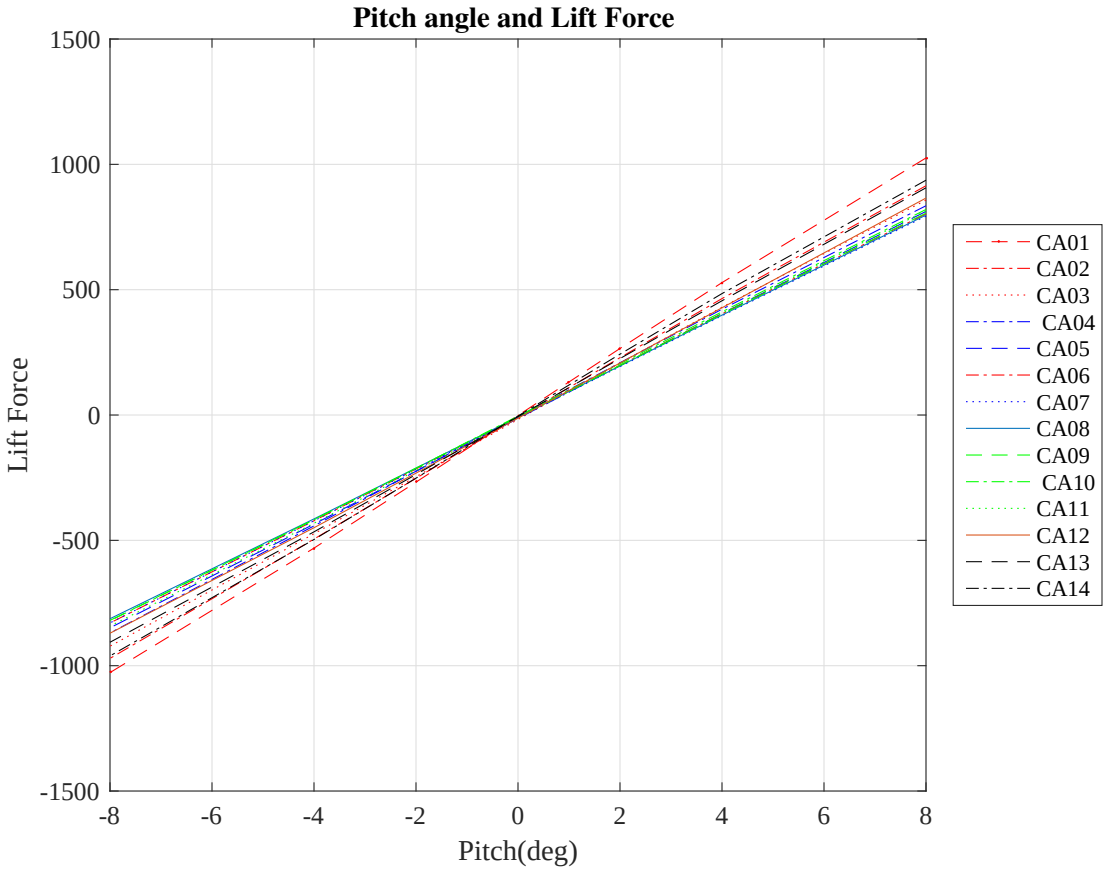

Figure 5.4: Steady Lift With Pitch

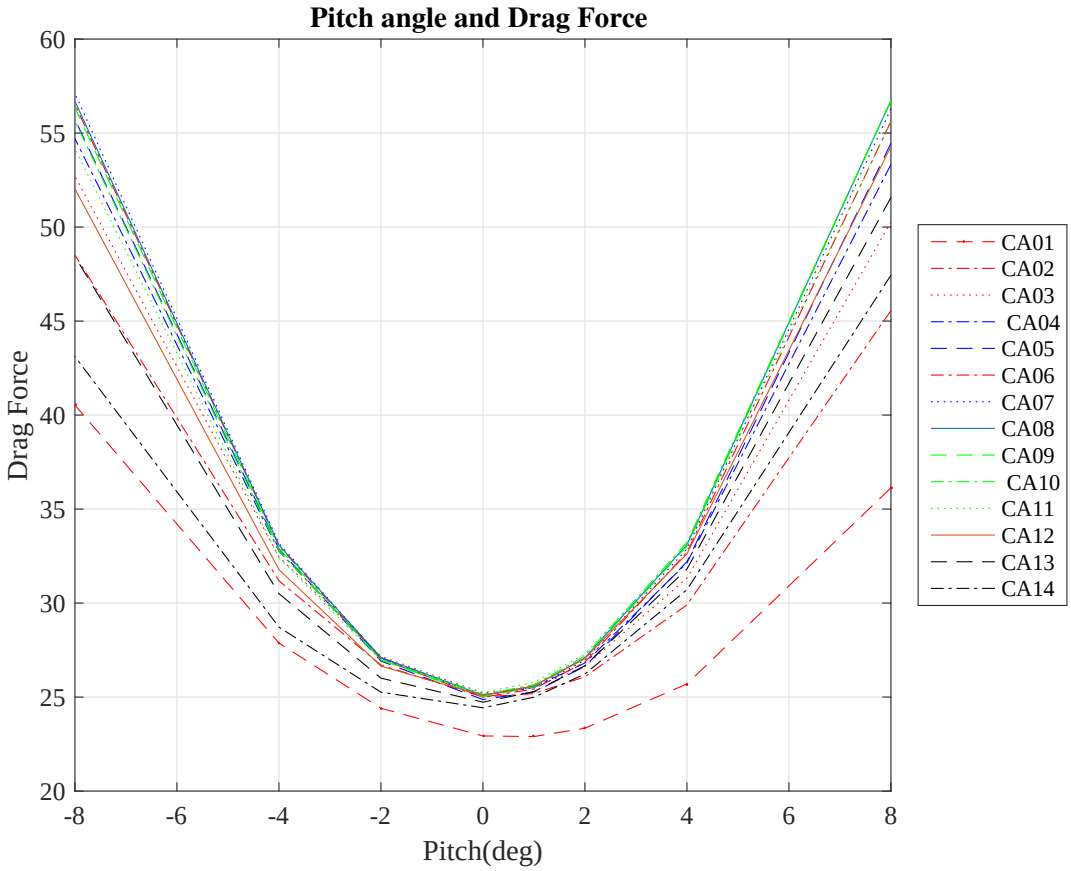

Figure 5.5: Steady Drag With Pitch

The variation of drag force with pitch angle is almost parabolic for all the cases of hydrofoil. The least drag for all the pitch angles is for the case CA01 with HMXX, which is expected, with maximum drag of 40N and minimum of 22N. The highest drag is shown by the case CA10 with HM08 of 56.7N. The base modified case CA02 with HM00 have a maximum of 45.56N and minimum of 25N. The selected case for RTS CA14 with HM12 have a maximum of 47.38N and minimum of 24.4N.

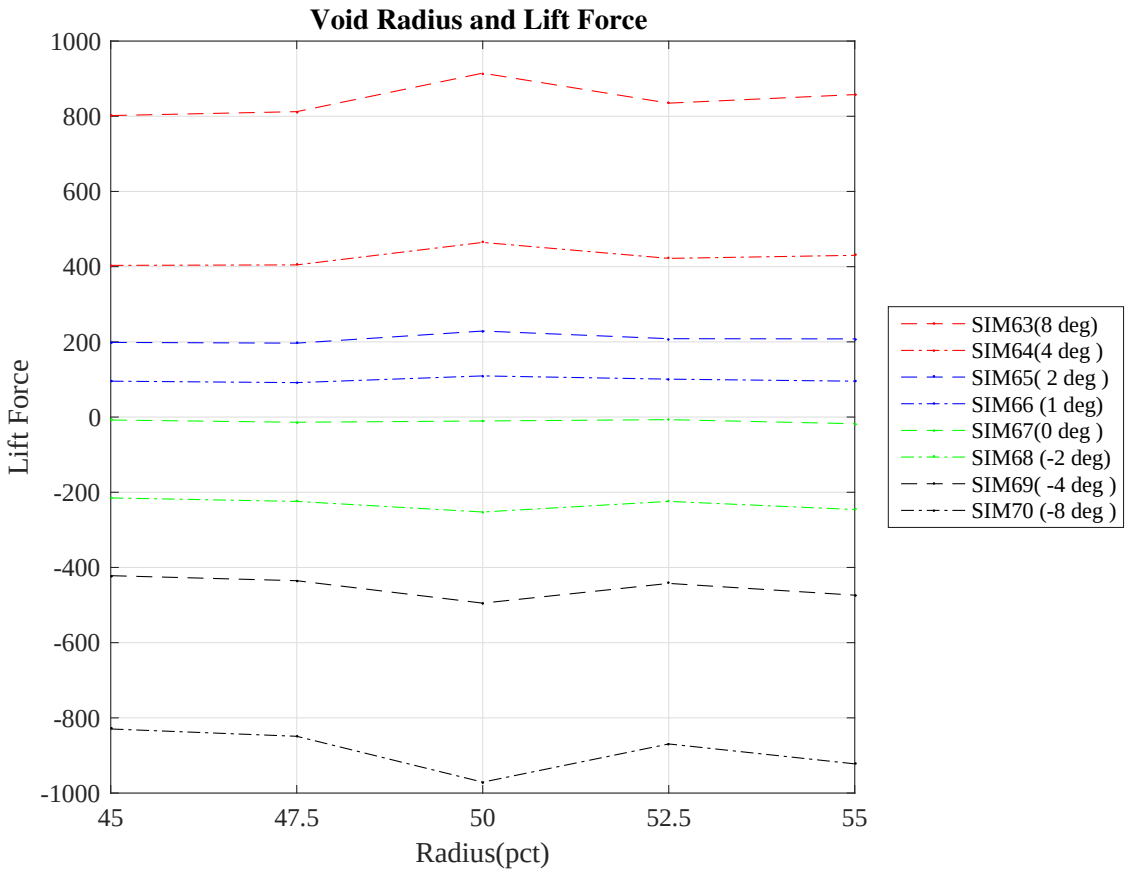

Figure 5.6: Steady Lift With Void Radius

The variation of lift force with void radius R_V shows that the maximum lift force is shown by the base modified case CA02 with HM00. This case which have an R_V value of 50 (percentage of maximum thickness) shows a lift of 914.68N. The value of negative lift for negative pitch angles is higher by around 10% for all the modified cases. The case with smallest R_V have the least lift of 801.86N. Lift force have a peak at $R_V = 50$ and then it reduces on further increase of R_V. So the best R_V value found out to be 50 considering lift performance.

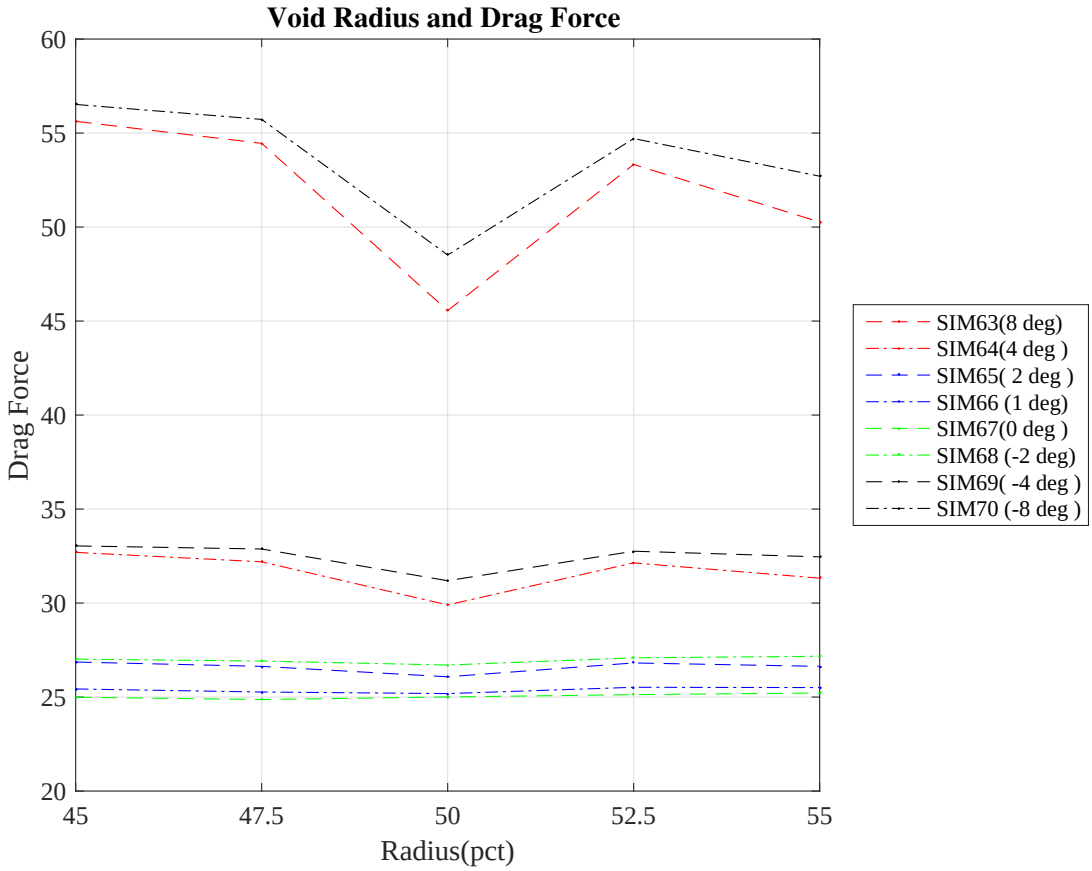

Figure 5.7: Steady Drag With Void Radius

The variation of drag force with void radius R_V shows that the minimum drag force is shown by the base modified case CA02 with HM00 for all pitch angles. This case which have an R_V value of 50 (percentage of maximum thickness) shows a drag of 45.55N for $\beta = 8°$. The case with smallest R_V of 45 have the highest drag of 55.6N. Drag force have a dip at $R_V = 50$ and then it increases on further increase of R_V. So the best R_V value found out to be 50 considering drag performance.

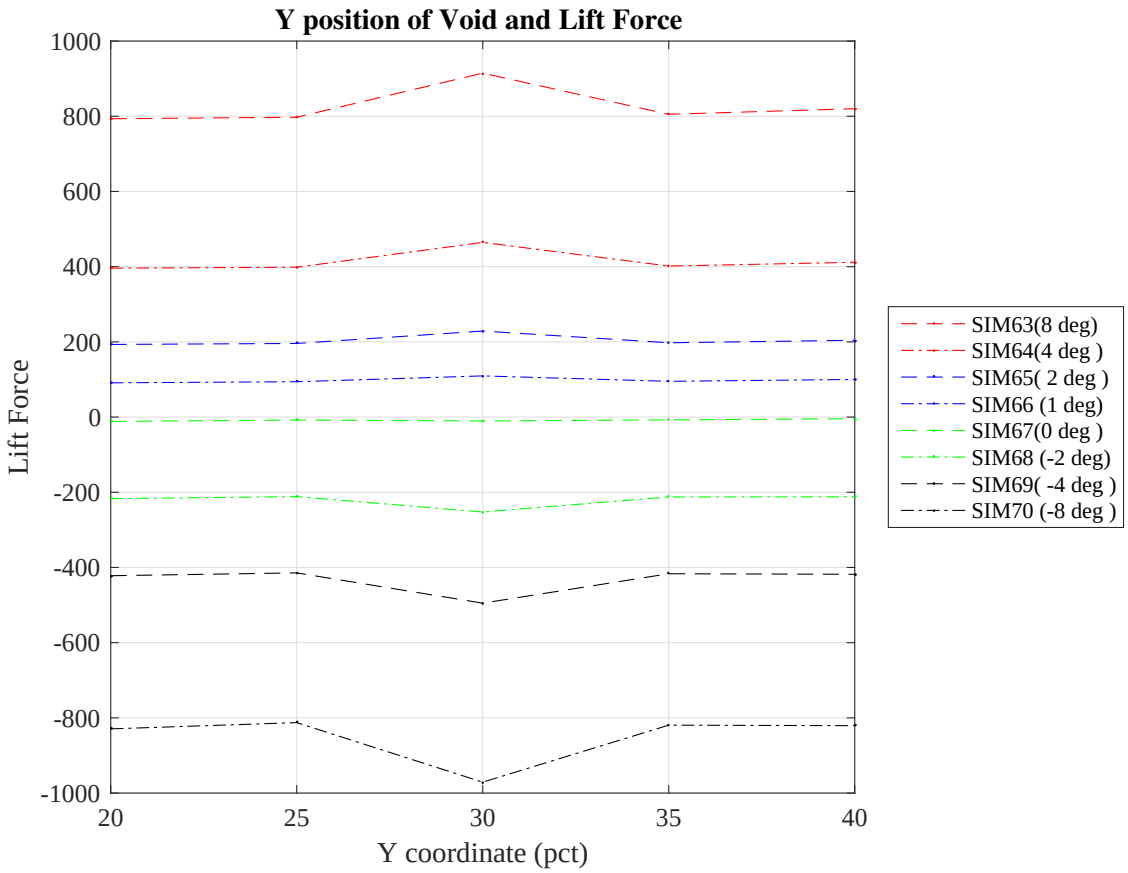

Figure 5.8: Steady Lift With Y Coordinate of Void

The variation of lift force with Y_V shows that the maximum lift force is shown by the base modified case CA02 with HM00. This case which have an Y_V value of 30 (percentage of maximum thickness) shows a lift of 914.68N. The case with smallest Y_V have the least lift of 793.32N. Lift force have a peak at $Y_V = 30$ and then it reduces on further increase of Y_V. So the best Y_V value found out to be 30 considering lift performance.

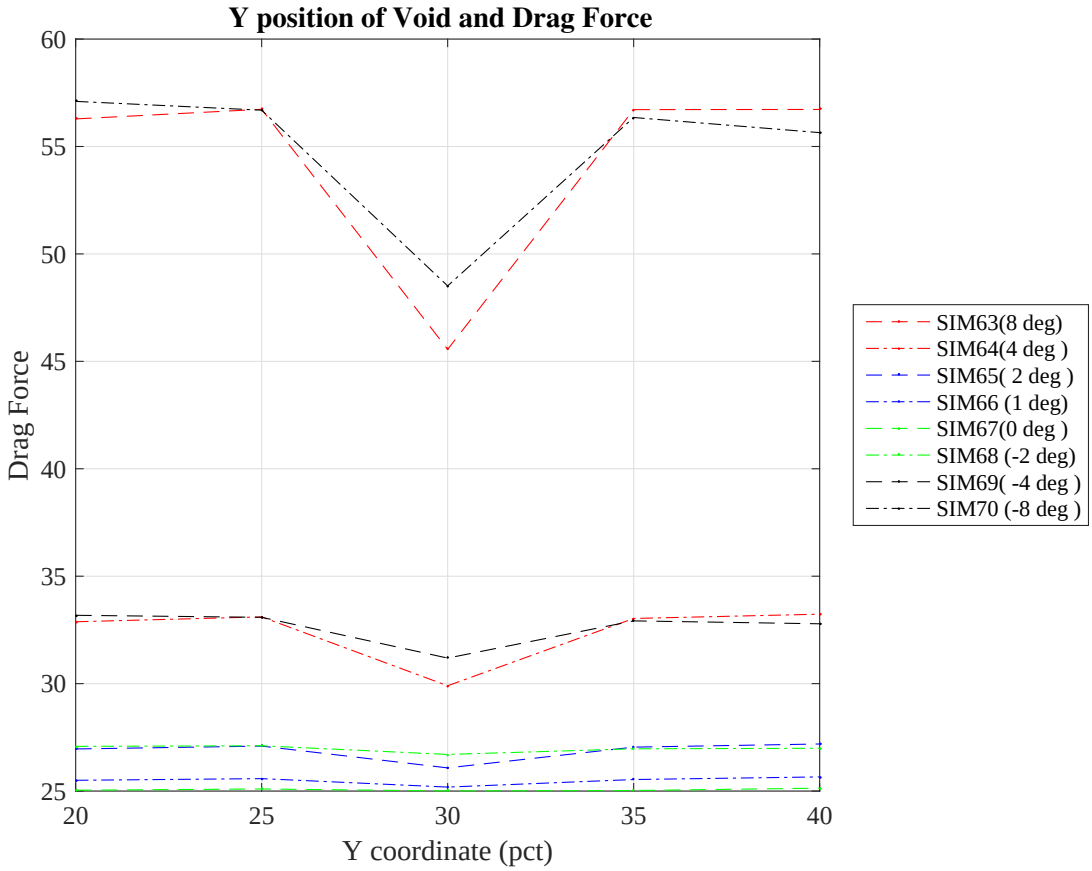

Figure 5.9: Steady Drag With Y Coordinate of Void

The variation of drag force with Y_V shows that the minimum drag force is shown by the base modified case CA02 with HM00 for all pitch angles. This case which have an Y_V value of 30 (percentage of maximum thickness) shows a drag of 45.55N for $\beta = 8°$. The case with highest Y_V of 40 have the highest drag of 56.28N. Drag force have a dip at $Y_V = 30$ and then it increases on further increase of Y_V. So the best Y_V value found out to be 30 considering drag performance.

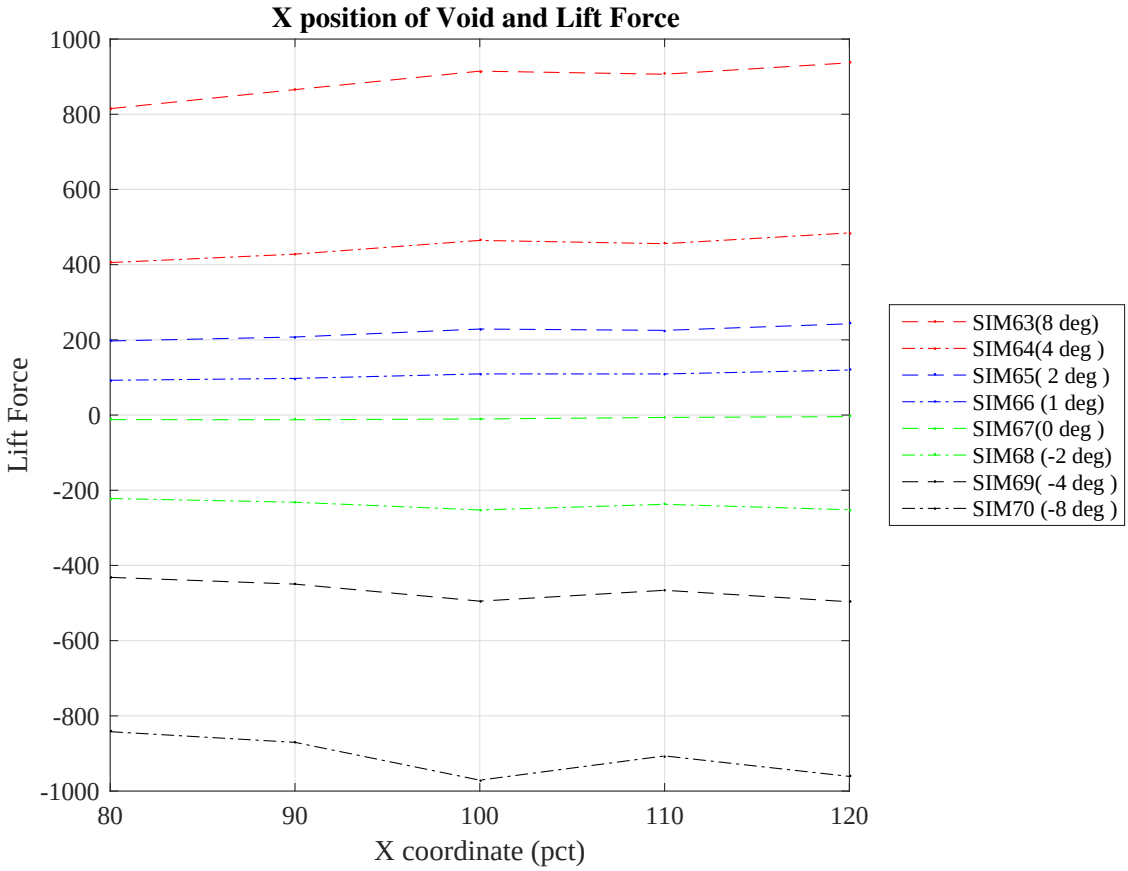

Figure 5.10: Steady Lift With X Coordinate of Void

The variation of lift force with X_V shows that the maximum lift force is shown by the selected modified case CA14 with HM12. This case which have an X_V value of 120 (percentage of X position of maximum thickness) shows a lift of 936.81N. The case with smallest X_V have the least lift of 814.88N. Lift force seems to increase as X_V increases but it has a peak at $X_V = 100$ but smaller than for $X_V = 120$. So the best Y_V value found out to be 120 considering lift performance.

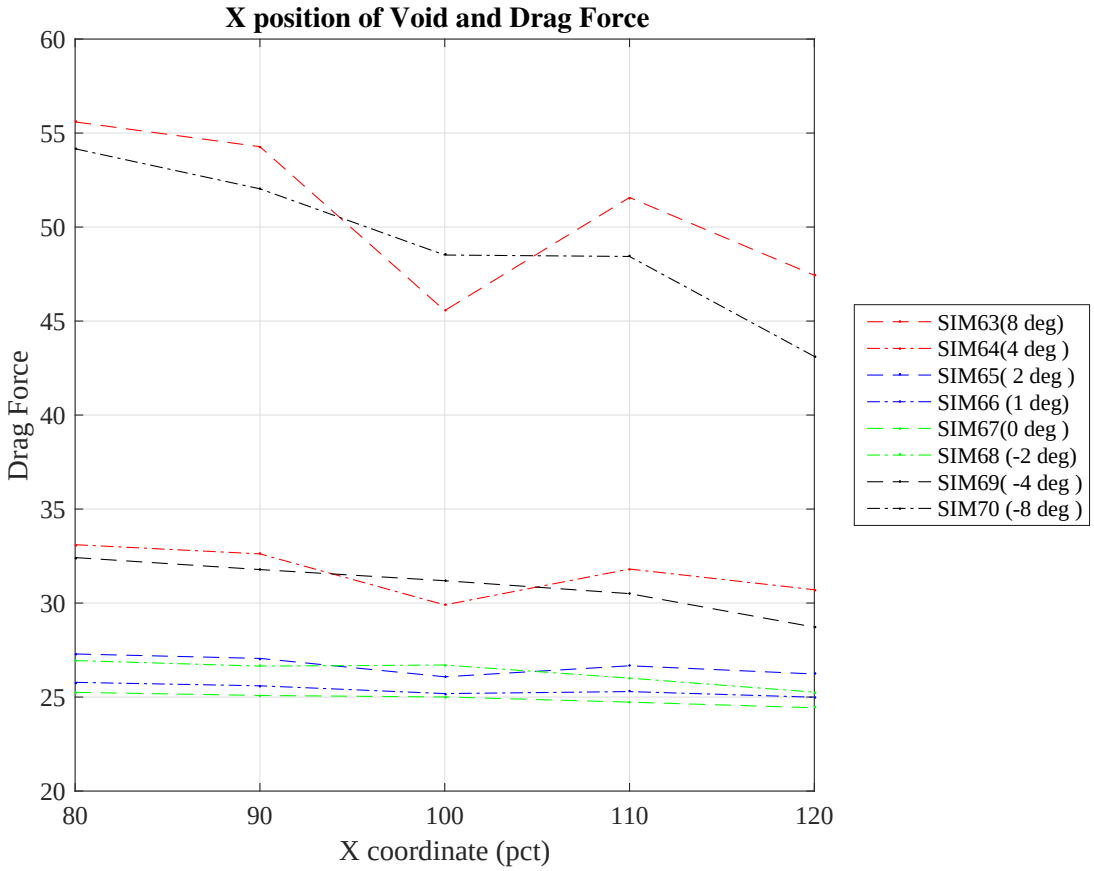

Figure 5.11: Steady Drag With X Coordinate of Void

The variation of drag force with X_V shows that the minimum drag force is shown by the base modified case CA02 with HM00 for all pitch angles. This case which have an X_V value of 100 (percentage of maximum thickness) shows a drag of 45.55N for $\beta = 8°$. The case with lowest X_V of 80 have the highest drag of 55.59N. Drag force have a dip at $X_V = 100$ and then it increases on further increases and then decreases with X_V. So the best X_V value found out to be 100 considering drag performance. The results of 9 rotating turbine simulations for finding the best modification for hydrofoil shape are given in the Table 5.1. The average moment and efficiency of RTS with modified hydrofoils is

compared with RTS with same other input parameter except no modification in hydrofoil shape H, HMXX. AM stands for average moment and η is the power efficiency in percentage.

Table 5.1: Comparison of Average Moment and Power Efficiency With HM

SIM	HM	CM	AM (Nm)	η %	SIM XX	AM XX (Nm)	η XX %
SIM14	HM09	1	110.53	28.48	SIM13	122.47	31.56
SIM22	HM09	2	128.723	33.16	SIM13	122.47	31.56
SIM29	HM13	1	107.73	27.76	SIM04	135.72	34.97
SIM31	HM09	2	124.53	32.09	SIM04	135.72	34.97
SIM33	HM12	2	136.52	35.18	SIM04	135.72	34.97
SIM40	HM12	2	138.03	44.46	SIM39	138.64	44.66
SIM42	HM12	2	136.74	49.92	SIM41	132.76	48.46
SIM44	HM12	2	118.89	48.21	SIM43	119.95	48.94
SIM46	HM12	2	106.81	48.16	SIM45	108.59	48.97

From the comparison it could be seen that in for three simulations, modified hydrofoil showed better efficiency than that of hydrofoil with no modifications. For simulation SIM22 with HM09 void pointing inwards have an efficiency of 33.16% while for simulation SIM13 which uses same hydrofoil but without modification HMXX shows an efficiency of only 31.56%. The increase in average power for SIM22 compared to SIM13 is 5.1%. For simulation SIM33 with HM12 void pointing inwards have an efficiency of 35.18% while for simulation SIM04 which uses same hydrofoil but without modification HMXX shows an efficiency of 34.97%. The increase in average power for SIM33 compared to SIM04 is small 0.6%. For simulation SIM42 with HM12 void pointing inwards have an efficiency of 49.92% which is the maximum efficiency among all simulations, while for simulation SIM41 which uses same hydrofoil but without modification HMXX

shows an efficiency of 48.46%. The increase in average power for SIM42 compared to SIM41 is 3.0%.

5.3 Section III Simulations

Simulations in this section are rotating turbine simulations (RTS) with 5 different pitch angles $\beta = -4°, -2°, 0°, 2°$ and 4°. The simulations considered for this section are given in the Table 4.9. The average moment and efficiency of RTS with non-zero pitch angle is compared with RTS with zero pitch angle. This results are shown in the Table 4.10 where AM is the average moment, η is the power efficiency in percentage. The results of section III simulation could be seen from three figures which shows their average moment, average power produced and average power efficiency. Fig. 5.12 shows the average moment, Fig. 5.13 shows the average power produced and Fig. 5.14 shows the predicted average power efficiency.

The average moment, power and power efficiency have the same pattern for section III simulations. It can be seen that power efficiency increases as the pitch angle increases from $-4°$ and reaches a maximum at 2° and reduces for further increase in pitch angle. In all cases of hydrofoils without modification with positive pitch angle of 2° shows higher efficiency than base case which is 0°. The efficiency of SIM25 (NACA0020 V with 2° pitch is 32.25% compared with SIM13 with 31.55% with $\beta = 0°$. Maximum Increase in power produced with changing pitch angle is about 2.2%. For modified hydrofoils 0° pitch angle seems to be better and for non-modified cases 2°.

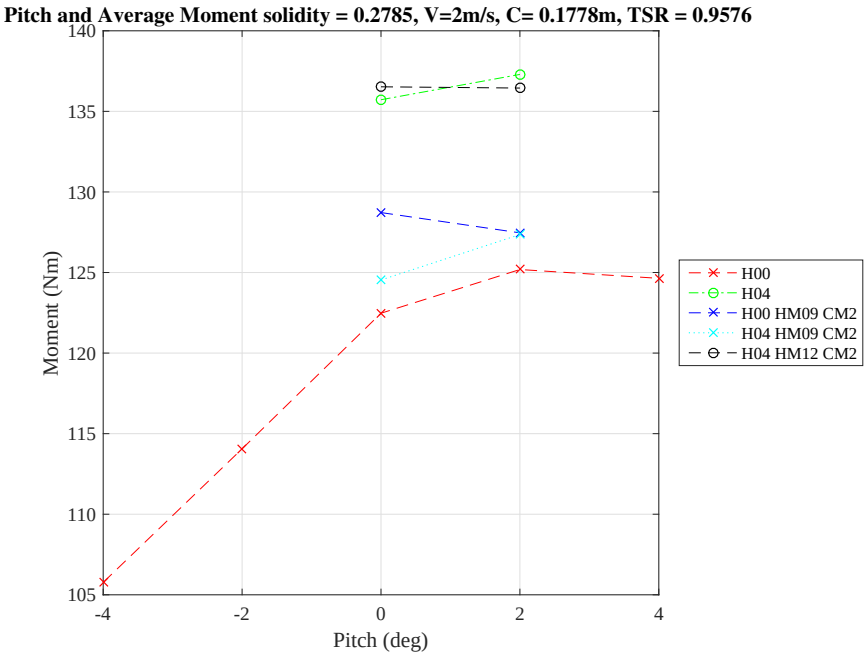

Figure 5.12: Average Moment of Section III Simulations

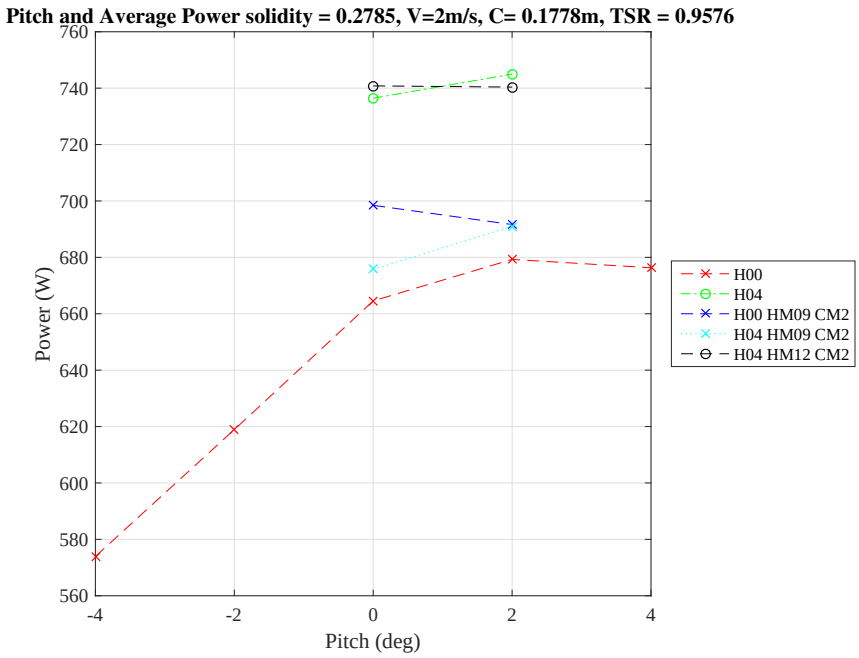

Figure 5.13: Average Power of Section III Simulations

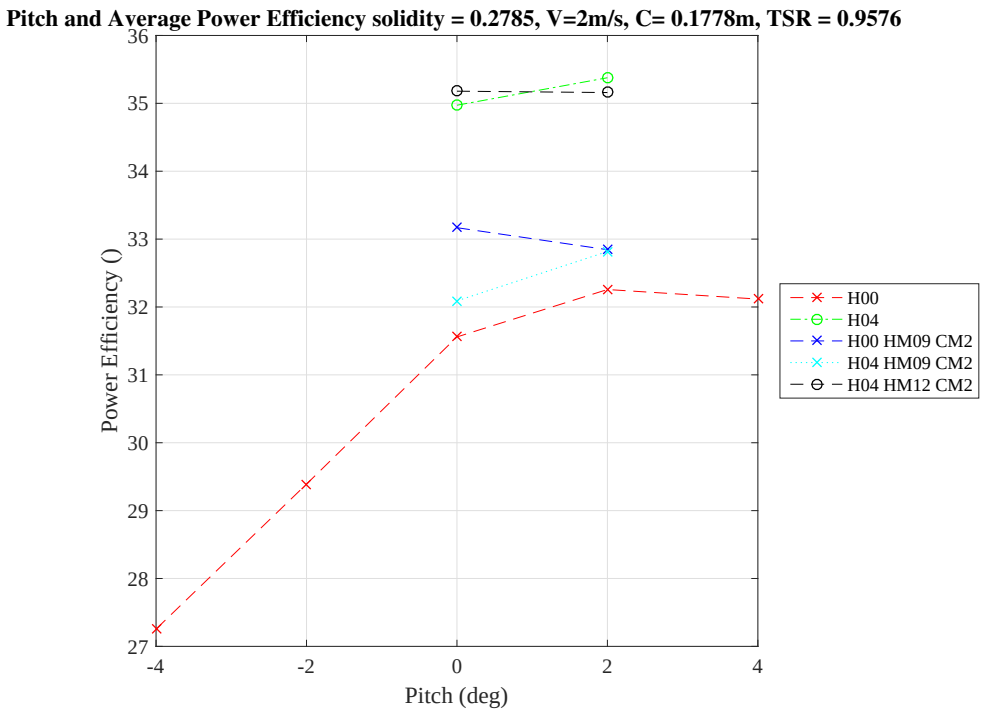

Figure 5.14: Average Power Efficiency of Section III Simulations

5.4 Section IV Simulations

This Section consists of 7 rotating turbine simulations with varying tip speed ratio. The tip speed ratio considered for these simulations are L01, L02, L04, L05, L07, L09 and L10 The simulations considered for this section are given in the Table 4.11. The results are shown in the Table 4.12 where AM is the average moment, η is the power efficiency in percentage. The results of section IV simulation could be seen from three figures which shows their average moment, average power produced and average power efficiency. Fig. 5.15 shows the average moment, Fig. 5.16 shows the average power produced and Fig. 5.17 shows the predicted average power efficiency.

It can be seen from the figure that moment increases as the tip speed ratio increases,

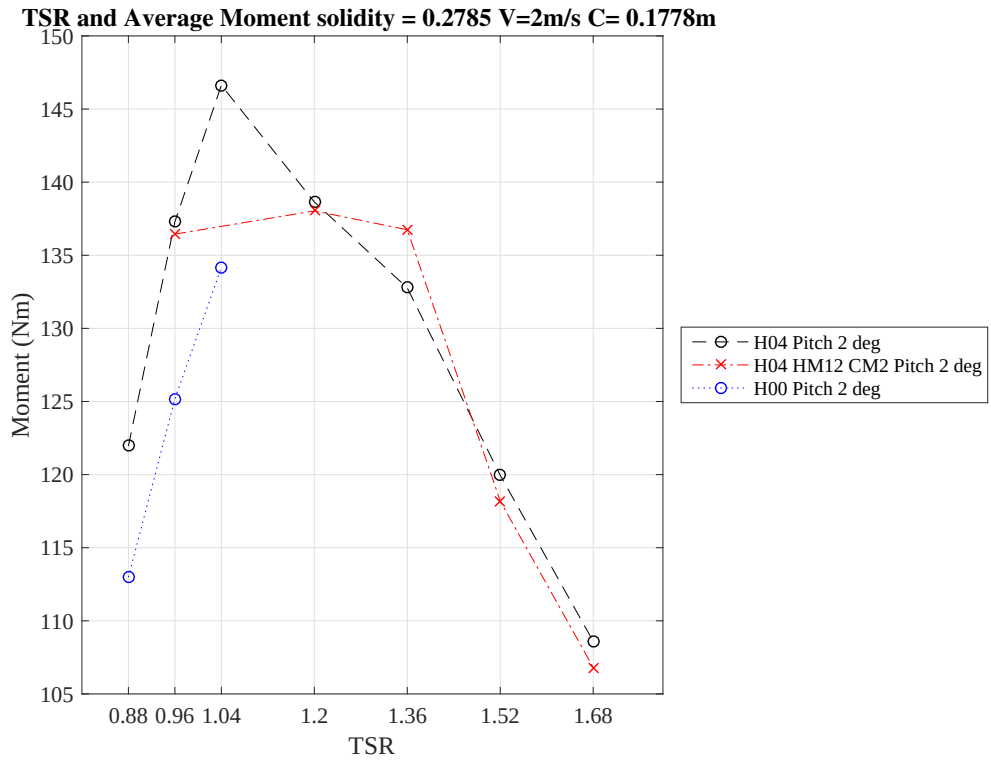

Figure 5.15: Average Moment of Section IV Simulations

from 113Nm for $\lambda = 0.88$ to 134.2Nm for $\lambda = 134.2Nm$ for hydrofoil shape with H00 with 2° pitch. Pitch increases in the same manner from 122Nm to 146Nm for H04 with 2° pitch and the reduces on further increase in tip speed ratio. For H04 HM14 maximum moment occurs at 1.2, a value of 138Nm then reduces.

It can be seen from the figure that power and efficiency increases as the tip speed ratio increases and reaches slightly steady state from $\lambda = 1.36$. For H04 HM12 maximum power and efficiency occurs at 1.36, a value of 1051W and 49.92% respectively and then reduces. For H04 HMXX maximum power and efficiency reaches steady from $\lambda = 1.52$ a value of 1030W and 48.9% respectively. The maximum increase in power from base case with $\lambda = 0.96$ and power 740W is 41.89%. when λ change to 1.36 for H04 HM12.

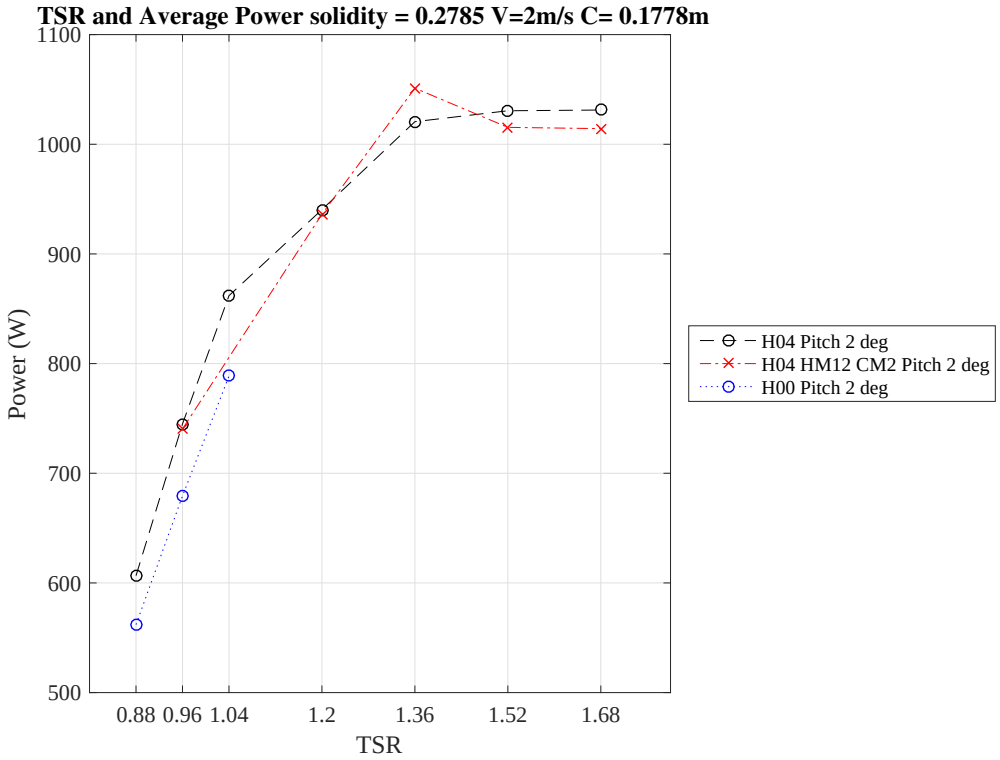

Figure 5.16: Average Power of Section IV Simulations

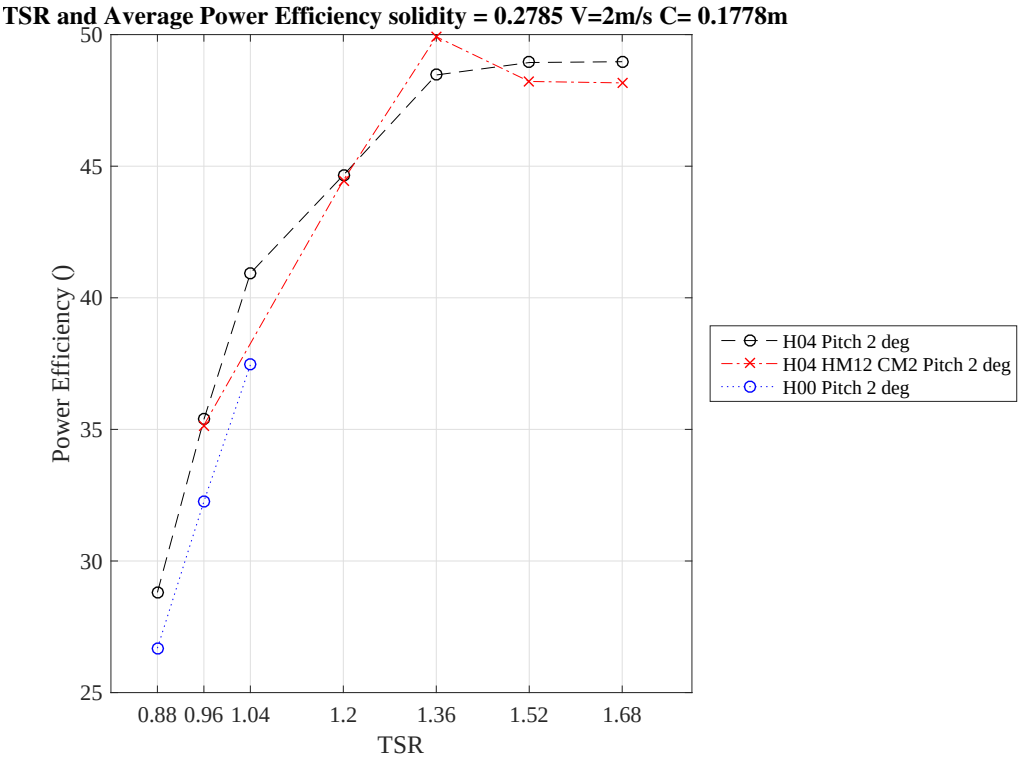

Figure 5.17: Average Power Efficiency of Section IV Simulations

5.5 Section V Simulations

This Section consists of 5 rotating turbine simulations with varying solidity. The solidity values considered for these simulations are S1 to S6. The simulations considered for this section are given in the Table 4.13. The results are shown in the Table 4.14 where AM is the average moment, η is the power efficiency in percentage. The results of section IV simulation could be seen from three figures which shows their average moment, average power produced and average power efficiency. Fig. 5.18 shows the average moment, Fig. 5.19 shows the average power produced and figure g 5.20 shows the predicted average power efficiency.

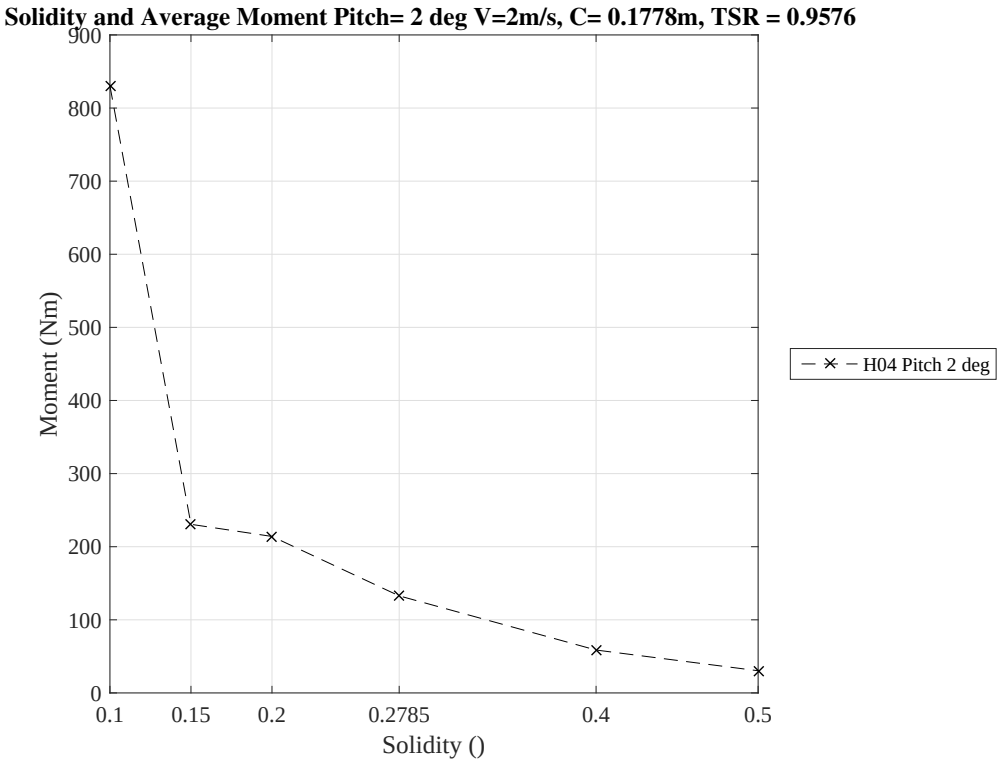

Figure 5.18: Average Moment of Section V Simulations

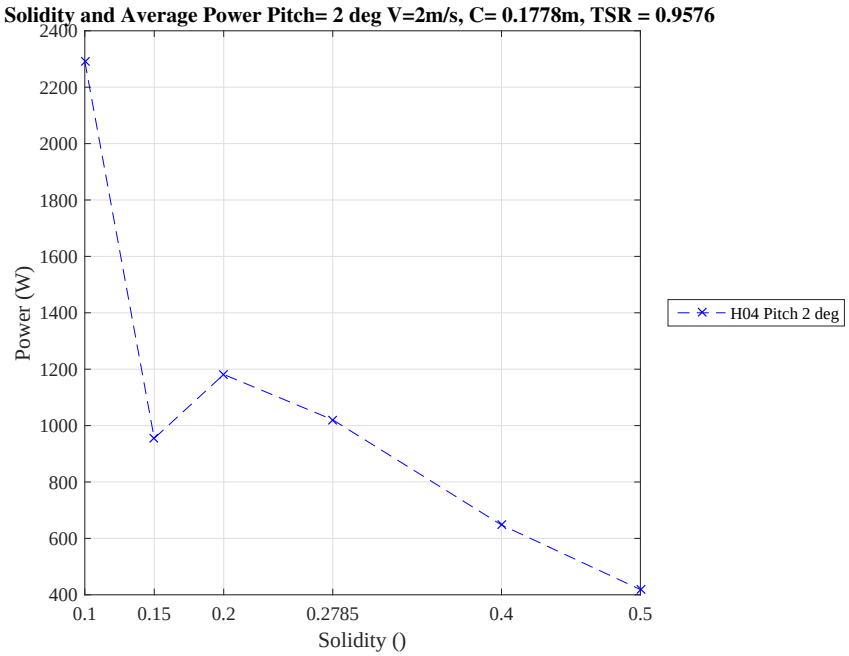

Figure 5.19: Average Power of Section V Simulations

Maximum moment and power is achieved for smallest solidity σ value of 0.1 (S1). Maximum moment is 830Nm and power is 2292W. This is the case with maximum moment and power among all simulations. The moment and power for base case (S4) are 39.02% 132.8Nm and 1021W. This is expected as the solidity reduces sweep area increases and available power increases. however, power efficiency is found to be highest for the base case $\sigma = 0.2785$ (S4) with a value of 48.47% whereas for $\sigma = 0.1$. So the best σ suggestion is base case S4.

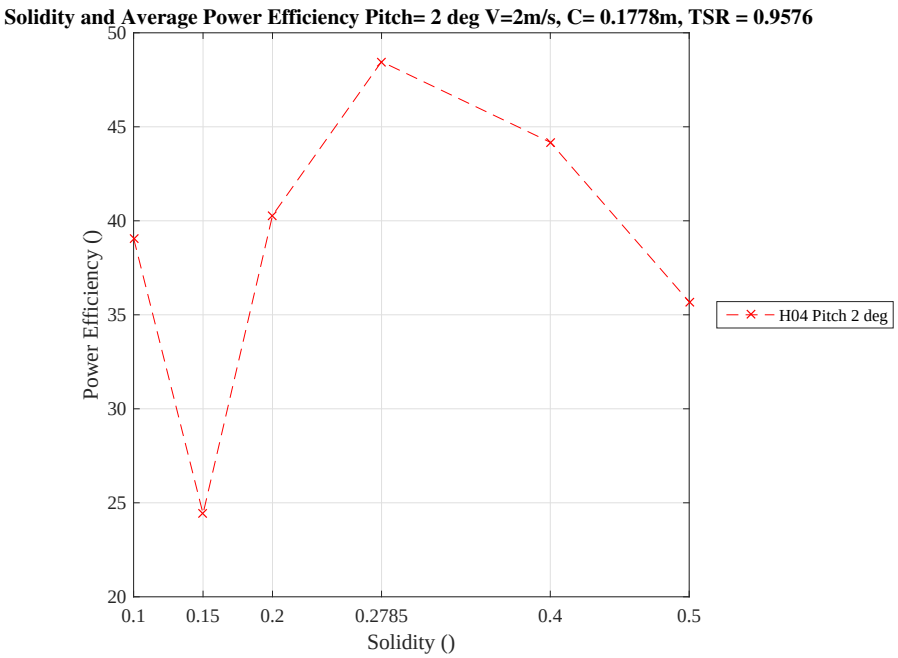

Figure 5.20: Average Power Efficiency of Section V Simulations

5.6 Summary of Results

The major objective of this research is suggest a water turbine design with higher power efficiency by conducting a parametric study of hydrofoil shapes, hydrofoil shape modifications with circular void, tip speed ratio, pitch angle and solidity. The design is intended to specific case of Gulf Stream ocean currents with flow velocity of 2m/s. The base water turbine design which was selected for this research is a Gorlov turbine and the base geometry was selected according to its inventor himself Alexander Gorlov [16]. Hydrofoil section which was selected is symmetric hydrofoil H00 (NACA0020) with a chord length of $C = 0.1778m$, with three blades $n = 3$, diameter of $D = 0.6096m$, Solidity of $\sigma = 0.2785$, tip speed ratio of $\lambda = 0.958$, pitch angle of $\beta = 0°$ and height of $h = 0.8696m$. For this thesis results from 70 CFD simulation research has been used. The 70 simulations can be

divided in to five sections and two kinds. The two kinds of simulation are Rotating Turbine Simulations (RTS) and Steady State Simulations (SSS) where RTS is 2D simulations with rotating hydrofoils of turbine and stead state simulations are 2D simulations in which hydrofoils are motionless or in steady state. Two dimensional simulations are used based on blade element theory (BET). The power efficiency of the base case simulation was found to be 31.55% and the power output was 664.5W. Among sections, the first section consists of 20 Rotating Turbine simulations (RTS). These simulations are done for find the best hydrofoil shape (H). All the hydrofoil shapes used for this research are NACA 4 digit foils. 13 NACA foils were used among which six are symmetric and seven for asymmetric. So after section I simulations best hydrofoil shape was selected which was H04 (NACA0018). The increase in power for H04 from H00 was 10.8%. The section II simulations consists of simulations for finding the best modified hydrofoil shape (HM) This section uses 8 steady state simulations (SSS) and 9 rotating turbine simulations (RTS). From the SSS, for 8 pitch angles each with thirteen modifications, hydrofoil modification was chosen based on overall lift and drag performance. The thirteen modifications were performed on base hydrofoil shape H00 (NACA0020). The modifications included 5 cases each with three different parameter of modification which are radius of the circular void R_V, Y coordinate of the center of void in local coordinate (LC) Y_V and X coordinate of the center of void in local coordinate (LC) X_V. R_V and Y_V are given as percentage of maximum thickness of hydrofoil and percentage of Y coordinate of maximum thickness and X_V as the percentage of X coordinate of maximum thickness. The selected modification was HM12 with

$R_V = 50$, $Y_V = 30$ and $X_V = 120$. This modification HM12 along with HM09 with X_V=80 and other values same of HM12 were selected for 9 RTS. From these simulations a maximum increase in power due to the modification came out to be 5.1%. In all cases when efficiency was higher than non-modified case void was pointing inwards to the center of turbine. The section III simulations consists simulations for finding the best pitch angle (β). This RTS with 5 different pitch angles $\beta = -4°, -2°, 0°, 2°$ and $4°$. Maximum Increase in power produced with changing pitch angle is about 2.2%. For modified hydrofoils 0° pitch angle seems to be better and for non-modified cases, pitch of 2°. The fourth section consists of simulations for finding the best tip speed ratio (λ), This section consists of 7 rotating turbine simulations with varying tip speed ratio. The tip speed ratio considered for these simulations are L01, L02, L04, L05, L07, L09 and L10 whose values range from 0.88 to 1.68 L02 being the base case. The best λ was found to be L07 (1.36) for H04 with modification HM12 and L10(1.68) for H04 without modification HMXX. The maximum increase in power from base case by changing tip speed ratio was found to be 41.89% for H04 HM12. The fifth section consists of simulations for finding the best solidity value (σ). This Section consists of 5 rotating turbine simulations with varying solidity. The solidity values considered for these simulations are S1 to S6 ranging from 0.1 to 0.5 with base case being S4($\sigma = 0.2785$). Power efficiency is found to be highest for the base case $\sigma = 0.2785$ (S4). So the σ s4 itself is the best case.

6 SUMMARY AND CONCLUSIONS

The major objective of this research was to suggest a water turbine design with higher power efficiency by conducting a parametric study of hydrofoil shapes, hydrofoil shape modifications with circular void, tip speed ratio, pitch angle and solidity. This design for Gulf Stream ocean currents is based on a specific Gorlov turbine design. The power efficiency of the base case turbine was improved from 31.5%. to 49.92% according to simulation results. A new modification with a circular void in the hydrofoil cross section was introduced in this research to increase the efficiency. The maximum increase in power due to changing hydrofoil shape was 10.81%. By introducing circular void in hydrofoil maximum increment was 5.1%. By varying tip speed ratio, it was 41.89%. By changing pitch angle it was 2.2% and for solidity no increase as base case was the best case. The major objective of this research is successfully completed as a design with higher power efficiency is suggested. The other main objective of this research was to see whether a modification with void in hydrofoil cross section can improve the efficiency. From the simulation results the answer is yes and maximum increase for studied modifications came about 5.1%.

According to results from this research using CFD it can be said that Gorlov turbines can be used efficiently for ocean currents in gulf stream from perspective of power efficiency. The results got from this research may be used only qualitatively, but it shows efficiency can be increased considerably by changing different parameters. The concept of

introducing void into turbine blade cross section is a new concept. Even though the maximum increment in power due to modification for cases considered is around 5%, since there can be infinite shapes and positions of void, it is a very open area for future research. Since the physics for turbine blade considered for this research is similar to other turbines like horizontal water turbines and wind turbines, especially vertical axis wind turbines, future research could be done in those perspectives also. But even if we can increase the efficiency considerably with modifications using voids, other major issues due to void such as reduction in structural strength, difficulty in manufacture and cavitation need to solved.

REFERENCES

[1] M. Shiono, K. Suzuki, S. Kiho, *et al.*, "Output characteristics of darrieus water turbine with helical blades for tidal current generations," in *The Twelfth International Offshore and Polar Engineering Conference*, International Society of Offshore and Polar Engineers, 2002.

[2] J. Zanette, D. Imbault, and A. Tourabi, "A design methodology for cross flow water turbines," *Renewable Energy*, vol. 35, no. 5, pp. 997–1009, 2010.

[3] "Tidal turbines, http://www.soue.org.uk/souenews/issue7/tidalturbines.html,"

[4] N. Fujisawa and S. Shibuya, "Observations of dynamic stall on darrieus wind turbine blades," *Journal of Wind Engineering and Industrial Aerodynamics*, vol. 89, no. 2, pp. 201–214, 2001.

[5] F. Vanek and L. Albright, *Energy systems engineering*. Mcgraw-Hill Education, 2016.

[6] ExxonMobil, "The outlook for energy: a view to 2040 technical report," 2012.

[7] S. Shafiee and E. Topal, "When will fossil fuel reserves be diminished?," *Energy policy*, vol. 37, no. 1, pp. 181–189, 2009.

[8] X. Yang, K. A. Haas, H. M. Fritz, S. P. French, X. Shi, V. S. Neary, and B. Gunawan, "National geodatabase of ocean current power resource in usa," *Renewable and Sustainable Energy Reviews*, vol. 44, pp. 496–507, 2015.

[9] H. M. Stommel, *The Gulf Stream: a physical and dynamical description*. Univ of California Press, 1958.

[10] D. M. Fratantoni, "North atlantic surface circulation during the 1990's observed with satellite-tracked drifters," *Journal of Geophysical Research: Oceans*, vol. 106, no. C10, pp. 22067–22093, 2001.

[11] P. Lissaman, "The coriolis program.," *Oceanus*, vol. 22, no. 4, pp. 23–28, 1979.

[12] M. M. S. R. Energy and A. U. P. U. D. of the Interior, "Technology white paper on ocean current energy potential on the u.s. outer continental shelf," 2006.

[13] W. S. Von Arx, H. Stewart, and J. R. Apel, "The florida current as a potential source of useable energy," in *Proceedings of the MacArthur Workshop on the Feasibility of Extracting Useable Energy from the Florida Current*, February, 1974.

[14] A. E. Duerr and M. R. Dhanak, "An assessment of the hydrokinetic energy resource of the florida current," *Oceanic Engineering, IEEE Journal of*, vol. 37, no. 2, pp. 281–293, 2012.

[15] X. Yang, K. A. Haas, and H. M. Fritz, "Evaluating the potential for energy extraction from turbines in the gulf stream system," *Renewable Energy*, vol. 72, pp. 12–21, 2014.

[16] A. M. Gorlov, "Helical turbines for the gulf stream: conceptual approach to design of a large-scale floating power farm," *Marine Technology and Sname News*, vol. 35, no. 3, p. 175, 1998.

[17] M. R. Castelli and E. Benini, "Comparison between lift and drag-driven vawt concepts on low-wind site aeo," in *ICAMME 2012: International Conference on Applied Mechanics and Mechanical Engineering*, pp. 28–30, 2012.

[18] R. H. Karsten, J. McMillan, M. Lickley, and R. Haynes, "Assessment of tidal current energy in the minas passage, bay of fundy," *Proceedings of the Institution of Mechanical Engineers, Part A: Journal of Power and Energy*, vol. 222, no. 5, pp. 493–507, 2008.

[19] F. O. Rourke, F. Boyle, and A. Reynolds, "Tidal energy update 2009," *Applied Energy*, vol. 87, no. 2, pp. 398–409, 2010.

[20] N. Mehmood, Z. Liang, and J. Khan, "Harnessing ocean energy by tidal current technologies," *Research Journal of Applied Sciences, Engineering and Technology*, vol. 4, no. 18, pp. 3476–3487, 2012.

[21] F. Chen, S.-M. Lu, K.-T. Tseng, S.-C. Lee, and E. Wang, "Assessment of renewable energy reserves in taiwan," *Renewable and sustainable energy reviews*, vol. 14, no. 9, pp. 2511–2528, 2010.

[22] K. S. Lee, K.-D. Yum, J.-S. Park, and J. W. Park, "Tidal current power development in korea," in *Korean Ocean Research and Development Institute (KORDI), presentation at East Asian Sea Congress*, 2009.

[23] "Andritz hydro, http://www.hammerfeststrom.com/,"

[24] A. Gorlov, "Helical turbine and fish safety," tech. rep., Tech. Rep. Half-moon Cove Tidal Power Project P-12704, Tidewalker Associates, 2010.

[25] D. Coiro, A. De Marco, F. Nicolosi, S. Melone, and F. Montella, "Dynamic behaviour of the patented kobold tidal current turbine: numerical and experimental aspects," *Acta Polytechnica*, vol. 45, no. 3, 2005.

[26] A. M. Gorlov, "Helical turbine assembly operable under multidirectional fluid flow for power and propulsion systems," July 1 1997. US Patent 5,642,984.

[27] A. M. Gorlov, "Helical turbine assembly operable under multidirectional gas and water flow for power and propulsion systems," Mar. 14 2000. US Patent 6,036,443.

[28] A. M. Gorlov, "System for providing wind propulsion of a marine vessel using a helical turbine assembly," Sept. 25 2001. US Patent 6,293,835.

[29] S.-H. Han, K.-S. Lee, K.-D. Yum, W.-S. Park, and J.-S. Park, "Evaluation of helical turbine efficiency for tidal current power plant based on in-situ experiment," in *Proceedings of the 5th International Conference on Asian and Pacific Coasts, Singapore*, vol. 4, pp. 315–321, World Scientific, 2009.

[30] V. J. Rossow, "Lift enhancement by an externally trapped vortex," *Journal of Aircraft*, vol. 15, no. 9, pp. 618–625, 1978.

[31] S. Chernyshenko, B. Galletti, A. Iollo, and L. Zannetti, "Trapped vortices and a favourable pressure gradient," *Journal of Fluid Mechanics*, vol. 482, pp. 235–255, 2003.

[32] F. O. Ringleb, "Separation control by trapped vortices," *Boundary Layer and Flow Control*, vol. 1, pp. 265–294, 1961.

[33] F. O. Ringleb, "Separation control by trapped vortices," *Boundary Layer and Flow Control*, vol. 1, pp. 265–294, 1961.

[34] A. Iollo and L. Zannetti, "Trapped vortex optimal control by suction and blowing at the wall," *European Journal of Mechanics-B/Fluids*, vol. 20, no. 1, pp. 7–24, 2001.

[35] W. Batten, A. Bahaj, A. Molland, and J. Chaplin, "Hydrodynamics of marine current turbines," *Renewable energy*, vol. 31, no. 2, pp. 249–256, 2006.

[36] C. Consul, R. Willden, E. Ferrer, and M. McCulloch, "Influence of solidity on the performance of a cross-flow turbine," in *Proceedings of the 8th European Wave and Tidal Energy Conference., Uppsala, Sweden*, 2009.

[37] P. Fraunie, C. Beguier, I. Paraschivoiu, and G. Brochier, "Water channel experiments of dynamic stall on darrieus wind turbine blades," *Journal of Propulsion and Power*, vol. 2, no. 5, pp. 445–449, 1986.

APPENDIX A

MISCELLANEOUS

In this chapter there are three sections, results, comparison and verification. The results section shows outputs of all the simulations, comparison section shows the comparison with the published experimental result and verification section shows the mesh size verification, time step verification and inner iteration verification.

A.1 Results

The details of input parameters for all the simulations for improving the basic turbine design is given in the tables Table A.1 to Table A.7. The results of RTS can be reached by clicking the figure names of the required figure in the tables Table A.1 to Table A.6. The results of steady state simulations (SSS) is given in Table A.7. Note that figure name doesn't have 'Fig.' due to the space constraint inside table. In the table S denotes simulation name without SIM. V denotes velocity profile, P for pressure profile, M is Moment results, DG is drag force results in global coordinate, LG is lift force in global coordinate, DLL stands for drag and lift forces in local coordinate system.

Table A.1: Results for Simulations SIM01 to SIM10

S	Name	Mesh	V	P	M	DG	LG	DLL
01	S11010XX0244	A.1	A.2	A.3	A.4	A.5	A.6	A.7
02	S11020XX0244	A.8	A.9	A.10	A.11	A.12	A.13	A.14
03	S11030XX0244	A.15	A.16	A.17	A.18	A.19	A.20	A.21
04	S11040XX0244	A.22	A.23	A.24	A.25	A.26	A.27	A.28
05	S11050XX0244	A.29	A.30	A.31	A.32	A.33	A.34	A.35
06	S11061XX0244	A.36	A.37	A.38	A.39	A.40	A.41	A.42
07	S11071XX0244	A.43	A.44	A.45	A.46	A.47	A.48	A.49
08	S11081XX0244	A.50	A.51	A.52	A.53	A.54	A.55	A.56
09	S11091XX0244	A.57	A.58	A.59	A.60	A.61	A.62	A.63
10	S11101XX0244	A.64	A.65	A.66	A.67	A.68	A.69	A.70

Table A.2: Results for Simulations SIM11 to SIM20

S	Name	Mesh	V	P	M	DFG	LG	DLL
11	S11110XX0244	A.71	A.72	A.73	A.74	A.75	A.76	A.77
12	S11120XX0244	A.78	A.79	A.80	A.81	A.82	A.83	A.84
13	S11000XX0244	A.85	A.86	A.87	A.88	A.89	A.90	A.91
14	S11001090244	A.92	A.93	A.94	A.95	A.96	A.97	A.98
15	S11062XX0244	A.99	A.100	A.101	A.102	A.103	A.104	A.105
16	S11072XX0244	A.106	A.107	A.108	A.109	A.110	A.111	A.112
17	S11082XX0244	A.113	A.114	A.115	A.116	A.117	A.118	A.119
18	S11092XX0244	A.120	A.121	A.122	A.123	A.124	A.125	A.126
19	S11102XX0244	A.127	A.128	A.129	A.130	A.131	A.132	A.133
20	S11112XX0244	A.134	A.135	A.136	A.137	A.138	A.139	A.140

Table A.3: Results for Simulations SIM21 to SIM30

S	Name	Mesh	V	P	M	DFG	LG	DLL
21	S11122XX0244	A.141	A.142	A.143	A.144	A.145	A.146	A.147
22	S11002090244	A.148	A.149	A.150	A.151	A.152	A.153	A.154
23	S11000XX0234	A.155	A.156	A.157	A.158	A.159	A.160	A.161
24	S11000XX0224	A.162	A.163	A.164	A.165	A.166	A.167	A.168
25	S11000XX0264	A.169	A.170	A.171	A.172	A.173	A.174	A.175
26	S11000XX0274	A.176	A.177	A.178	A.179	A.180	A.181	A.182
27	S11040XX0264	A.183	A.184	A.185	A.186	A.187	A.188	A.189
28	S11002090264	A.190	A.191	A.192	A.193	A.194	A.195	A.196
29	S11001130244	A.197	A.198	A.199	A.200	A.201	A.202	A.203
30	S11001130244	A.204	A.205	A.206	A.207	A.208	A.209	A.210

Table A.4: Results for Simulations SIM31 to SIM40

S	Name	Mesh	V	P	M	DFG	LG	DLL
31	S11042090244	A.211	A.212	A.213	A.214	A.215	A.216	A.217
32	S11042090264	A.218	A.219	A.220	A.221	A.222	A.223	A.224
33	S11042120244	A.225	A.226	A.227	A.228	A.229	A.230	A.231
34	S11042120264	A.232	A.233	A.234	A.235	A.236	A.237	A.238
35	S11040XX0164	A.239	A.240	A.241	A.242	A.243	A.244	A.245
36	S11000XX0164	A.246	A.247	A.248	A.249	A.250	A.251	A.252
37	S11040XX0464	A.253	A.254	A.255	A.256	A.257	A.258	A.259
38	S11000XX0464	A.260	A.261	A.262	A.263	A.264	A.265	A.266
39	S11040XX0564	A.267	A.268	A.269	A.270	A.271	A.272	A.273
40	S11042120564	A.274	A.275	A.276	A.277	A.278	A.279	A.280

Table A.5: Results for Simulations SIM41 to SIM50

S	Name	Mesh	V	P	M	DFG	LG	DLL
41	S11040XX0764	A.281	A.282	A.283	A.284	A.285	A.286	A.287
42	S11042120764	A.288	A.289	A.290	A.291	A.292	A.293	A.294
43	S11040XX0964	A.295	A.296	A.297	A.298	A.299	A.300	A.301
44	S11042120964	A.302	A.303	A.304	A.305	A.306	A.307	A.308
45	S11040XX1064	A.309	A.310	A.311	A.312	A.313	A.314	A.315
46	S11042121064	A.316	A.317	A.318	A.319	A.320	A.321	A.322
47	S1104212AU44	A.323	A.324	A.325	A.326	A.327	A.328	A.329
48	S11040XXAU64	A.330	A.331	A.332	A.333	A.334	A.335	A.336
49	S11000XXAU64	A.337	A.338	A.339	A.340	A.341	A.342	A.343
50	S12040XX0744	A.344	A.345	A.346	A.347	A.349	A.351	A.353

Table A.6: Results for RTS SIM51 to SIM62

S	Name	Mesh	V	P	M	DFG	LG	DLL
51	S12042120744	A.355	A.356	A.357	A.358	A.360	A.362	A.364
52	S12040XX0764	A.366	A.367	A.368	A.369	A.371	A.373	A.375
53	S11040XX0761	A.377	A.378	A.379	A.380	A.381	A.382	A.383
54	S11040XX0762	A.384	A.385	A.386	A.387	A.388	A.389	A.390
55	S11040XX0763	A.391	A.392	A.393	A.394	A.395	A.396	A.397
56	S11040XX0765	A.398	A.399	A.400	A.401	A.402	A.403	A.404
57	S11040XX0766	A.405	A.406	A.407	A.408	A.409	A.410	A.411
58	SC11040XX0845	A.412	A.413	A.414	A.415	A.416	A.417	A.418
59	SC11040XX0345	A.419	A.420	A.421	A.422	A.423	A.424	A.425
60	SC11040XX0645	A.426	A.427	A.428	A.429	A.430	A.431	A.432
61	SC11040XX1145	A.433	A.434	A.435	A.436	A.437	A.438	A.439
62	SC11040XX1245	A.440	A.441	A.442	A.443	A.444	A.445	A.446

Table A.7: Results for Simulations SIM61 to SIM70

S	Name	Lift Force	Drag Force
63	SS2008	A.447	A.455
64	SS2007	A.448	A.456
65	SS2006	A.449	A.457
66	SS2005	A.450	A.458
67	SS2004	A.451	A.459
68	SS2003	A.452	A.460
69	SS2002	A.453	A.461
70	SS2001	A.454	A.462

A.1.1 SIM01

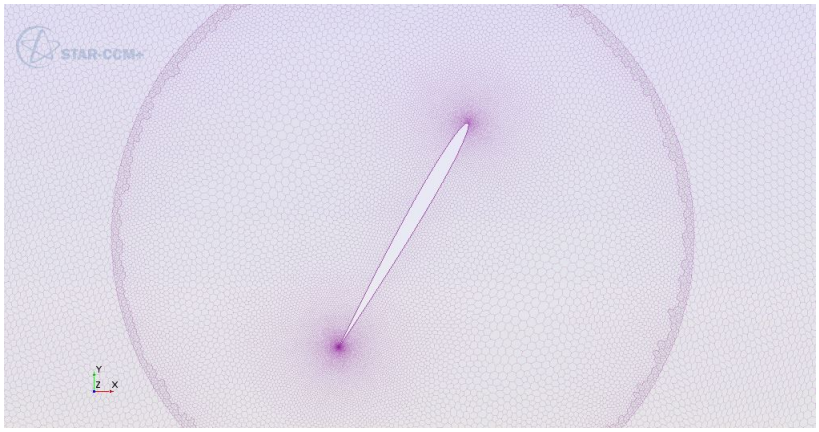

Figure A.1: Mesh SIM01

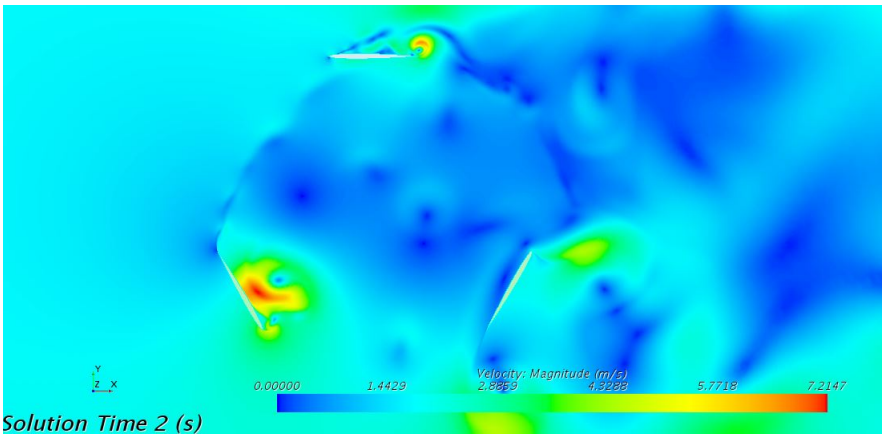

Figure A.2: Velocity SIM01

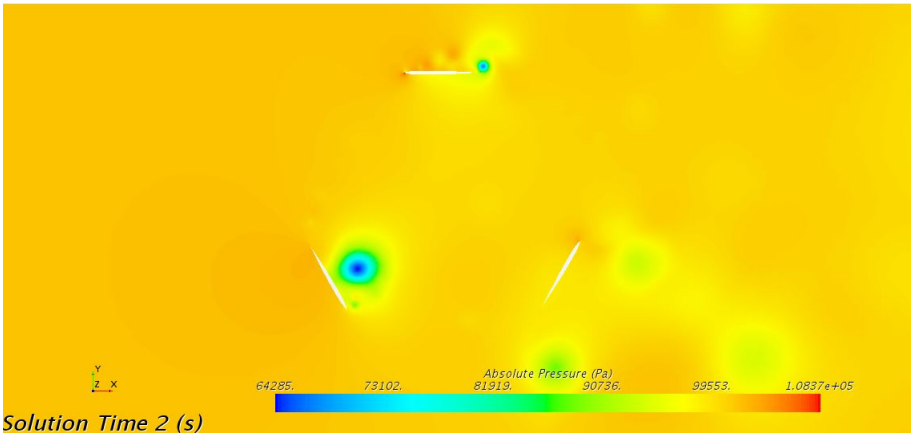

Figure A.3: Pressure SIM01

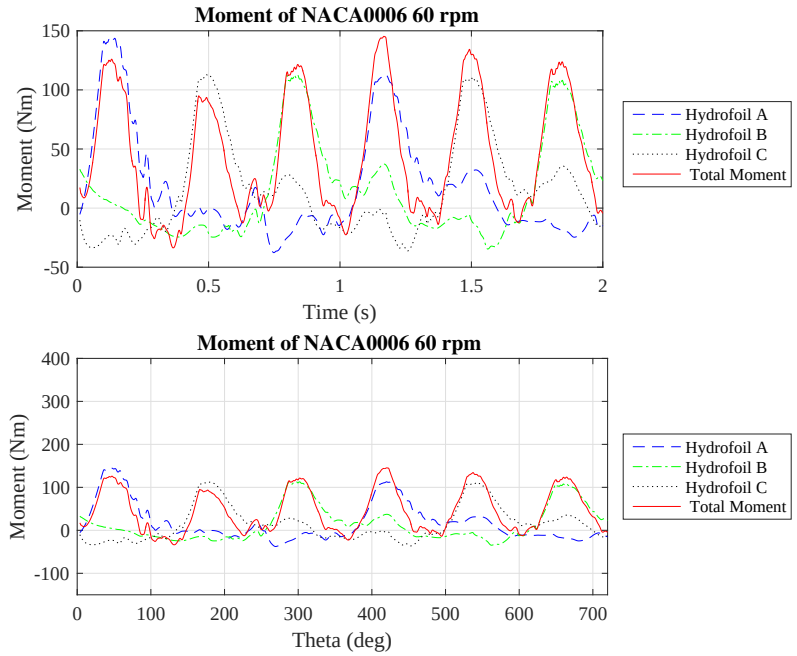

Figure A.4: Moment SIM01

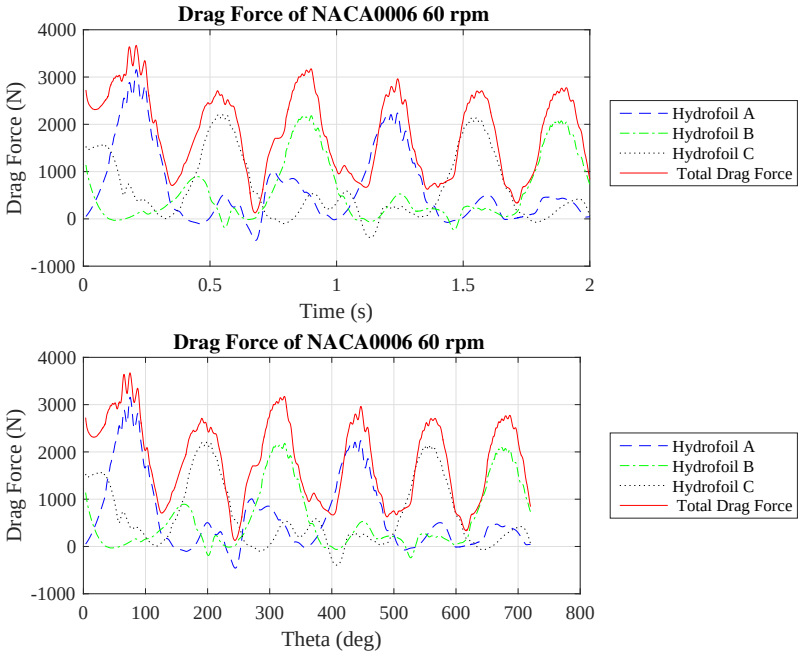

Figure A.5: Drag Force (GC) SIM01

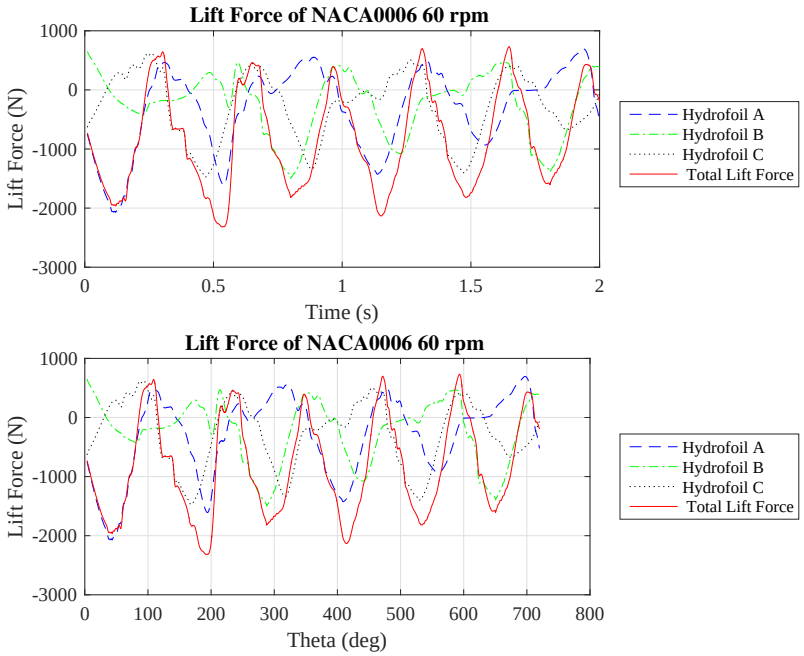

Figure A.6: Lift Force (GC) SIM01

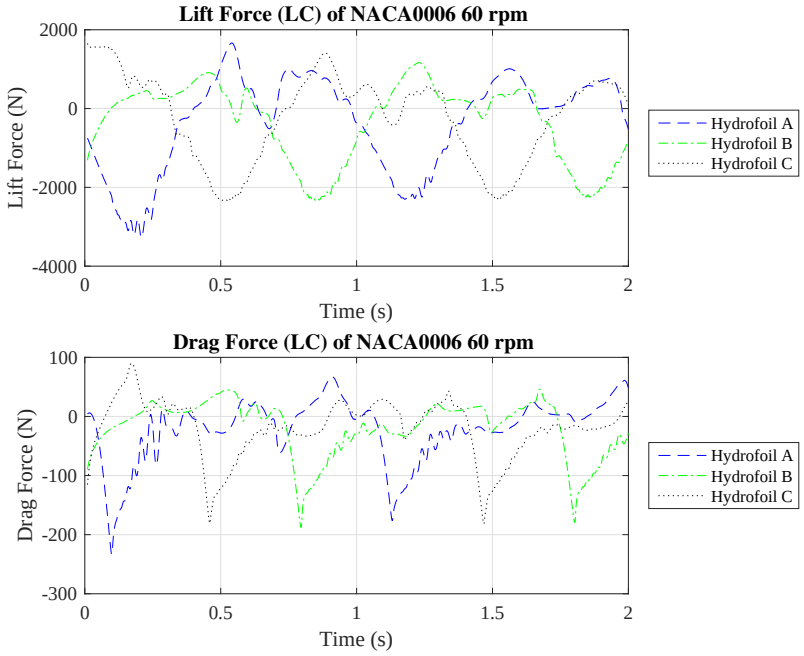

Figure A.7: Lift and Drag Force (LC) SIM01

A.1.2 SIM02

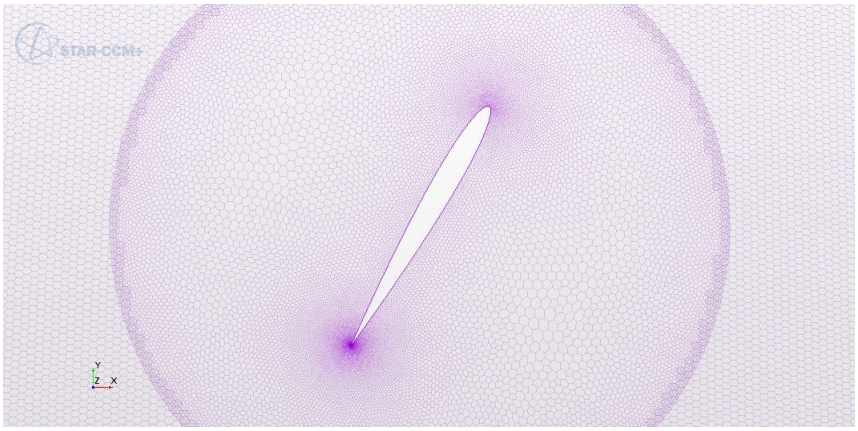

Figure A.8: Mesh SIM02

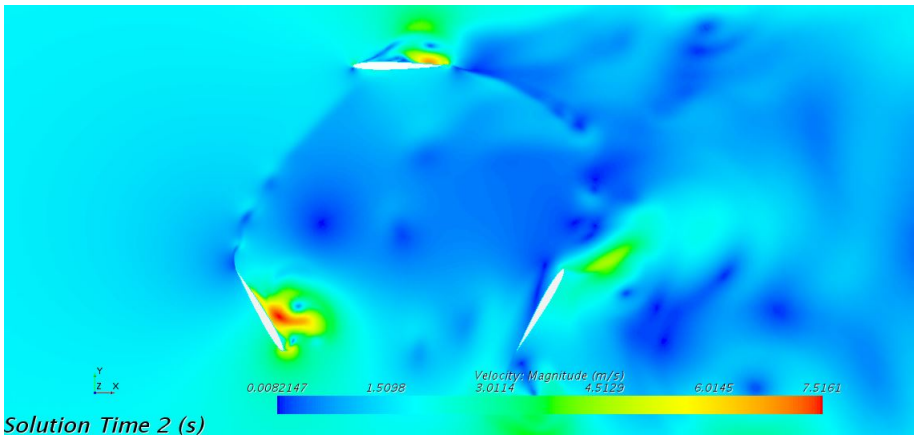

Figure A.9: Velocity SIM02

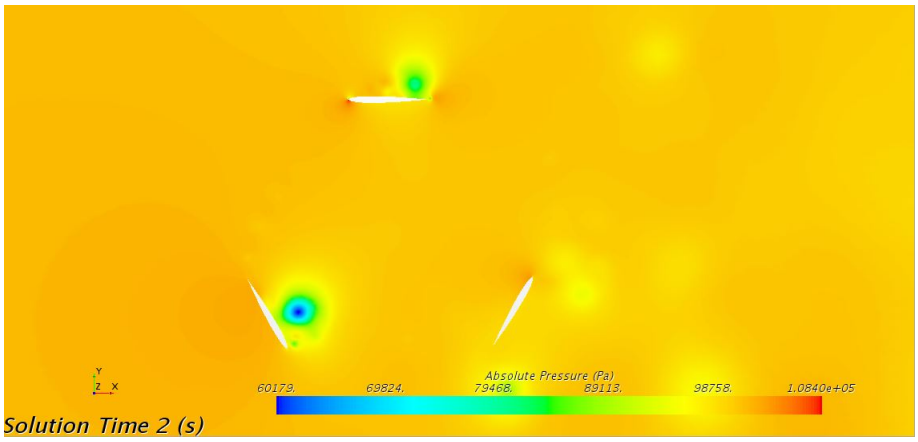

Figure A.10: Pressure SIM02

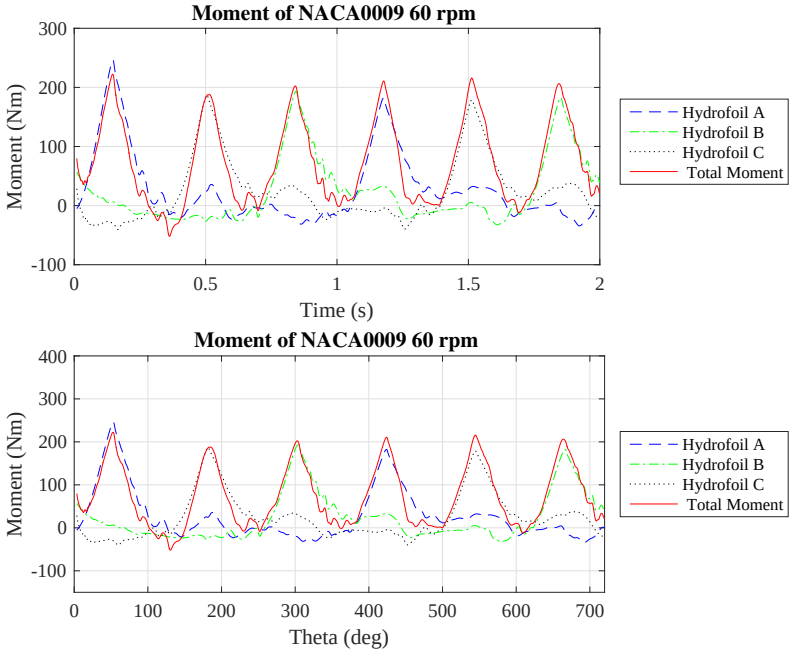

Figure A.11: Moment SIM02

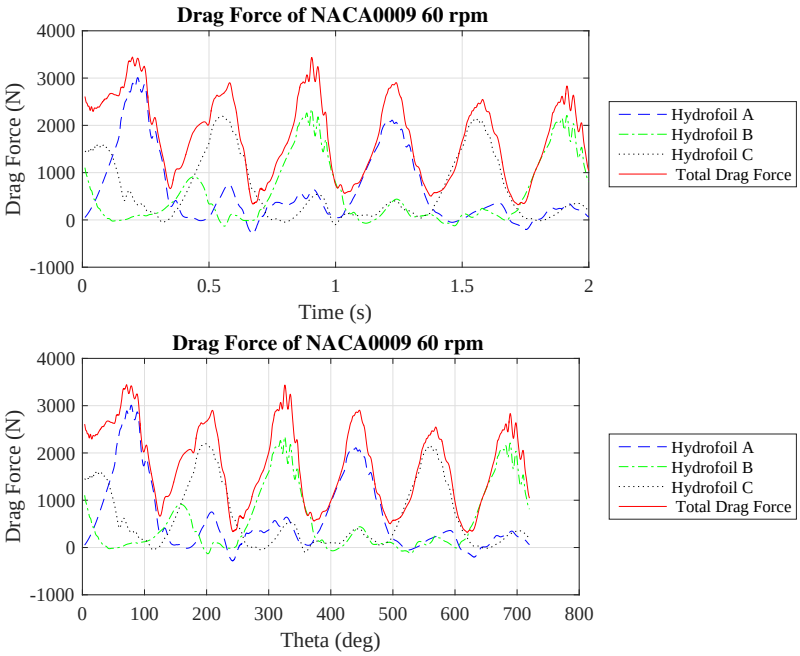

Figure A.12: Drag Force SIM02

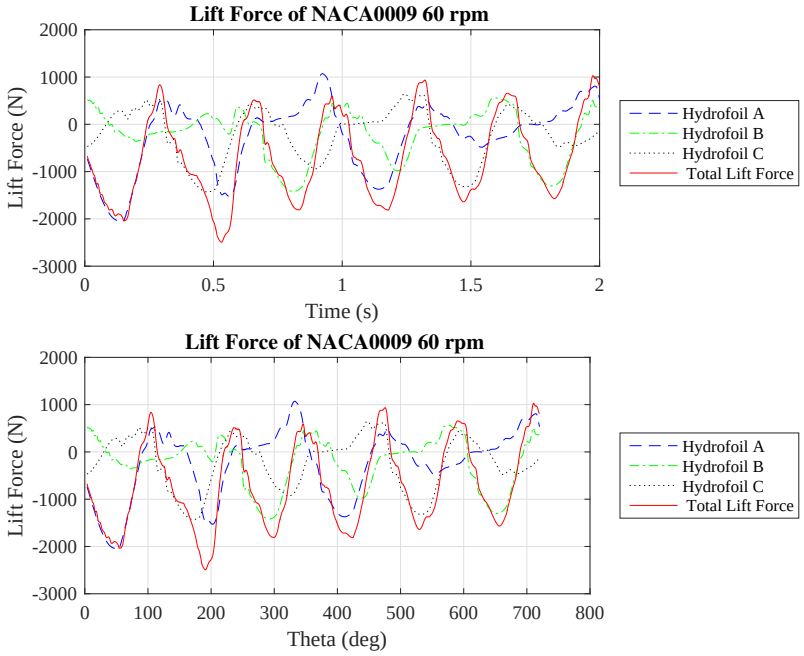

Figure A.13: Lift Force SIM02

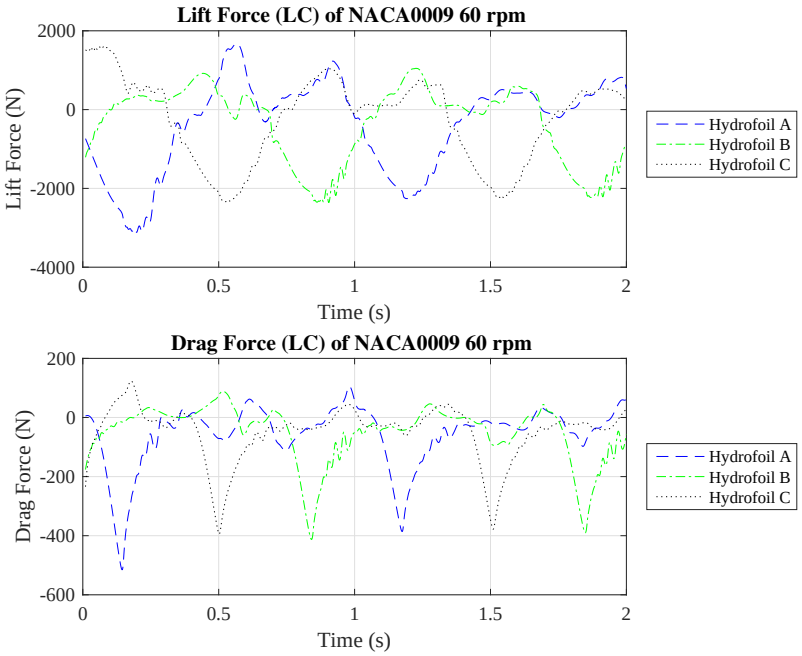

Figure A.14: Lift and Drag Force (LC) SIM02

A.1.3 SIM03

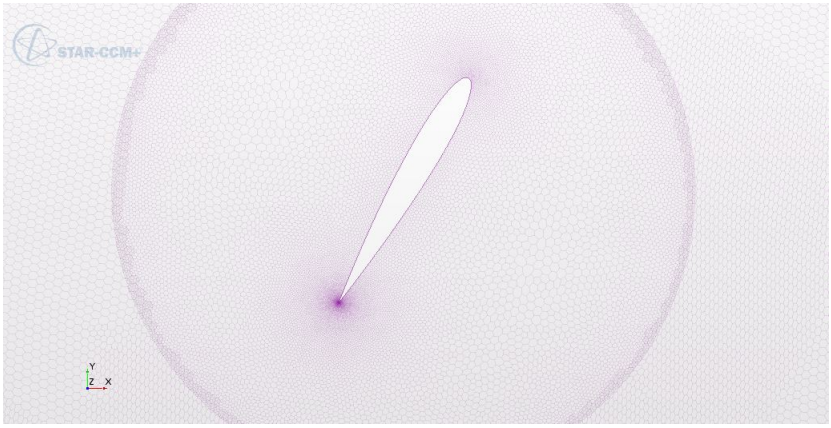

Figure A.15: Mesh SIM03

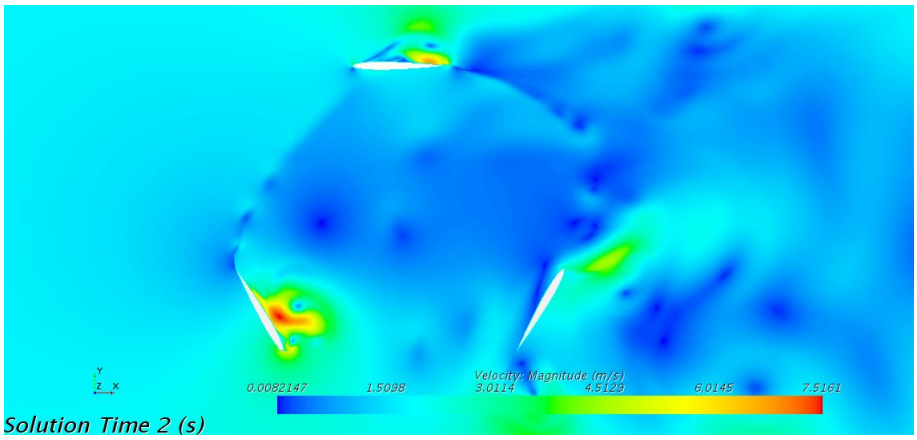

Figure A.16: Velocity SIM03

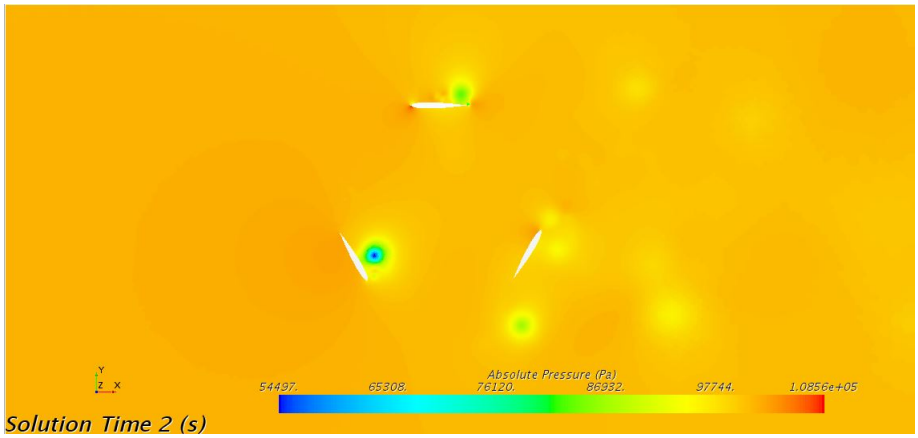

Figure A.17: Pressure SIM03

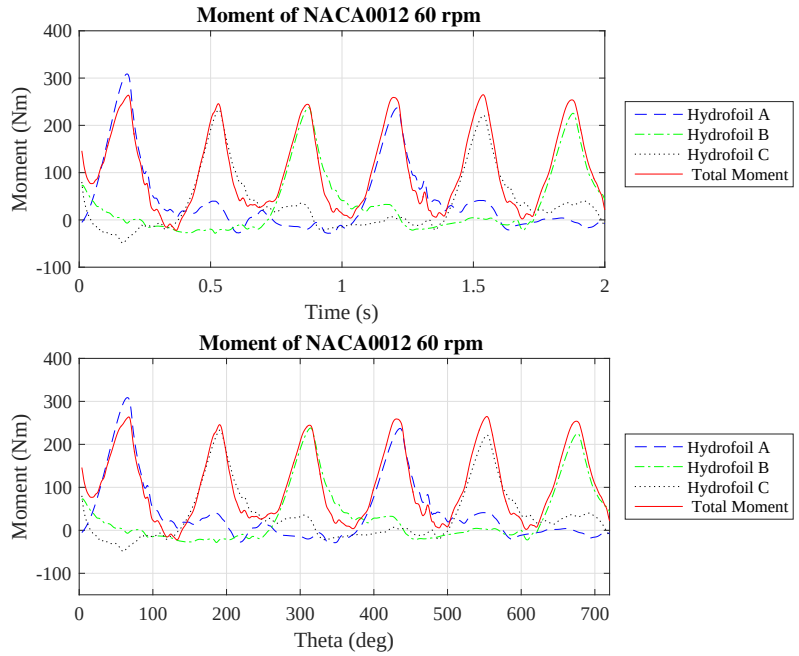

Figure A.18: Moment SIM03

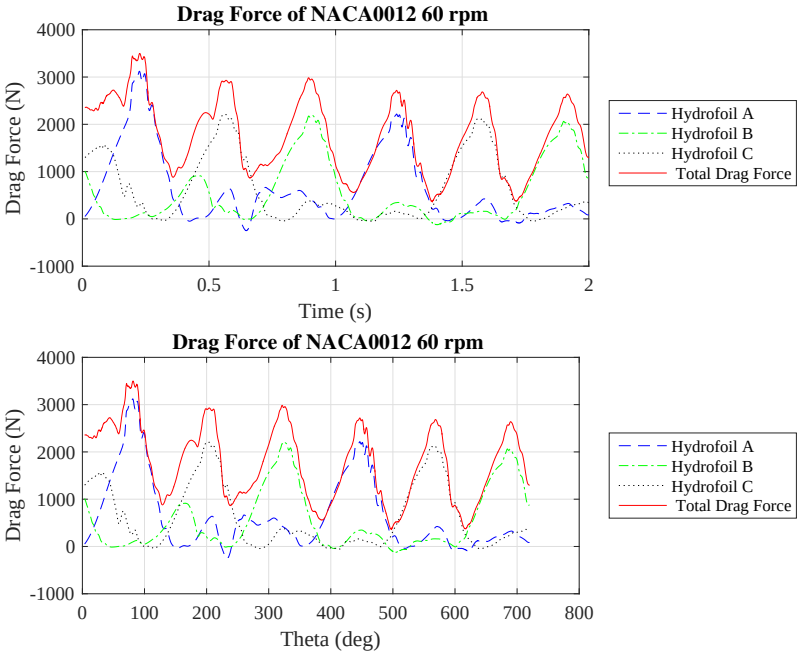

Figure A.19: Drag Force SIM03

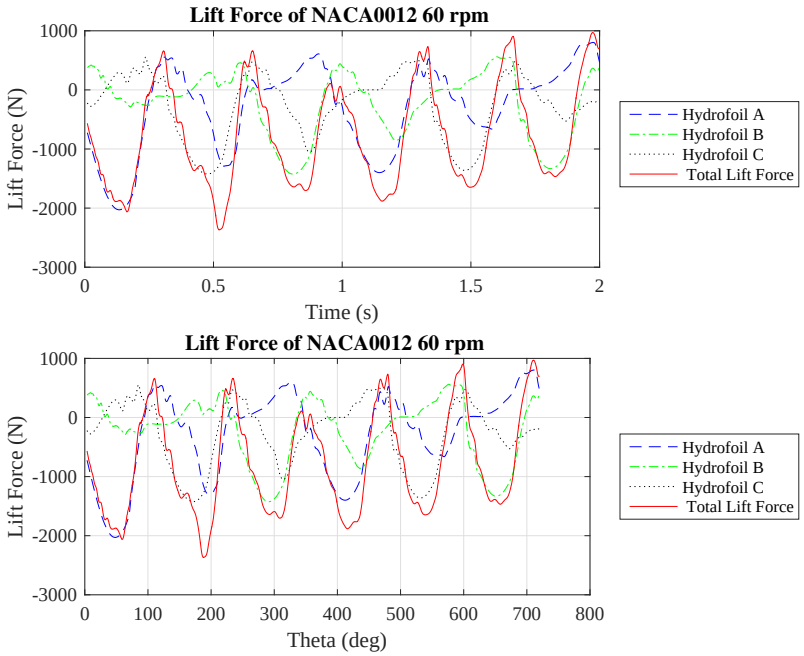

Figure A.20: Lift Force SIM03

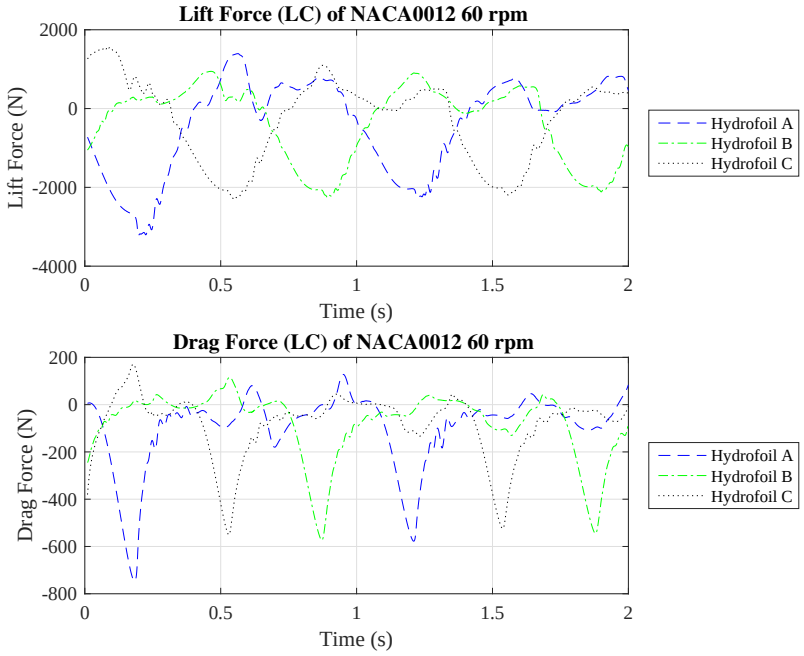

Figure A.21: Lift and Drag Force (LC) SIM03

A.1.4 SIM04

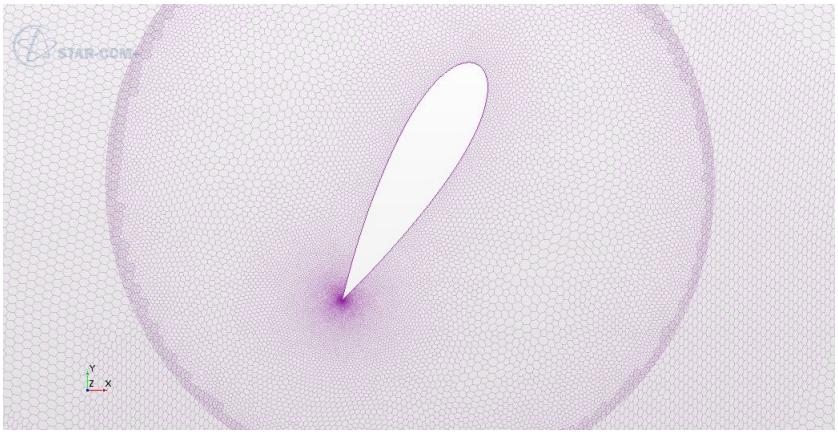

Figure A.22: Mesh SIM04

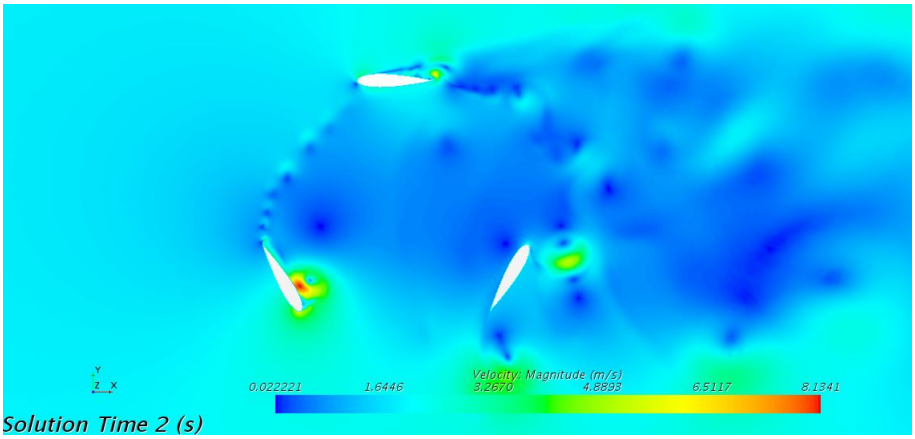

Figure A.23: Velocity SIM04

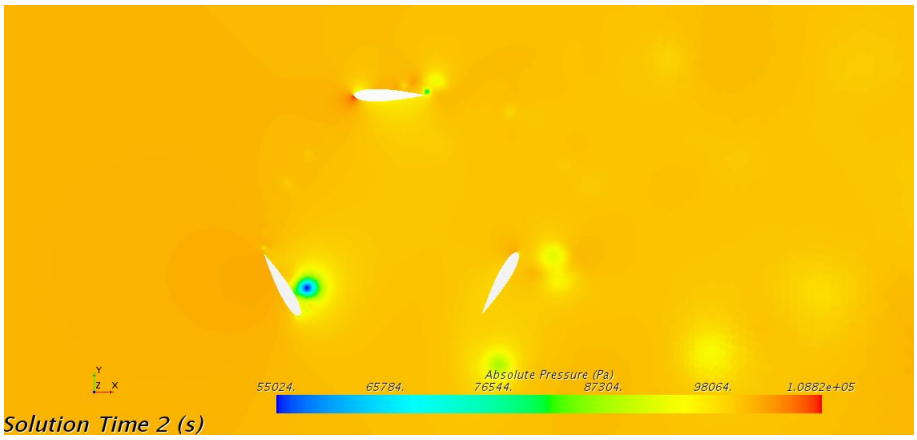

Figure A.24: Pressure SIM04

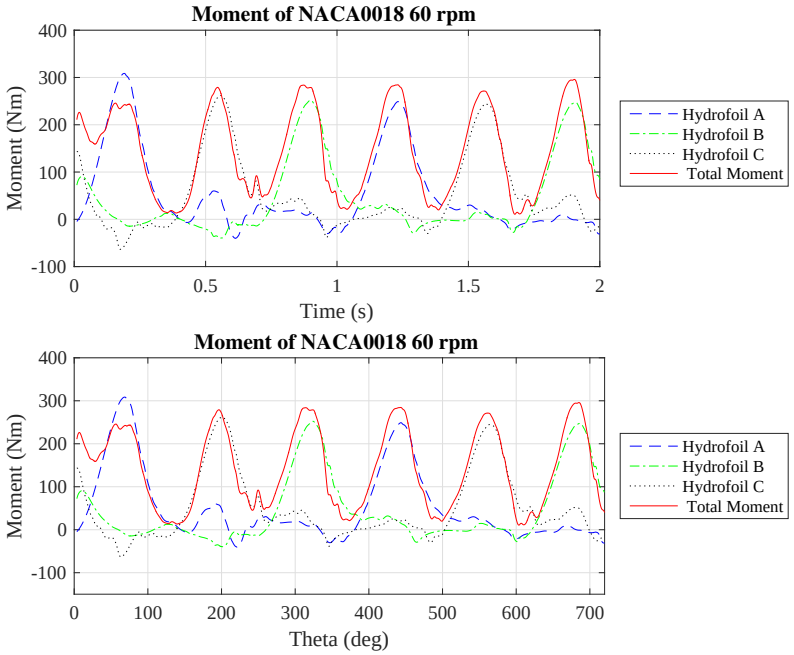

Figure A.25: Moment SIM04

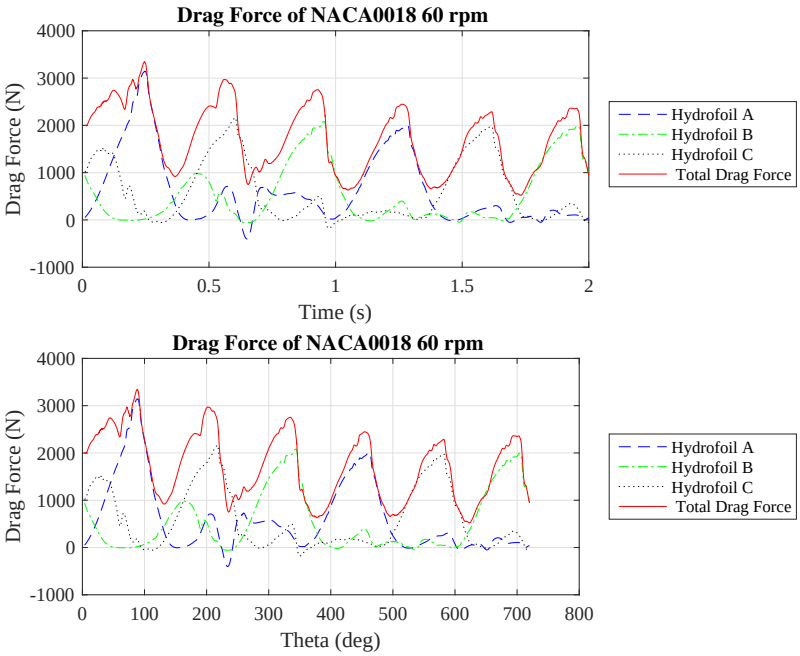

Figure A.26: Drag Force SIM04

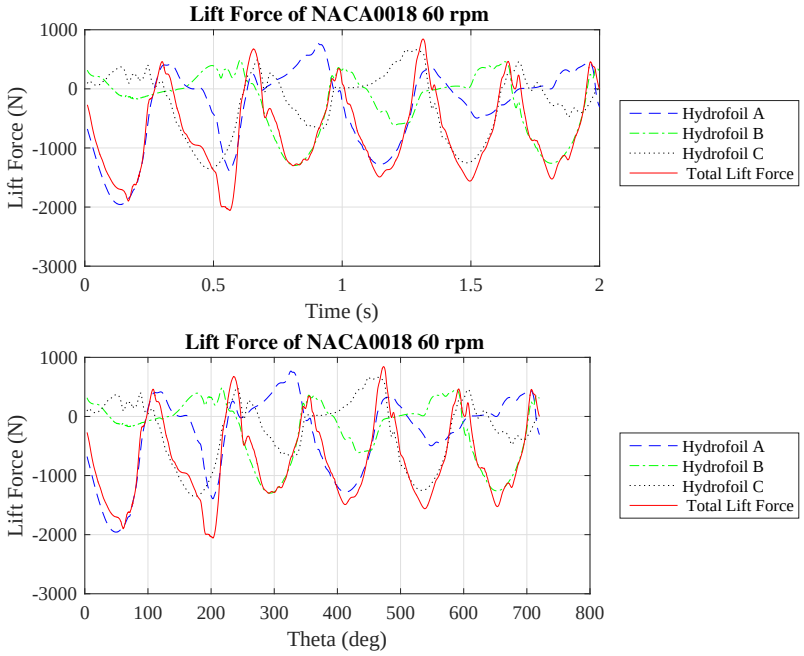

Figure A.27: Lift Force SIM04

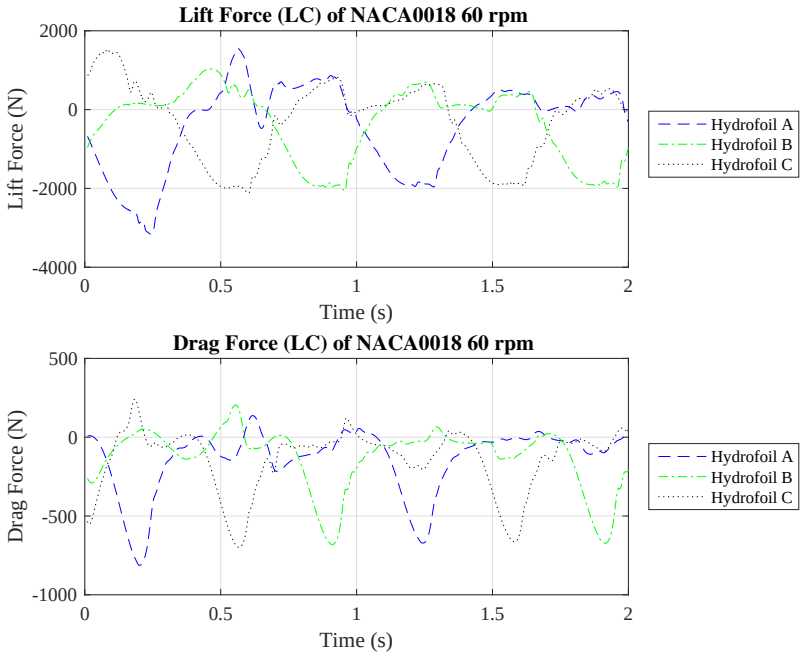

Figure A.28: Lift and Drag Force (LC) SIM04

A.1.5 SIM05

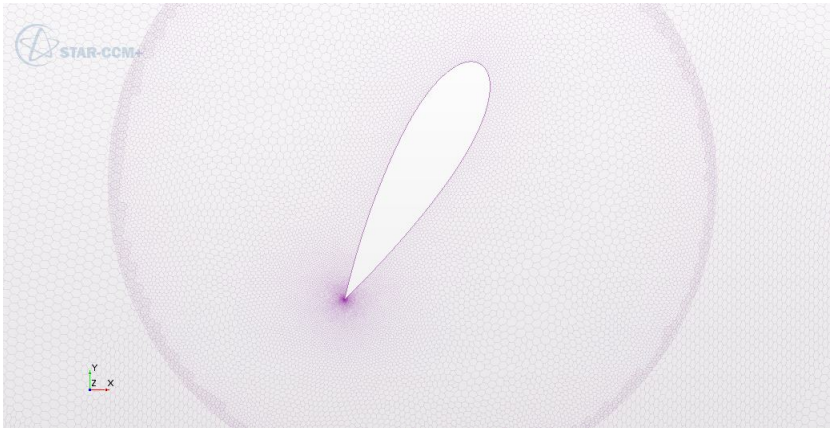

Figure A.29: Mesh SIM05

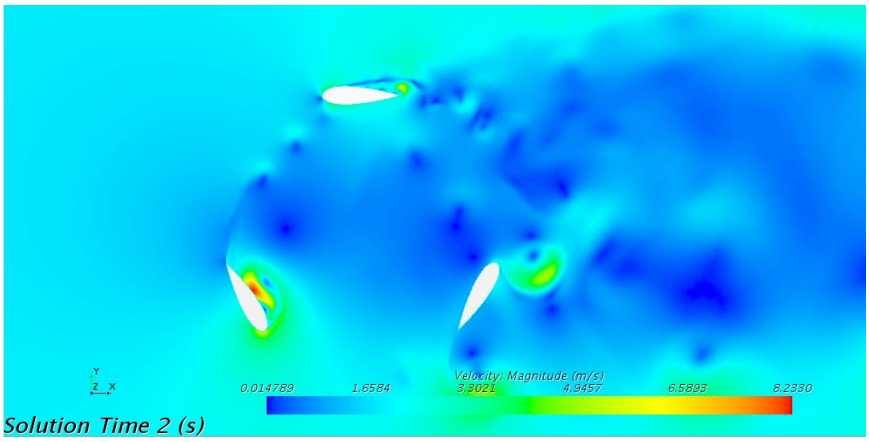

Figure A.30: Velocity SIM05

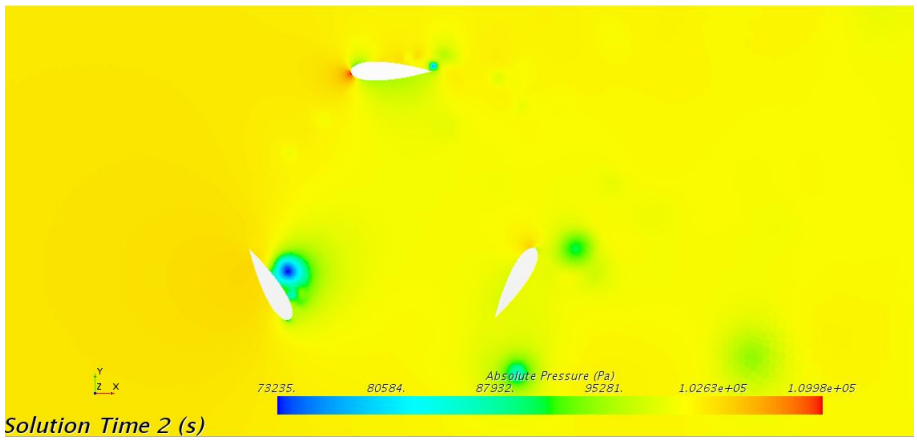

Figure A.31: Pressure SIM05

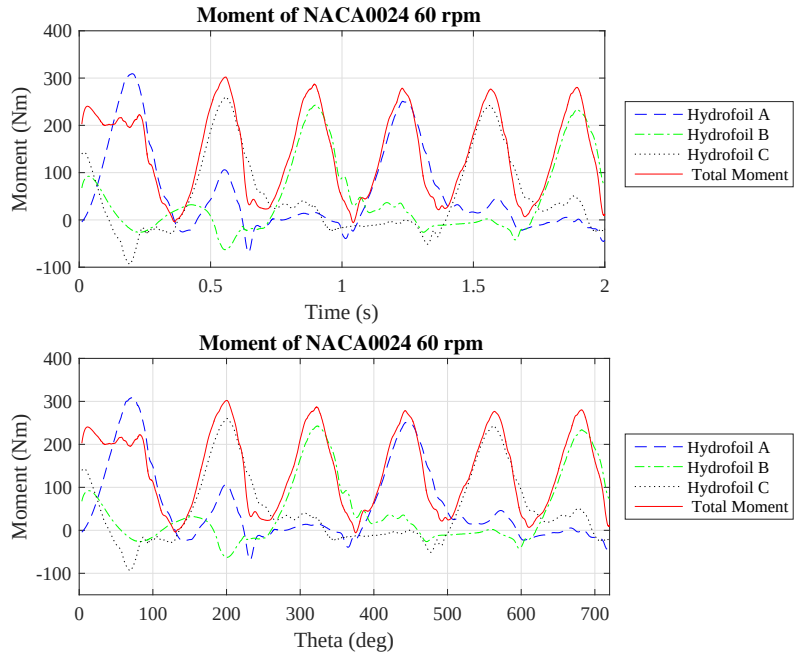

Figure A.32: Moment SIM05

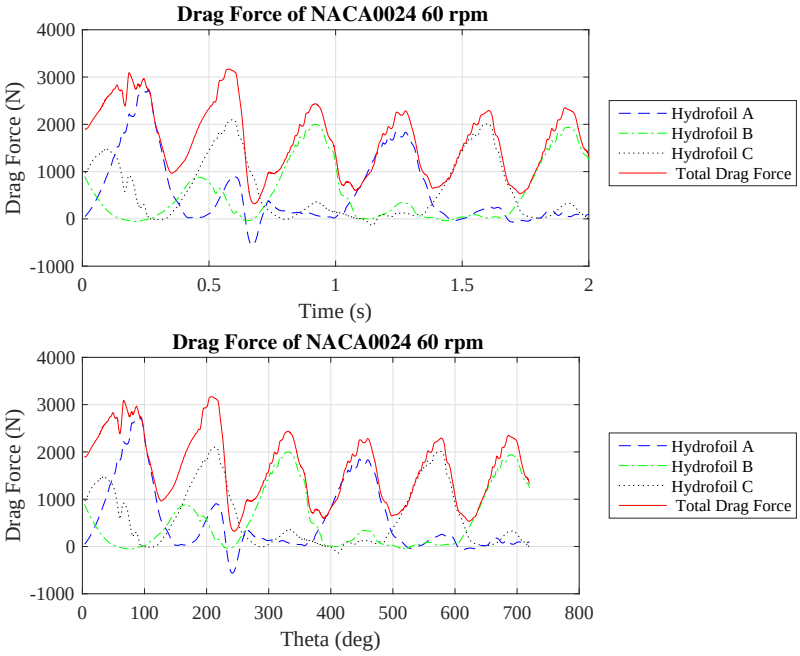

Figure A.33: Drag Force SIM05

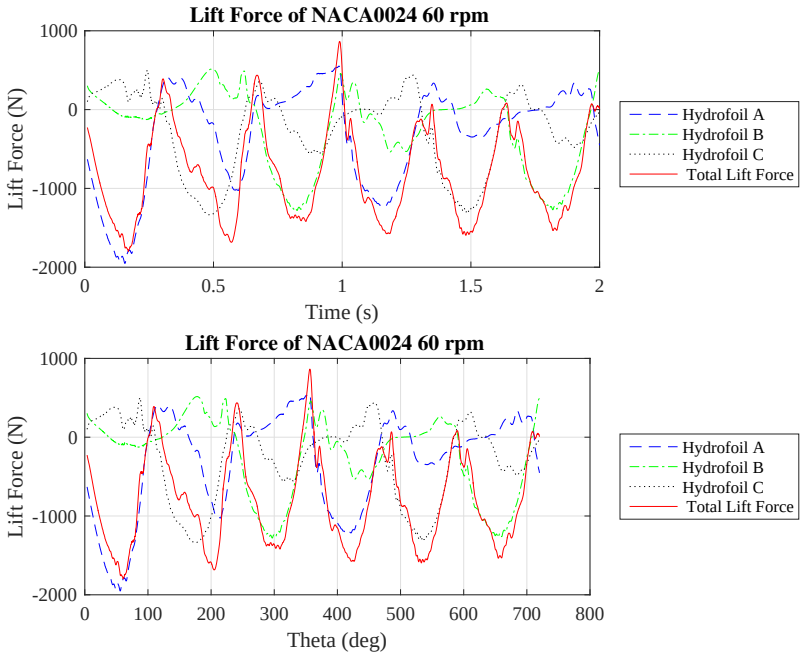

Figure A.34: Lift Force SIM05

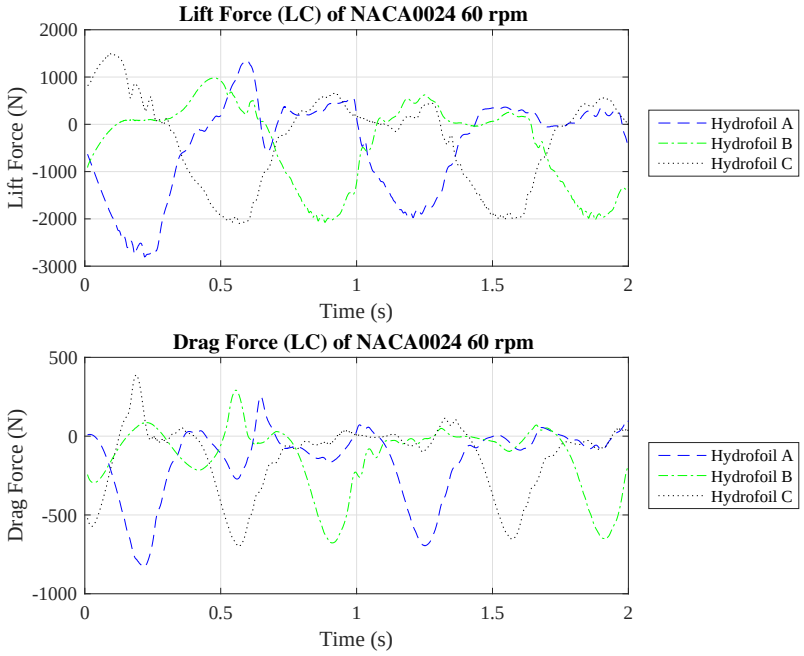

Figure A.35: Lift and Drag Force (LC) SIM05

A.1.6 SIM06

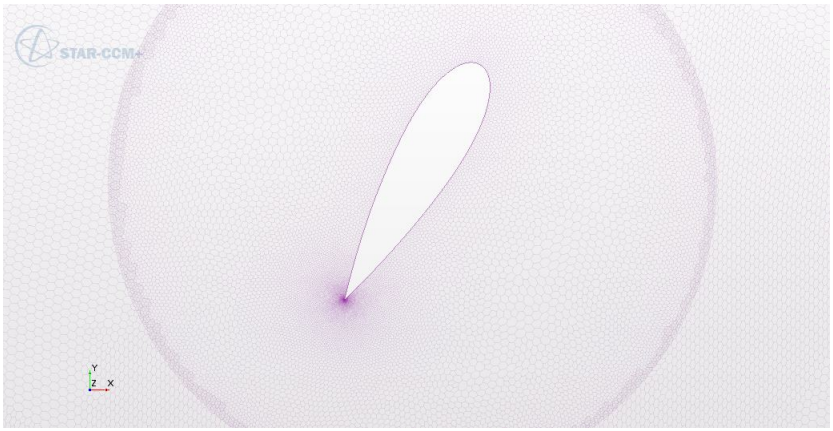

Figure A.36: Mesh SIM06

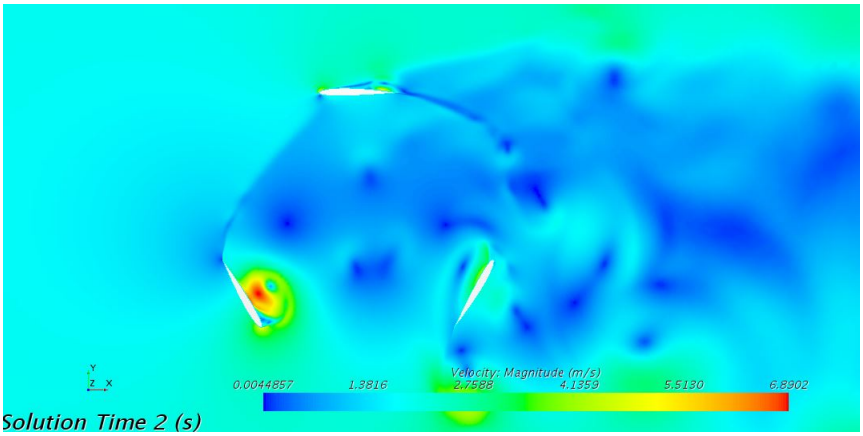

Figure A.37: Velocity SIM06

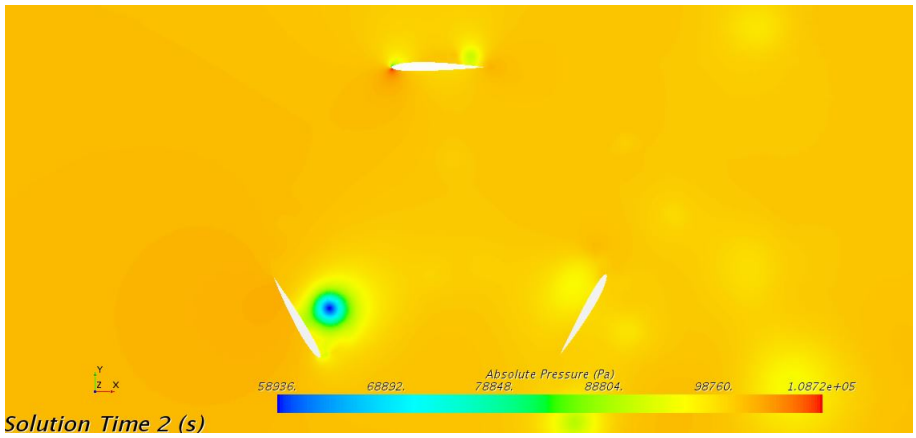

Figure A.38: Pressure SIM06

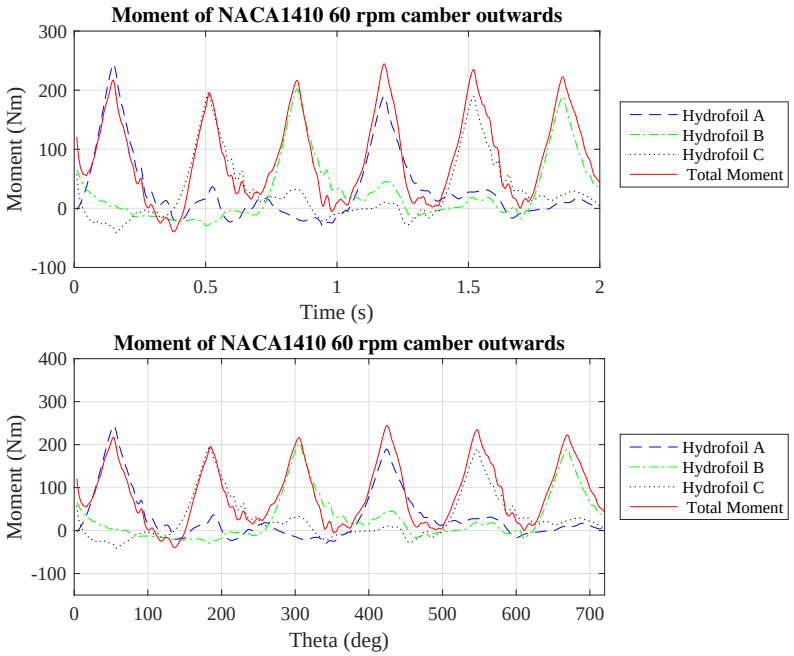

Figure A.39: Moment SIM06

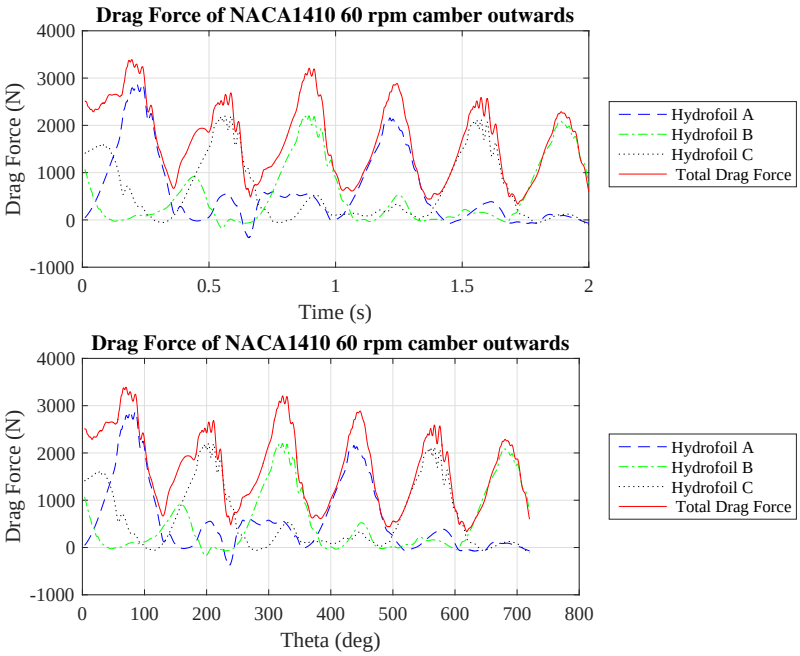

Figure A.40: Drag Force SIM06

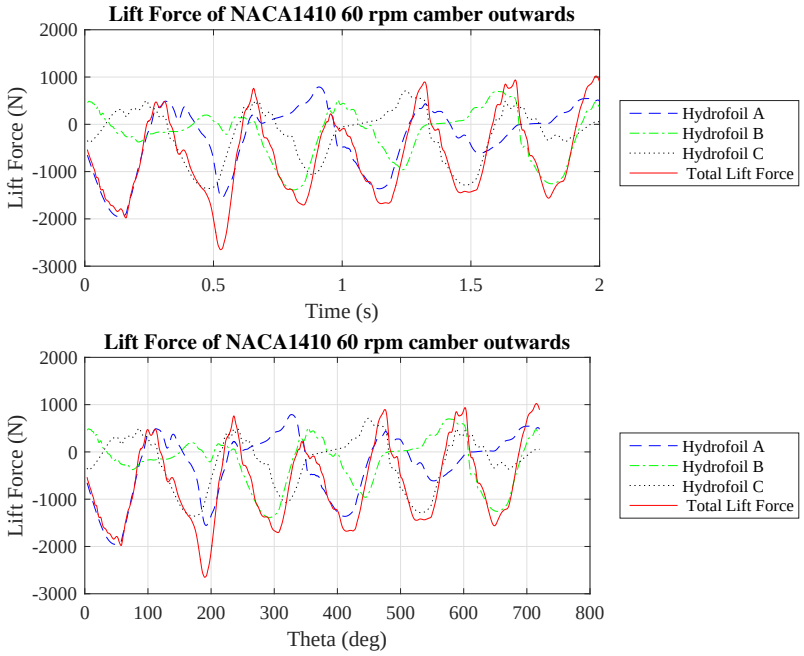

Figure A.41: Lift Force SIM06

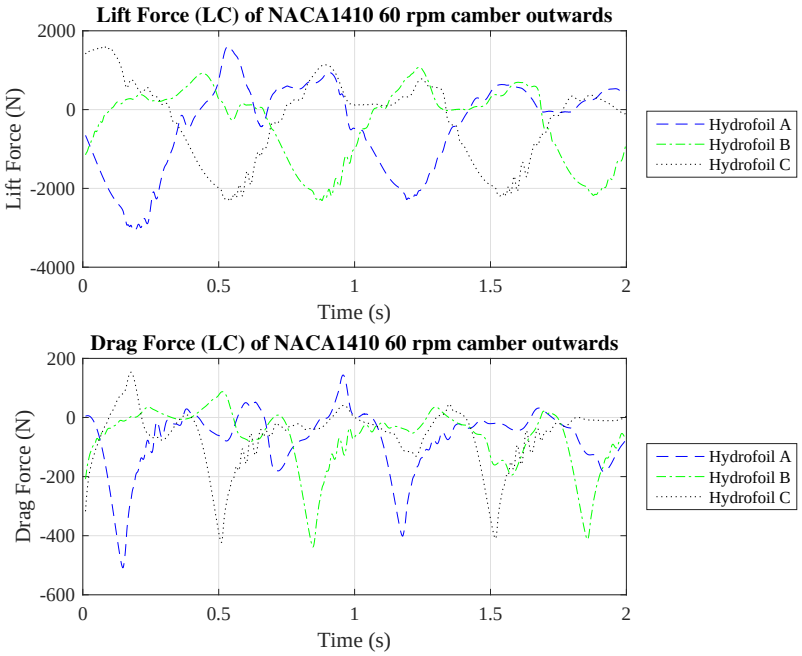

Figure A.42: Lift and Drag Force (LC) SIM06

A.1.7 SIM07

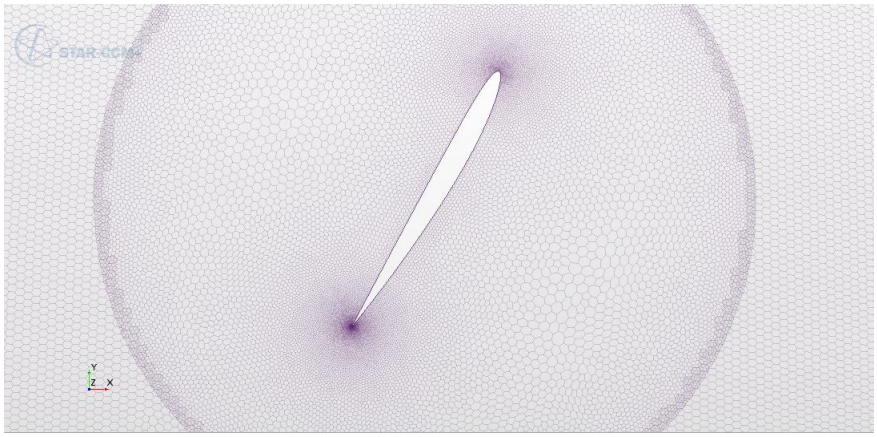

Figure A.43: Mesh SIM07

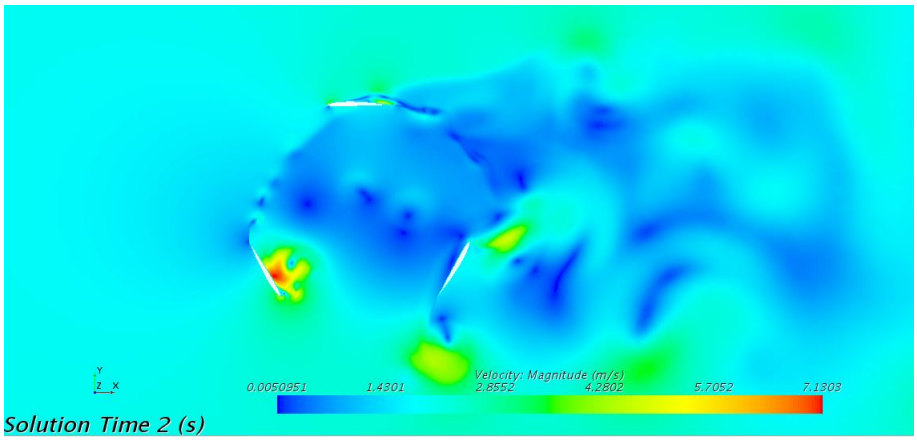

Figure A.44: Velocity SIM07

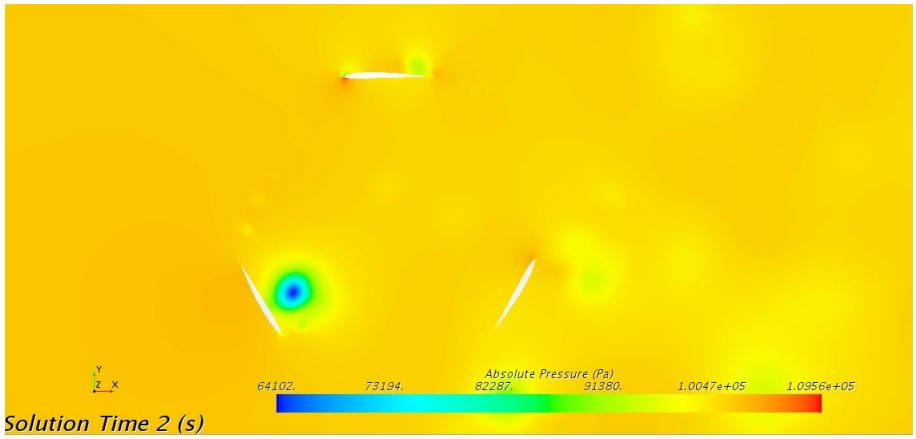

Figure A.45: Pressure SIM07

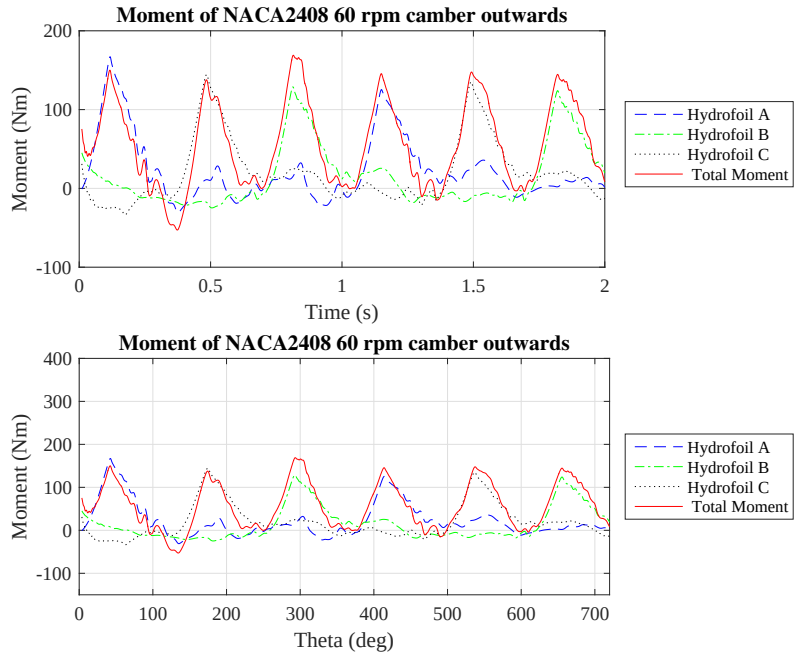

Figure A.46: Moment SIM07

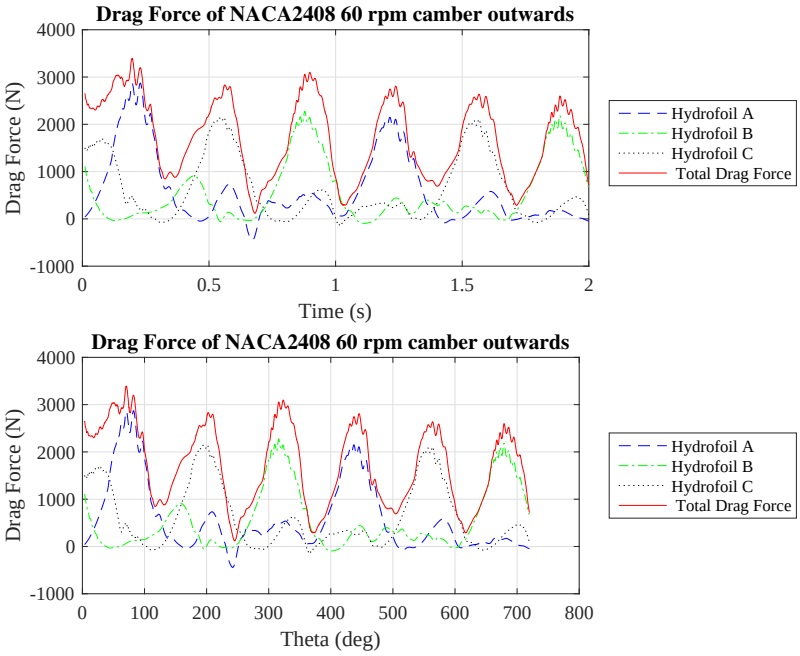

Figure A.47: Drag Force SIM07

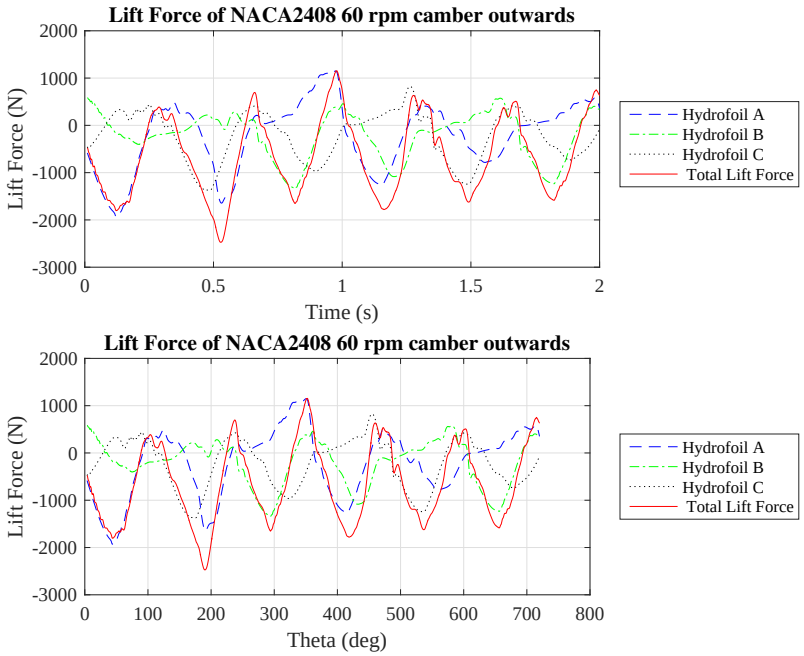

Figure A.48: Lift Force SIM07

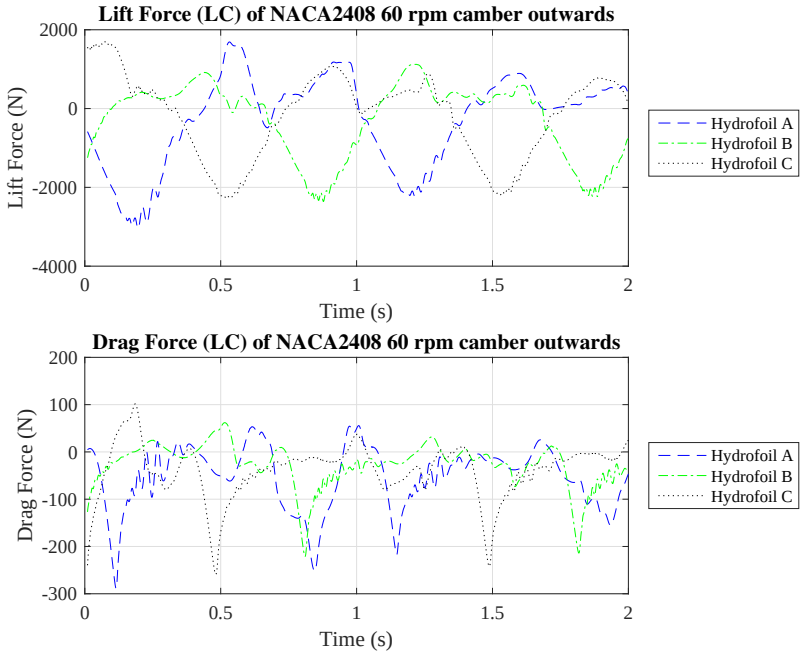

Figure A.49: Lift and Drag Force (LC) SIM07

A.1.8 SIM08

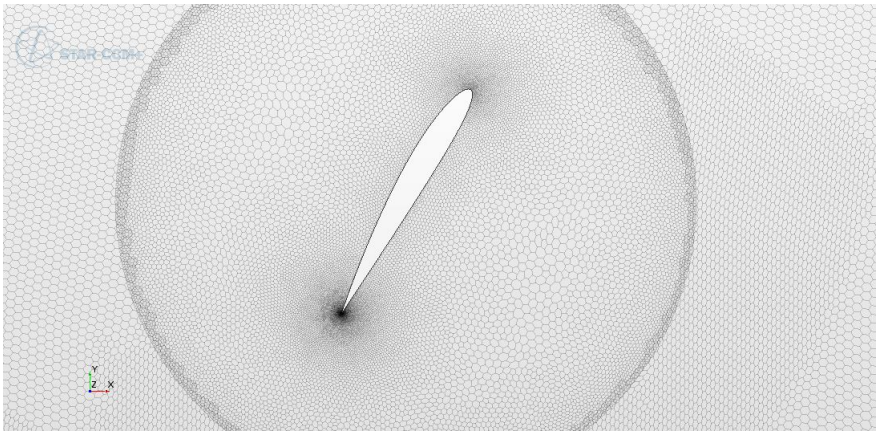

Figure A.50: Mesh SIM08

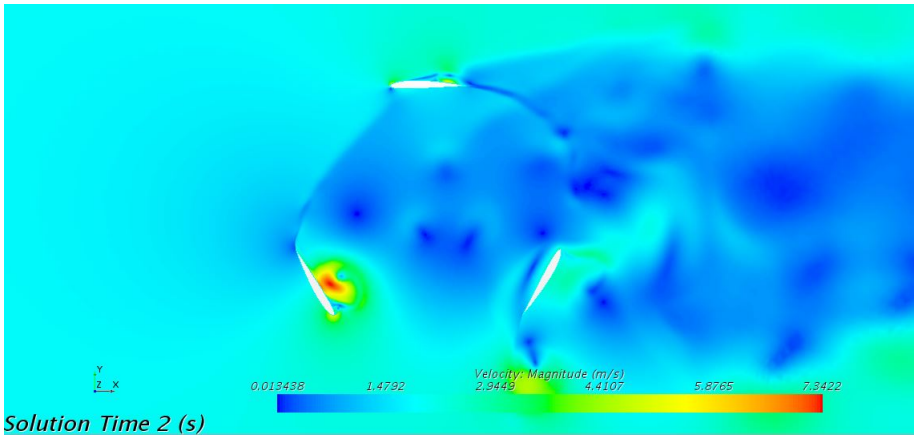

Figure A.51: Velocity SIM08

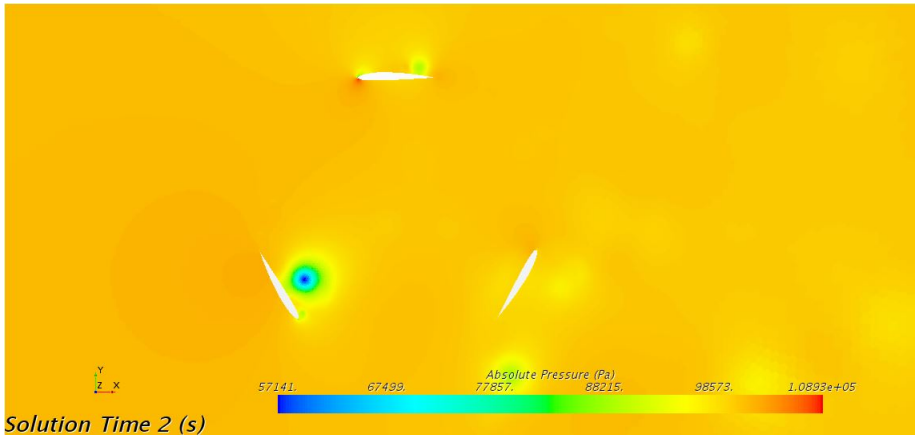

Figure A.52: Pressure SIM08

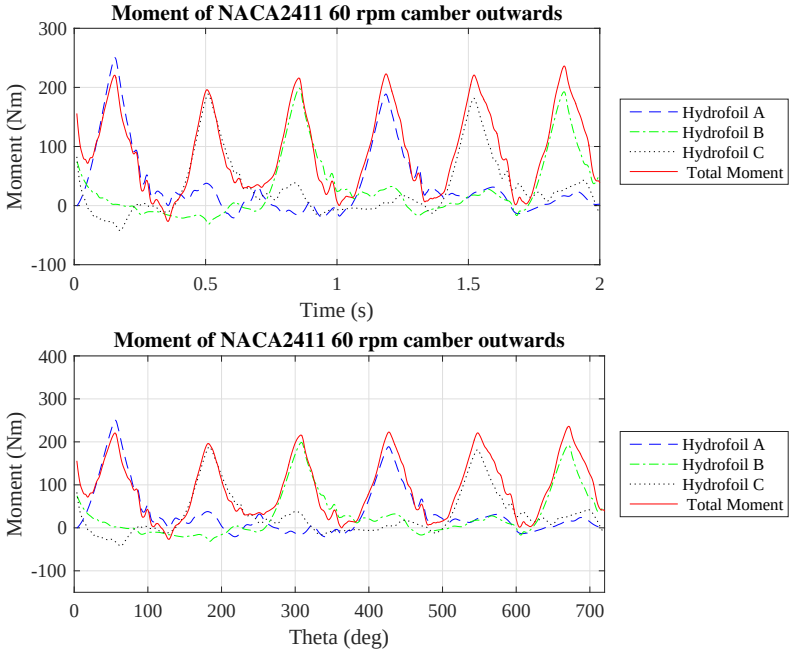

Figure A.53: Moment SIM08

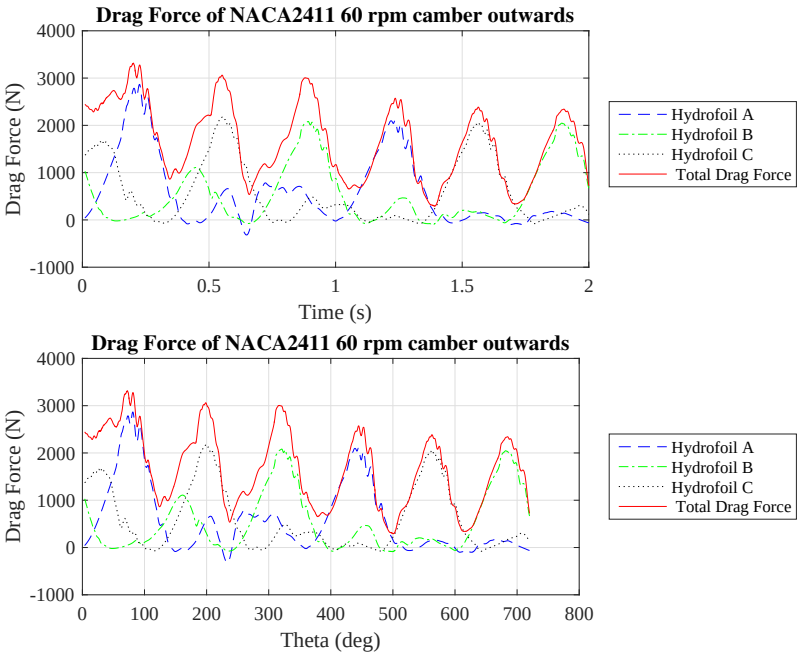

Figure A.54: Drag Force SIM08

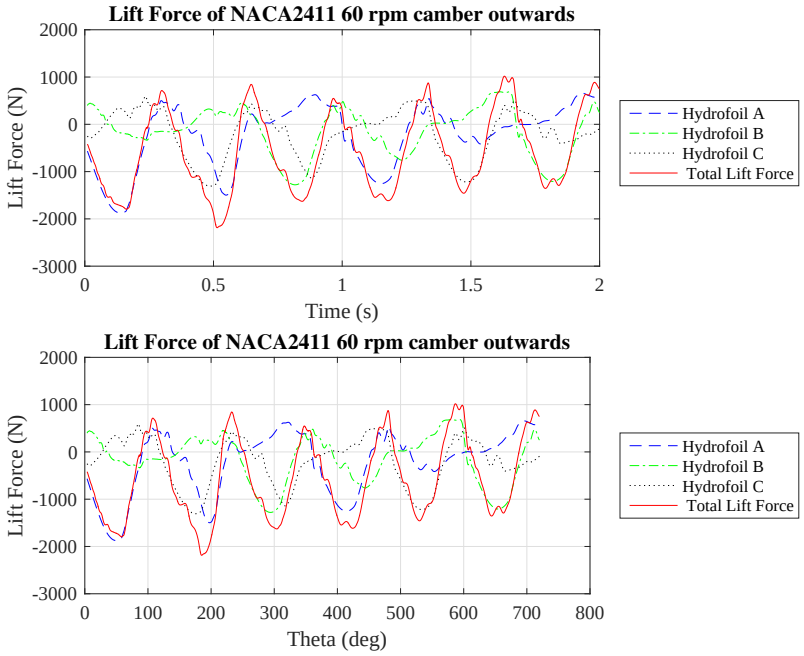

Figure A.55: Lift Force SIM08

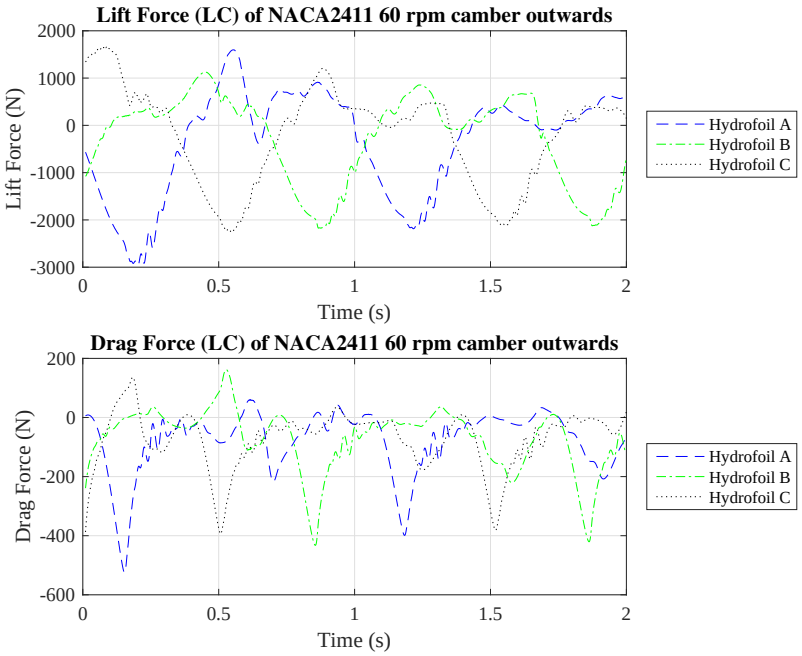

Figure A.56: Lift and Drag Force (LC) SIM08

A.1.9 SIM09

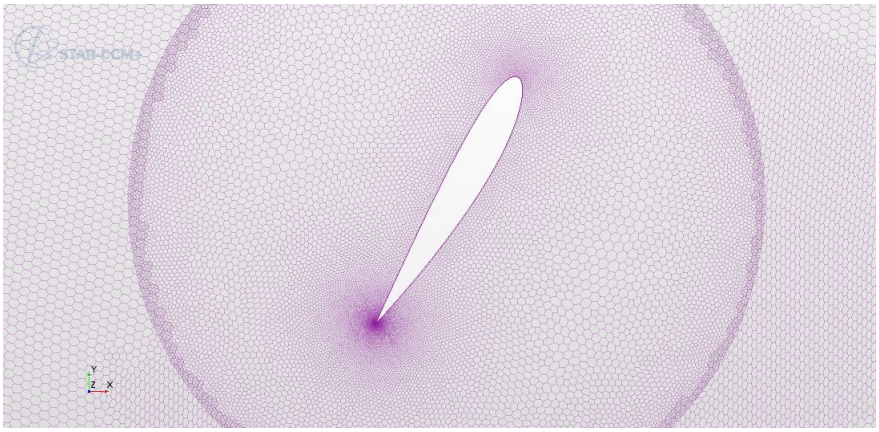

Figure A.57: Mesh SIM09

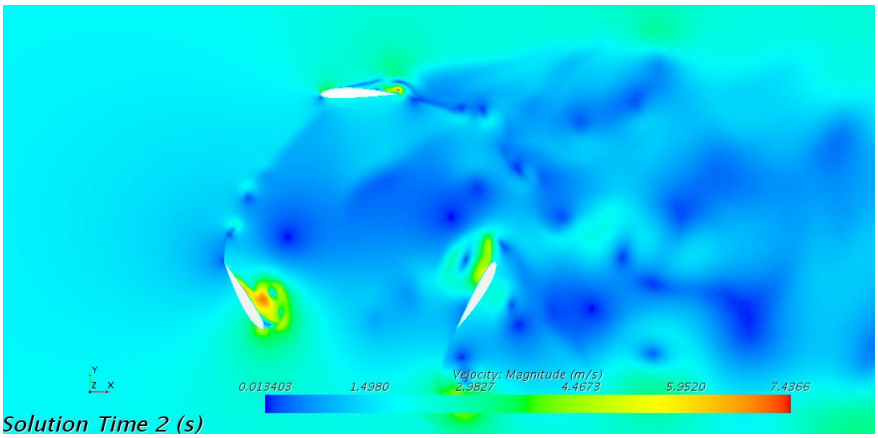

Figure A.58: Velocity SIM09

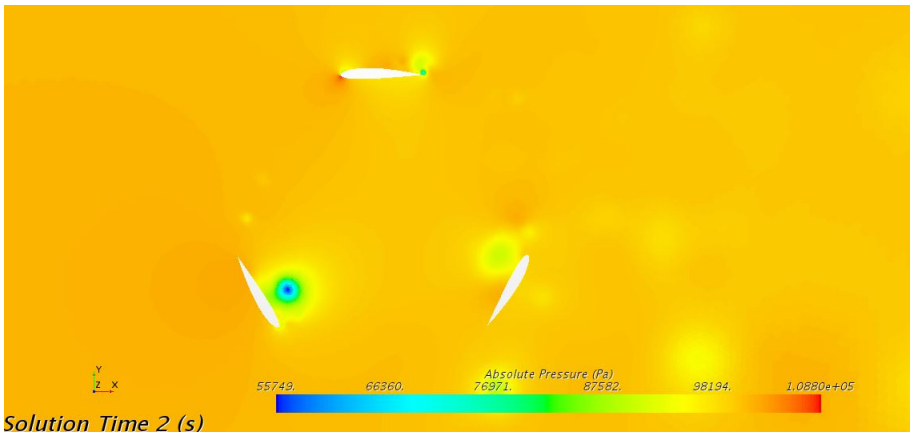

Figure A.59: Pressure SIM09

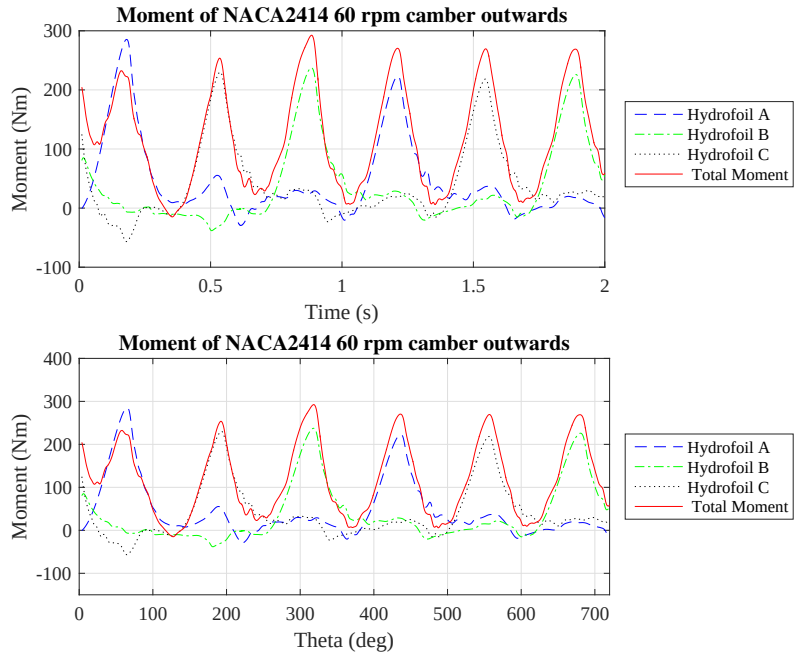

Figure A.60: Moment SIM09

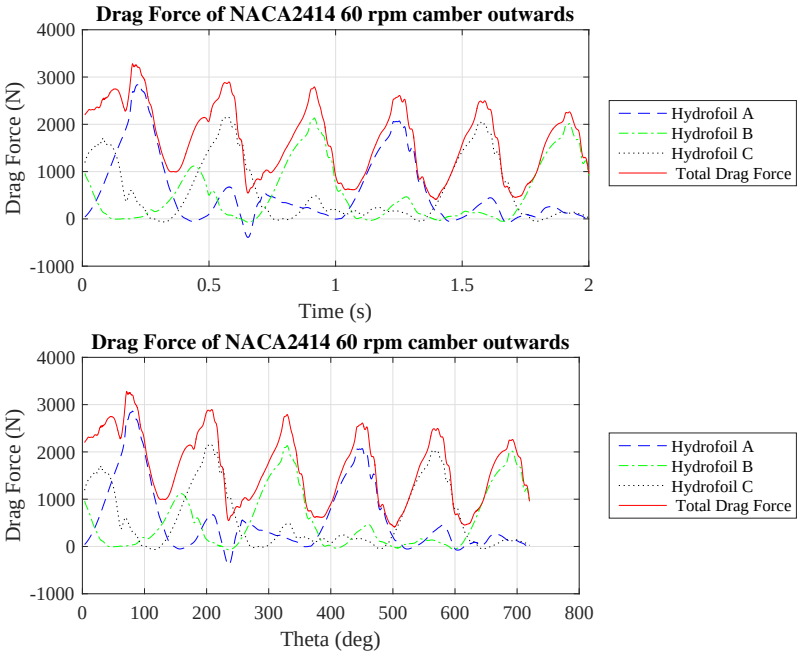

Figure A.61: Drag Force SIM09

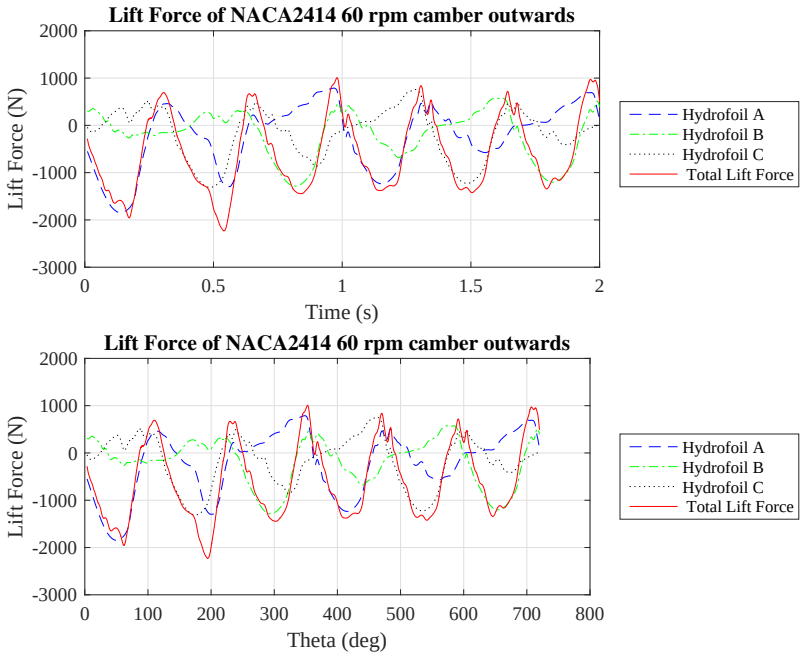

Figure A.62: Lift Force SIM09

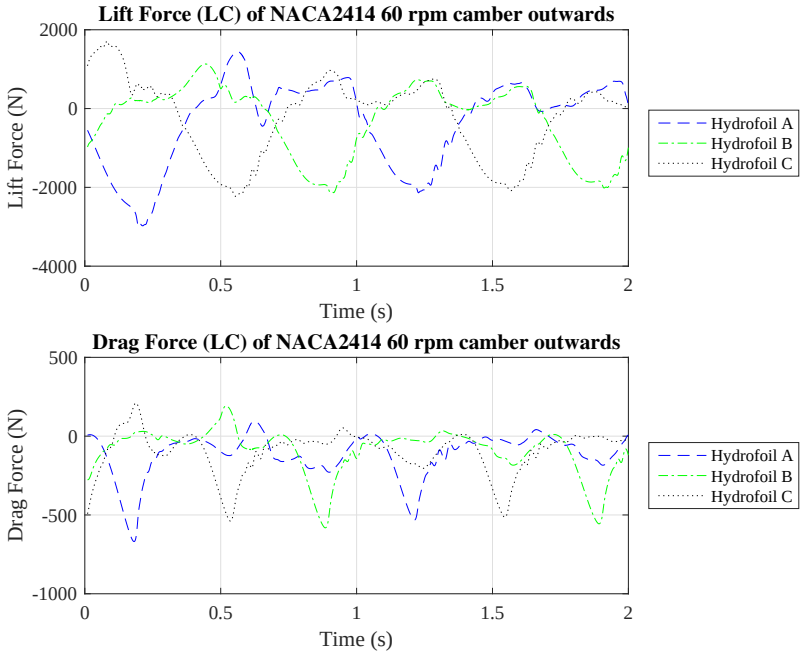

Figure A.63: Lift and Drag Force (LC) SIM09

A.1.10 SIM10

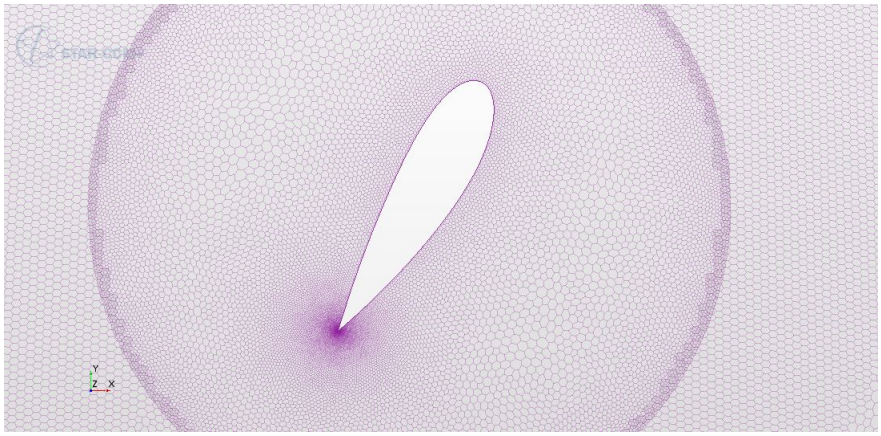

Figure A.64: Mesh SIM10

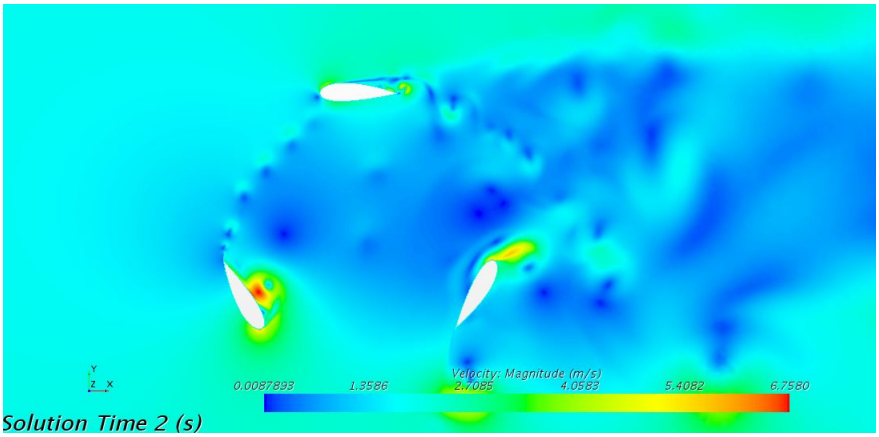

Figure A.65: Velocity SIM10

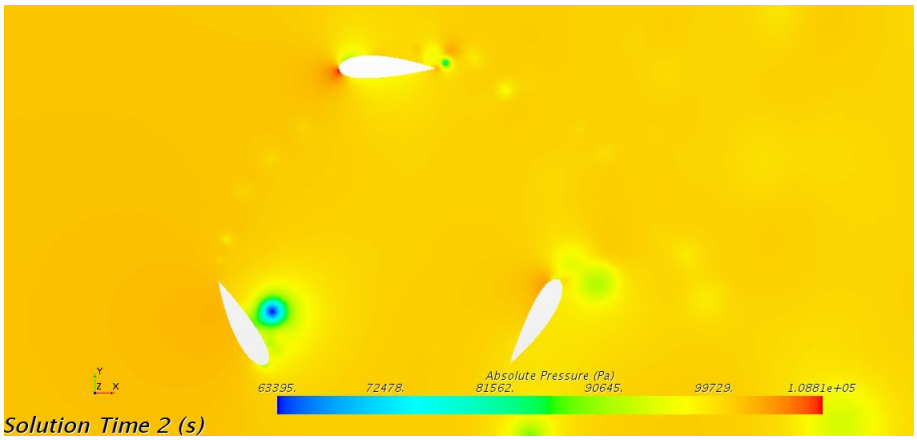

Figure A.66: Pressure SIM10

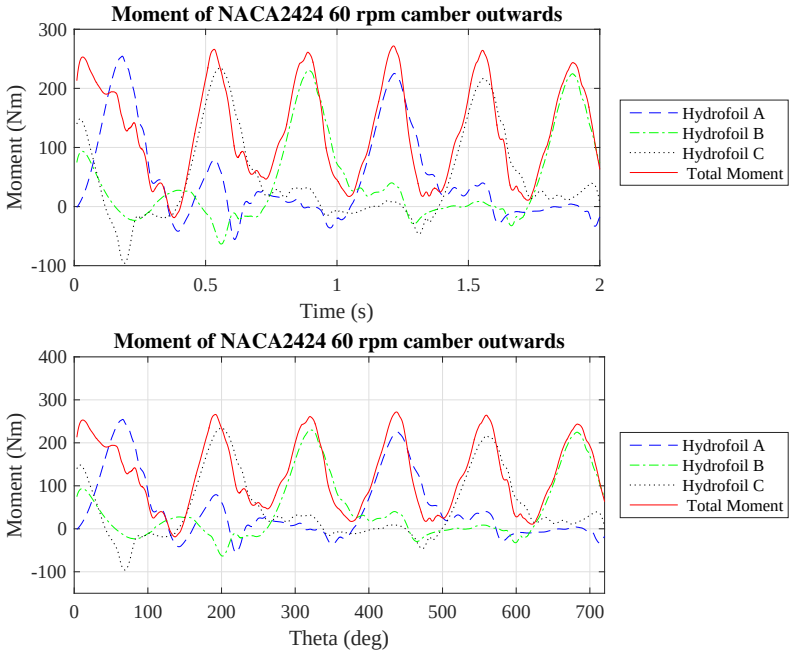

Figure A.67: Moment SIM10

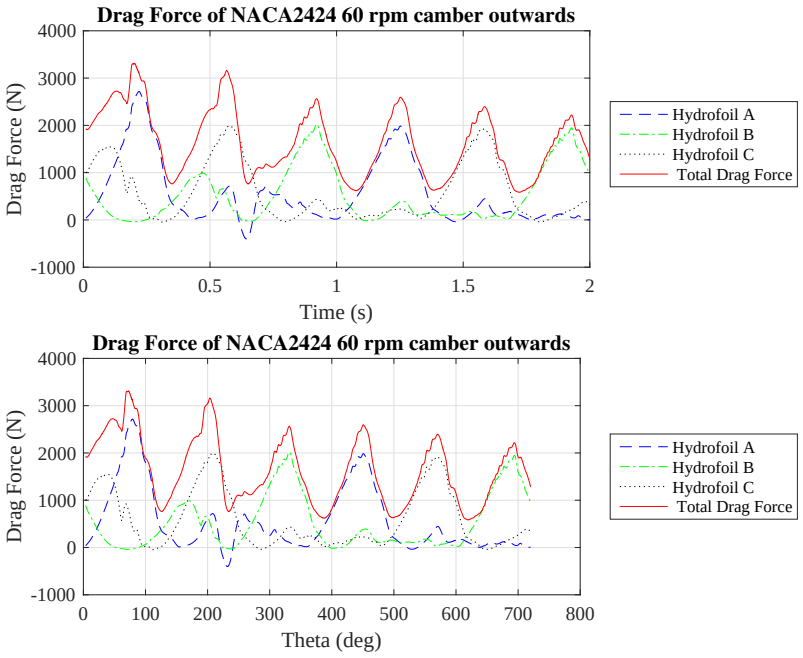

Figure A.68: Drag Force SIM10

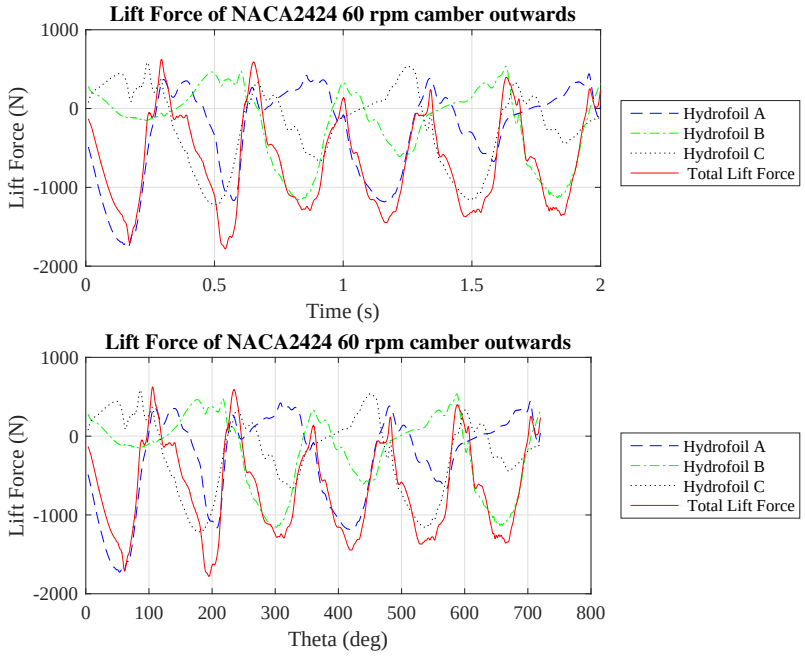

Figure A.69: Lift Force SIM10

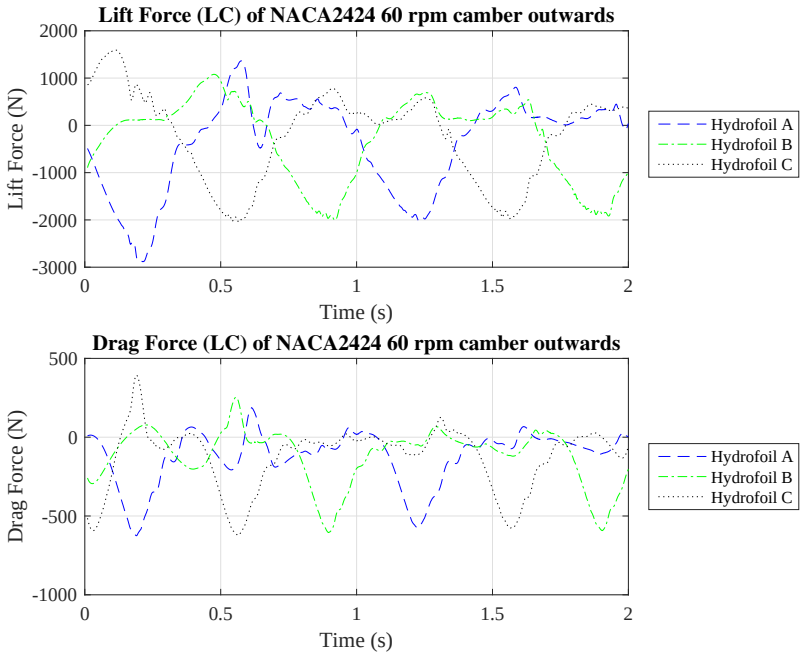

Figure A.70: Lift and Drag Force (LC) SIM10

A.1.11 SIM11

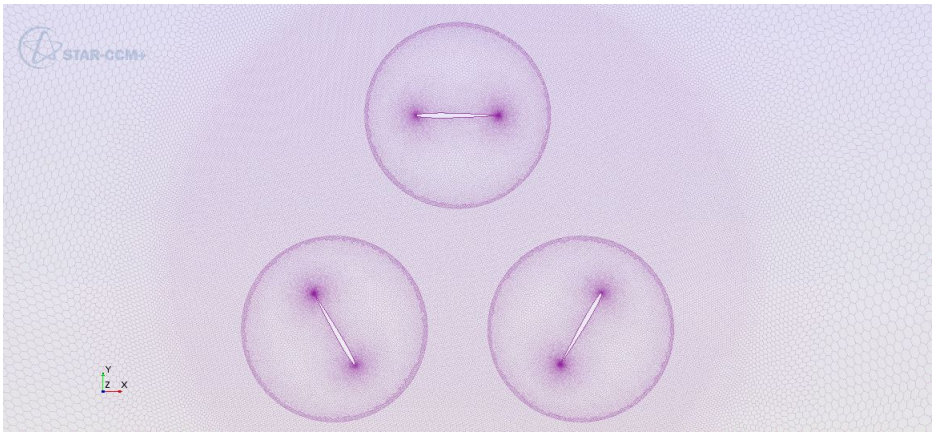

Figure A.71: Mesh SIM11

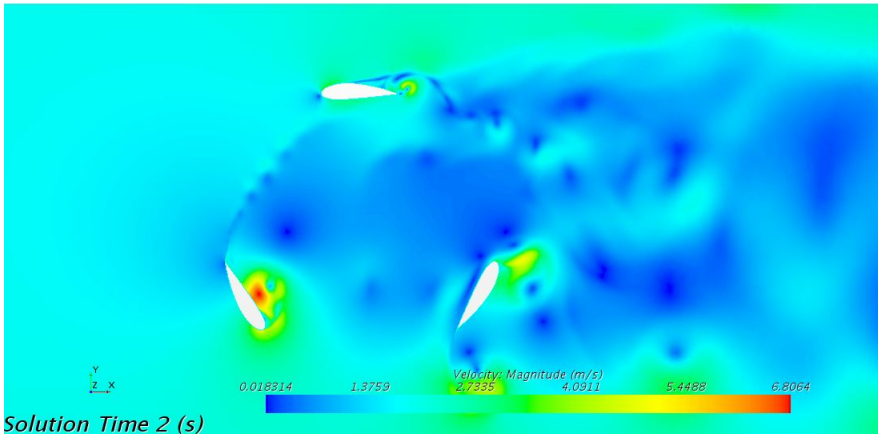

Figure A.72: Velocity SIM11

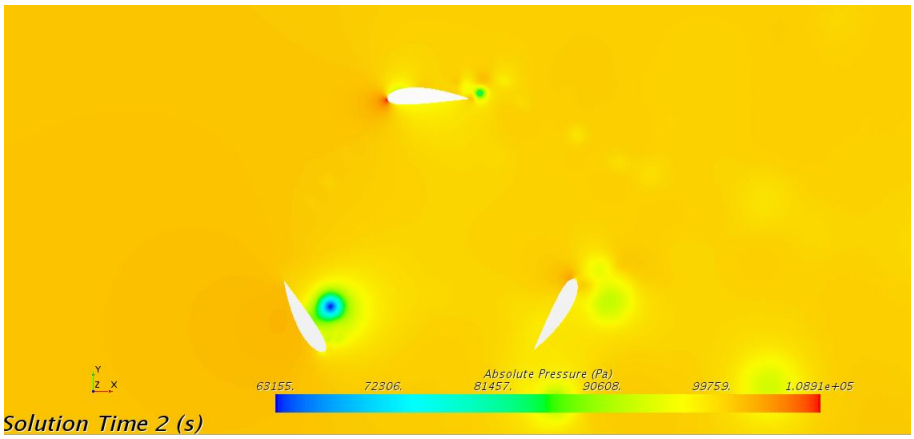

Figure A.73: Pressure SIM11

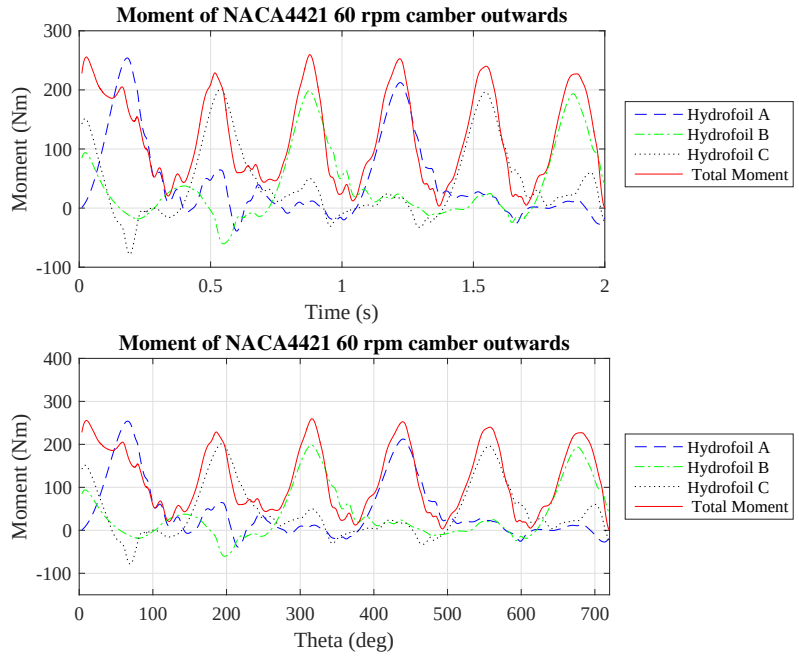

Figure A.74: Moment SIM11

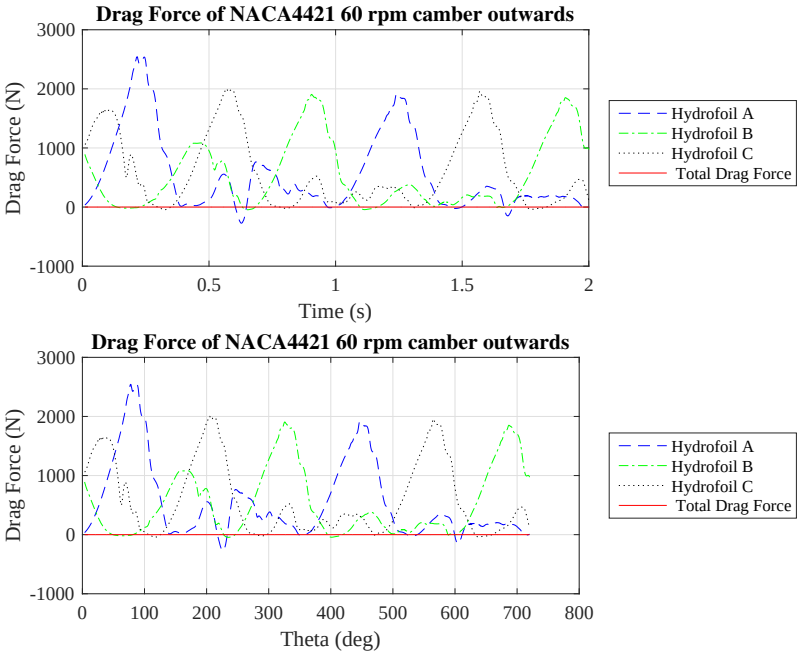

Figure A.75: Drag Force SIM11

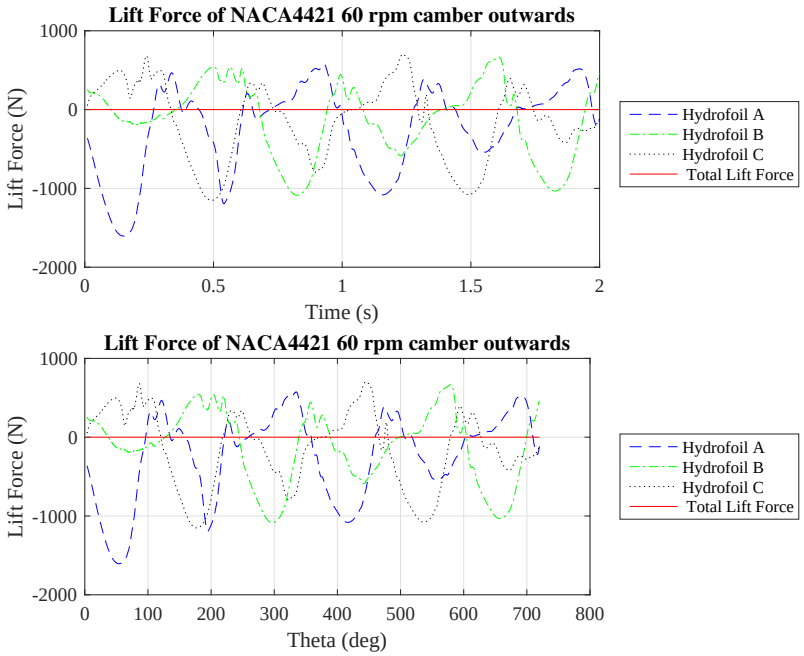

Figure A.76: Lift Force SIM11

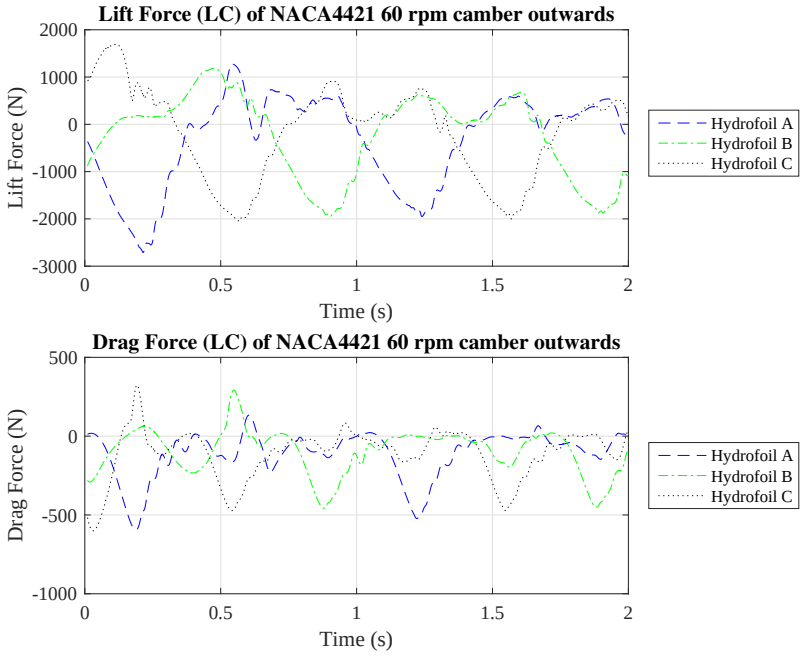

Figure A.77: Lift and Drag Force (LC) SIM11

A.1.12 SIM12

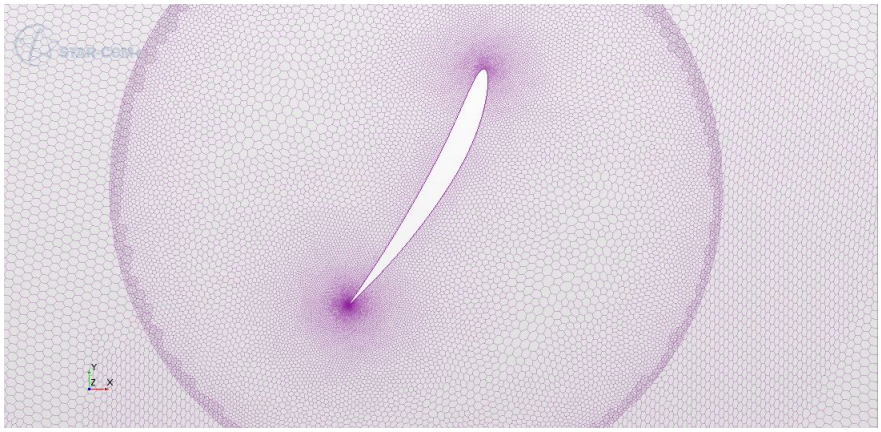

Figure A.78: Mesh SIM12

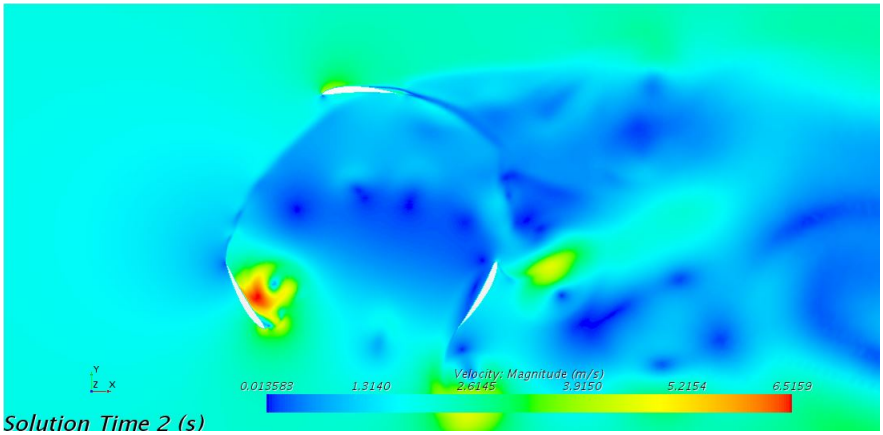

Figure A.79: Velocity SIM12

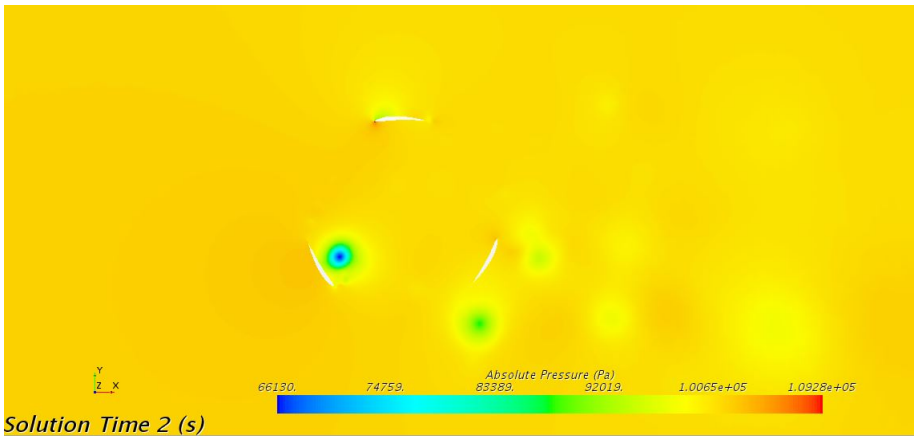

Figure A.80: Pressure SIM12

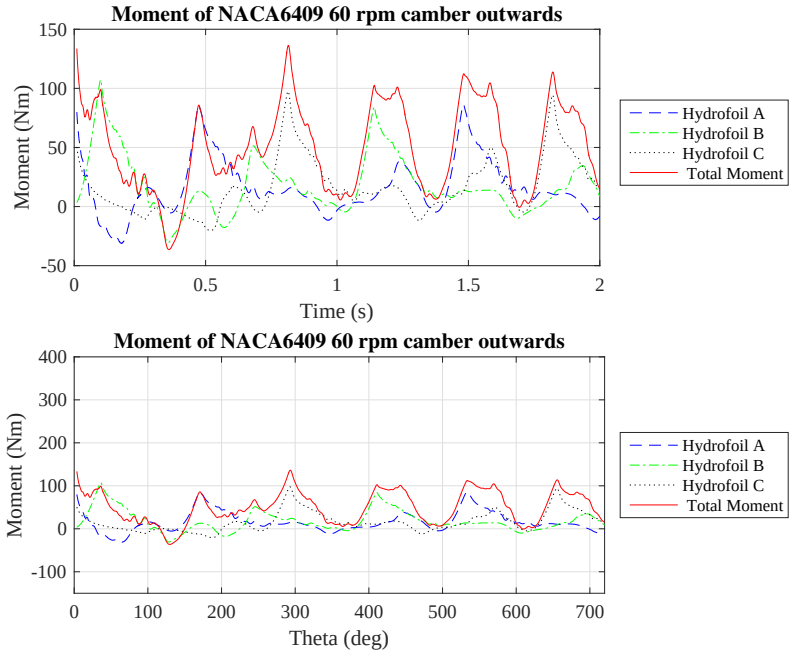

Figure A.81: Moment SIM12

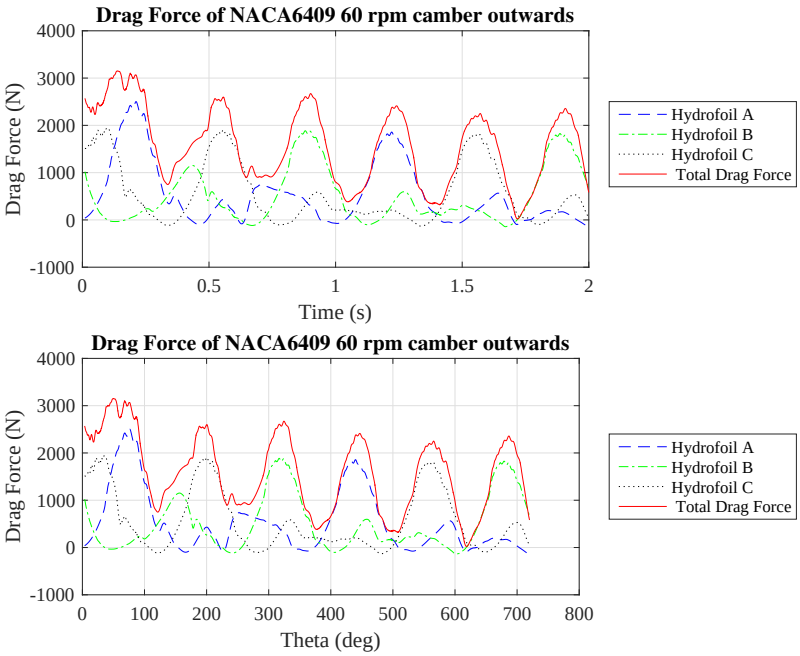

Figure A.82: Drag Force SIM12

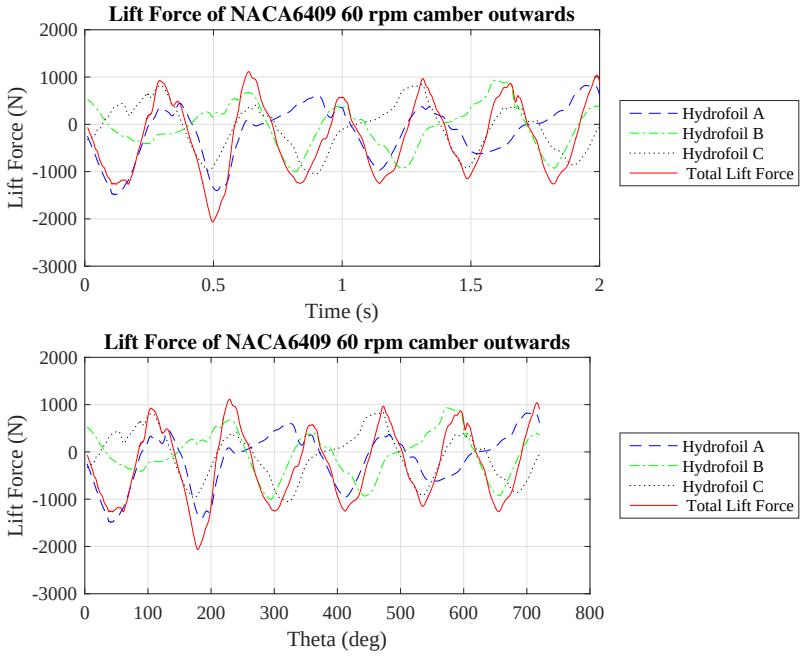

Figure A.83: Lift Force SIM12

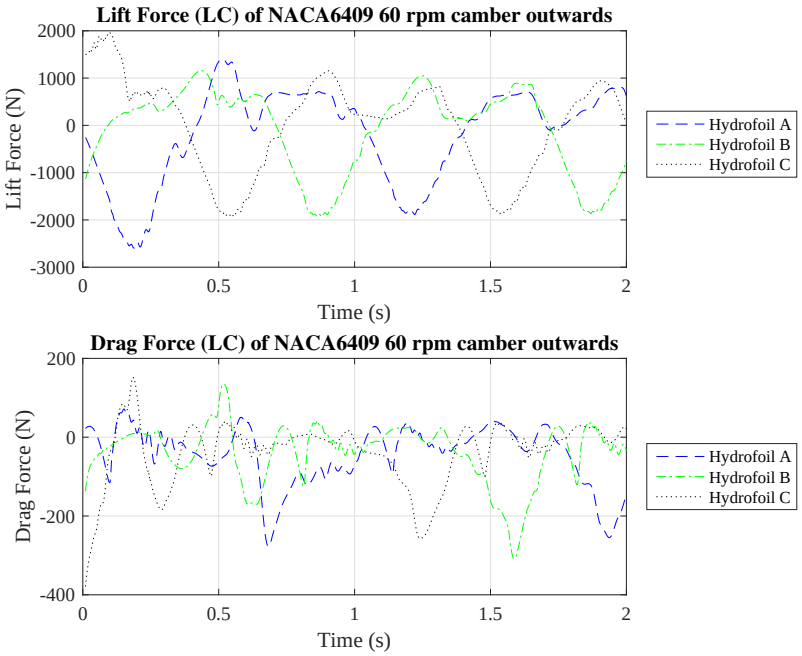

Figure A.84: Lift and Drag Force (LC) SIM12

A.1.13 SIM13

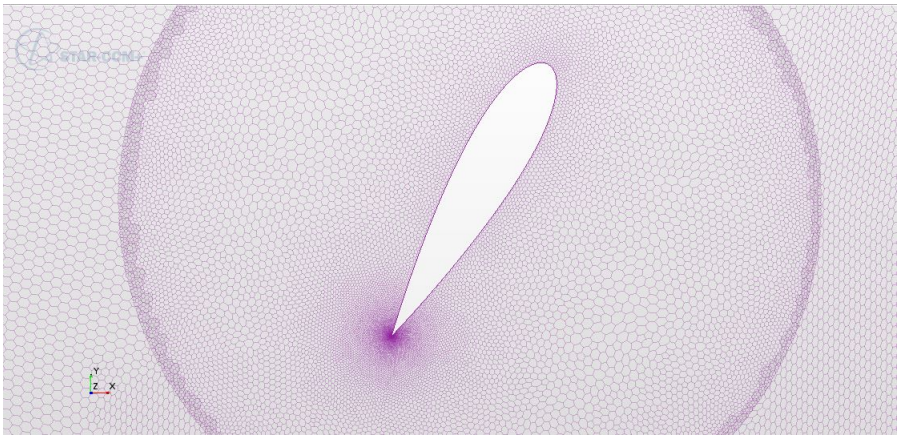

Figure A.85: Mesh SIM13

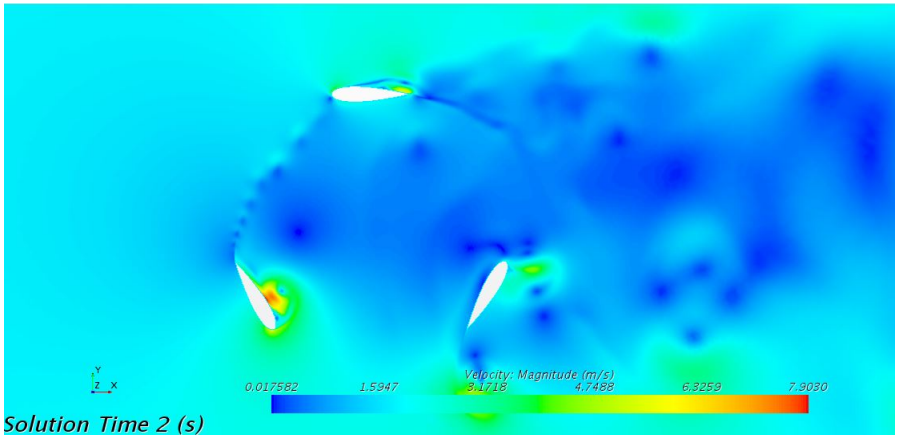

Figure A.86: Velocity SIM13

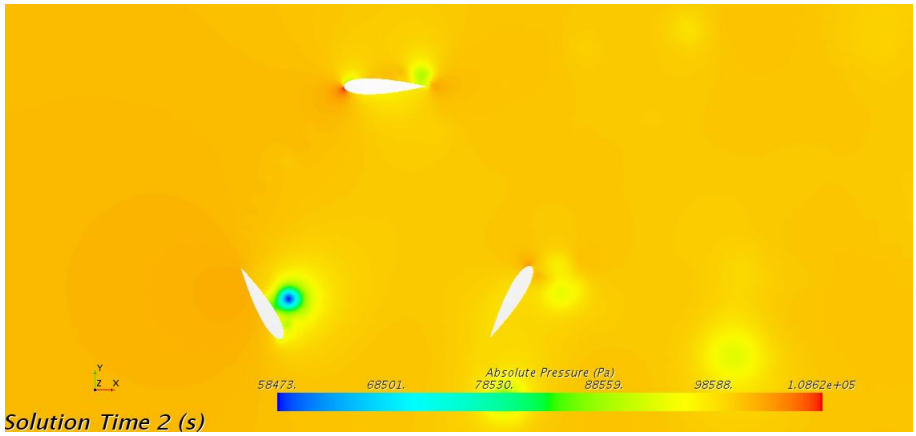

Figure A.87: Pressure SIM13

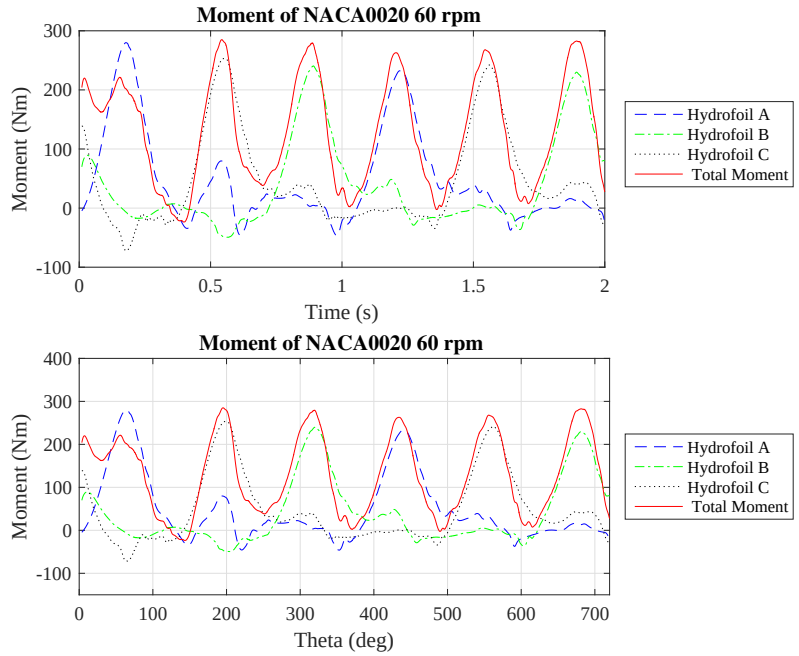

Figure A.88: Moment SIM13

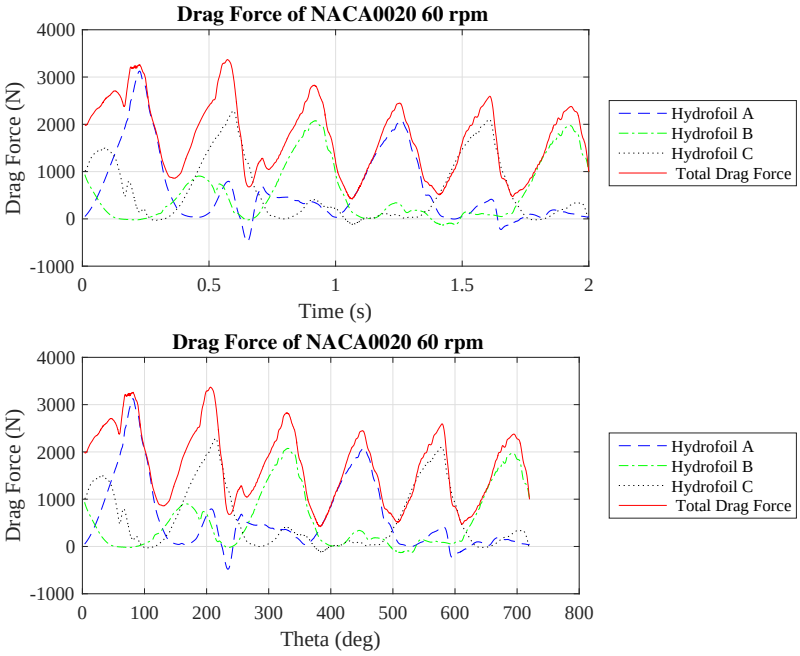

Figure A.89: Drag Force SIM13

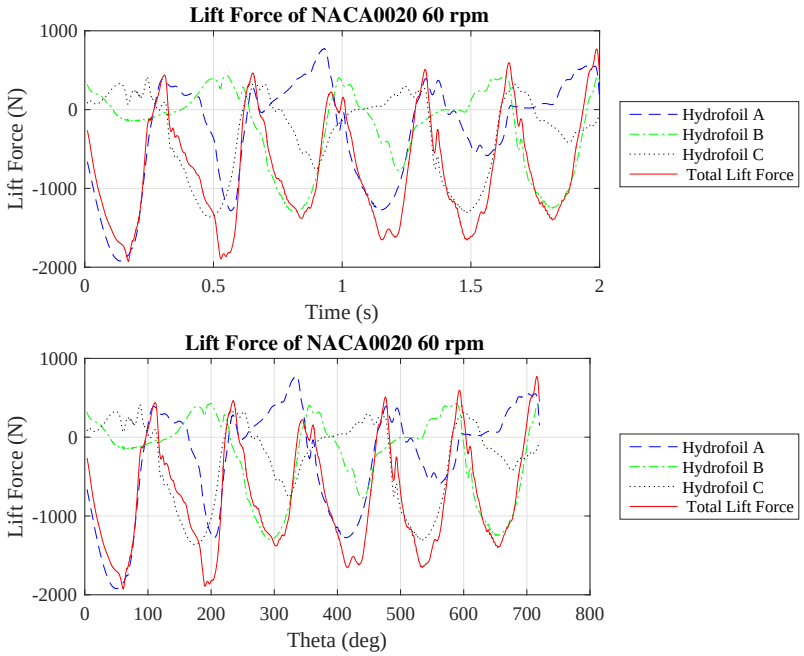

Figure A.90: Lift Force SIM13

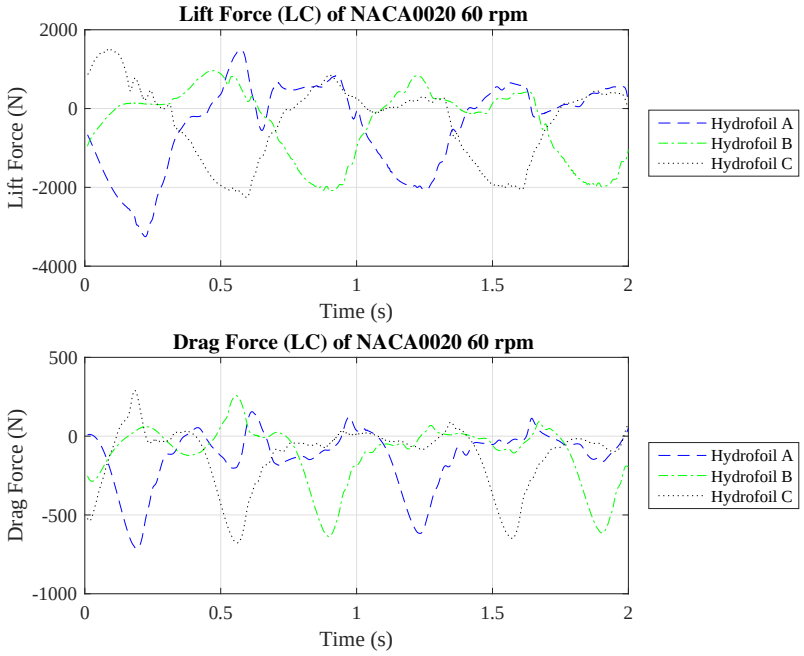

Figure A.91: Lift and Drag Force (LC) SIM13

A.1.14 SIM14

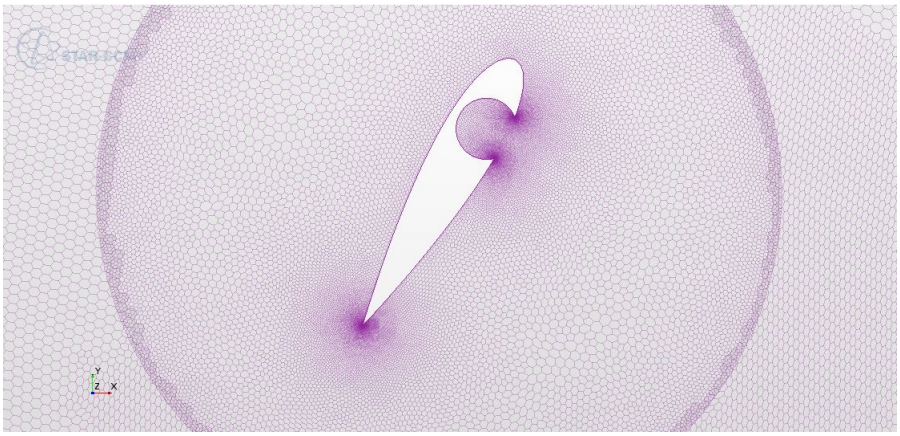

Figure A.92: Mesh SIM14

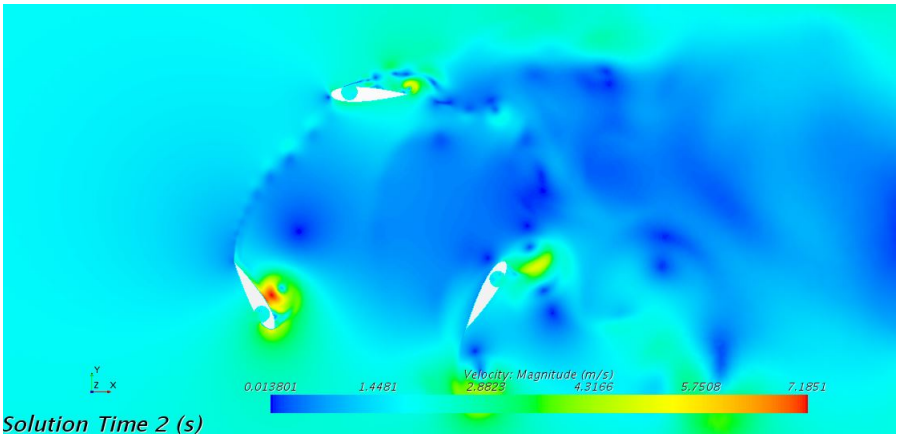

Figure A.93: Velocity SIM14

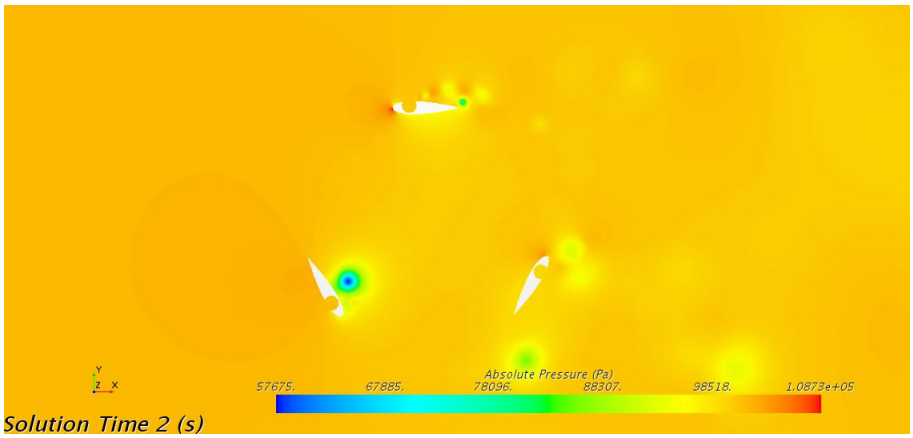

Figure A.94: Pressure SIM14

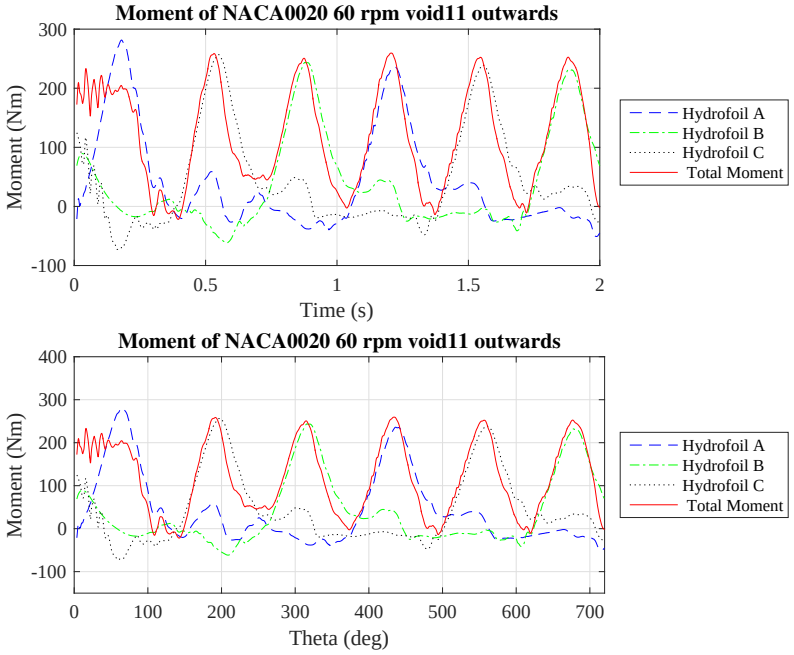

Figure A.95: Moment SIM14

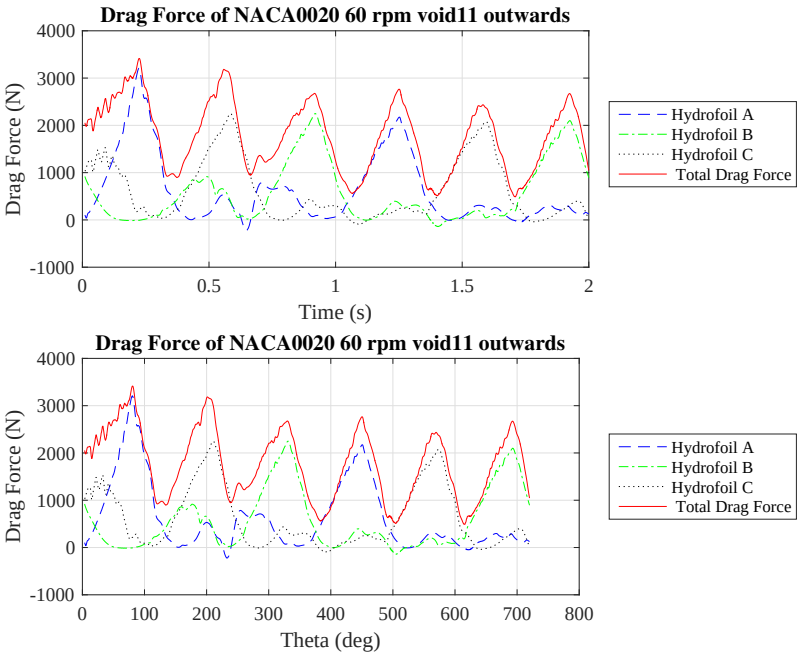

Figure A.96: Drag Force SIM14

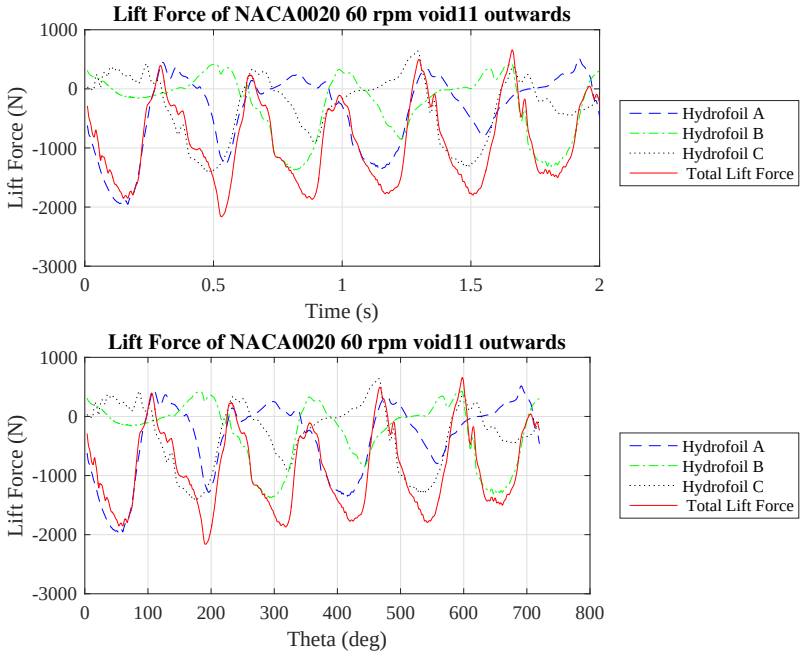

Figure A.97: Lift Force SIM14

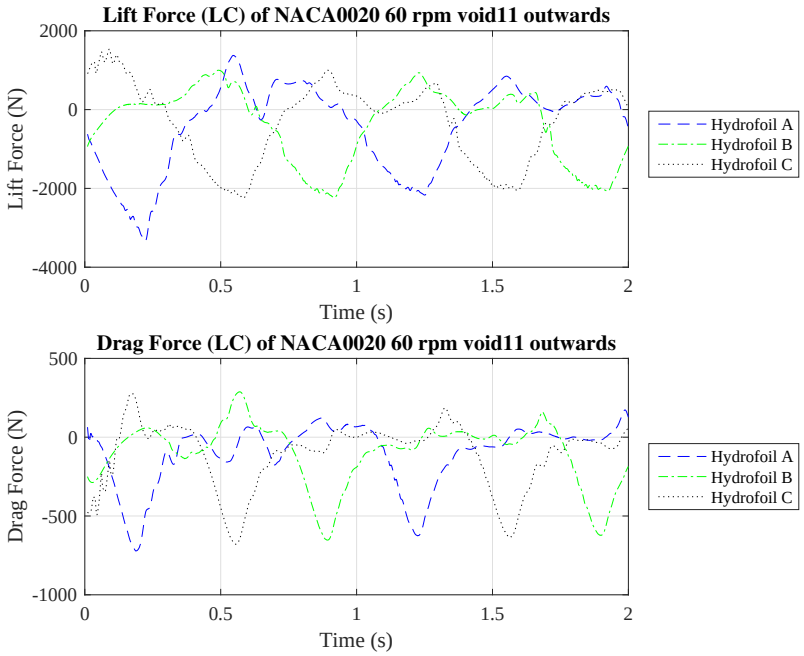

Figure A.98: Lift and Drag Force (LC) SIM14

A.1.15 SIM15

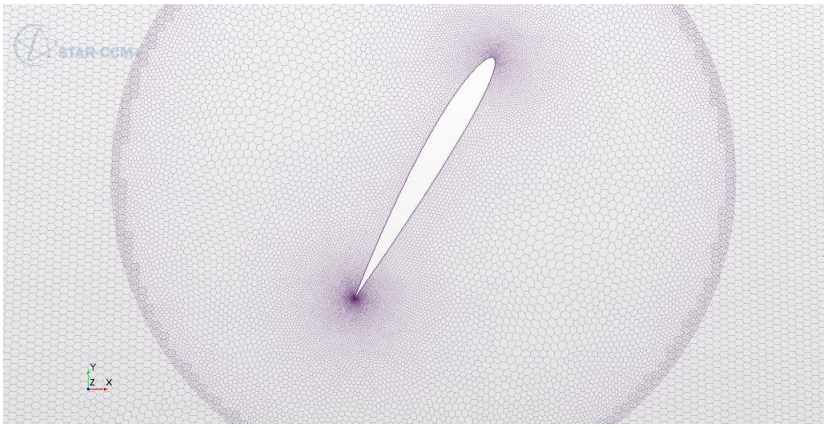

Figure A.99: Mesh SIM15

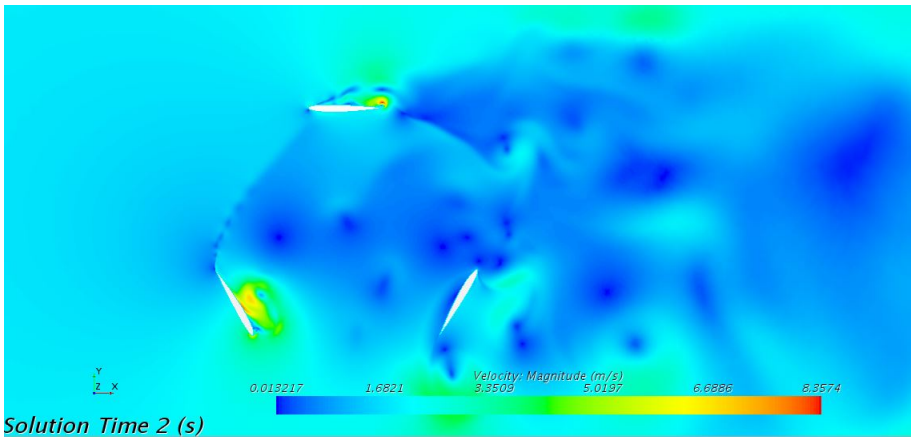

Figure A.100: Velocity SIM15

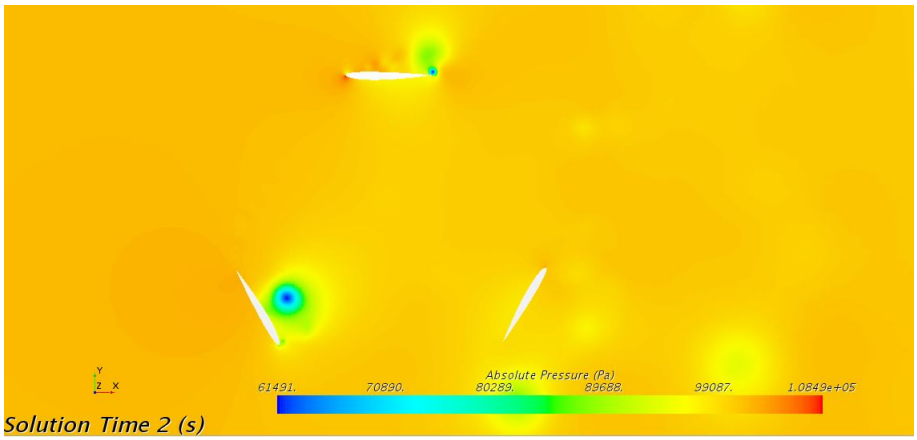

Figure A.101: Pressure SIM15

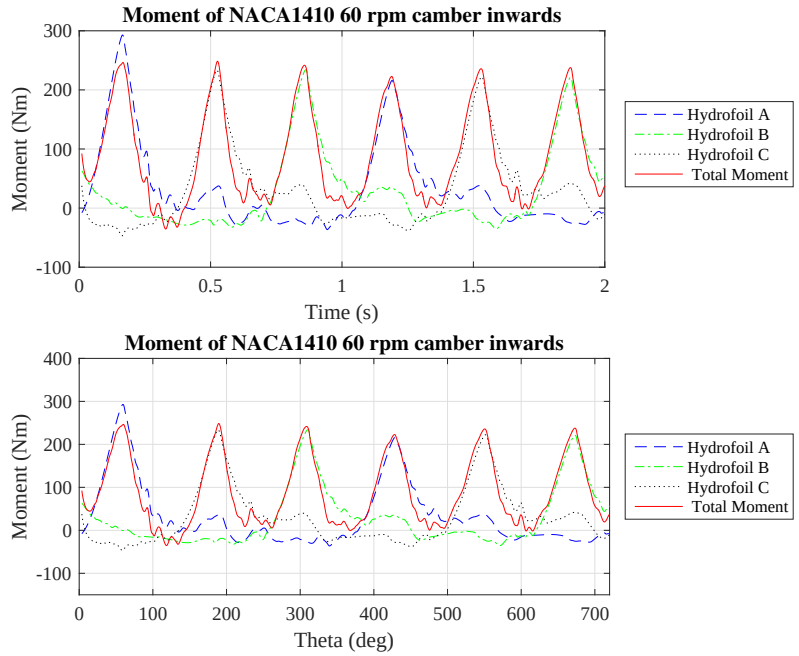

Figure A.102: Moment SIM15

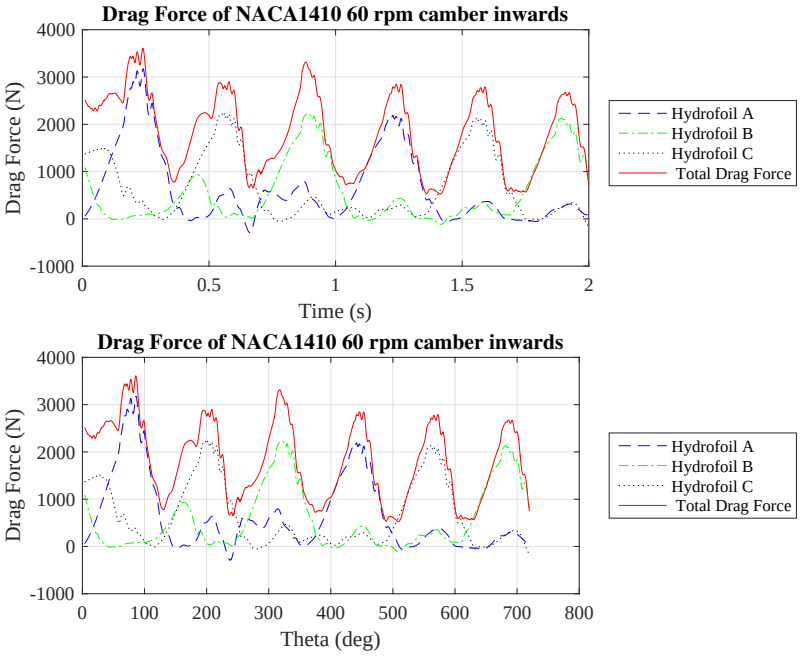

Figure A.103: Drag Force SIM15

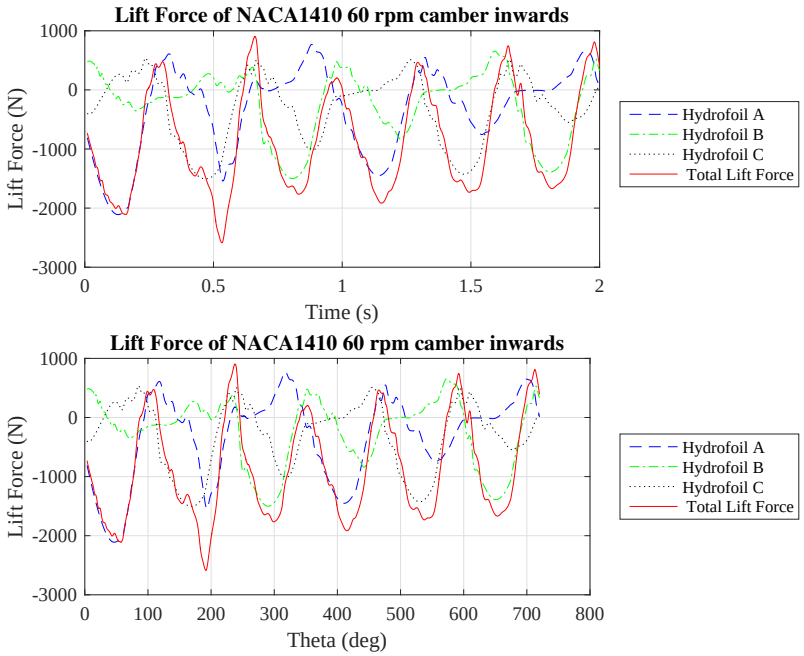

Figure A.104: Lift Force SIM15

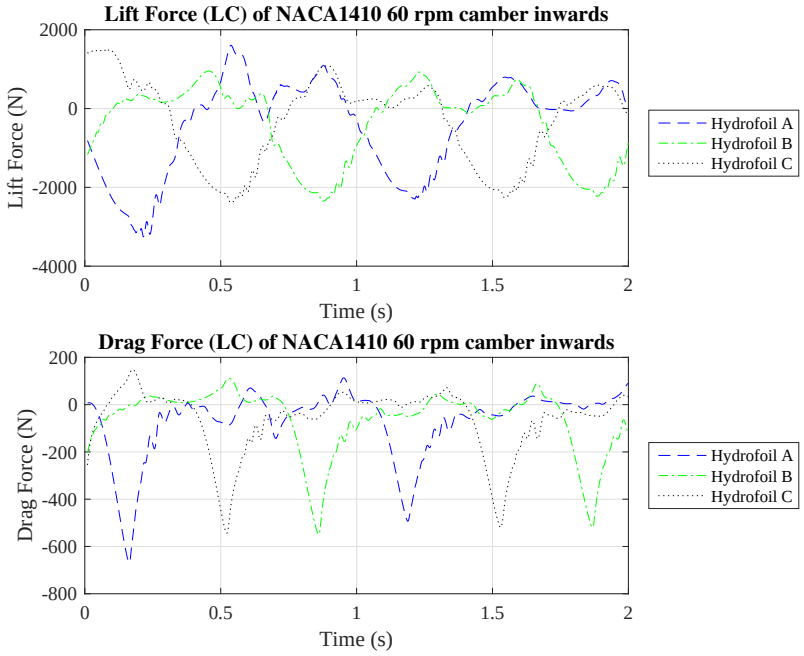

Figure A.105: Lift and Drag Force (LC) SIM15

A.1.16 SIM16

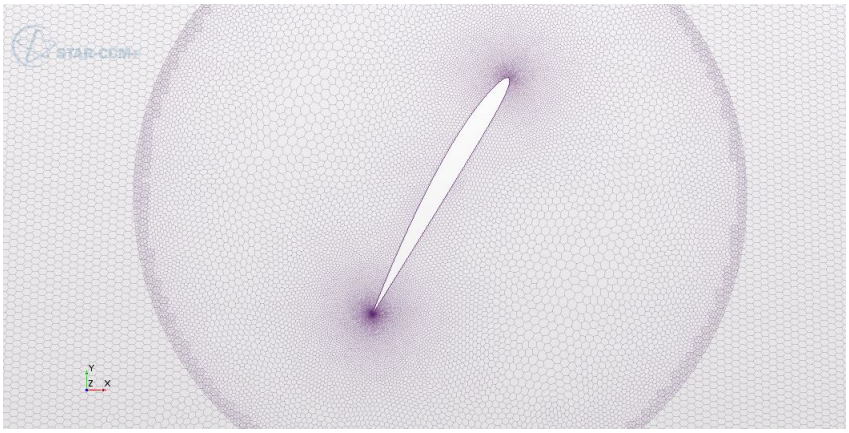

Figure A.106: Mesh SIM16

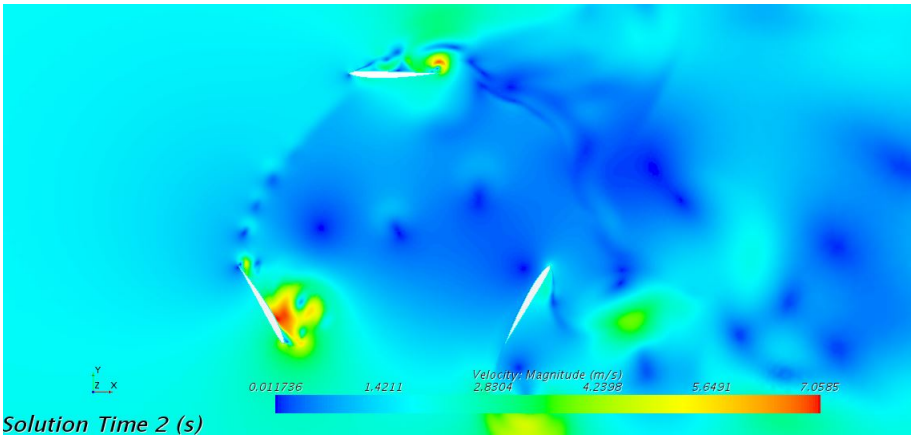

Figure A.107: Velocity SIM16

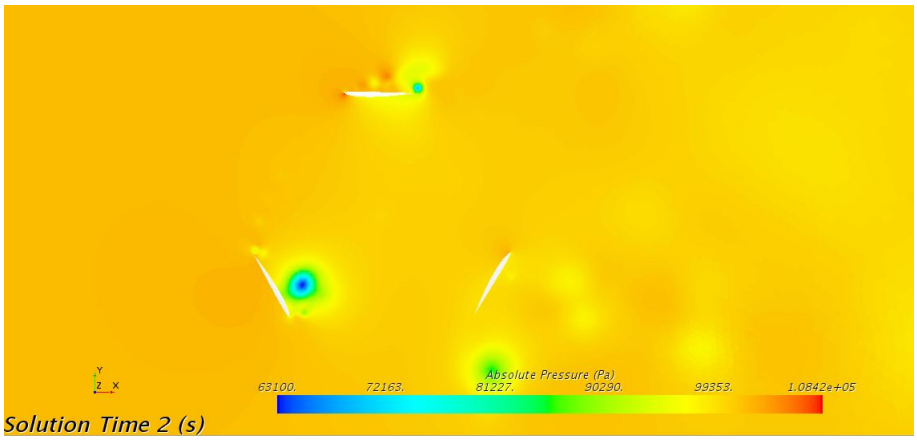

Figure A.108: Pressure SIM16

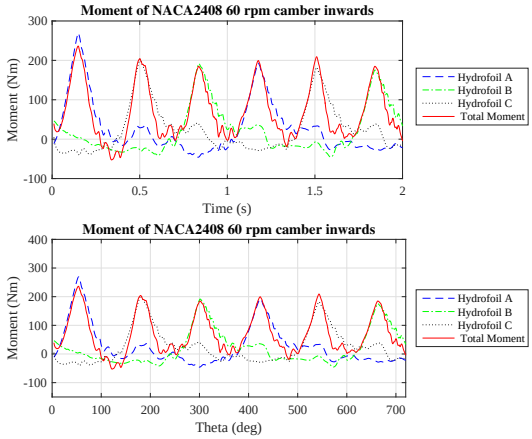

Figure A.109: Moment SIM16

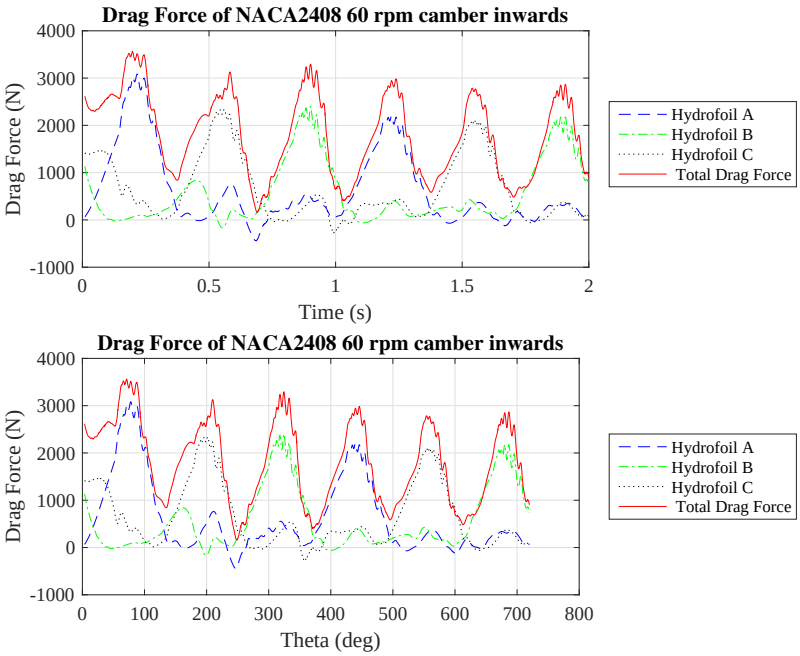

Figure A.110: Drag Force SIM16

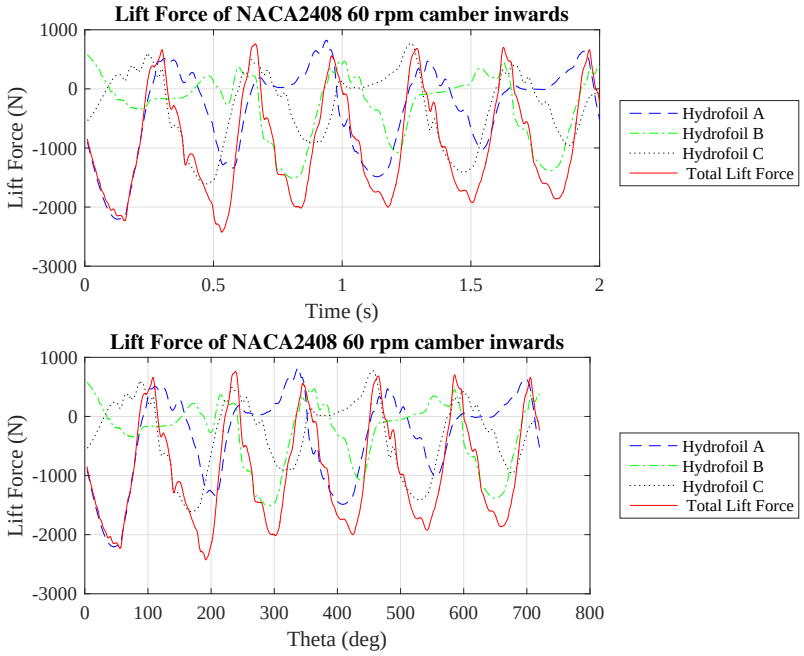

Figure A.111: Lift Force SIM16

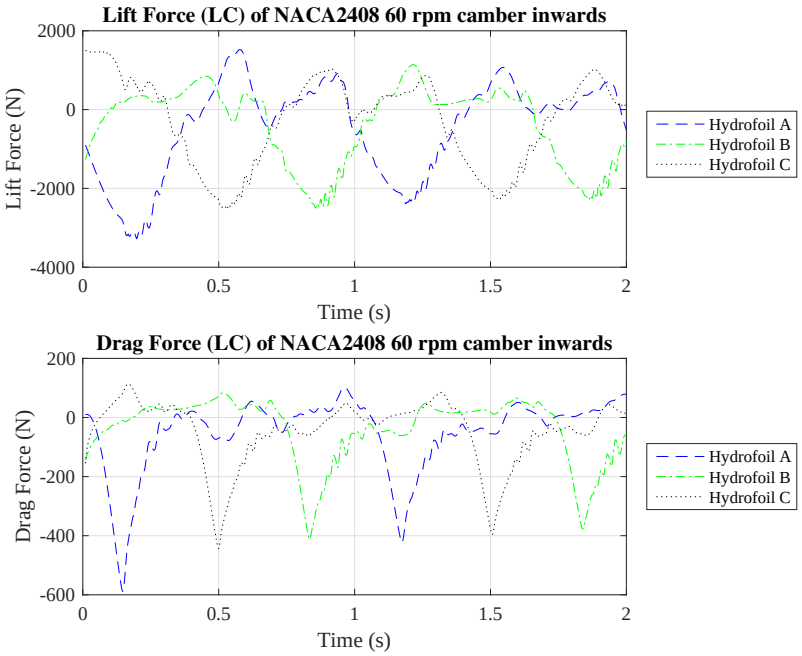

Figure A.112: Lift and Drag Force (LC) SIM16

A.1.17 SIM17

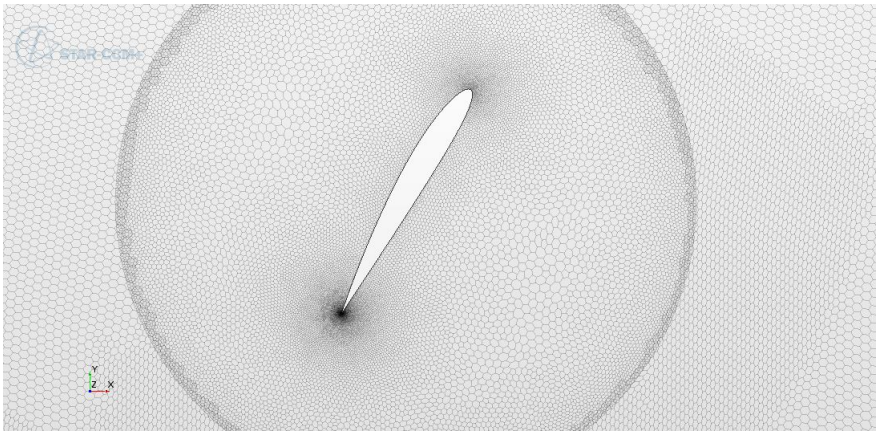

Figure A.113: Mesh SIM17

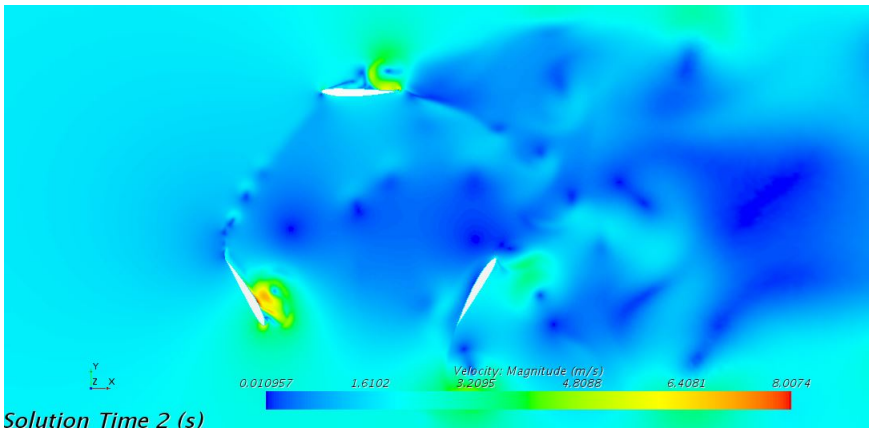

Figure A.114: Velocity SIM17

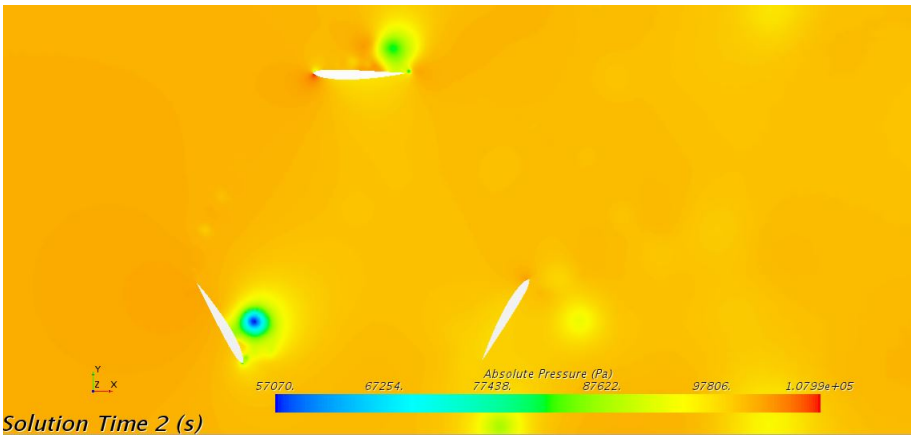

Figure A.115: Pressure SIM17

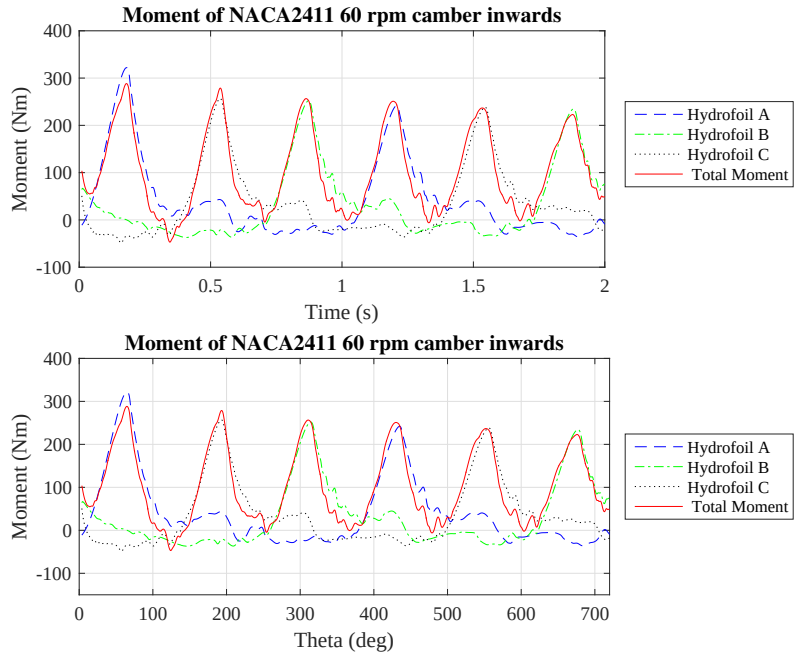

Figure A.116: Moment SIM17

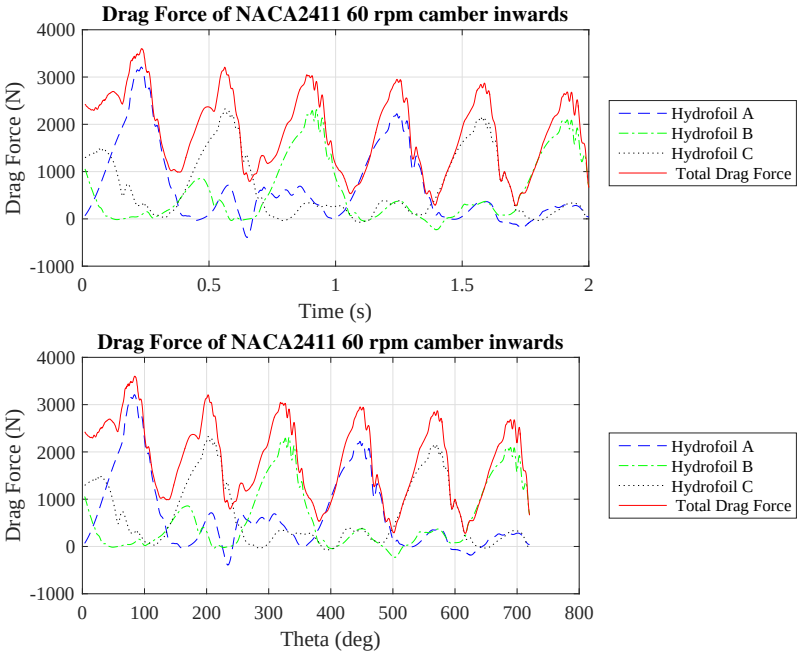

Figure A.117: Drag Force SIM17

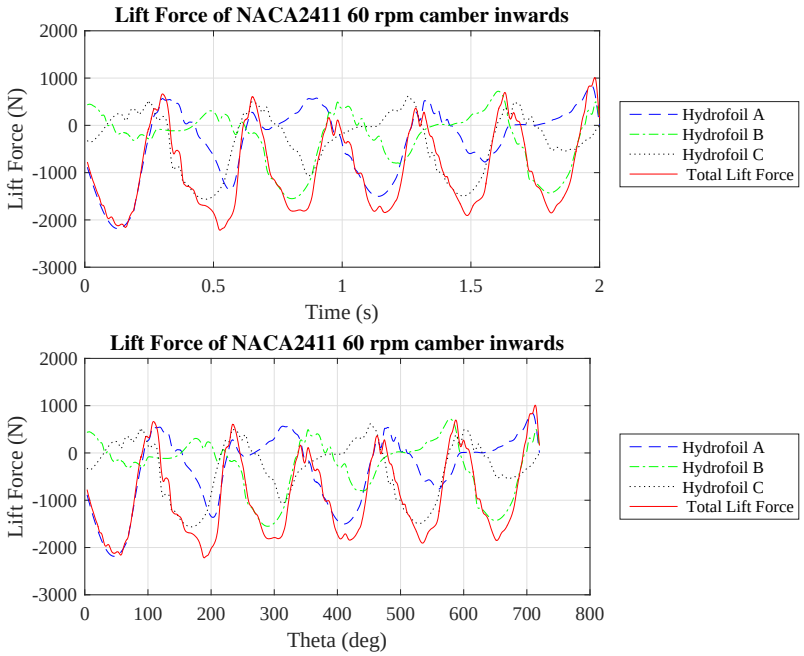

Figure A.118: Lift Force SIM17

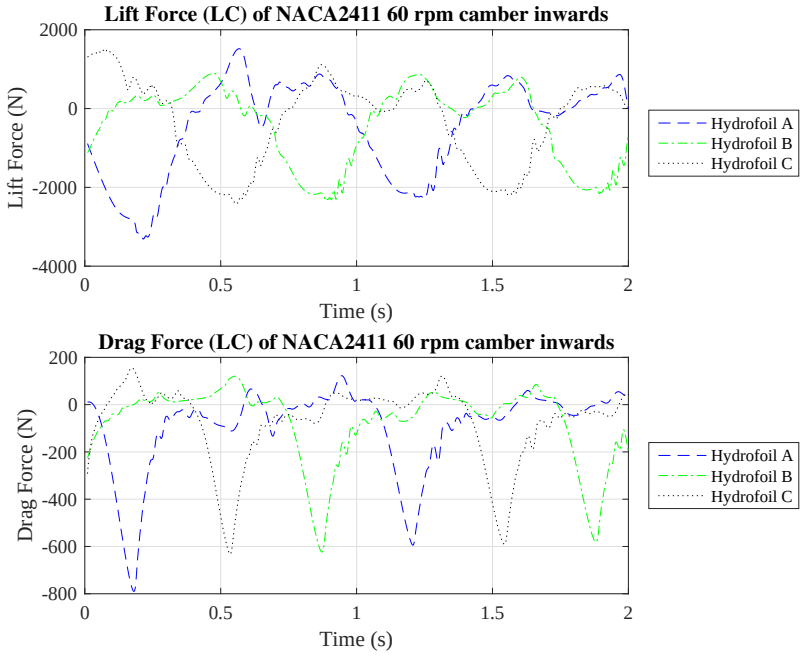

Figure A.119: Lift and Drag Force (LC) SIM17

A.1.18 SIM18

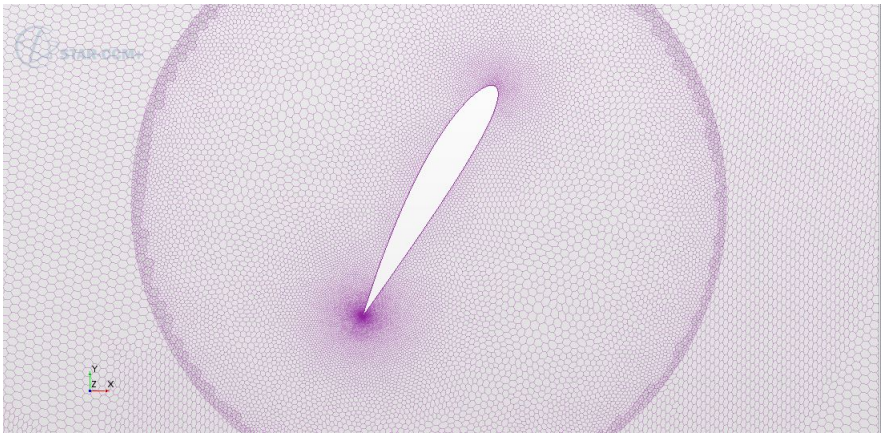

Figure A.120: Mesh SIM18

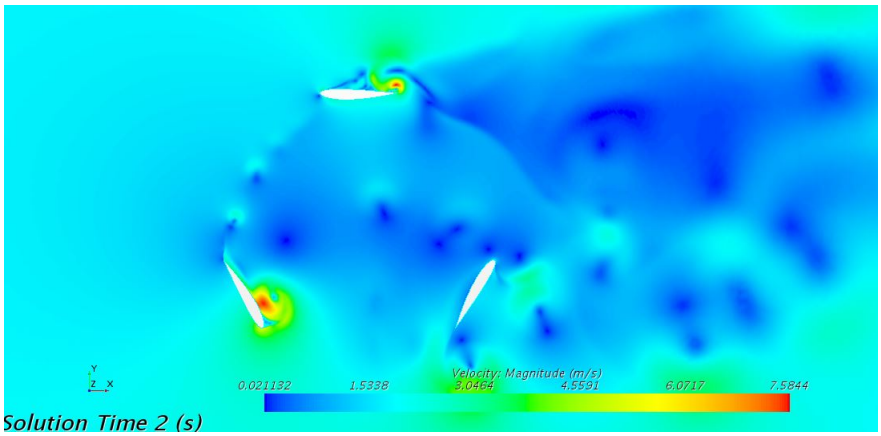

Figure A.121: Velocity SIM18

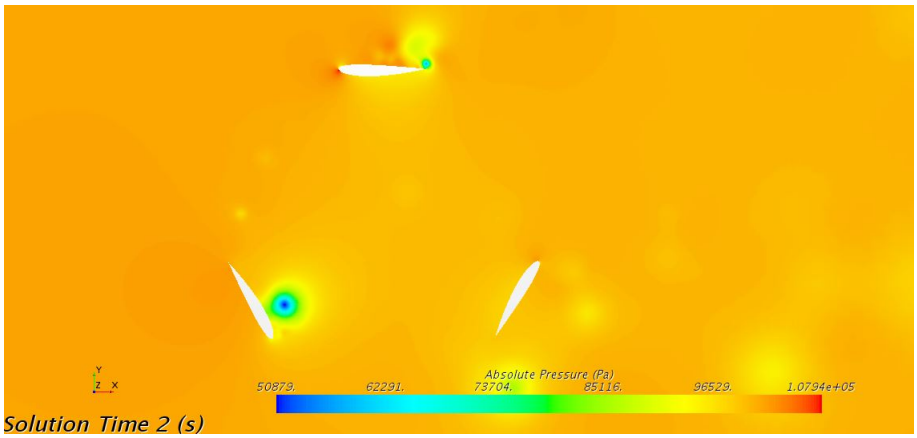

Figure A.122: Pressure SIM18

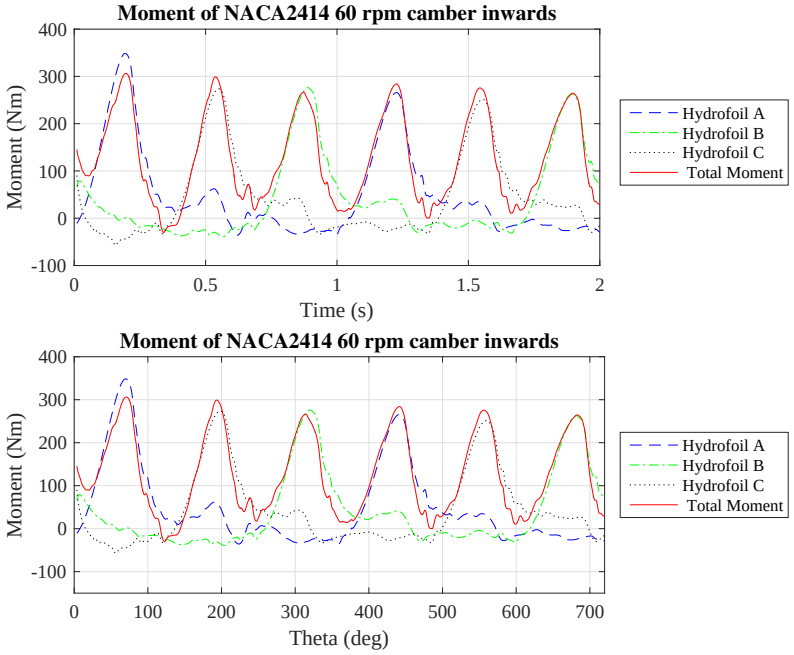

Figure A.123: Moment SIM18

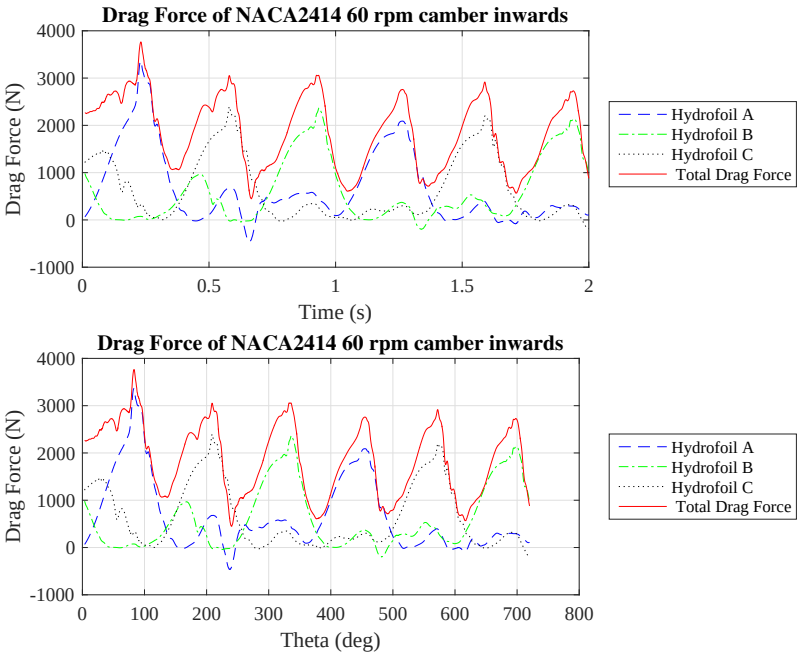

Figure A.124: Drag Force SIM18

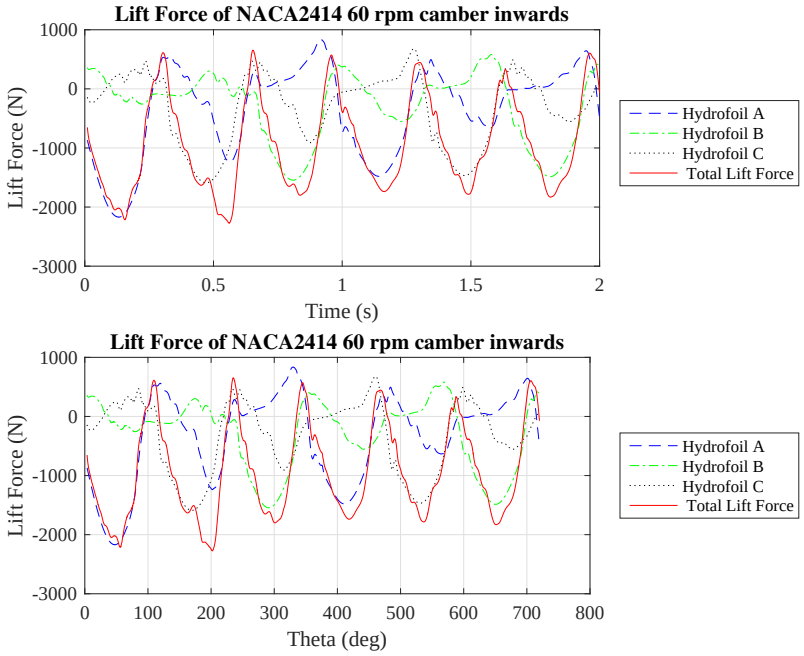

Figure A.125: Lift Force SIM18

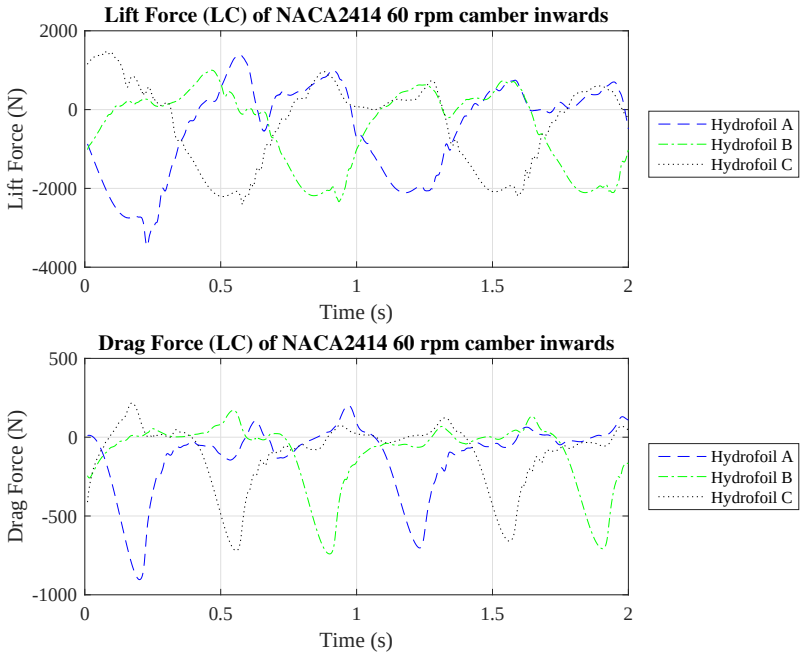

Figure A.126: Lift and Drag Force (LC) SIM18

A.1.19 SIM19

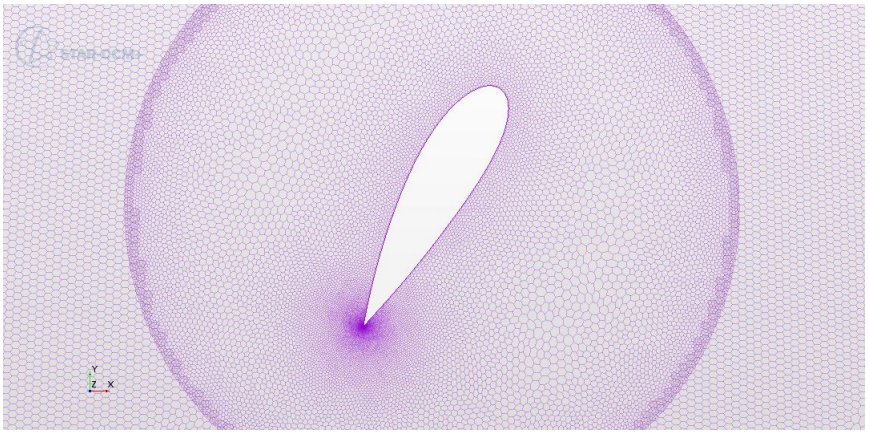

Figure A.127: Mesh SIM19

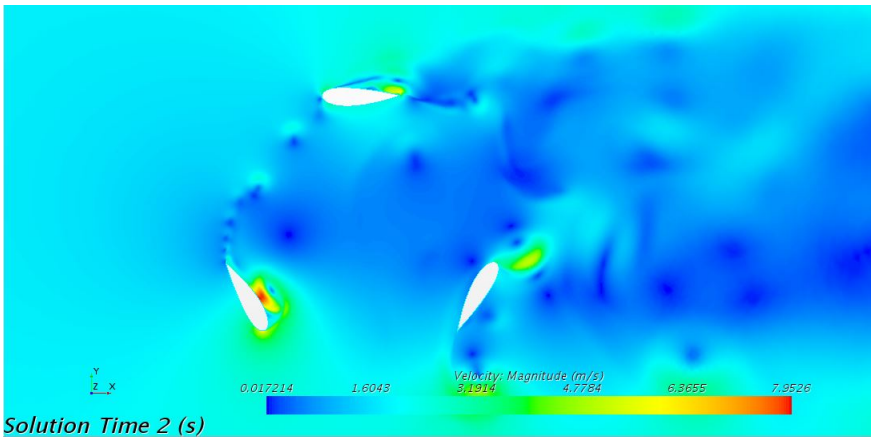

Figure A.128: Velocity SIM19

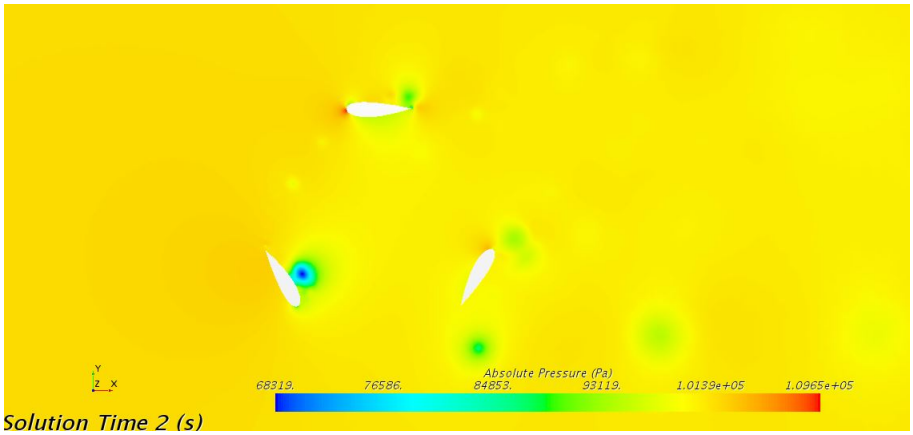

Figure A.129: Pressure SIM19

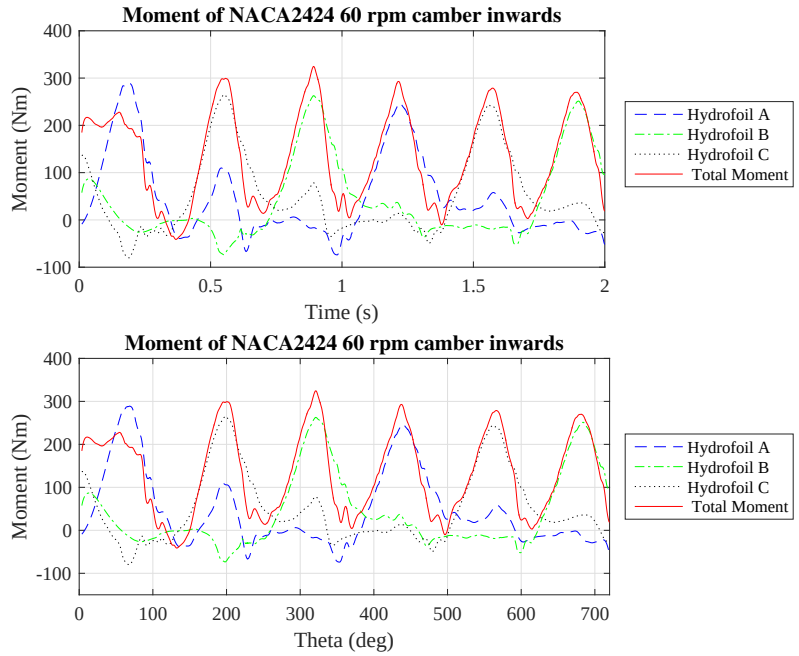

Figure A.130: Moment SIM19

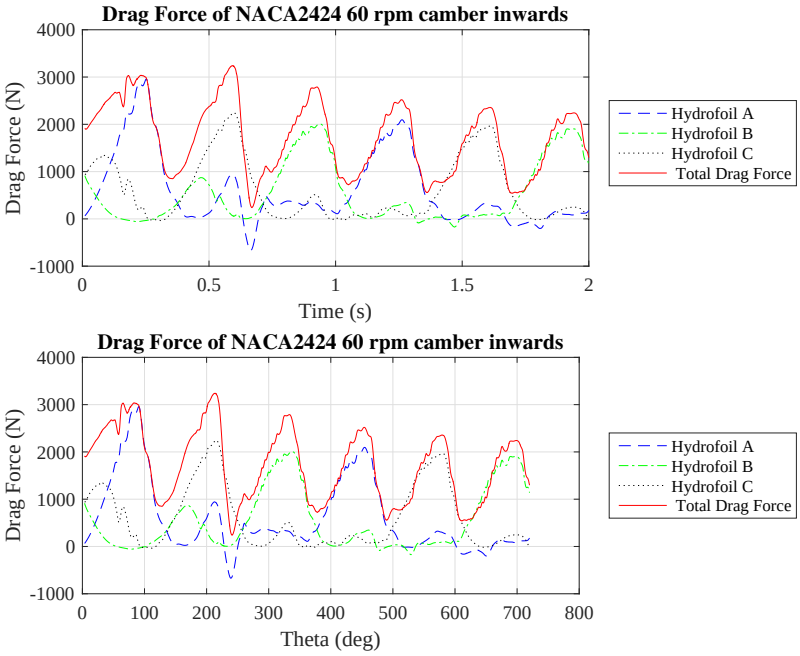

Figure A.131: Drag Force SIM19

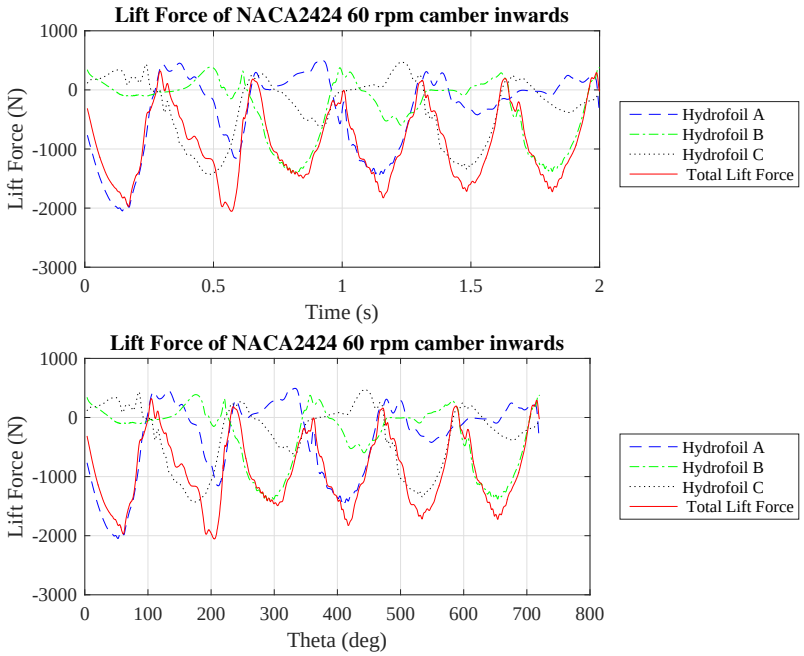

Figure A.132: Lift Force SIM19

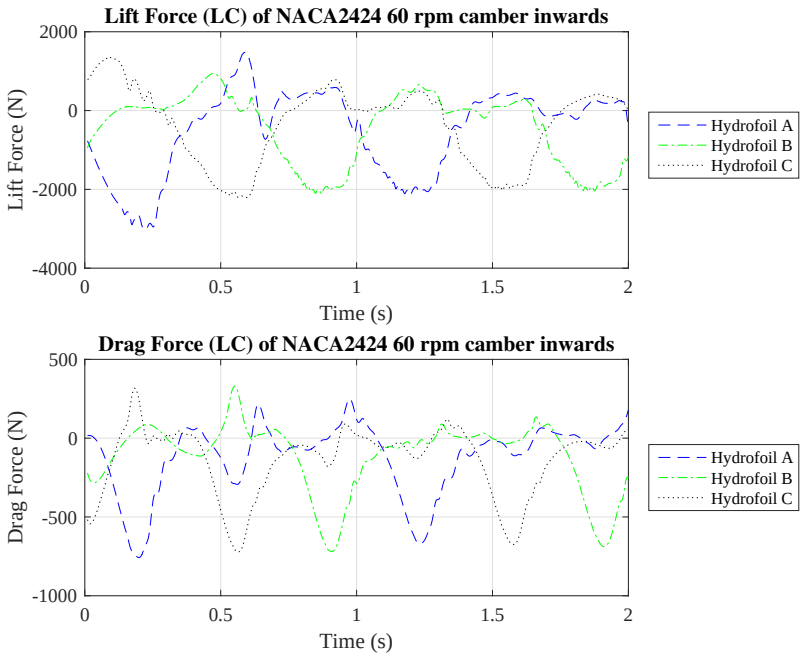

Figure A.133: Lift and Drag Force (LC) SIM19

A.1.20 SIM20

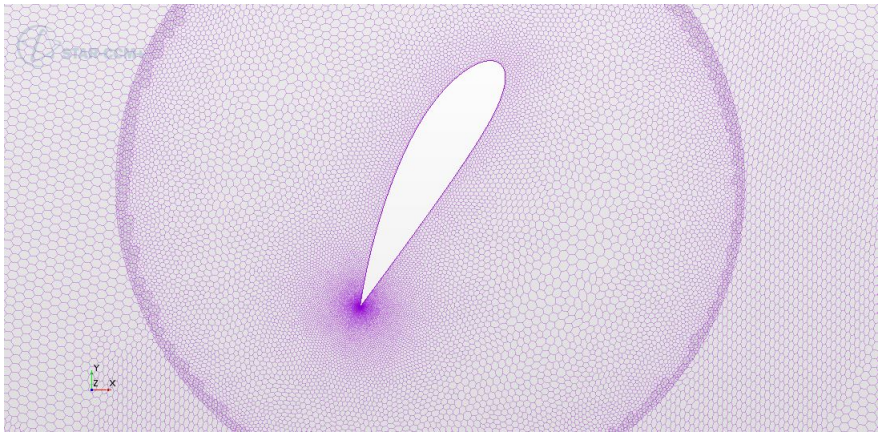

Figure A.134: Mesh SIM20

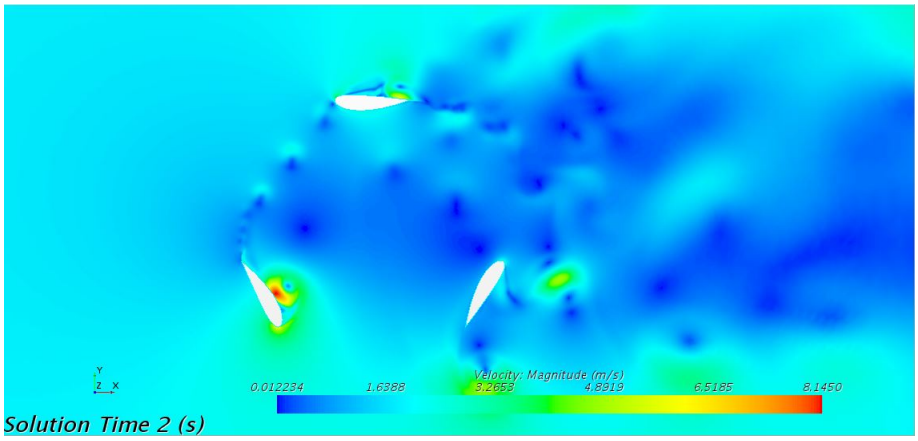

Figure A.135: Velocity SIM20

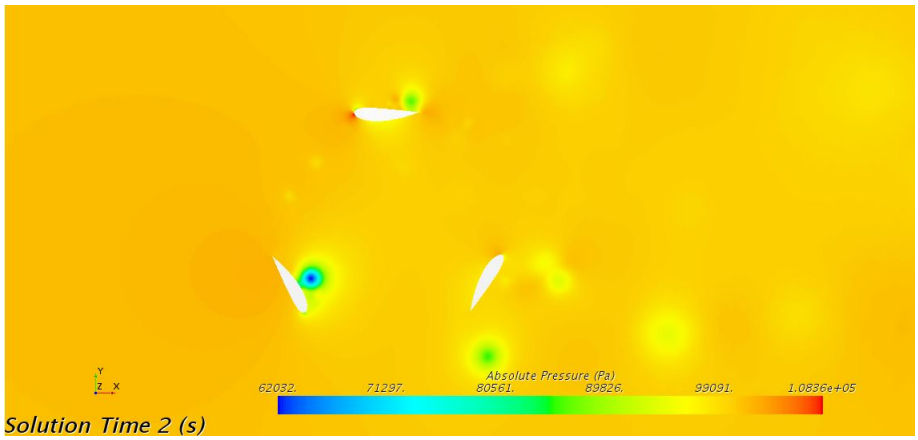

Figure A.136: Pressure SIM20

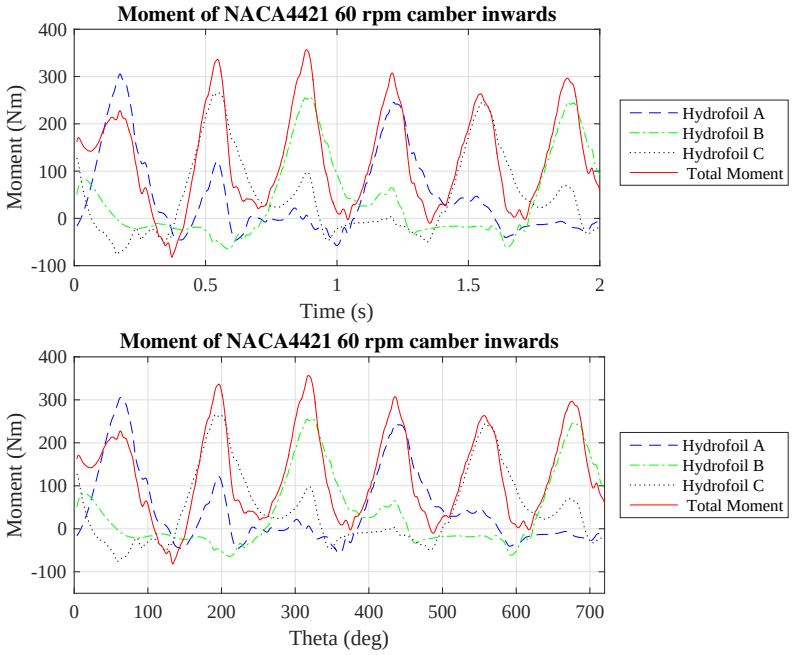

Figure A.137: Moment SIM20

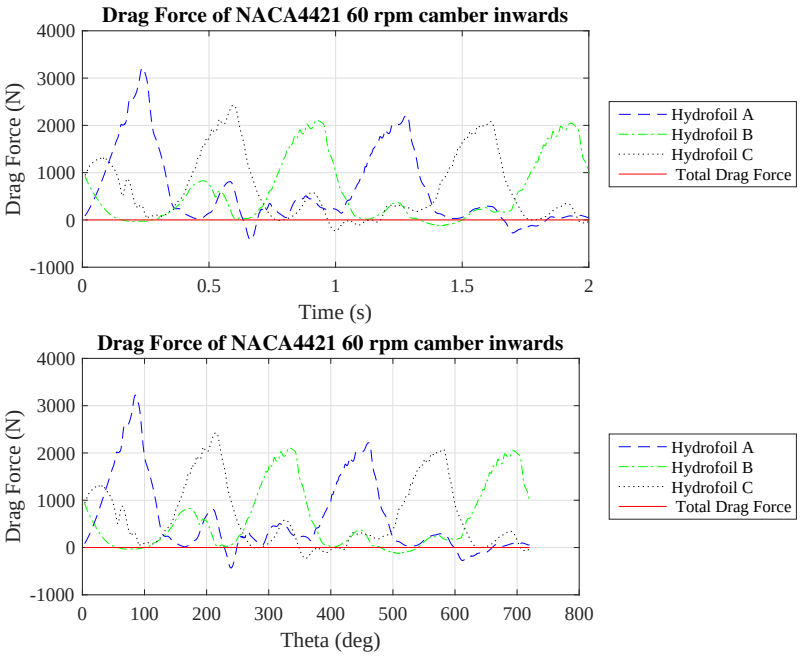

Figure A.138: Drag Force SIM20

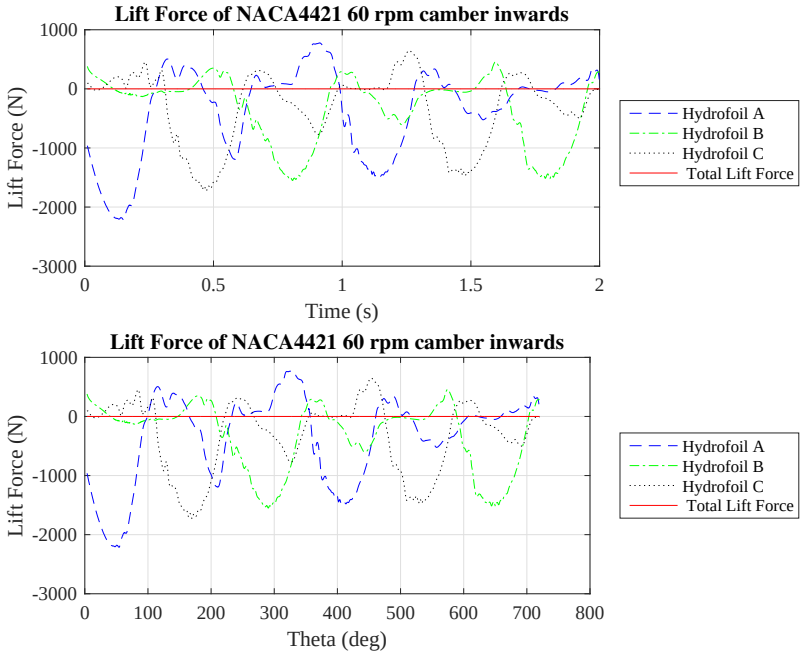

Figure A.139: Lift Force SIM20

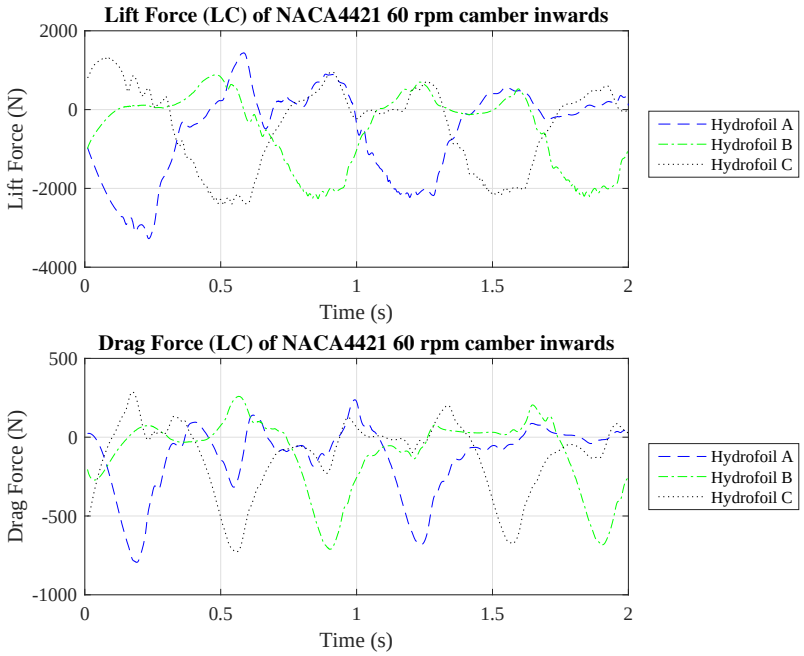

Figure A.140: Lift and Drag Force (LC) SIM20

A.1.21 SIM21

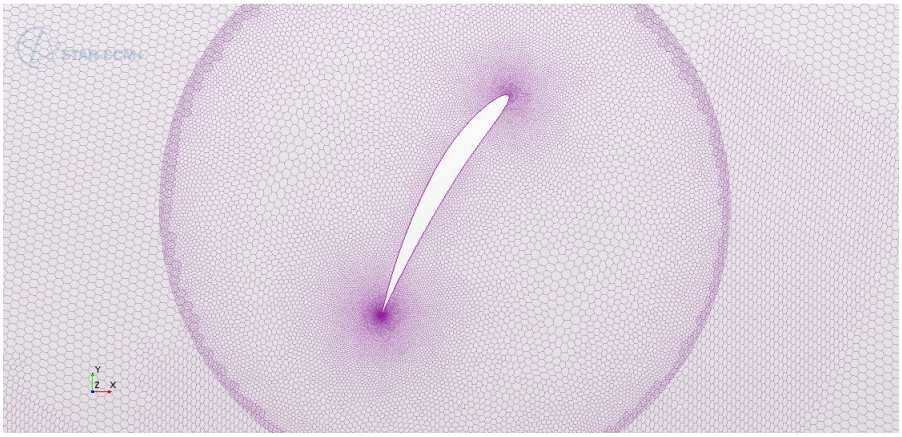

Figure A.141: Mesh SIM21

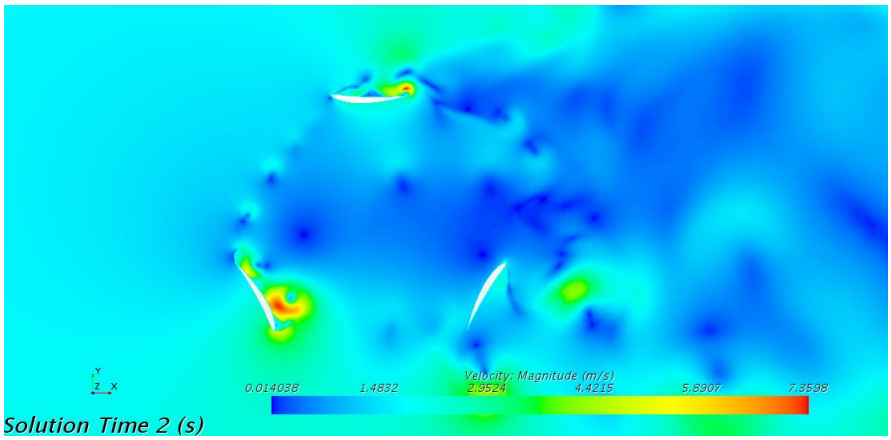

Figure A.142: Velocity SIM21

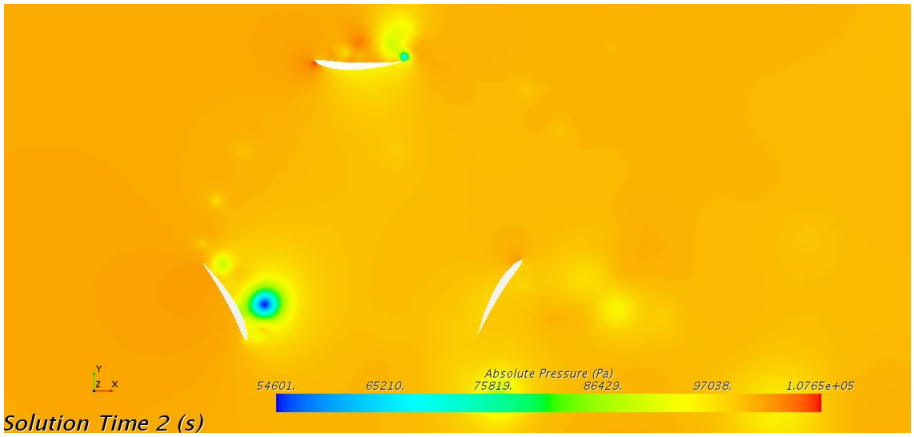

Figure A.143: Pressure SIM21

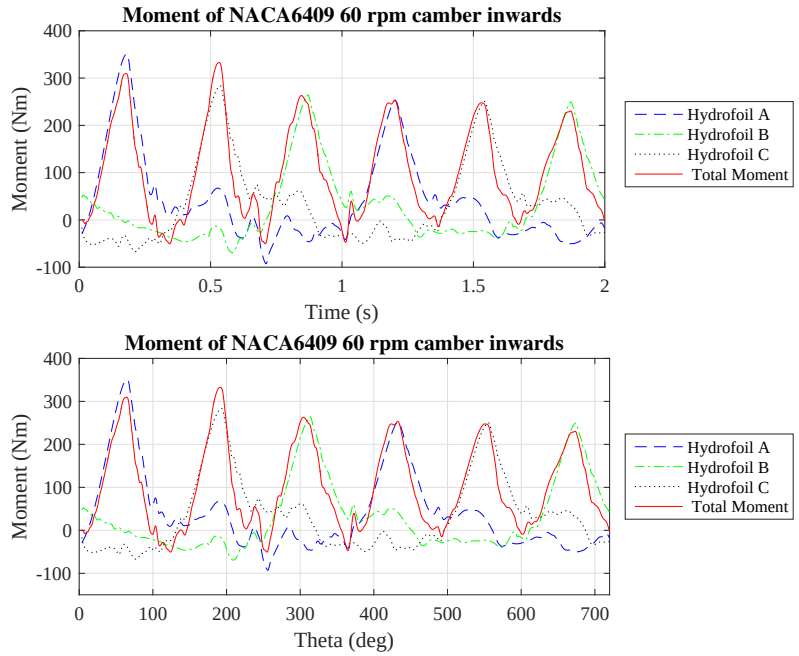

Figure A.144: Moment SIM21

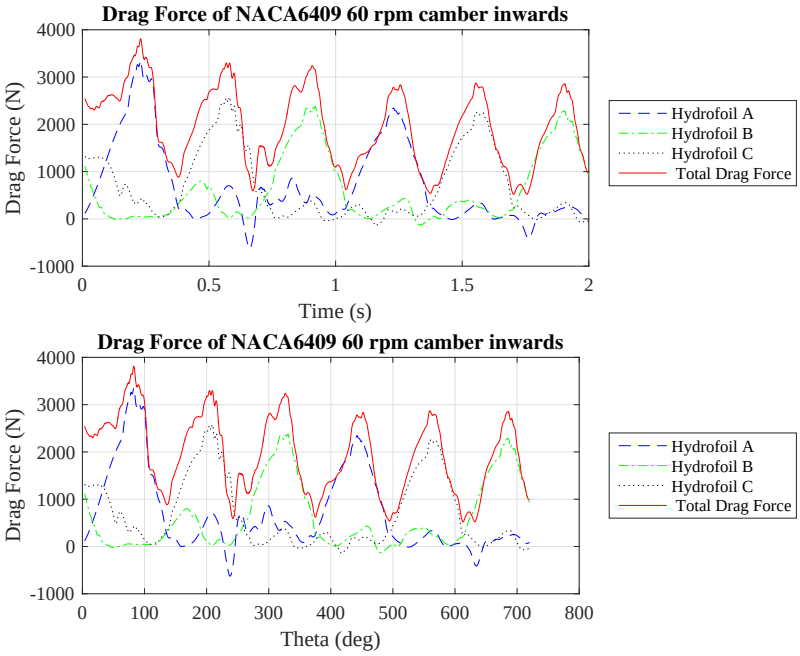

Figure A.145: Drag Force SIM21

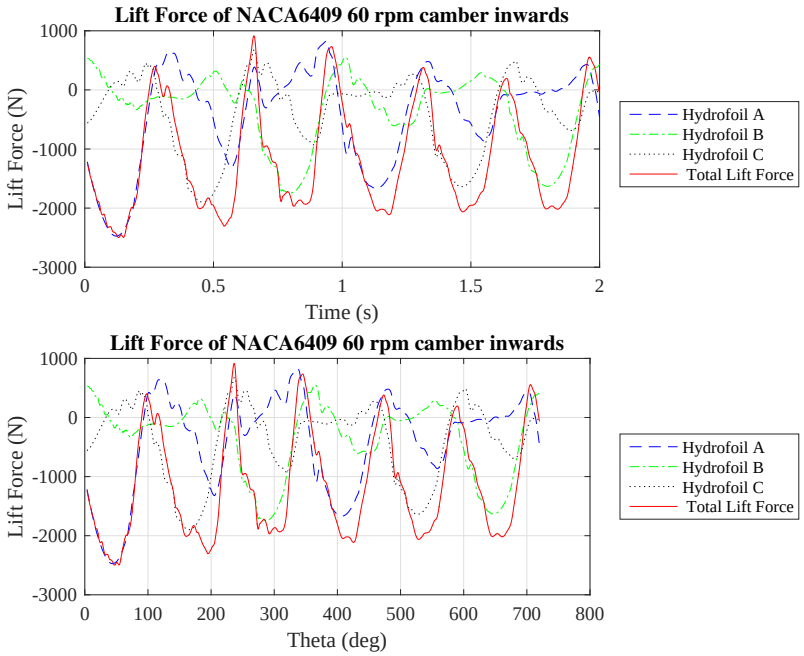

Figure A.146: Lift Force SIM21

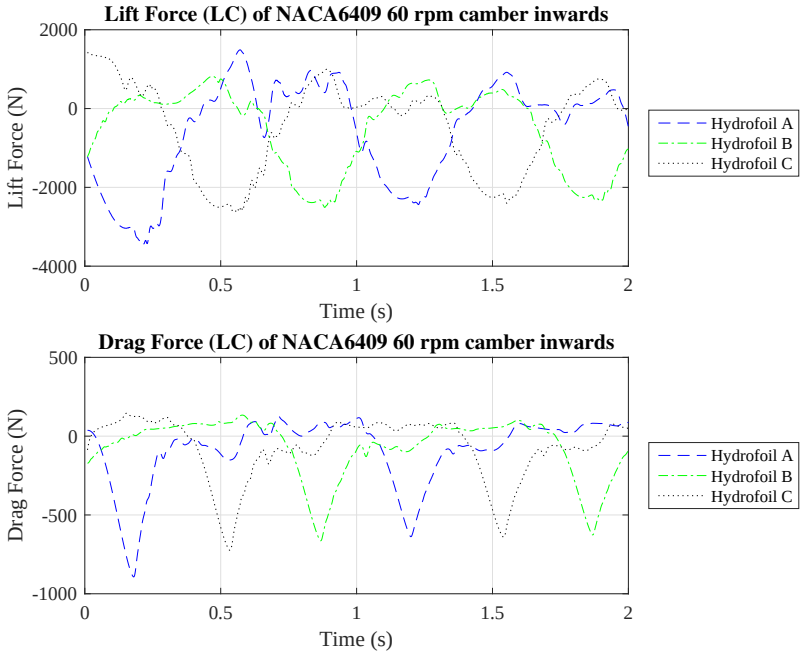

Figure A.147: Lift and Drag Force (LC) SIM21

A.1.22 SIM22

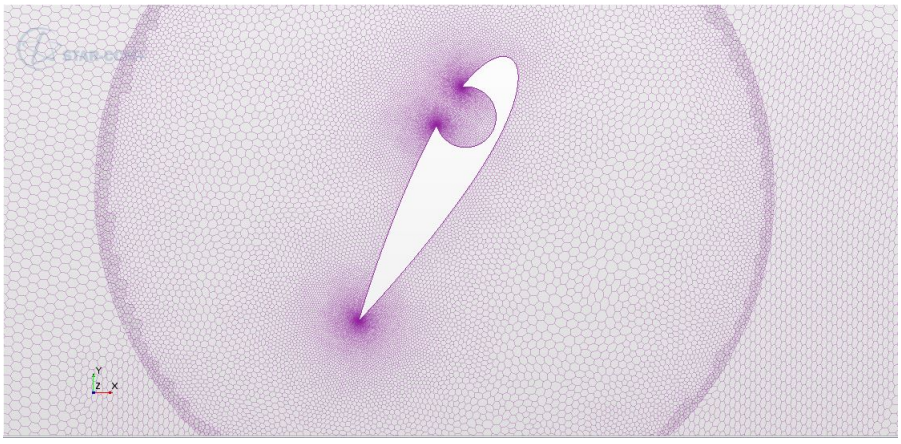

Figure A.148: Mesh SIM22

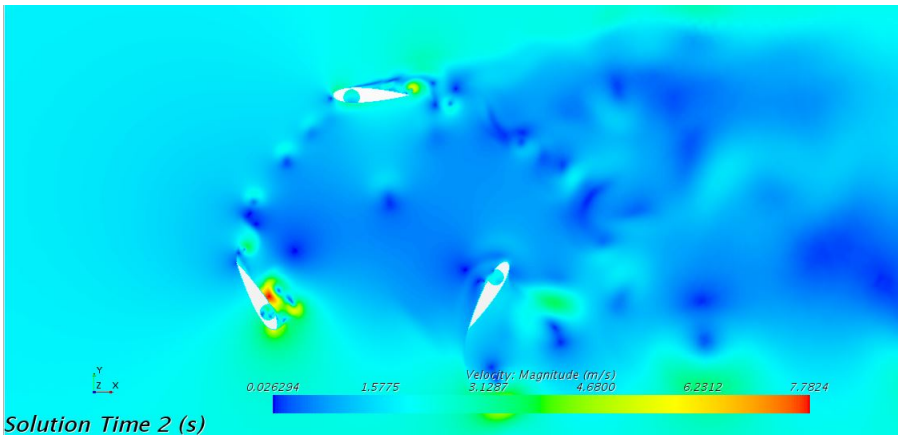

Figure A.149: Velocity SIM22

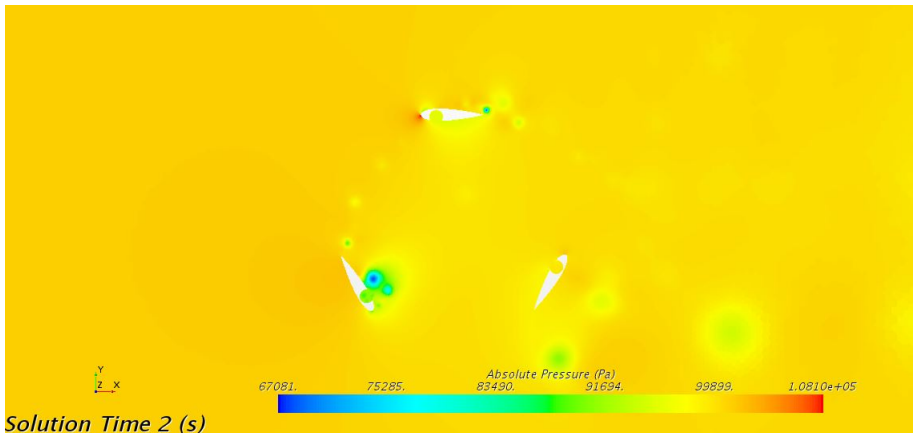

Figure A.150: Pressure SIM22

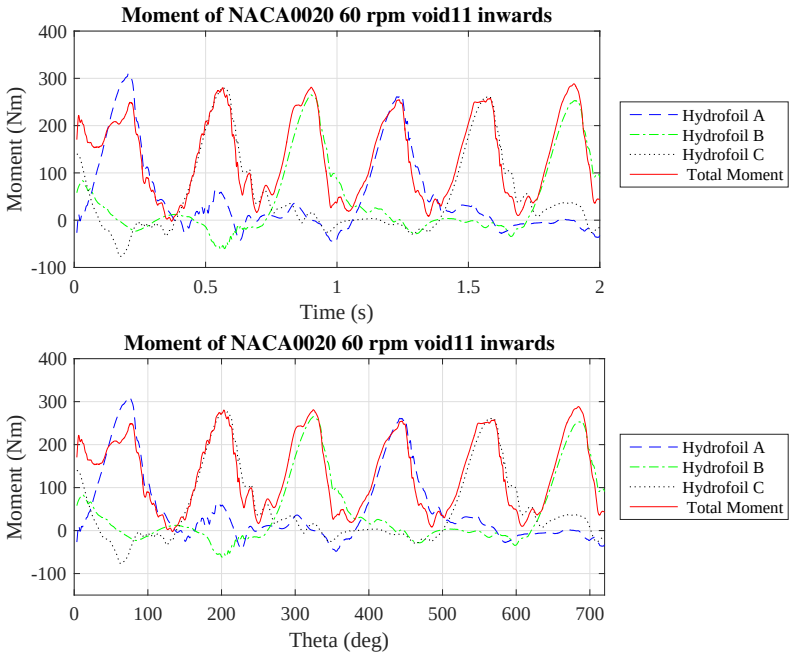

Figure A.151: Moment SIM22

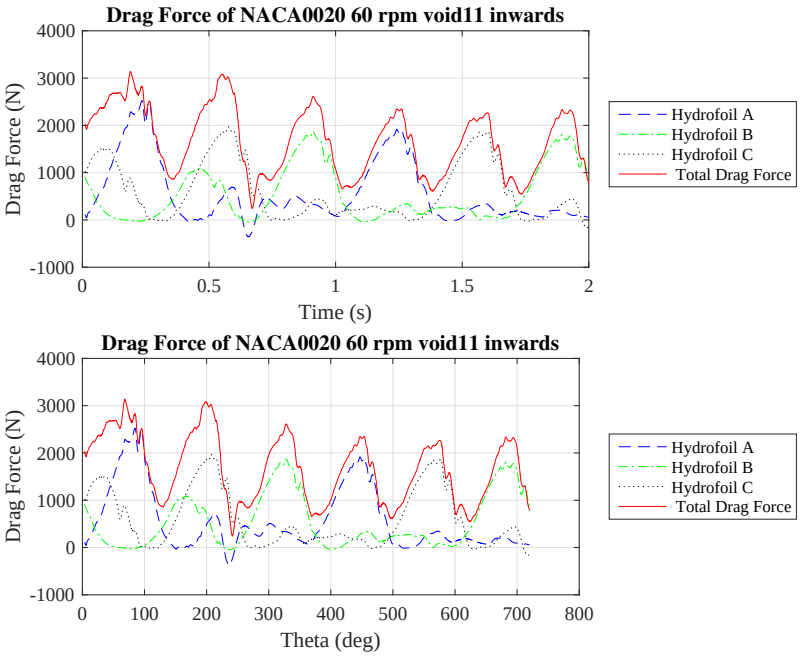

Figure A.152: Drag Force SIM22

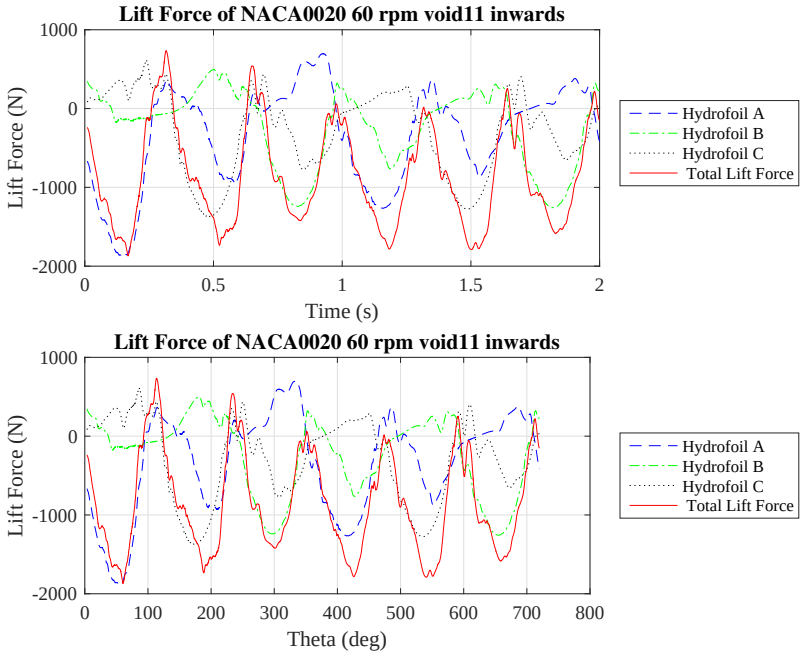

Figure A.153: Lift Force SIM22

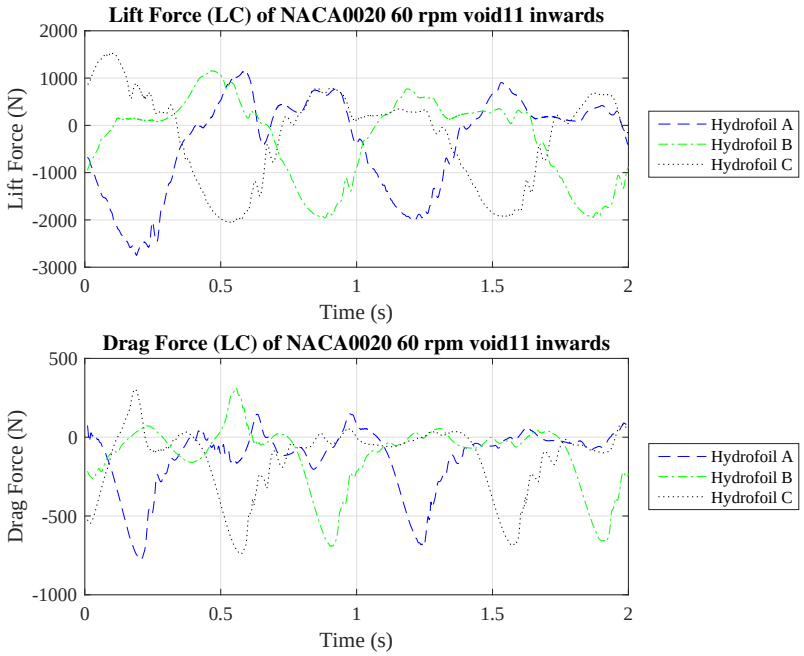

Figure A.154: Lift and Drag Force (LC) SIM22

A.1.23 SIM23

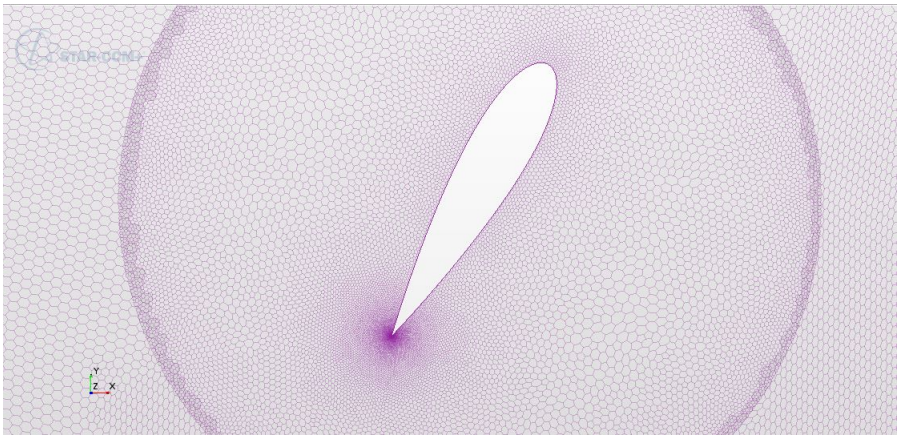

Figure A.155: Mesh SIM23

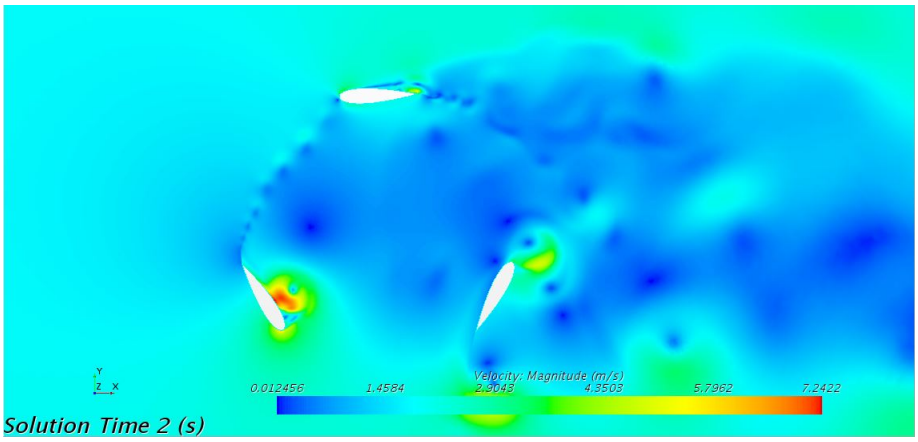

Figure A.156: Velocity SIM23

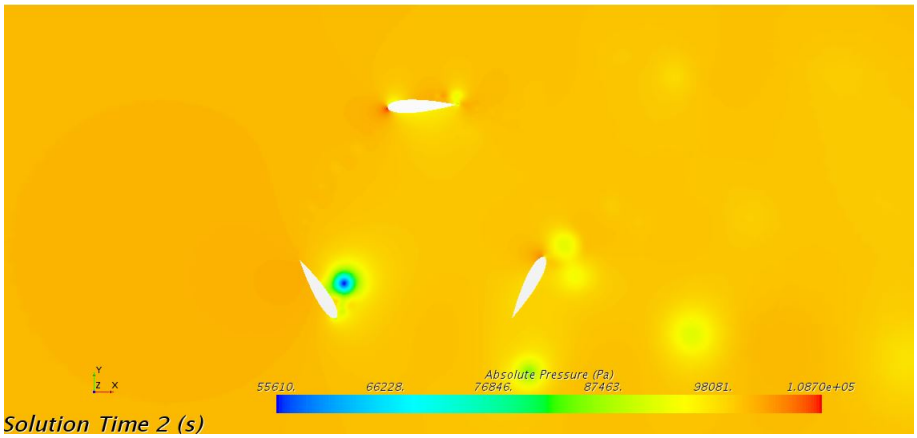

Figure A.157: Pressure SIM23

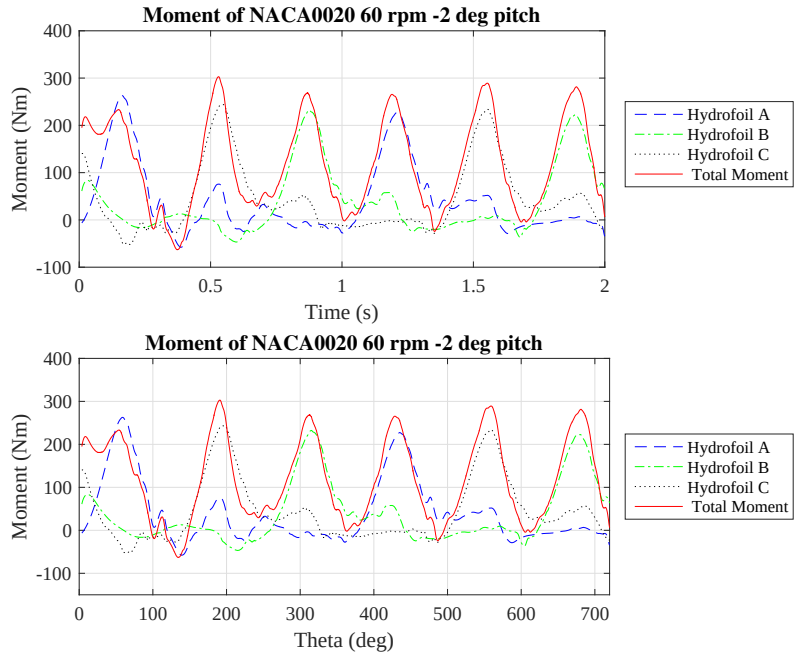

Figure A.158: Moment SIM23

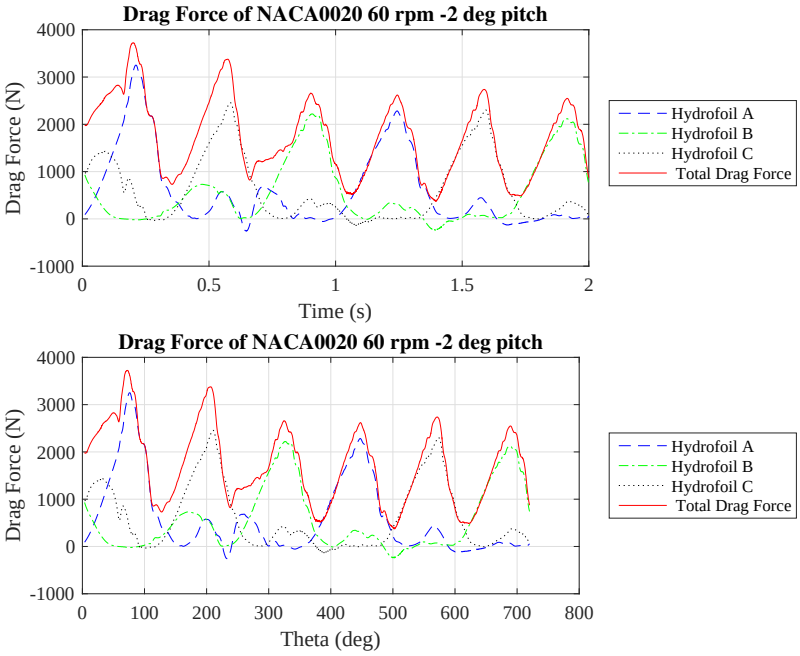

Figure A.159: Drag Force SIM23

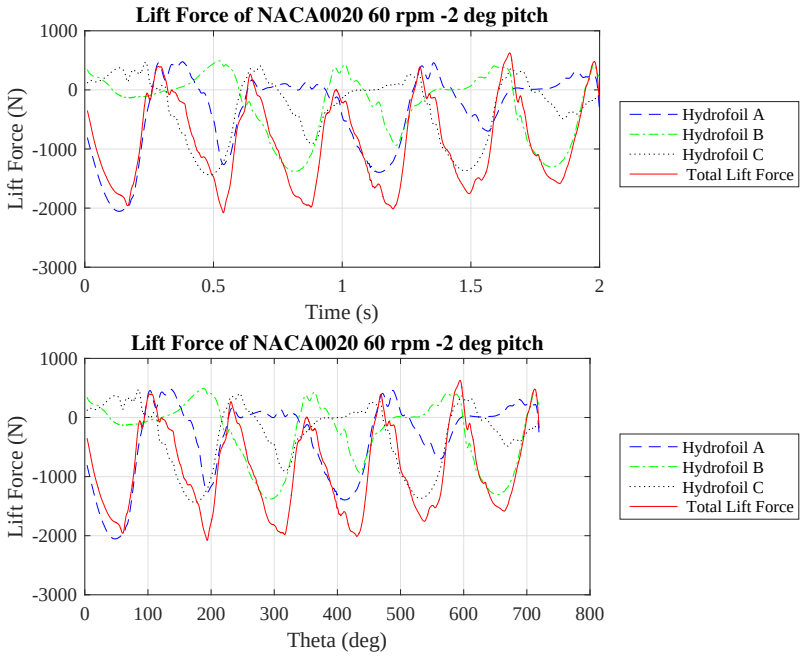

Figure A.160: Lift Force SIM23

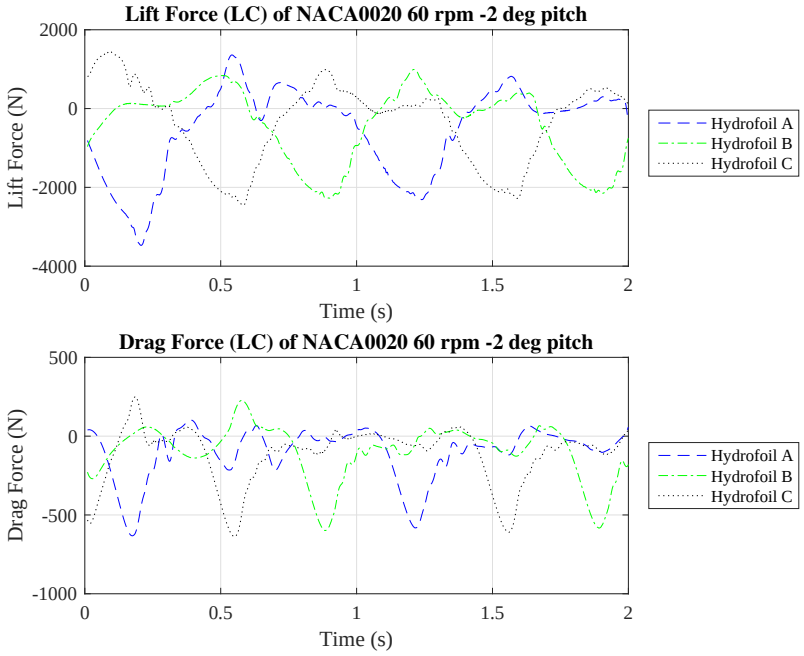

Figure A.161: Lift and Drag Force (LC) SIM23

A.1.24 SIM24

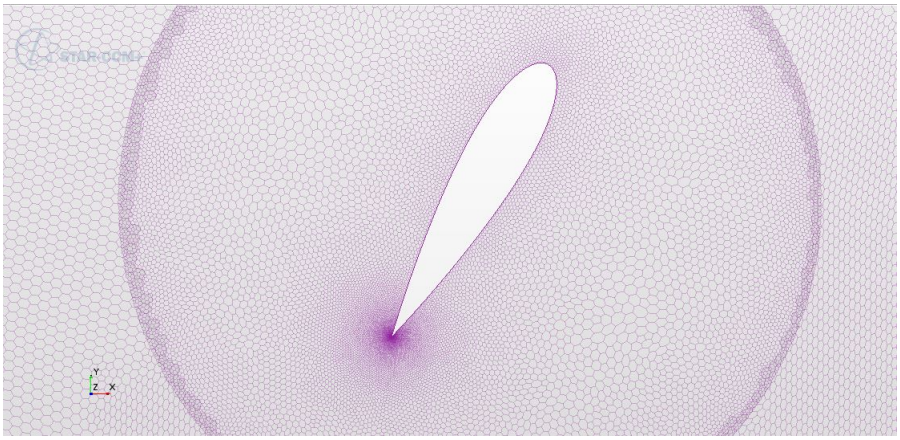

Figure A.162: Mesh SIM24

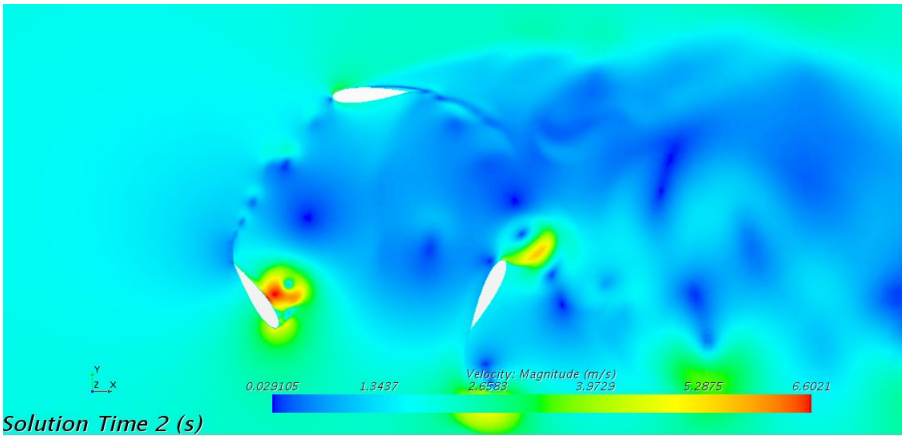

Figure A.163: Velocity SIM24

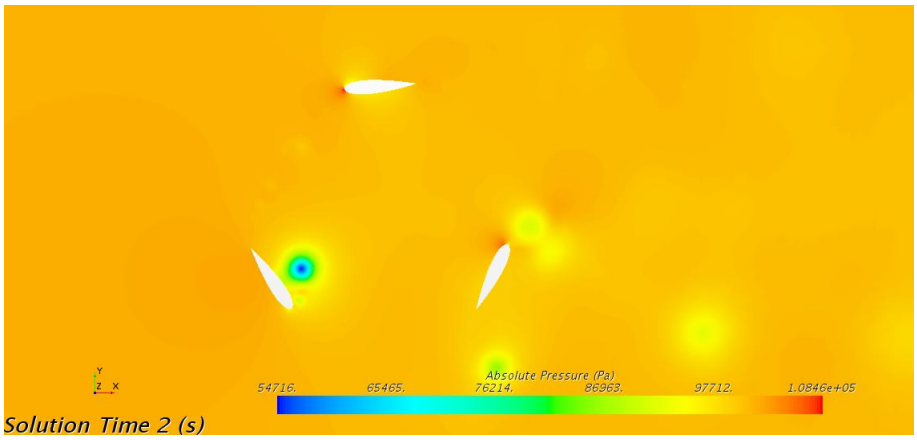

Figure A.164: Pressure SIM24

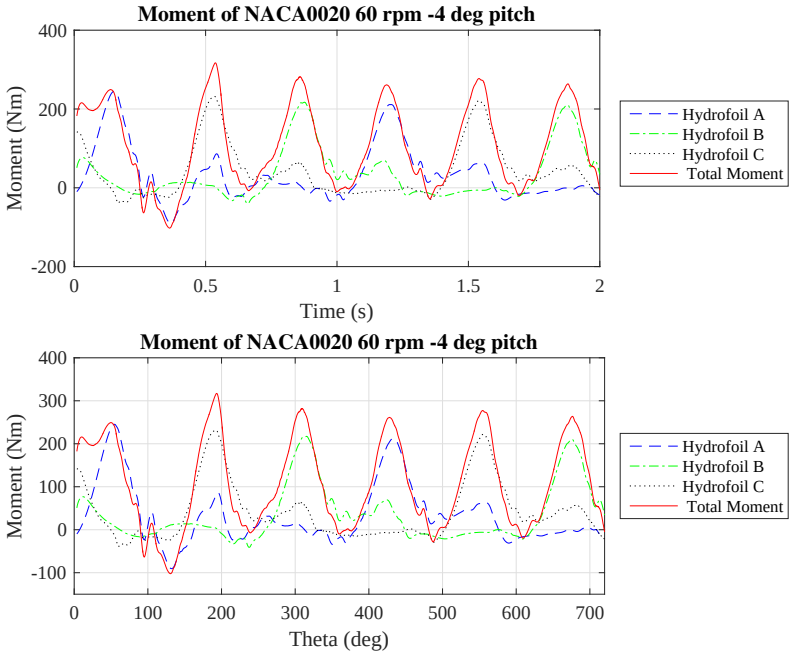

Figure A.165: Moment SIM24

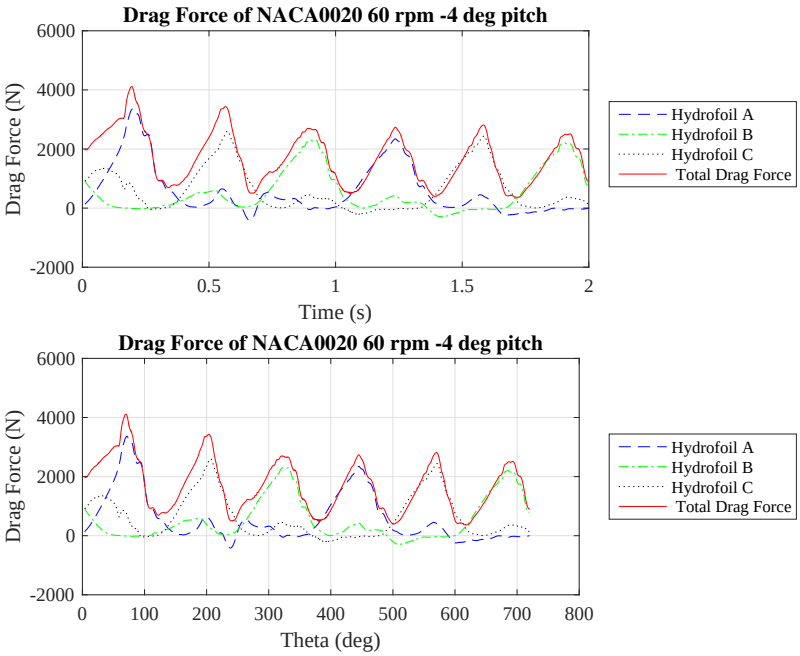

Figure A.166: Drag Force SIM24

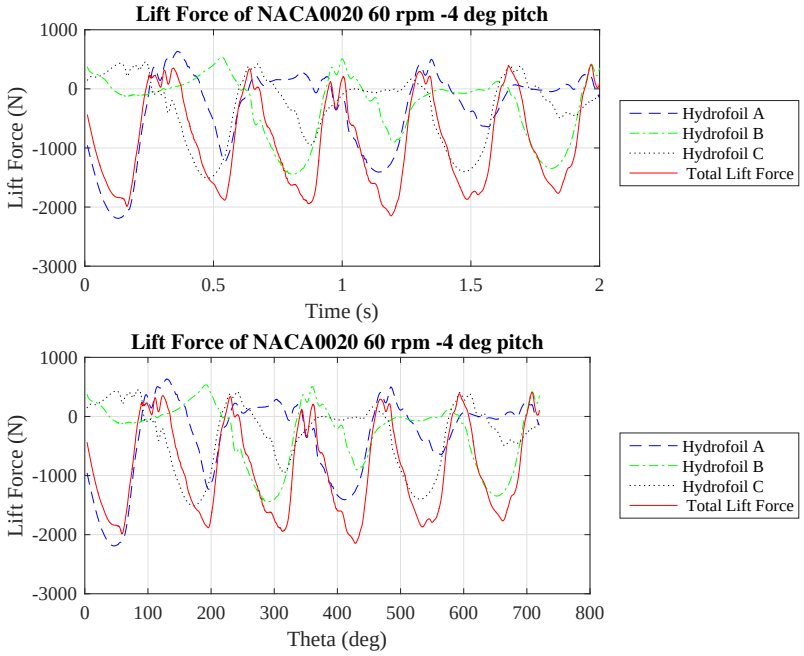

Figure A.167: Lift Force SIM24

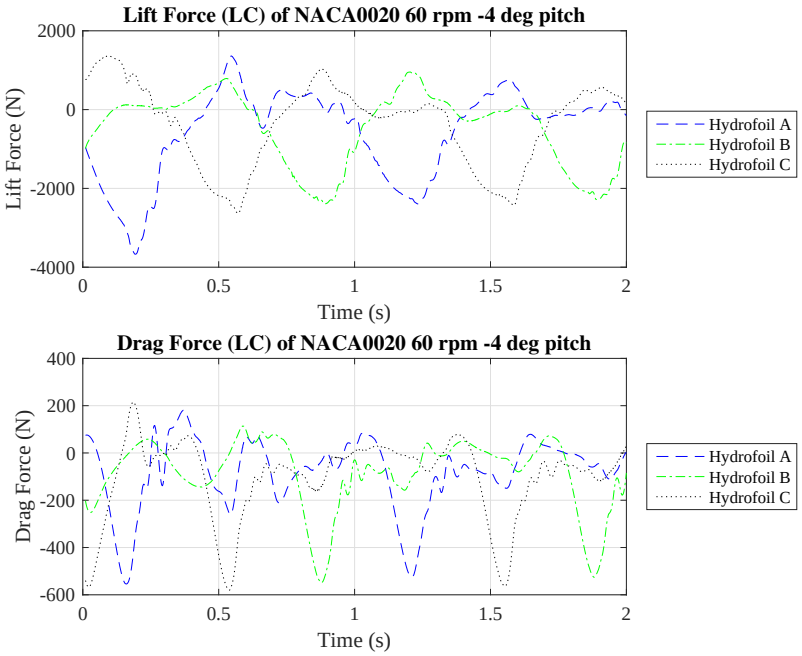

Figure A.168: Lift and Drag Force (LC) SIM24

A.1.25 SIM25

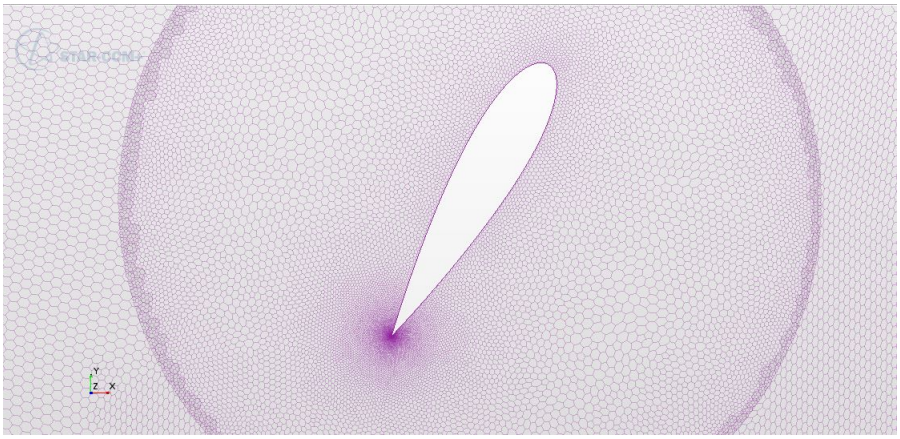

Figure A.169: Mesh SIM25

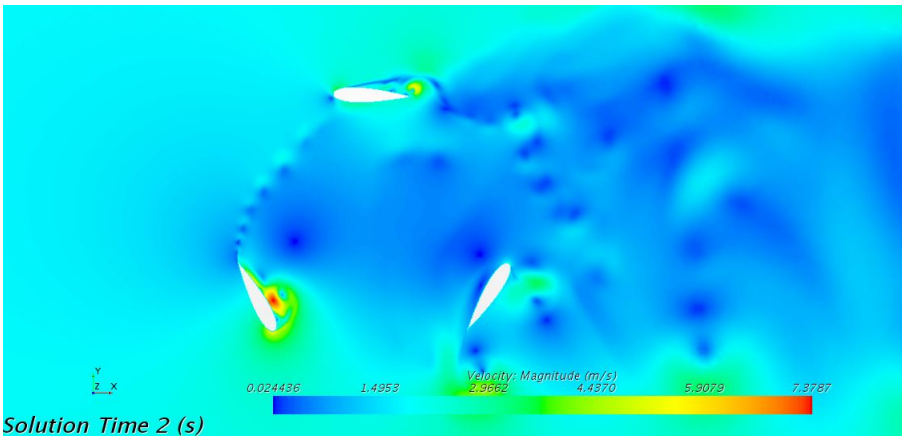

Figure A.170: Velocity SIM25

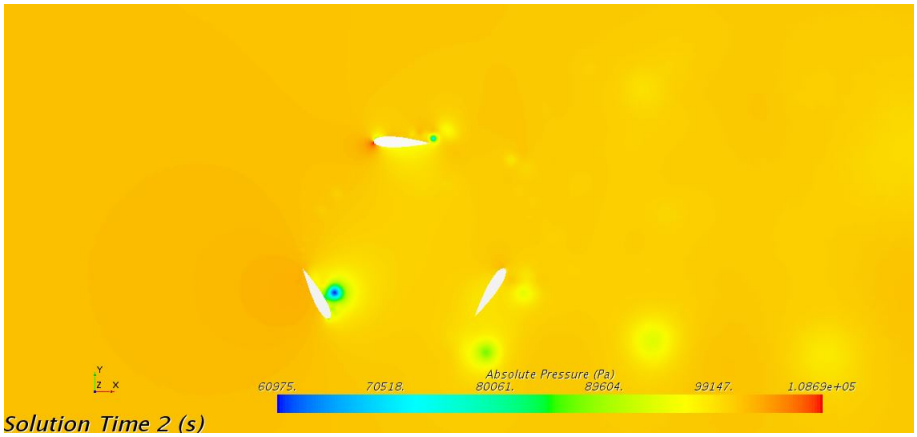

Figure A.171: Pressure SIM25

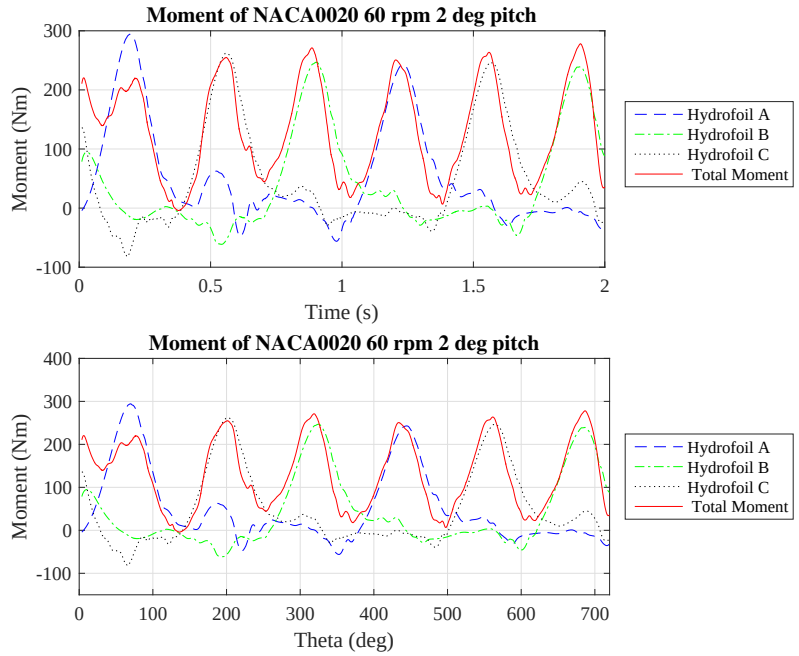

Figure A.172: Moment SIM25

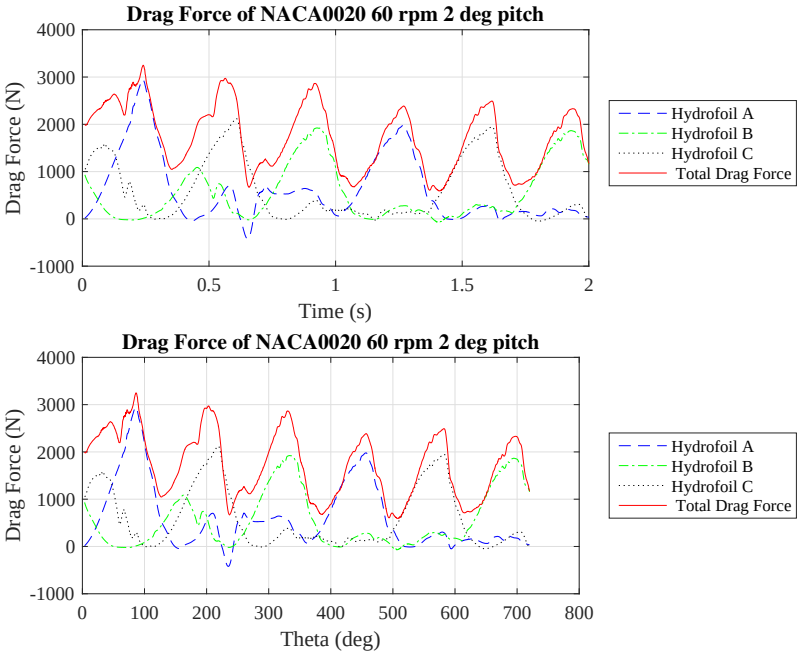

Figure A.173: Drag Force SIM25

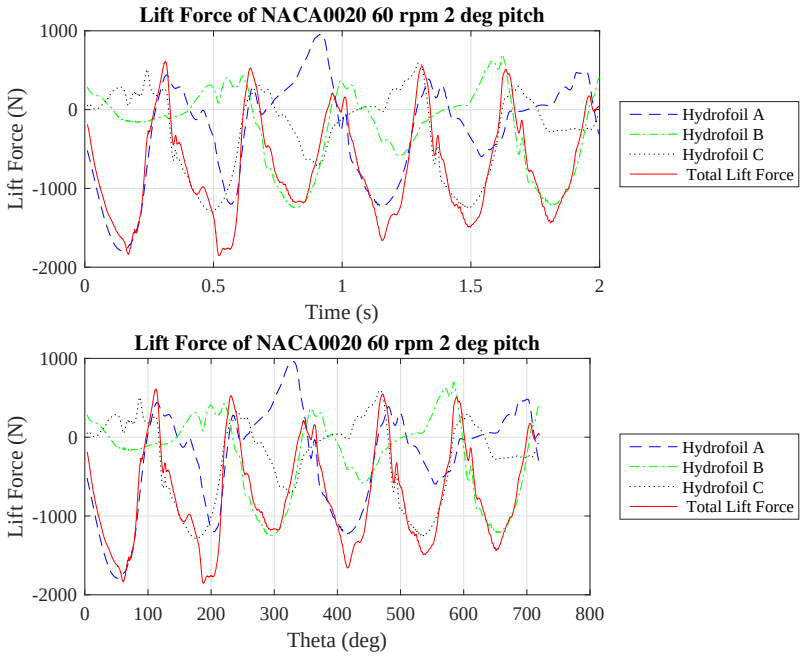

Figure A.174: Lift Force SIM25

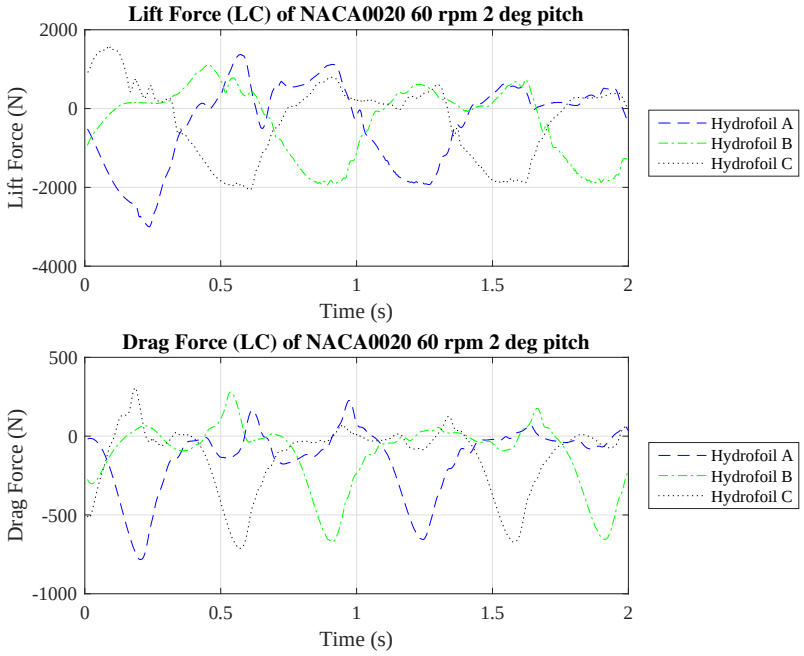

Figure A.175: Lift and Drag Force (LC) SIM25

A.1.26 SIM26

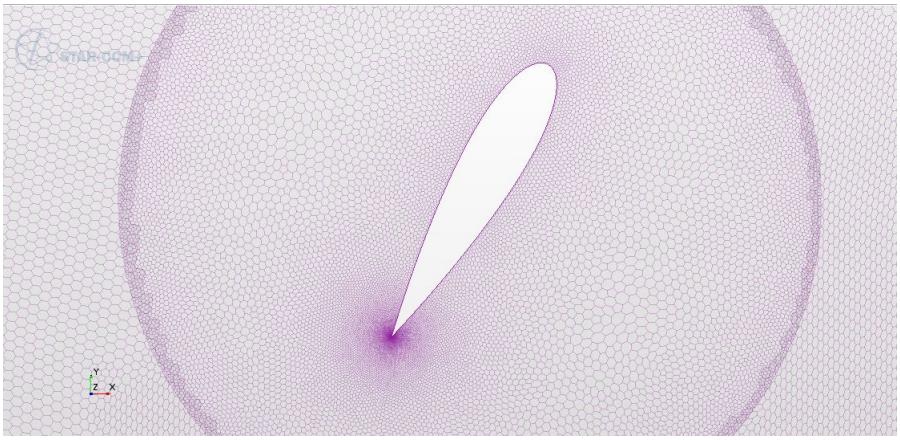

Figure A.176: Mesh SIM26

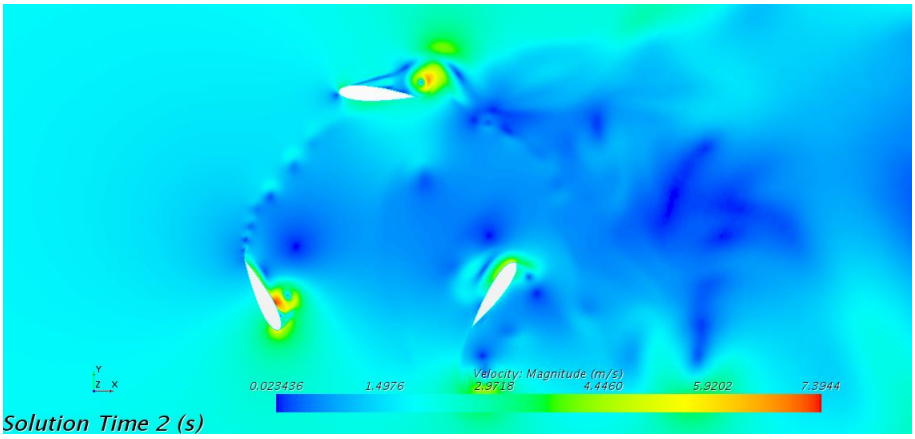

Figure A.177: Velocity SIM26

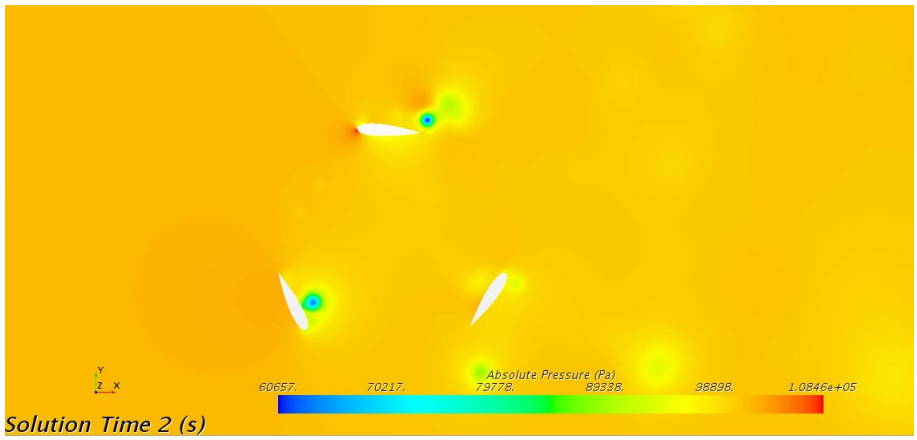

Figure A.178: Pressure SIM26

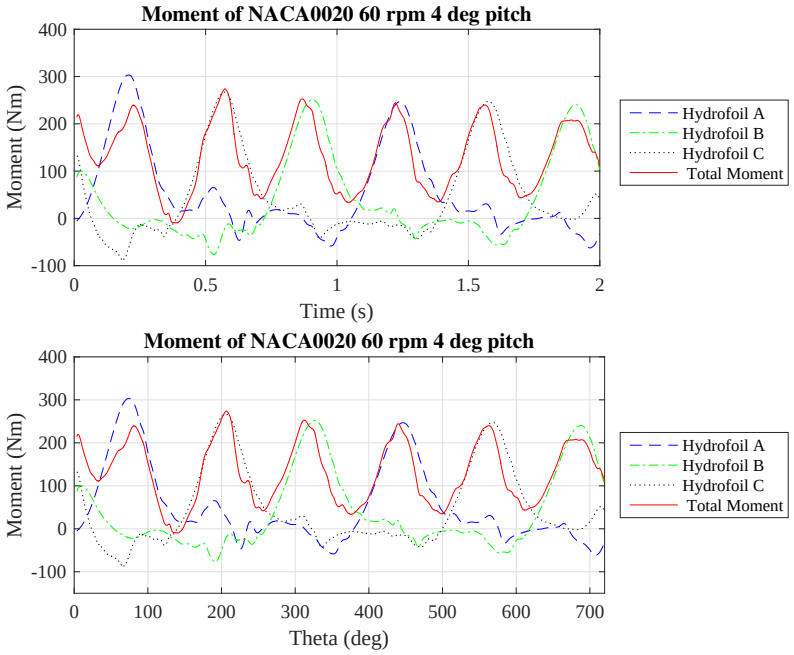

Figure A.179: Moment SIM26

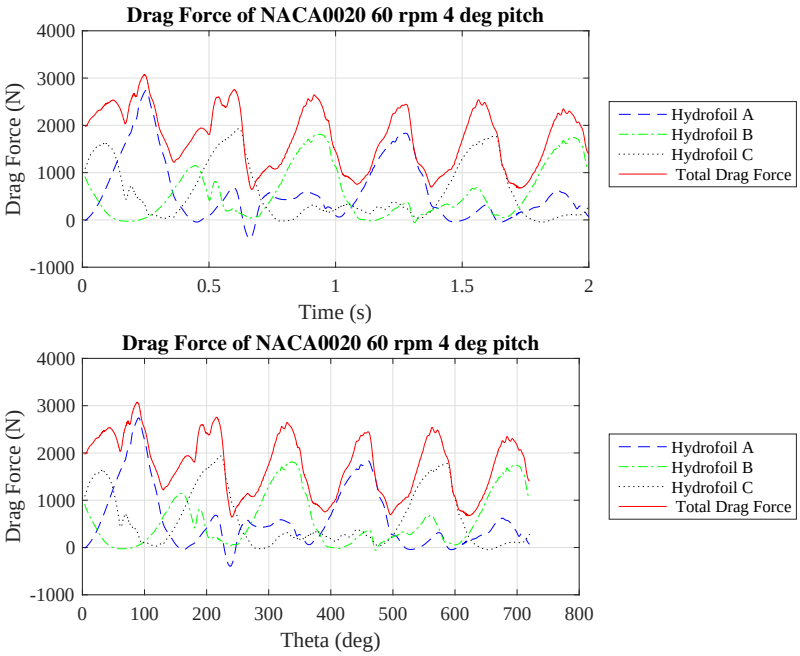

Figure A.180: Drag Force SIM26

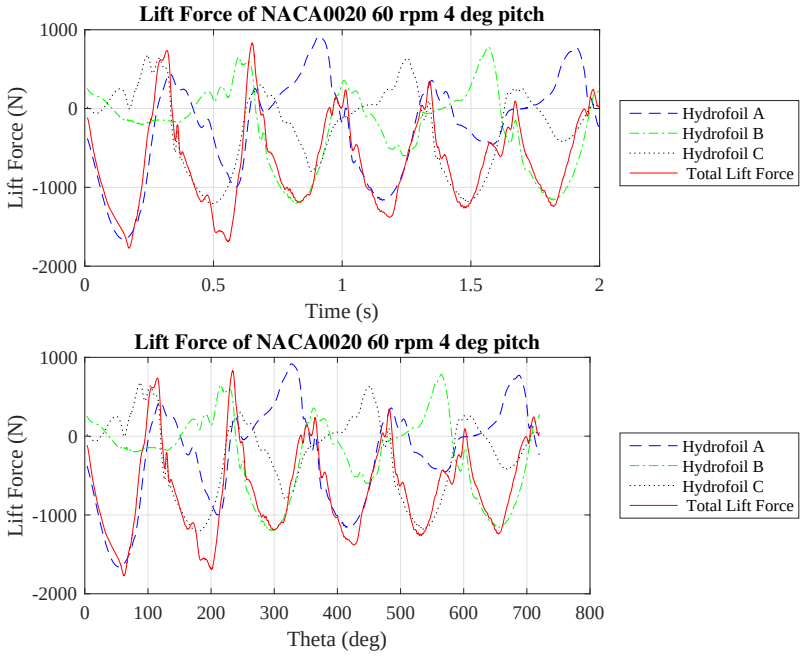

Figure A.181: Lift Force SIM26

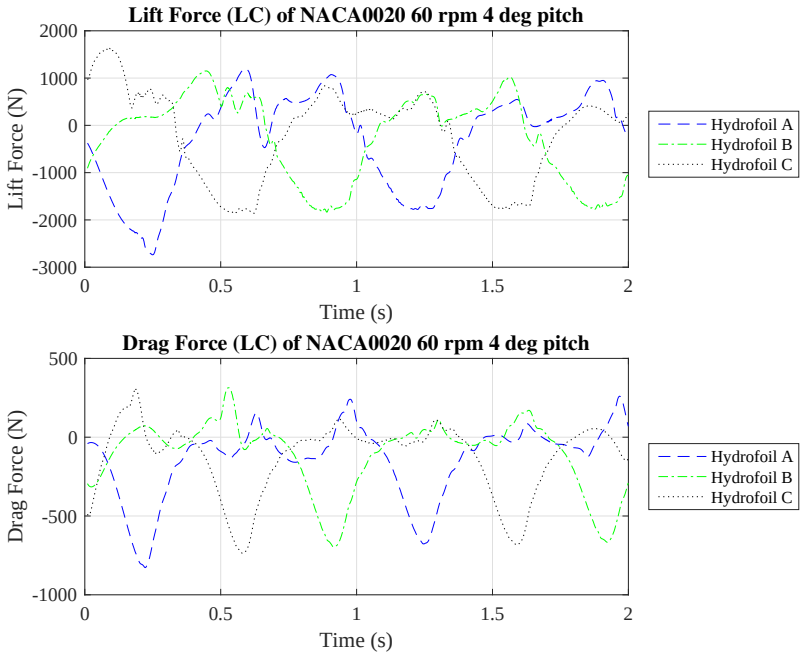

Figure A.182: Lift and Drag Force (LC) SIM26

A.1.27 SIM27

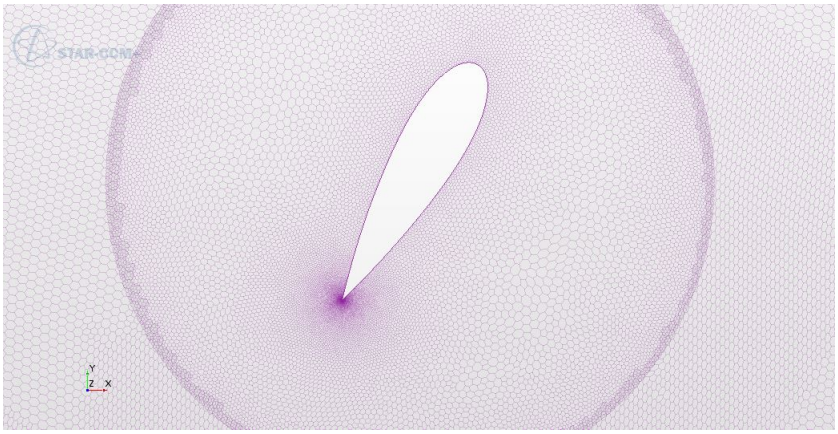

Figure A.183: Mesh SIM27

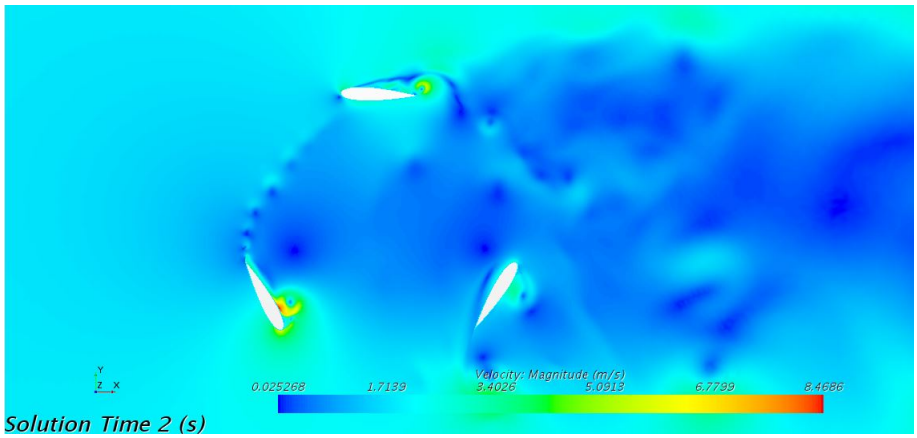

Figure A.184: Velocity SIM27

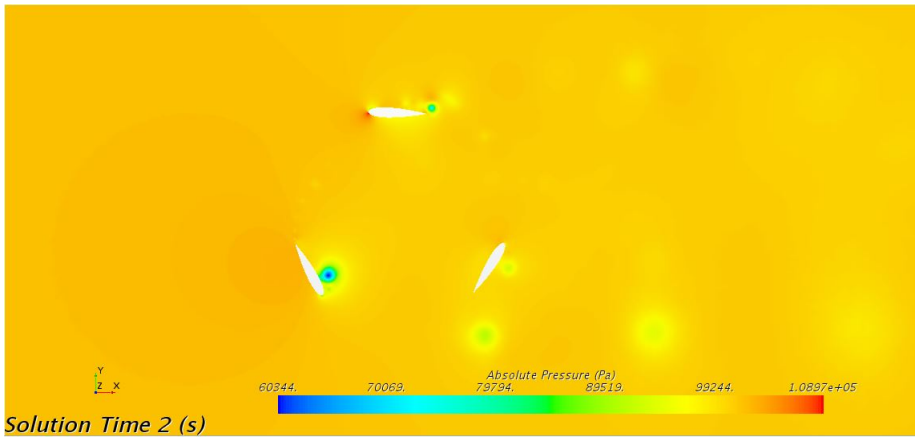

Figure A.185: Pressure SIM27

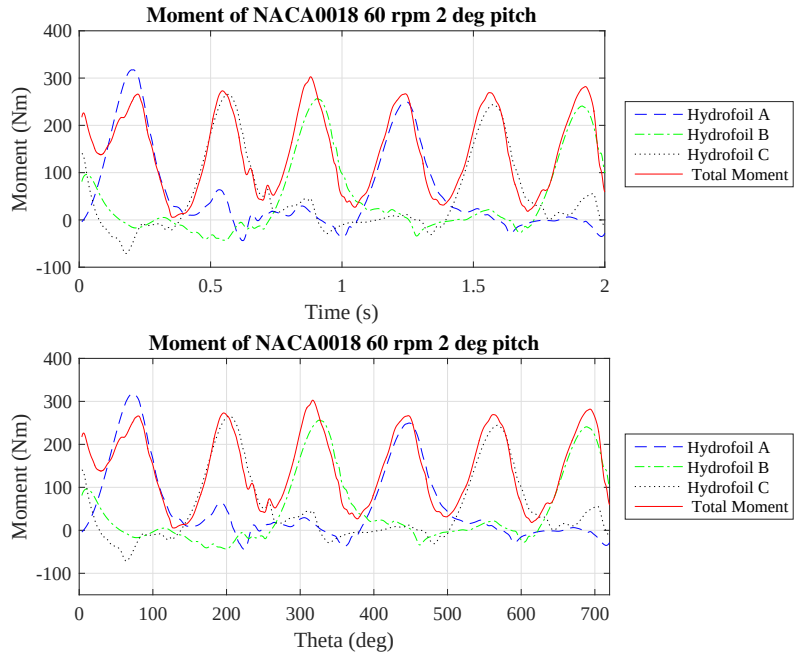

Figure A.186: Moment SIM27

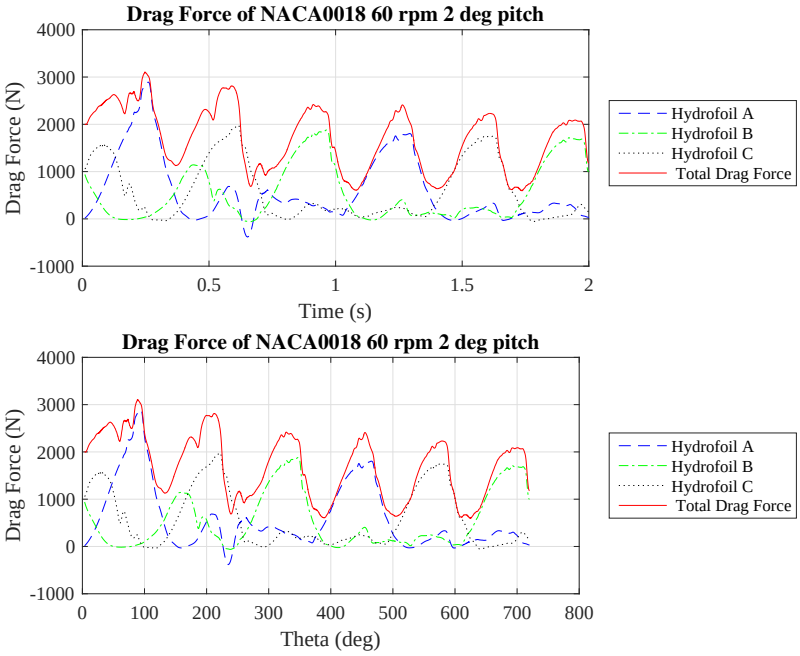

Figure A.187: Drag Force SIM27

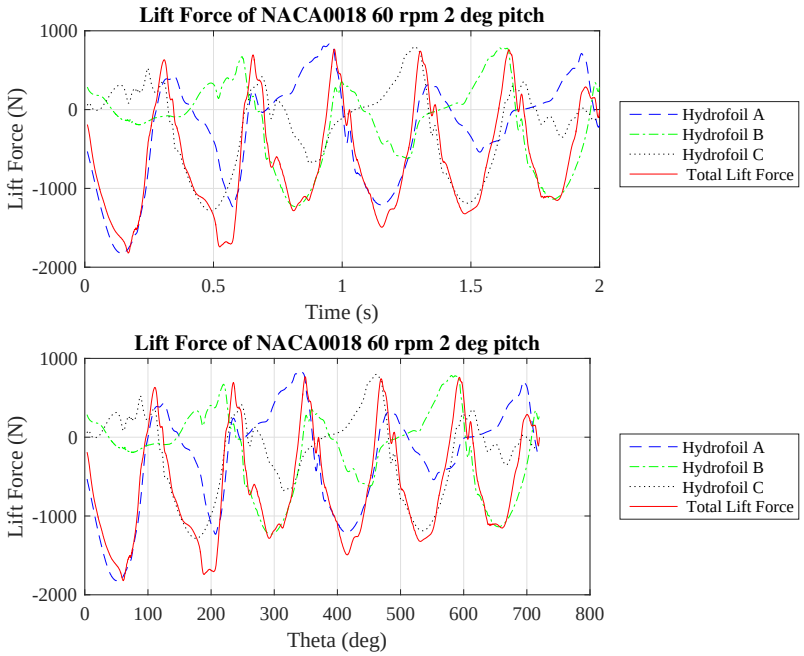

Figure A.188: Lift Force SIM27

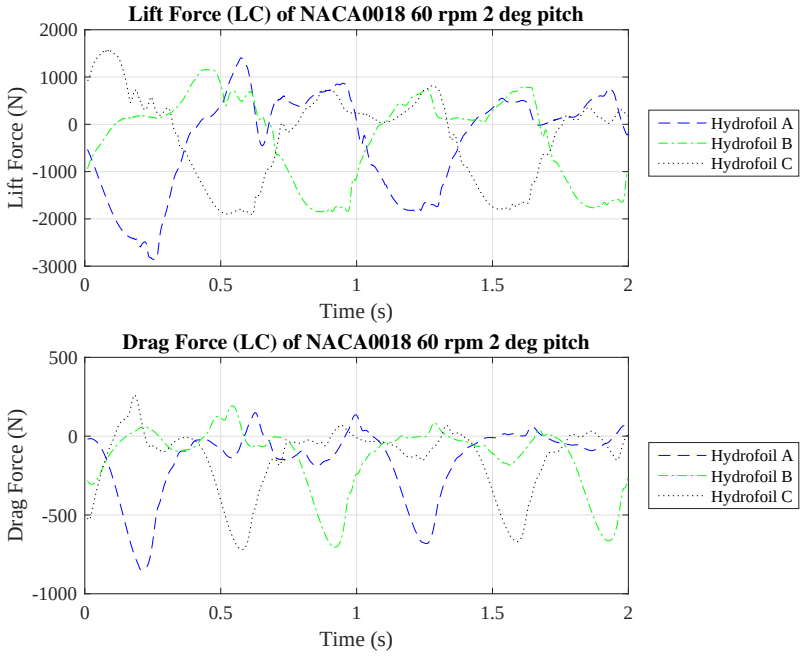

Figure A.189: Lift and Drag Force (LC) SIM27

A.1.28 SIM28

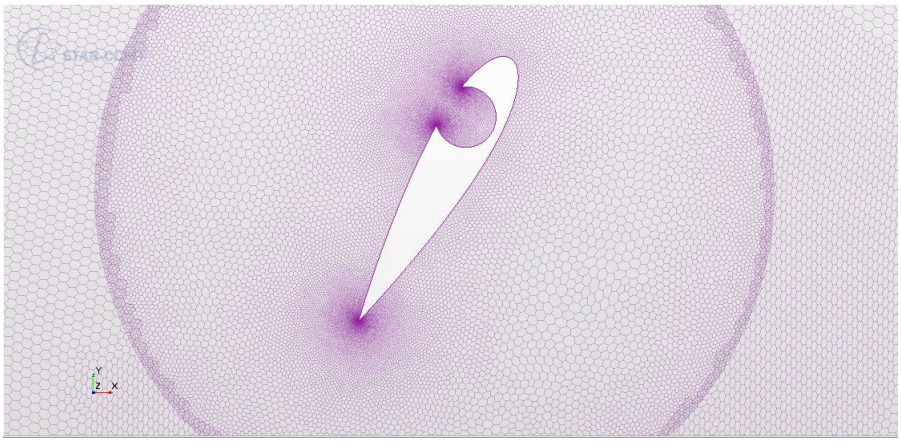

Figure A.190: Mesh SIM28

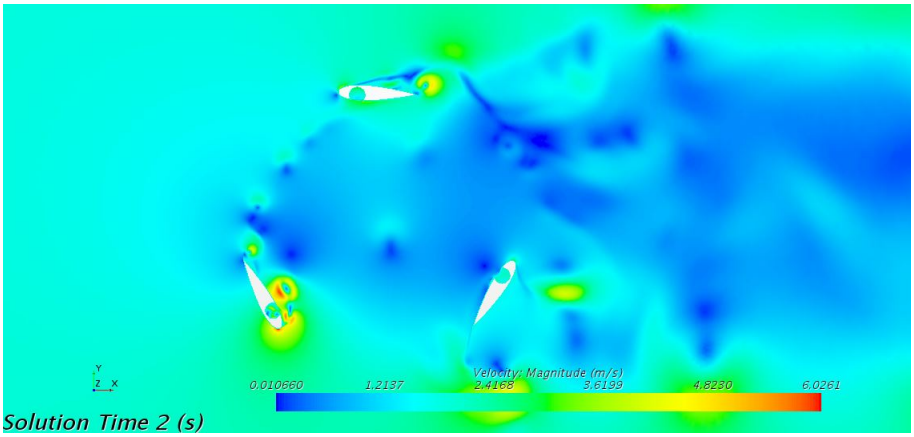

Figure A.191: Velocity SIM28

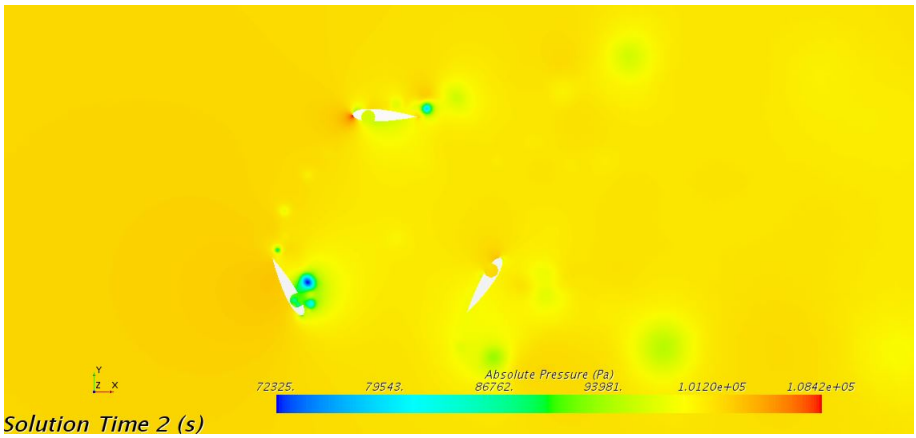

Figure A.192: Pressure SIM28

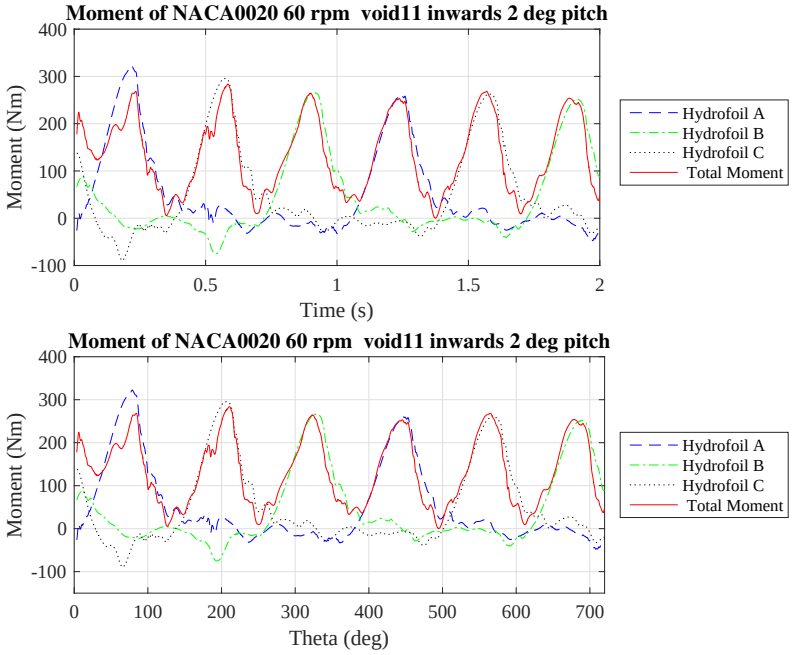

Figure A.193: Moment SIM28

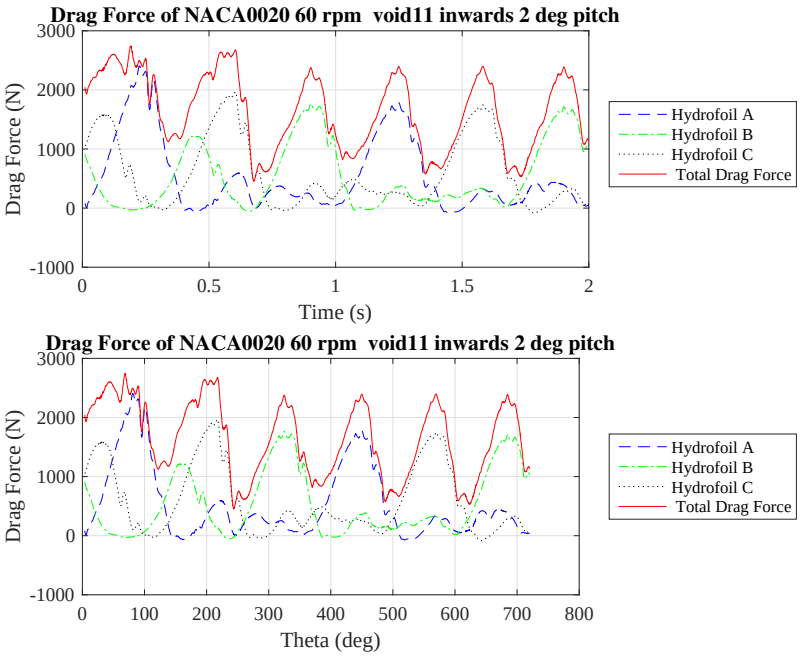

Figure A.194: Drag Force SIM28

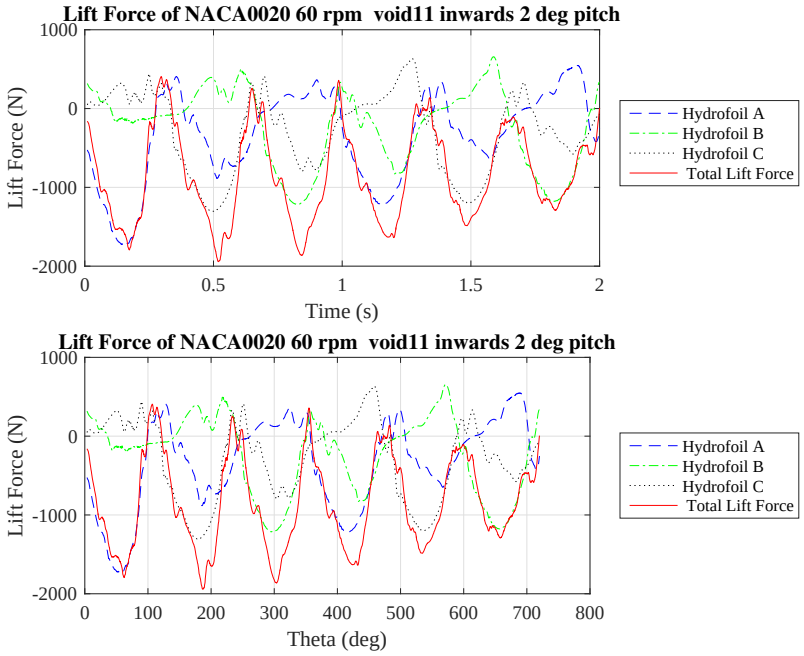

Figure A.195: Lift Force SIM28

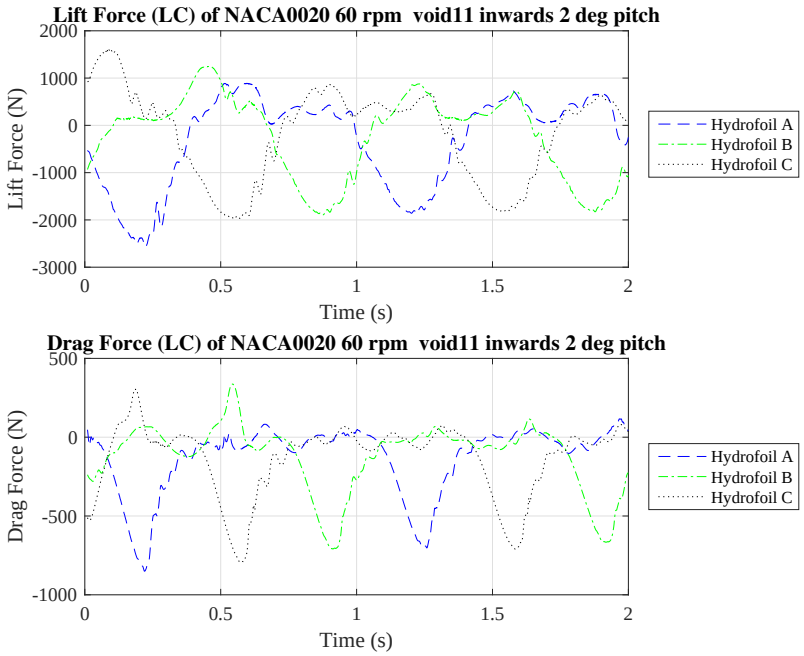

Figure A.196: Lift and Drag Force (LC) SIM28

A.1.29 SIM29

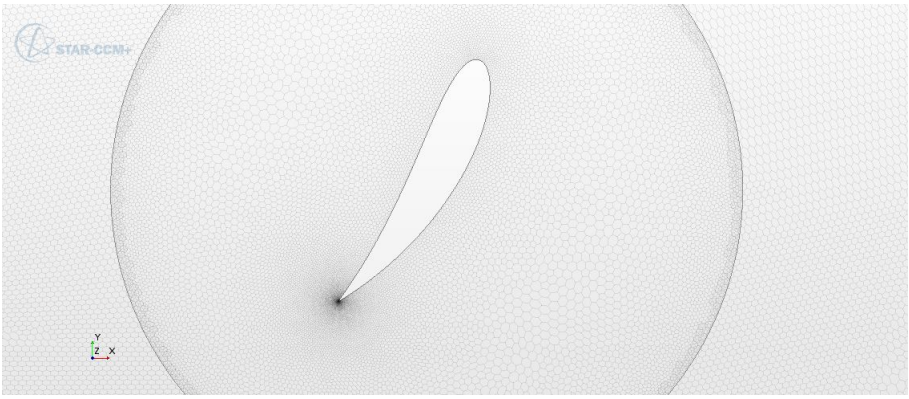

Figure A.197: Mesh SIM29

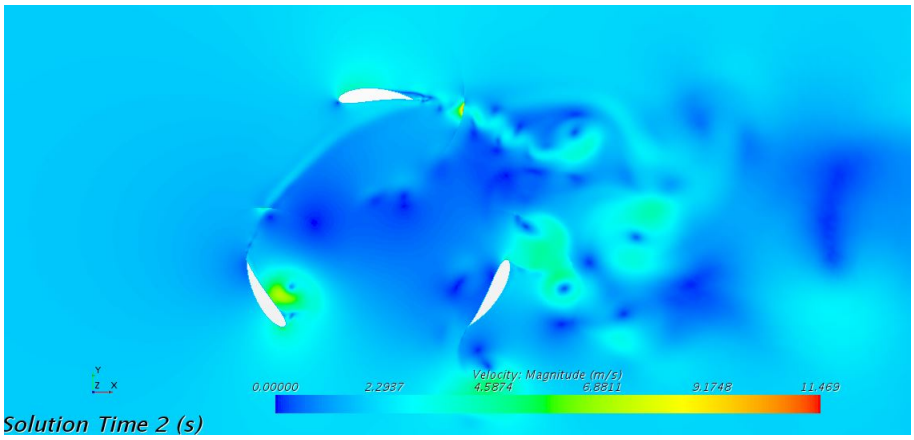

Figure A.198: Velocity SIM29

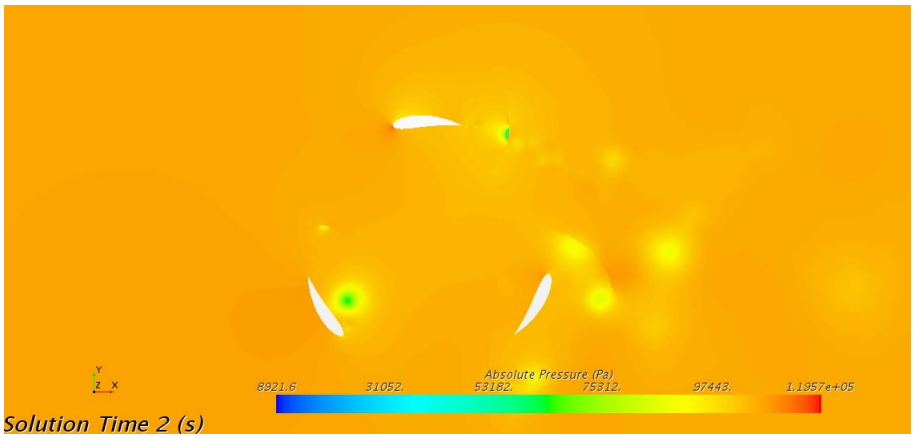

Figure A.199: Pressure SIM29

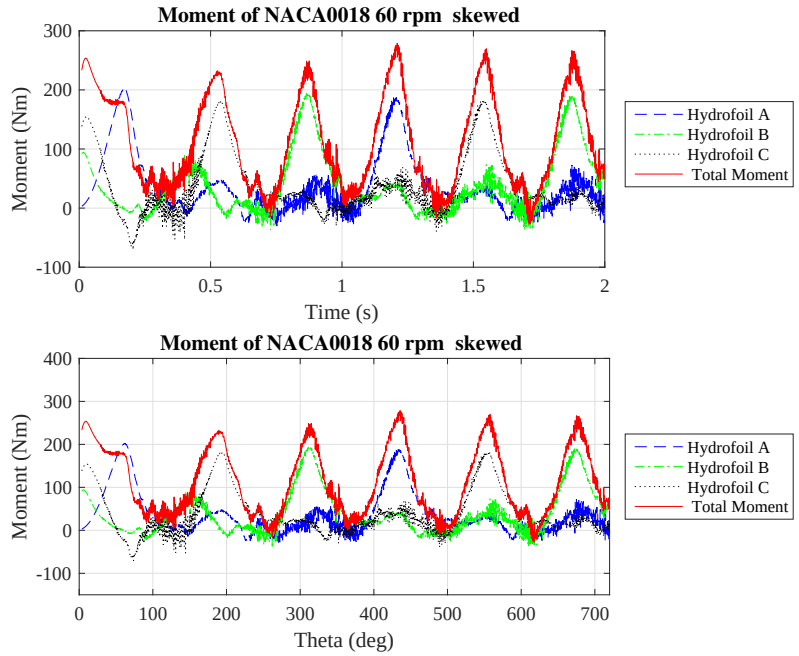

Figure A.200: Moment SIM29

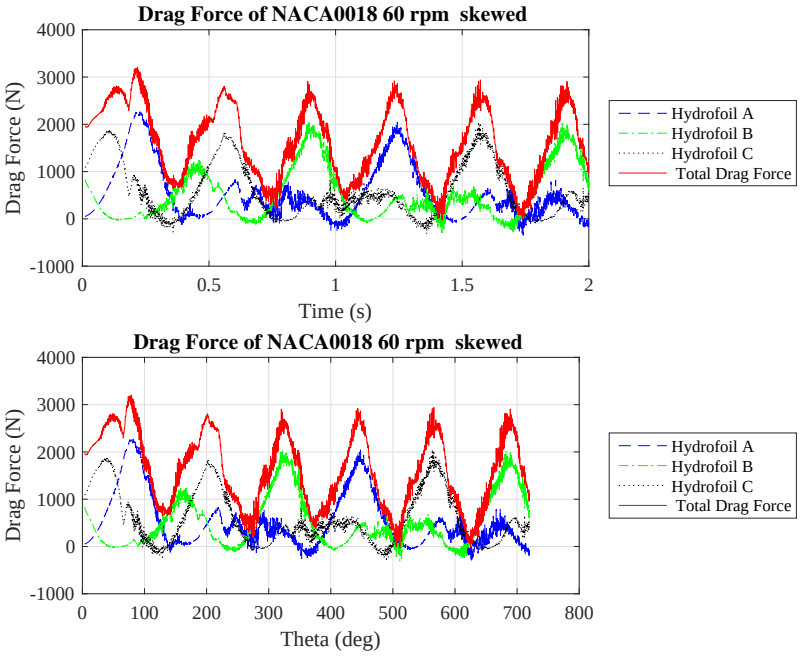

Figure A.201: Drag Force SIM29

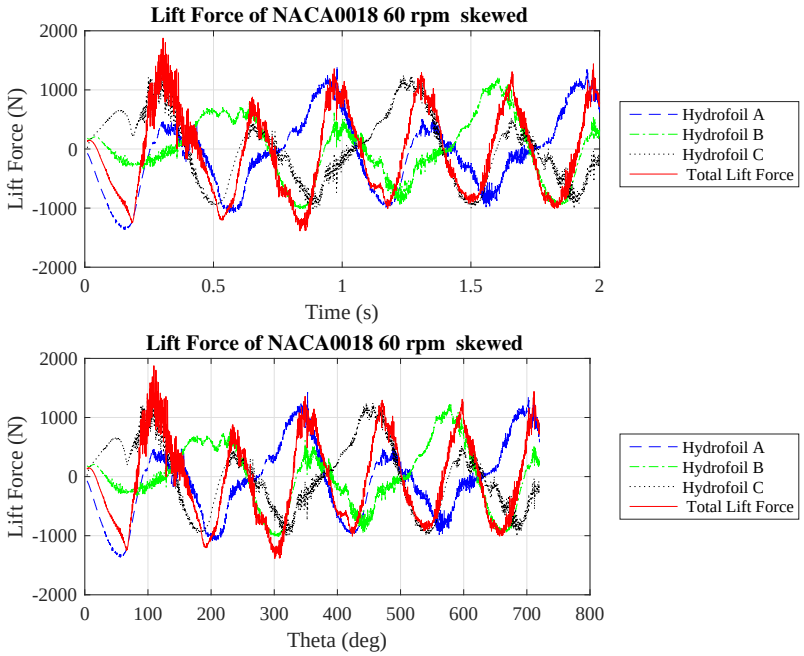

Figure A.202: Lift Force SIM29

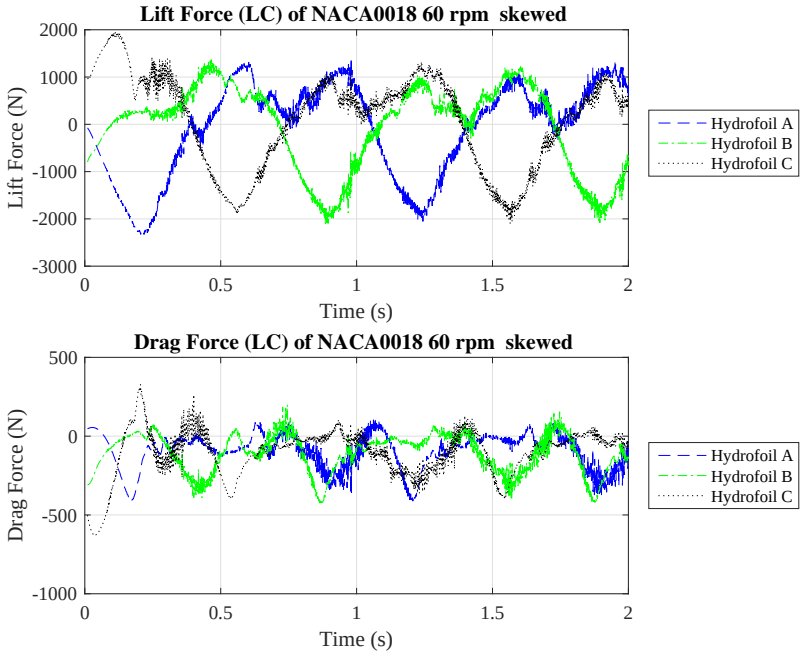

Figure A.203: Lift and Drag Force (LC) SIM29

A.1.30 SIM30

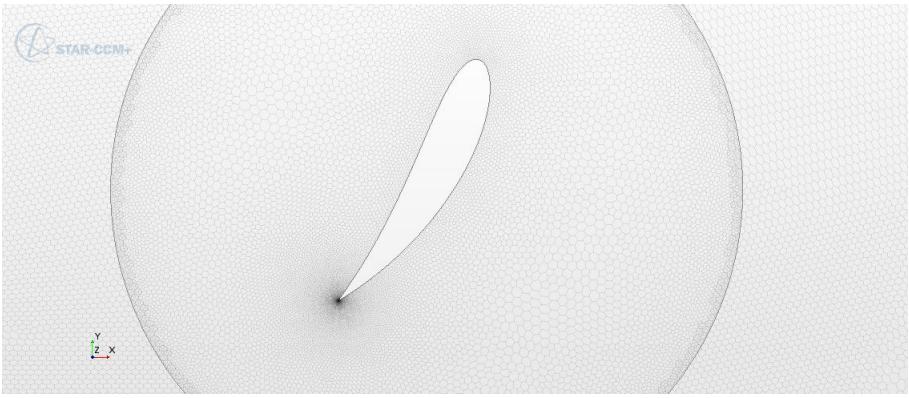

Figure A.204: Mesh SIM30

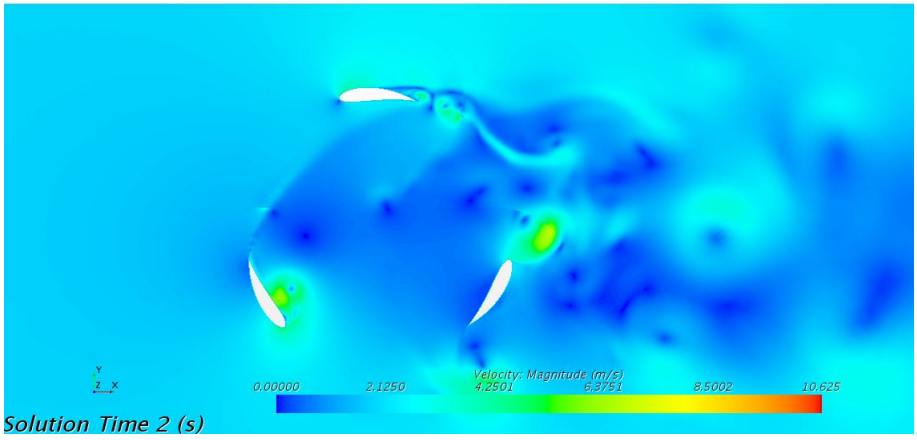

Figure A.205: Velocity SIM30

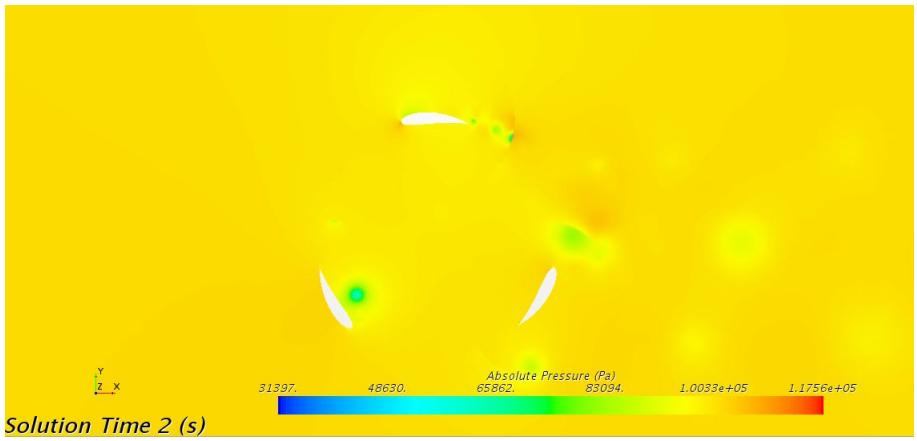

Figure A.206: Pressure SIM30

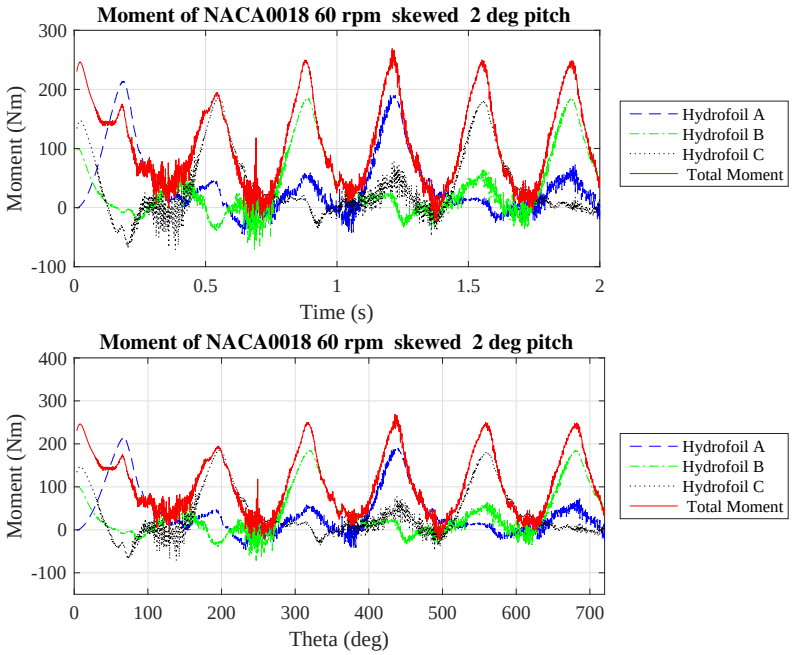

Figure A.207: Moment SIM30

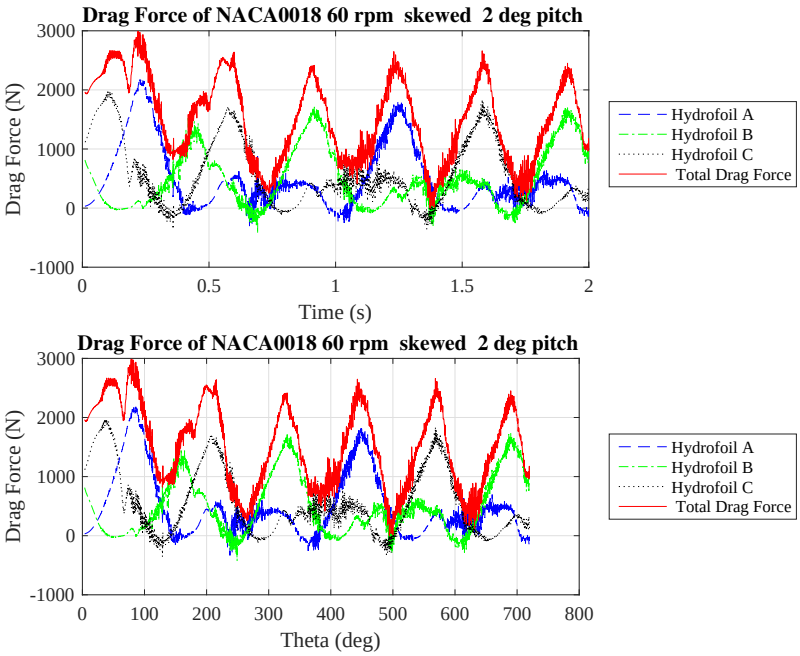

Figure A.208: Drag Force SIM30

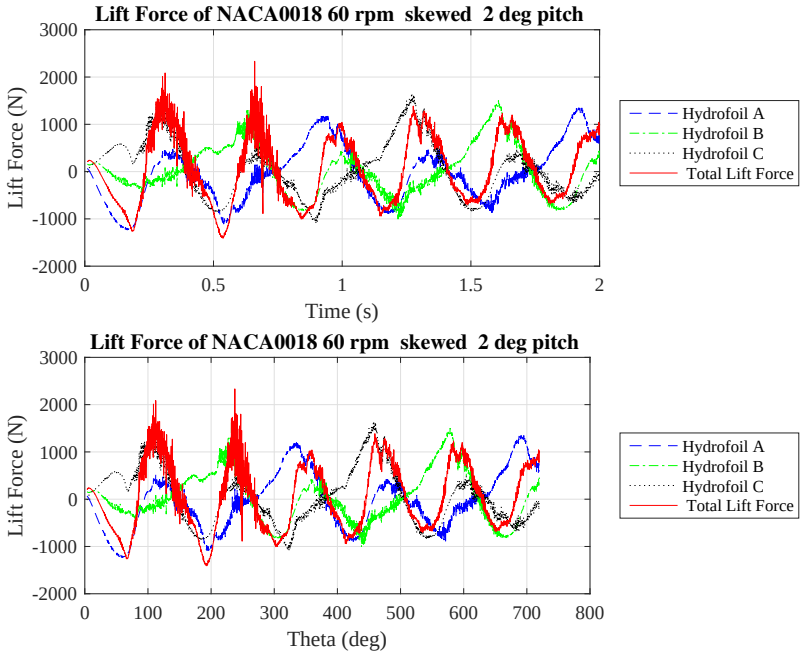

Figure A.209: Lift Force SIM30

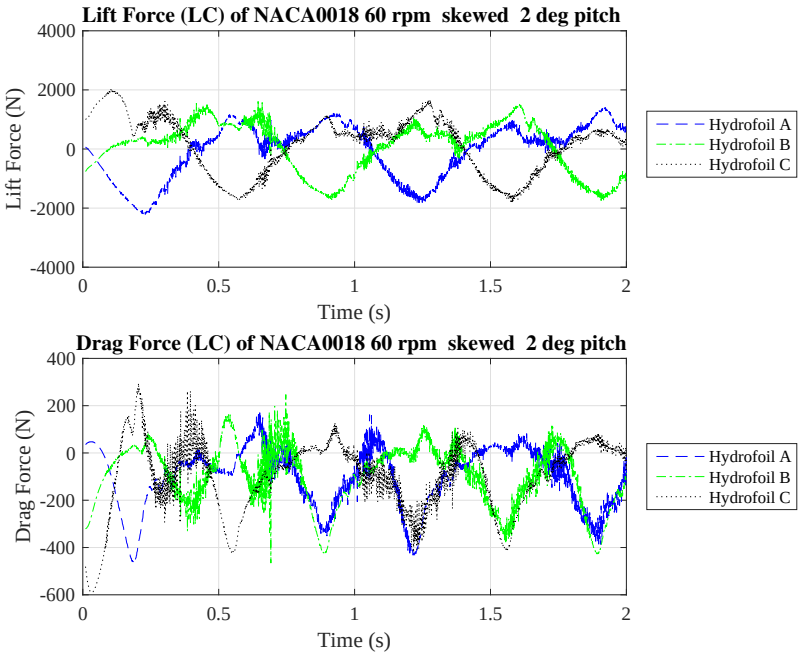

Figure A.210: Lift and Drag Force (LC) SIM30

A.1.31 SIM31

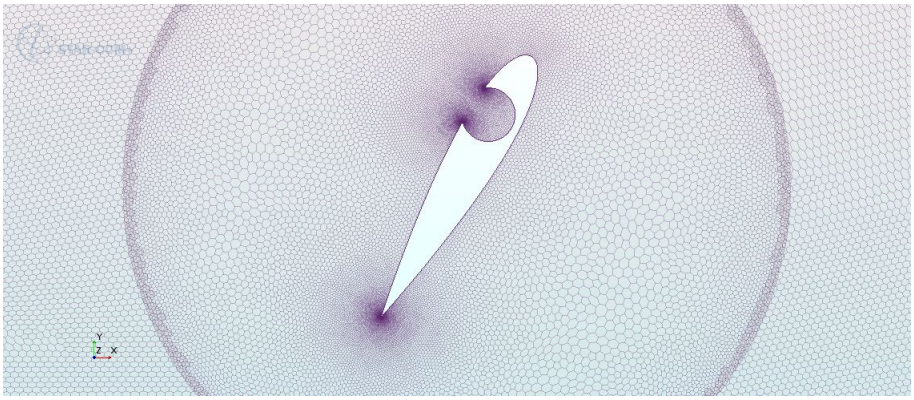

Figure A.211: Mesh SIM31

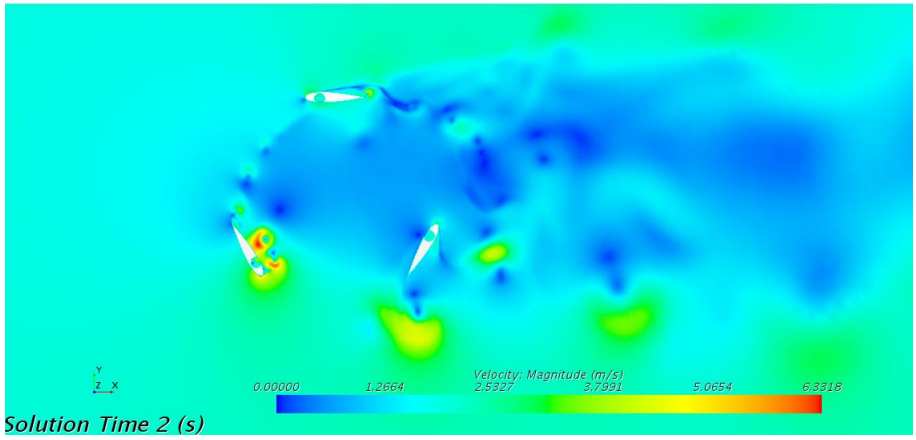

Figure A.212: Velocity SIM31

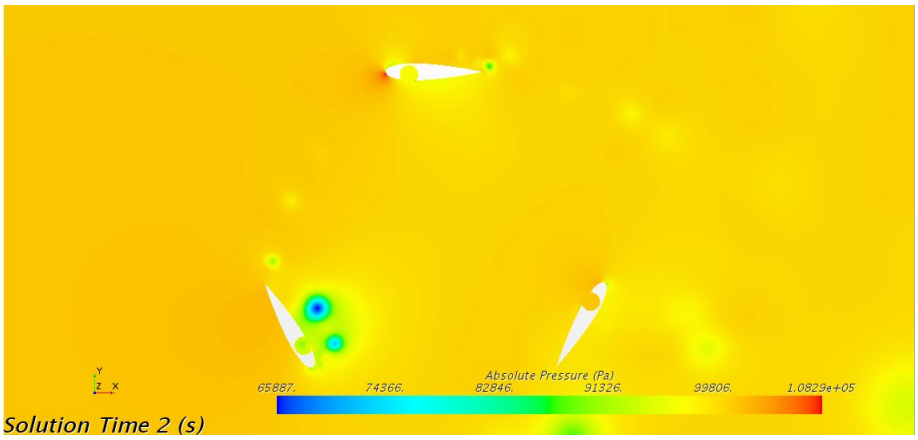

Figure A.213: Pressure SIM31

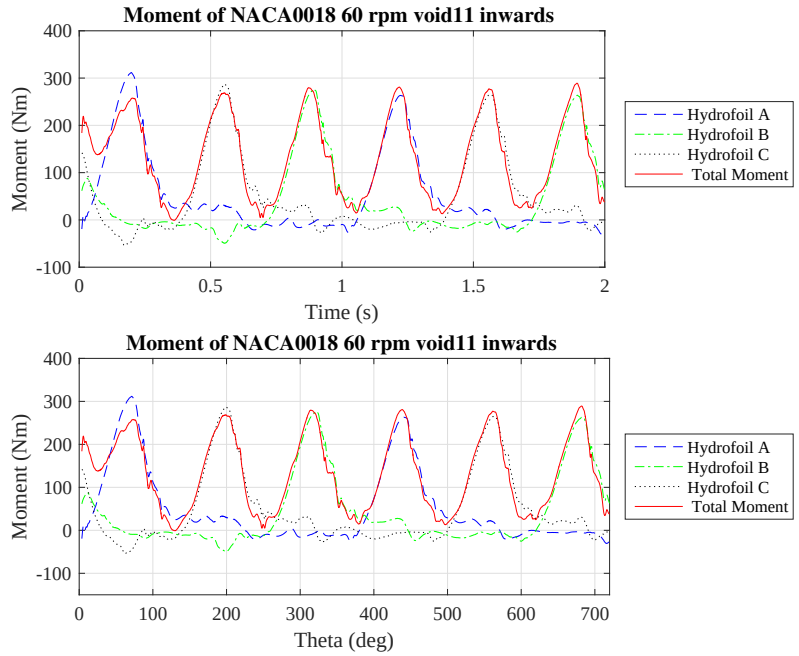

Figure A.214: Moment SIM31

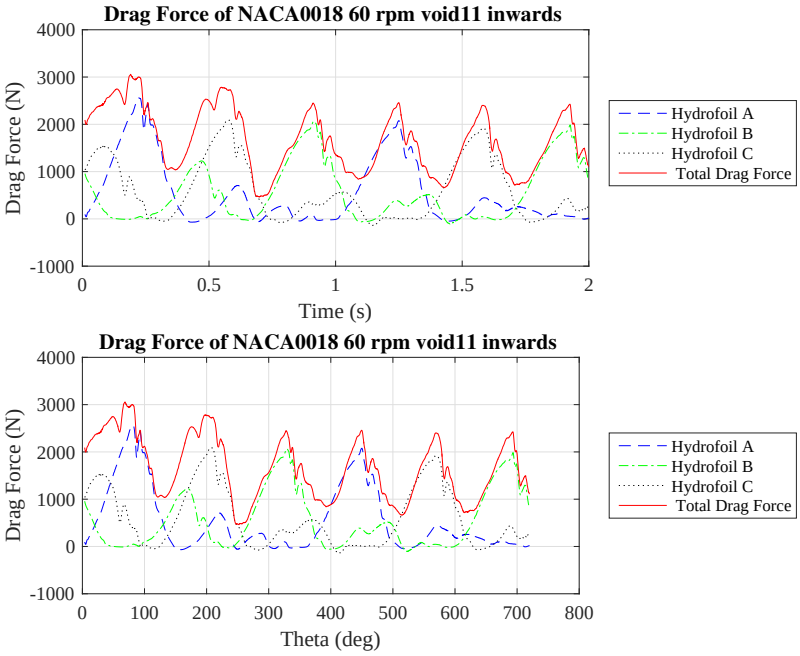

Figure A.215: Drag Force SIM31

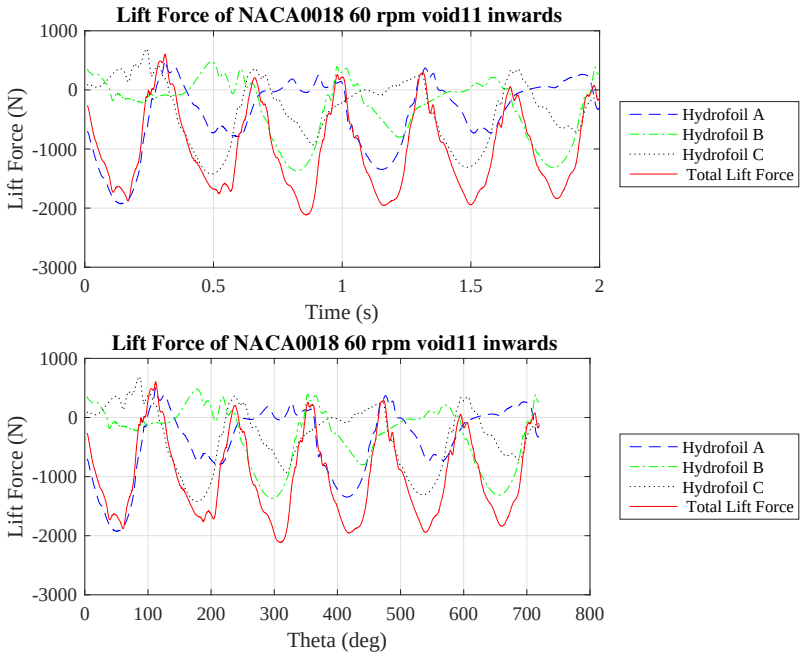

Figure A.216: Lift Force SIM31

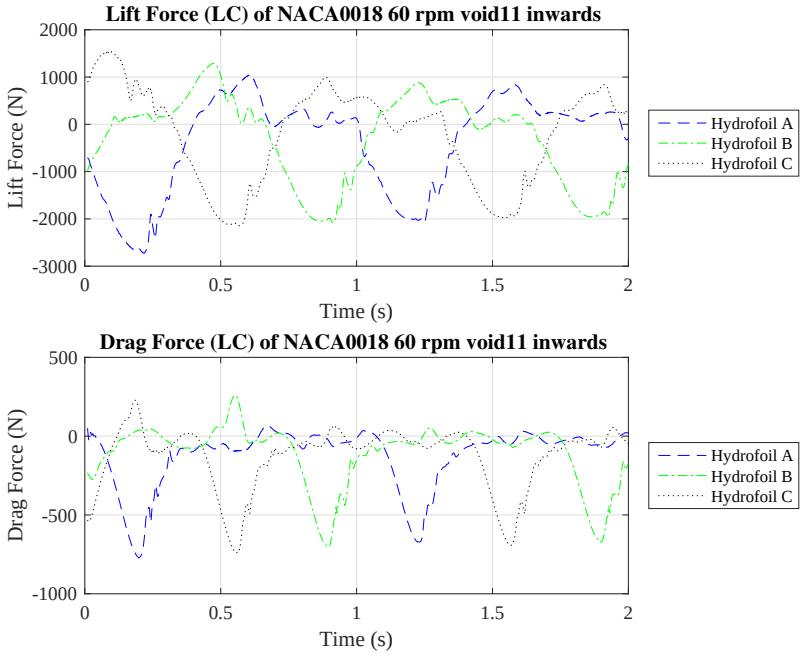

Figure A.217: Lift and Drag Force (LC) SIM31

A.1.32 SIM32

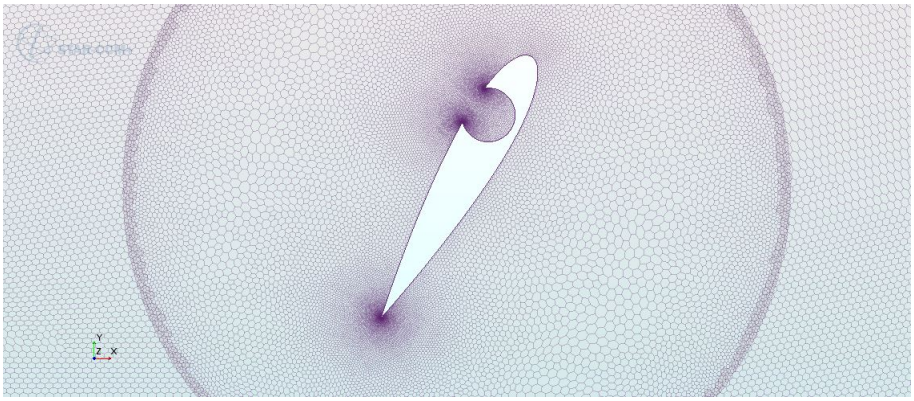

Figure A.218: Mesh SIM32

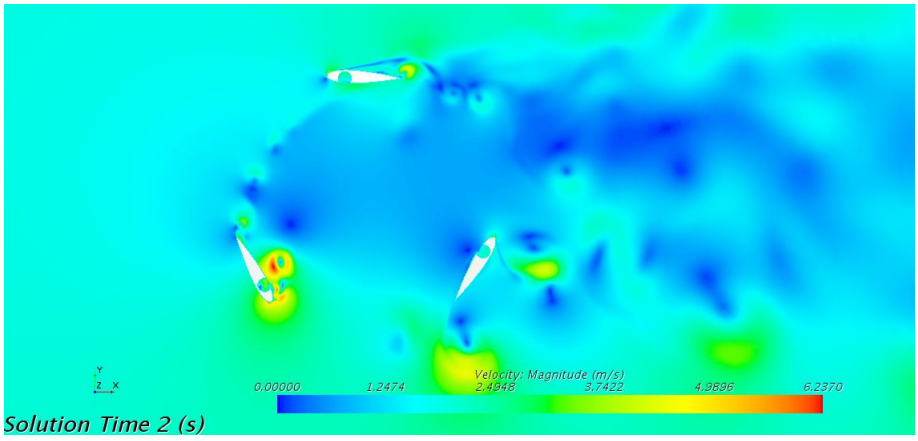

Figure A.219: Velocity SIM32

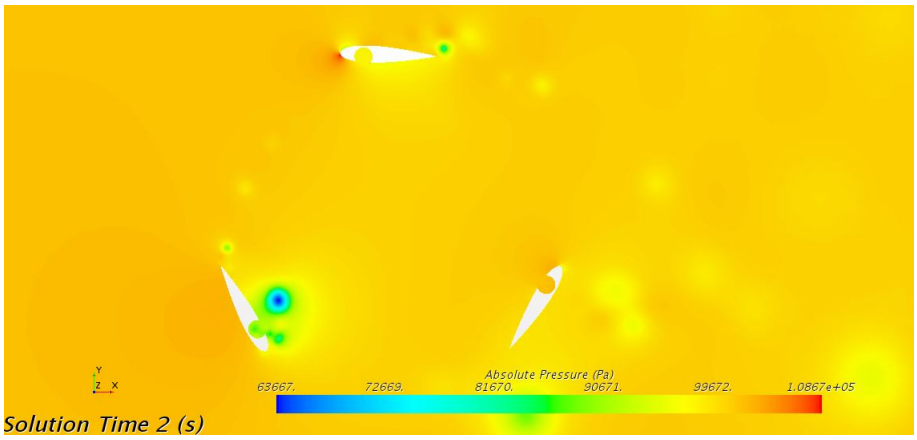

Figure A.220: Pressure SIM32

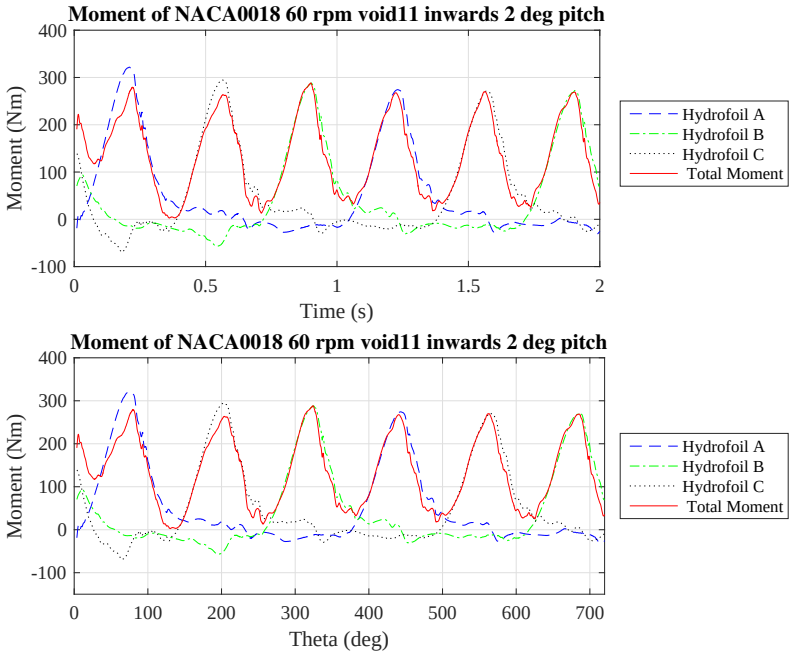

Figure A.221: Moment SIM32

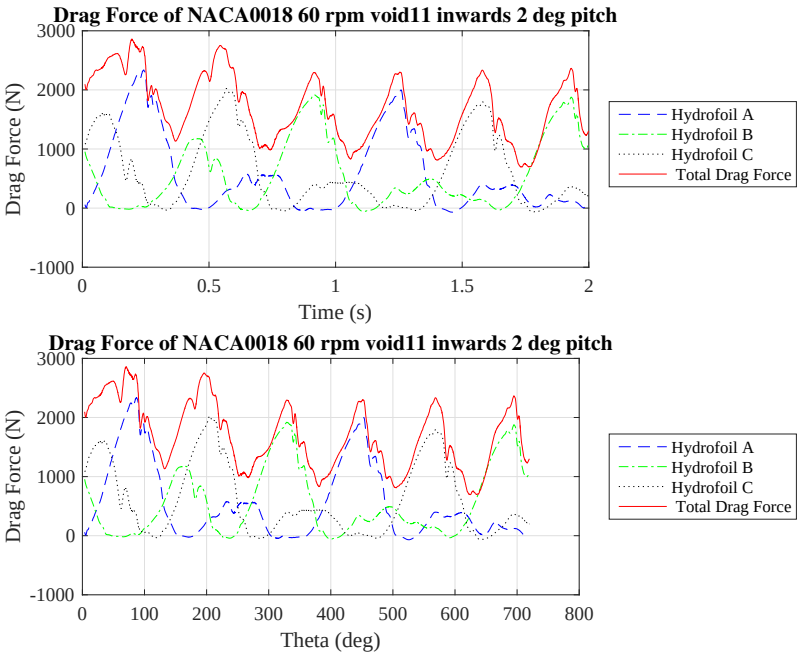

Figure A.222: Drag Force SIM32

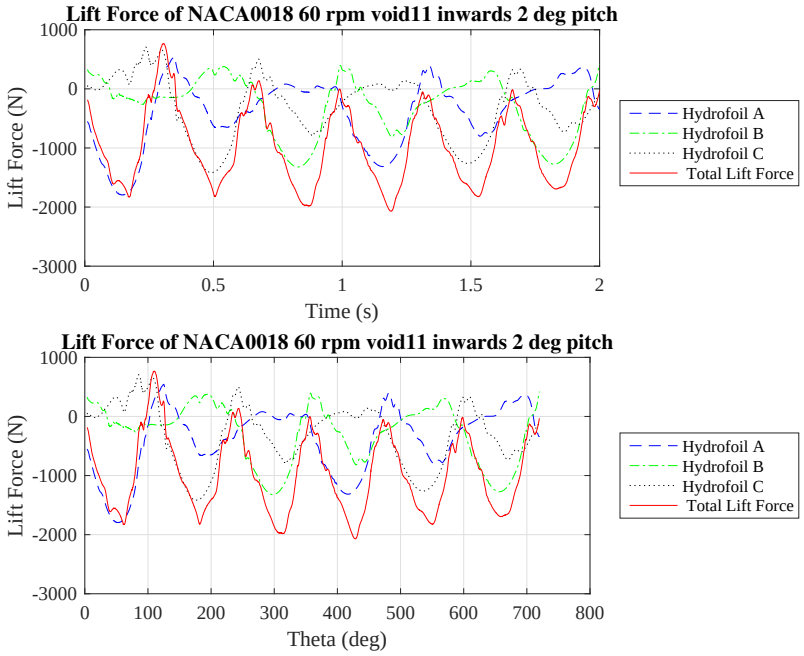

Figure A.223: Lift Force SIM32

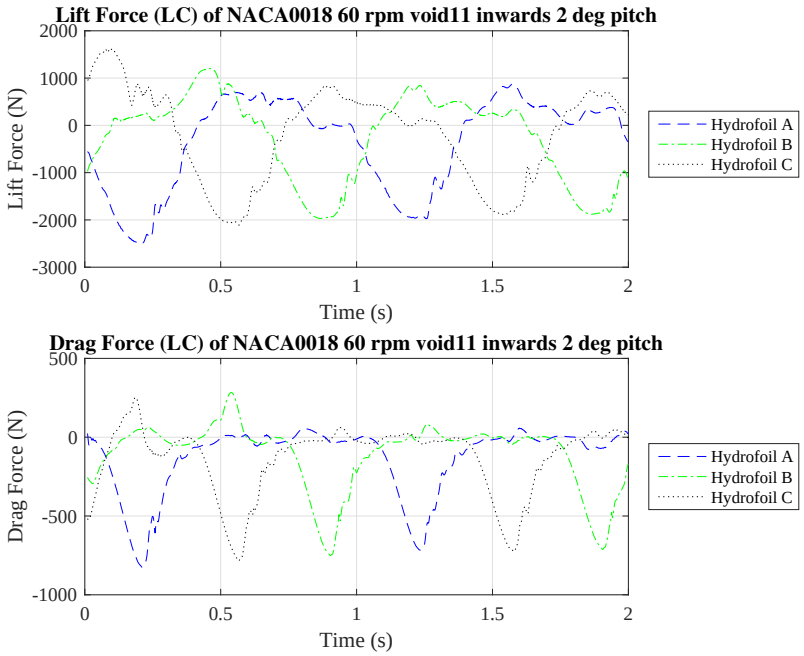

Figure A.224: Lift and Drag Force (LC) SIM32

A.1.33 SIM33

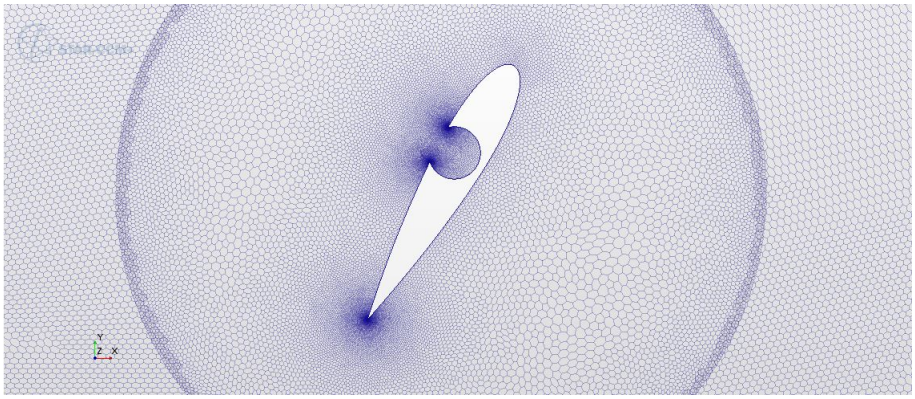

Figure A.225: Mesh SIM33

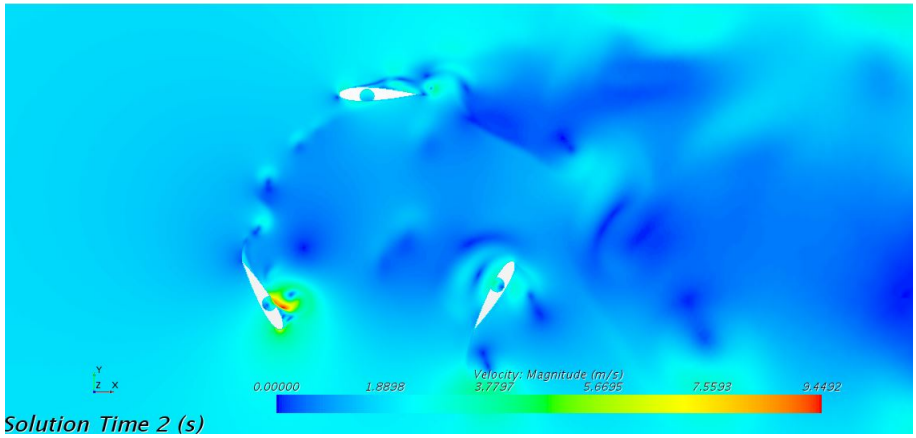

Figure A.226: Velocity SIM33

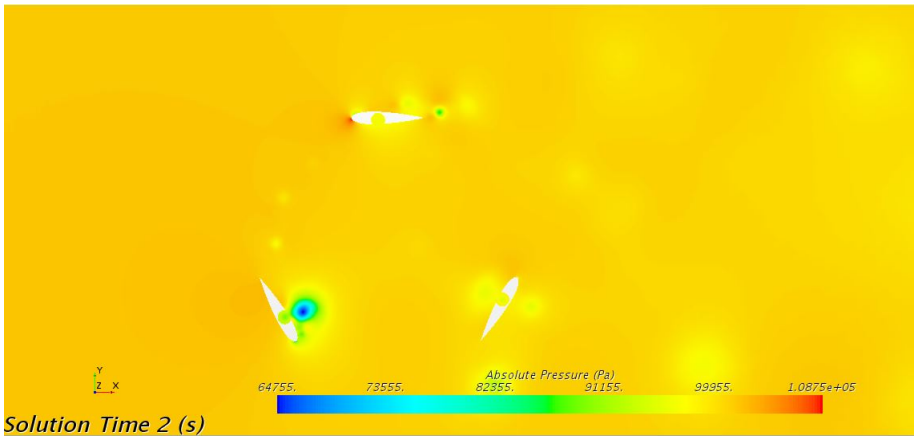

Figure A.227: Pressure SIM33

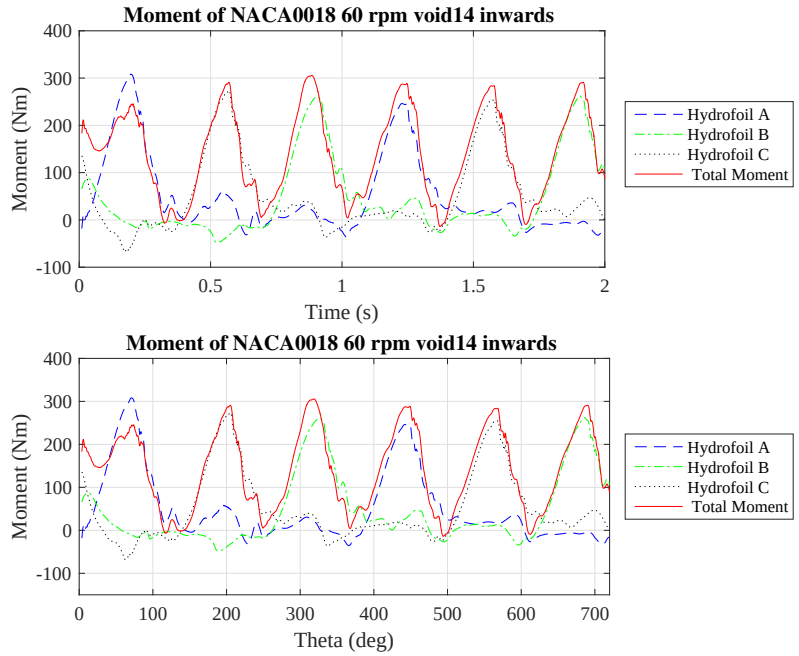

Figure A.228: Moment SIM33

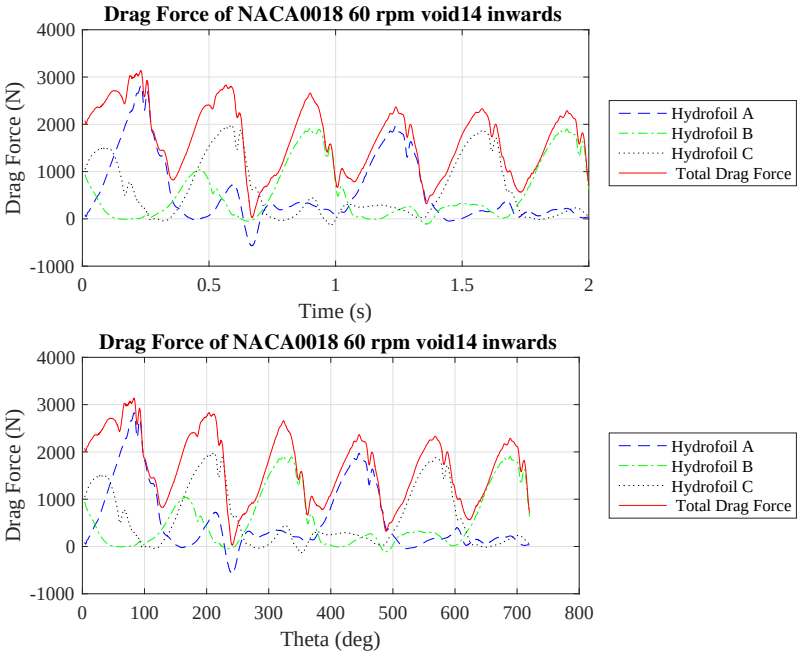

Figure A.229: Drag Force SIM33

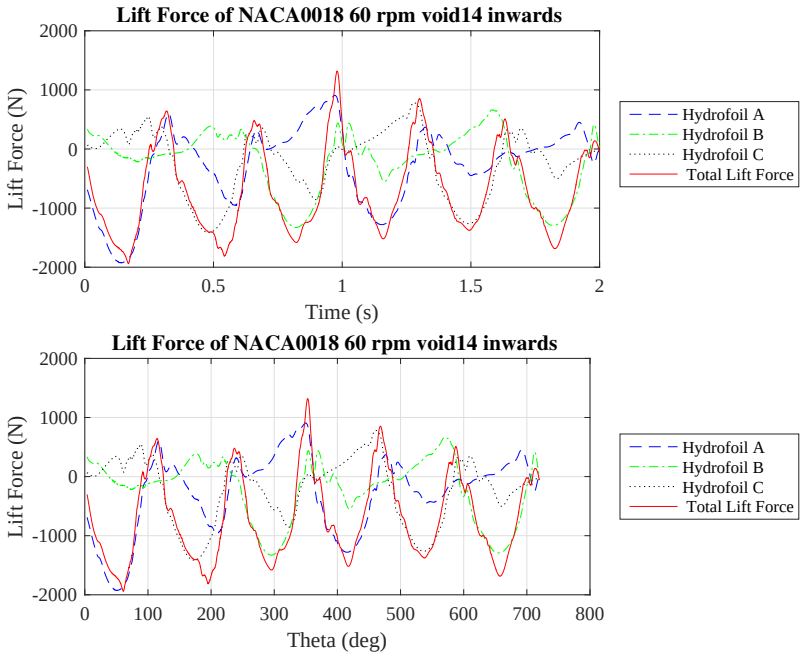

Figure A.230: Lift Force SIM33

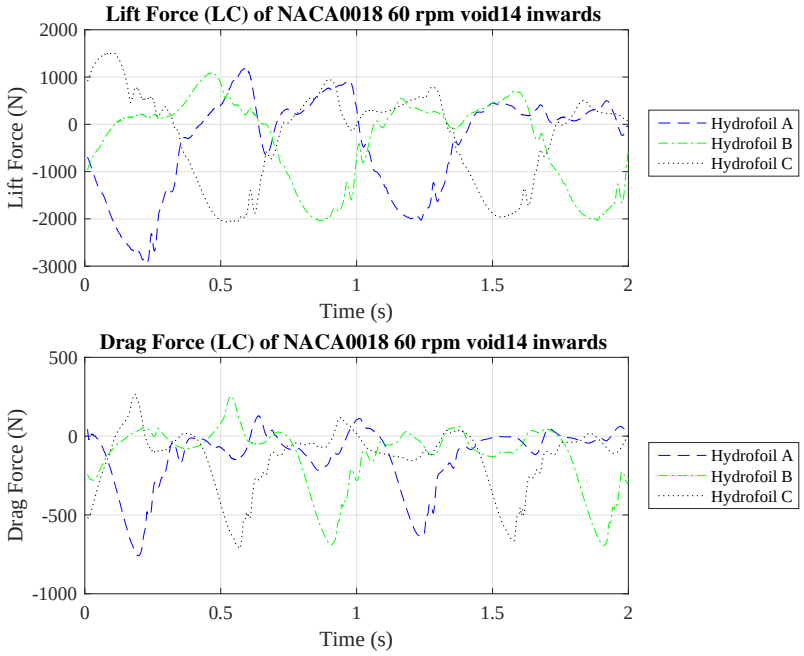

Figure A.231: Lift and Drag Force (LC) SIM33

A.1.34 SIM34

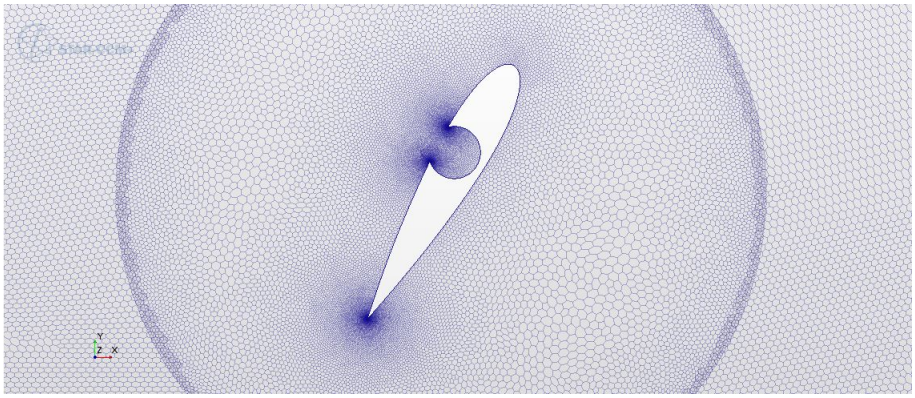

Figure A.232: Mesh SIM34

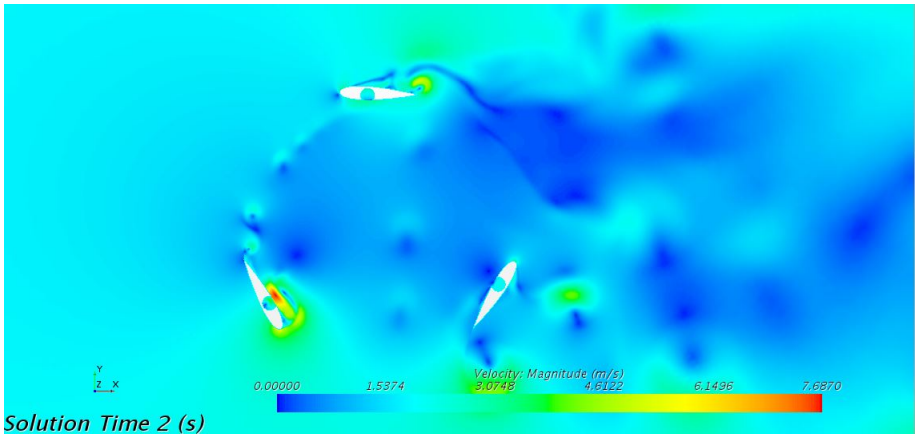

Figure A.233: Velocity SIM34

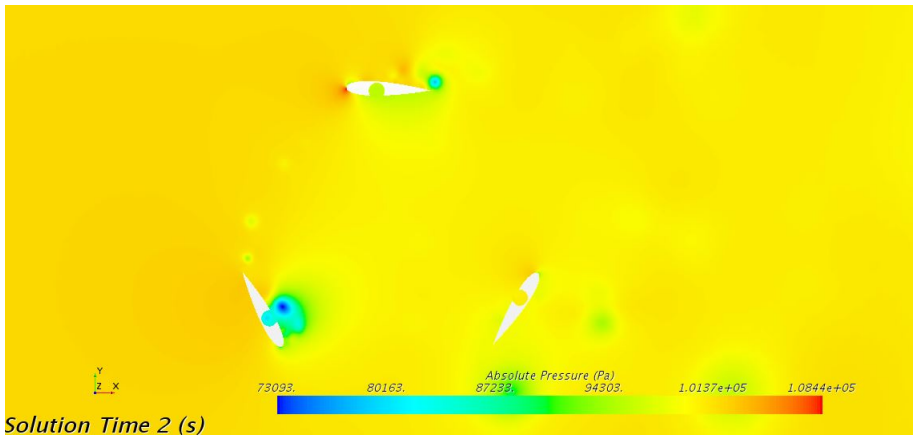

Figure A.234: Pressure SIM34

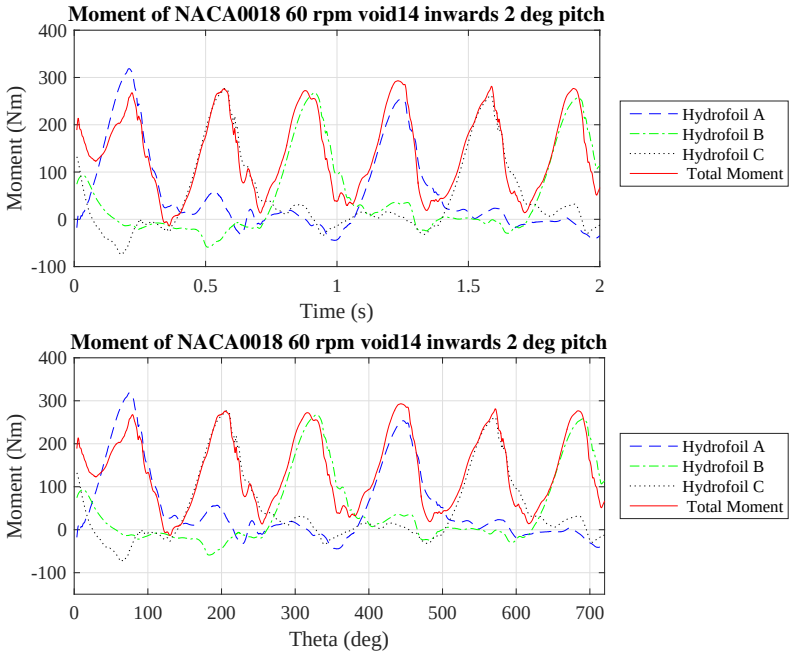

Figure A.235: Moment SIM34

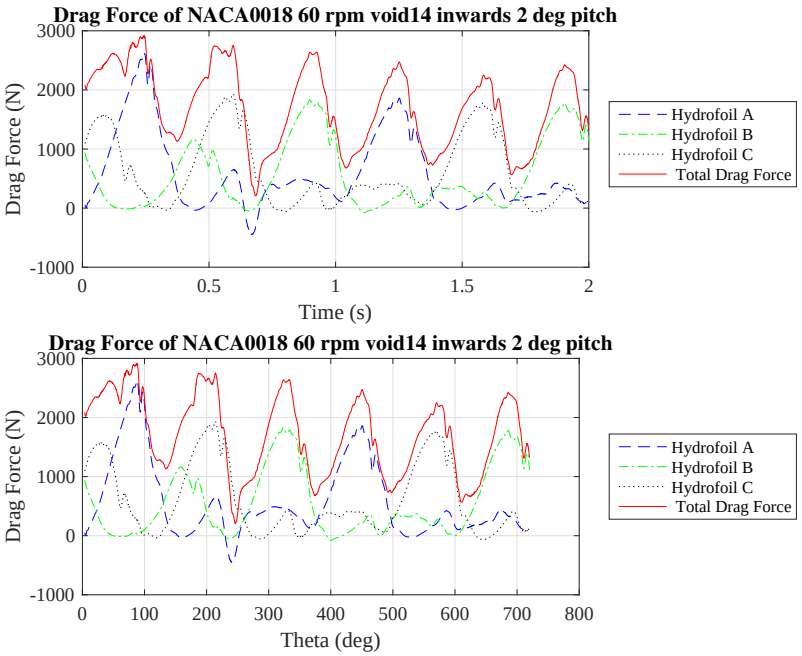

Figure A.236: Drag Force SIM34

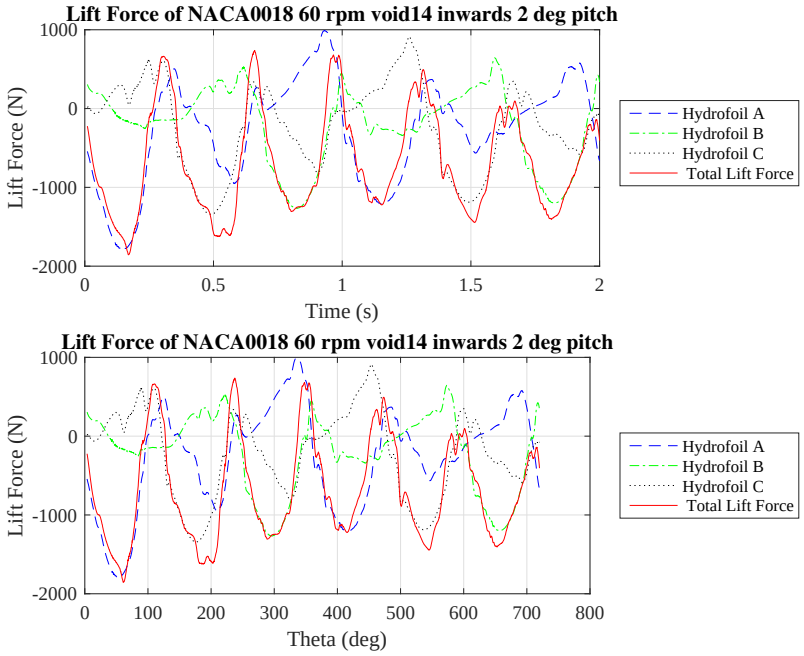

Figure A.237: Lift Force SIM34

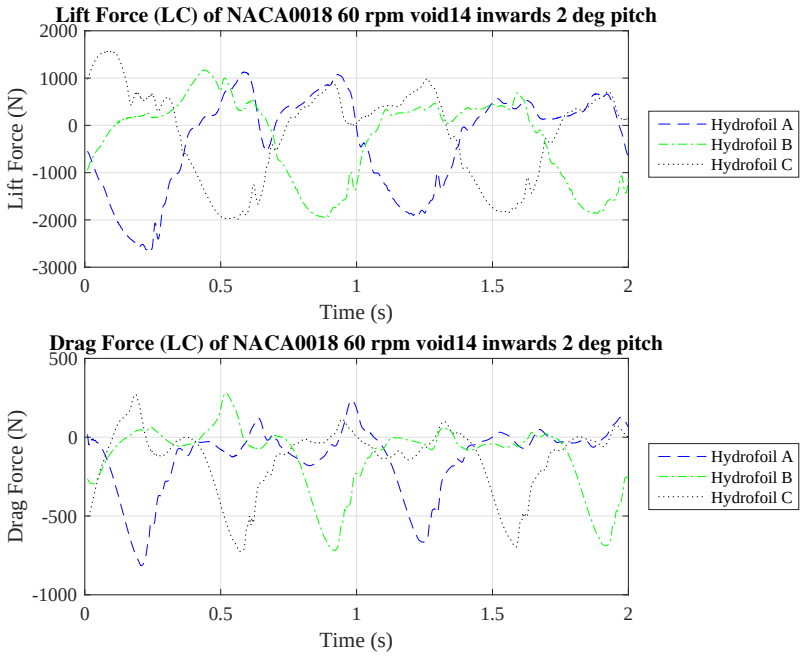

Figure A.238: Lift and Drag Force (LC) SIM34

A.1.35 SIM35

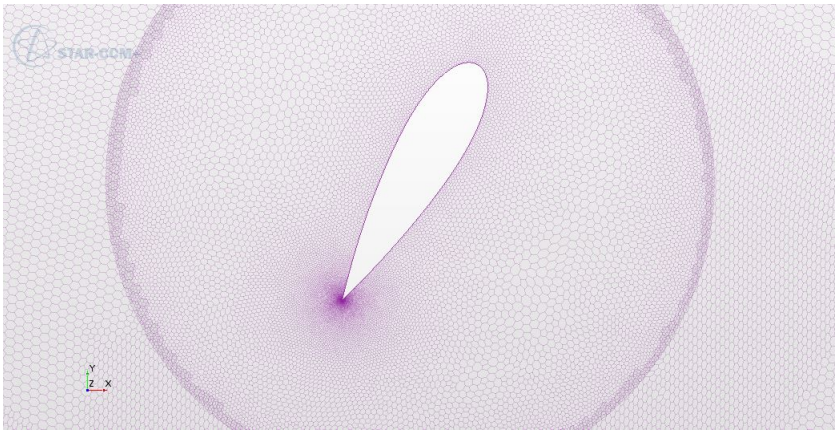

Figure A.239: Mesh SIM35

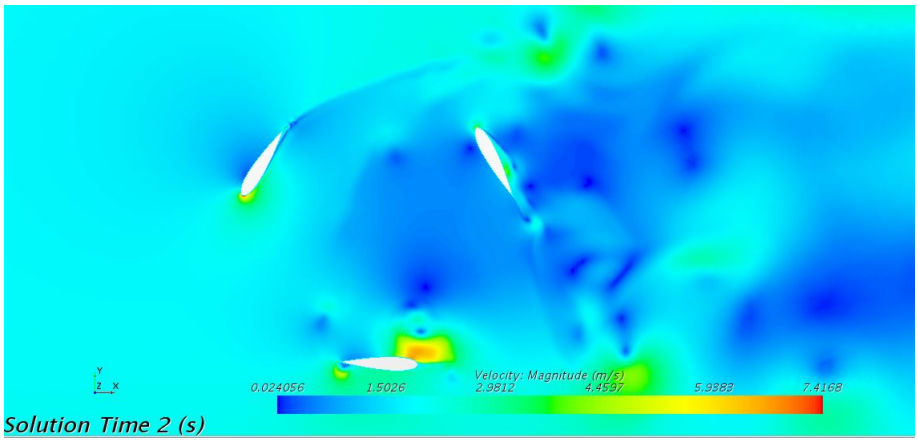

Figure A.240: Velocity SIM35

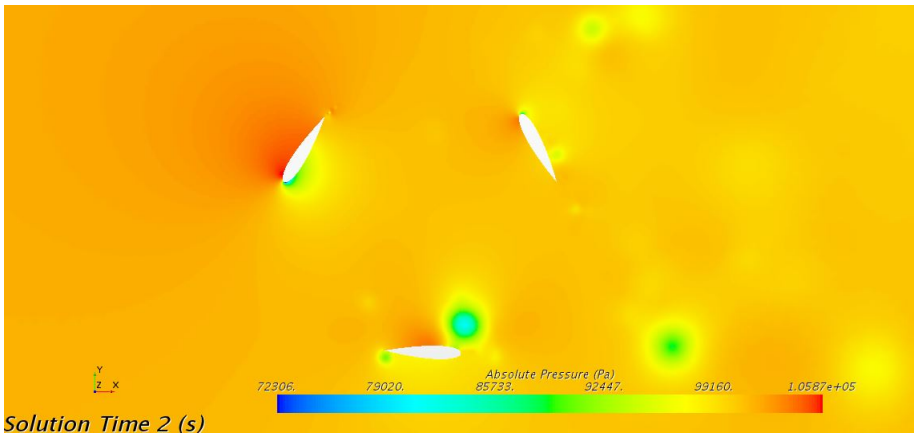

Figure A.241: Pressure SIM35

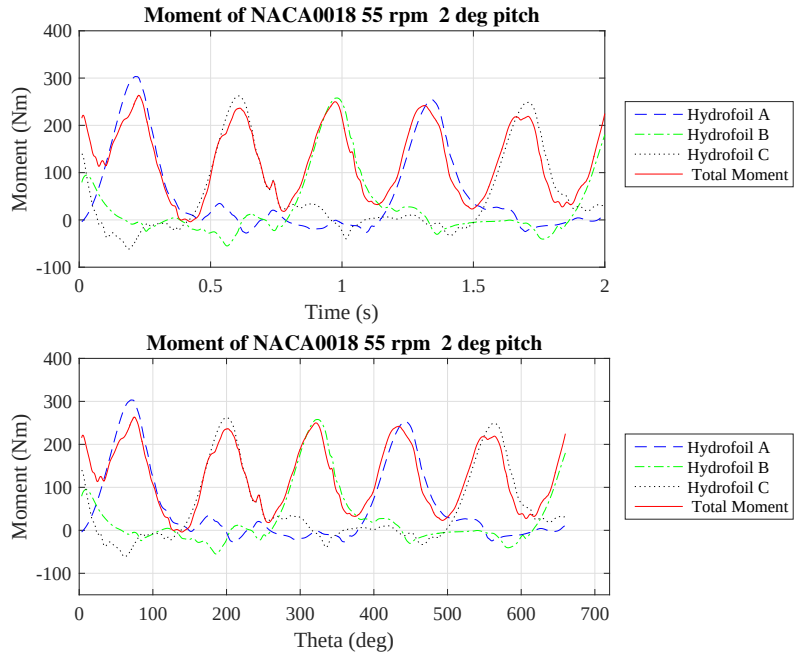

Figure A.242: Moment SIM35

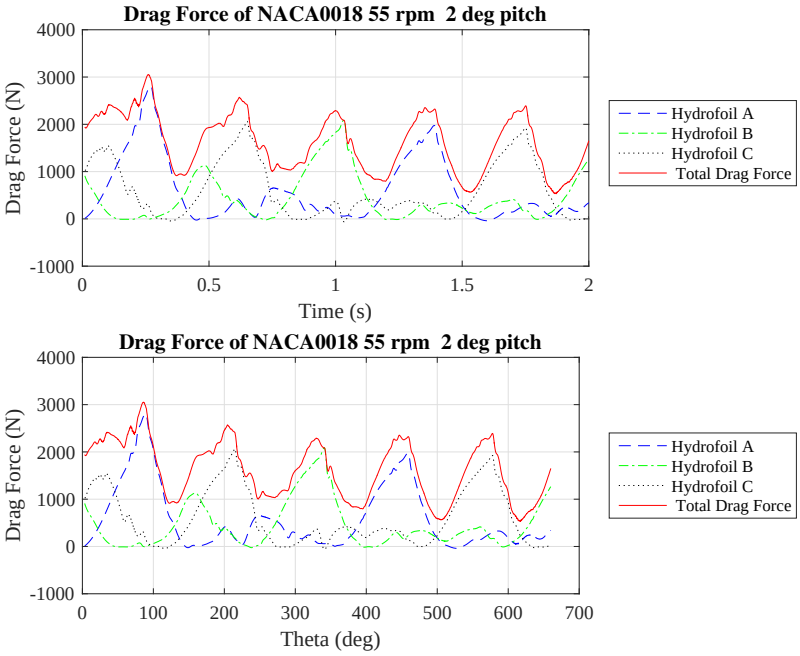

Figure A.243: Drag Force SIM35

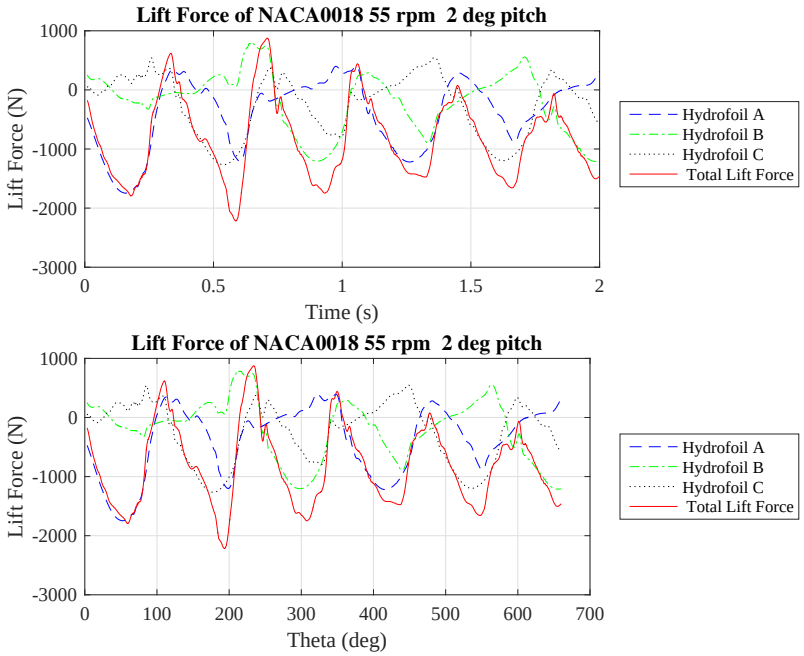

Figure A.244: Lift Force SIM35

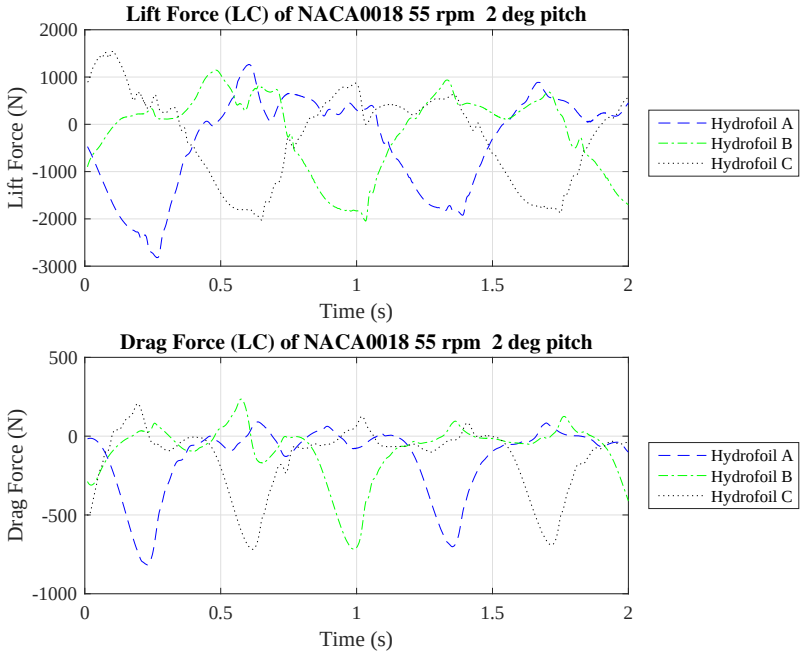

Figure A.245: Lift and Drag Force (LC) SIM35

A.1.36 SIM36

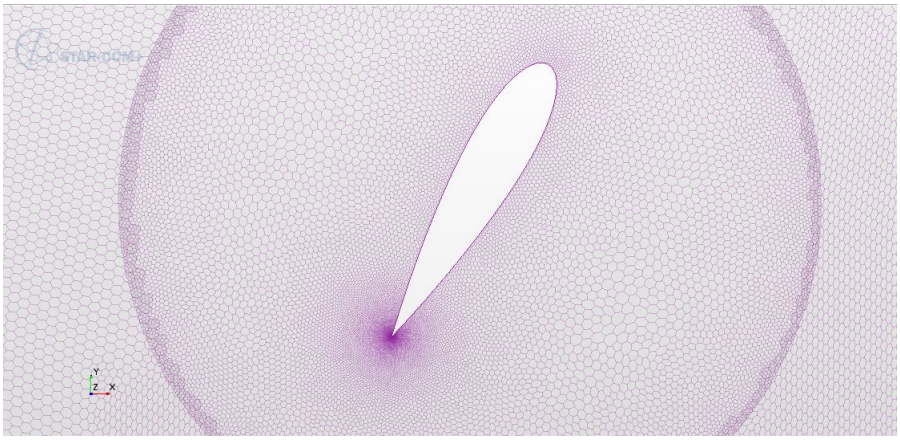

Figure A.246: Mesh SIM36

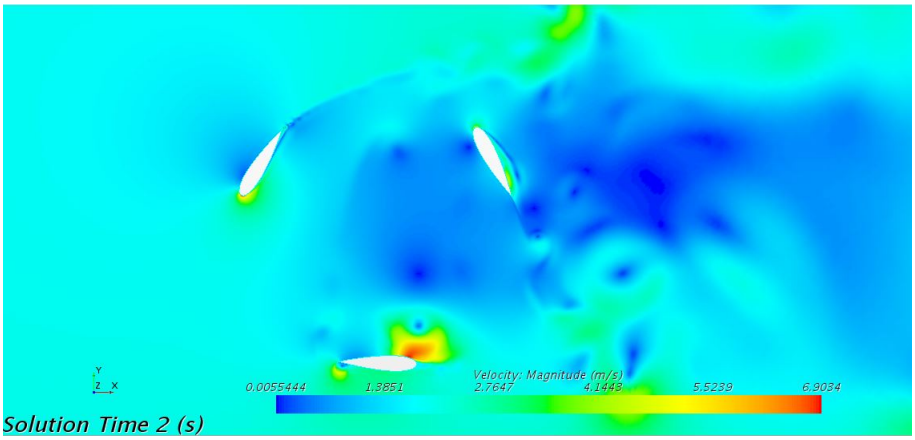

Figure A.247: Velocity SIM36

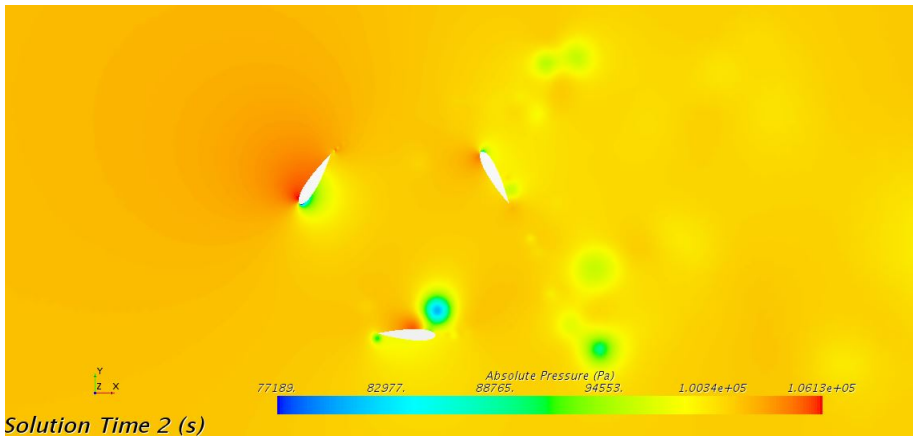

Figure A.248: Pressure SIM36

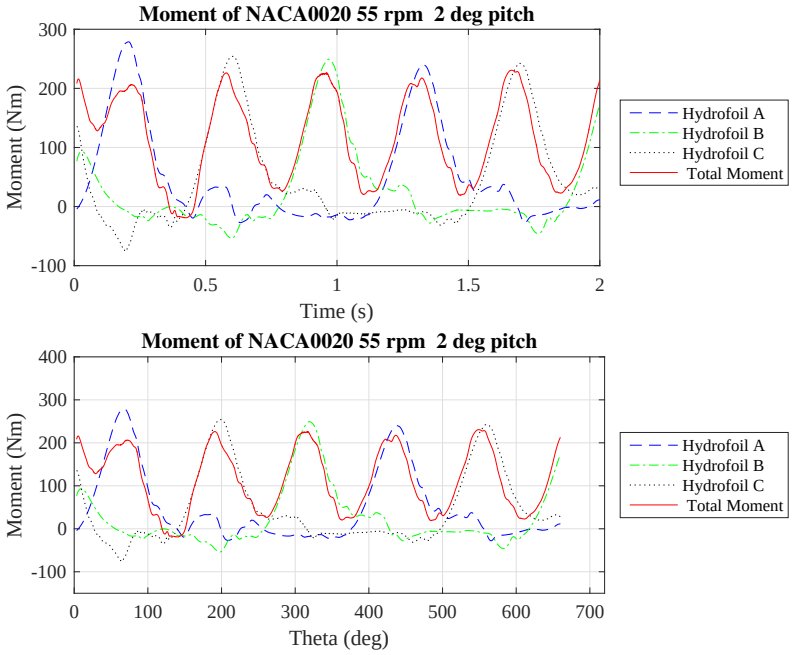

Figure A.249: Moment SIM36

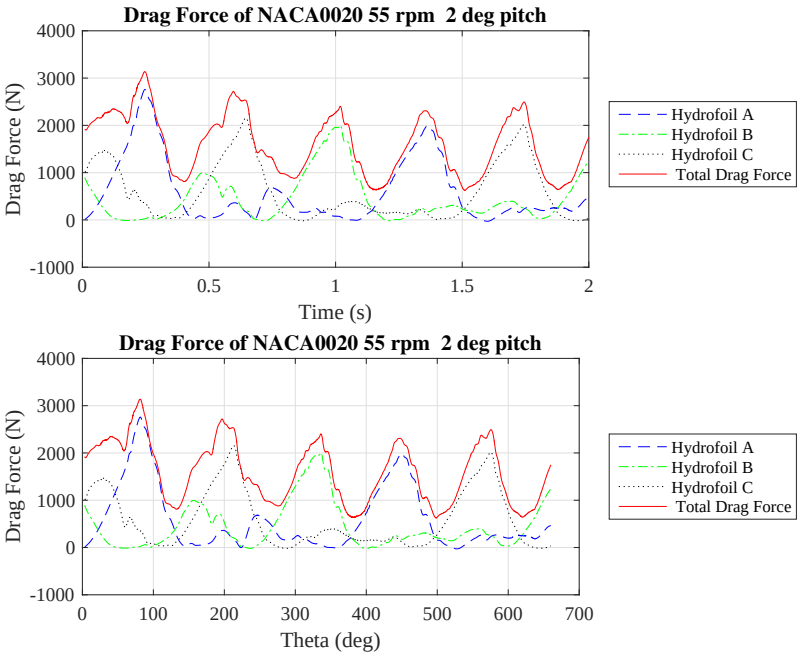

Figure A.250: Drag Force SIM36

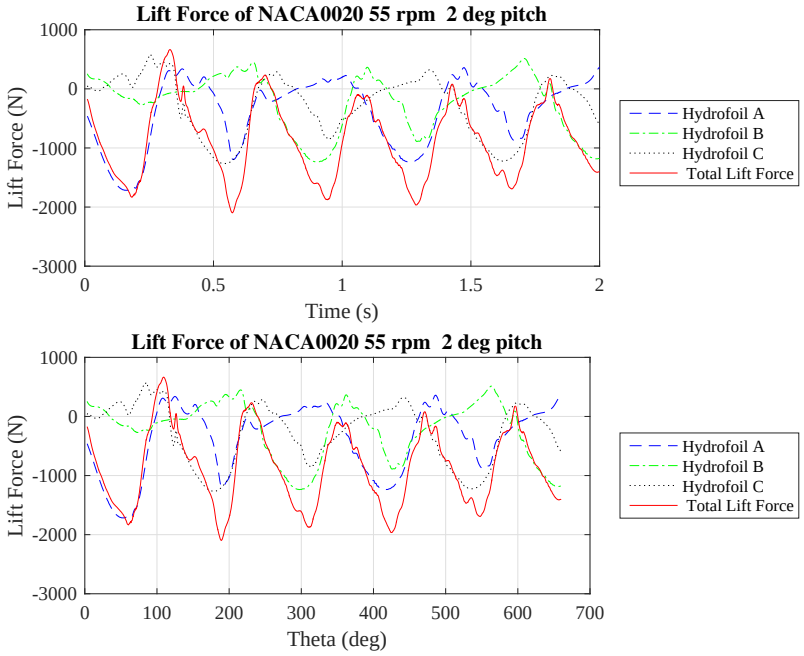

Figure A.251: Lift Force SIM36

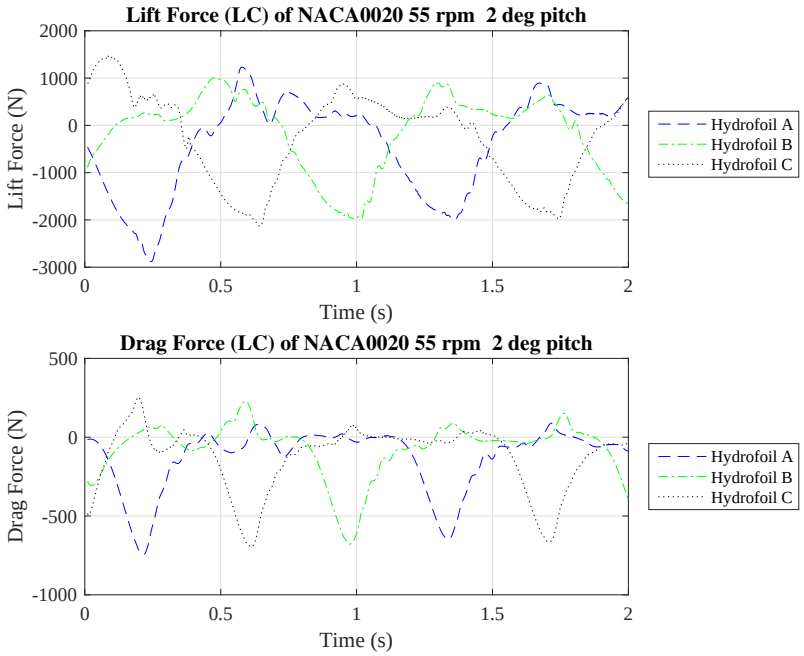

Figure A.252: Lift and Drag Force (LC) SIM36

A.1.37 SIM37

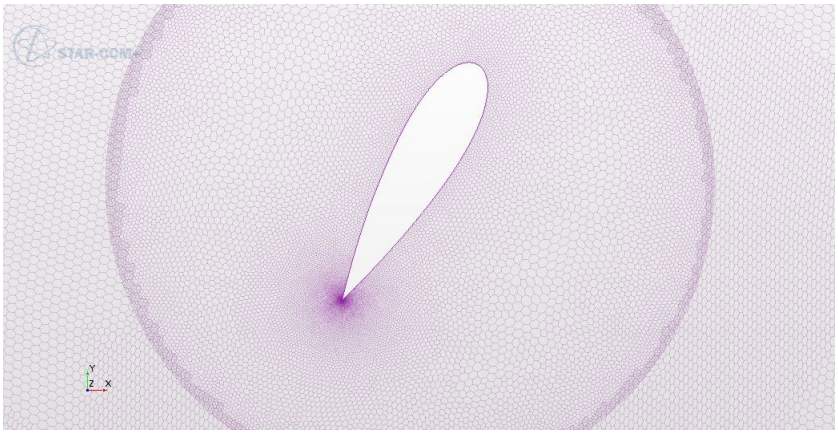

Figure A.253: Mesh SIM37

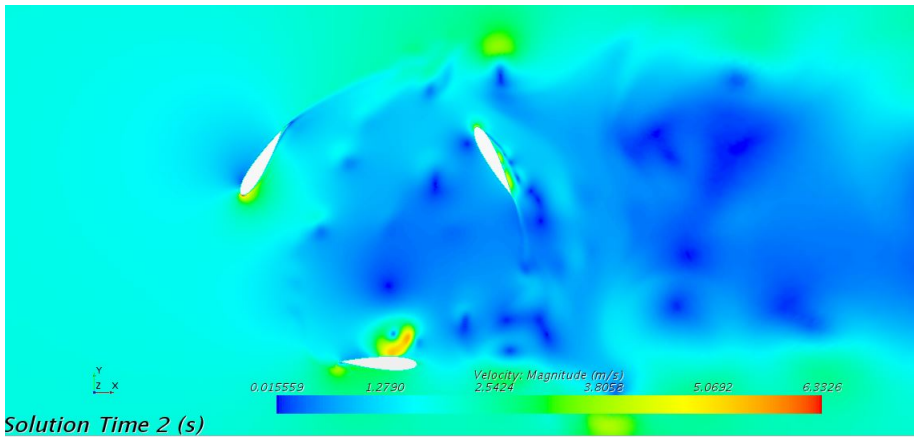

Figure A.254: Velocity SIM37

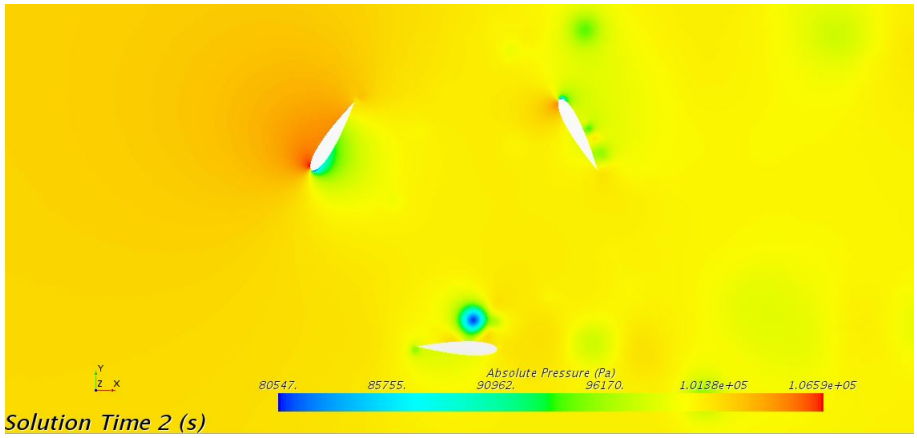

Figure A.255: Pressure SIM37

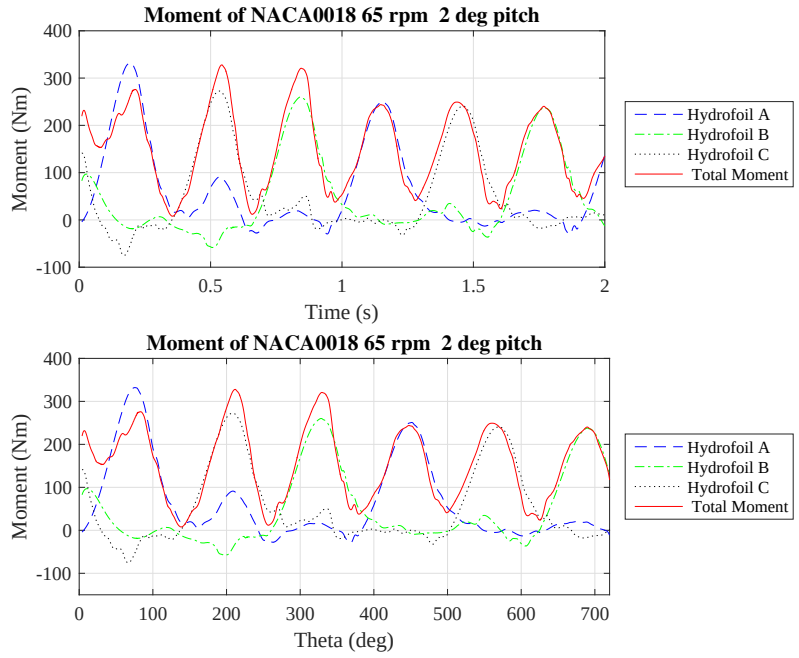

Figure A.256: Moment SIM37

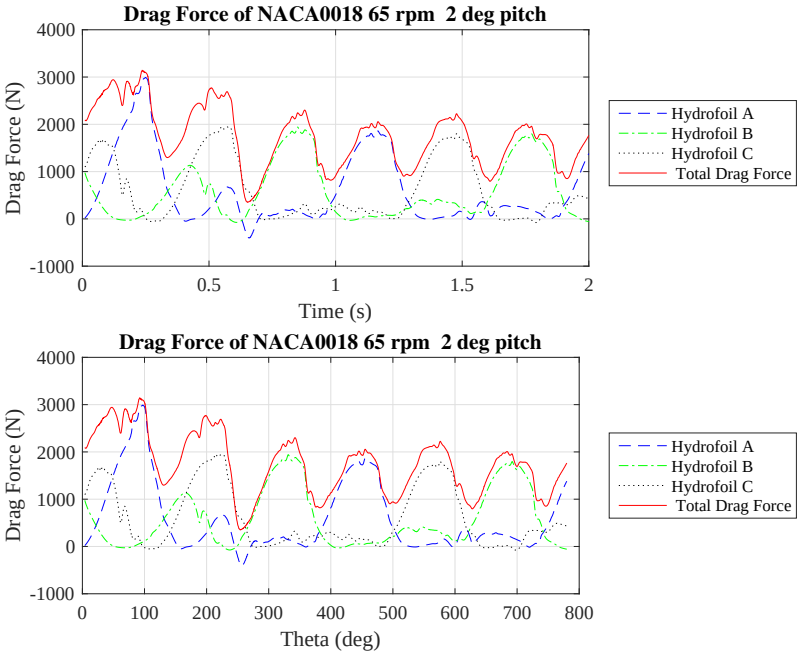

Figure A.257: Drag Force SIM37

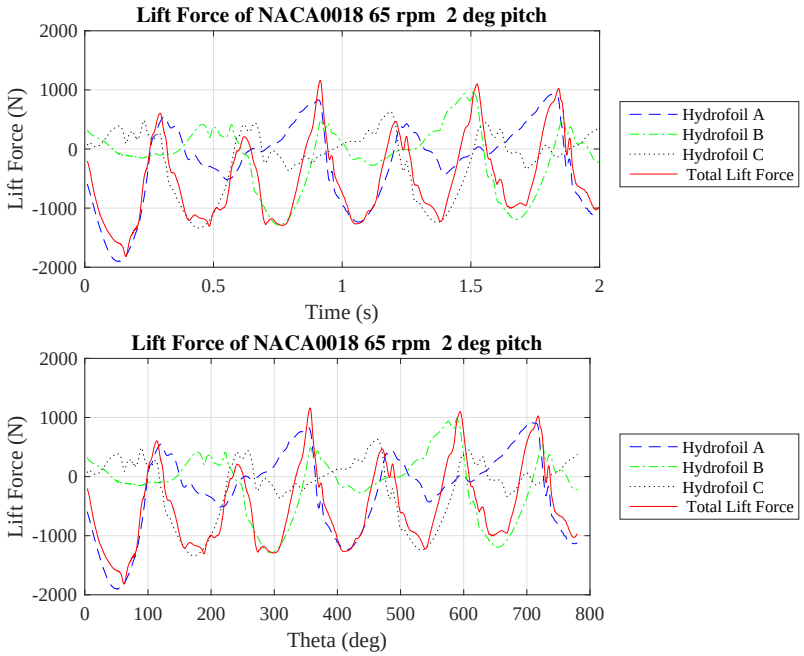

Figure A.258: Lift Force SIM37

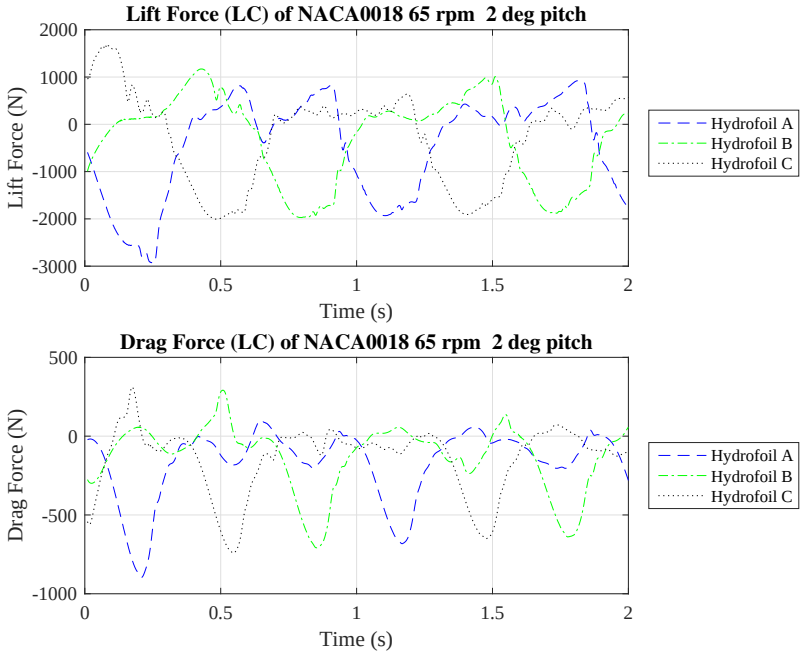

Figure A.259: Lift and Drag Force (LC) SIM37

A.1.38 SIM38

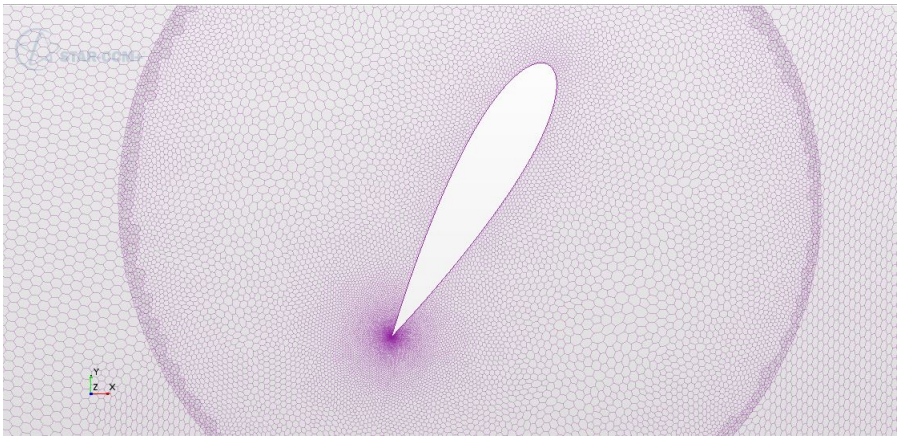

Figure A.260: Mesh SIM38

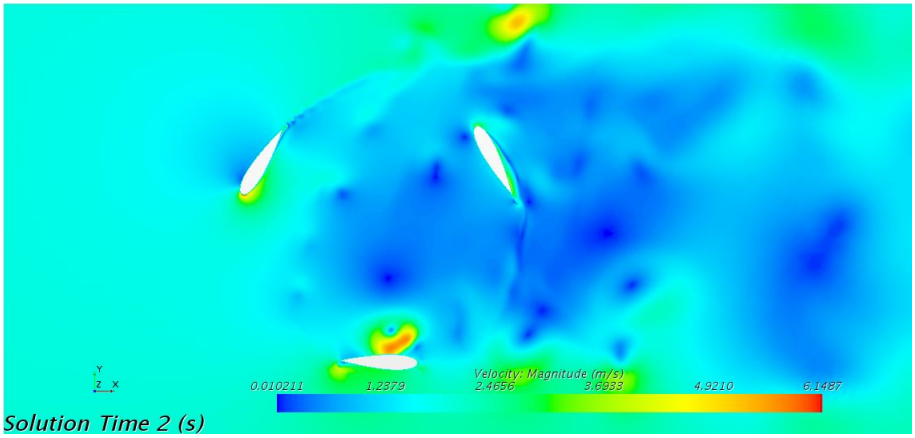

Figure A.261: Velocity SIM38

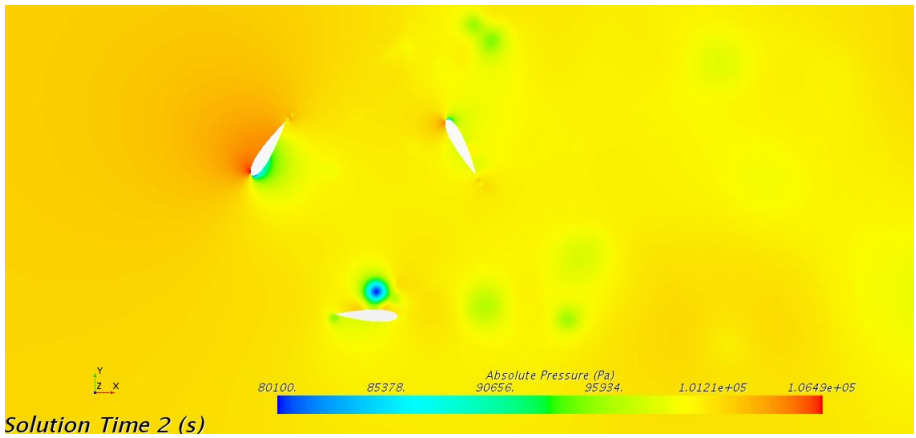

Figure A.262: Pressure SIM38

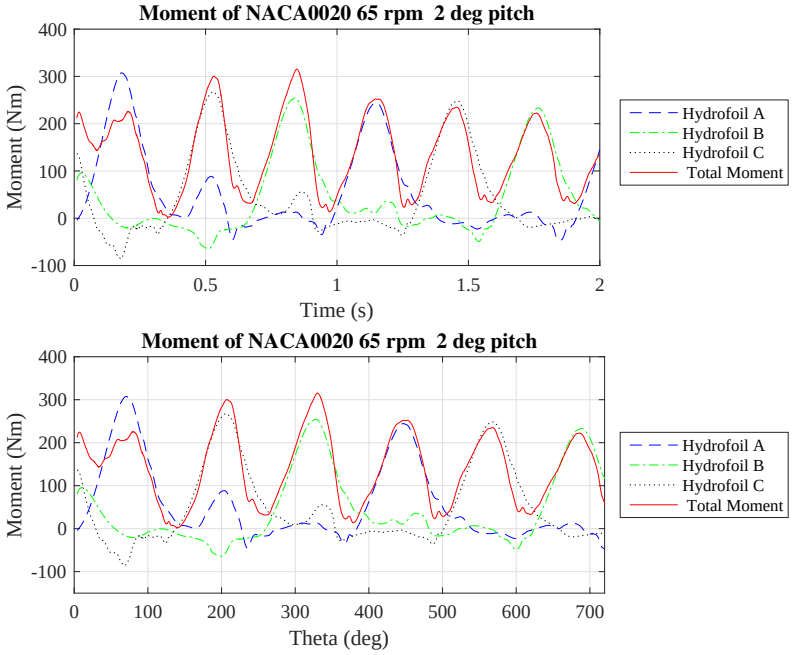

Figure A.263: Moment SIM38

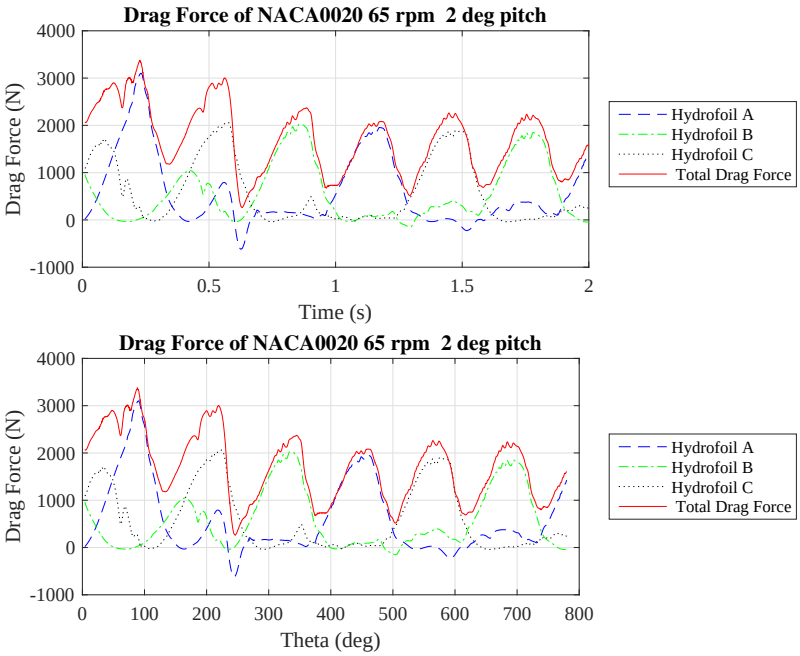

Figure A.264: Drag Force SIM38

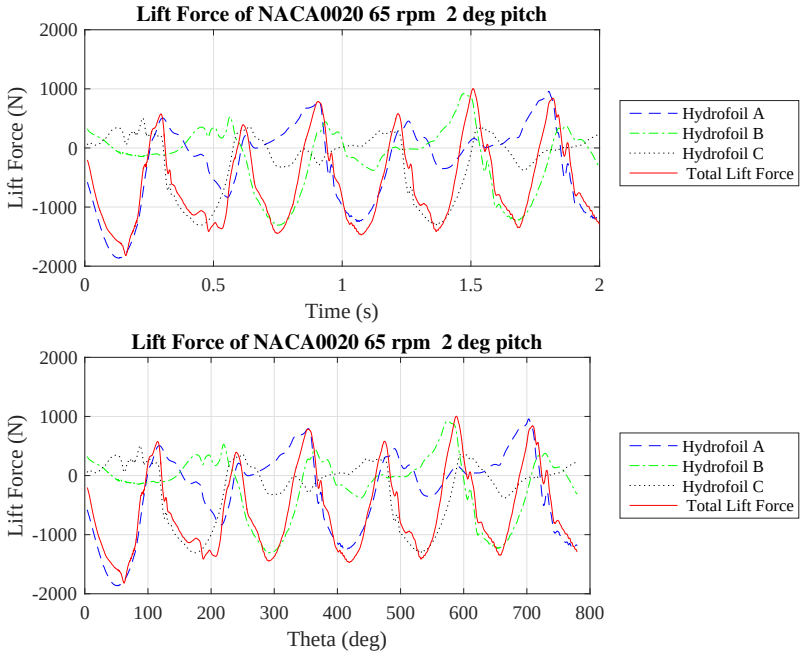

Figure A.265: Lift Force SIM38

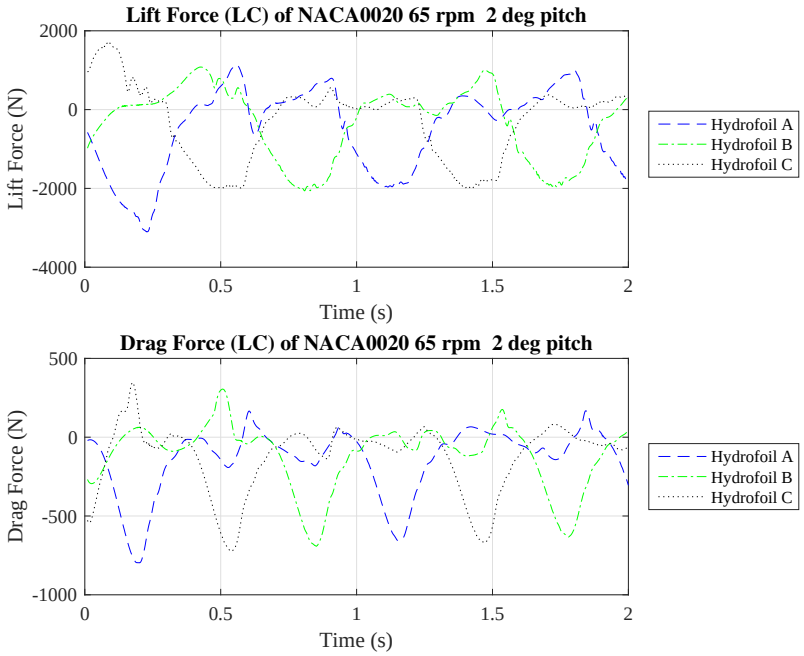

Figure A.266: Lift and Drag Force (LC) SIM38

A.1.39 SIM39

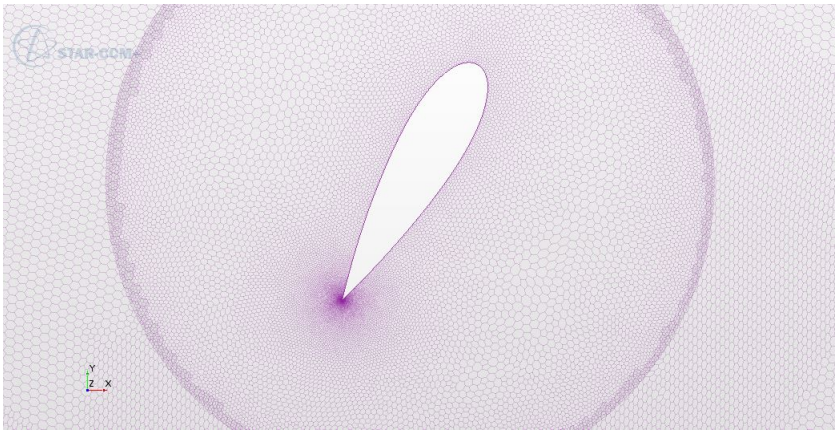

Figure A.267: Mesh SIM39

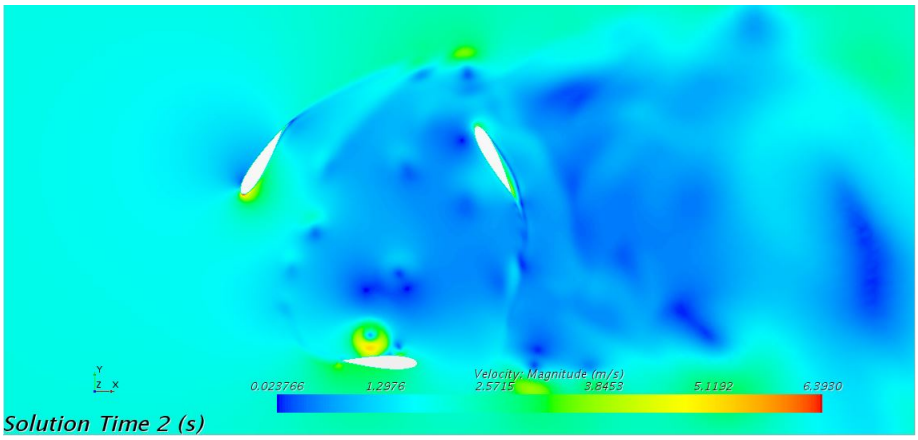

Figure A.268: Velocity SIM39

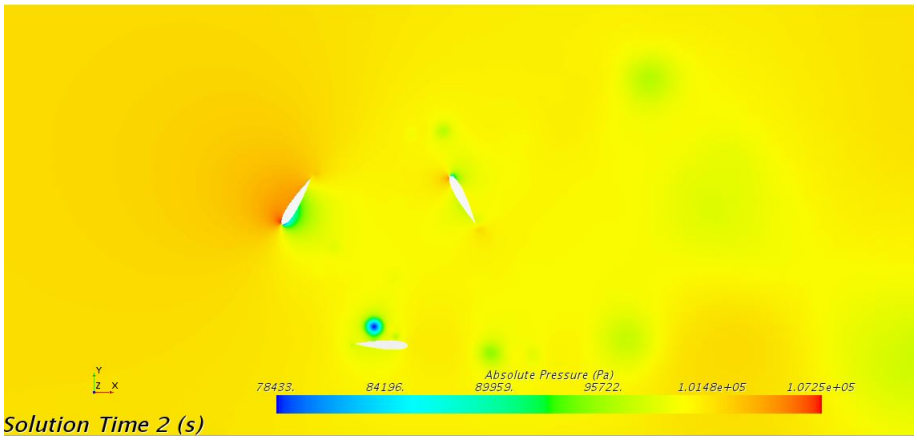

Figure A.269: Pressure SIM39

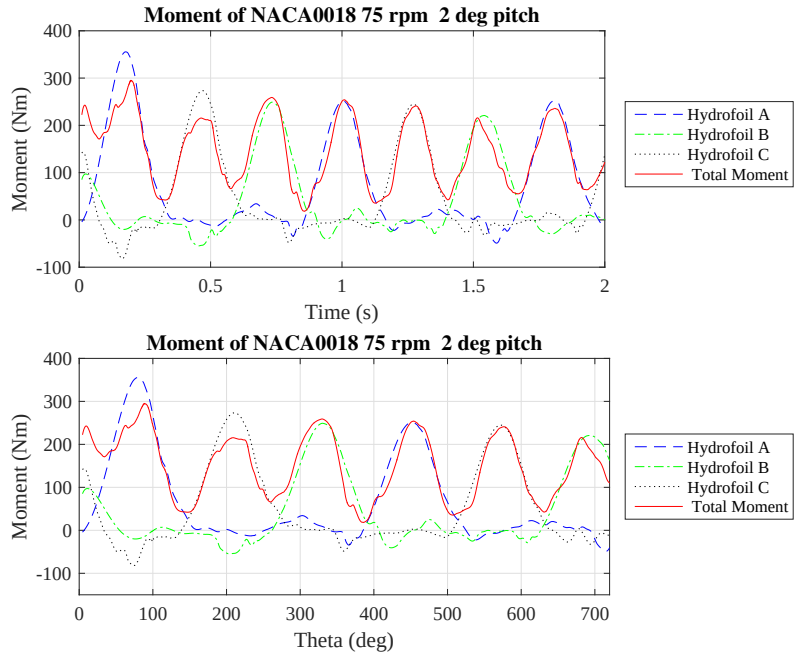

Figure A.270: Moment SIM39

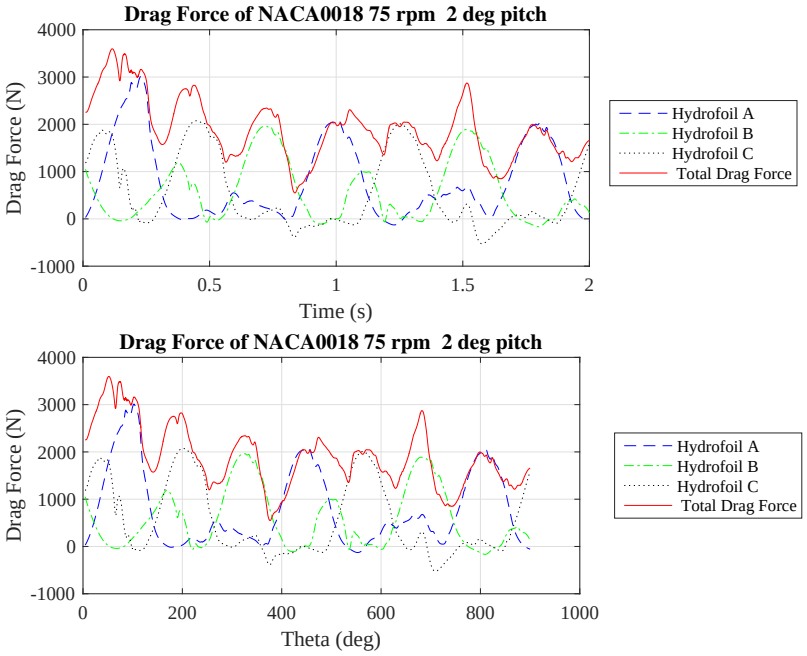

Figure A.271: Drag Force SIM39

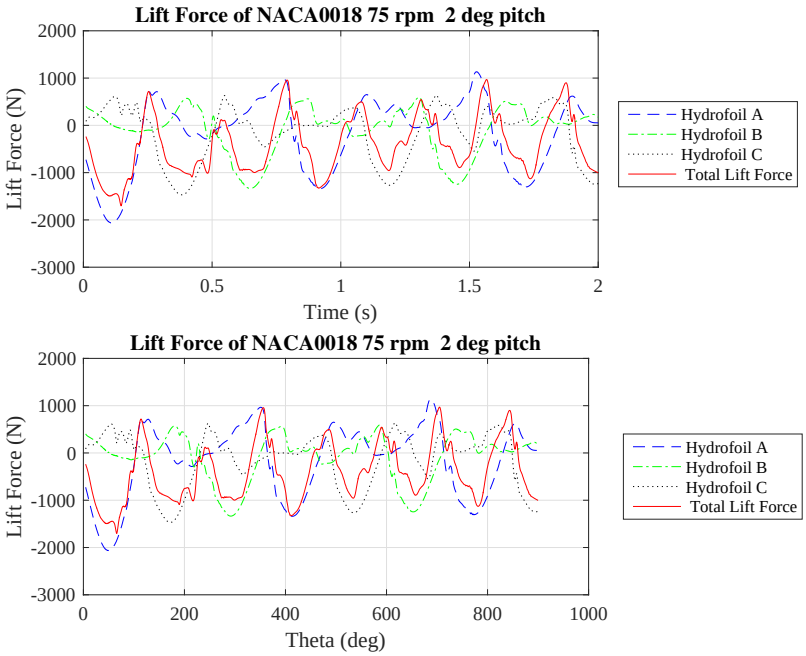

Figure A.272: Lift Force SIM39

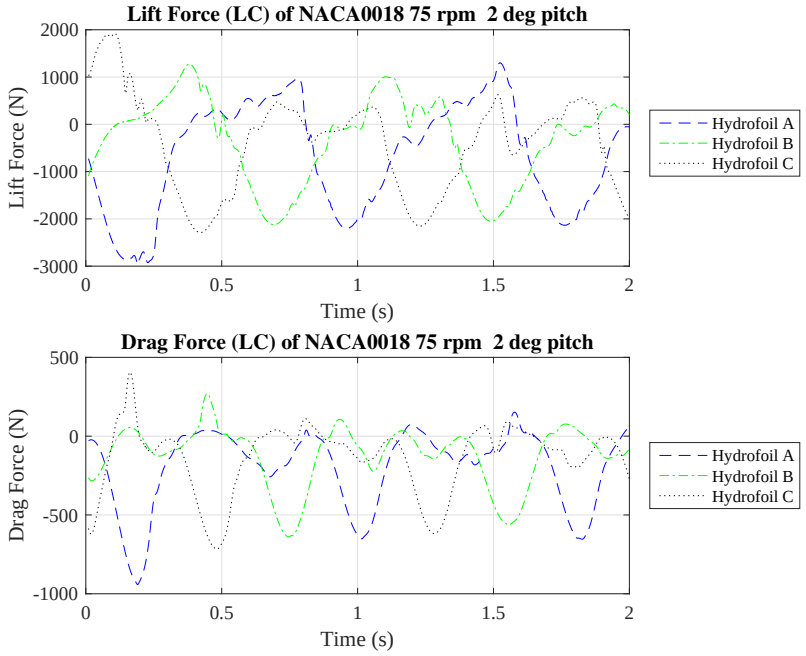

Figure A.273: Lift and Drag Force (LC) SIM39

A.1.40 SIM40

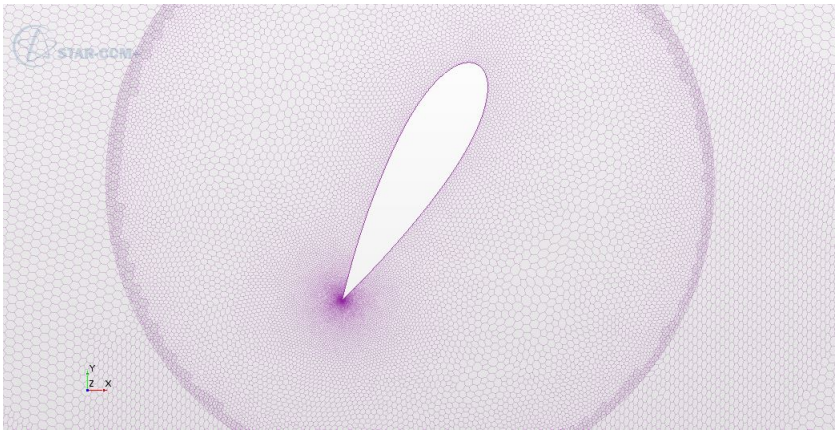

Figure A.274: Mesh SIM40

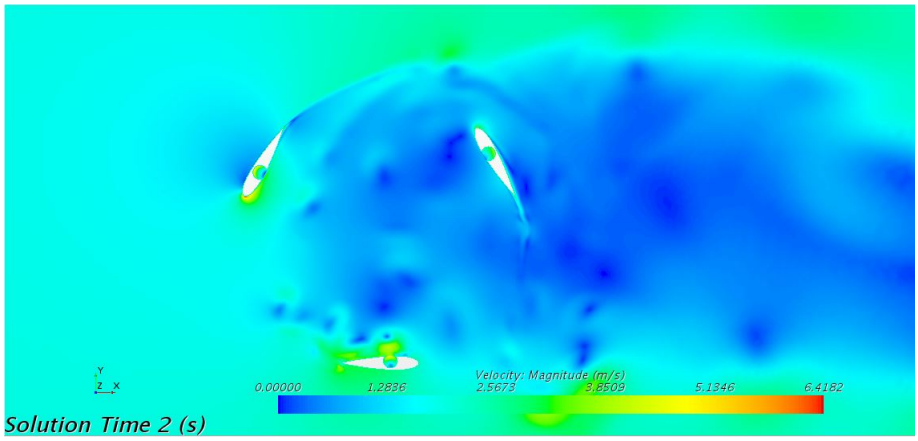

Figure A.275: Velocity SIM40

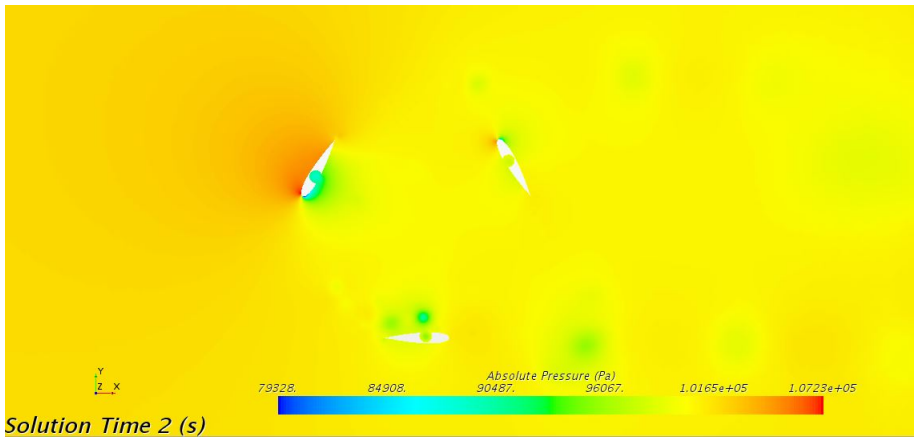

Figure A.276: Pressure SIM40

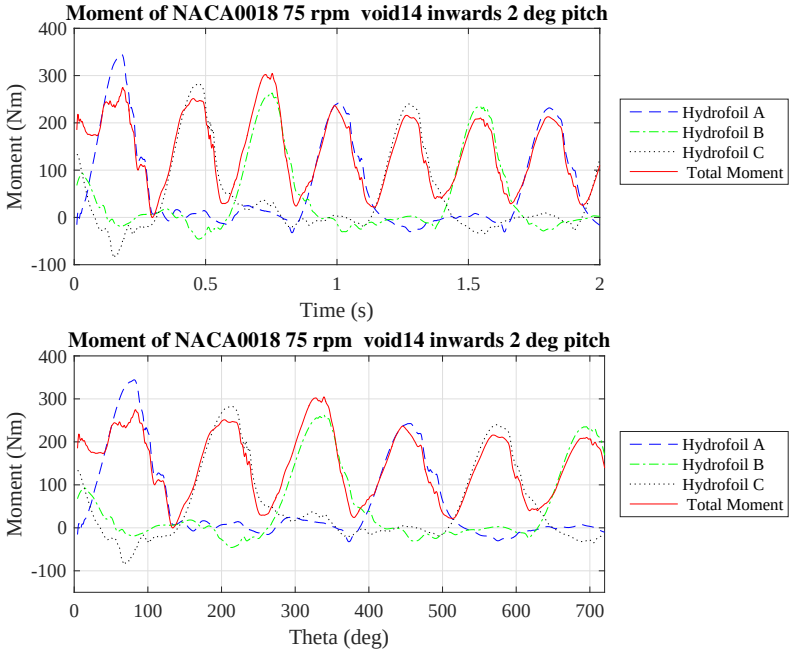

Figure A.277: Moment SIM40

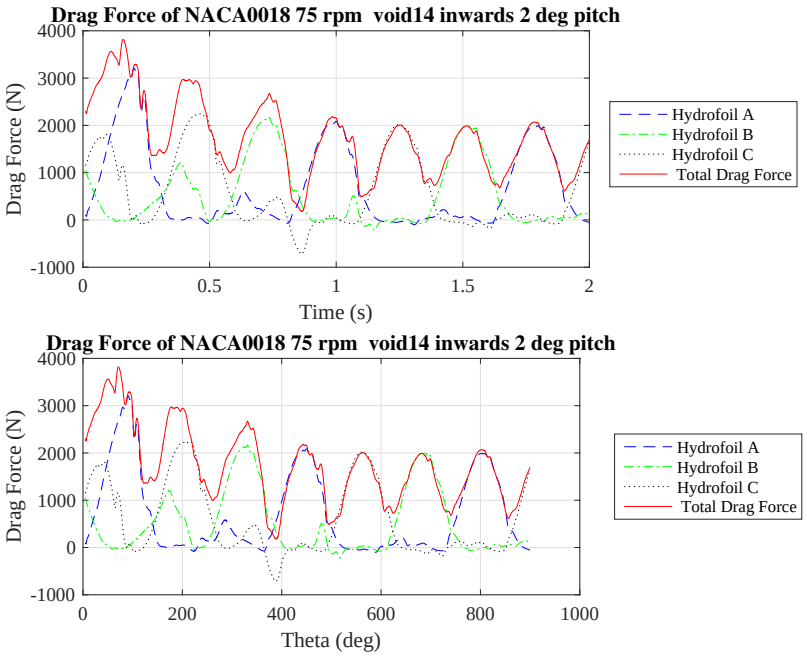

Figure A.278: Drag Force SIM40

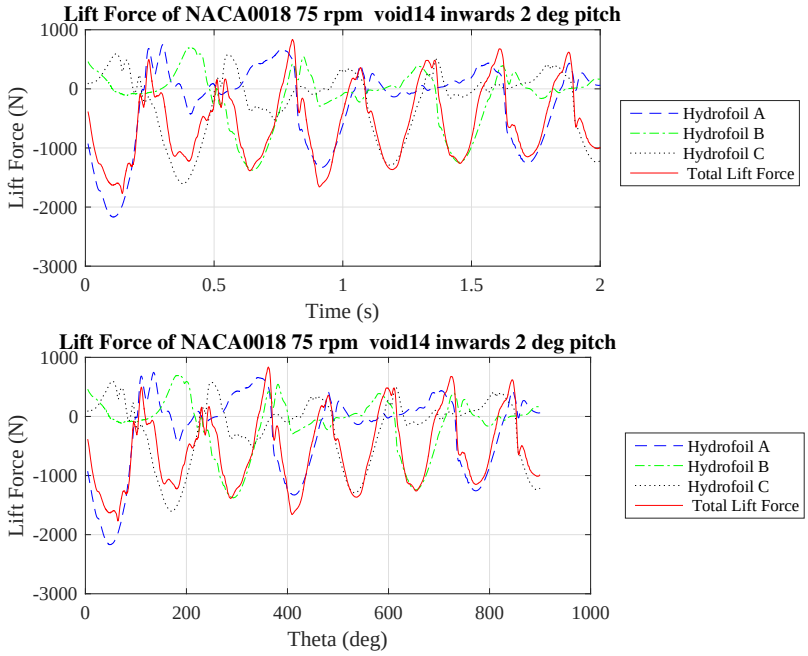

Figure A.279: Lift Force SIM40

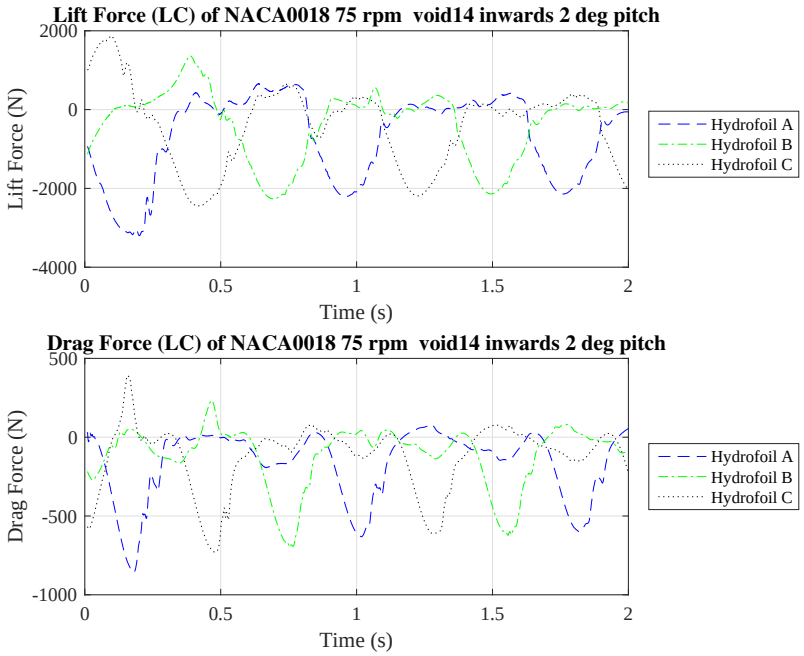

Figure A.280: Lift and Drag Force (LC) SIM40

A.1.41 SIM41

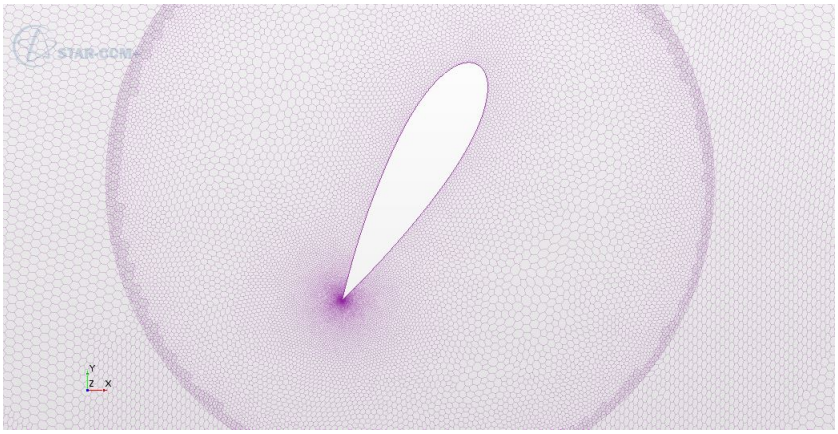

Figure A.281: Mesh SIM41

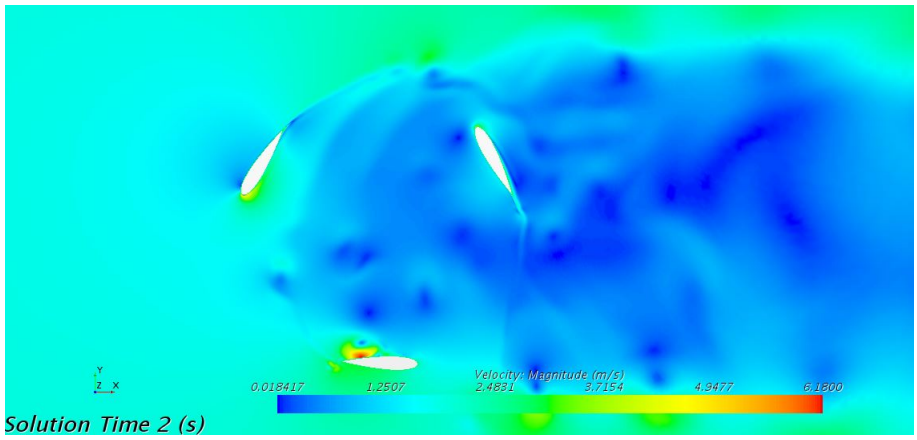

Figure A.282: Velocity SIM41

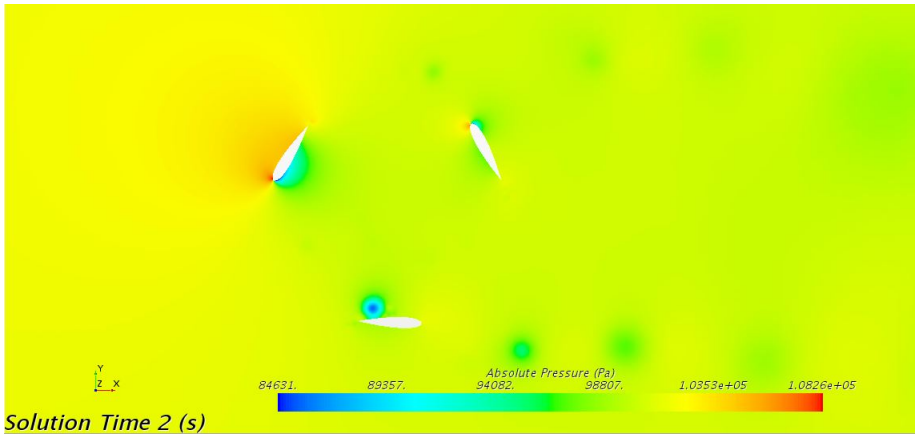

Figure A.283: Pressure SIM41

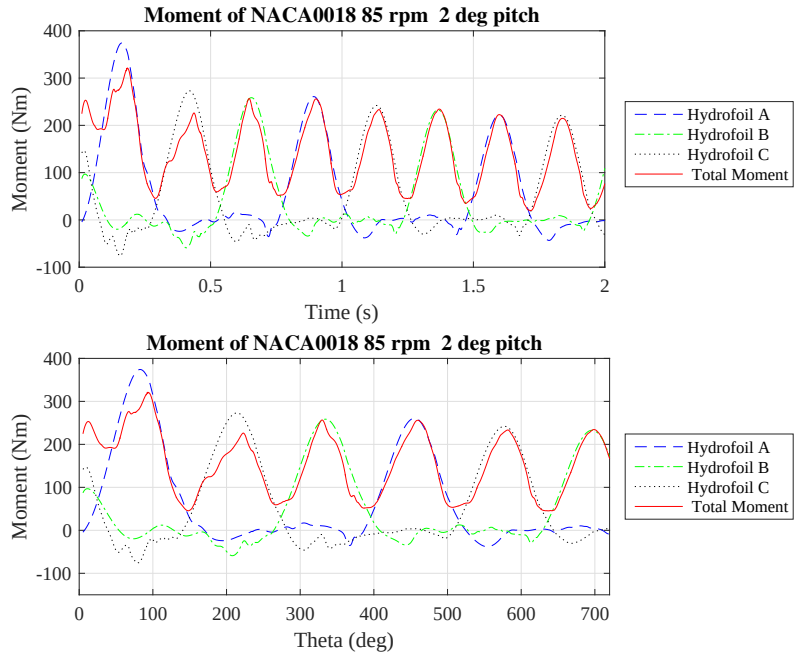

Figure A.284: Moment SIM41

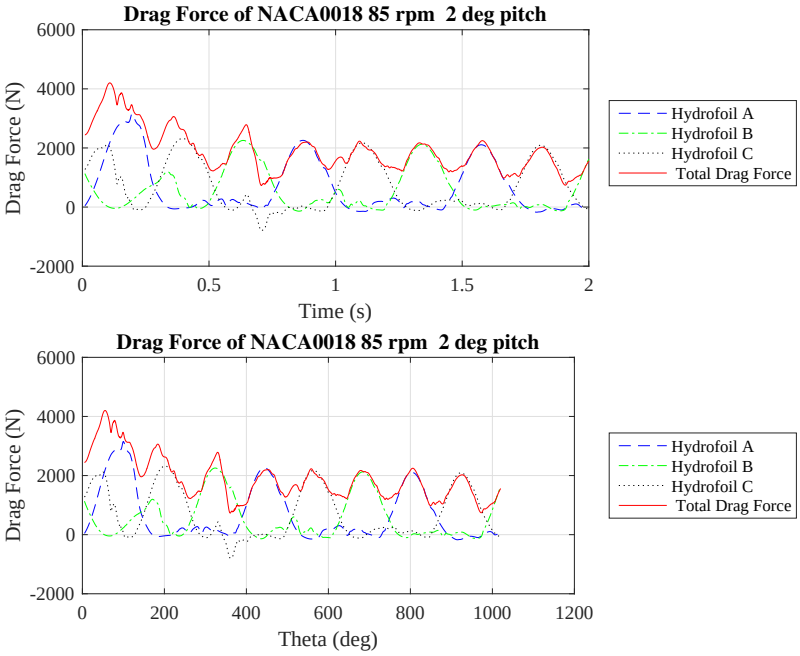

Figure A.285: Drag Force SIM41

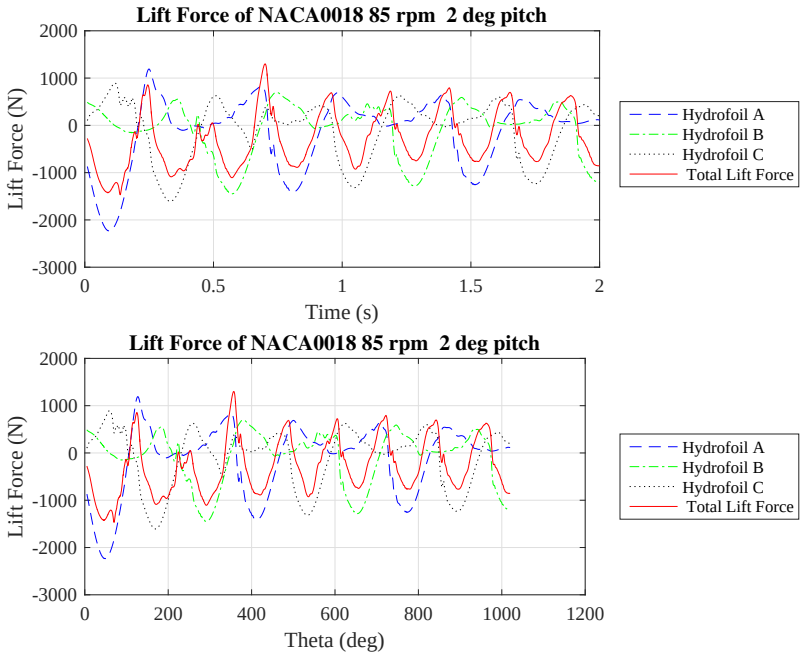

Figure A.286: Lift Force SIM41

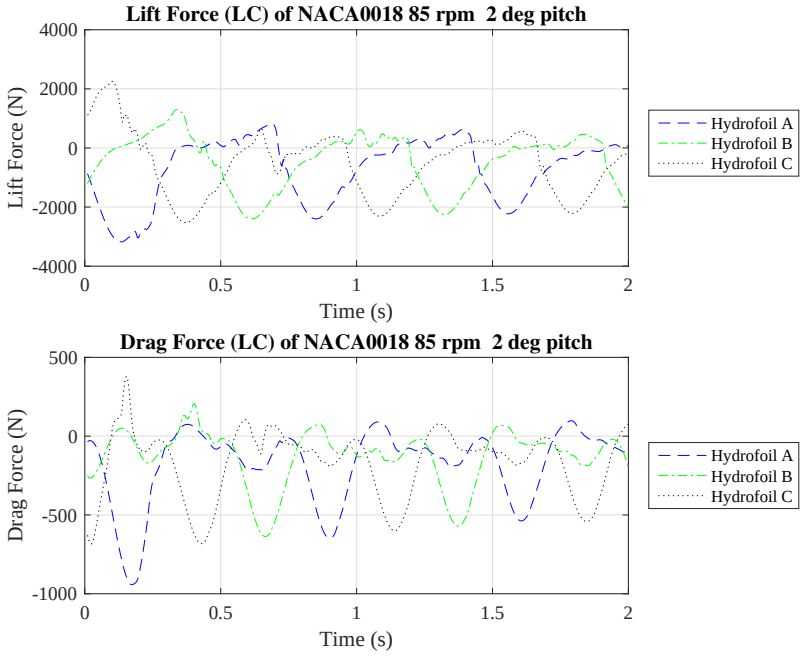

Figure A.287: Lift and Drag Force (LC) SIM41

A.1.42 SIM42

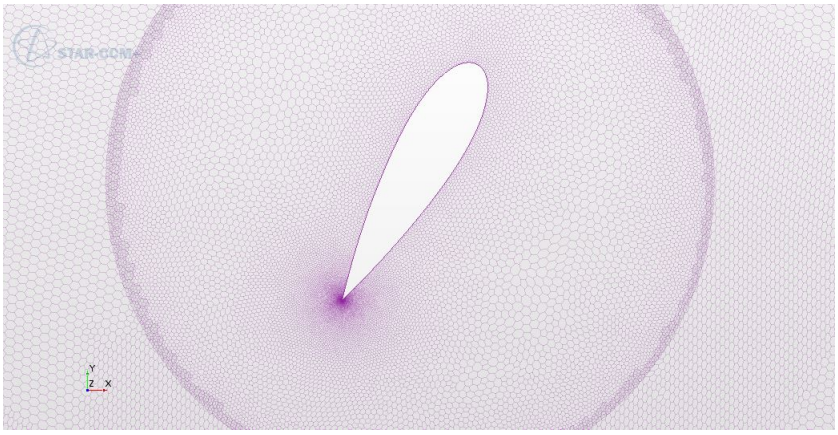

Figure A.288: Mesh SIM42

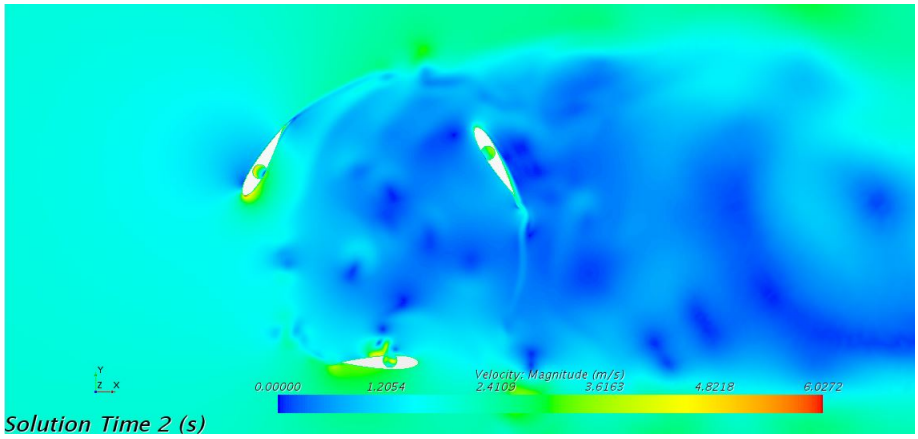

Figure A.289: Velocity SIM42

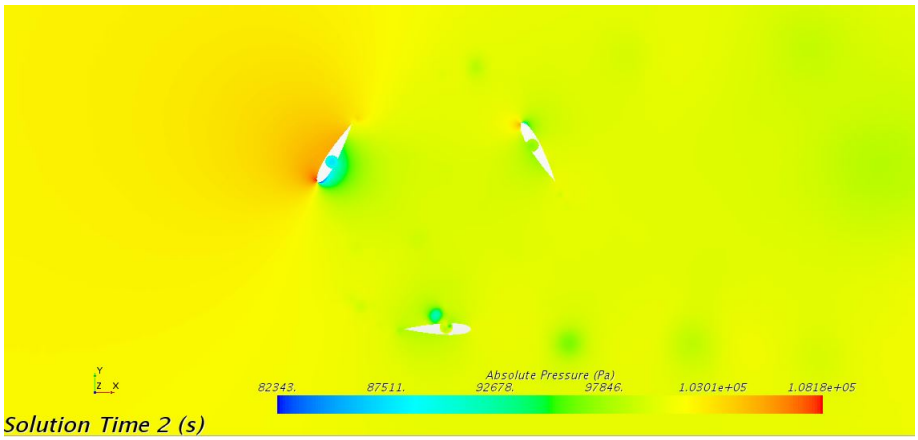

Figure A.290: Pressure SIM42

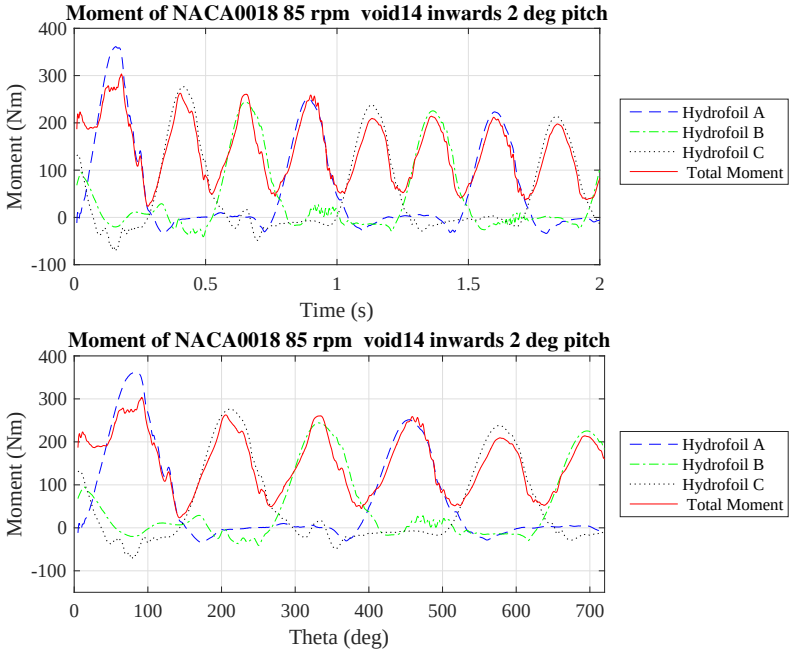

Figure A.291: Moment SIM42

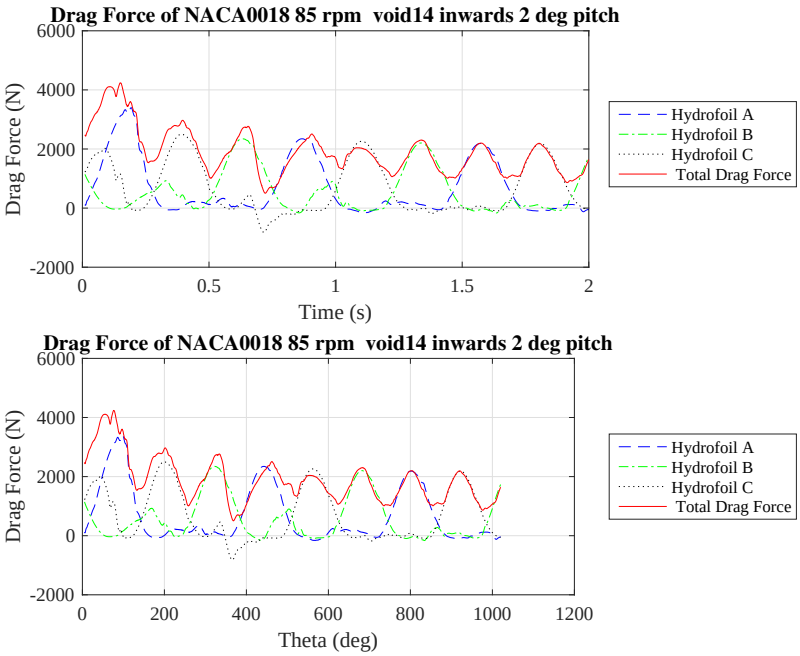

Figure A.292: Drag Force SIM42

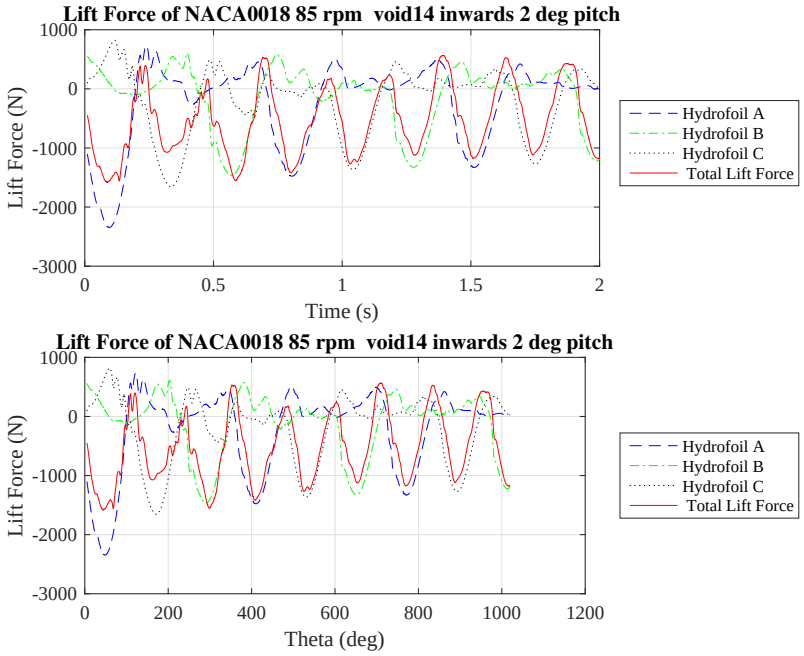

Figure A.293: Lift Force SIM42

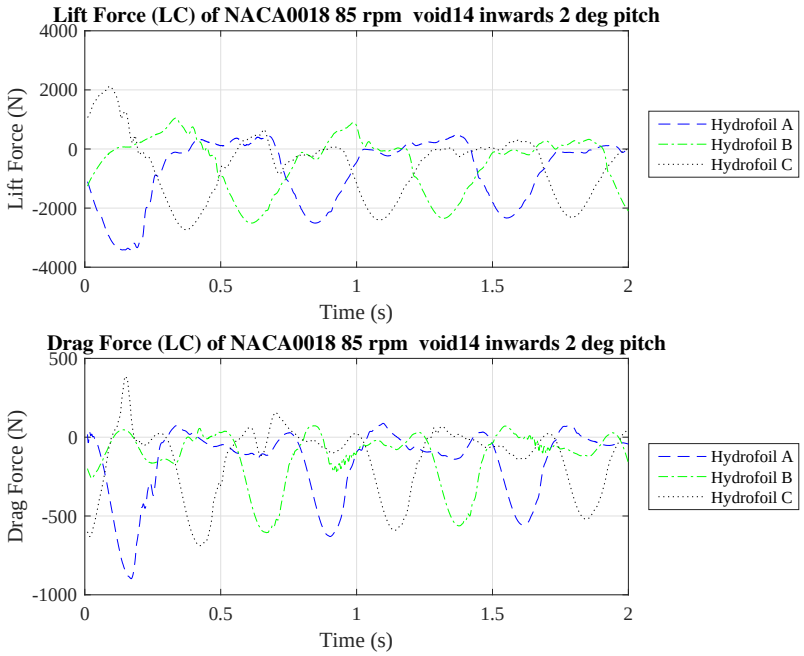

Figure A.294: Lift and Drag Force (LC) SIM42

A.1.43 SIM43

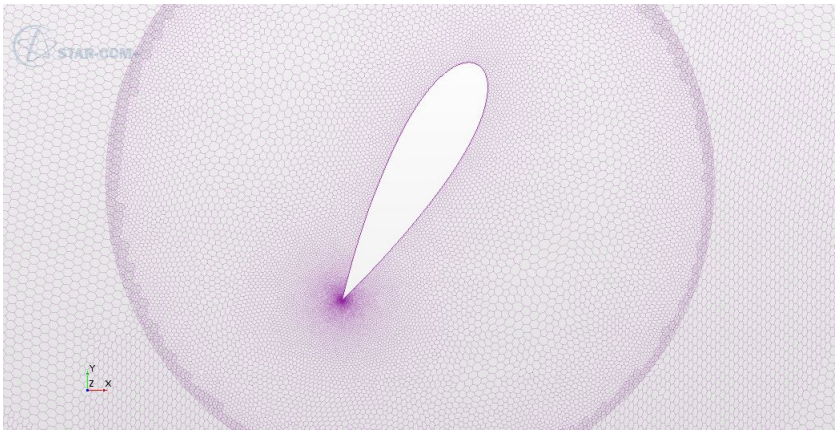

Figure A.295: Mesh SIM43

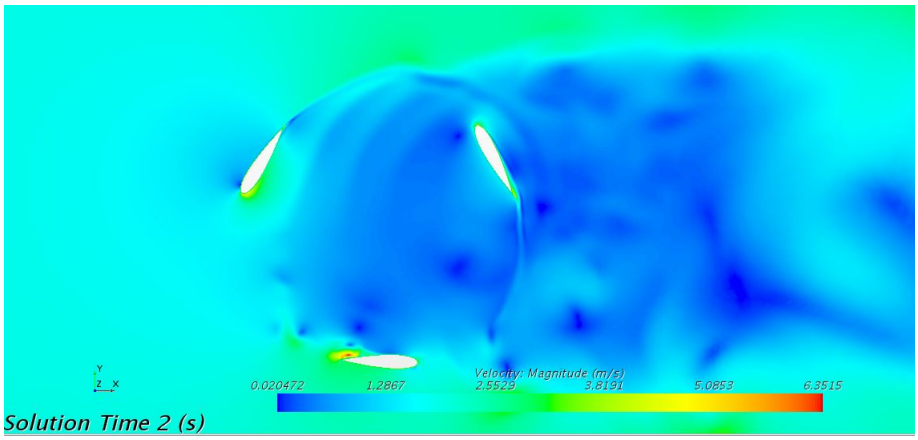

Figure A.296: Velocity SIM43

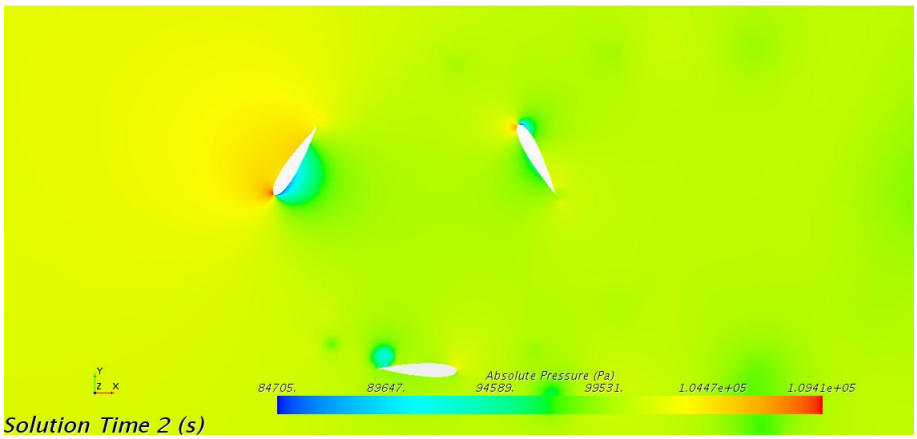

Figure A.297: Pressure SIM43

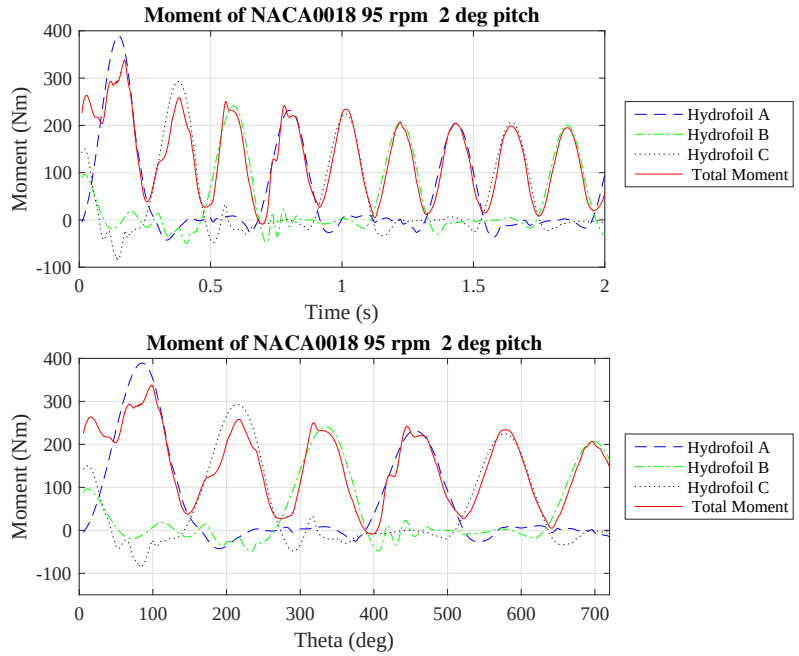

Figure A.298: Moment SIM43

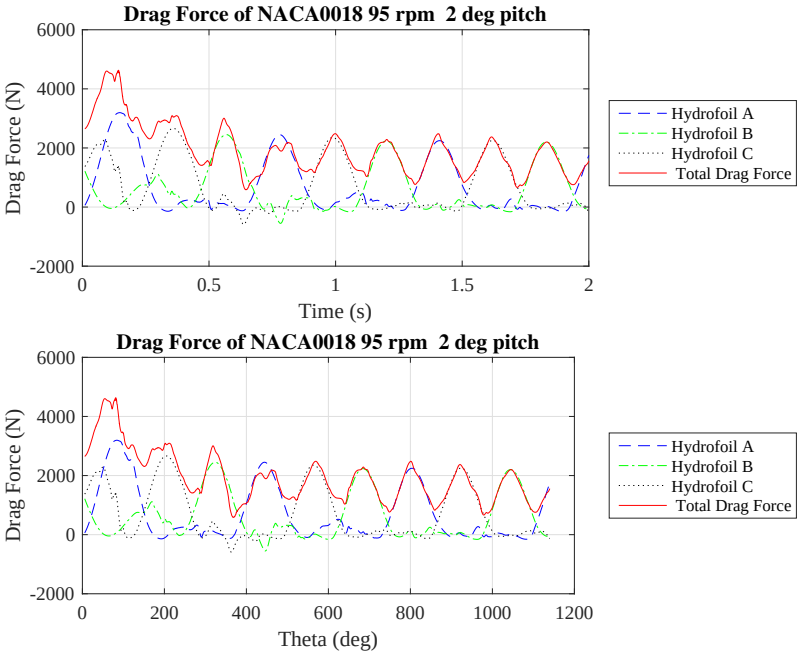

Figure A.299: Drag Force SIM43

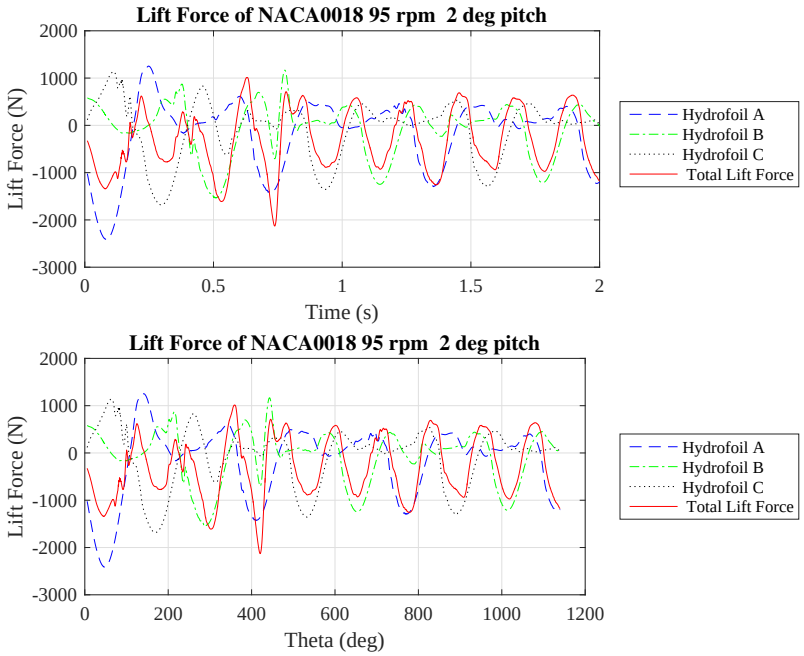

Figure A.300: Lift Force SIM43

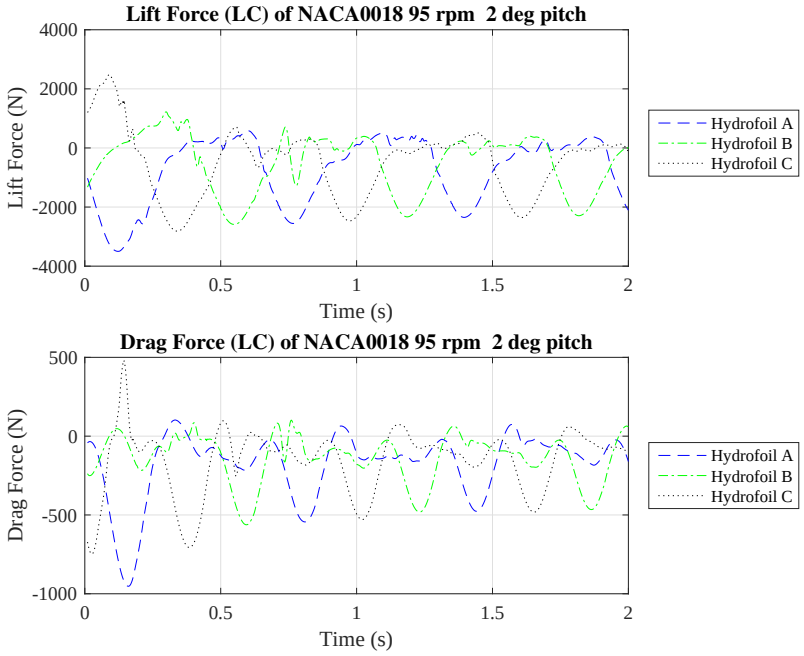

Figure A.301: Lift and Drag Force (LC) SIM43

A.1.44 SIM44

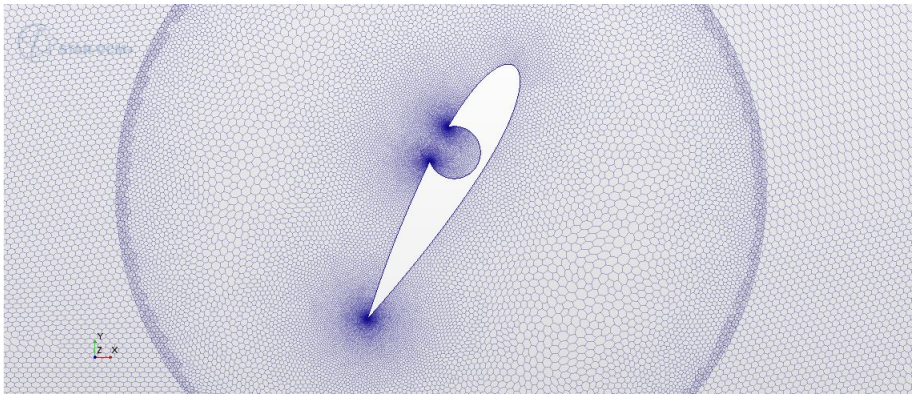

Figure A.302: Mesh SIM44

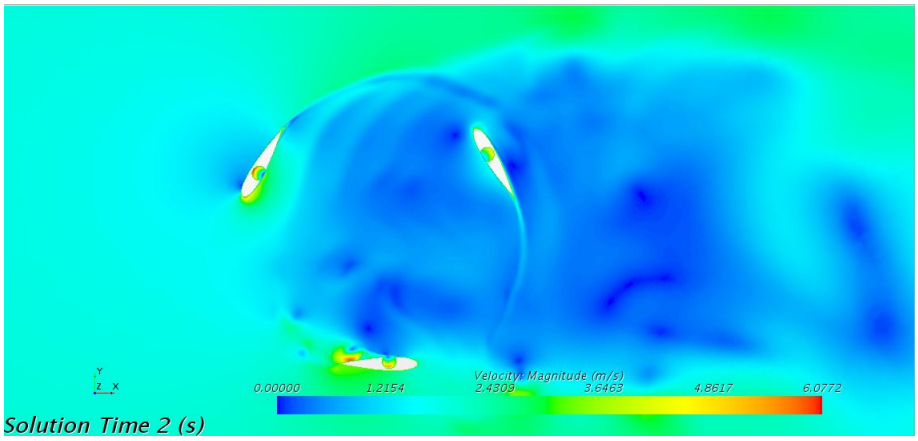

Figure A.303: Velocity SIM44

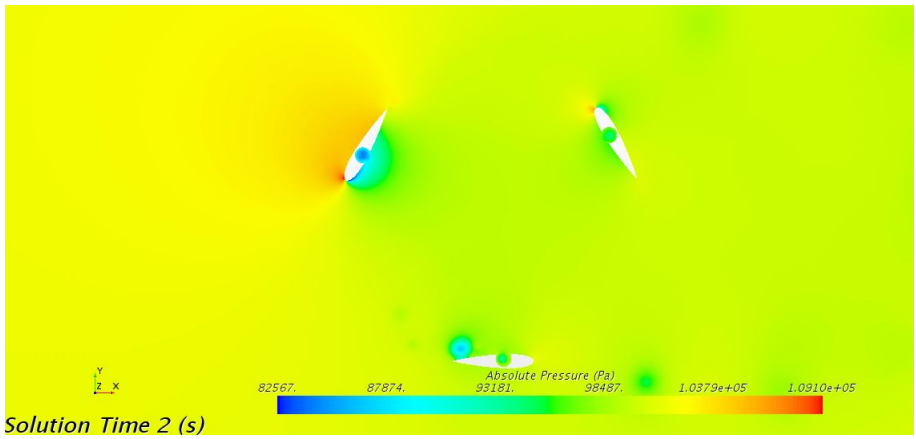

Figure A.304: Pressure SIM44

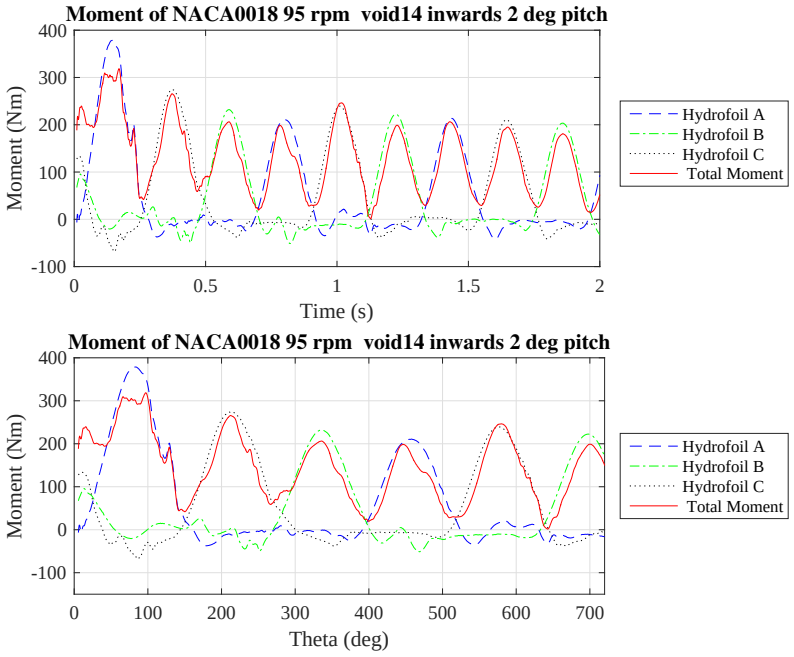

Figure A.305: Moment SIM44

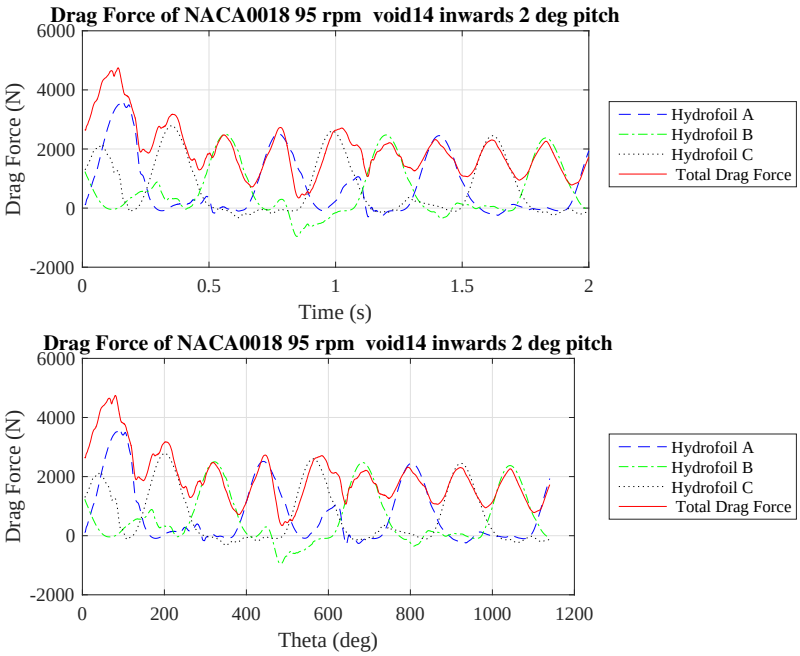

Figure A.306: Drag Force SIM44

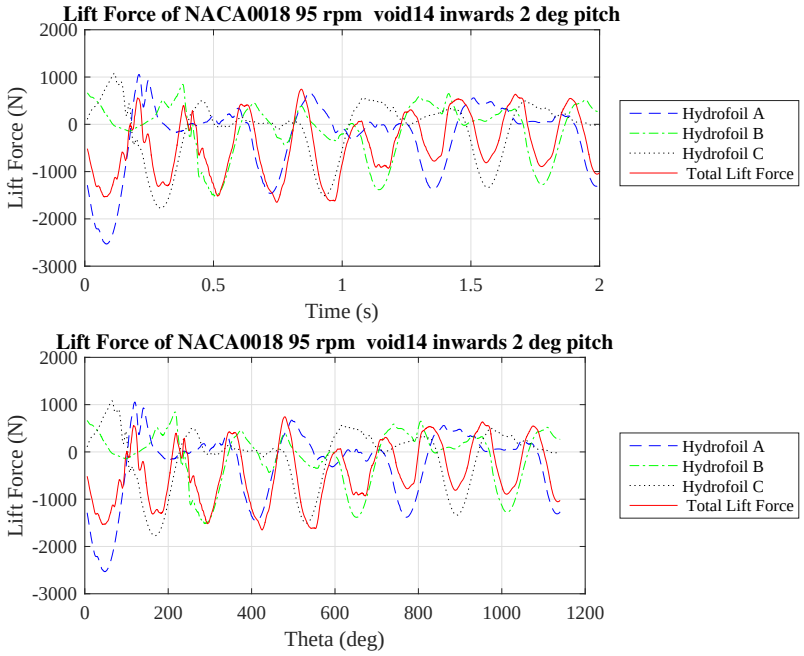

Figure A.307: Lift Force SIM44

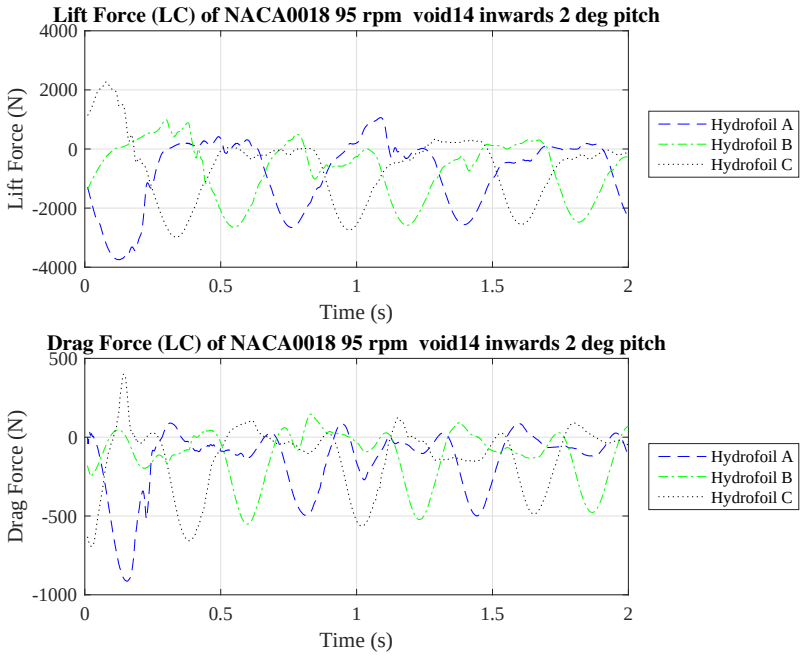

Figure A.308: Lift and Drag Force (LC) SIM44

A.1.45 SIM45

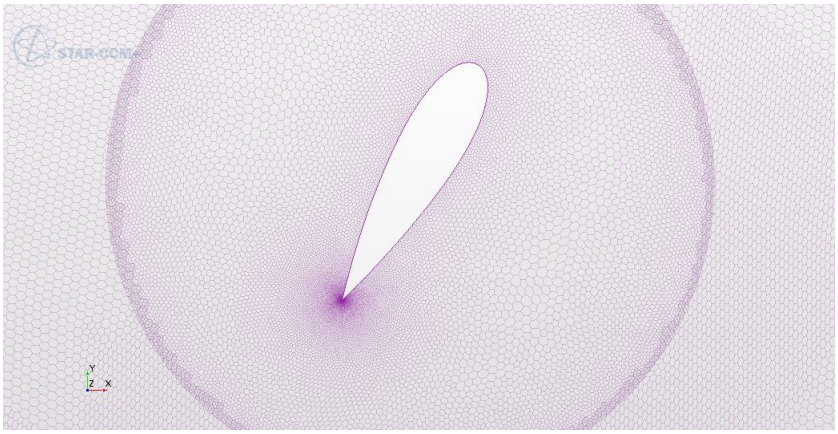

Figure A.309: Mesh SIM45

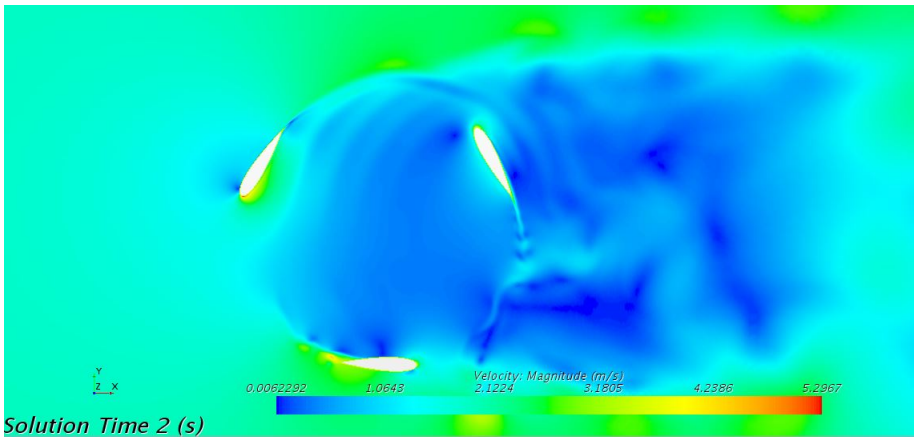

Figure A.310: Velocity SIM45

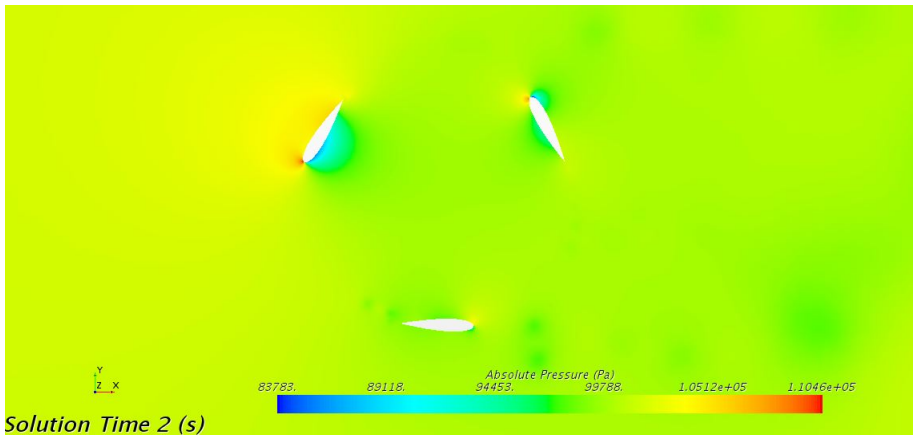

Figure A.311: Pressure SIM45

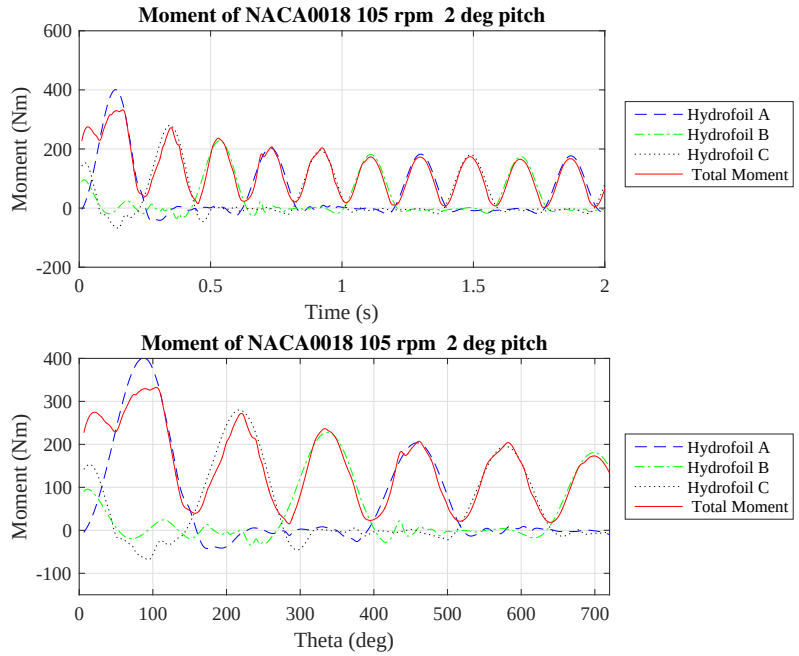

Figure A.312: Moment SIM45

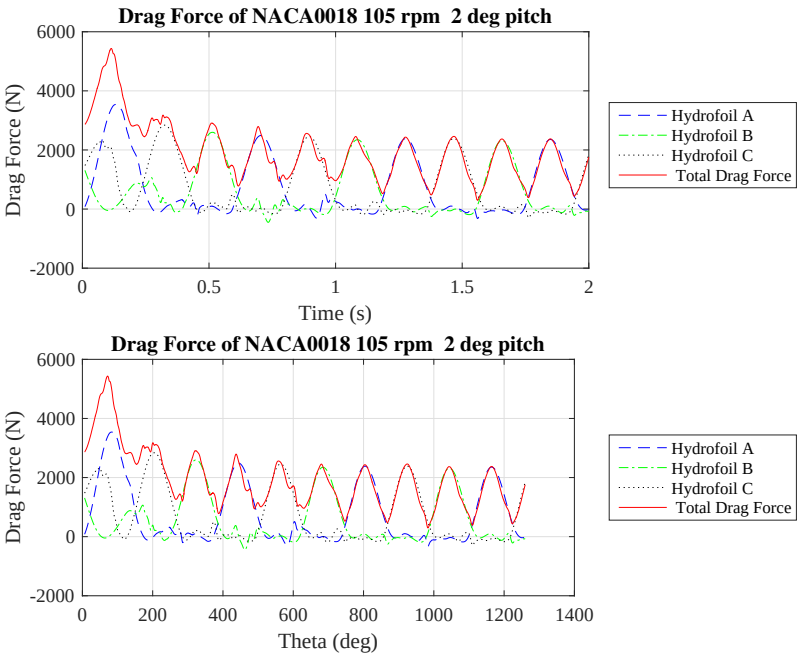

Figure A.313: Drag Force SIM45

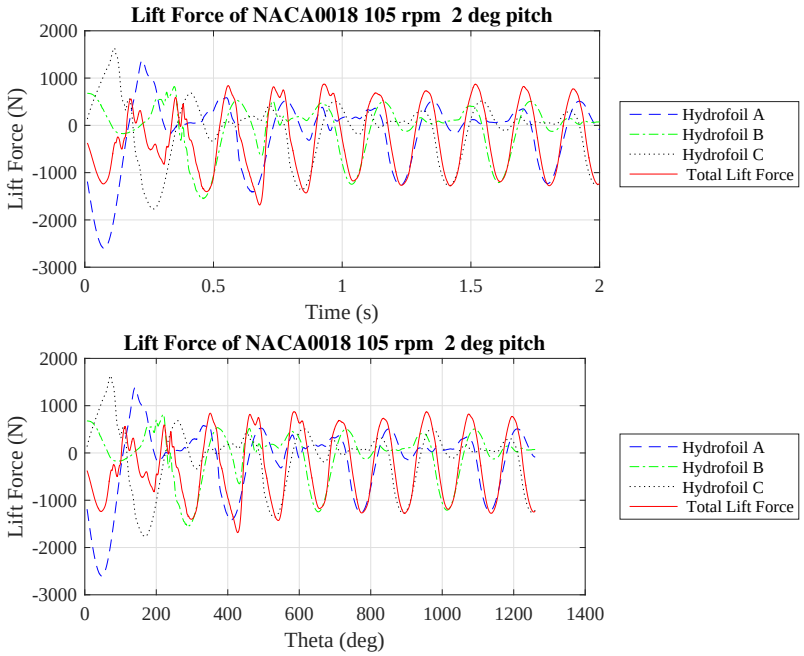

Figure A.314: Lift Force SIM45

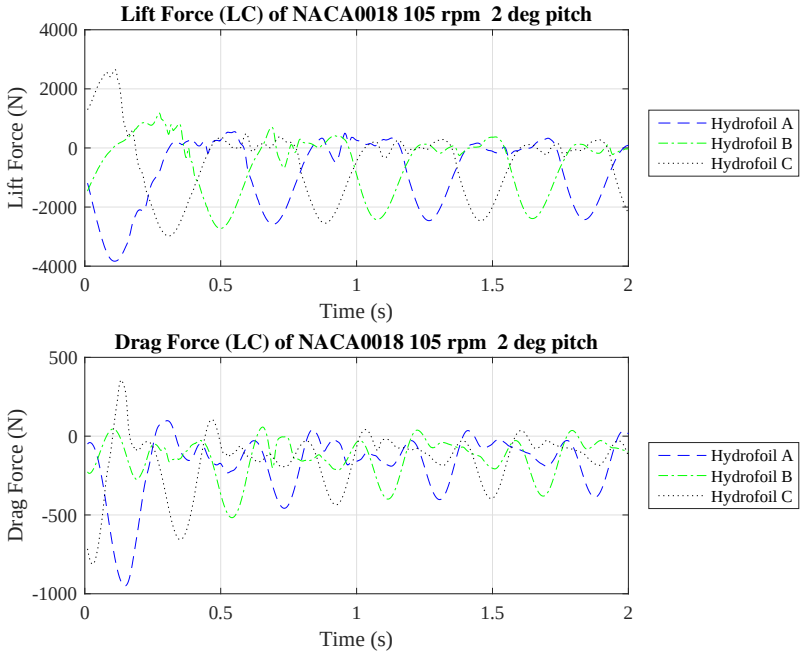

Figure A.315: Lift and Drag Force (LC) SIM45

A.1.46 SIM46

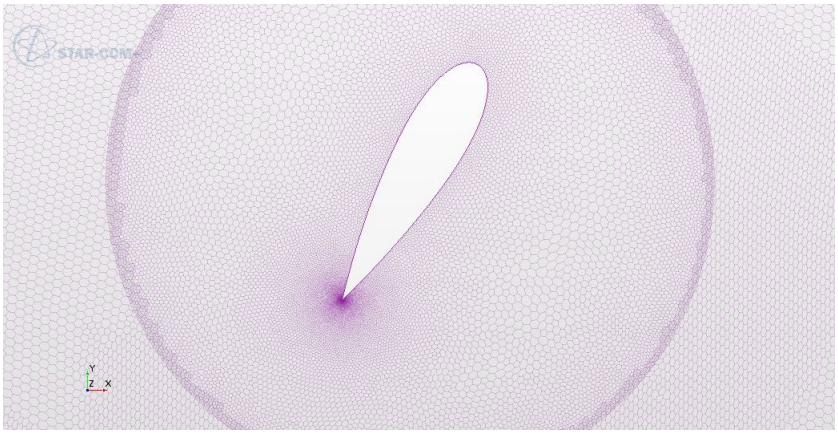

Figure A.316: Mesh SIM46

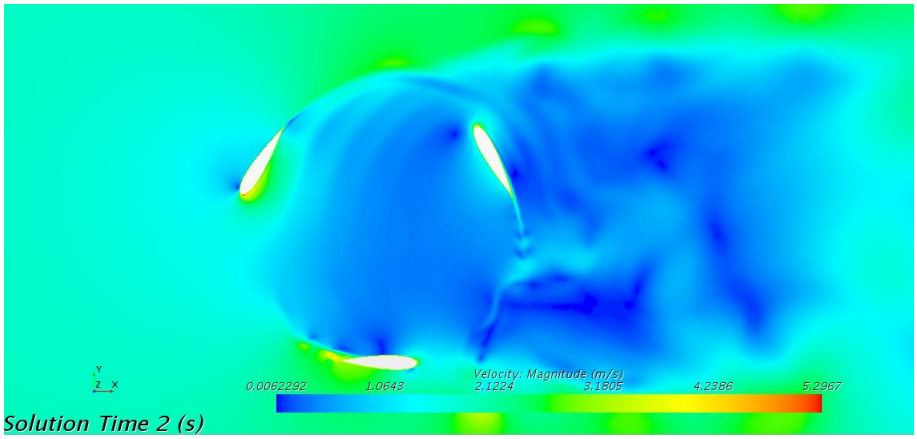

Figure A.317: Velocity SIM46

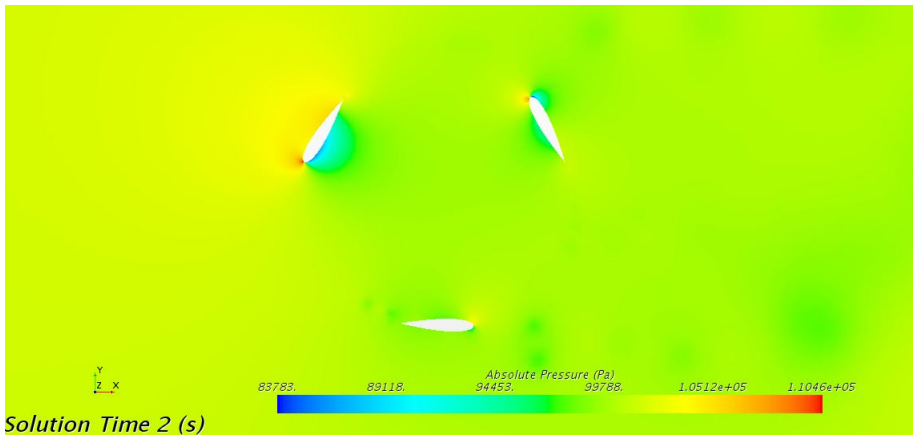

Figure A.318: Pressure SIM46

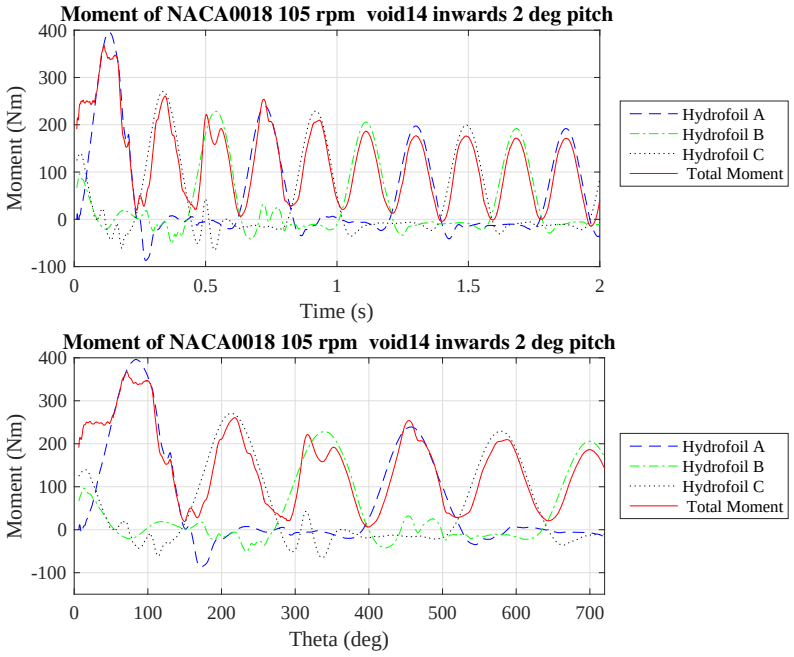

Figure A.319: Moment SIM46

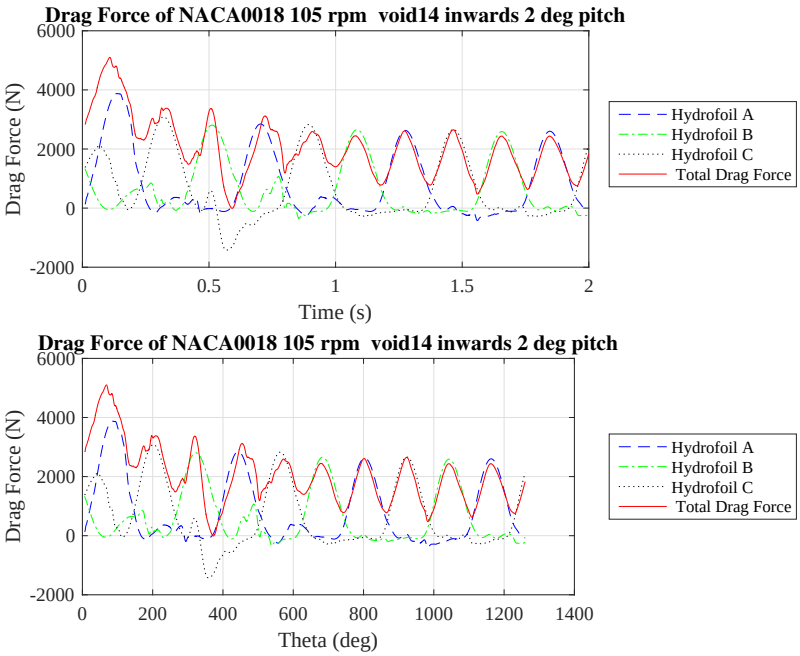

Figure A.320: Drag Force SIM46

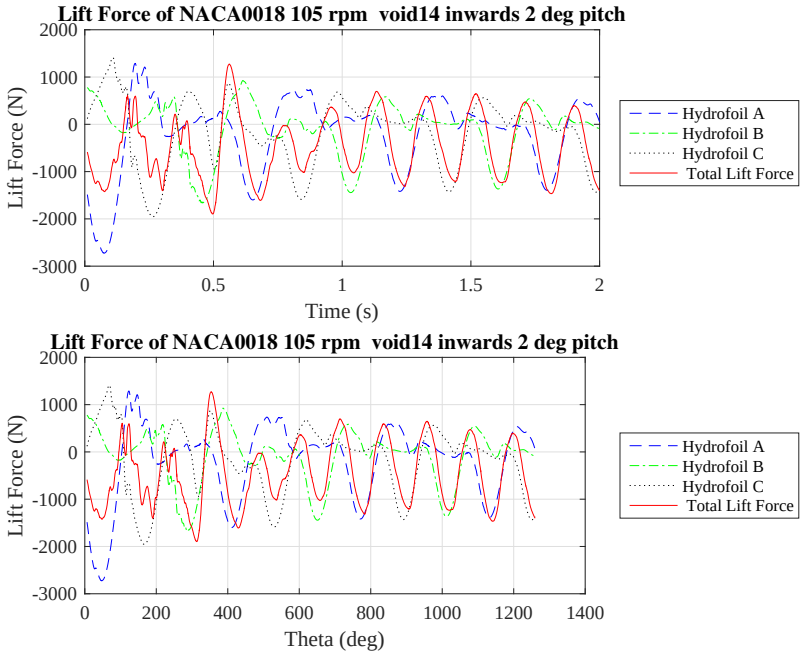

Figure A.321: Lift Force SIM46

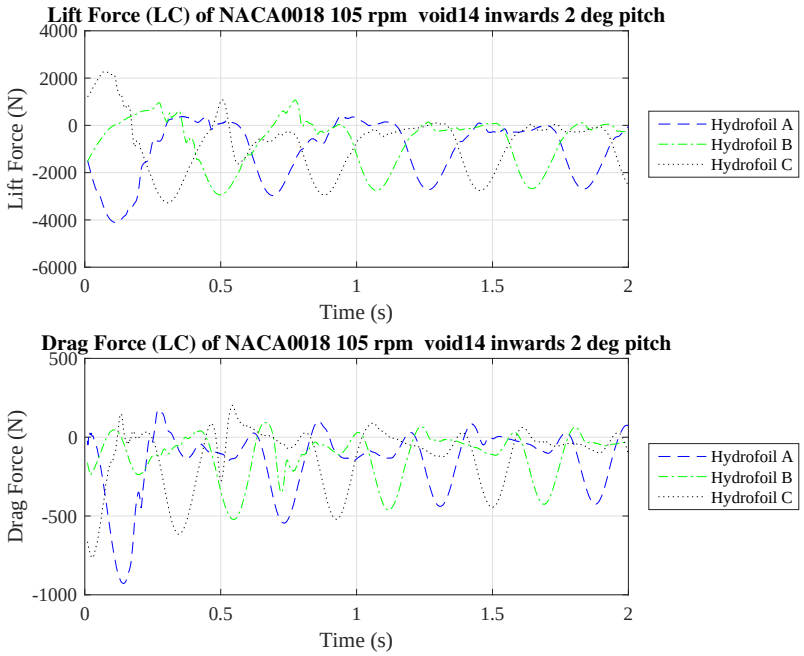

Figure A.322: Lift and Drag Force (LC) SIM46

A.1.47 SIM47

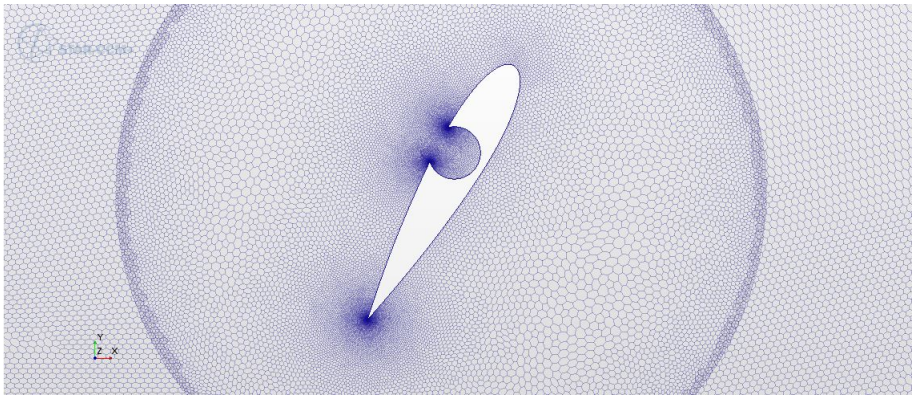

Figure A.323: Mesh SIM47

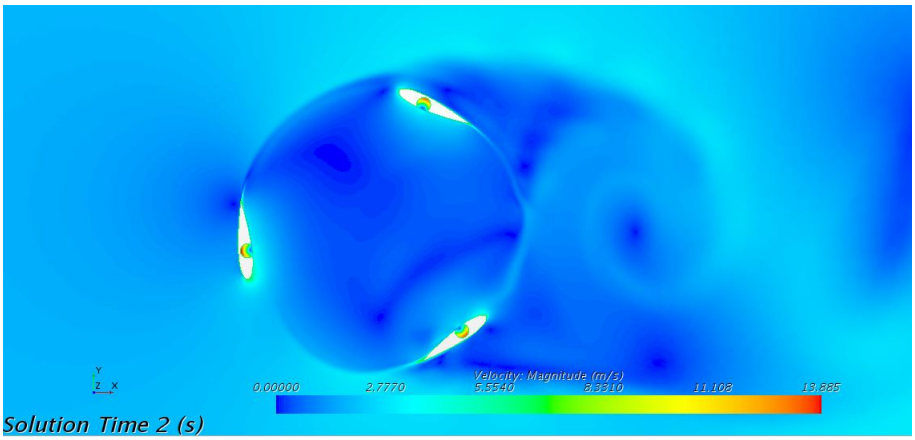

Figure A.324: Velocity SIM47

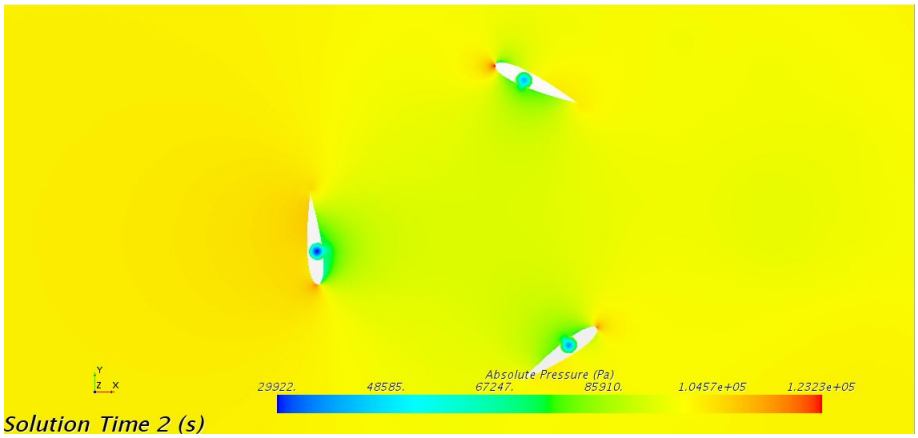

Figure A.325: Pressure SIM47

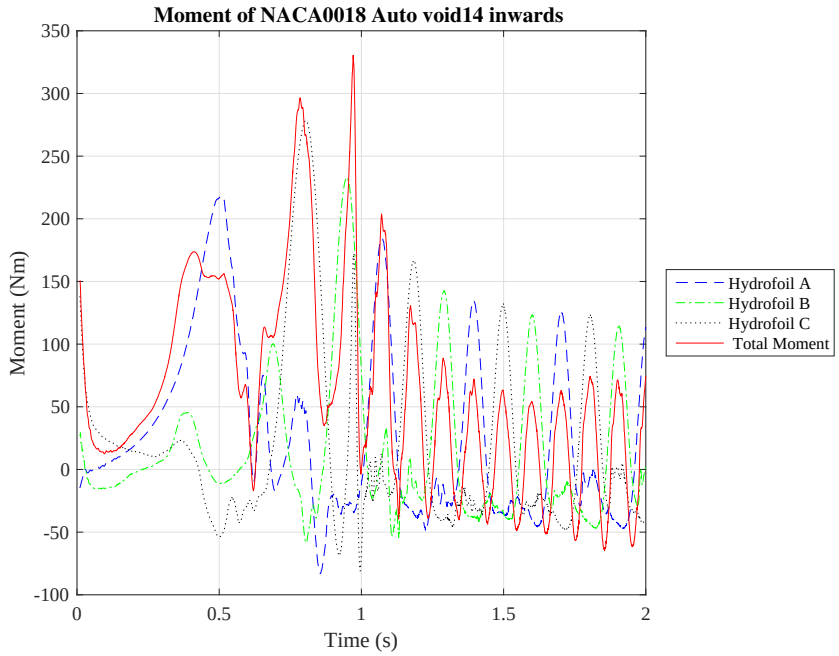

Figure A.326: Moment SIM47

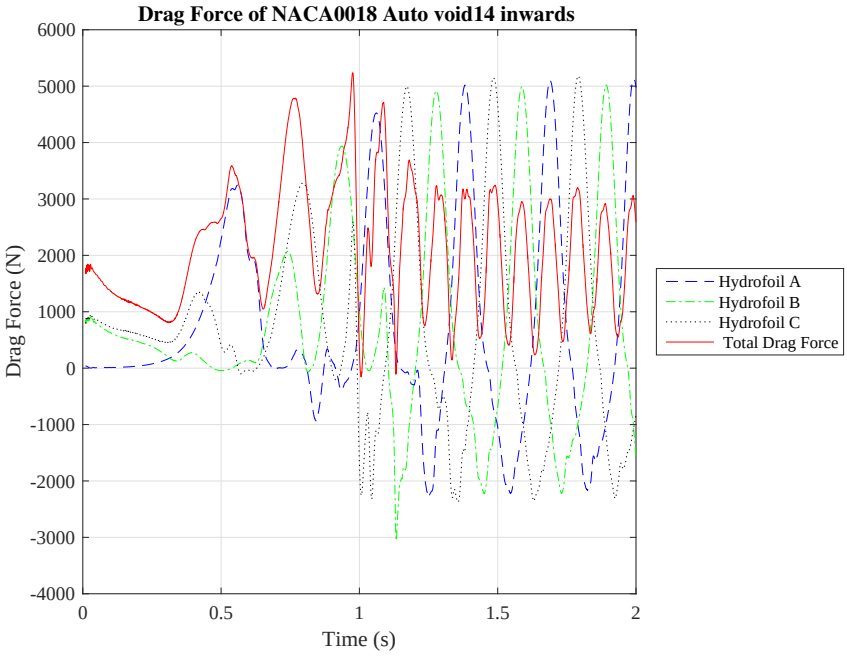

Figure A.327: Drag Force SIM47

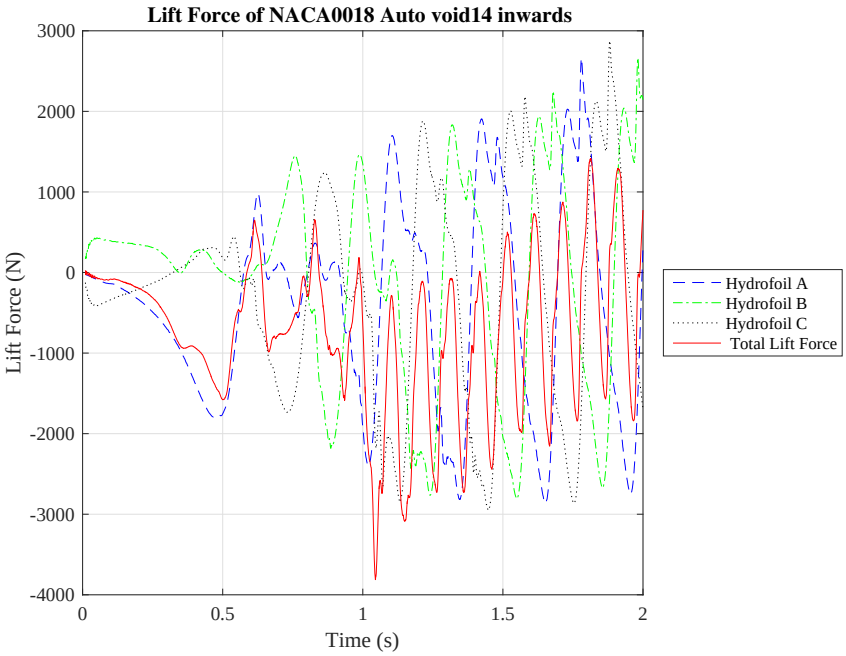

Figure A.328: Lift Force SIM47

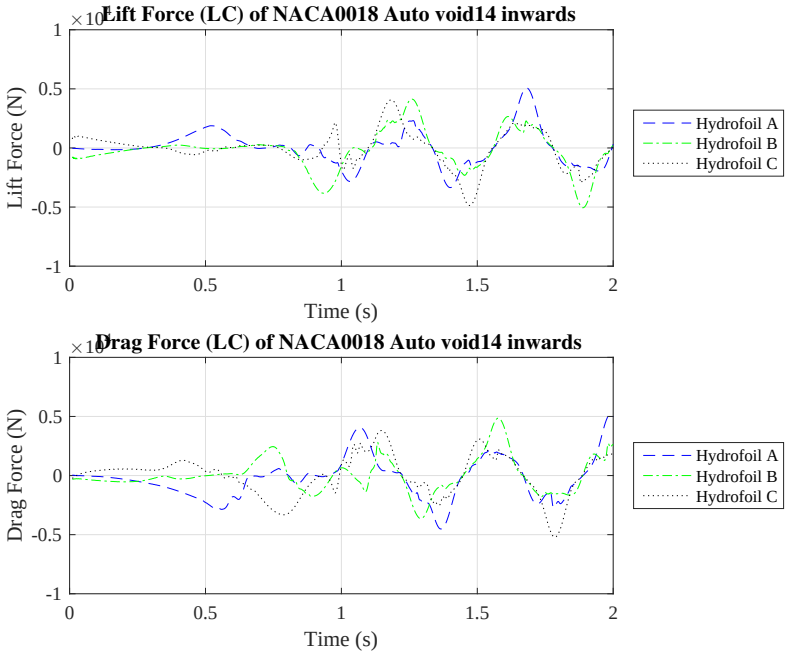

Figure A.329: Lift and Drag Force (LC) SIM47

A.1.48 SIM48

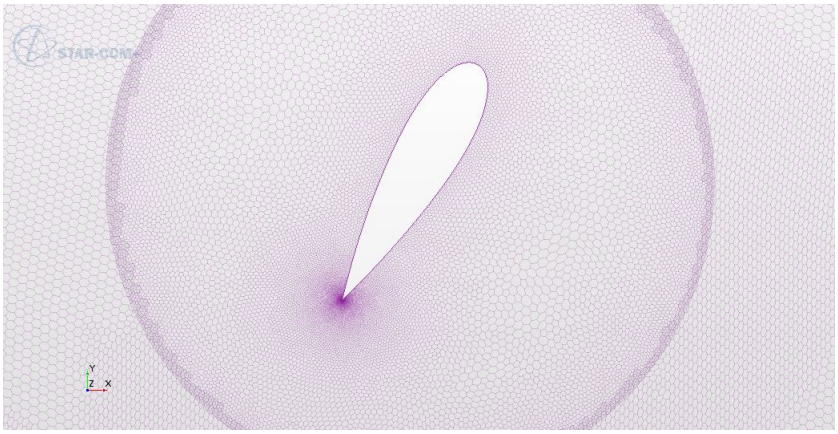

Figure A.330: Mesh SIM48

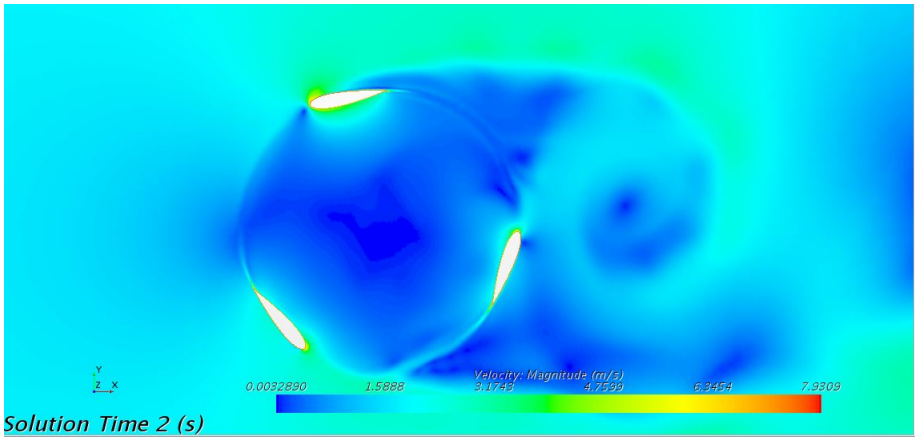

Figure A.331: Velocity SIM48

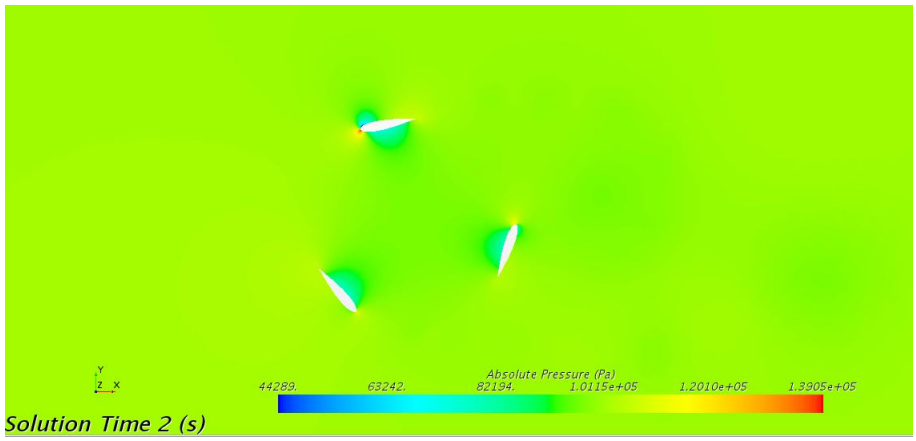

Figure A.332: Pressure SIM48

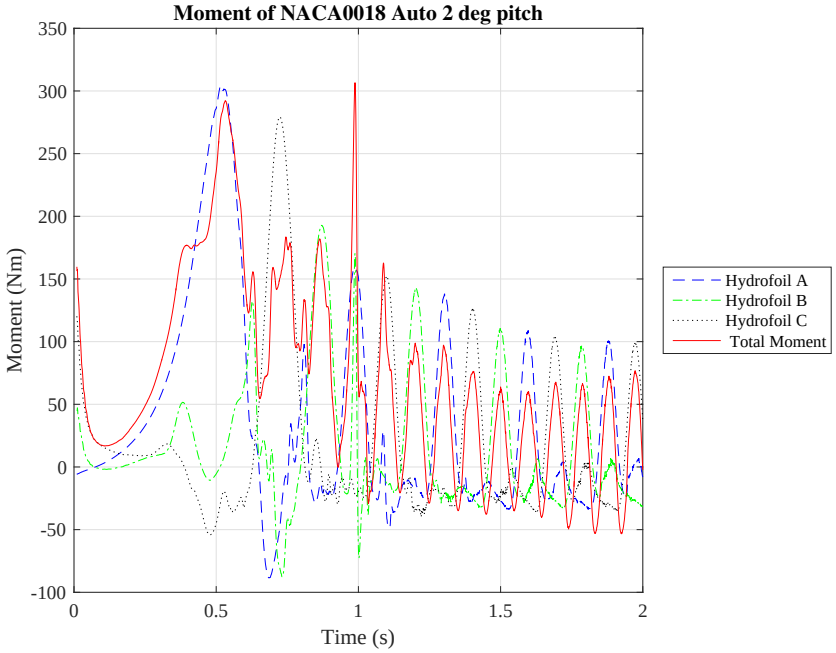

Figure A.333: Moment SIM48

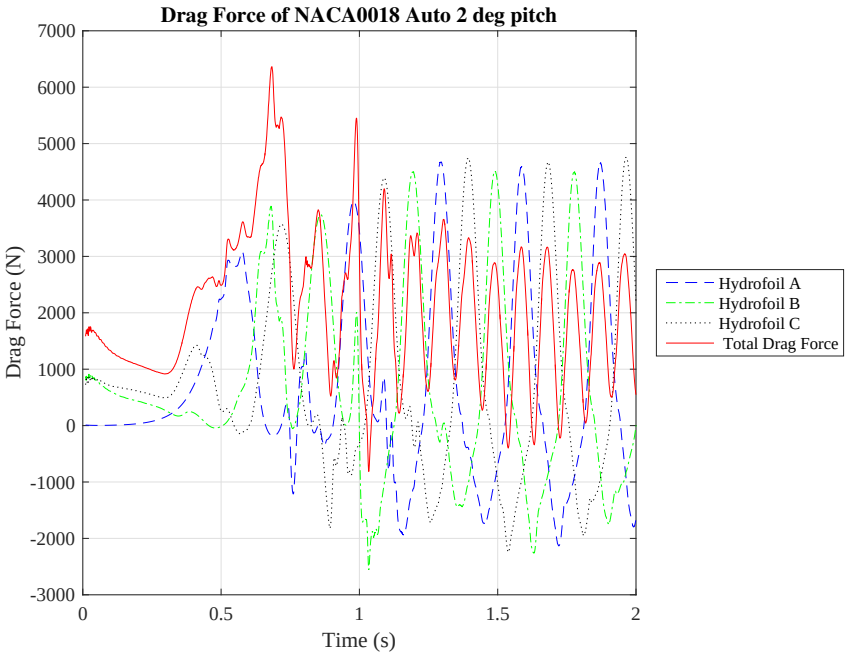

Figure A.334: Drag Force SIM48

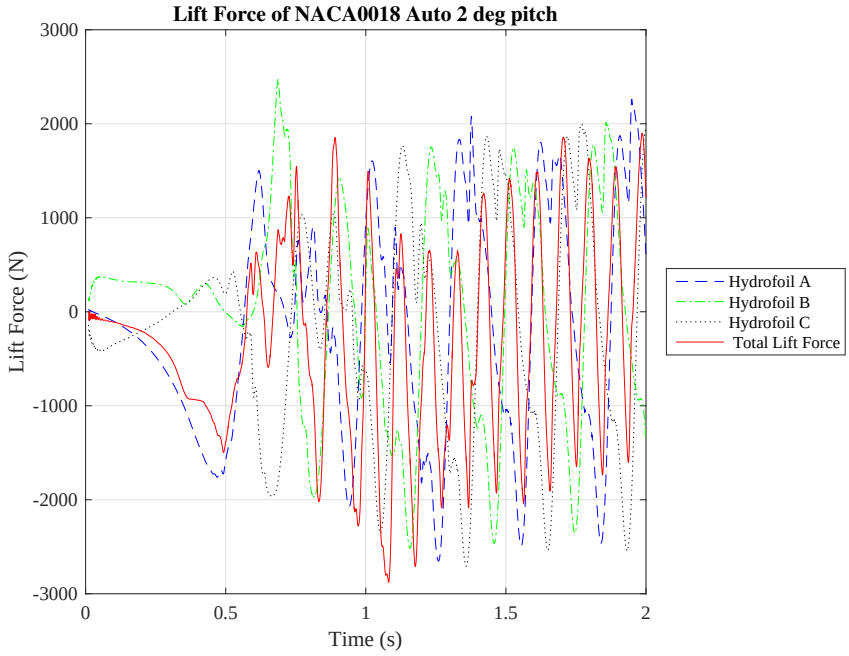

Figure A.335: Lift Force SIM48

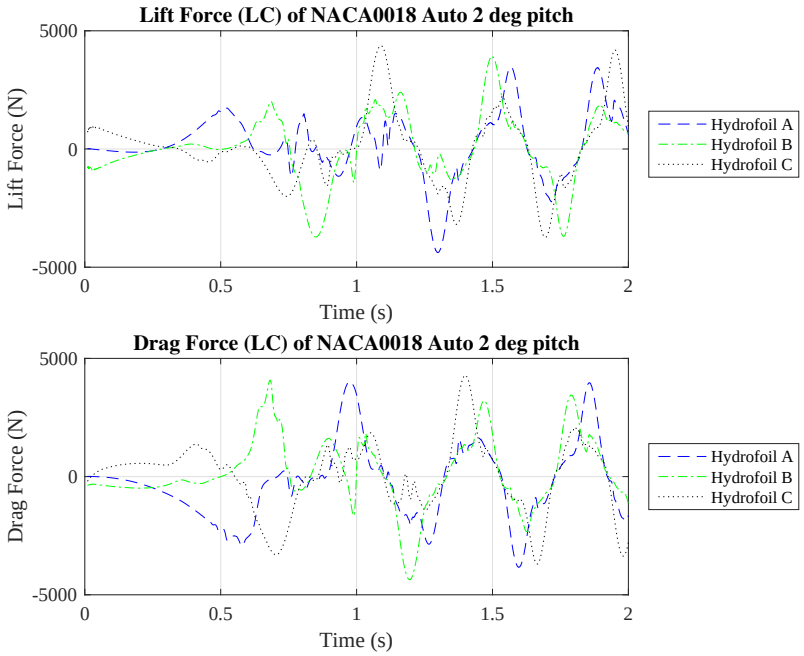

Figure A.336: Lift and Drag Force (LC) SIM48

A.1.49 SIM49

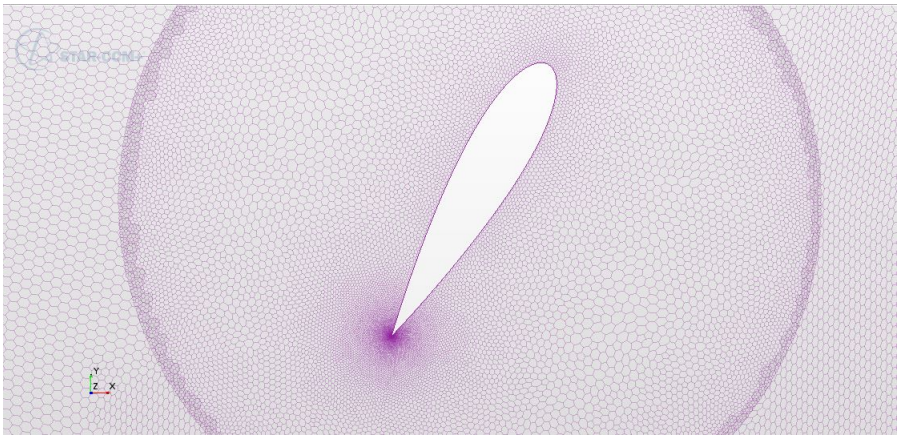

Figure A.337: Mesh SIM49

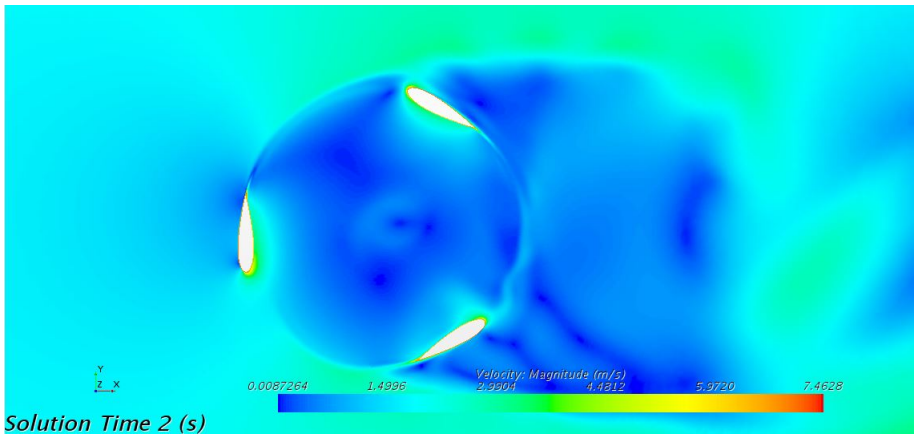

Figure A.338: Velocity SIM49

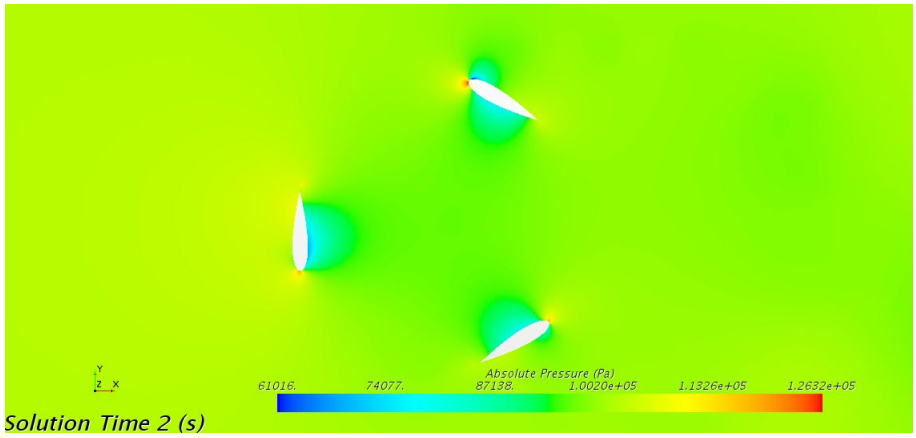

Figure A.339: Pressure SIM49

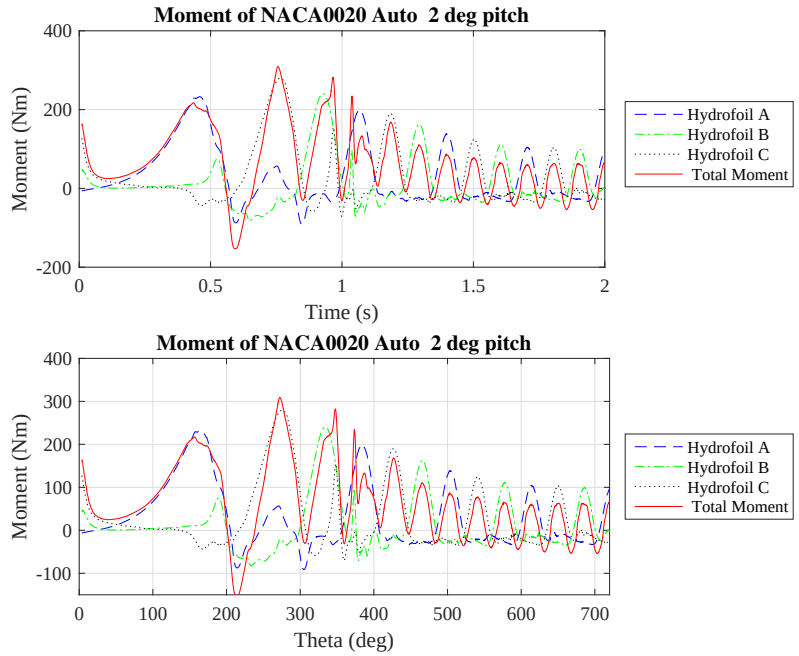

Figure A.340: Moment SIM49

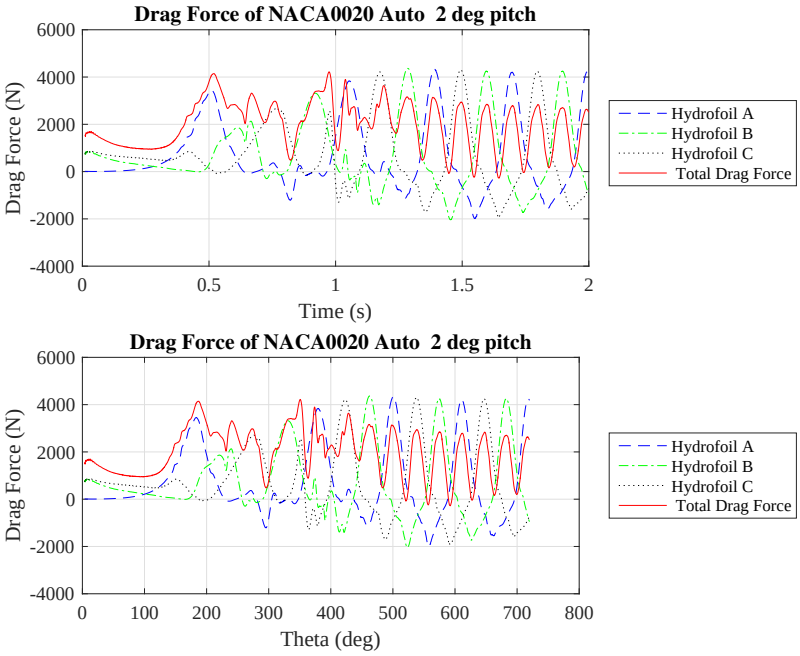

Figure A.341: Drag Force SIM49

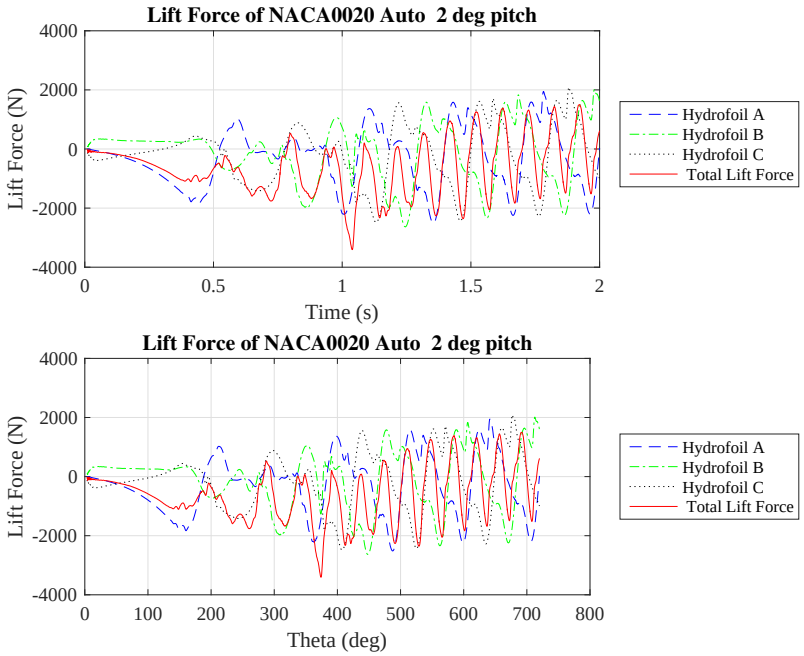

Figure A.342: Lift Force SIM49

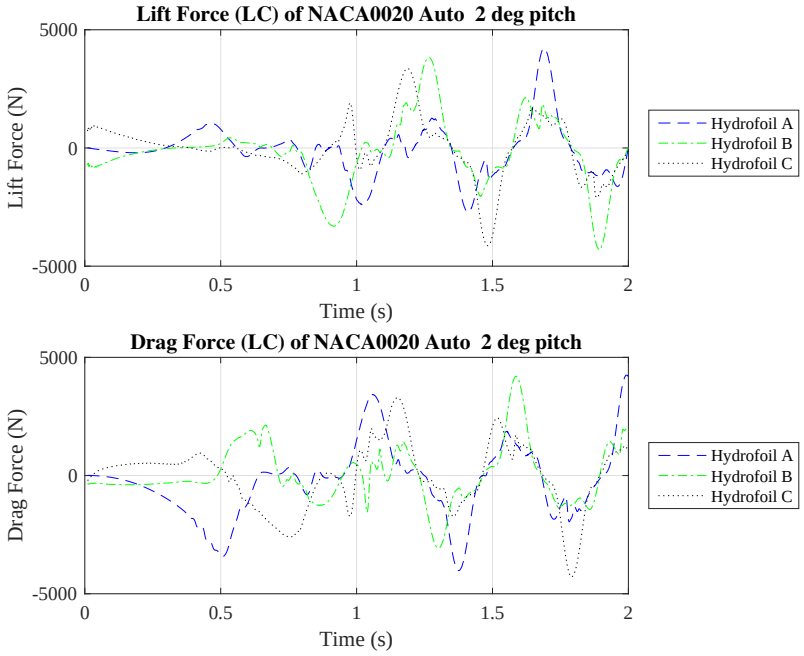

Figure A.343: Lift and Drag Force (LC) SIM49

A.1.50 SIM50

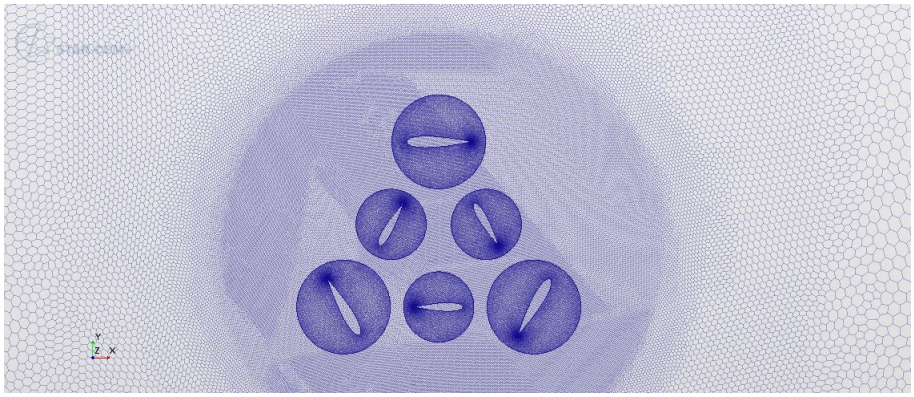

Figure A.344: Mesh SIM50

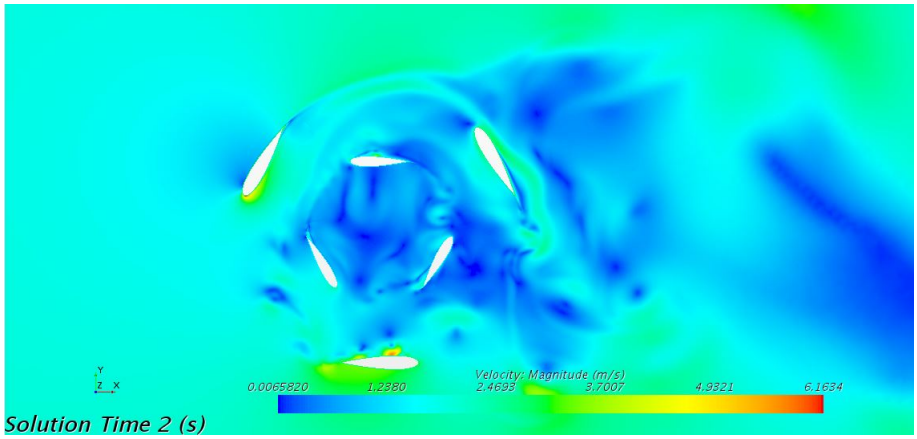

Figure A.345: Velocity SIM50

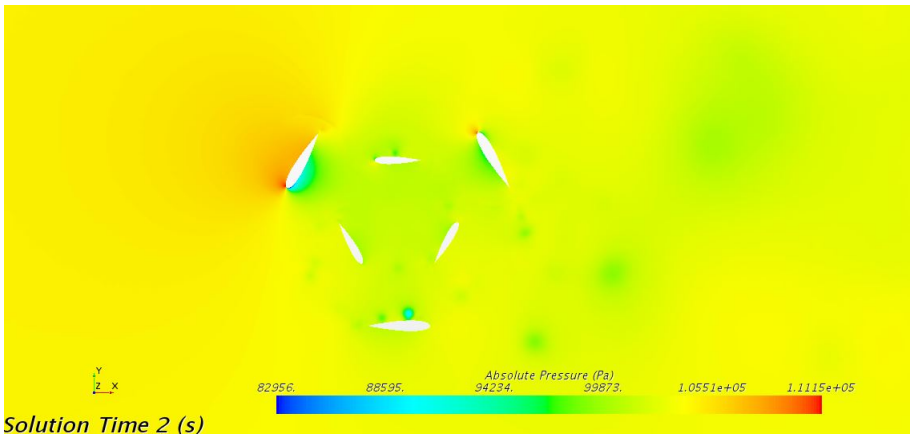

Figure A.346: Pressure SIM50

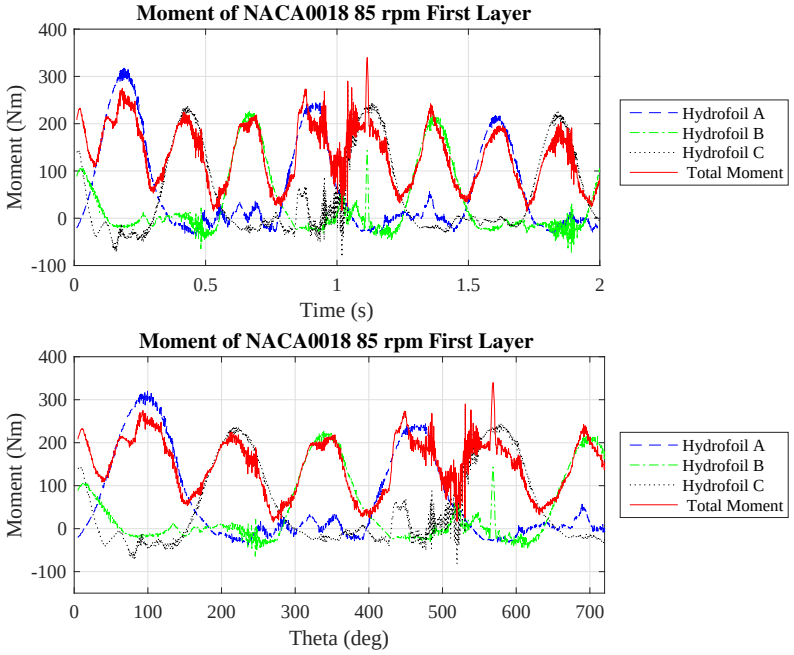

Figure A.347: Moment SIM50 1

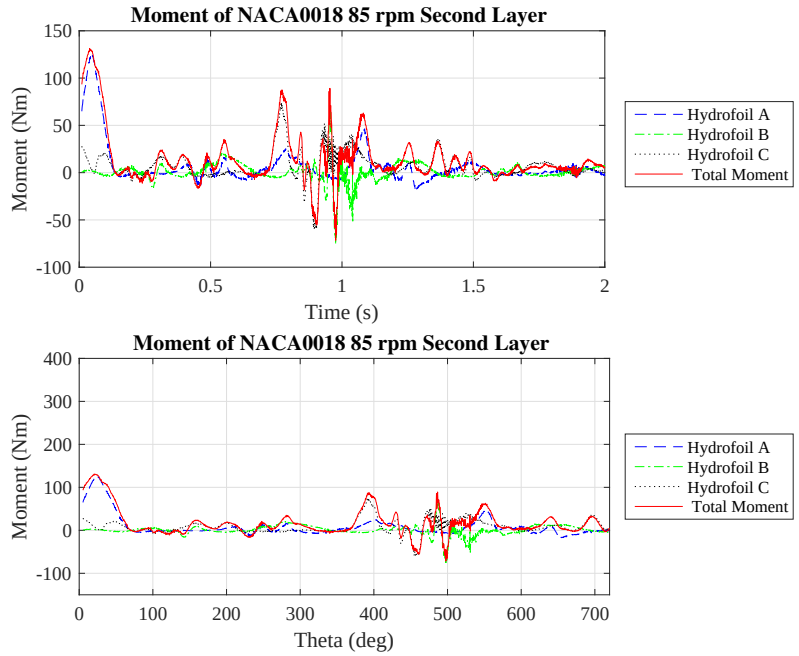

Figure A.348: Moment SIM50 2

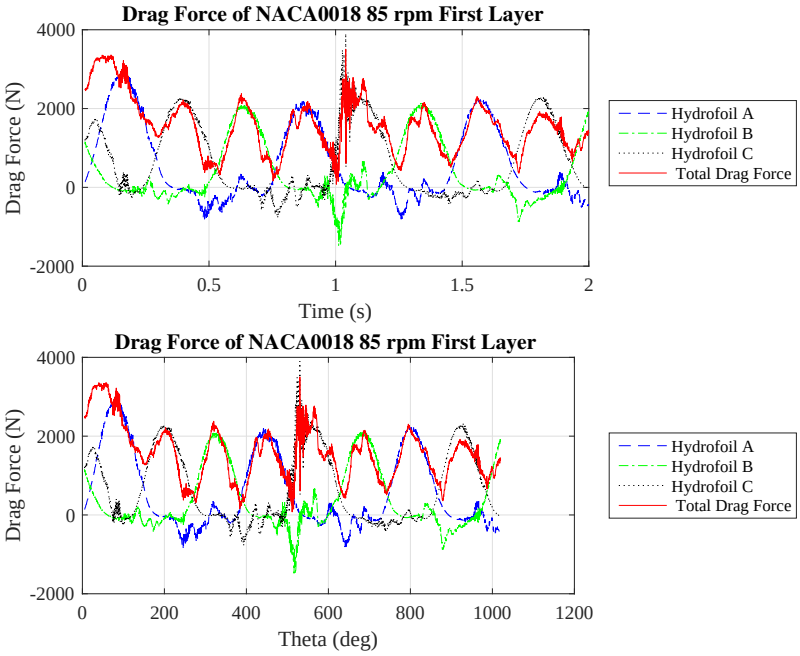

Figure A.349: Drag Force SIM50 1

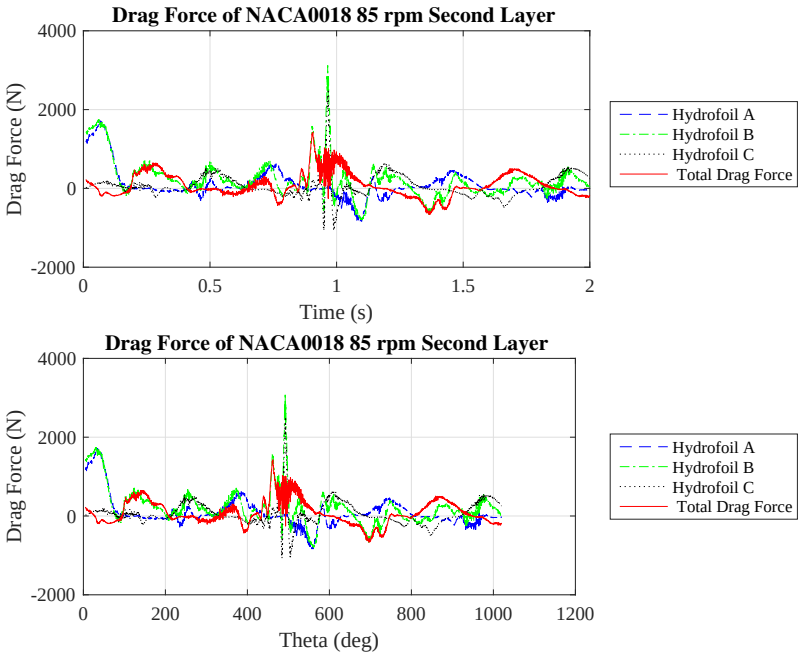

Figure A.350: Drag Force SIM50 2

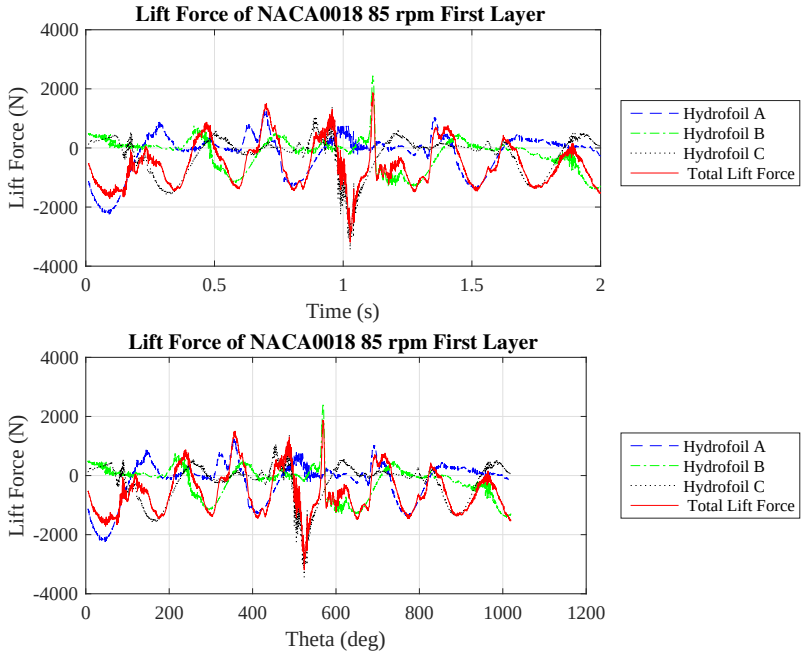

Figure A.351: Lift Force SIM50 1

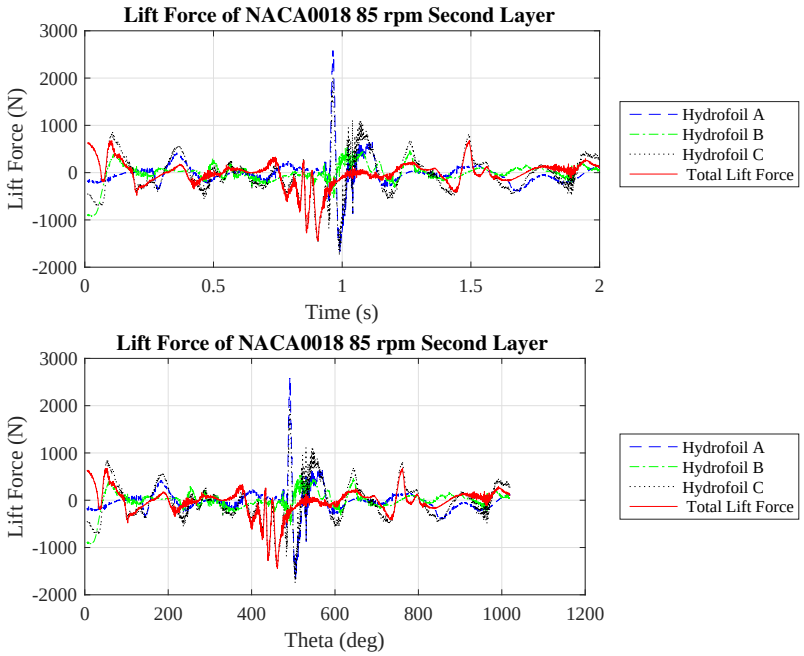

Figure A.352: Lift Force SIM50 2

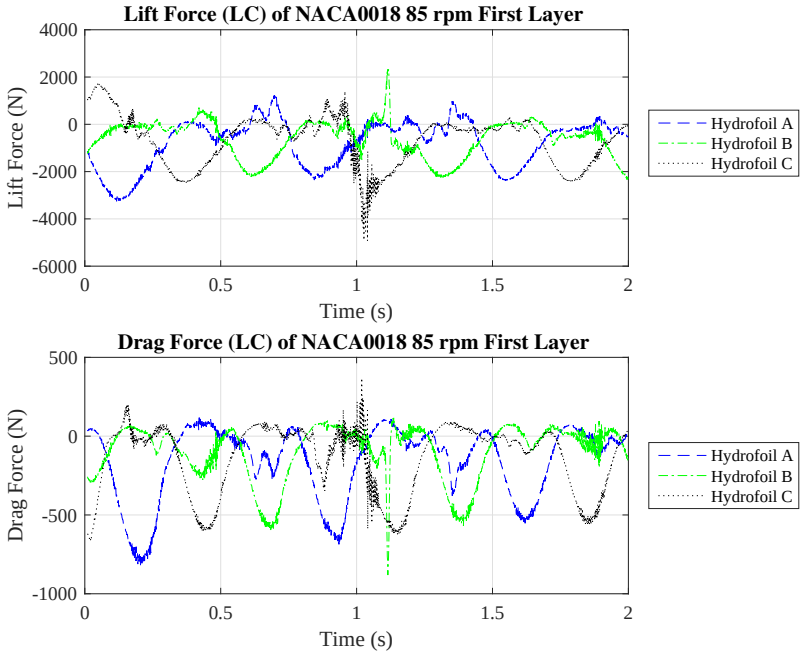

Figure A.353: Lift and Drag Force (LC) SIM50

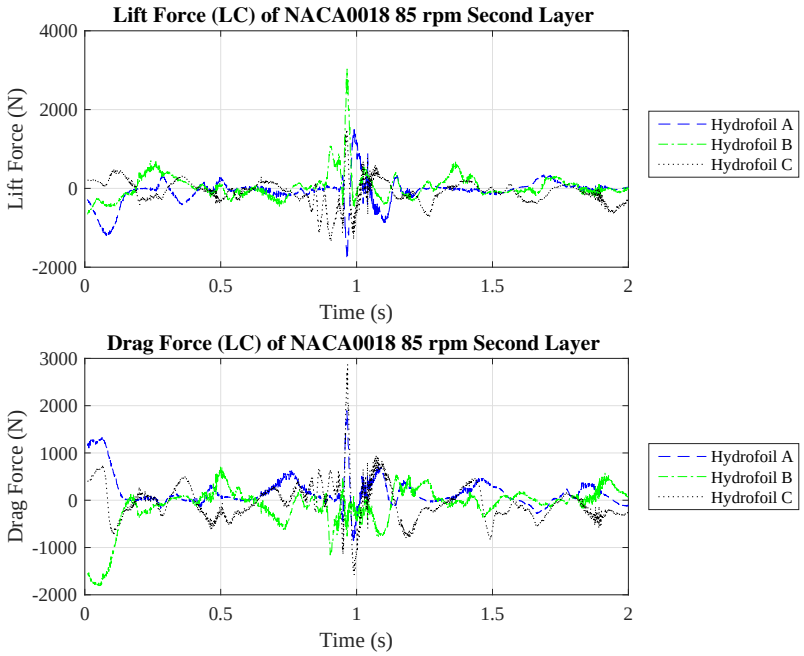

Figure A.354: Lift and Drag Force (LC) SIM50

A.1.51 SIM51

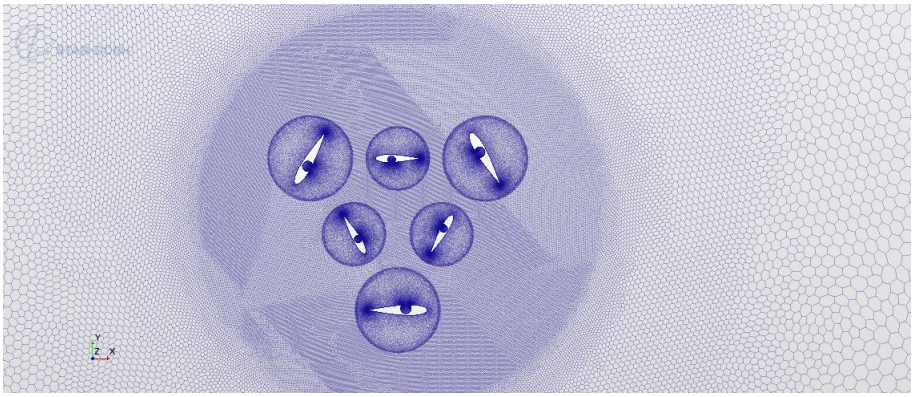

Figure A.355: Mesh SIM51

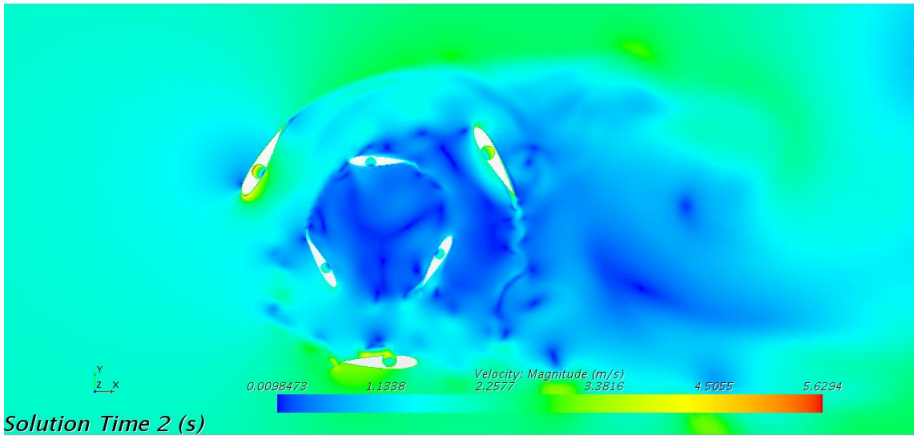

Figure A.356: Velocity SIM51

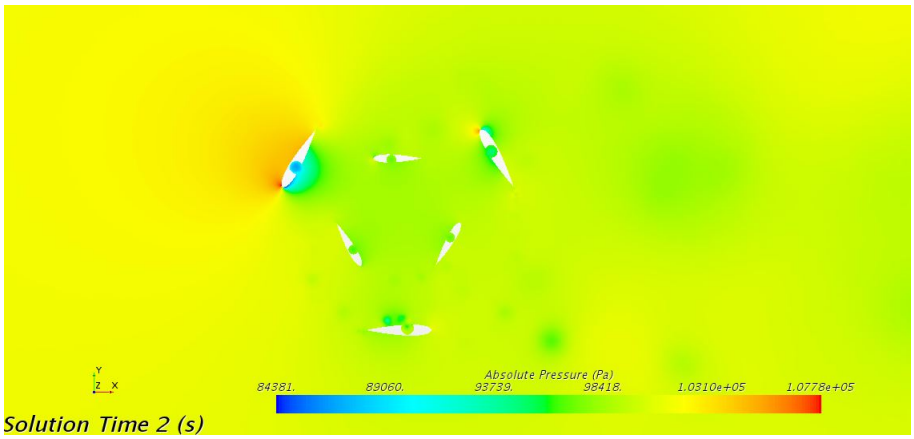

Figure A.357: Pressure SIM51

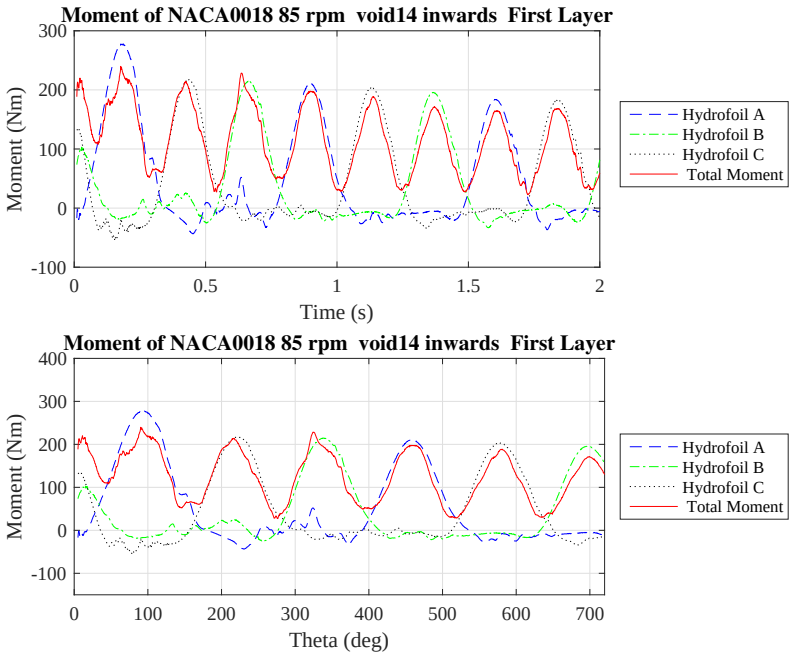

Figure A.358: Moment SIM51 1

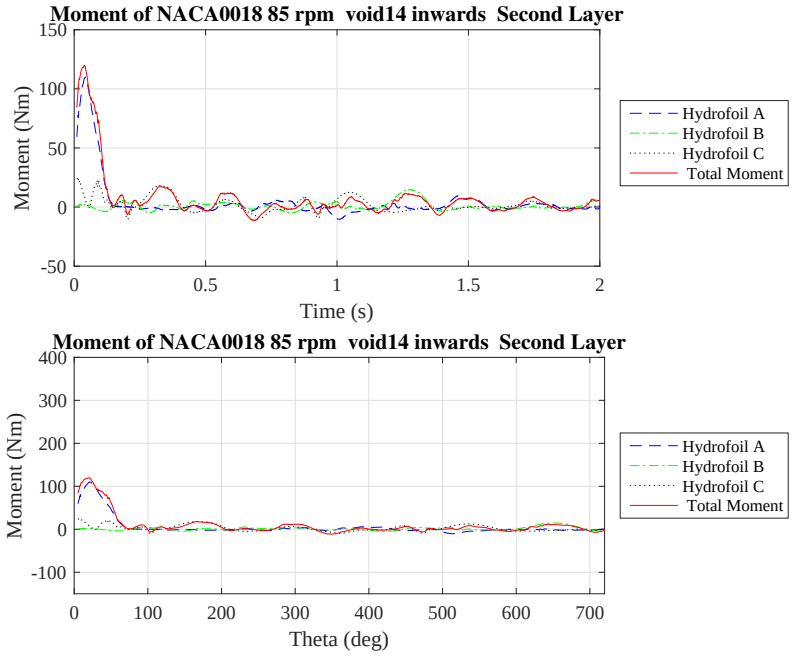

Figure A.359: Moment SIM51 2

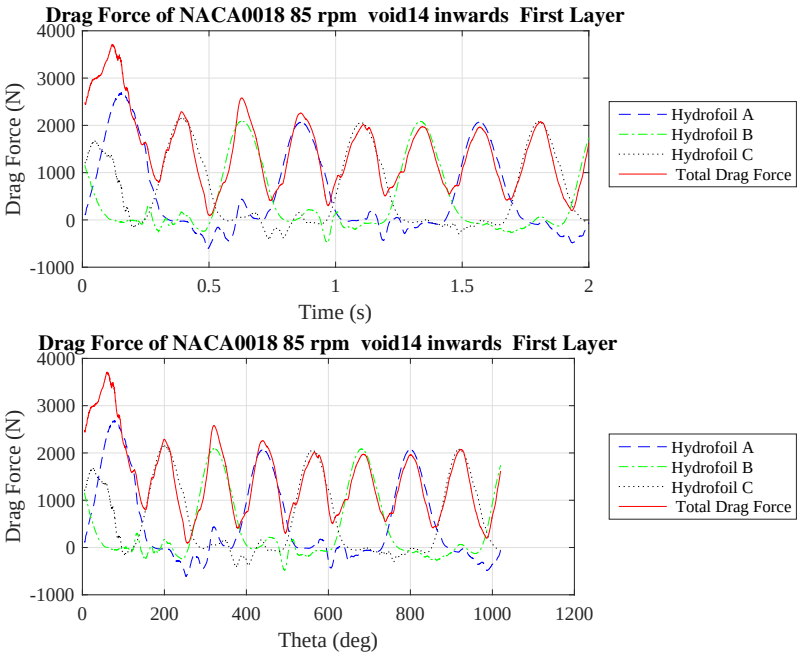

Figure A.360: Drag Force SIM51 1

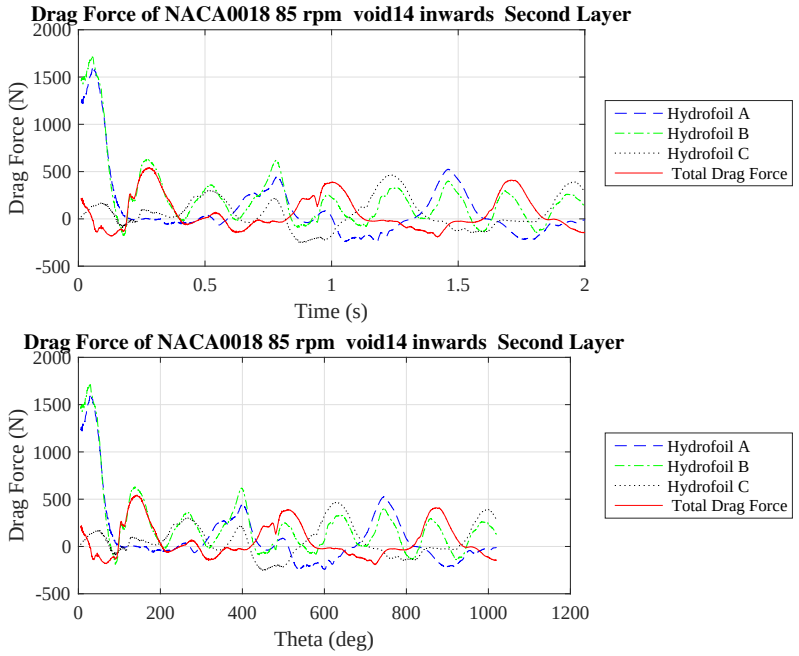

Figure A.361: Drag Force SIM51 2

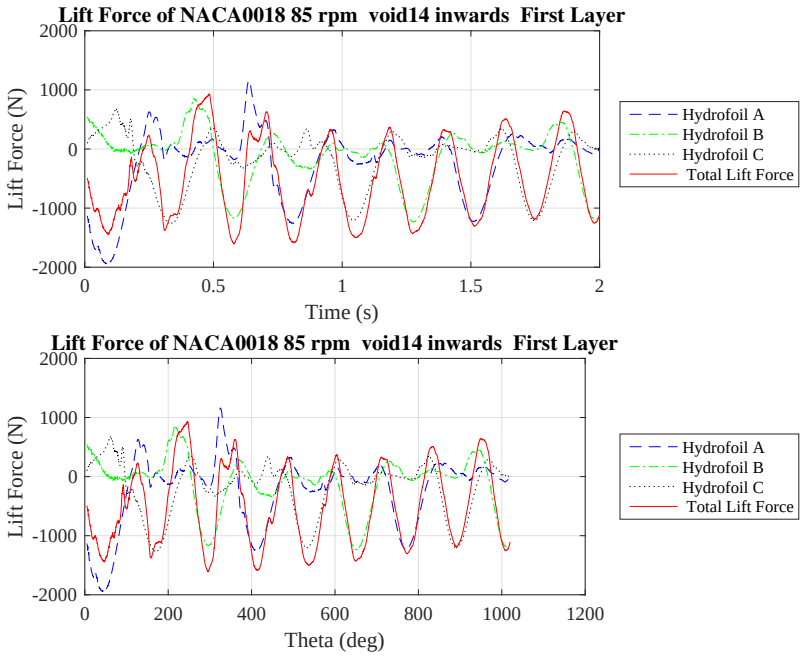

Figure A.362: Lift Force SIM51 1

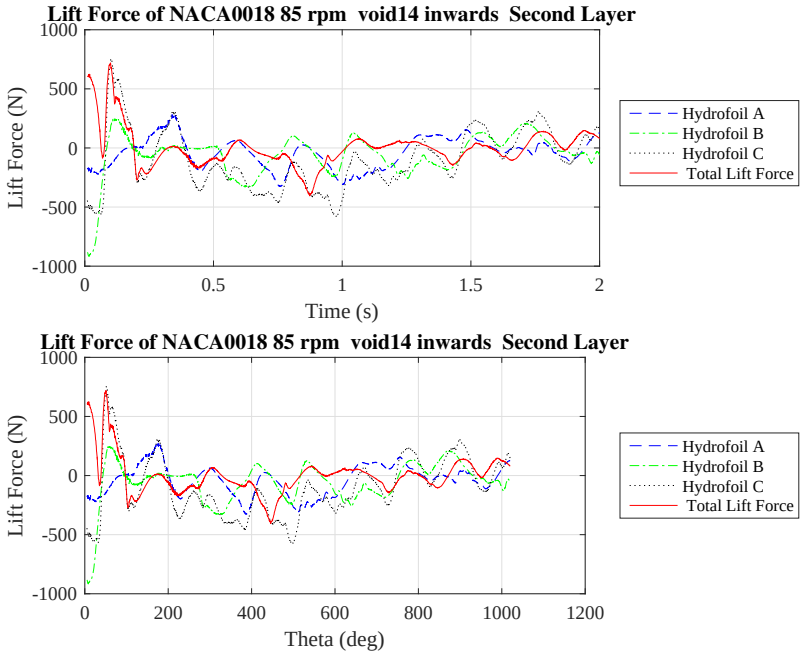

Figure A.363: Lift Force SIM51 2

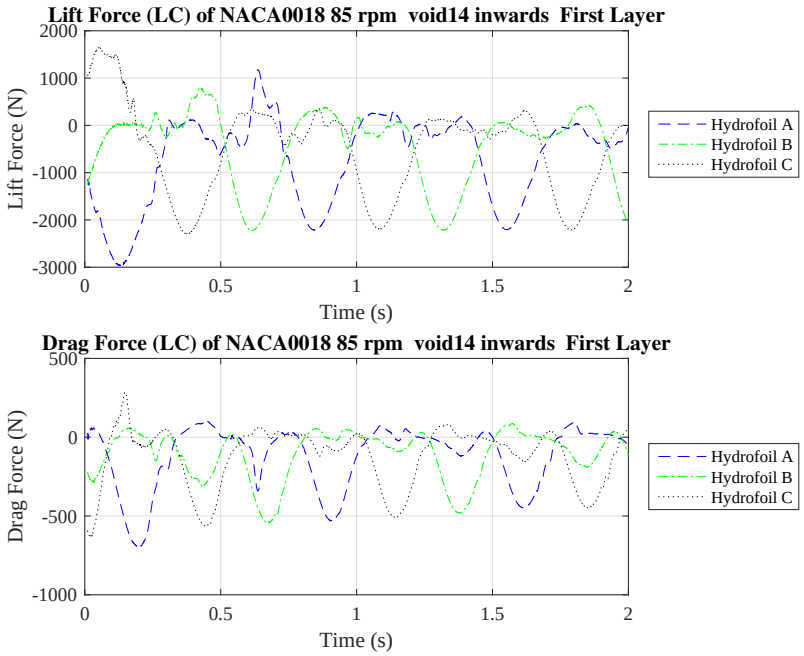

Figure A.364: Lift and Drag Force (LC) SIM51

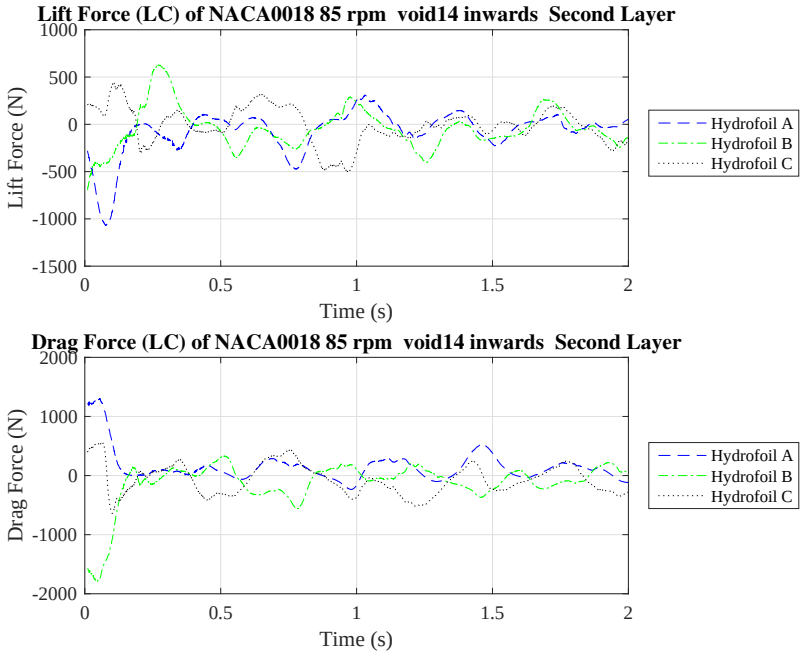

Figure A.365: Lift and Drag Force (LC) SIM51

A.1.52 SIM52

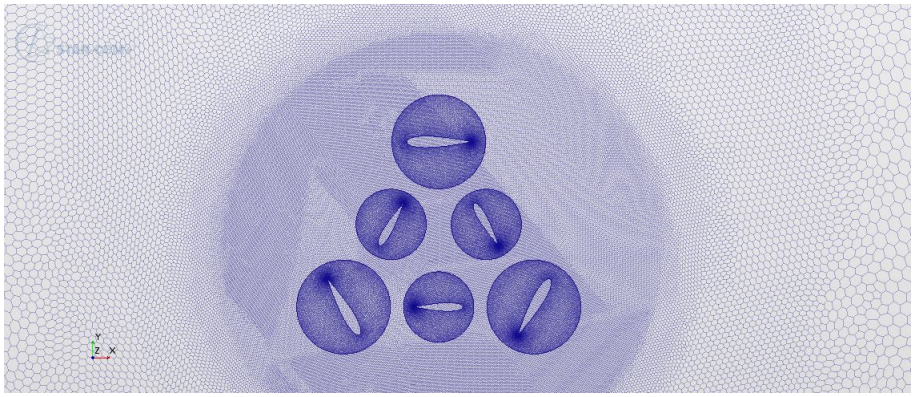

Figure A.366: Mesh SIM52

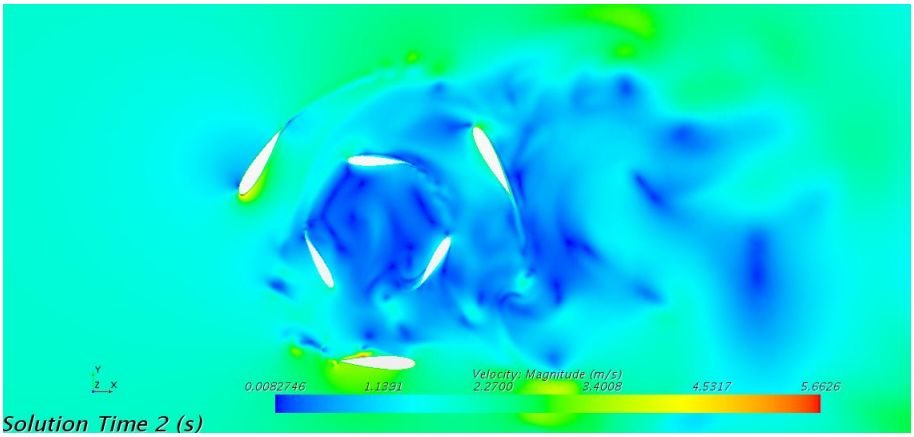

Figure A.367: Velocity SIM52

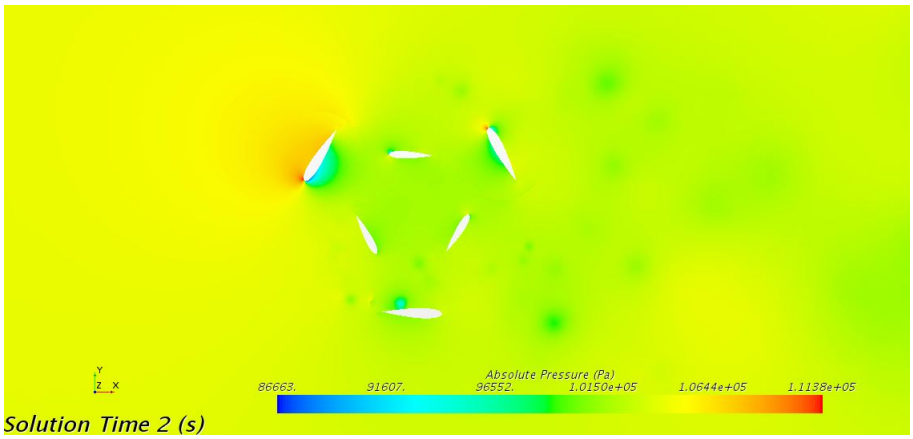

Figure A.368: Pressure SIM52

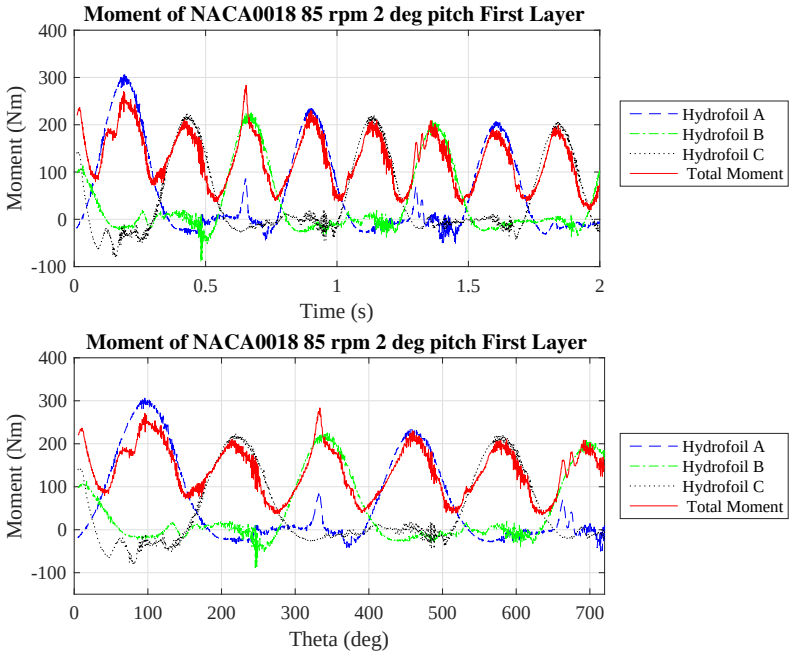

Figure A.369: Moment SIM52 1

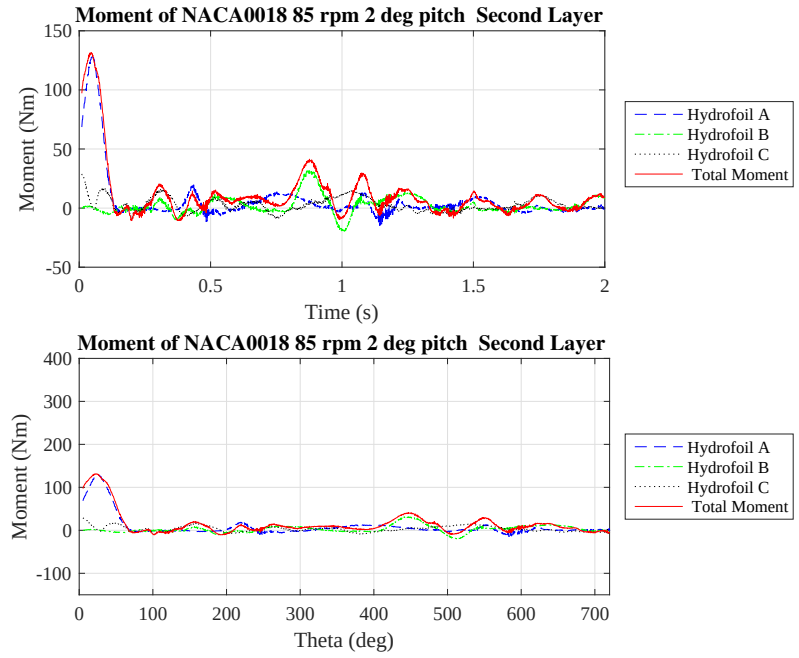

Figure A.370: Moment SIM52 2

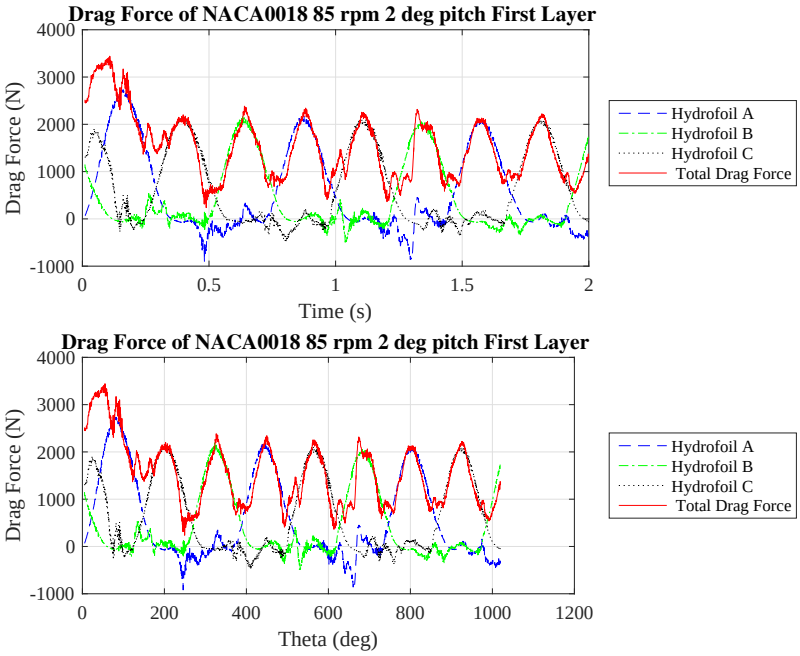

Figure A.371: Drag Force SIM52 1

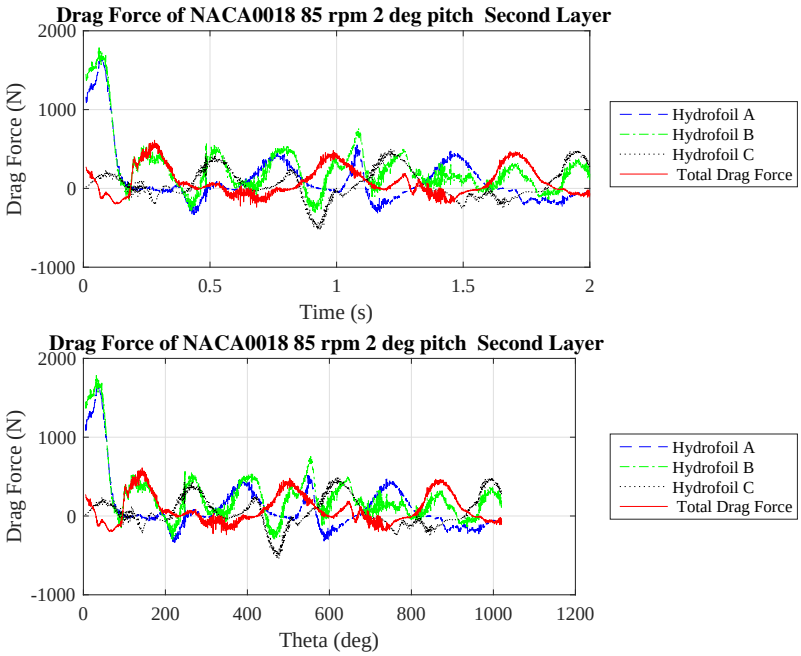

Figure A.372: Drag Force SIM52 2

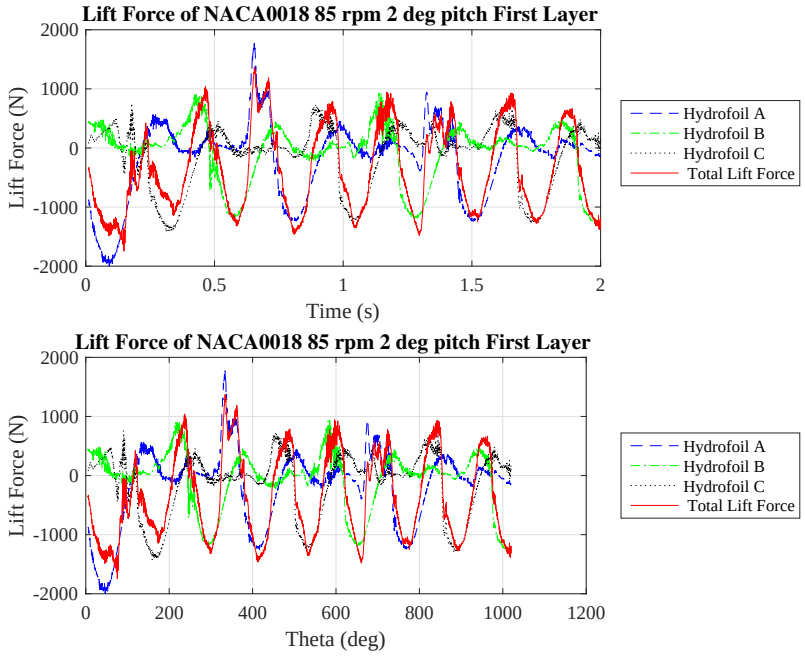

Figure A.373: Lift Force SIM52 1

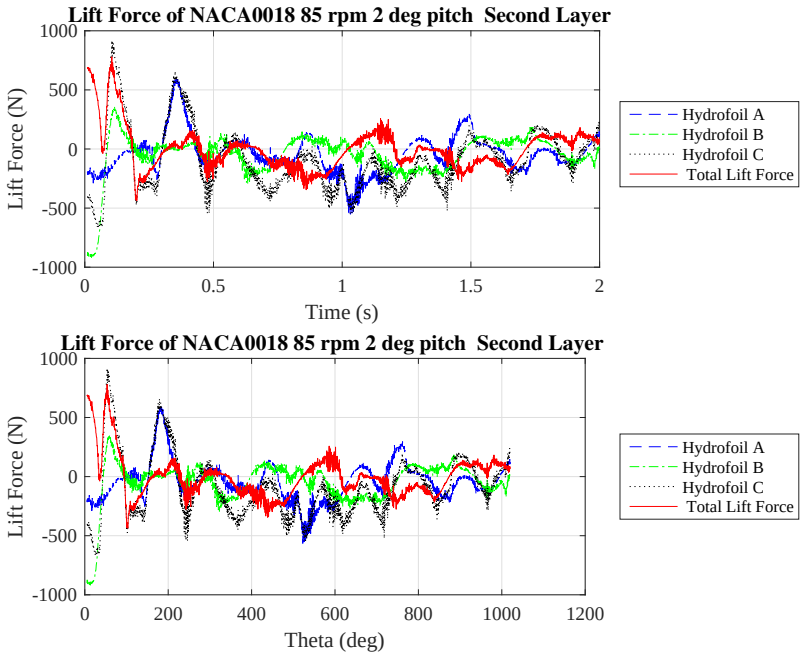

Figure A.374: Lift Force SIM52 2

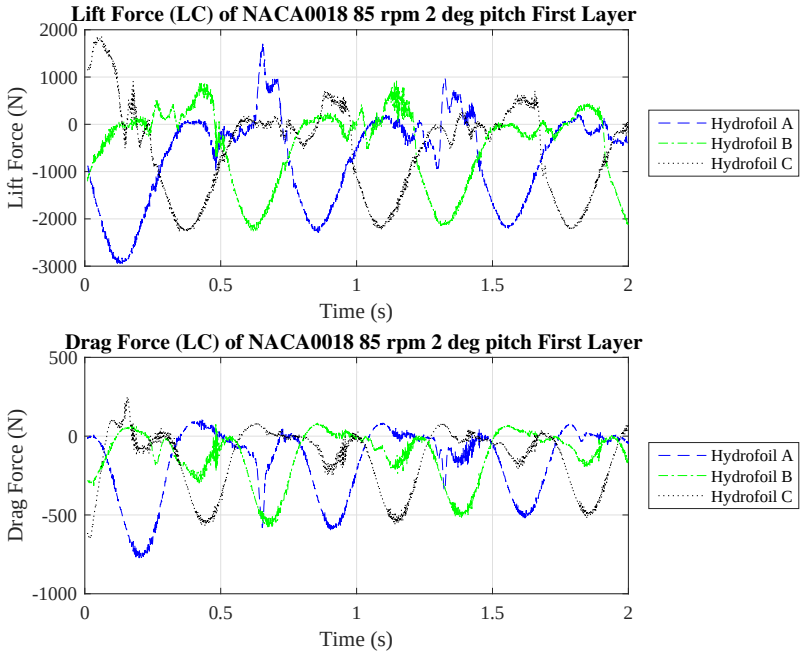

Figure A.375: Lift and Drag Force (LC) SIM52

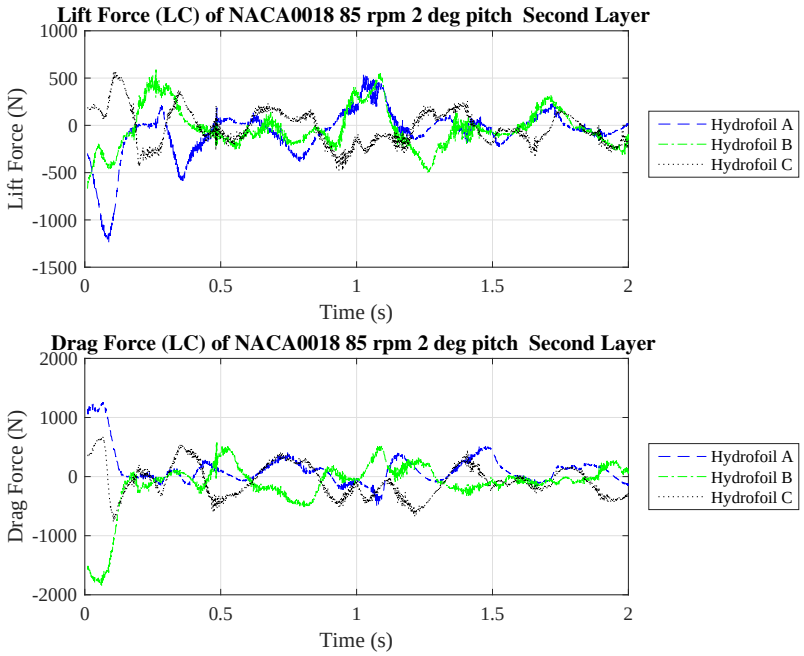

Figure A.376: Lift and Drag Force (LC) SIM52

A.1.53 SIM53

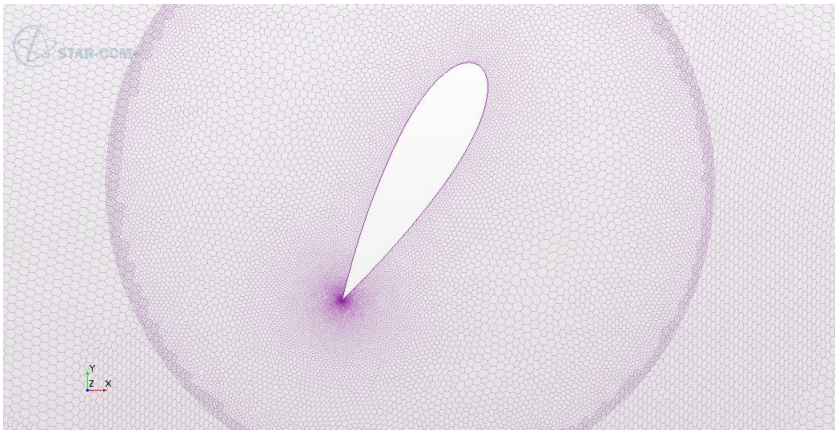

Figure A.377: Mesh SIM53

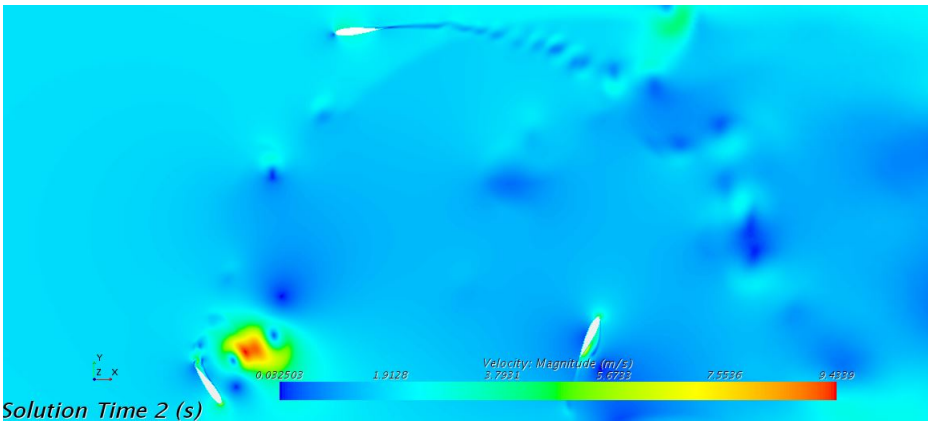

Figure A.378: Velocity SIM53

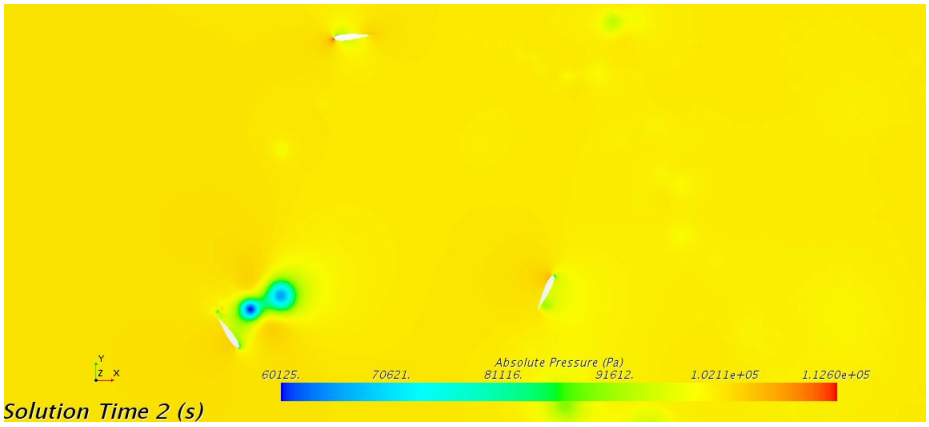

Figure A.379: Pressure SIM53

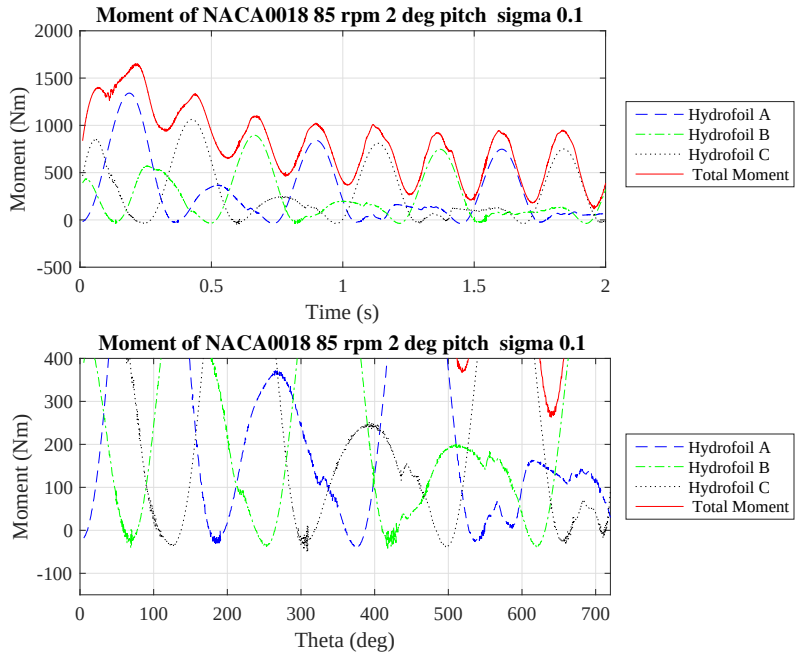

Figure A.380: Moment SIM53

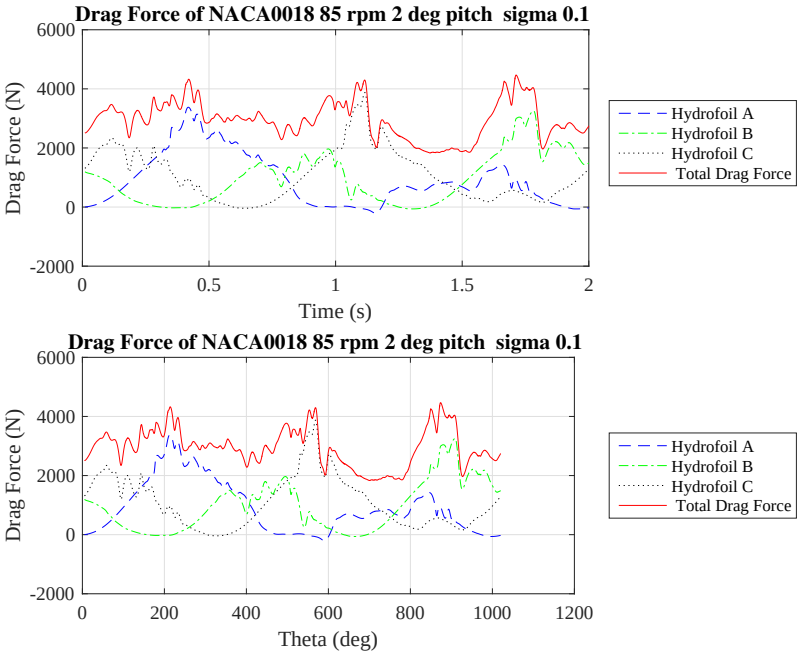

Figure A.381: Drag Force SIM53

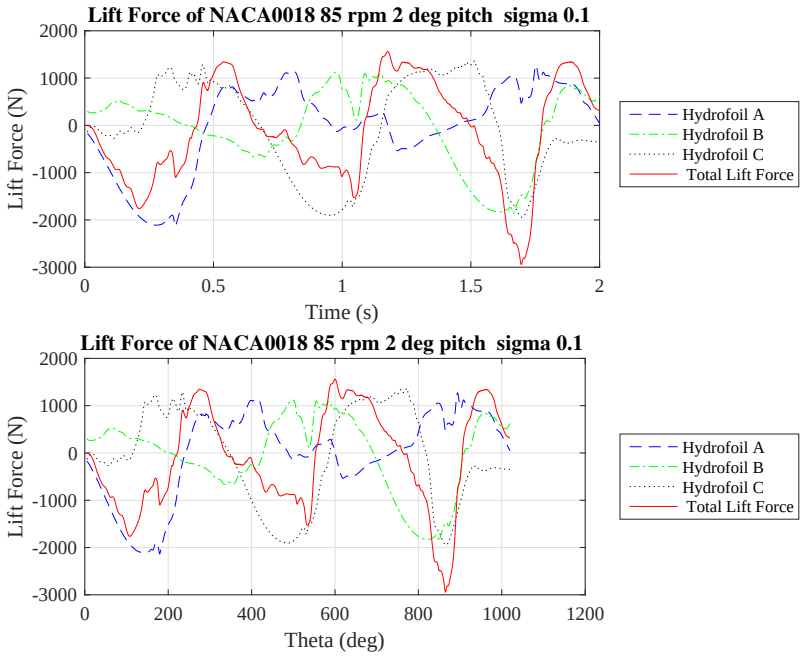

Figure A.382: Lift Force SIM53

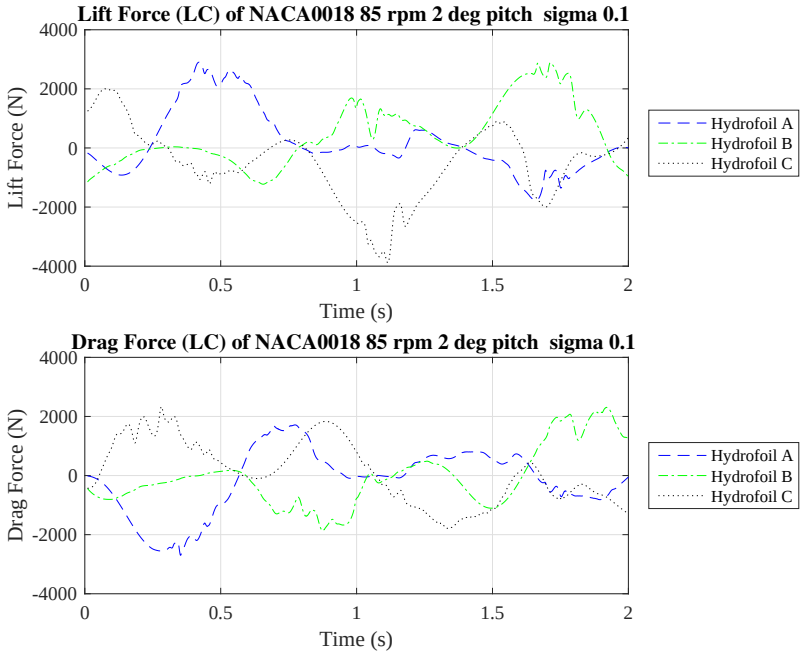

Figure A.383: Lift and Drag Force (LC) SIM53

A.1.54 SIM54

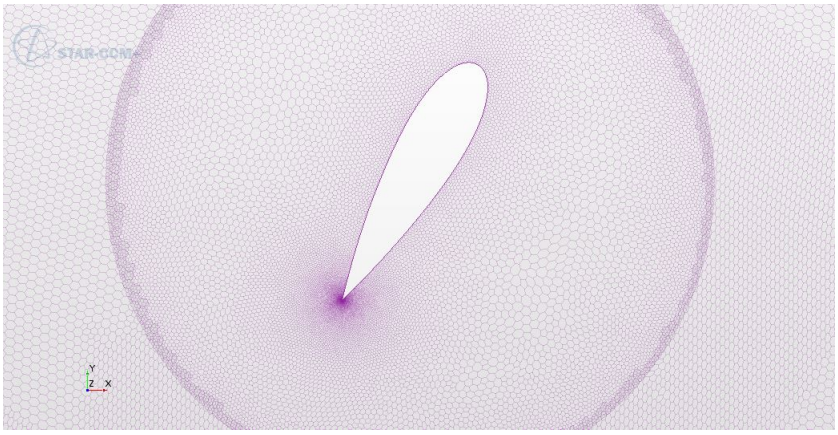

Figure A.384: Mesh SIM54

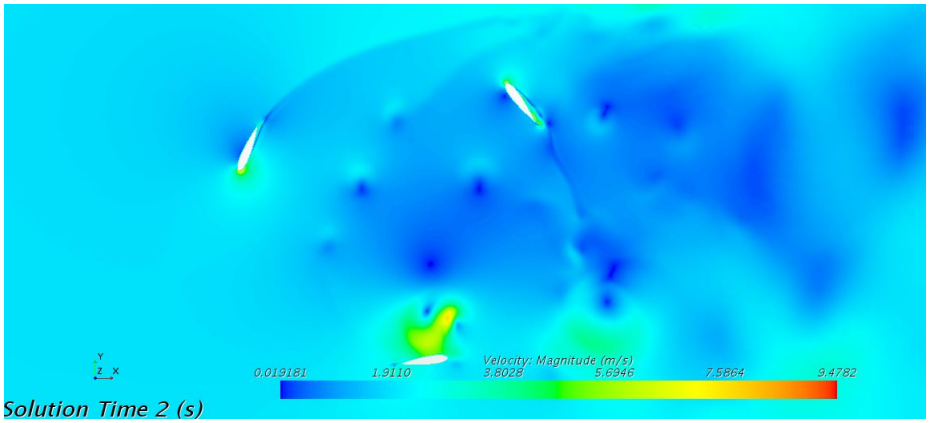

Figure A.385: Velocity SIM54

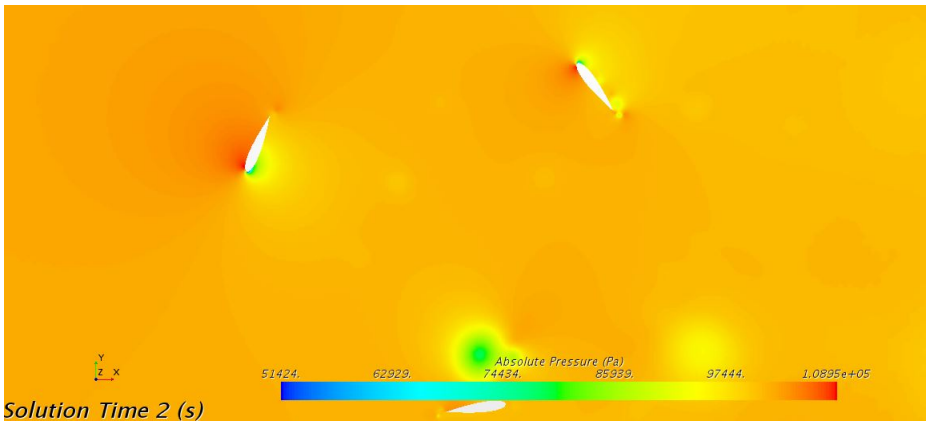

Figure A.386: Pressure SIM54

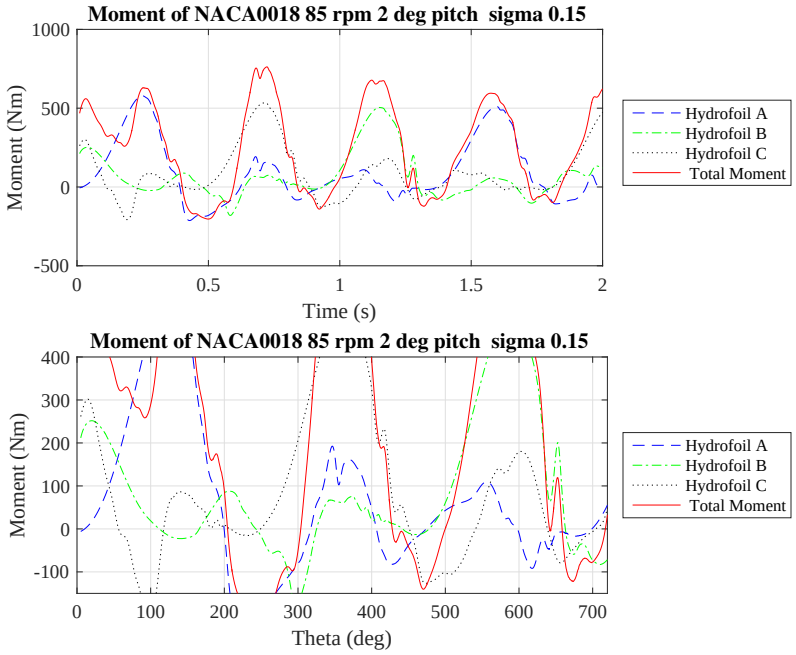

Figure A.387: Moment SIM54

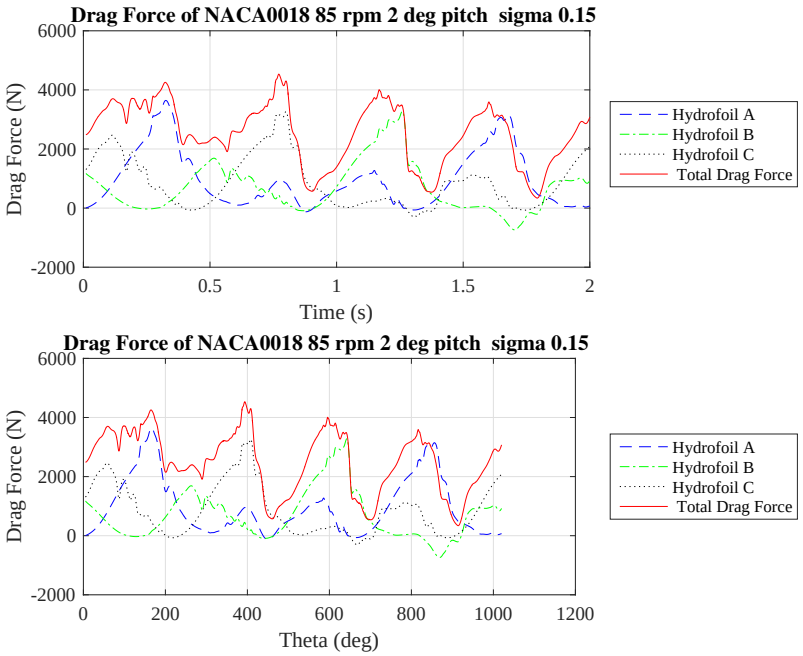

Figure A.388: Drag Force SIM54

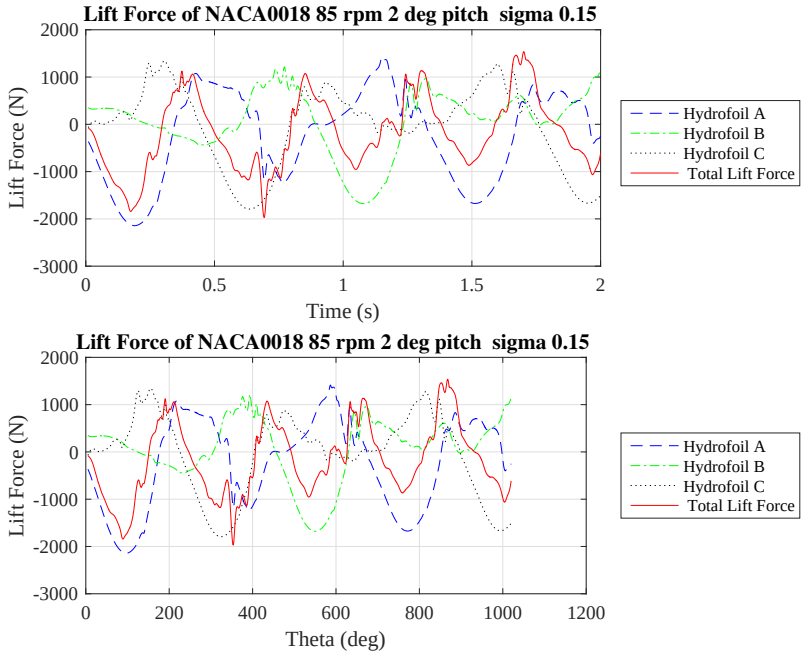

Figure A.389: Lift Force SIM54

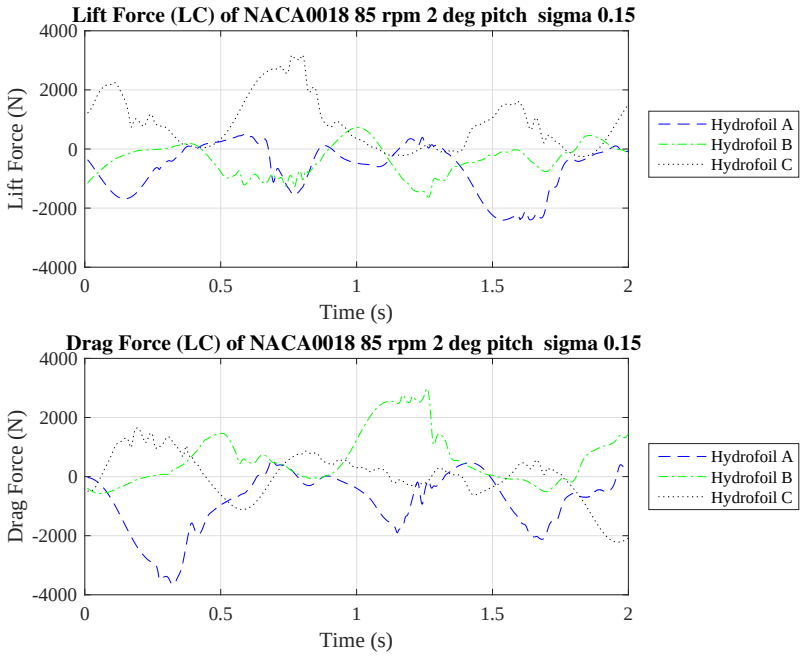

Figure A.390: Lift and Drag Force (LC) SIM54

A.1.55 SIM55

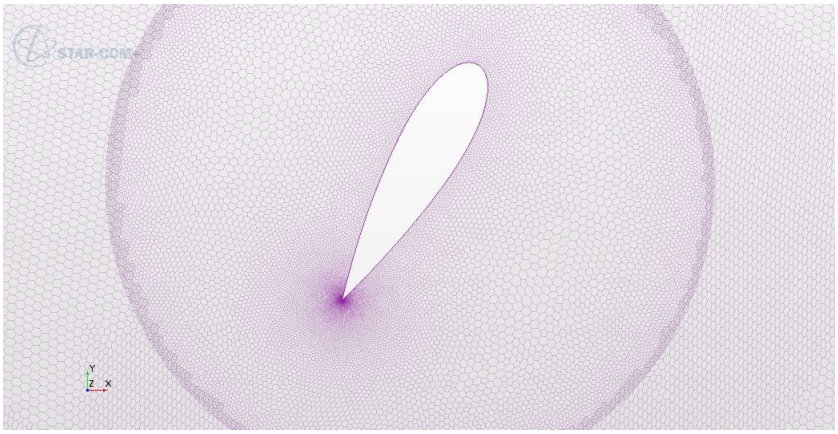

Figure A.391: Mesh SIM55

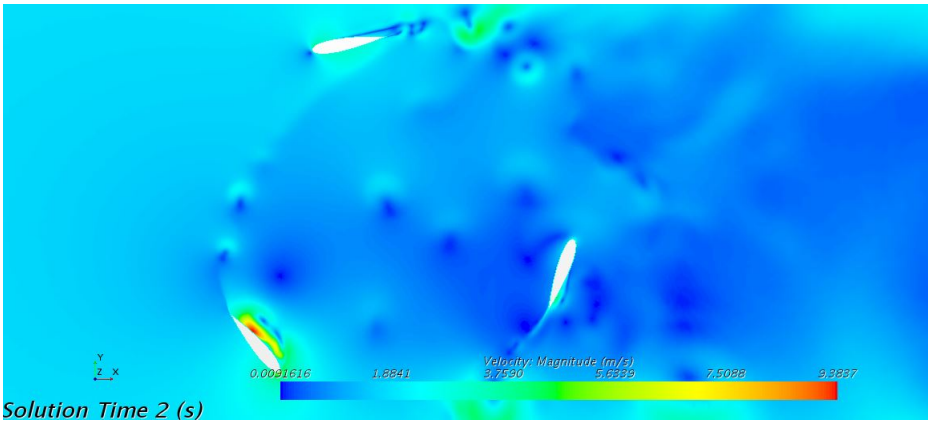

Figure A.392: Velocity SIM55

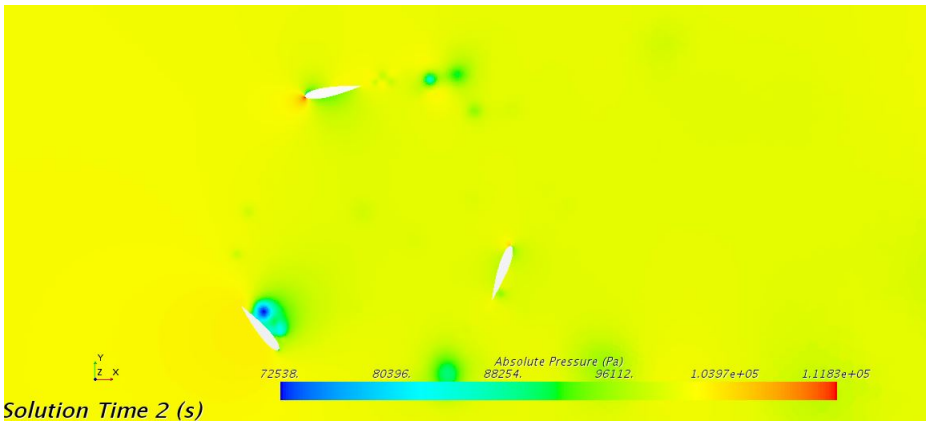

Figure A.393: Pressure SIM55

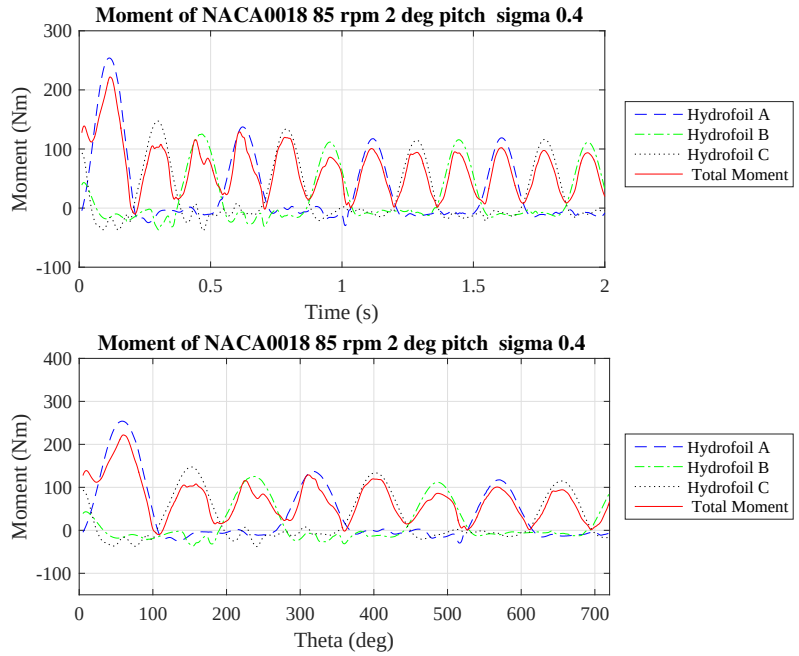

Figure A.394: Moment SIM55

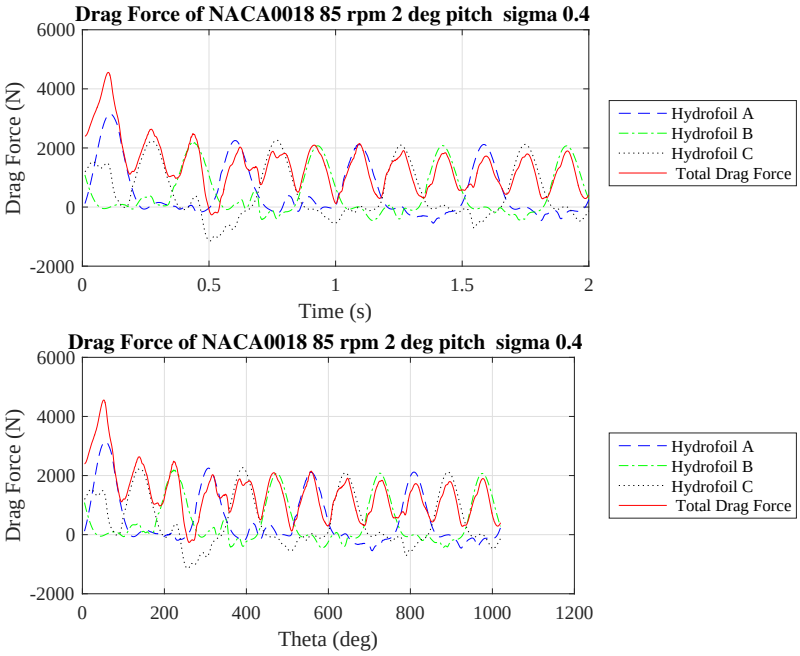

Figure A.395: Drag Force SIM55

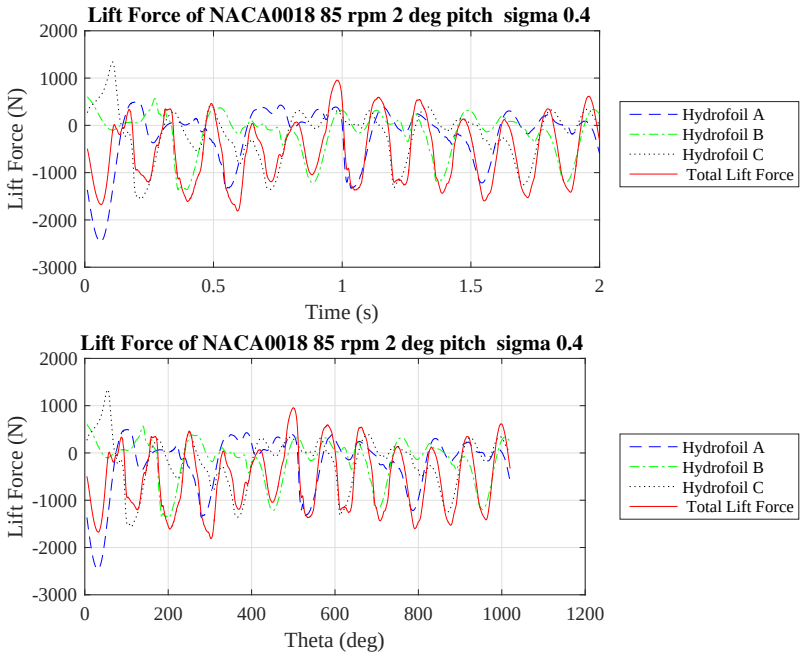

Figure A.396: Lift Force SIM55

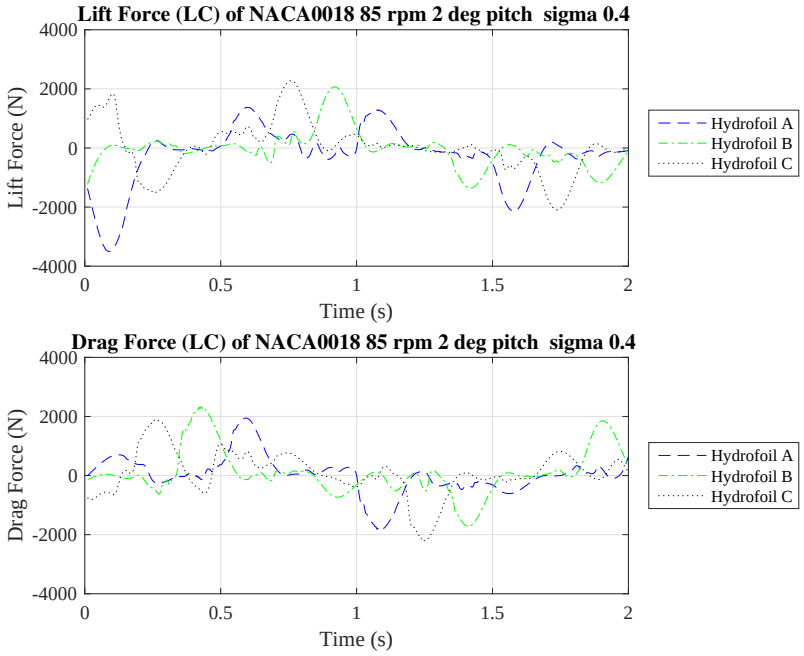

Figure A.397: Lift and Drag Force (LC) SIM55

A.1.56 SIM56

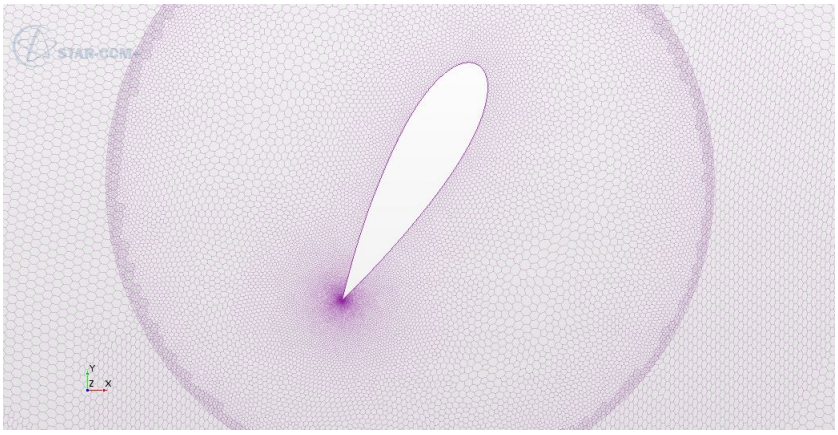

Figure A.398: Mesh SIM56

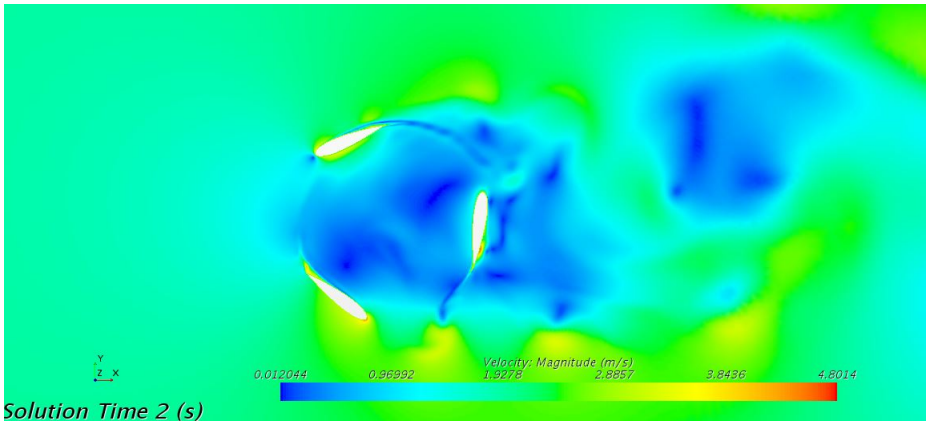

Figure A.399: Velocity SIM56

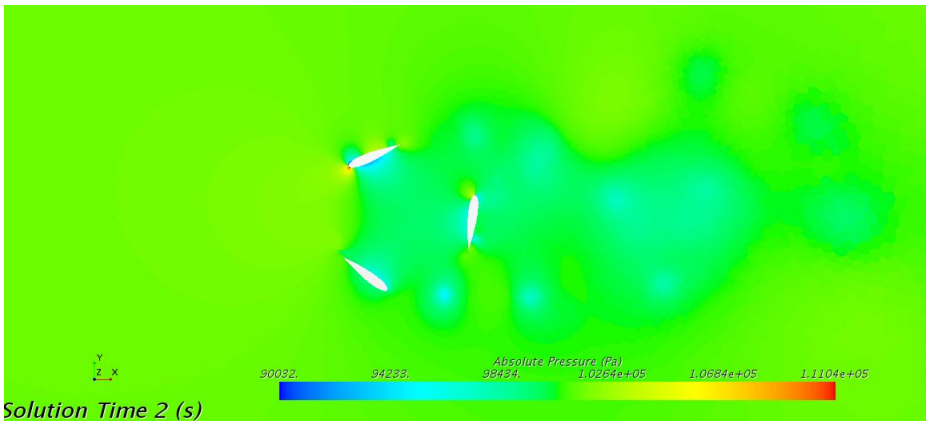

Figure A.400: Pressure SIM56

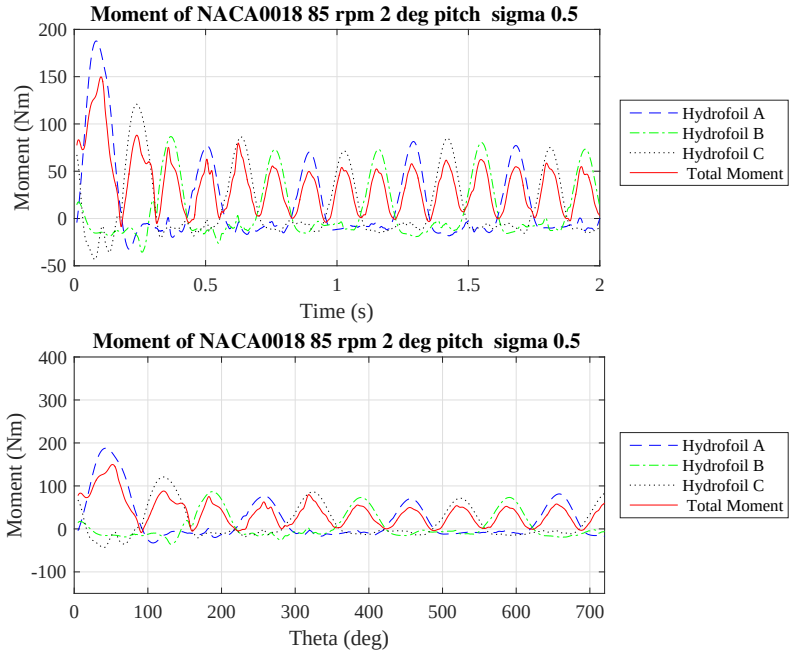

Figure A.401: Moment SIM56

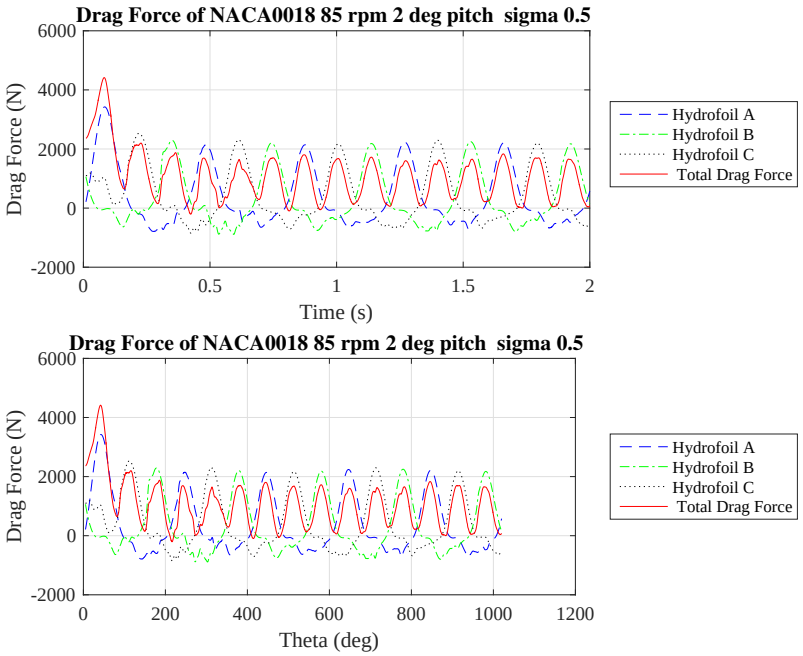

Figure A.402: Drag Force SIM56

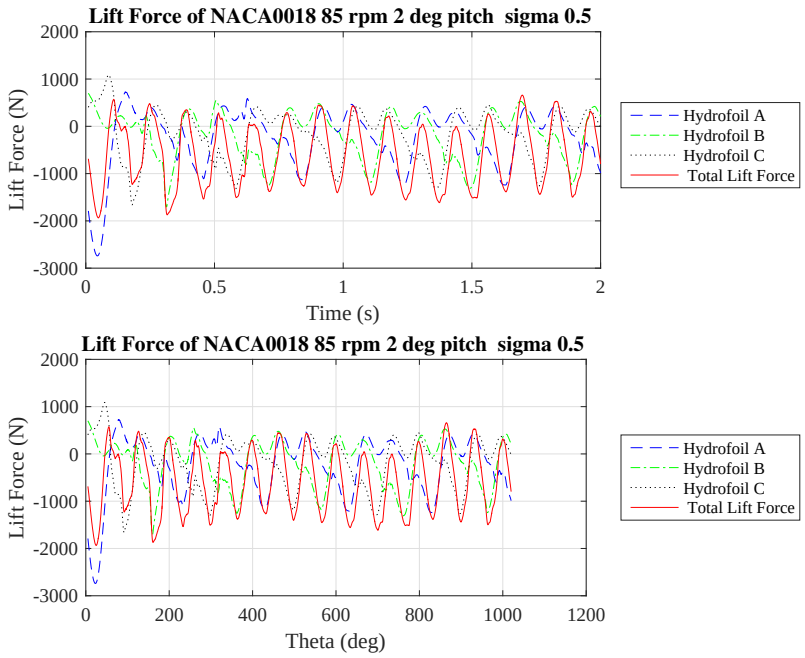

Figure A.403: Lift Force SIM56

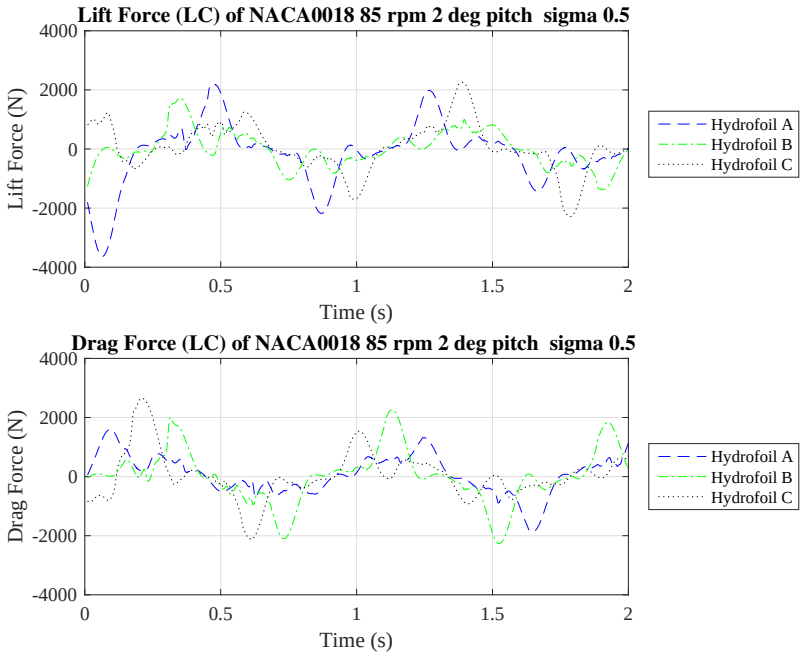

Figure A.404: Lift and Drag Force (LC) SIM56

A.1.57 SIM57

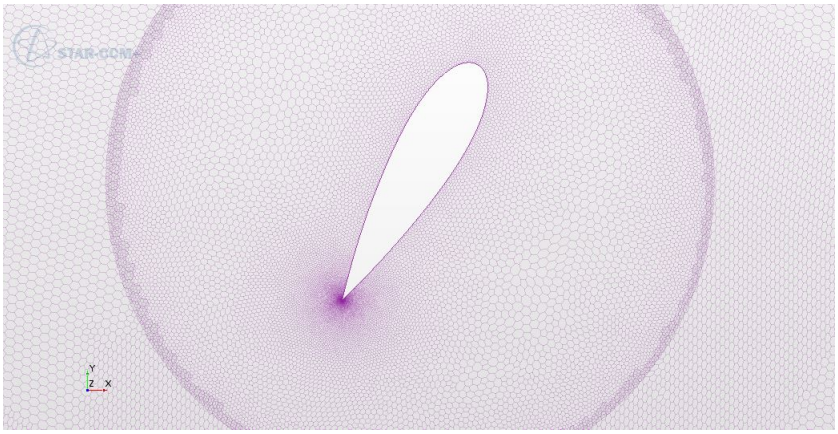

Figure A.405: Mesh SIM57

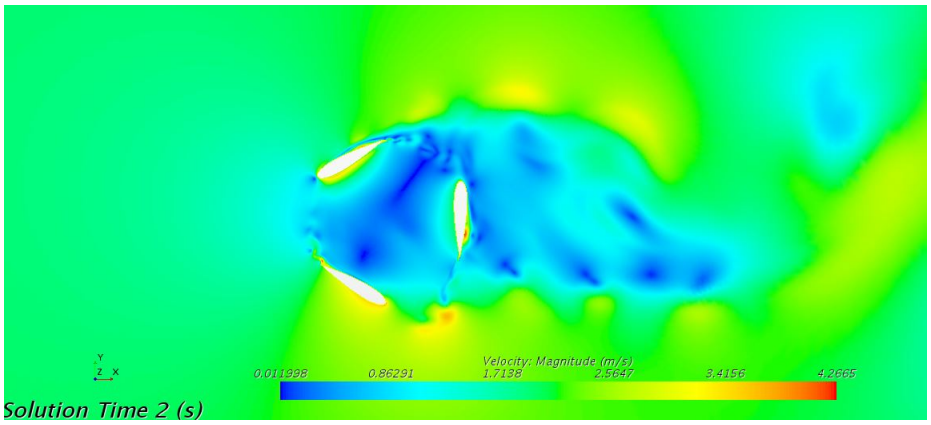

Figure A.406: Velocity SIM57

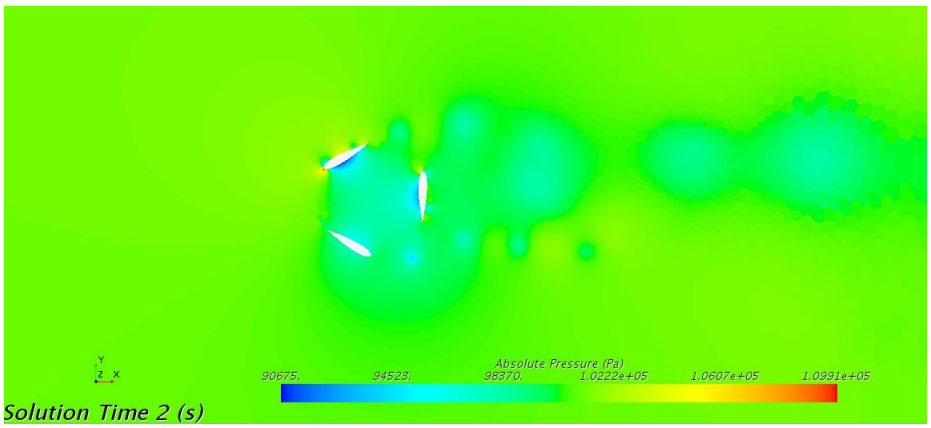

Figure A.407: Pressure SIM57

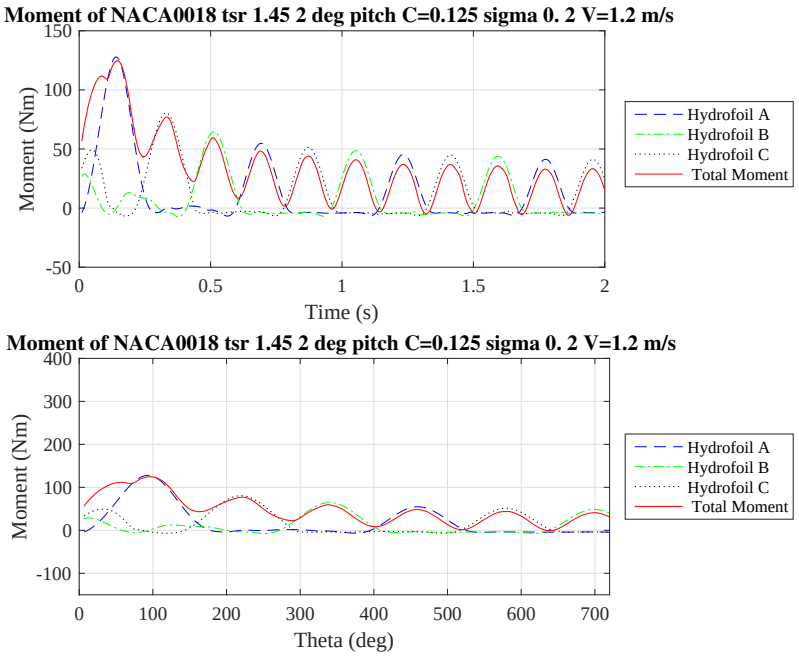

Figure A.408: Moment SIM57

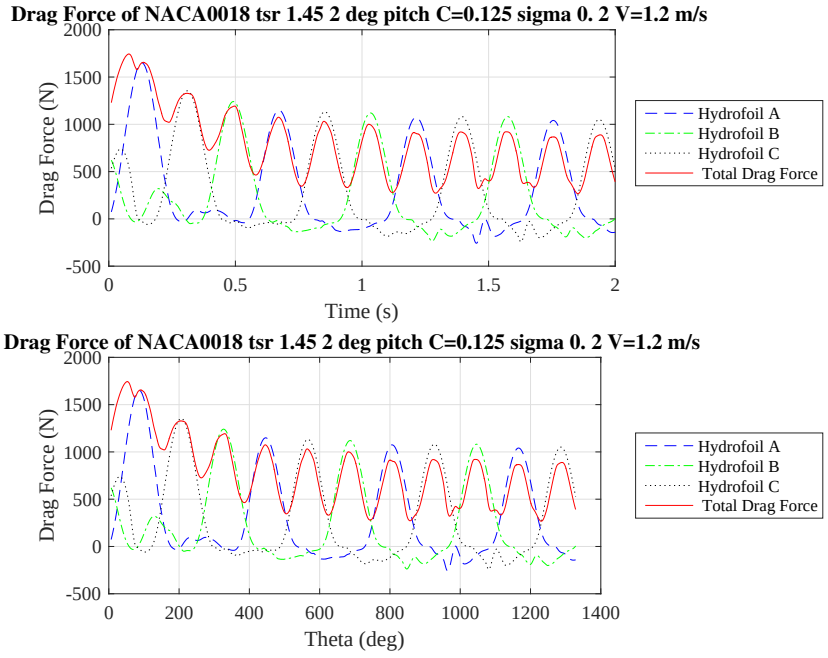

Figure A.409: Drag Force SIM57

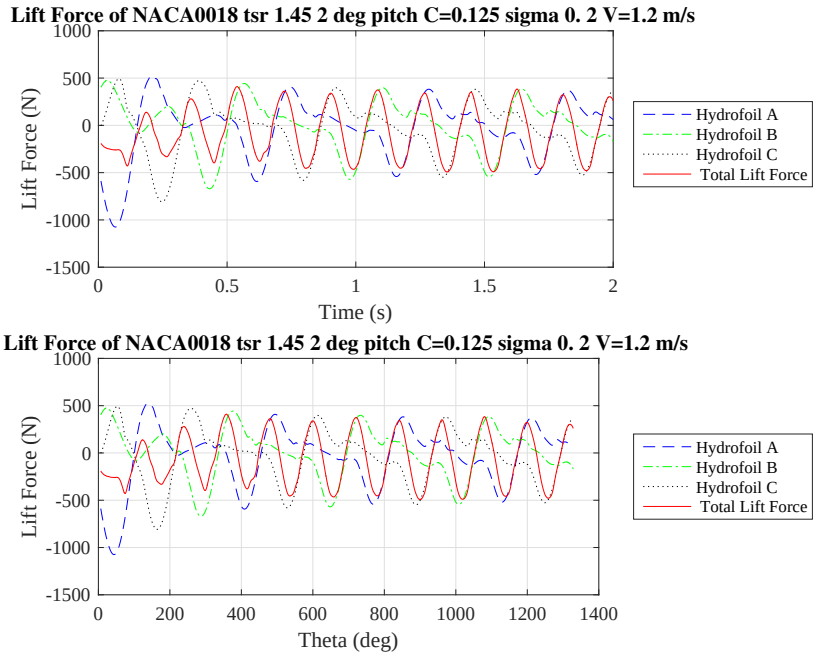

Figure A.410: Lift Force SIM57

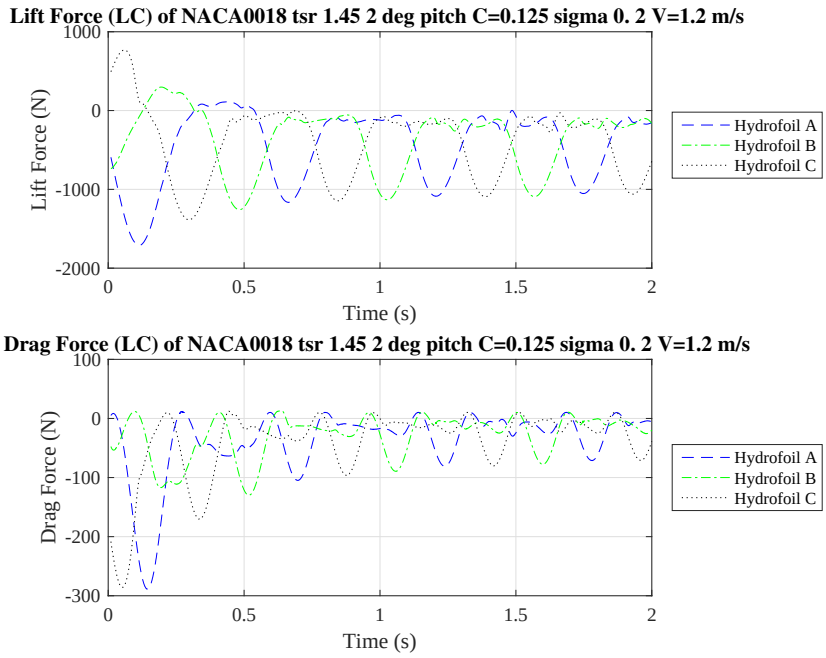

Figure A.411: Lift and Drag Force (LC) SIM57

A.1.58 SIM58

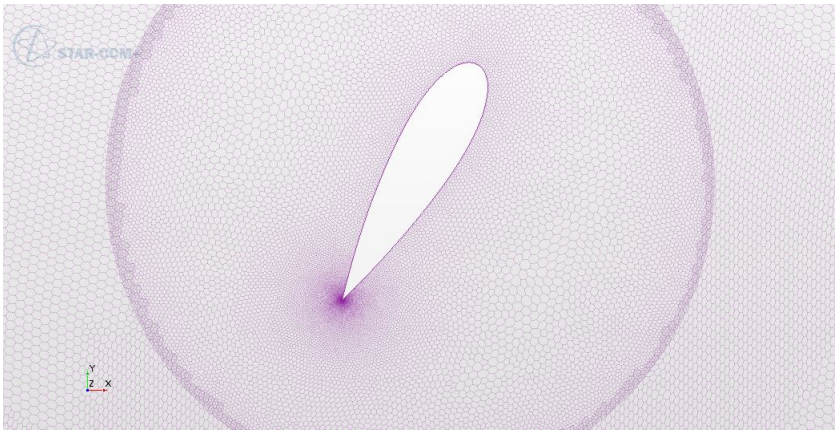

Figure A.412: Mesh SIM58

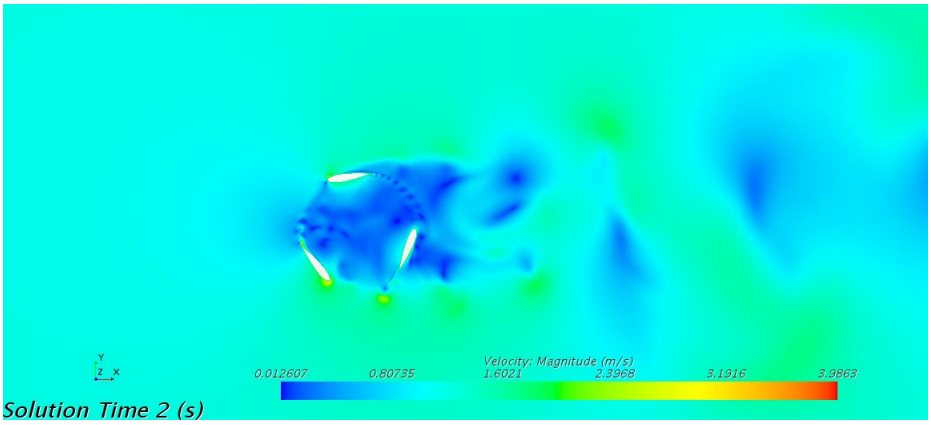

Figure A.413: Velocity SIM58

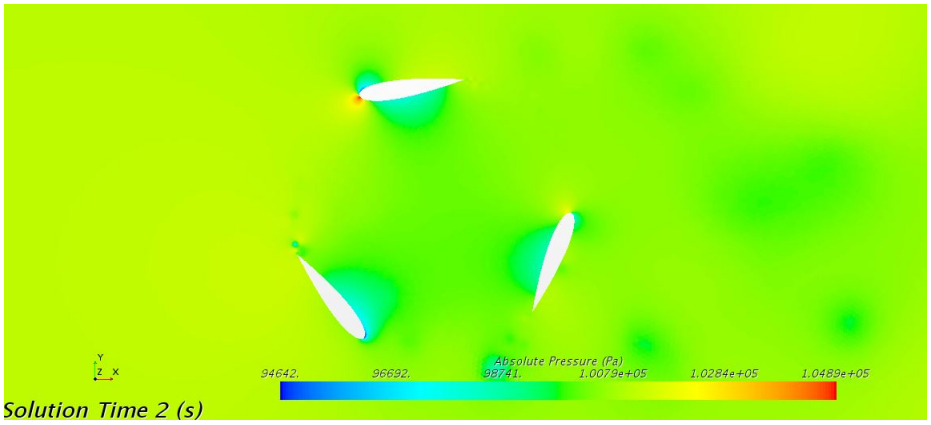

Figure A.414: Pressure SIM58

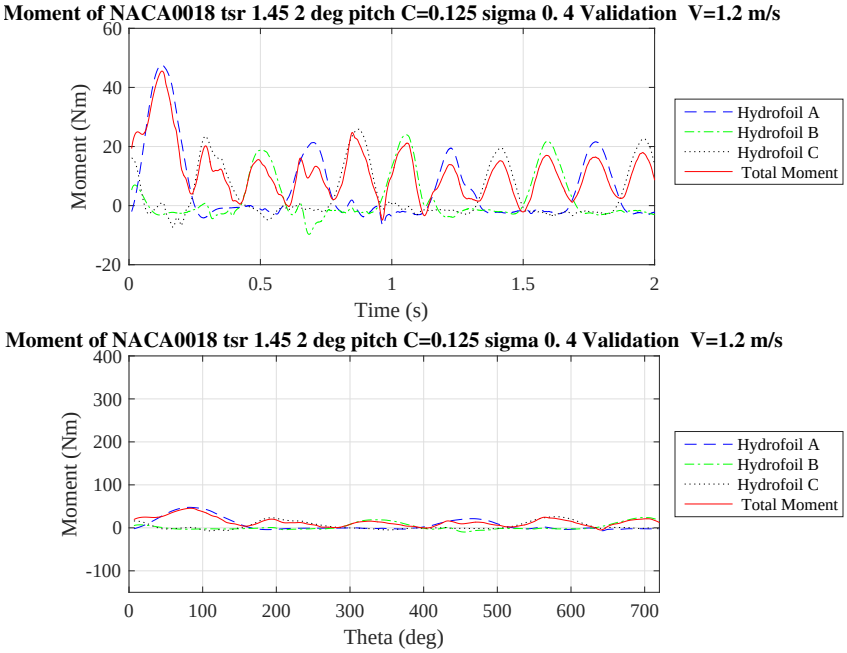

Figure A.415: Moment SIM58

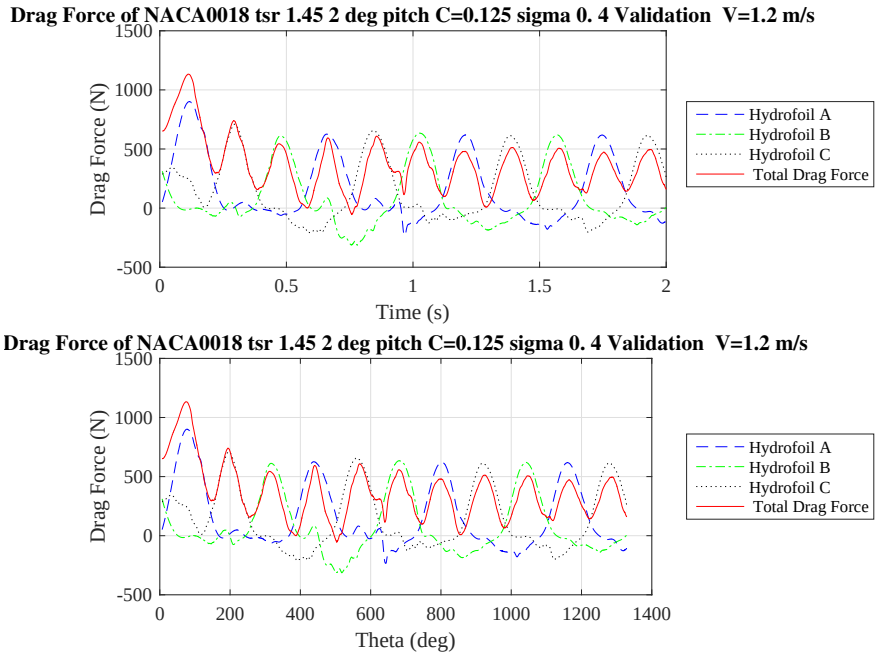

Figure A.416: Drag Force SIM58

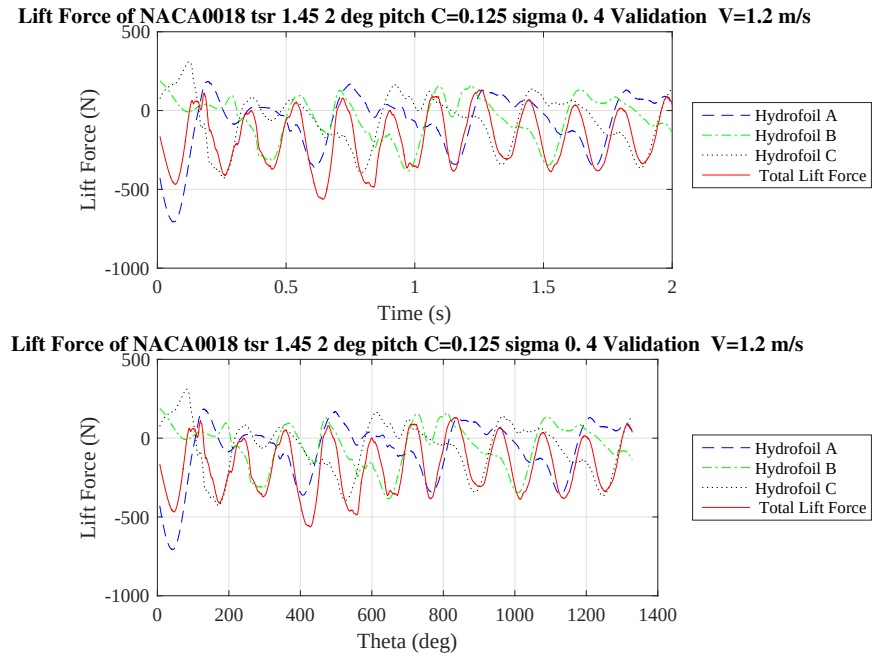

Figure A.417: Lift Force SIM58

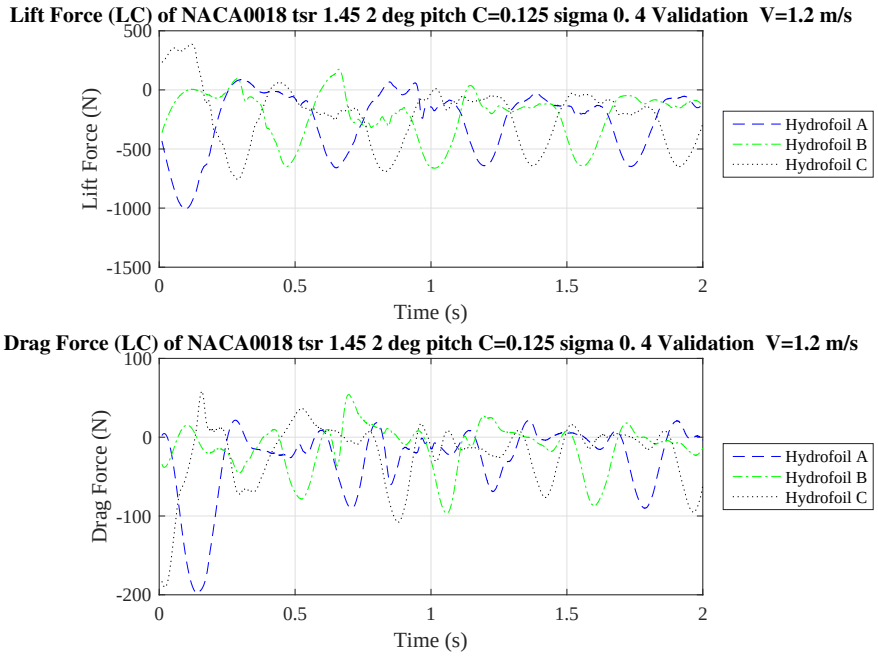

Figure A.418: Lift and Drag Force (LC) SIM58

A.1.59 SIM59

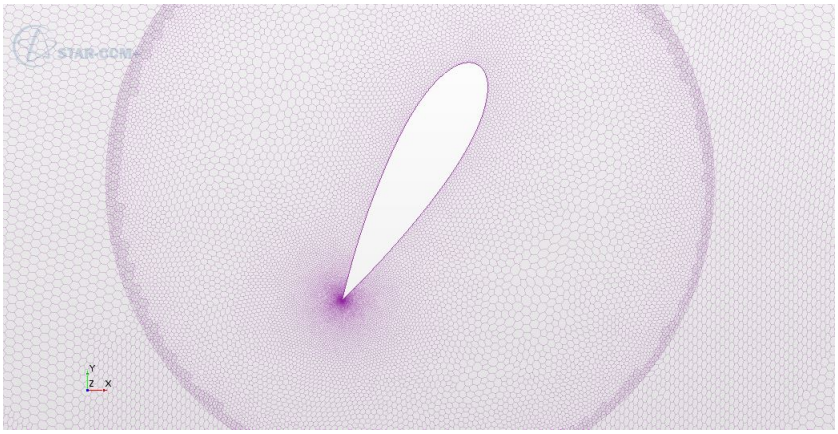

Figure A.419: Mesh SIM59

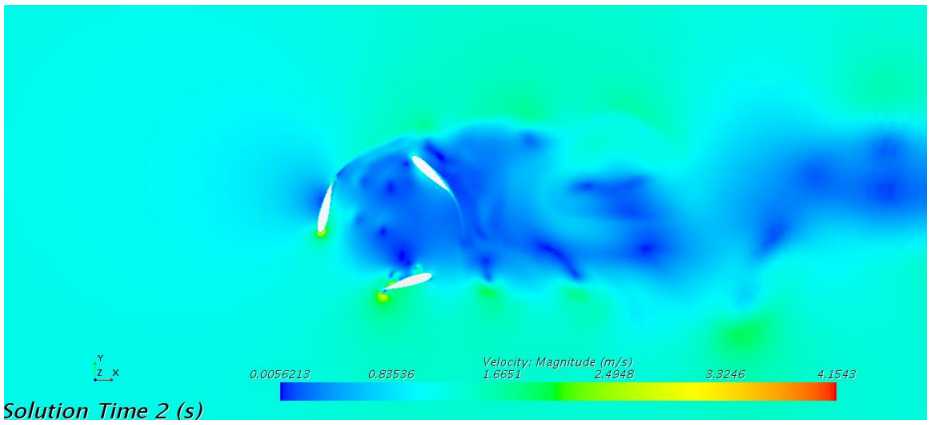

Figure A.420: Velocity SIM59

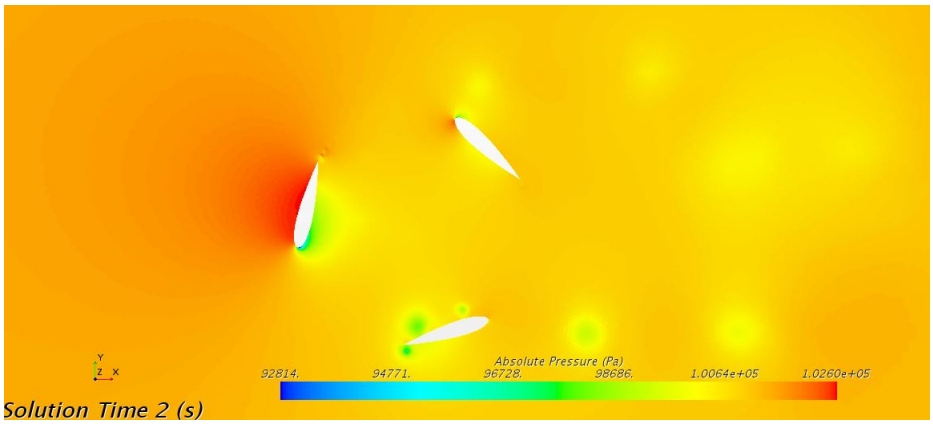

Figure A.421: Pressure SIM59

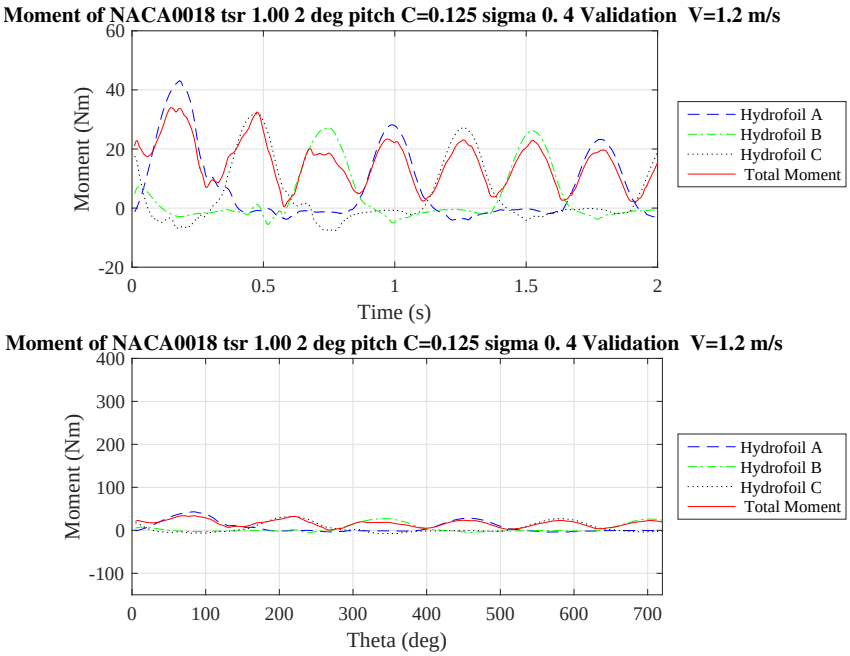

Figure A.422: Moment SIM59

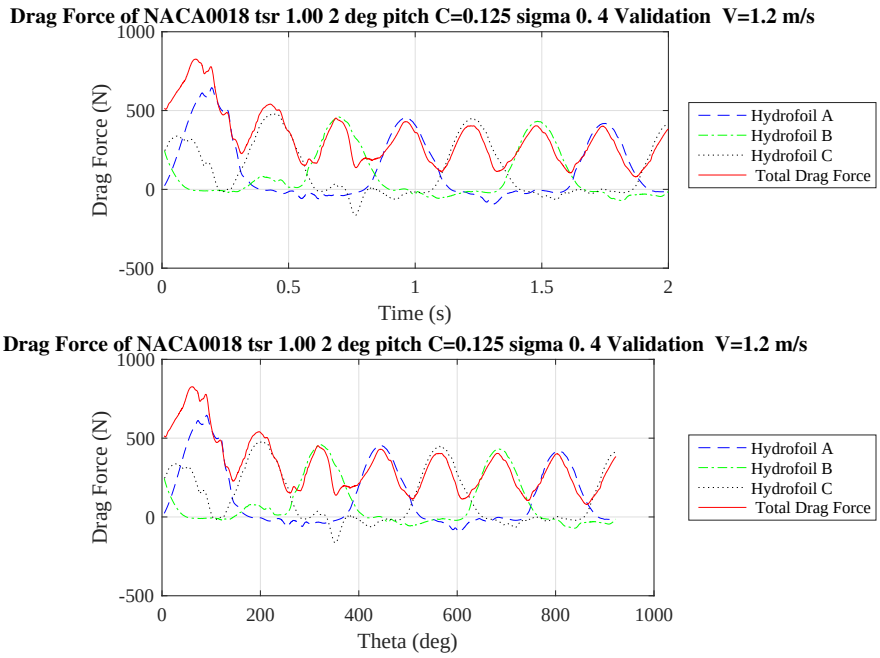

Figure A.423: Drag Force SIM59

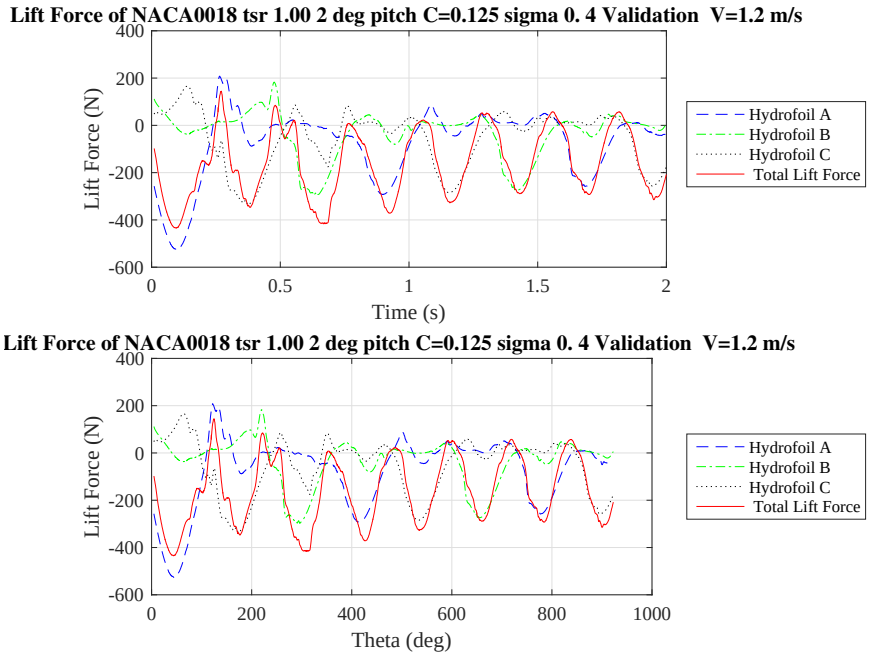

Figure A.424: Lift Force SIM59

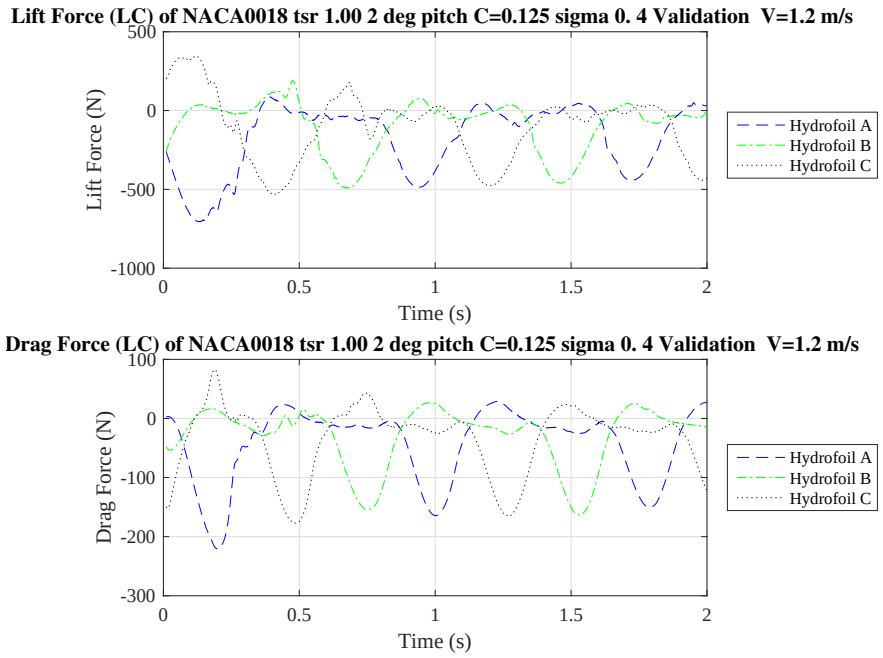

Figure A.425: Lift and Drag Force (LC) SIM59

A.1.60 SIM60

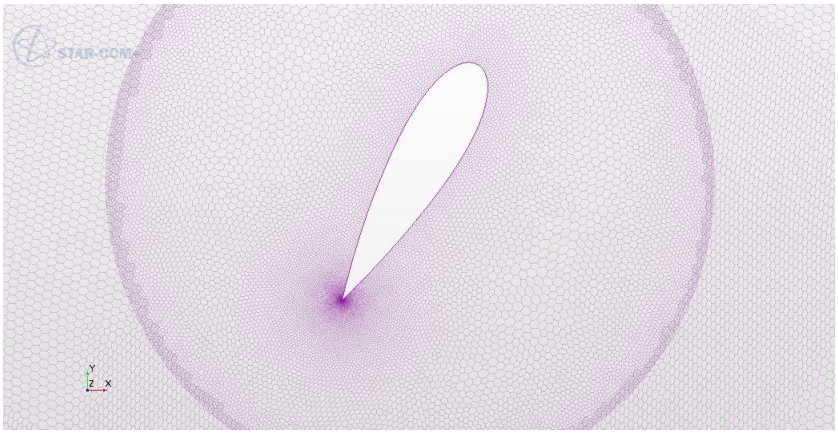

Figure A.426: Mesh SIM60

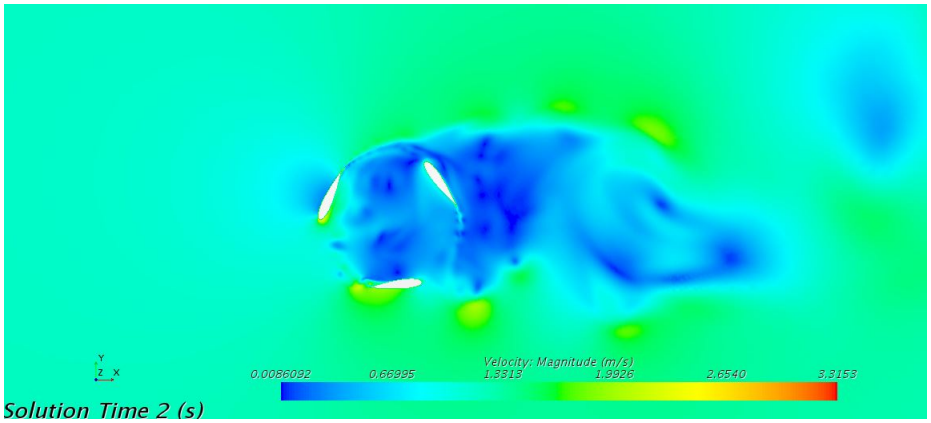

Figure A.427: Velocity SIM60

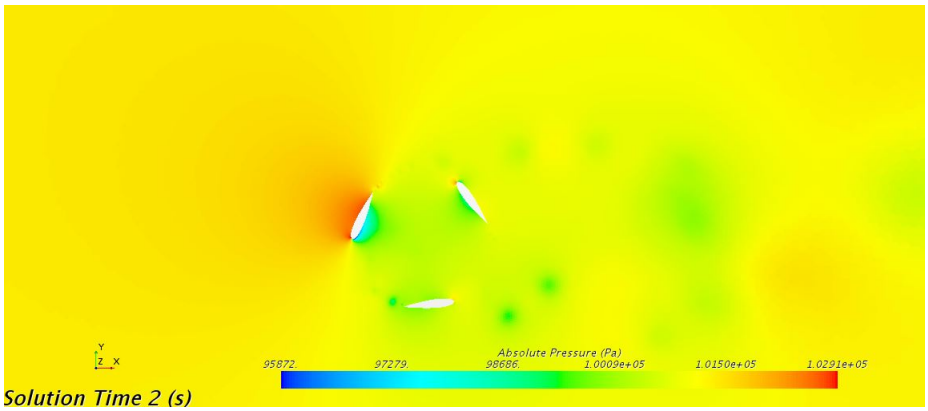

Figure A.428: Pressure SIM60

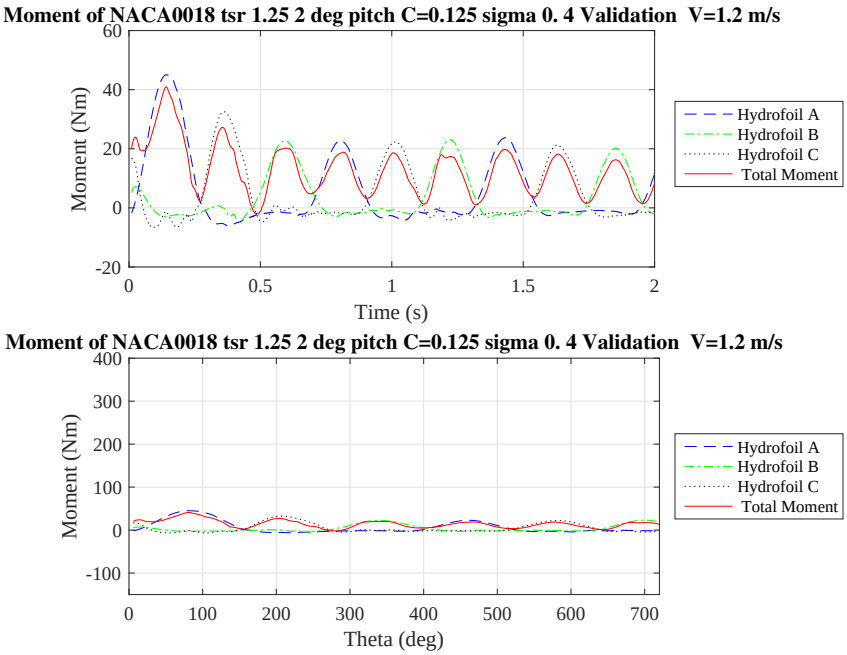

Figure A.429: Moment SIM60

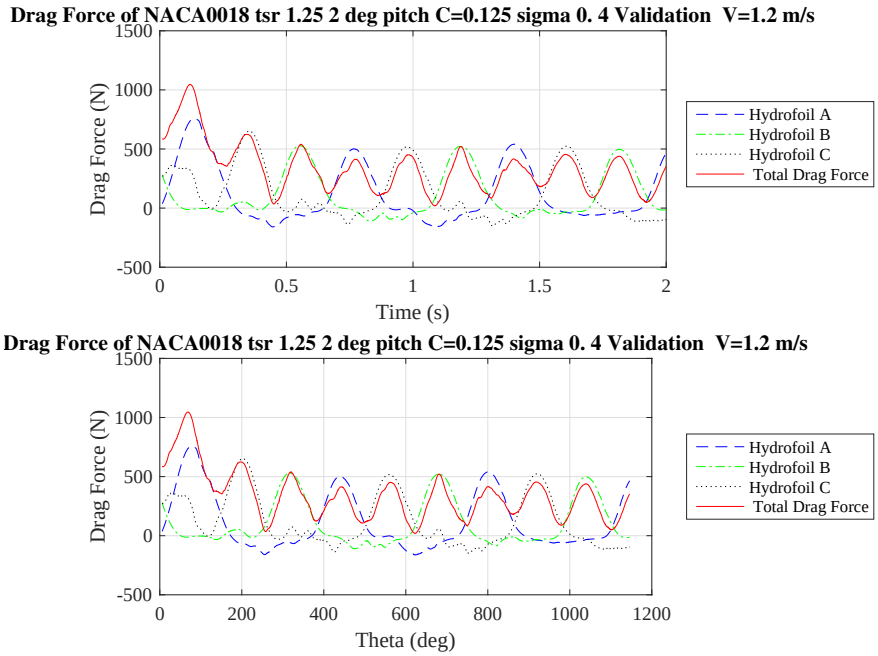

Figure A.430: Drag Force SIM60

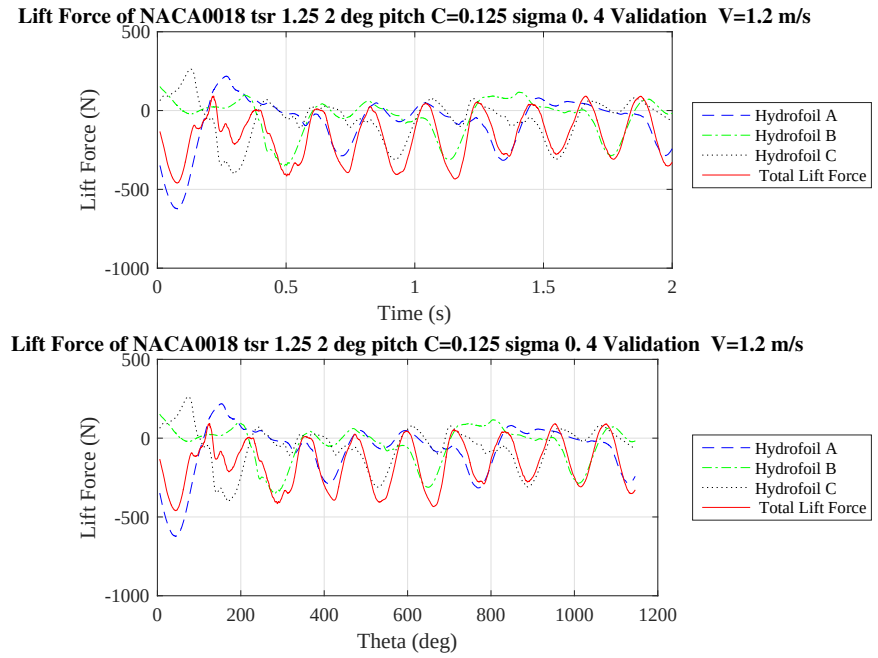

Figure A.431: Lift Force SIM60

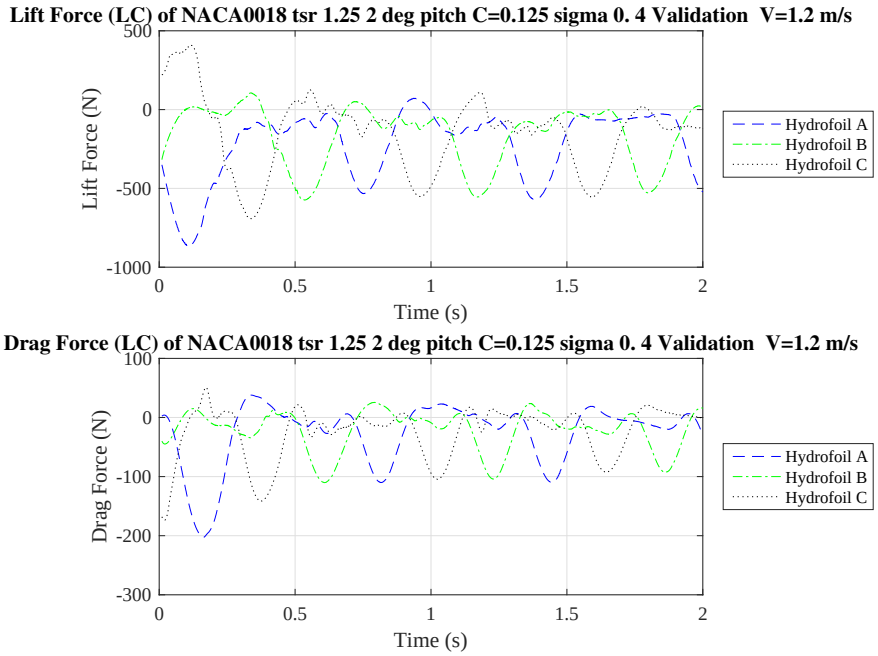

Figure A.432: Lift and Drag Force (LC) SIM60

A.1.61 SIM60

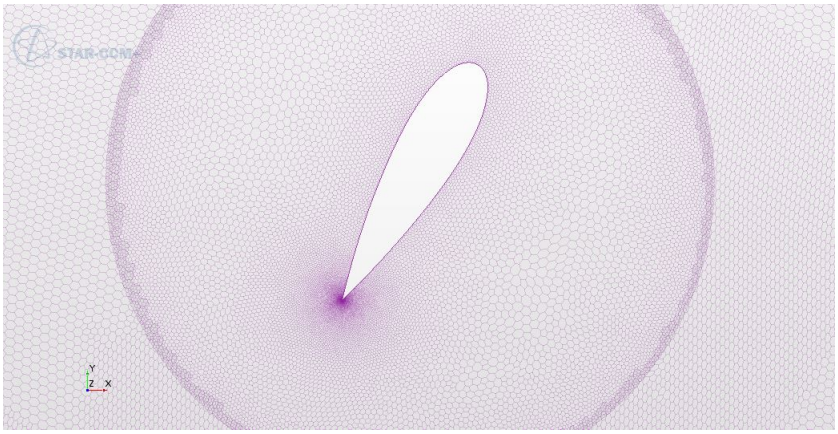

Figure A.433: Mesh SIM61

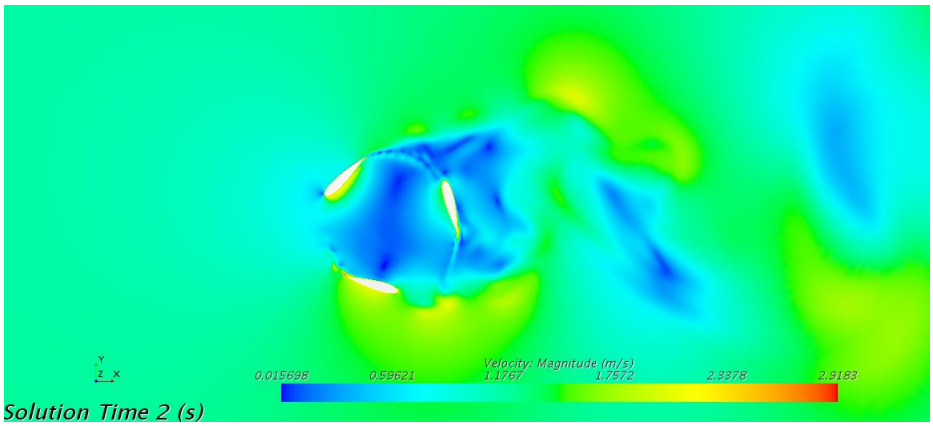

Figure A.434: Velocity SIM61

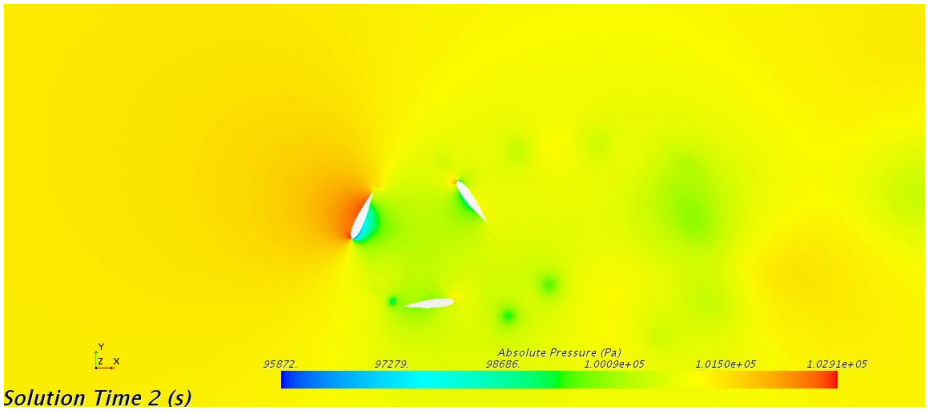

Figure A.435: Pressure SIM61

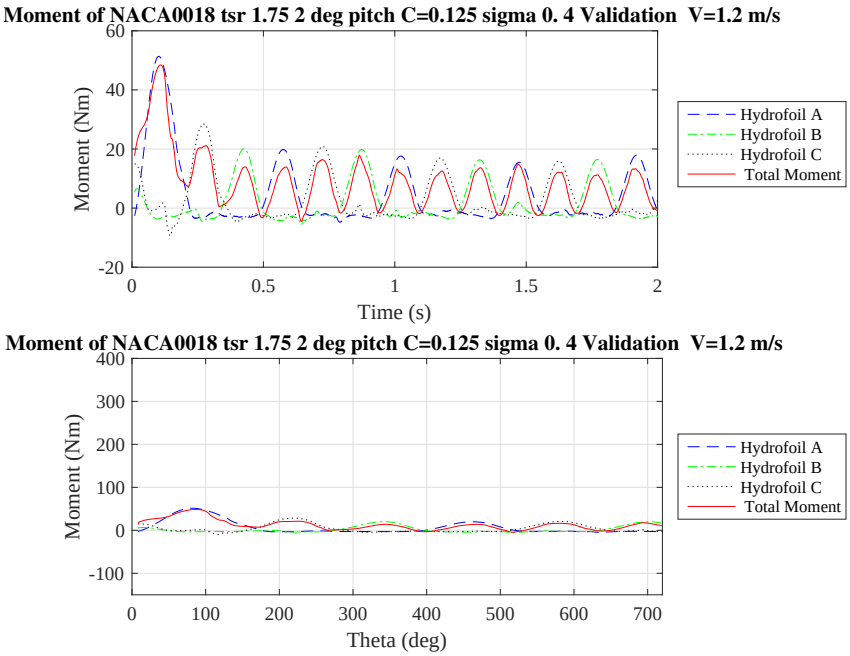

Figure A.436: Moment SIM61

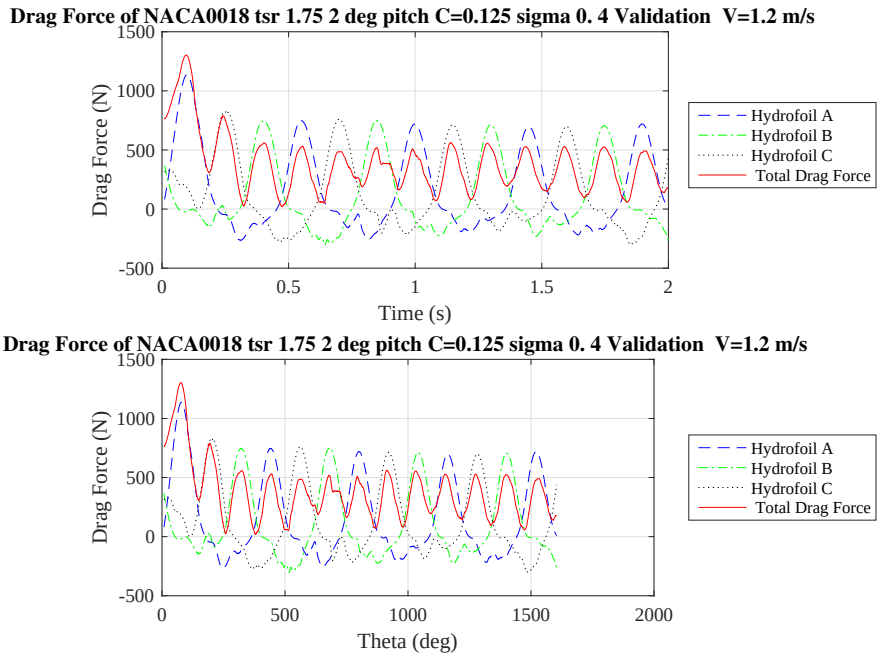

Figure A.437: Drag Force SIM61

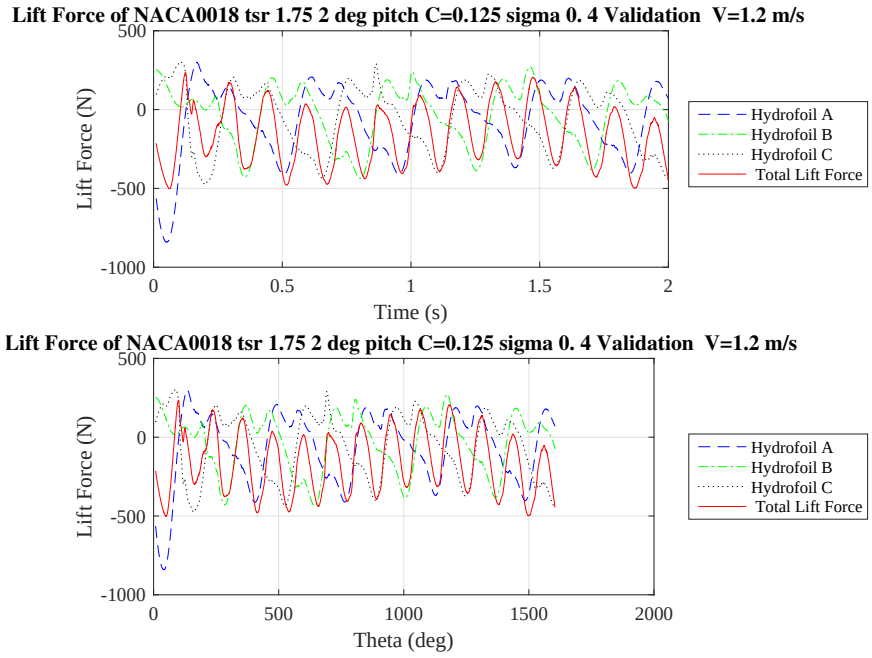

Figure A.438: Lift Force SIM61

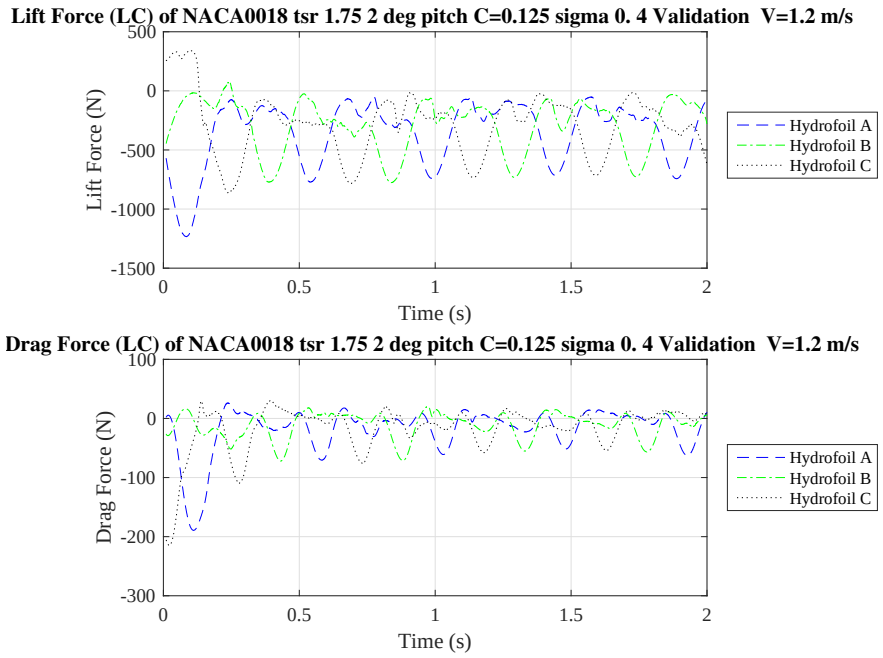

Figure A.439: Lift and Drag Force (LC) SIM61

A.1.62 SIM62

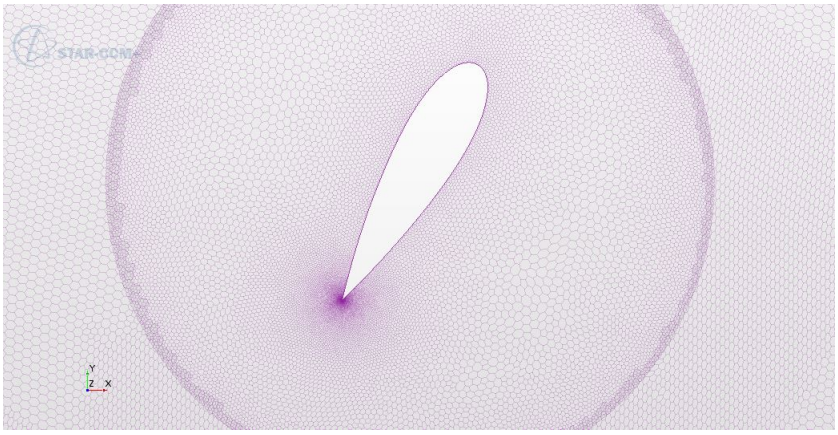

Figure A.440: Mesh SIM62

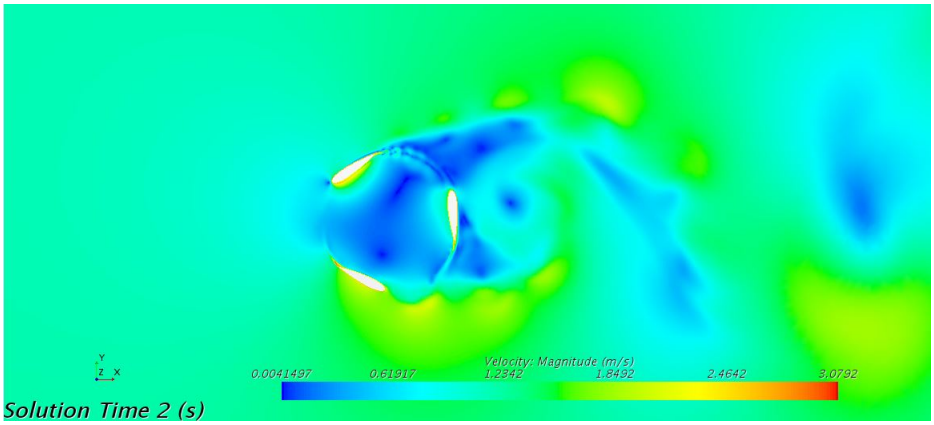

Figure A.441: Velocity SIM62

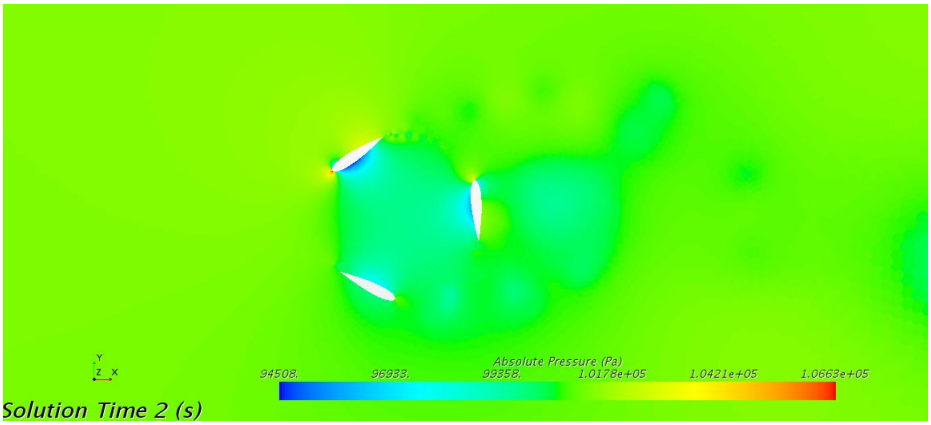

Figure A.442: Pressure SIM62

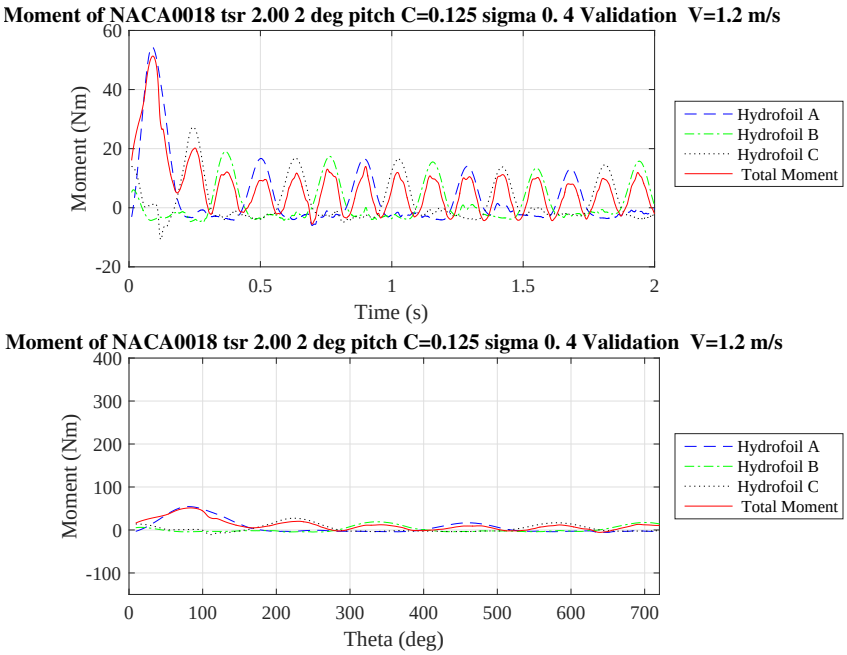

Figure A.443: Moment SIM62

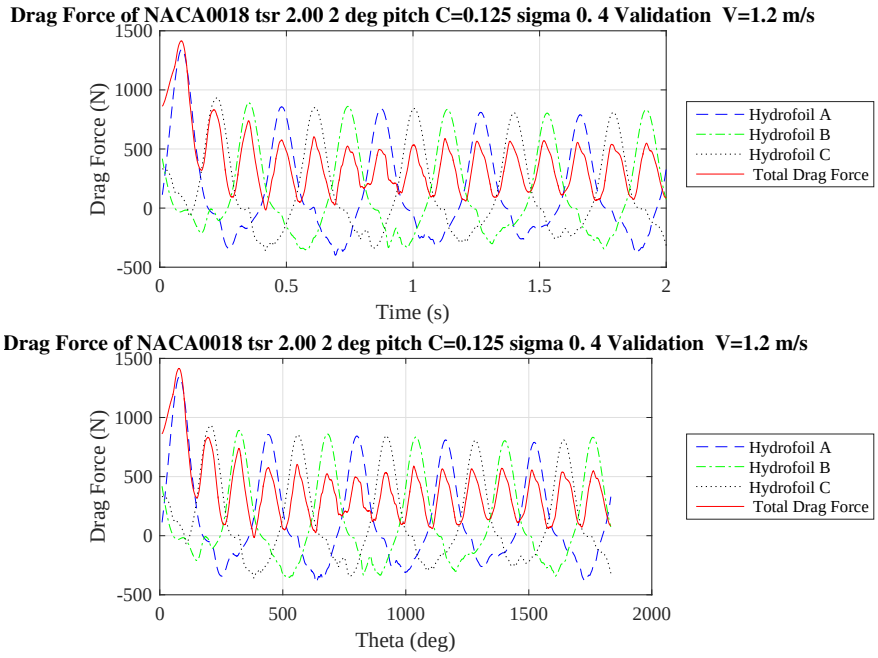

Figure A.444: Drag Force SIM62

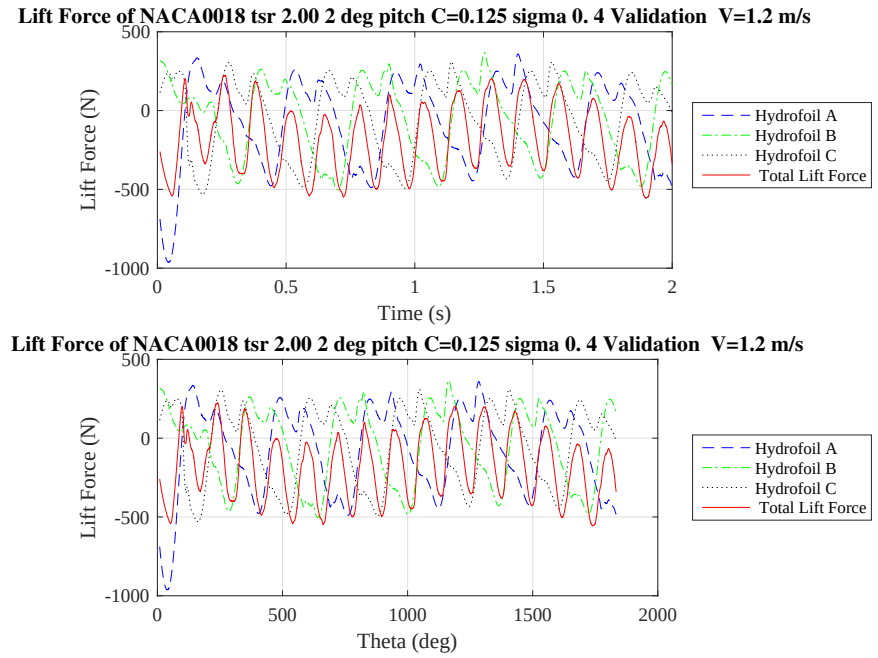

Figure A.445: Lift Force SIM62

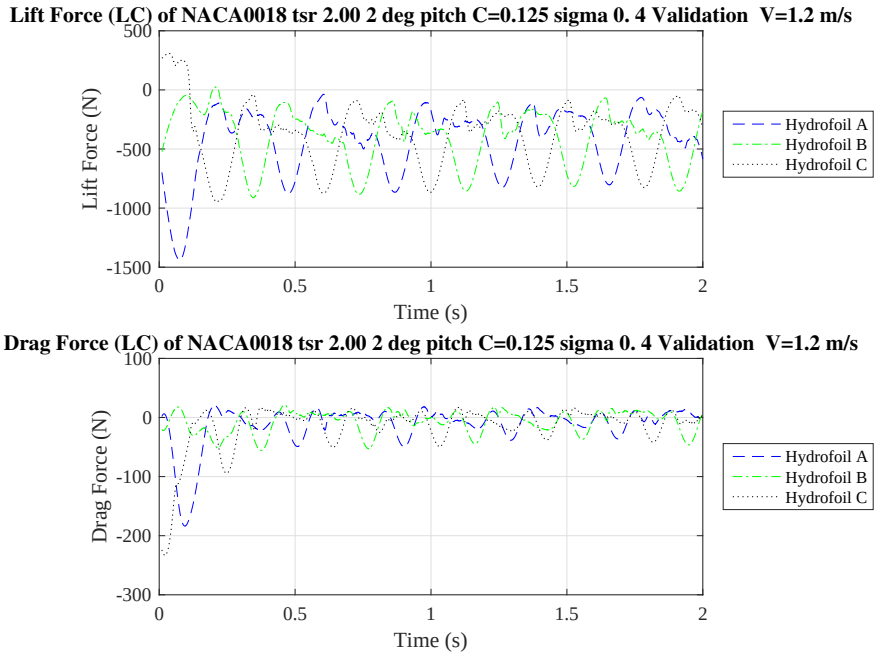

Figure A.446: Lift and Drag Force (LC) SIM62

A.1.63 Lift and Drag Forces of Steady State Simulations (SSS)

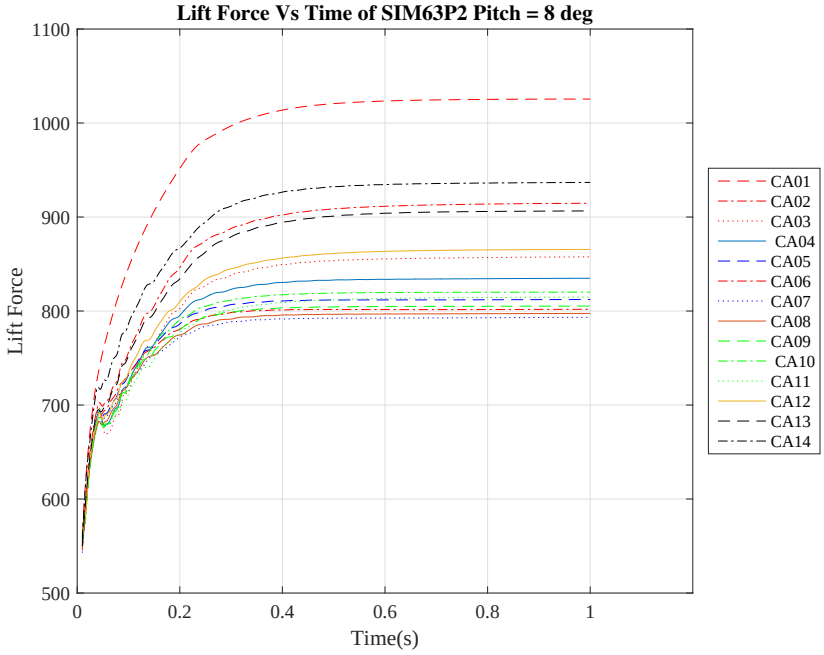

Figure A.447: Lift Force for Pitch 8 deg SIM63

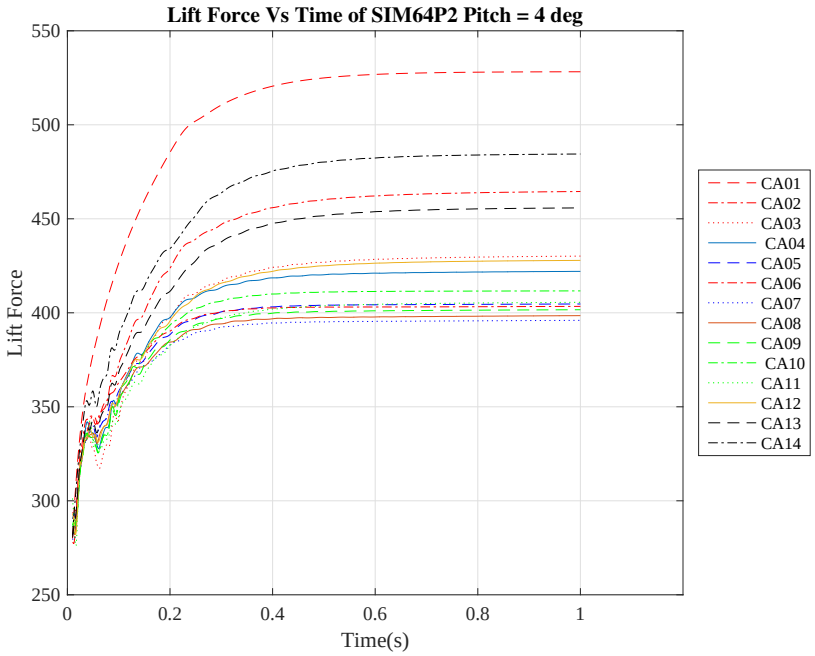

Figure A.448: Lift Force for Pitch 4 deg SIM64

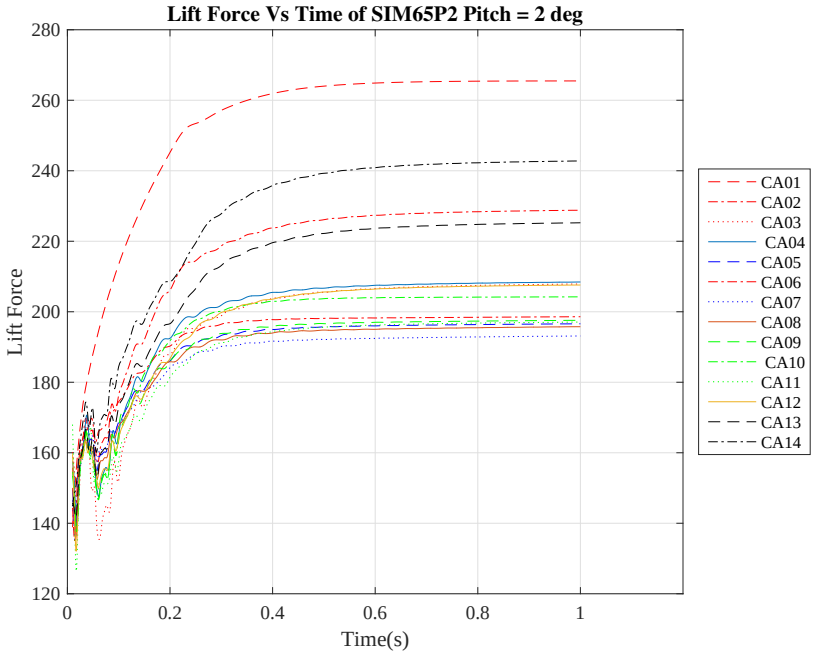

Figure A.449: Lift Force for Pitch 2 deg SIM65

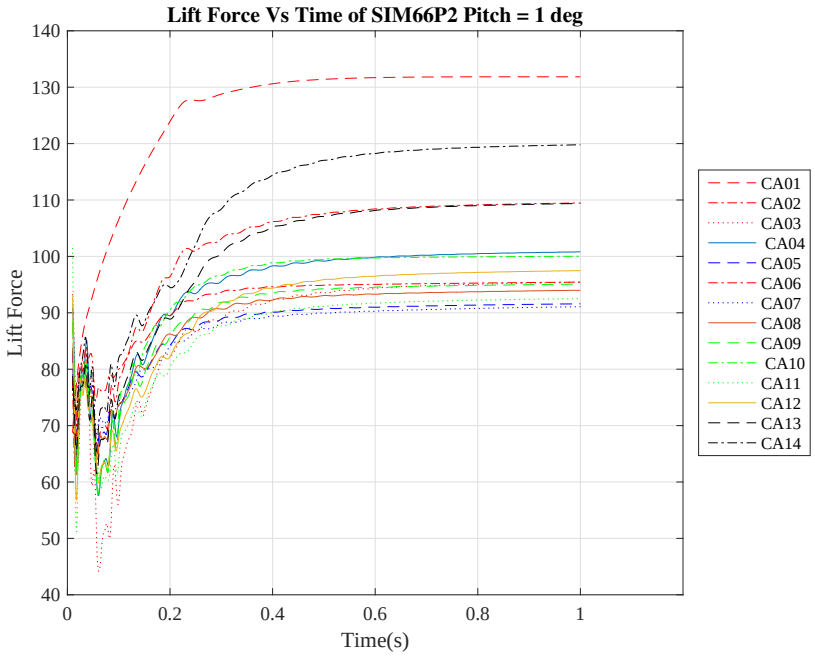

Figure A.450: Lift Force for Pitch 1 deg SIM66

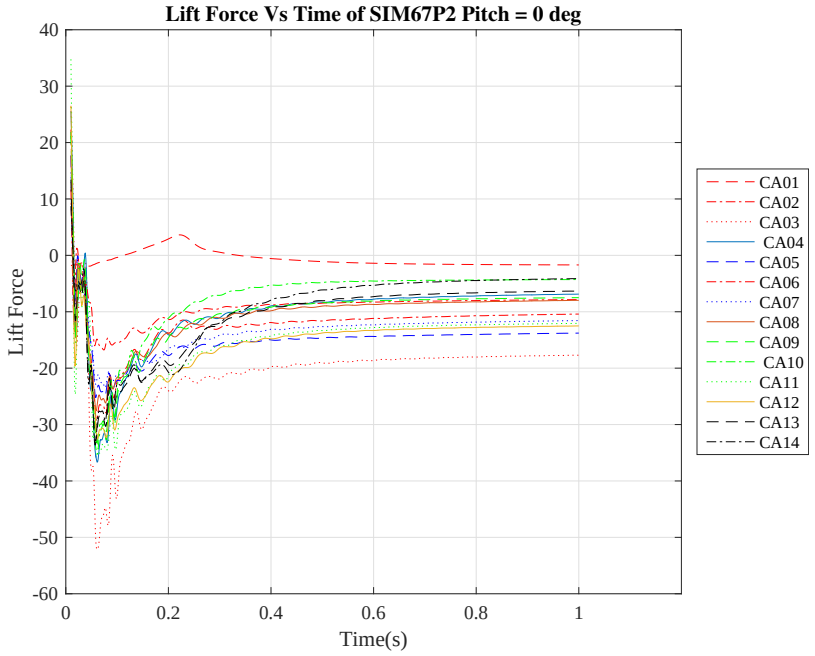

Figure A.451: Lift Force for Pitch 0 deg SIM67

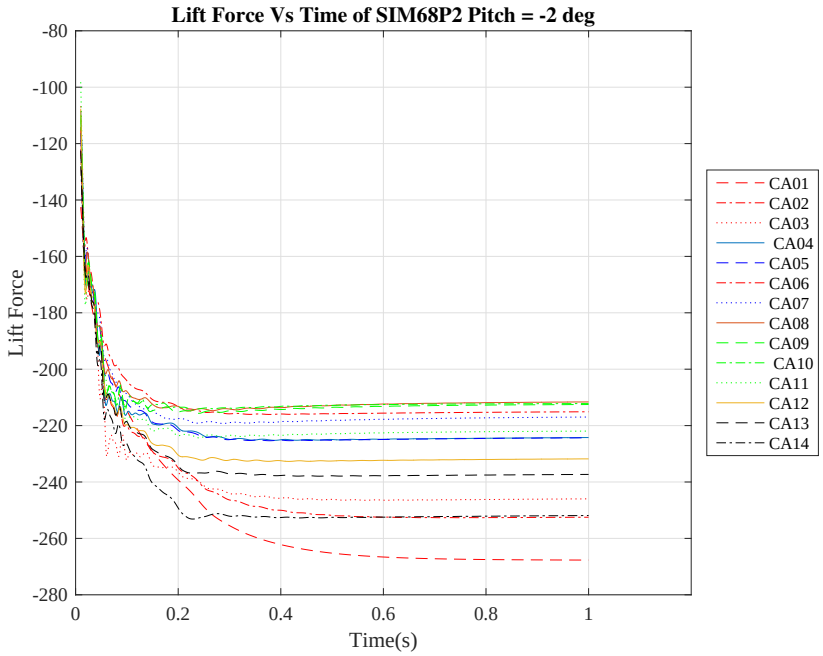

Figure A.452: Lift Force for Pitch -2 deg SIM68

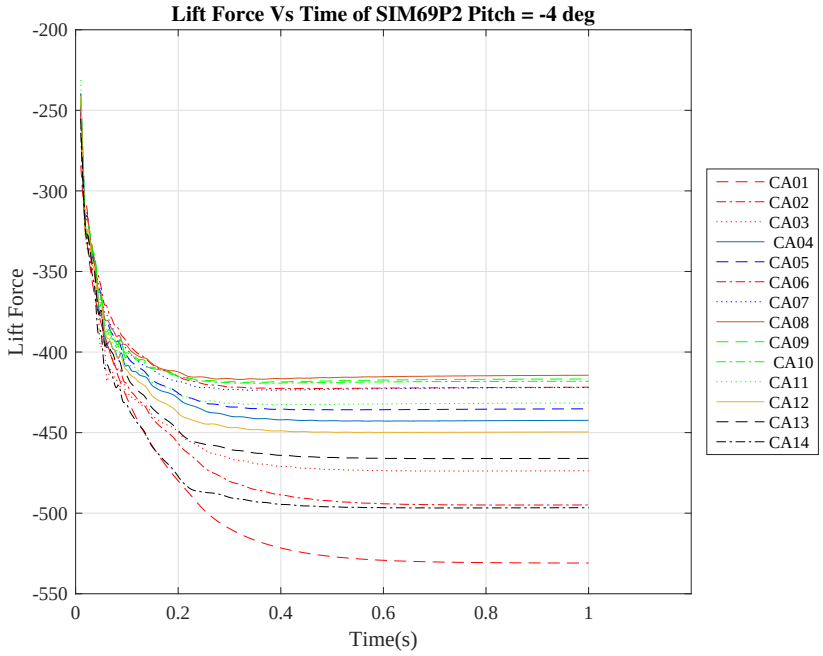

Figure A.453: Lift Force for Pitch -4 deg SIM69

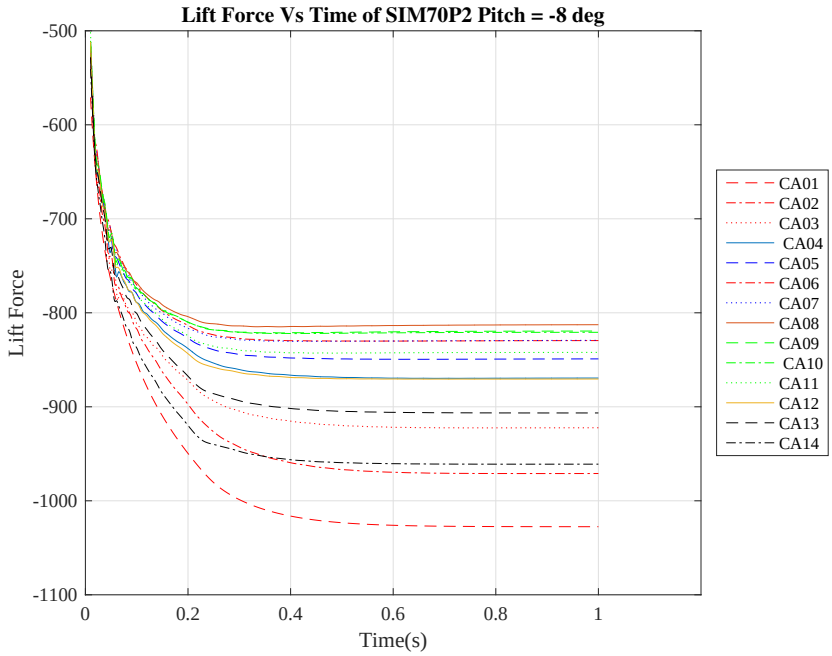

Figure A.454: Lift Force for Pitch -8 deg SIM70

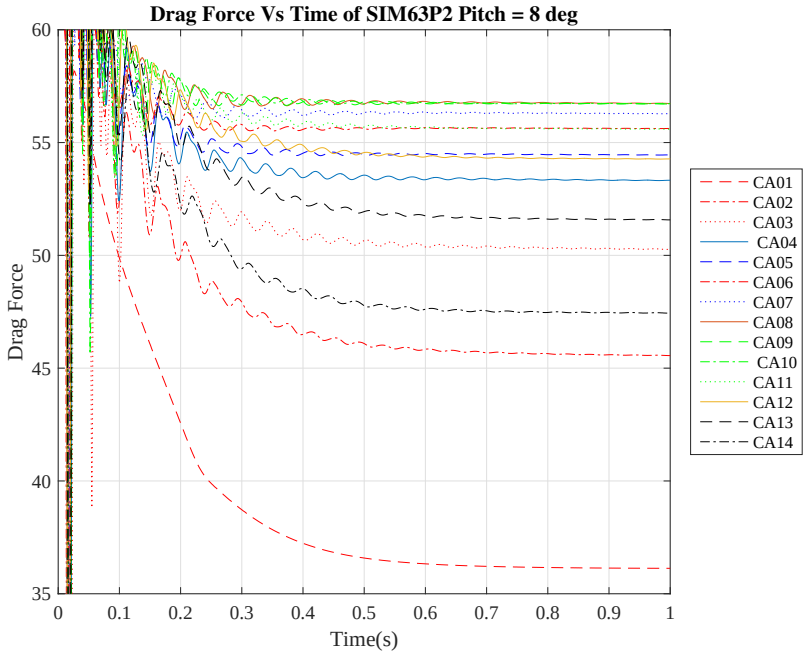

Figure A.455: Drag Force for Pitch 8 deg SIM63

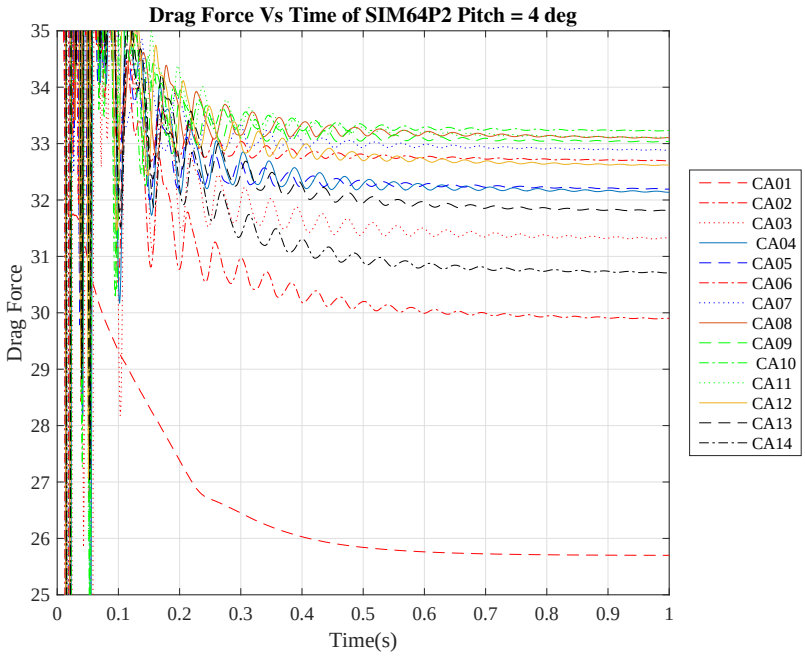

Figure A.456: Drag Force for Pitch 4 deg SIM64

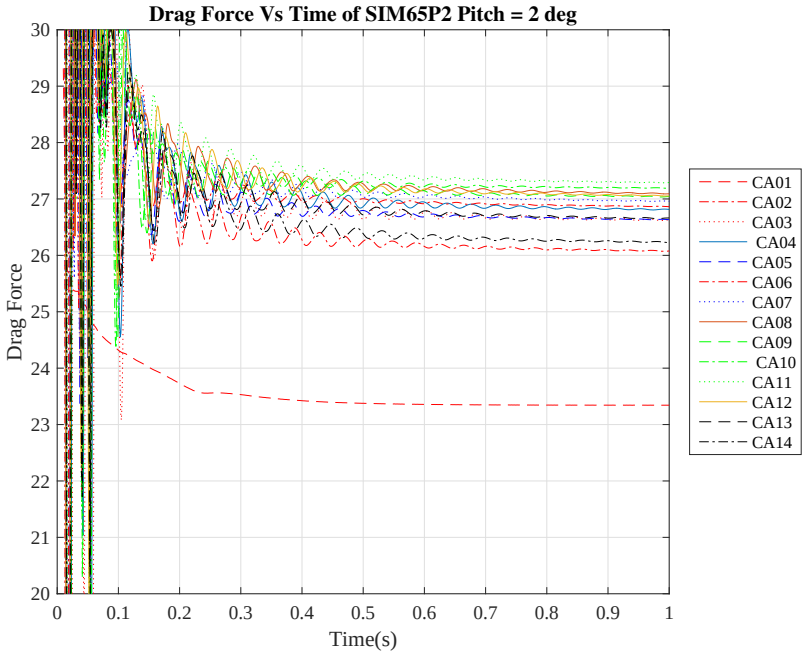

Figure A.457: Drag Force for Pitch 2 deg SIM65

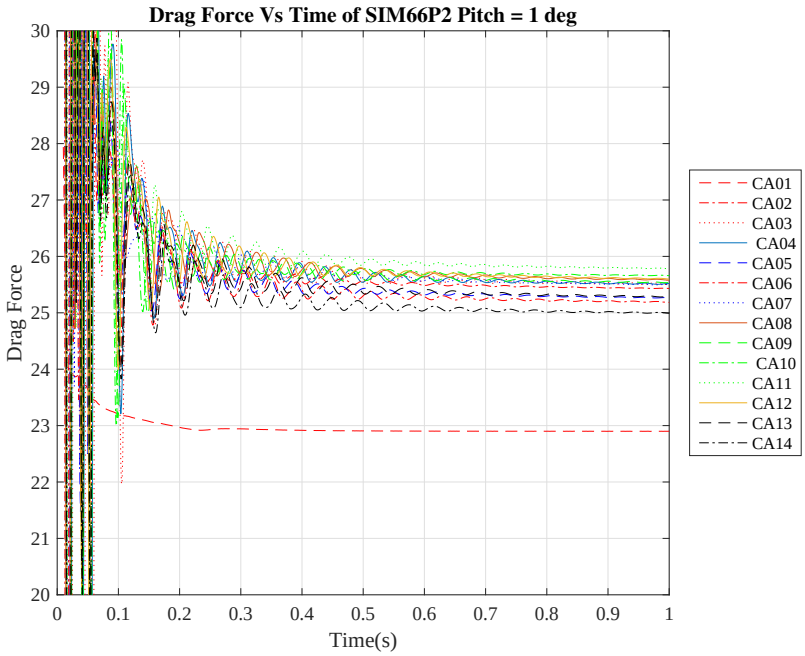

Figure A.458: Drag Force for Pitch 1 deg SIM66

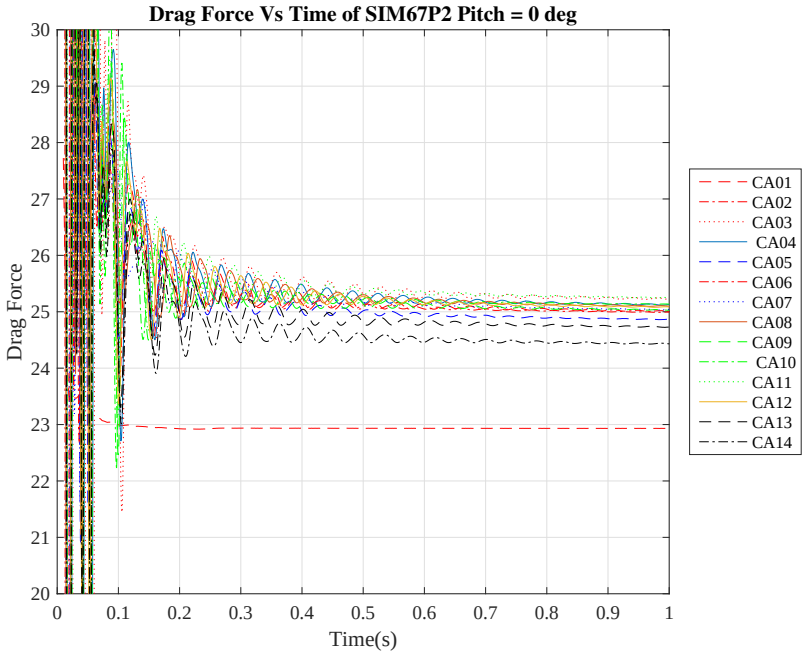

Figure A.459: Drag Force for Pitch 0 deg SIM67

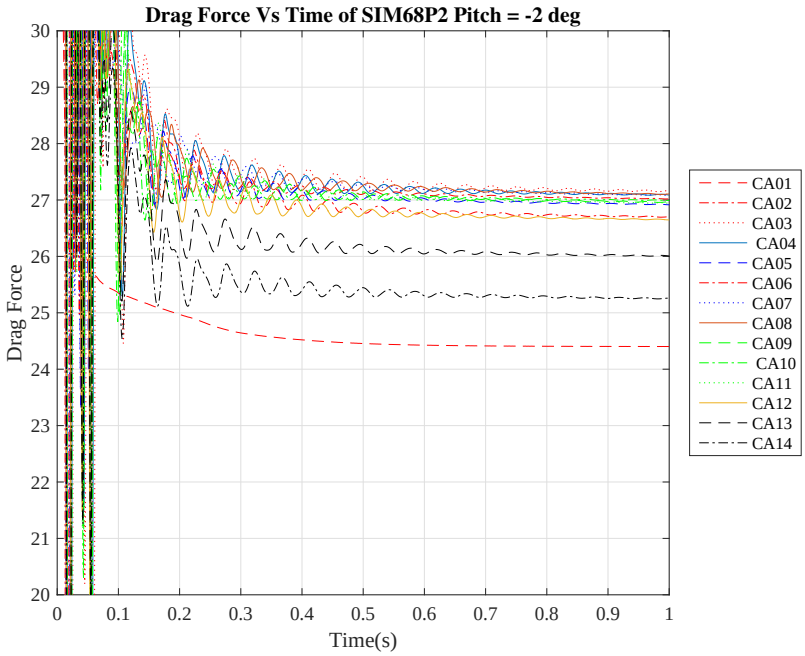

Figure A.460: Drag Force for Pitch -2 deg SIM68

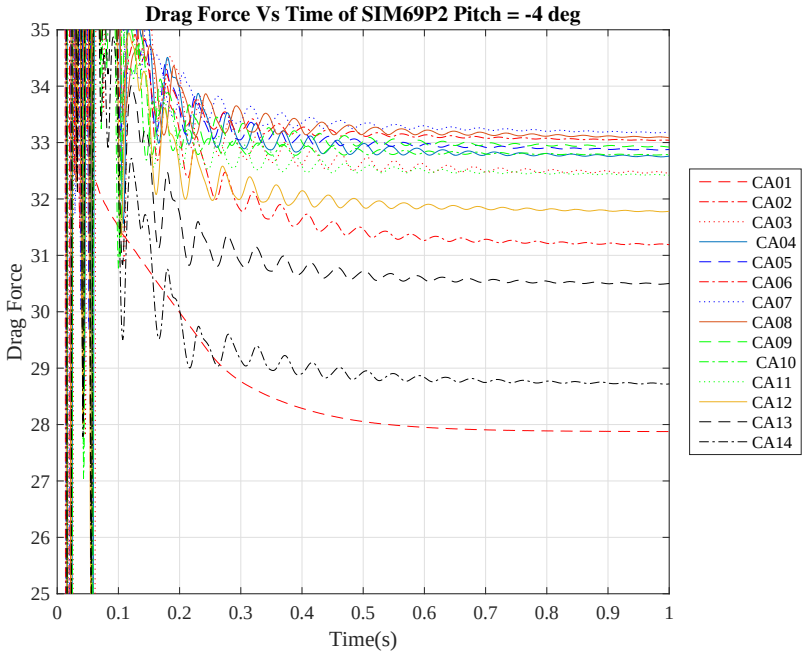

Figure A.461: Drag Force for Pitch -4 deg SIM69

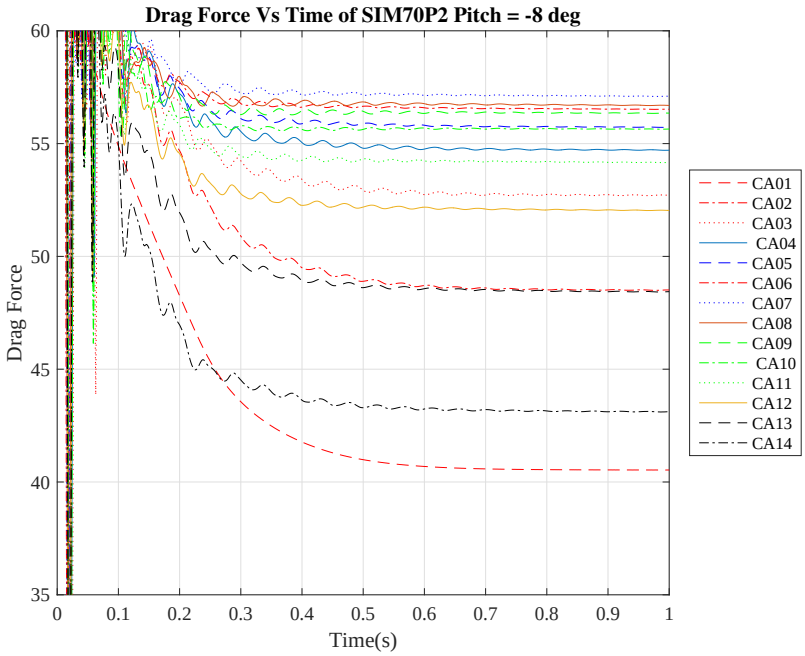

Figure A.462: Drag Force for Pitch -8 deg SIM70

A.2 Comparison

The simulation results were compared to experimental results did by Shion et. al [1]. The base case for comparison was hydrofoil shape H04 (NACA0018) with a chord length of $C = 0.125m$, with three blades $n = 3$, Solidity of $\sigma = 0.4$, pitch angle of $\beta = 0°$ and varying tip speed ratio λ. The moment comparison is given in the figure Fig. A.463. The power efficiency is compared and given in the figure Fig. A.464. It can be seen that both experimental and simulation results have the same pattern of efficiency. The predicted efficiency by 2D simulation is higher. Note that the hydrofoil shape used for the experiment by Shion et. al is different. The intention behind comparison was to find out whether results are in the same order of magnitude and whether they show a similar pattern. From the comparison it can be seen both expectations are met.

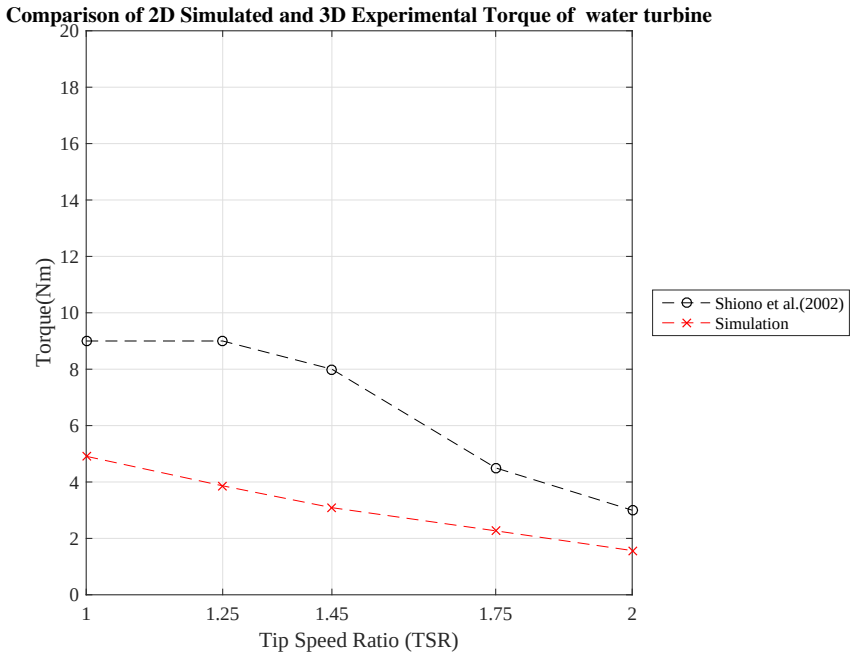

Figure A.463: Moment Comparison

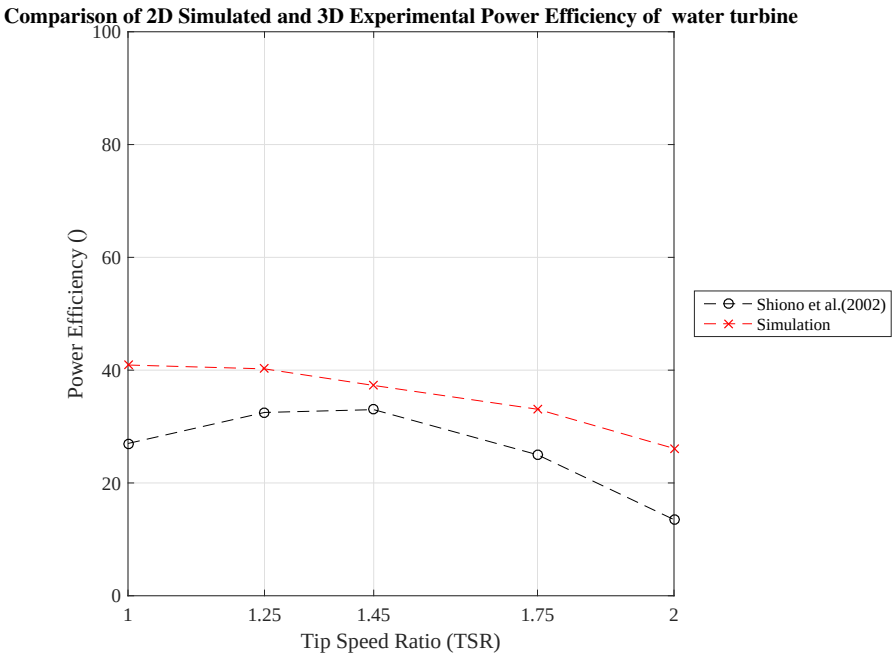

Figure A.464: Power Efficiency Comparison

A.3 Verification

In this section few of the verifications did for this research is mentioned. Figure Fig. A.465 show how the computing time and number of parallel core varies for the simulations carried out. This is for Ada super computer. The number of cores selected for research were 15. The relation between number of inner iterations and net computing time is given in figure Fig. A.466. The simulation result variation with number of inner iteration is given in figure Fig. A.467. The change in net computing time with time step is given in figure Fig. A.468 while the change in estimated lift force with time steps is given in figure Fig. A.469. The mesh selection for RTS was based on the given Table A.8. FBS stands for base size of hydrofoil mesh. CBS and SBS denotes cylindrical base size and spherical mesh base size respectively in percentage of FBS. BBS stands for the base mesh size of back ground fluid domain.

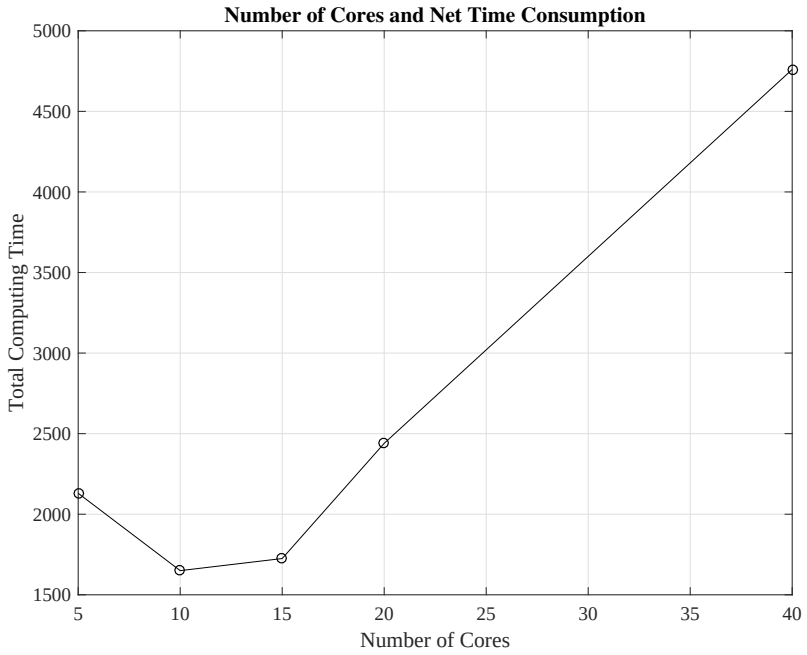

Figure A.465: Number of Cores and Net Time Consumption

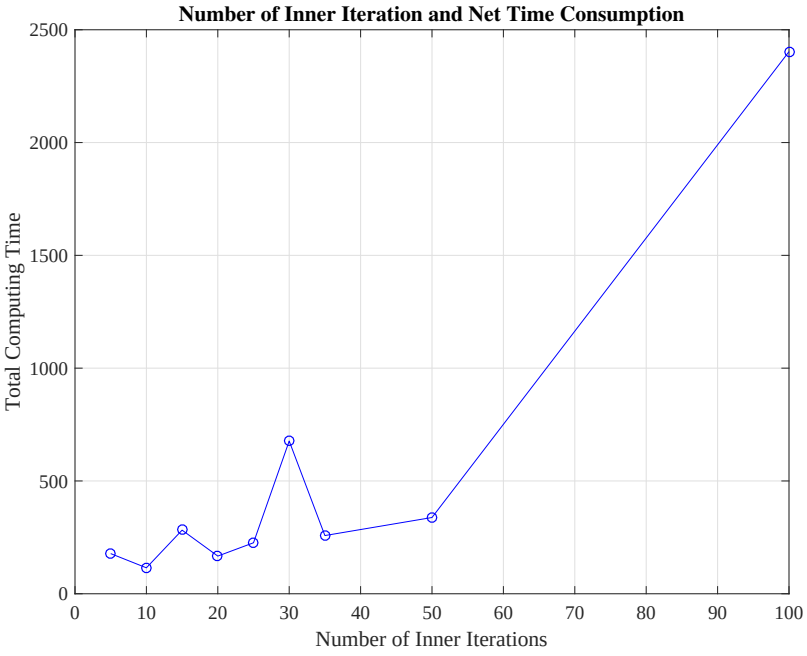

Figure A.466: Number of Inner Iteration and Net Time Consumption

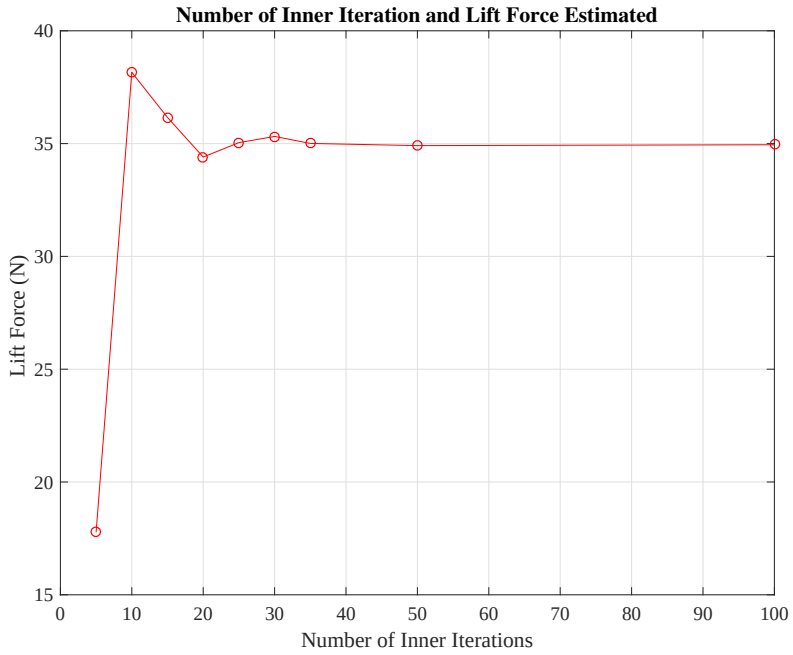

Figure A.467: Number of Inner Iterations

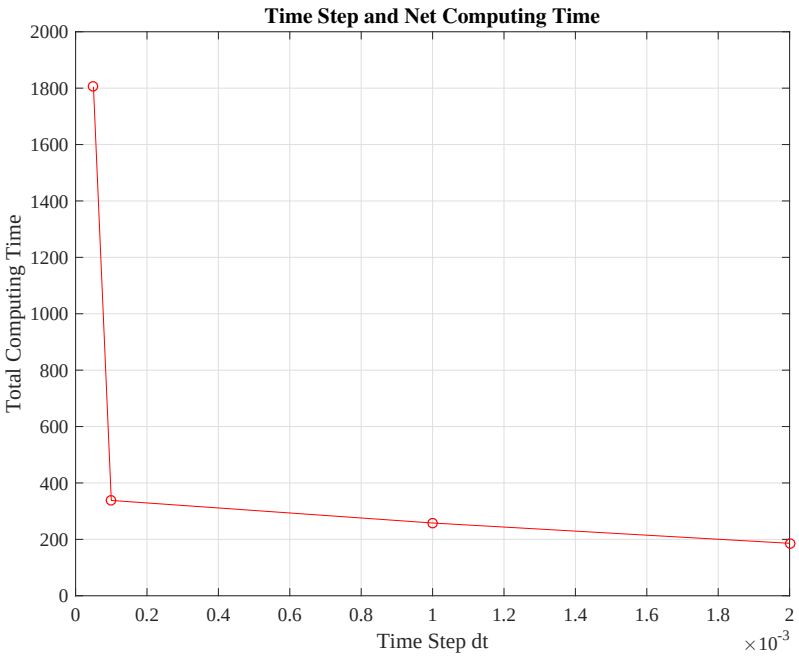

Figure A.468: Time Step and Net Computing Time

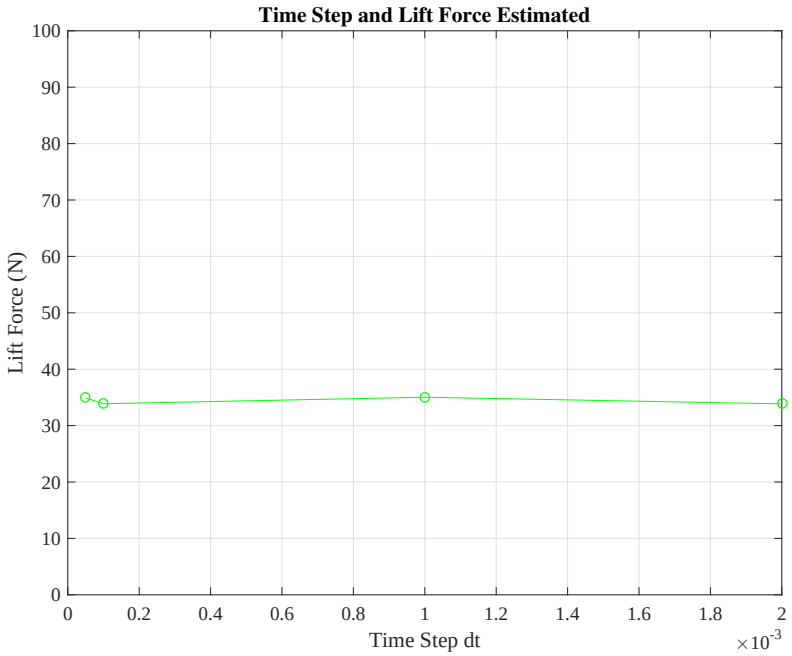

Figure A.469: Time Step and Lift Force Estimated

Table A.8: Section V Simulation Results

FBS (m)	CBS(%)	SBS (%)	BBS (m)	Moment (Nm)
0.002	20	2	0.1	171.409
0.002	20	5	0.1	174.86
0.001	20	2	0.1	181.78
0.004	20	2	0.1	178.292
0.002	20	2	0.05	171.622
0.002	20	2	30.2	170.438
0.002	20	0.1	30.2	174.093